Graz University of Technology

Dipl.-Ing. Erik Leitinger, BSc.

Cognitive Indoor Positioning and Tracking using Multipath Channel Information

Dissertation

for the degree of:

Doctor of Technical Sciences

submitted at

Graz University of Technology

Supervisor and First Examiner:

Assoc.Prof. Dipl.-Ing. Dr. Klaus Witrisal

Signal Processing and Speech Communications Laboratory
Graz University of Technology, Austria

Second Examiner:

Prof. Fredrik Tufvesson, PhD.

Department of Electrical and Information Technology
Lund University, SE

Graz, November, 2015

This work was partly supported by the Austrian Science Fund (FWF) within the National Research Network "SISE", project S10610, and by the Austrian Research Promotion Agency (FFG) within the project "REFlex", number 845630.

Abstract

This thesis presents a *robust* and *accurate* positioning system that adapts its behavior to the surrounding environment like the visual brain, mimicking its capability of filtering out clutter and focusing attention on activity and relevant information. Especially in indoor environments, which are characterized by harsh multipath propagation, it is still elusive to achieve the needed level of accuracy *robustly* under the constraint of reasonable infrastructural needs. In such environments it is essential to separate relevant from irrelevant information and attain an appropriate uncertainty model for measurements that are used for positioning.

The thesis has the goal to approach this objective more closely by implementing the four basic principles for *human cognition*, namely the *perception-action cycle (PAC)*, *memory*, *attention* and *intelligence*, into the positioning systems. To encounter all these principles, the concepts of multipath-assisted indoor navigation and tracking (MINT) are intertwined with the principles of cognitive dynamic systems (CDSs) that were developed by Simon Haykin and co-workers.

MINT exploits specular multipath components (MPCs) that can be associated to the local geometry using a known floor plan. In this way, MPCs can be seen as signals from additional virtual sources—so-called virtual anchors (VAs)—that are mirror-images of a physical anchor w.r.t. features of a floor plan. Hence additional *position-related information* is exploited that is contained in the radio signals. This position-related information is quantified based on the Cramér Rao lower bound (CRLB) of the position error for a geometry-based stochastic channel model (GSCM) to account for geometry dependent MPCs as well as for stochastically modeled diffuse/dense multipath (DM). It shows that the signal-to-interference-plus-noise-ratio (SINR) quantifies the amount of position-related information.

However, inaccuracies in the floor plan and the resulting uncertainties in the VAs, are not considered at this stage. Hence, *probabilistic MINT* is introduced in this thesis that has the aims (i) to remove the requirement of a precisely known a-priori floor plan and (ii) to cope with uncertainties in the environment representation. In probabilistic MINT the VAs are comprised in a geometry-based probabilistic environment model (GPEM). In a consecutive step, this algorithm is extended to a probabilistic multipath-assisted feature-based simultaneous localization and mapping (SLAM) approach that can operate without *any* prior knowledge of the floor plan.

The GSCM and GPEM represent the built-in *memory* of the developed cognitive positioning system. In contrast, the *attention* is executed by the algorithm itself by enabling separation between relevant and irrelevant information and focusing onto the memorized model parameters. Closing the PAC with transmit waveform adaptation based on a cognitive controller (CC) supports this separation process and also facilitates (i) the feature of gaining new position-related information from the surrounding environment and (ii) suppression of additional noise. The interplay of all these characteristics is the key facilitator of *intelligent* behavior of the cognitive positioning algorithm.

Kurzfassung

Die vorliegende Dissertation präsentiert ein *robustes* und *genaues* Lokalisierungssystem basierend auf Funksignalen, welches sich in seinem Verhalten an die jeweilige Umgebung anpasst. Wie das visuelle Gehirn, soll es zwischen relevanter Information und störenden Signalkomponenten unterscheiden und auf Aktivität fokussieren können. Speziell in Innenräumen ist funkbasierte Lokalisierung sehr herausfordernd und oft mit großen Fehlern behaftet, da die Ausbreitungscharakteristik in Räumen durch eine große Anzahl und Dichte von Mehrwegekomponenten geprägt ist. Auch wenn ein Lokalisierungssystem eine hohe Positionsgenauigkeit aufweist, ist nicht garantiert, dass es diese auch *robust* in einer großen Anzahl von Messungen erreichen kann. Daher ist es von großer Wichtigkeit, positionsrelevante Information, welche in den Mehrwegekomponenten enthalten ist, zu nutzen und von irrelevanten bzw störenden Signalkomponenten zu trennen.

Um diese Anforderungen zu erfüllen, soll in dieser Dissertation ein Lokalisierungssystem entwickelt werden, welches auf den vier Grundeigenschaften des menschlichen Gehirns: (i) der Wahrnehmungs-Handlungs-Regelung, (ii) dem Gedächtnis, (iii) der Aufmerksamkeit und (iv) der Intelligenz, basiert. Um diese Eigenschaften zu erhalten, wird das Konzept von *mehrwegekomponenten-unterstützter Lokalisierung* mit den Eigenschaften eines *kognitiven dynamischen Systems* verwoben. Die Grundlagen zu *kognitiven dynamischen Systemen* wurden von Prof. Simon Haykin und seinen Mitarbeitern ausgearbeitet.

Mehrwegekomponenten-unterstützte Lokalisierung nutzt das a-priori Wissen eines Raumplans, sodass geometrisch modellierte Mehrwegekomponenten zur Positionierung genutzt werden können. Die Signalpfade sind dabei durch sogenannte *virtuelle Quellen* modelliert, die die Spiegelbilder der Basisstation an ebenen Flächen darstellen. Die hierdurch *deterministisch* modellierten Mehrwegekomponenten beinhalten nützliche *positionsrelevante Information*, welche durch nichtauflösbare, interferierende Mehrwegekomponenten reduziert wird, die stochastisch modelliert werden. Um diese Information mathematisch formal bewerten zu können, wird aus diesem *geometrisch-stochastischen Kanalmodell* die untere Fehlerschranke für einen Positions-Schätzer hergeleitet. Es zeigt sich, dass die positionsrelevante Information direkt mit dem Signal-zu-Inteferenz-und-Rausch-Abstand der einzelnen Mehrwegekomponenten quantifiziert werden kann.

Bis dahin wird ein wichtiges Faktum noch nicht berücksichtigt: Die möglichen Ungenauigkeiten in den als bekannt angenommenen Raumplänen bzw. in den daraus abgeleiteten virtuellen Quellen. Um den Anspruch auf einen exakten Raumplan zu lockern, wurde im Zuge dieser Arbeit ein *probabilistischer* mehrwegekomponenten-unterstützte Lokalisierungsalgorithmus entwickelt, welcher die Ungenauigkeiten in den virtuellen Quellen berücksichtigt, indem er diese durch Zufallsvariablen modelliert. Das sich daraus ergebende Geometrie-Modell wurde unter dem Begriff *geometrisch-probabilistisches Umgebungsmodell* zusammengefasst. Für den Fall, dass keine a-priori Information über den Raumplan gegeben ist, kann dieser Algorithmus simultan neue virtuelle Quellen finden und auch Lokalisierung durchführen.

Das vom Algorithmus erlernte *geometrisch-stochastische Kanalmodell* und *geometrisch- probabilistische Umgebungsmodell* sind als *Gedächtnis* des daraufhin entwickelten kognitiven Lokalisierungsalgorithmus zu interpretieren, wohingegen die *Aufmerksamkeit* durch die Eigenschaft des Algorithmus, relevante von irrelevanter Information zu trennen und auf die erlernten Mo-

dellparameter zu fokussieren, gegeben ist. Dieses Verhalten wird durch die Möglichkeit von Signalparameter-Adaption unterstützt, welche auf einem kognitiven Regelsystem basiert. Dieses kognitive Regelsystem arbeitet wiederum auf Basis der geschätzten Parameter des Lokalisierungsalgorithmus. Das Zusammenspiel von all diesen Teilen, ermöglicht ein *intelligentes Verhalten* des kognitiven Lokalisierungssystems.

Acknowledgment – Danke!

First of all I want to thank Prof. Klaus Witrisal for being a great PhD advisor. I really enjoyed our discussions with which almost every time new scientific ideas were raised. Especially your ability to focus on the relevant information of a topic helped me a lot finding good ways to formulate the problems at hand. Further, I am thankful for the freedom in pursuing my research work and your faith in my work. I really hope that we continue our work together in the future.

At next I want to express my tremendous gratefulness to Paul, my coworker, office colleague and good friend. Without you I would not be where I am today. Our fruitful discussions and cooperation enhanced many aspects of my work and understanding of statistical signal processing. Also, I want to thank Josef for all our good conversations about work and any other topic. There is nothing else to say, only that you have become a good friend.

I want to thank Prof. Simon Haykin for hosting me at the Cognitive Dynamic System Laboratory at McMaster University. Another thanks goes to his PhD students, Ashkan Amiri, Mehdi Fatemi and Eduardo Santos-Diaz for providing such a pleasant working environment at McMaster. I hope we will meet again soon and work together.

I also want to thank Prof. Fredrik Tufvesson for taking the journey to Graz and being my second examiner. I hope we can keep in touch in the future.

A lot of thanks goes out to all my other colleagues and friends at SPSC: Franz, Bernhard, Katharina, Shuli, Andreas P.-E., Andreas L., Markus F., Robert, Jamilla, Christian, Stefan and all the others. I also want to thank all my long-term good friends, Florian, Stefan, Romana, Steve, Daniel, Klaus, Jan, Rudolf and all the others for their friendship, support and endless patience when I am talking about science whether the opponent is interested or not.

I want to thank my mother for her endless support and for giving me the freedom to live my life and to choose the way of education I preferred.

Most importantly, thanks to Christine for your support, love, encouragement when I am doubting myself and your endless patience with my sometimes uncompromising way of living. Also, your patience when I was talking too much about my topics helped me to organize my ideas and to get new perspectives on the matter at hand.

List of Acronyms

ACF autocorrelation function

AoA angle-of-arrival

AWGN additive white Gaussian noise

BCRLB Bayesian Cramér Rao lower bound

CC cognitive controller

CDF cumulative distribution function

CDS cognitive dynamic system

CIR channel impulse response

CP cognitive perceptor

CRLB Cramér Rao lower bound

DA data association

DFT discrete Fourier transform

DM diffuse multipath

EFIM equivalent Fisher information matrix

EKF extended Kalman filter

EM expectation maximization

FIM Fisher information matrix

GDOP geometric delusion of precision

GPEM geometry-based probabilistic environment model

GPS global positioning system

GSCM geometry-based stochastic channel model

HMM hidden Markov model

IMU inertial measurement unit

INR interference-plus-noise-ratio

KF Kalman filter

LOS line-of-sight

MAP maximum a-posteriori

MINT multipath-assisted indoor navigation and tracking

ML maximum likelihood

MPC multipath component

MSE mean square error

NLOS non-line-of-sight

PAC perception-action cycle

PCRLB posterior Cramér Rao lower bound

PDF probability density function

PDP power delay profile

PF particle filter

PEB position error bound

PMF probability mass function

PRM probabilistic reasoning machine

PSD power spectral density

PSO particle swarm optimization

RFID radio frequency identification

RFS random finite set

RL reinforcement learning

RRC root raised cosine

RLS recursive least square

RV random variable

SINR signal-to-interference-plus-noise-ratio

SIR sequential importance re-sampling

SLAM simultaneous localization and mapping

SNR signal-to-noise-ratio

SP sigma point

SVM support vector machine

TDMA time division multiple access

TDoA time-difference-of-arrival

ToA time-of-arrival

ToF time-of-flight

TR time reversal

UKF unscented Kalman filter

UT unscented transformation

UWB ultra-wideband

VA virtual anchor

ZZB Ziv-Zakai bound

Statutory Declaration

I declare that I have authored this thesis independently, that I have not used other than the declared sources/resources, and that I have explicitly indicated all material which has been quoted either literally or by content from the sources used. The text document uploaded to TUGRAZonline is identical to the present doctoral dissertation.

date	(signature)

Contents

Part I

Monographic Thesis

1 Introduction

Remark on the bibliography: This thesis contains a monographic dissertation in Part I and a collection of publications in Part II that hold many of the main contributions. The included papers are referenced in the text using labels in the form [O#], to distinguish them from conventional references to work of others.

1.1 What is this Thesis about?

The umbrella topic of this thesis is indoor positioning[1] with "almost" no infrastructural requirements. At first hand this sounds quite simple from a scientific perspective and the implications seem to be rather straightforward, but when someone is looking for the details and is asking the proper questions, the variety of scientific answers is very broad.

Roughly speaking, this thesis introduces and discusses a *positioning and tracking* system for harsh indoor environments that is *aware of its surrounding environment* and further is *able to act optimally on its environment, i.e. it controls the measurement information-return.* Such a system can be categorized as a cognitive indoor positioning system.

Let us take the human visual system as an example for the importance of cognitive aspects. It is quite clear that the visual brain and its capability to cognitively process images with context information from scenes as efficiently as possible, needs a broad range of functionalities, like

[1] The term positioning has been defined in [1] as follows: "*positioning describes the determination of the coordinates of an object in a defined coordinate system, while localization refers to the position of an object relative to topological relations. These terms are often used interchangeably in the literature, despite the fact that in most cases positioning is the more correct term".* Note that this conforms to [2]. In this thesis, coordinates of a mobile agent are estimated w.r.t. a floor plan or w.r.t. physical reference nodes with known positions, in principle allowing as in [1] for both terms.

the physiology of the human eye or the brains' ability of pattern recognition or the short and long-term memorized environment objects in the brain, etc. All of these important properties of the brain interplay together for providing the best possible image of a scene on which a following planned action, such as "switching on the light", could be based. Further, this means that also the a-priori planned actions of the brain are based on the objective to support the visualization and interpretation of objects, e.g. focusing the pupils dependent on the light conditions, i.e. adapt the eye (sensor) to its surrounding environmental state. Evidently, a perceptive system has to reason with measurements under *uncertainty* [3], i.e. it has to treat the gained information *probabilistically* [4–6], but it also has to deliberately take actions on the environment and consequently influence measurements to reason in favor of relevant information instead of irrelevant one.

These qualities should also be mapped to the design of a positioning system to facilitate the inevitable requirement of *robustness*[2]. Especially in indoor environments which are characterized by harsh multipath propagation, it is still elusive to achieve the needed level of accuracy *robustly* under the constraint of reasonable infrastructural needs. In such environments it is essential to separate relevant from irrelevant information and attain an appropriate uncertainty model for measurements that are used for positioning. Hence, cognitive processing of measurement data for positioning seems to be a natural choice to overcome such severe impairments.

The following two Sections (1.2 and 1.3) are a guideline through the scientific topics at hand. Sections 1.2 gives a literature overview about indoor positioning and introduces positioning methods that exploit multipath to overcome *robustness* issues. Section 1.3 introduces cognitive dynamic systems (CDSs) as processing units for perception, which thus provide proper system model concepts for *cognitive positioning*. "Armed" with theses techniques, we are able to state the precise research question of this thesis in Section 1.4.

1.2 Indoor Positioning

1.2.1 Conventional Indoor Positioning

Outdoors, determining ones position (i.e. the position of a mobile agent) is nowadays possible almost everywhere, whether it is for private purposes, e.g. for sightseeing, or for industrial needs, e.g. in logistics. This is enabled by technologies like the global positioning system (GPS) [2, 7] that use time-of-arrival (ToA)[3] measurements to satellites acting as so-called anchors[4] for determining the required position. The greatest challenges of such systems are regions of non-line-of-sight (NLOS) conditions, presence of strong multipath propagation and low available signal strength (as it is often the case in urban-canyons). Even, more challenging for a satellite-based positioning system is in-building positioning, since the needed level of signal-to-noise-ratio (SNR) for demodulation and decoding can not be reached. Hence, there is the necessity for

[2] We define robustness as the percentage of cases in which a system can achieve its given potential accuracy.

[3] Time-based positioning uses at least three ToA to anchors for trilateration. In general, GPS needs at least four satellites for also considering the differences in the time-basis, meaning that the time-difference-of-arrival (TDoA) measurements are utilized for multilateration.

[4] Anchors are defined as physical reference wireless nodes at precisely known positions [7].

self-contained indoor positioning systems that are able to deal with harsh multipath propagation conditions inside a building.

Promising indoor positioning candidate systems thus either use sensing technologies that provide remedies against multipath or they fuse information from multiple information sources [8–11]. A comprehensive overview about different indoor positioning methods and used technologies can be found in [1, 12]. The technologies can be categorized by the physical principles their sensors are using: (i) optical methods, e.g. time-of-flight (ToF) cameras, (ii) acoustic methods, e.g. ultra sonic measurements using ToA, (iii) inertial measurements, e.g. acceleration measurements comprised in an inertial measurement unit (IMU) for dead-reckoning and (iv) radio-based measurements, e.g. GPS using TDoA. A universal framework for theoretical analysis and interpretation of information fusion in networks is provided in [9]. In there, agents determine their positions by exploiting so-called spatial and temporal cooperation to infer information from different sources. The presented framework establishes a deep understanding of joint information evolution in navigation networks based on the Fisher information matrix (FIM) [13, 14]. In this thesis, we focus on radio-based methods, especially on methods that use ultra-wideband (UWB) signals [15–17] because of their superior time resolution facilitating the separation of multipath components (MPCs) [18]. Before continuing with positioning methods that can actively exploit these MPCs, a brief overview of "conventional" radio-based indoor positing systems is provided.

WLAN-based fingerprinting systems, based on the IEEE 802.11x standards [19], make use of existing infrastructure and exploit the position dependence of the received signal strength [20–22]. A major drawback of WLAN-based systems is the required large amount of labeled training samples needed to train the classifier model (e.q. support vector machines (SVMs)) that growths significantly with the size of the deployment area. These systems show a relatively large variance w.r.t. the position-related parameters such as the distance, even with an optimized deployment [23].

Conventional UWB signal-based positioning systems, extensively described in [24], use in the most cases ToA/TDoA based positioning. The superior time resolution of UWB signals enables inherently high-accuracy ToA ranging [25, 26] that lays the foundation for accurate positioning. The need of a large bandwidth is theoretically shown in [25] by utilizing the insight given by the Cramér Rao lower bound (CRLB) [13] and the Ziv-Zakai bound (ZZB) [27] on the ranging error variance. However, NLOS situations and harsh multipath propagation potentially lead to large ranging biases that in turn result in large position errors.

UWB fingerprinting systems apply the location fingerprinting concept to channel impulse responses (CIRs) of UWB signals. Such systems, extensively investigated in [28], are capable of highly accurate positioning in challenging indoor environments, with a performance depending on the spatial resolution of the fingerprint-cells. Thus, also a large amount of accurate measuring training data is needed. To relax the need for manually measured training data, a virtual source model is used in [29].

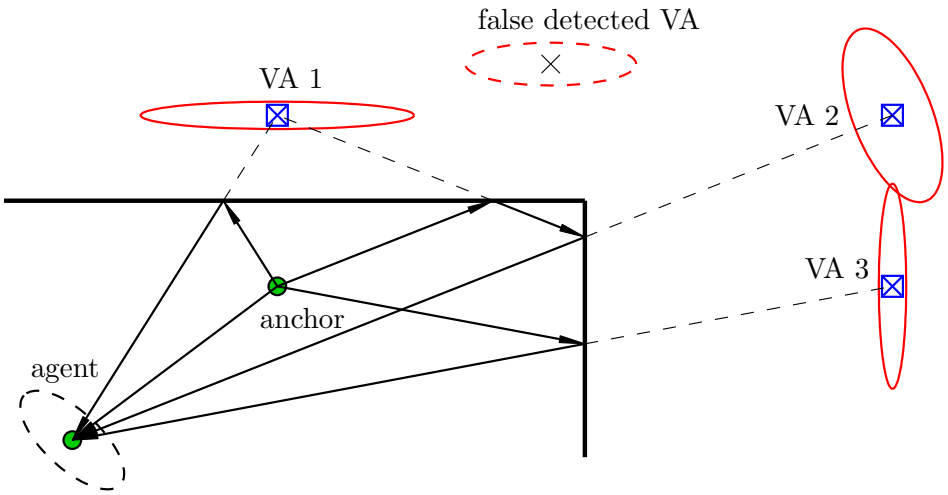

Figure 1.1: Illustration of an anchor and an agent (green dots) and a subset of virtual anchors (VAs) (blue square-crosses). Position uncertainties are represented by marginal PDFs (error ellipses in black and red). Specular MPC paths between the anchor and the agent are depicted in black.

1.2.2 Multipath-assisted Indoor Positioning – Related Work

Multipath-assisted positioning systems exploit specular MPCs (by black lines) that can be associated to the local geometry as illustrated in Fig. 1.1 [1], [O4, O6–O8]. MPCs can be seen as signals from additional virtual sources, so-called virtual anchors (VAs), that are mirror-images of a physical anchor w.r.t. the floor plan (blue square-crosses in Fig. 1.1) [1, 30, 31]. Hence, additional *position-related information* is exploited that is contained in the radio signals.

Methods that actually exploit multipath propagation require prior knowledge [32, 33]. This can be the floor plan, like in our work and related approaches (e.g. [34]), or a set of known antenna locations to enable beamforming (e.g. in imaging [35]). In an inverse problem, the room geometry can be inferred from the multipath and known measurement locations [36, 37]. In [36, 37] MPCs of acoustic sources are exploited in a similar manner as in [1] and this thesis.

This contrasts to competing approaches, which either (i) detect and avoid NLOS measurements [38], (ii) mitigate errors induced by strong multipath conditions [39], or employ more realistic statistical models for the distribution of the range estimates by introducing a ranging likelihood function [40]. Cooperation between agents is another method to increase the amount of available information [10, 41–44] and thus to reduce the position outage[5].

Insight on the position-related information that is conveyed in the signals [45] can be gained by an analysis of performance bounds, such as the CRLB[6]. Using the concept of equivalent Fisher information matrix (EFIM) [42, 46], allows for analytic evaluation of the CRLB on the position error by blockwise inversion of the FIM [47, 48].

To obtain expressions for the EFIM that yield insight on multipath-assisted positioning, a proper channel model is paramount to capture the information contained in MPCs. It is common to differentiate between resolvable MPCs which origin from specular reflections or distinct scatterers [49–52] and so-called dense multipath, which comprises all other "energy producing" components that can not be resolved by the measurement aperture [53–58]. This part of

[5] The position of an agent is said to be in outage when its position error exceeds a predefined threshold, say e.g 0.1 m.

[6] The CRLB is a lower bound of the covariance matrix of an unbiased estimator for a vector parameter.

the channel is often modeled statistically since many unresolvable components add up in this window of aperture. An established approach to describe these statistics is to use parametric models for the power delay profile (PDP) [54–56]. For the analysis presented in this thesis, propagation effects other than the geometrically modeled specular MPCs constitute interference to useful position-related information. This interference is called *diffuse multipath (DM)* [59], [O7] that also comprises the dense multipath. diffuse multipath (DM) is modeled as a colored noise process with non-stationary statistic. The overall models are often referred to as hybrid geometry-based stochastic channel models (GSCMs). Based on a GSCM the CRLB on the corresponding position error and its theoretical implications are comprehensively analyzed in [59], [O7].

For tracking and positioning applications, robustness and accuracy of multipath-assisted indoor navigation and tracking (MINT) have been reported in [1], [O3–O5]. However, neither of these works have considered uncertainties in the floor plan, including partly or entirely unknown floor plans.

1.2.3 Simultaneous Localization and Mapping (SLAM) using Multipath Channel Information

In MINT the measurement uncertainties are already properly treated based on the results of the CRLB analysis, however inaccuracies in the floor plan and the resulting uncertainties in the VAs were not considered. Hence the next step to take is to introduce the VAs as random variables (RVs) jointly with the agent position, as shown in Fig 1.1. Naturally, this leads to a simultaneous localization and mapping (SLAM) approach that has the capability to learn an unknown environment map, i.e. floor plan.

SLAM [60,61] is all about inferring an agent's pose (including the position) and the surrounding environment (represented by a map or extracted map features) using uncertain data. The uncertainty presents itself on different levels: The measurement data may come from different sensors, giving rise to different measurement variances. When these data are processed by an algorithm, the algorithm needs to take into account this heterogeneity by two type of uncertainties: (i) associating measurements to their respective origin using data association (DA) and (ii) weighting the measurements according to their respective (possibly a-priori unknown) sensor uncertainties.

In general, there are two major classes of feature-based SLAM[7] approaches, (a) vector-based feature mapping and in contrast (b) set-based feature mapping ones [62–64]. Approaches based on (a) apply DA and subsequent Bayesian filtering meaning that the uncertainties in (i) and (ii) are somehow separated from one another. Approaches based on (b) comprise both types of uncertainties in (i) and (ii) in a Bayesian approach using random finite sets (RFSs) [65, 66]. An extensive mathematical treatment of RFSs can be found in [67]. As the ordering of extracted measurement parameters and of map features as well as the DA are not explicitly defined, naturally their uncertainties should be considered also, not only the uncertainties in the sensor models. The first kind of uncertainties could lead to inconsistencies in the map features

[7] In feature-based SLAM, instead of the map itself, landmarks of the map are estimated. These landmarks can then be used to reconstruct the actual map.

that consequently result in significant agent position errors. Thus a meaningful probabilistic reasoning with its uncertainty [68] is of great importance. RFSs would be a natural choice for describing there map features.

In classical feature-based SLAM implementations, much of the *measurement origin uncertainty*[8] is alleviated by using sensors that allow for a resolution of the measurement origin. In the popular example of laser scanners, distance estimates to features are obtained that are labeled with a corresponding angle w.r.t. the pose of the agent. Independent of the physical measurement principle, this is called range-bearing sensor setup and is widely used in robotics [70, 71].

The aims of this thesis (and of the work in [O8]) are (i) to remove the requirement of a precisely known a-priori floor plan and (ii) to cope with uncertainties in the environment representation given by the VAs, as shown in Fig 1.1, in which the marginal PDFs of the VAs are illustrated by red error ellipses. To keep requirements on the agent simple, only single-antenna terminals are considered. Hence, only a single signal per anchor (nodes at known positions in the environment) is available per time step. Using an online estimated channel characterization, measurements from past estimated agent positions are fused efficiently, giving rise to probabilistic feature-based SLAM using multipath channel information. The required spatially consistent information about the environment is embedded in the MPCs and the associated VAs. The MPCs estimated from the received signals of the moving agent over time deliver the spatially consistent geometric data for tracking and for the update of the floor plan features, i.e. VA positions. An online estimation of the influence of the DM on the range uncertainties to the VAs allows for an efficient selection of the VAs that can reliably be updated and used for the agent tracking. This is a key difference to existing radio-based SLAM approaches like [72, 73]. The importance of position-related multipath information and its inherent need for DA is also the reason why the approach in [O8] is based on the more "simple" vector-based feature mapping approach instead of the set-based feature mapping approach using RFS statistic.

1.3 Cognitive Dynamic System (CDS)

As stated in Section 1.1, cognitive processing is a natural choice for positioning in harsh environments. We adopt the vision of a cognitive dynamic system (CDS) described by S. Haykin and co-workers in their seminal works as a "step toward bridging the gap between neuroscience and engineering" [74, 75]. The information processing in the visual brain, which has been extensively studied in neuroscience, gives valuable insight in the unparalleled capability of the brain of filtering out clutter and focusing attention on activity, i.e. to separate relevant from irrelevant information. In their earlier paper [76], a bat has been discussed as an example showing the efficiency of cognitive processing in nature, in a setting that closely resembles a multistatic radar. The bat adapts its emitted ultrasound pulses e.g. while approaching its bait. In doing so, it acts on the environment in an adaptive fashion. Its sonar comprises a closed PAC. *Memory* and *attention* are considered to be key facilitators of *"intelligence"*, both of which can be mapped to signal processing functionalities of a CDS [74–77]. According to [78] the four basic principles

[8] As opposed to the *inaccuracy* of the measurements themselves [69].

for *human cognition*[9], having our application in mind, are [75, 78]:

- Perception-Action Cycle: Environmental measurements, having their source in the action part and coming into the perception part of the brain, are processed to extract relevant information. This process continues from one cycle to the next.
- Multilayered Memory: Basically, there are three parts:
  - perceptual memory that holds the relevant information gained from perception
  - executive memory that builds on feedback information about the perceived environment to reason on future actions on the environment
  - working memory that reciprocally couples the perceptual and the executive memories
- Attention: Whereas either the PAC and memory occupy physical places in the brain, attention is algorithmic in nature. It is an enabler for efficient resource management in the brain and also to focus the perceptor on relevant information and the executive side on important future actions.
- Intelligence: Based on all previously mentioned principles, it represents the most powerful property in human cognition. The primary objective is optimal control of a target of interest [78].

Keeping these four principles in mind and following the philosophy of [75,79], the building blocks of a CDS describe a perception system that is directly coupled with its surrounding physical environment. Its elements are the cognitive perceptor (CP), the cognitive controller (CC) and the probabilistic reasoning machine (PRM) (described in detail in Section 2.4). From a mathematical point of view, a CDS can be interpreted as an advanced scheme for solving online probabilistic inverse problems in a *robust* and *efficient*[10] manner by also adapting the measured data to the problem at hand.

The reason why we think about using CDS concepts for indoor positioning is: To improve the *robustness* of radio-based MINT—beside its high level of *position accuracy*—in harsh multipath environments. The idea is to gain control over the observed environment information to (i) provide as much position-related information to the Bayesian state estimator as possible for achieving the highest level of reliability/robustness in position estimation, (ii) to improve the separation between relevant and irrelevant information, and (iii) building up a consistent environment and action memory.

[9] In general, there are five principles, including also language.

[10] In terms of (indoor) localization, "efficient" means highest possible position accuracy, when using limited system resources, i.e. signal bandwidth.

1.4 Research Question of this Thesis

This leads to the statement of the research question addressed in this thesis:

> Starting without any a-priori known floor plan or with an uncertain, partly unknown one, is it possible to consistently infer an agent's position and a feature map from received UWB signals by actively sensing the surrounding environment?

1.5 Organization and Contributions of this Thesis

1.5.1 Organization of this Thesis

The thesis is structured into two main parts: Part I contains the mono-graphic thesis that is mostly based on papers listed in Section 1.5.3 and Part II contains these papers.

In Part I, Chapter 2 introduces the GSCM, the GPEM and the basic concept of the cognitive positioning and tracking system that are further needed in the follow-up chapters. In Chapter 3, the CRLB on the position error is derived and analyzed for MINT. Different measurement scenarios, are analyzed to get insights on different effects of interest: (i) Multipath-Sync with known clock-offset between anchors and agents, (ii) Multipath-NSync with unknown clock-offset between anchors and agents and optionally also between the individual anchors, and (iii) Multipath-Coop with cooperation between the agents, monostatic measurements, and possibly additional fixed anchors. Chapter 4 deals with a positioning algorithm for initializing the agent position within the floor plan that is able to cope with a large number of local maxima in the likelihood function. Chapter 5 discusses tracking algorithms. Further, a joint agent and VA tracking algorithm is presented that considers the uncertainties in the VAs, while in Chapter 6 the stage for the multipath channel based SLAM algorithm is set. Finally, Chapter 7 wraps up the cognitive positioning and tracking system by closing the PAC, enabling cognitive control of the information gained by the surrounding environment.

1.5.2 Summary of Contributions of this Thesis

- The importance of a **theoretical quantification** of the **position-related channel information** and its effects on the position error bound is shown for multipath-assisted positioning. A **rigorous mathematical analysis** is conducted for different measurement scenarios, channel parameter and geometry setups, e.g. known or unknown noise statistics, VA positions as deterministic unknowns or RVs, etc. Thus, the gained insights expose the significance of "optimal" treatment of certain model parameters and give a guideline for estimating and influencing them.
- An maximum likelihood (ML) algorithm for **initial position estimation using multipath channel information** that is able to cope with the multi-modality of the likelihood function. For this a hybrid probabilistic-heuristic approach is used which combines a

sequential importance re-sampling (SIR) particle filter (PF) with the concept of particle swarm optimization (PSO), which is able to find the global maximum in the parameter space.

- A **framework of Bayesian state-space estimators** is presented that (i) use extracted multipath channel parameters and DA or (ii) the entire received signal. The former ones are based on different Kalman filter (KF) approaches with prior DA. Additionally, the position-related channel information that is needed for a proper measurement model is extracted and updated online. The latter is are based on PFs using the entire received signal.

- The Bayesian estimator framework is **extended to a probabilistic environment model**, i.e. the VAs are treated as RVs and included into the state space.

- A **new Simultaneous Localization and Mapping (SLAM) approach** is proposed that allows to learn the floor plan representation (VAs) and to deal with inaccurate information. Again a key feature is the position-related channel information that is estimated online and enables an efficient combination of the measurements as it yields a reasonable uncertainty model for the VAs. For detection and estimation of new VAs, different algorithms are presented based on recursive least square (RLS) estimation and PF.

- Finally, **closed-loop cognitive positioning and tracking** is introduced that uses multipath channel information. The algorithm actively controls the information gained from the surrounding environment using waveform parameter optimization based on the perceptor's entropy, thus the perceptor is able to optimally **separate relevant from irrelevant information** contained in the received signal.

1.5.3 Contributions of Included Papers

The contributions in the individual papers contained in Part I are:

[O1] In this paper, we propose to jointly employ a narrowband radio to interrogate radio frequency identification (RFID) transponders and an adaptive UWB backscatter radio for target tracking and for actuating, sensing, and learning the radio environment. The paper explores the system model and key processing steps of such a cognitive secondary radar.

[O2] In this paper, we derive the CRLB on the position error for an RFID tag localizaion system exploiting multipath on backscatter radio channels. The backscatter channel is modeled with a GSCM. Time reversal (TR) processing on the uplink channel is analyzed using the deterministic MPCs to overcome the degenerate nature of the backscatter channel. The CRLB shows the potential gain obtained from time reversal (TR) processing as well as its strong dependence on the geometry.

[O3] In this work, we introduce a cooperative algorithm that utilizes multipath components for localization. The algorithm uses two types of measurements: (i) bistatic measurements between agents and (ii) monostatic (bat-like) measurements by the individual agents.

[O4] In this work, we develop an ML algorithm for agent position estimation using multipath channel information. A hybrid probabilistic-heuristic approach is used which combines a SIR PF with the concept of PSO.

[O5] This paper presents an evaluation of a demonstration system for MINT. With the real-time demonstration system, performance evaluations are possible without the need to rely on pre-recorded measurement trajectories or simulated radio channels. Hence, the robustness and accuracy of MINT in different environments can be tested easily and a proof-of-concept is obtained in close-to-practical conditions.

[O6] This letter presents the improvement of a multipath-assisted tracking approach using information about the relevance of deterministic multipath components in an environment. This information is fed to a tracking filter as observation noise model. It is estimated from a few training signals between anchors and an agent at known positions.

[O7] In this article, a unified framework is presented for the quantification of GSCM based position-related multipath information, using the concept of equivalent Fisher information. We derive analytical results for the CRLB of multipath-assisted positioning, considering bistatic transmissions between agents and fixed anchors, monostatic transmissions from agents, cooperative measurements inbetween agents, and combinations thereof, including the effect of clock offsets.

[O8] In this paper, we propose a new SLAM approach that allows to learn the floor plan representation and to deal with inaccurate information. A key feature is an online estimated channel characterization that enables an efficient combination of the measurements. Starting with just the known anchor positions, the proposed method includes the VA positions also in the state space and is thus able to adapt the VA positions during agent tracking.

[O9] This paper provides an in-deph analysis of position-realated information provided by monostatic measurements. The CRLB on the position error is computed and used to analyze the impact of the indoor geometries and to find the limitations of such measurements. A general form of multipath delay gradients, crucial terms in the CRLB relating geometry and channel parameters, is derived for this purpose.

[O10] This article discusses the potential of future high-accuracy localization systems as a key component of assisted living (AL) applications. Accurate location information can be tremendously useful to realize, e.g. behavioral monitoring, fall detection, and real-time assistance. Such services are expected to provide older adults and people with disabilities with more independence and thus to reduce the cost for caretaking. The paper therefore places its focus on (i) discussing radiolocalization methods that reduce the required infrastructure by exploiting information from reflected multipath components and (ii) showing that knowledge about the propagation environment enables localization with high accuracy and robustness. It is demonstrated that new millimeter-wave (mm-wave) technology, under investigation for 5G communications systems, will be able to provide cm-accuracy indoor localization in a robust manner, ideally suited for AL.

In addition to these, the papers [80–83] were published during this thesis. Parts of the localization and tracking methods that were developed during this thesis were published as a patent

specification with the title “Method, device and system for indoor localization and tracking using ultrawideband radio signals” [84]. Furthermore, the master’s theses [85–88] were supervised, which are directly related to this PhD thesis.

List of Included Papers

[O1] K. Witrisal, E. Leitinger, P. Meissner, and D. Arnitz, "Cognitive radar for the localization of RFID transponders in dense multipath environments," in *Radar (RadarCon), 2013 IEEE International Conference on*, April 2013.

[O2] E. Leitinger, P. Meissner, M. Froehle, and K. Witrisal, "Performance bounds for multipath-assisted indoor localization on backscatter channels," in *IEEE RadarCon 2014*, 2014.

[O3] M. Froehle, E. Leitinger, P. Meissner, and K. Witrisal, "Cooperative multipath-assisted indoor navigation and tracking (co-mint) using uwb signals," in *IEEE ICC 2013 Workshop on Advances in Network Localization and Navigation (ANLN)*, 2013.

[O4] E. Leitinger, M. Fröhle, P. Meissner, and K. Witrisal, "Multipath-Assisted Maximum-Likelihood Indoor Positioning using UWB Signals," in *Communications Workshops (ICC), 2014 IEEE International Conference on*, June 2014, pp. 170–175.

[O5] P. Meissner, E. Leitinger, M. Lafer, and K. Witrisal, "Real-time demonstration of multipath-assisted indoor navigation and tracking (MINT)," in *Communications Workshops (ICC), 2014 IEEE International Conference on*, June 2014, pp. 144–149.

[O6] P. Meissner, E. Leitinger, and K. Witrisal, "UWB for robust indoor tracking: Weighting of multipath components for efficient estimation," *Wireless Communications Letters, IEEE*, vol. 3, no. 5, pp. 501–504, Oct 2014.

[O7] E. Leitinger, P. Meissner, C. Rudisser, G. Dumphart, and K. Witrisal, "Evaluation of position-related information in multipath components for indoor positioning," *Selected Areas in Communications, IEEE Journal on*, vol. 33, no. 11, pp. 2313–2328, Nov 2015.

[O8] E. Leitinger, P. Meissner, M. Lafer, and K. Witrisal, "Simultaneous localization and mapping using multipath channel information," in *Communications Workshops (ICC), 2015 IEEE International Conference on*, June 2015.

[O9] G. Dumphart, E. Leitinger, P. Meissner, and K. Witrisal, "Monostatic indoor localization: Bounds and limits," in *Communications Workshops (ICC), 2015 IEEE International Conference on*, June 2015.

[O10] K. Witrisal, P. Meissner, E. Leitinger, Y. Shen, C. Gustafson, F. Tufvesson, K. Haneda, D. Dardari, A. F. Molisch, A. Conti, and M. Z. Win, "High-accuracy localization for assisted living," *IEEE Signal Processing Magazine*, 2016.

2

Cognitive Geometry-based Stochastic Environment Model

This chapter introduces the features of the floor plan, i.e. virtual anchors (VAs) and the multipath channel model in detail. Also, the overall probabilistic model of the surrounding environment and cognitive positioning systems are defined to provide the basis for the subsequent chapters.

2.1 Geometry-based Probabilistic Environment Model (GPEM)

The basic work on multipath-assisted indoor navigation and tracking (MINT) can be found in [1], [O4, O6, O7]. In [1], a detailed mathematical description of how reflectors can be represented using virtual sources and how their positions are computed using optical ray-tracing with a-priori knowledge of a floor plan. As already stated in Section 1, MINT systems exploit specular MPCs (black lines in Fig 2.1) that can be associated to the local geometry using a known floor plan. In this way, MPCs can be seen as signals from additional virtual sources, i.e. VAs (blue square-crosses in Fig 1.1) that are mirror-images of an physical anchor w.r.t. the floor plan [1, 30, 31].

Explanation of VAs using electromagnetic field equations: An electromagnetic wave, emitted from the transmit antenna, placed in a closed room (bounded by walls), is traveling to the receive antenna, assuming far-field condition. For this setup, plane waves represent a solution for the wave equation, which uniqueness is yielded by introducing boundary conditions. In a room, these conditions are defined by the reflective properties of the walls [37]. Solving the wave equation with this boundary conditions, one gets the multipath-channel impulse response between transmitter and receiver, as described in [37] for acoustic waves. To fulfill the

boundary conditions for the electromagnetic wave on walls[11], a virtual source model for the transmitter/source can be used to describe the behavior of the wave on the wall.

2.1.1 A-Priori Known Floor Plan – Exact Virtual Anchors (VA) Positions

In this case, VA positions are computed with *exact floor plan, i.e. room geometry, knowledge.* By mirroring the j-th anchor w.r.t. walls, first-order VAs are constructed. Higher-order VAs are computed by mirroring VAs w.r.t. walls [O6] and [30, 31].

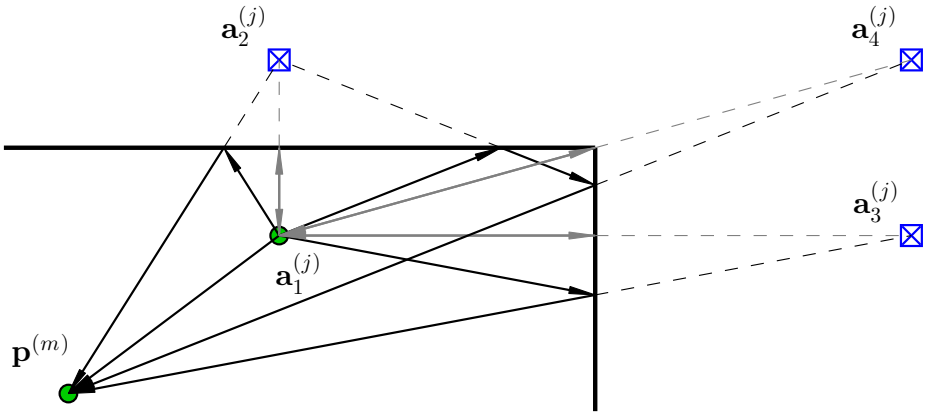

Figure 2.1: Illustration of multipath geometry using VAs for (i) bistatic transmissions (black) between an anchor at $\mathbf{a}_1^{(j)}$ and an agent at $\mathbf{p}^{(m)}$ and for (ii) a monostatic measurement (gray) by an agent at $\mathbf{a}_1^{(j)}$.

Fig. 2.1 illustrates the geometric model for multipath-assisted positioning. A signal exchanged between an anchor at position $\mathbf{a}_1^{(j)}$ and an agent at $\mathbf{p}^{(m)}$ contains specular reflections at the room walls, indicated by the black lines[12]. These reflections can be modeled geometrically using the VAs $\mathbf{a}_k^{(j)}$ with $k = 1, \ldots, K^{(j)}$ that are mirror-images of the j-th anchor w.r.t. walls [1, 30, 31]. The number of expected VAs per anchor j is defined as $K^{(j)}$. We call this the *bistatic* [13] setup, where the fixed anchors and the floor plan constitute the available infrastructure. Assuming also a *cooperative* setup, agents localize themselves using bistatic measurements inbetween them. Here, the node at $\mathbf{a}_1^{(j)}$ is an agent that plays the role of an anchor (and thus provides a set of VAs) for the agent at $\mathbf{p}^{(m)}$. If the agents are equipped accordingly, they can use *monostatic*[14] measurements, indicated in Fig. 2.1 by the gray lines. Here, the node at $\mathbf{a}_1^{(j)}$ acts as an anchor for itself with its own set of VAs. This means that the node transmits and receives the radio-signal by itself.

[11] E.g., the tangential electrical field vector has to be zero on the surface on an ideal conductor. This means that the phase of the electrical field vector has to change with 180°.
[12] Since the radio channel is reciprocal, the assignment of transmitter and receiver roles to anchors and agents is arbitrary and this choice can be made according to the application scenario.
[13] Bistatic in the sense of Radar: Transmit and the receive antenna have different locations.
[14] Monostatic in the sense of Radar: Transmit and receive antennas are co-located

2.1.2 A-Priori Known Floor Plan with uncertainties – Probabilistic VA Positions

To be able to cope with uncertainties in the floor plan the deterministic geometric model of the VA positions $\mathbf{a}_k^{(j)}$ of the j-th anchor, is extended to a probabilistic one as shown in Fig. 2.2. The VA positions and the agent position $\mathbf{p}^{(m)}$ are represented by a joint PDF $p\big(\mathbf{p}^{(m)}, \mathbf{a}_1^{(j)}, \mathbf{a}_2^{(j)}, \ldots, \mathbf{a}_{K^{(j)}}^{(j)}\big)$. If the position of the j-th anchor is assumed to be known exactly, the joint PDF reduces to $p\big(\mathbf{p}^{(m)}, \mathbf{a}_2^{(j)}, \ldots, \mathbf{a}_{K^{(j)}}^{(j)}\big)$.

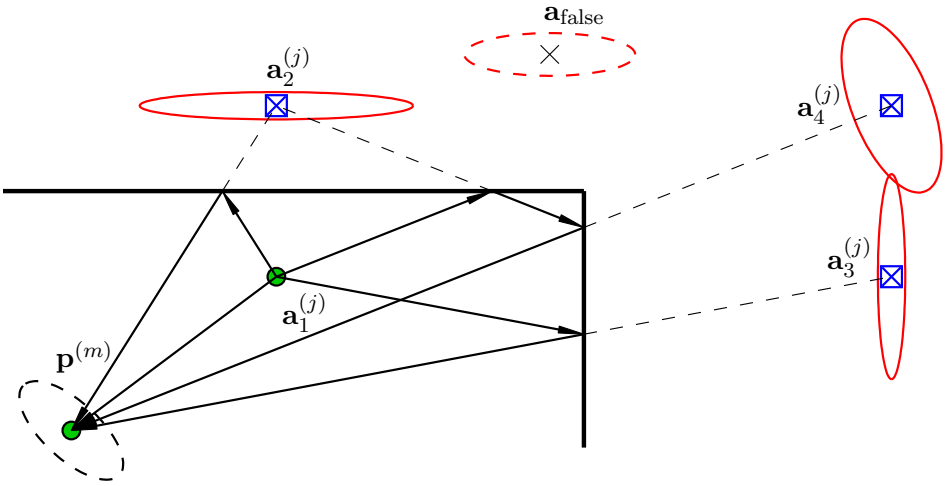

Figure 2.2: Illustration of the VAs for the j-th anchor and an agent with PDFs $p\big(\mathbf{a}_k^{(j)}\big)$ and $p\big(\mathbf{p}^{(m)}\big)$, respectively. The VA at position $\mathbf{a}_{\text{false}}$ represents a false detected VA.

Fig. 2.2 illustrates the probabilistic geometric environment model. The joint PDF of the agent and the VA positions is represented by a multivariate Gaussian RV, where the figure shows the marginal distributions of the agent $p\big(\mathbf{p}^{(m)}\big)$ (dashed black ellipses) and the VA positions $p\big(\mathbf{a}_k^{(j)}\big)$ (red ellipses). The marginal distribution $p\big(\mathbf{a}_{\text{false}}\big)$ (dashed red ellipse) defines a wrongly detected VA at position $\mathbf{a}_{\text{false}}$. The anchor position $\mathbf{a}_1^{(j)}$ is assumed to be known perfectly. Uncertainty in the floor plan does not just mean that the VA positions are uncertain and thus described by RVs, but also that floor plan information is incorrect/inconsistent or entirely missing. This means that positioning and tracking algorithms based on VAs, have to consider this lack of knowledge.

2.2 Geometry-based Stochastic Channel and Signal Model (GSCM)

In general, a *baseband* UWB signal $s(t)$ with effective pulse duration T_{p} is exchanged between the j-th anchor located at position $\mathbf{a}_1^{(j)} \in \mathbb{R}^2$ and the m-th agent at position $\mathbf{p}_n^{(m)} \in \mathbb{R}^2$ at time instance n. Note that two-dimensional position coordinates are used throughout the thesis, for the sake of simplicity. The extension to three dimensional coordinates is straightforward. The corresponding received signal is modeled as [59], [O7]

$$\begin{aligned} r_n^{(j,m)}(t) &= r_{\text{det},n}^{(j,m)}(t) + r_{\text{diff},n}^{(j,m)}(t) + w(t) \\ &= \sum_{k=1}^{K_n^{(j,m)}} \alpha_{k,n}^{(j,m)} s(t - \tau_{k,n}^{(j,m)}) + (s * \nu_n^{(j,m)})(t - \epsilon^{(j,m)}) + w(t). \end{aligned} \tag{2.1}$$

The first term $r_{\text{det},n}^{(j,m)}(t)$ describes a sum of $K_n^{(j,m)}$ deterministic MPCs with complex amplitudes $\{\alpha_{k,n}^{(j,m)}\}$[15] and delays $\{\tau_{k,n}^{(j,m)}\}$, with $k = 1 \dots K_n^{(j,m)}$. If it is needed, the channel parameter are comprised into the vectors $\boldsymbol{\alpha}_n^{(j,m)}$ and $\boldsymbol{\tau}_n^{(j,m)}$, respectively. These delays are modeled by a deterministic relation to the VAs at position $\mathbf{a}_k^{(j)} \in \mathbb{R}^2$ (see Fig 2.1), defined as $\tau_{k,n}^{(j,m)} = \frac{1}{c} d(\mathbf{a}_k^{(j)}, \mathbf{p}_n^{(m)}) + \epsilon^{(j,m)} = \frac{1}{c} \|\mathbf{p}_n^{(m)} - \mathbf{a}_k^{(j)}\| + \epsilon^{(j,m)} = \frac{1}{c} d_{k,n}^{(j,m)} + \epsilon^{(j,m)}$, where c is the speed of light and $\epsilon^{(j,m)}$ represents the clock-offset due to clock asynchronism between the j-th anchor and the m-th agent. The delay $\tau_{1,n}^{(j,m)}$ defines the direct line-of-sight (LOS) delay between the anchor and the agent. The number of MPCs $K_n^{(j,m)}$ is equivalent to the number of visible VAs at the agent position $\mathbf{p}_n^{(m)}$ [1]. The energy of signal $s(t)$ is assumed to be normalized to one.

The second term $r_{\text{diff},n}^{(j,m)}(t)$ denotes the convolution of the transmitted signal $s(t)$ with the DM $\nu_n^{(j,m)}(t)$, which is modeled as a zero-mean Gaussian random process. For DM we assume uncorrelated scattering along the delay axis τ, hence the autocorrelation function (ACF) of $\nu_n^{(j,m)}(t)$ is given by

$$K_{\nu,n}^{(j,m)}(\tau, u) = \mathbb{E}_\nu \left\{ \nu_n^{(j,m)}(\tau) \Big(\nu_n^{(j,m)}(u) \Big)^* \right\} = S_{\nu,n}^{(j,m)}(\tau) \delta(\tau - u), \tag{2.2}$$

where $S_{\nu,n}^{(j,m)}(\tau)$ is the PDP of DM at the agent position $\mathbf{p}_n^{(m)}$. The DM process is assumed to be quasi-stationary in the spatial domain, which means that $S_{\nu,n}^{(j,m)}(\tau)$ does not change in the vicinity of position $\mathbf{p}_n^{(m)}$ [89–91]. The last term, $w(t)$ denotes an additive white Gaussian noise (AWGN) process with double-sided power spectral density (PSD) of $N_0/2$.

The correlation function of both noise terms $w(t) + r_{\text{diff}}(t)$ is given by

$$\begin{aligned} \mathrm{K}_{\mathrm{n},n}^{(j,m)}(t, u) &= K_{\mathrm{w}}(t, u) + \mathrm{K}_{\mathrm{c},n}^{(j,m)}(t, u) = \mathbb{E}_w \left\{ w(t) \big(w(u) \big)^* \right\} + \mathbb{E}_\nu \left\{ r_{\text{diff},n}^{(j,m)}(t) \Big(r_{\text{diff},n}^{(j,m)}(u) \Big)^* \right\} \\ &= N_0 \delta(t - u) + \int_{-\infty}^{\infty} S_{\nu,n}^{(j,m)}(\tau) s(t - \tau) s(u - \tau) d\tau, \end{aligned} \tag{2.3}$$

where the second term, related to $r_{\text{diff}}(t)$, describes the non-stationary behavior of the noise process in the delay domain. Note that the statistic of $r_{\text{diff}}(t)$ is non-stationary in the delay domain and it is colored due to the convolution with $s(t)$. The PDP $S_{\nu,n}^{(j,m)}(\tau)$ in $\mathrm{K}_{\mathrm{n},n}^{(j,m)}(t, u)$ is crucial to represent the power ratio between useful deterministic MPCs and DM (along the delay axis τ). The PDP can be represented by an arbitrary function [55,56] or by an parametric PDP function [54]. Both are estimated from an ensemble of measurements taken in the vicinity of the agent position.

In the following Sections, the time index n, the anchor j and the agent index m are just used if necessary. For example, if there is one agent only, the index m need not to be used. We will also drop the clock-offset $\epsilon^{(j,m)}$ and re-introduce it in Section 3.5.2, where the synchronization aspects between the agent and anchors are studied.

[15] We assume a non-coherent channel model, otherwise the complex amplitudes split up into $\alpha_k = a_k \mathrm{e}^{-2\pi f_c \tau_k}$, where a_k is the complex reflection coefficient of the k-th VA and f_c is the carrier frequency.

2.2.1 MPC Signal Parameter Estimation

The MPC arrival time estimation at agent position $\mathbf{p}_n$ is realized as an iterative least-squares approximation of the received signal [O6]. The arrival times of the k-th MPC is obtained from

$$\hat{\tau}_{k,n}^{(j)} = \arg\min_{\tau} \int_0^T \left| r_n^{(j)}(t) - \hat{r}_{n,k-1}^{(j)}(t) - \hat{\alpha}(\tau) s(t-\tau) \right|^2 dt \tag{2.4}$$

using a template signal for all MPCs up to the $(k-1)$-th defined as $\hat{r}_{n,k-1}^{(j)}(t) = \sum_{k'=1}^{k-1} \hat{\alpha}_{k',n}^{(j)} s(t - \hat{\tau}_{k',n}^{(j)})$. The complex path amplitudes are nuisance parameters, estimated using a projection of $\left(r_n^{(j)}(t) - \hat{r}_{n,k-1}^{(j)}(t) \right)$ onto a unit energy pulse $s(t)$ as

$$\hat{\alpha}(\tau) = \int_0^T \left[r_n^{(j)}(t) - \hat{r}_{n,k-1}^{(j)}(t) \right]^* s(t-\tau) dt; \quad \hat{\alpha}_{k,n}^{(j)} = \hat{\alpha}(\hat{\tau}_{k,n}^{(j)}). \tag{2.5}$$

The number of estimated MPCs $\hat{K}_n^{(j)}$ should be chosen according to the number of expected specular paths in an environment. With the assumptions of separable MPCs and white noise, (2.4) and (2.5) correspond to a maximum-likelihood (ML) estimation of the deterministic MPCs. The estimated MPC delays/distances are collected in the finite set

$$\mathcal{Z}_n = \bigcup_j \mathcal{Z}_n^{(j)} = \bigcup_j \{\hat{d}_{k,n}^{(j)}\}_{k=1}^{\hat{K}_n^{(j)}},$$

where $\hat{d}_{k,n}^{(j)} = c\hat{\tau}_{k,n}^{(j)}$, and the according complex amplitudes in the finite set

$$\Gamma_n = \bigcup_j \Gamma_n^{(j)} = \bigcup_j \{\hat{\alpha}_{k,n}^{(j)}\}_{k=1}^{\hat{K}_n^{(j)}}.$$

In addition, after convergence to $\hat{K}_n^{(j)}$, a DM process realization $r_{\text{diff},n}^{(j)}(t) \approx r_n^{(j)}(t) - \hat{r}_{n,\hat{K}_n^{(j)}}^{(j)}(t)$ can be derived. With a set of measurements in the vicinity of the agent position, the DM PDP can be estimated from the according set of DM process realizations by

$$\hat{S}_{\nu,n}^{(j)}(\tau) \approx \text{var}\left\{ r_{\text{diff},n}^{(j)}(t) \right\}, \tag{2.6}$$

where the samples of DM realizations $r_{\text{diff},n}^{(j)}(t)$ have to be whitened by the spectrum of the transmit pulse $s(t)$. An iterative expectation maximization (EM) approach is described in Section 4.1.1 for estimating the deterministic channel parameters and the noise parameters.

2.2.2 A First Glance on the Multipath Channel Information

As a first step, we will assume in Section 3 that the DM statistic is known a-priori to be able to analyze the influence of DM on the CRLB in closed form, with no parametric restriction on the DM PDP $S_{\nu,n}^{(j)}(\tau)$. With this, our results will show that information coming from MPCs is

quantified by an SINR

$$\mathrm{SINR}_{k,n}^{(j)} := \frac{\left|\alpha_{k,n}^{(j)}\right|^2}{N_0 + T_\mathrm{p} S_{\nu,n}^{(j)}(\tau_{k,n}^{(j)})}, \tag{2.7}$$

which represents the power ratio between useful deterministic MPC and impairing DM plus measurement noise. The derivation of the SINRs can be found in Section 3.3.2. In this case the SINRs are computed via 2.7 or 3.18, the "simple" iterative least-squares approximation of the received signal is the inappropriate choice, since the DM process is not considered in the estimator. As the path amplitudes are computed using the projection integral (2.5), they partly are composted of deterministic, diffuse and AWGN, $\hat{\alpha}_{k,n}^{(j)} = \alpha_{k,n}^{(j)} + \nu_{k,n}^{(j)} + w_{k,n}$. However, the method-of-moments estimator described in [45] and Section 5.1.3 is used to directly compute the SINRs using the complex amplitudes $\hat{\alpha}_{k,n}^{(j)}$ in (2.5), instead of explicitly estimating the deterministic amplitudes and noise parameters as they would be needed in (2.7).

2.3 Probabilistic Geometric Position Model

To gain deeper insights into probabilistic description of the GSCM and the GPEM, we formulate the joint posterior PDF of agent position and the VA positions, assuming that all model parameters are RVs. By a step by step reduction of the probabilistic parameter model to a model with deterministic unknown parameters, provides the PDFs on which the algorithm of the following Sections 4, 5, 6 and 7 are based on.

The finite set of expected VAs at time instance n is defined as $\mathcal{A}_n^{(j)} = \left\{\mathbf{a}_{k,n}^{(j)}\right\}_{k=1}^{K_n^{(j)}}$. The posterior PDF of agent position $\mathbf{p}_n$ and the VA positions $\mathbf{a}_{k,n}^{(j)}$ (with perfect knowledge of the anchor positions), conditioned on the set of received signals $r_{1:n}^{(j)}(t) = [r_1^{(j)}(t), \ldots, r_n^{(j)}(t)]$, is defined as

$$\begin{aligned}
p\big(\mathbf{p}_n, &\mathbf{a}_{1,n}^{(j)}, \ldots, \mathbf{a}_{K_n^{(j)},n}^{(j)} \big| r_{1:n}^{(j)}(t)\big) = p\big(\mathbf{p}_n, \mathcal{A}_n^{(j)} | r_{1:n}^{(j)}(t)\big) \qquad (2.8)\\
&= \int_{\boldsymbol{\alpha}^{(j)}, \boldsymbol{\tau}^{(j)}} p\big(\mathbf{p}_n, \mathcal{A}_n^{(j)} | r_{1:n}^{(j)}(t), \boldsymbol{\alpha}^{(j)}, \boldsymbol{\tau}^{(j)}\big) p(\boldsymbol{\alpha}^{(j)}, \boldsymbol{\tau}^{(j)}) \mathrm{d}\boldsymbol{\alpha}^{(j)} \mathrm{d}\boldsymbol{\tau}^{(j)}\\
&\vdots \quad \rightarrow \text{Bayesian Rule}\\
&= \int_{\boldsymbol{\alpha}^{(j)}, \boldsymbol{\tau}^{(j)}} p\big(r_{1:n}^{(j)}(t), \boldsymbol{\alpha}^{(j)}, \boldsymbol{\tau}^{(j)} | \mathbf{p}_n, \mathcal{A}_n^{(j)}\big) p\big(\mathbf{p}_n, \mathcal{A}_n^{(j)}\big) \mathrm{d}\boldsymbol{\alpha}^{(j)} \mathrm{d}\boldsymbol{\tau}^{(j)}\\
&\vdots \quad \rightarrow \text{Chain Rule}\\
&= \int_{\boldsymbol{\alpha}^{(j)}, \boldsymbol{\tau}^{(j)}} p\big(r_{1:n}^{(j)}(t) | \boldsymbol{\alpha}^{(j)}, \boldsymbol{\tau}^{(j)}, \mathbf{p}_n, \mathcal{A}_n^{(j)}\big) p\big(\boldsymbol{\alpha}^{(j)}, \boldsymbol{\tau}^{(j)} \big| \mathbf{p}_n, \mathcal{A}_n^{(j)}\big) p\big(\mathbf{p}_n, \mathcal{A}_n^{(j)}\big) \mathrm{d}\boldsymbol{\alpha}^{(j)} \mathrm{d}\boldsymbol{\tau}^{(j)}\\
&= \int_{\boldsymbol{\alpha}^{(j)}, \boldsymbol{\tau}^{(j)}} p\big(r_{1:n}^{(j)}(t) | \boldsymbol{\alpha}^{(j)}, \boldsymbol{\tau}^{(j)}, \cancel{\mathbf{p}_n}, \cancel{\mathcal{A}_n^{(j)}}\big) p\big(\boldsymbol{\alpha}^{(j)}, \boldsymbol{\tau}^{(j)} | \mathbf{p}_n, \mathcal{A}_n^{(j)}\big) p\big(\mathbf{p}_n, \mathcal{A}_n^{(j)}\big) \mathrm{d}\boldsymbol{\alpha}^{(j)} \mathrm{d}\boldsymbol{\tau}^{(j)}
\end{aligned}$$

$$= \int\limits_{\boldsymbol{\alpha}^{(j)},\boldsymbol{\tau}^{(j)}} p\big(r_{1:n}^{(j)}(t)|\boldsymbol{\alpha}^{(j)},\boldsymbol{\tau}^{(j)}\big)p\big(\boldsymbol{\alpha}^{(j)}|\boldsymbol{\tau}^{(j)}\big)p\big(\boldsymbol{\tau}^{(j)}\big|\mathbf{p}_n,\mathcal{A}_n^{(j)}\big)p\big(\mathbf{p}_n,\mathcal{A}_n^{(j)}\big)\mathrm{d}\boldsymbol{\alpha}^{(j)}\mathrm{d}\boldsymbol{\tau}^{(j)},$$

where $p(x,y|z,w)$ describes the joint PDF of the RVs x and y conditioned on the RVs z and w. If we assume that the channel parameter vectors $\boldsymbol{\alpha}_n^{(j,m)}$ and $\boldsymbol{\tau}_n^{(j,m)}$ are deterministic unknowns, Eq. (2.8) reduces to

$$\begin{aligned} p\big(\mathbf{p}_n,\mathcal{A}_n^{(j)}|r_{1:n}^{(j)}(t)\big) &= p\big(r_{1:n}^{(j)}(t)|\boldsymbol{\alpha}^{(j)},\boldsymbol{\tau}^{(j)}\big)p\big(\boldsymbol{\alpha}^{(j)}|\boldsymbol{\tau}^{(j)}\big)p\big(\boldsymbol{\tau}^{(j)}\big|\mathbf{p}_n,\mathcal{A}_n^{(j)}\big)p\big(\mathbf{p}_n,\mathcal{A}_n^{(j)}\big) \\ &= p\big(r_{1:n}^{(j)}(t)|\mathbf{p}_n,\mathcal{A}_n^{(j)};\boldsymbol{\alpha}^{(j)};\boldsymbol{\tau}^{(j)}\big)p\big(\mathbf{p}_n,\mathcal{A}_n^{(j)}\big), \end{aligned} \tag{2.9}$$

where $p(x|z;w)$ describes the PDF of the RV x conditioned on the RV z and on the deterministic unknown parameter w. The evaluation of the likelihood function $p\big(r_{1:n}^{(j)}(t)|\boldsymbol{\alpha}^{(j)},\boldsymbol{\tau}^{(j)}\big)$ can be interpreted as a position and geometry dependent channel estimation with uncertainty in both, the agent position $\mathbf{p}_n$ and the VA positions $\mathcal{A}_n^{(j)} = \big\{\mathbf{a}_{k,n}^{(j)}\big\}_{k=1}^{K_n^{(j)}}$. The intermediate formulation (2.9) is mathematically not quite correct, since $\boldsymbol{\tau}^{(j)}$ and $\boldsymbol{\alpha}^{(j)}$ are no RVs anymore. This is because $p\big(\boldsymbol{\tau}^{(j)}\big|\mathbf{p}_n,\mathcal{A}_n^{(j)}\big)$ and $p\big(\boldsymbol{\alpha}^{(j)}|\boldsymbol{\tau}^{(j)}\big)$ describe a deterministic relation between realizations of the RVs $\mathbf{p}_n$ and $\mathcal{A}_n^{(j)}$ and deterministic channel parameters $\boldsymbol{\tau}^{(j)}$ and $\boldsymbol{\alpha}^{(j)}$. Nevertheless, (2.9) and the following equations (2.10) and (2.11) are very informative, concerning the uncertainty in the agent, anchor and VA positions.

2.3.1 Computation of the Agent Position Probability Density Function (PDF)

Floor Plan with uncertainty (see for Fig. 2.2): The marginal posterior PDF of the agent position $\mathbf{p}_n$ is computed by marginalizing out the uncertainty of the VAs of the j-th anchor

$$\begin{aligned} p\big(\mathbf{p}_n|r_{1:n}^{(j)}(t)\big) &= \int\limits_{\mathbf{a}_1^{(j)}} \cdots \int\limits_{\mathbf{a}_{K_n^{(j)},n}^{(j)}} p\big(r_{1:n}^{(j)}(t)|\boldsymbol{\alpha}^{(j)},\boldsymbol{\tau}^{(j)}\big) \\ &\qquad \times p\big(\boldsymbol{\alpha}^{(j)}|\boldsymbol{\tau}^{(j)}\big)p\big(\boldsymbol{\tau}^{(j)}|\mathbf{p}_n,\mathcal{A}_n^{(j)}\big)p\big(\mathbf{p}_n,\mathcal{A}_n^{(j)}\big)\mathrm{d}\mathbf{a}_{1,n}^{(j)}\cdots\mathrm{d}\mathbf{a}_{K_n^{(j)},n}^{(j)} \\ &= \int\limits_{\mathbf{a}_1^{(j)}} \cdots \int\limits_{\mathbf{a}_{K_n^{(j)},n}^{(j)}} p\big(r_{1:n}^{(j)}(t)|\mathbf{p}_n,\mathcal{A}_n^{(j)};\boldsymbol{\alpha}^{(j)};\boldsymbol{\tau}^{(j)}\big)p\big(\mathbf{p}_n,\mathcal{A}_n^{(j)}\big)\mathrm{d}\mathbf{a}_{1,n}^{(j)}\cdots\mathrm{d}\mathbf{a}_{K_n^{(j)},n}^{(j)}. \end{aligned} \tag{2.10}$$

Equation (2.10) shows the general case, with uncertainty in the j-th anchor position $\mathbf{a}_1^{(j)}$.

Perfect Floor Plan Knowledge (see for Fig. 2.1): In this case, when assuming deterministic unknown channel parameters, these parameters and further the agent position $\mathbf{p}_n$ are estimated by using the VA positions directly. The marginal posterior PDF of the agent position is then given by

$$\begin{aligned} p\big(\mathbf{p}_n|r_{1:n}^{(j)}(t)\big) &= p\big(r_{1:n}^{(j)}(t)|\boldsymbol{\alpha}^{(j)},\boldsymbol{\tau}^{(j)}\big)p\big(\boldsymbol{\alpha}^{(j)},\boldsymbol{\tau}^{(j)}|\mathbf{p}_n;\mathcal{A}_n^{(j)}\big)p\big(\mathbf{p}_n\big) \\ &= p\big(r_{1:n}^{(j)}(t)|\mathbf{p}_n;\boldsymbol{\alpha}^{(j)};\boldsymbol{\tau}^{(j)};\mathcal{A}_n^{(j)}\big)p(\mathbf{p}_n), \end{aligned} \tag{2.11}$$

where the likelihood function $p\big(r_{1:n}^{(j)}(t)|\mathbf{p}_n;\boldsymbol{\alpha}^{(j)};\boldsymbol{\tau}^{(j)};\mathcal{A}_n^{(j)}\big)$ dependents probabilistically on the

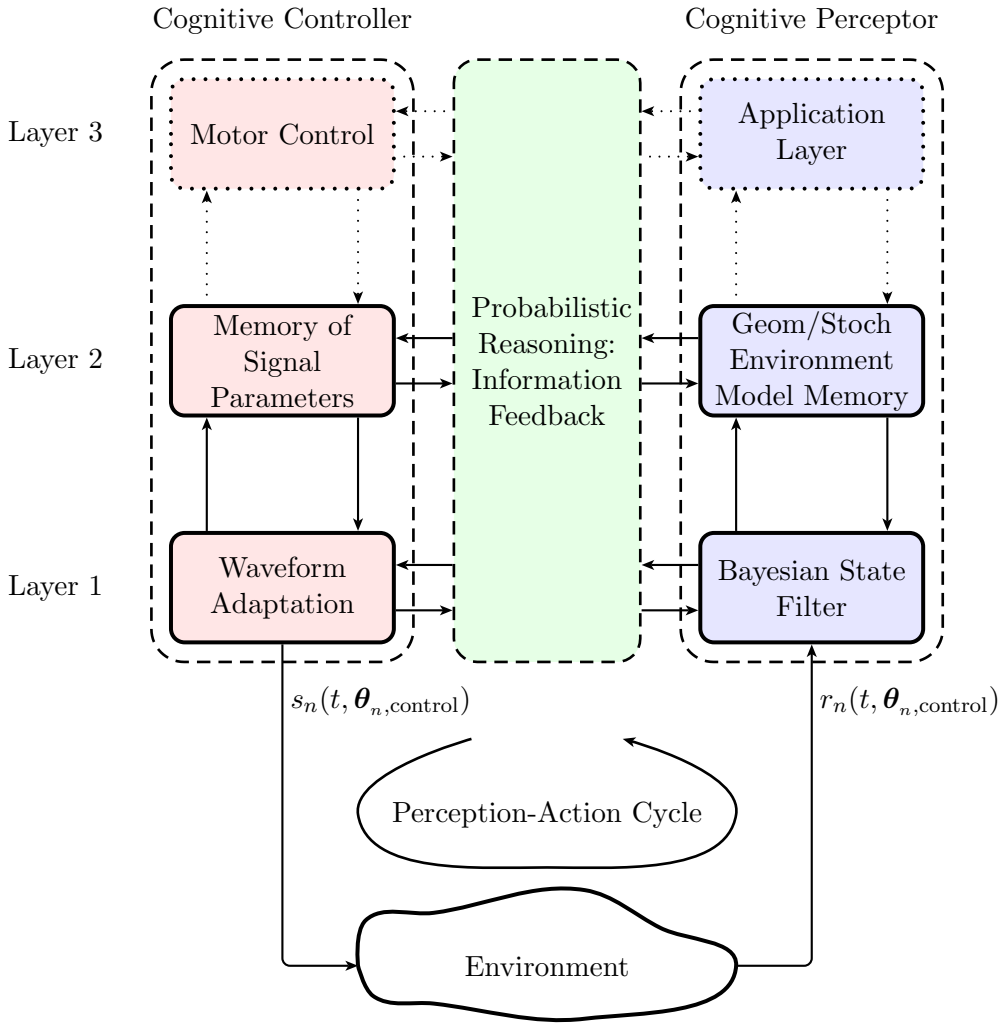

Figure 2.3: Block diagram of Cognitive Dynamic System (CDS) for indoor positioning and tracking.

agent position PDF and deterministically on the VA positions and the channel parameters.

2.4 Cognitive Positioning and Tracking System

The basic building blocks of a CDS as introduced in Section 1.3 are depicted on Fig. 2.3 and described as follows:

- *Cognitive perceptor (CP)*: Has the purpose to focus the attention on extracting and separating relevant information and irrelevant information from the received signal. Irrelevant information is coupled with uncertainty and is therefore used as probabilistic weighting for relevant information to increase the robustness of a Bayesian state estimator. Further, a higher-level environment model is learned and memorized.

- *Probabilistic reasoning machine (PRM) and information feedback*: Mediates the information flow between the cognitive perceptor and the controller. The feedback information is described by an *information-theoretic measure* of the probabilistic state of the CP.

- *Cognitive controller (CC)*: Has the purpose to act on the environment based on the feedback information of the CP and to memorize past actions and to enable predictive planning.
- *Perception-action cycle (PAC)*: Incorporates the sensed environment into the closed loop with the CP and the CC. This means that every action on the environment directly influences the CP in the next sensing period.
- *Reciprocal Coupling:* As shown in Figure 2.3, the left and the right parts of the CDS are reciprocally coupled via the PRM so that a persistent information flow between both sides is guaranteed. This means that the feedback information of the CP is driving the cognitive actions, but also the CC is interacting with the CP via the PRM to guarantee consistency in the chosen cognitive actions by using the perceptive memory.
- *Hierarchical Structure:* Enables the ability to interpret the environmental observables on different abstraction layers. The level of abstraction is increased as we go up from layer to layer, so that the characteristic probabilistic essence of the observables is partitioned over the CDS and the *robustness* of the state estimation can be controlled. The layers of the CP are interacting with one another to continuously adapt the memory of past environment experiences to the changes in the environment in a joint manner. In the same manner also the CC has to have this hierarchical structure to actively sense the environment for every aspect of abstraction in an optimal way.

2.4.1 Multipath-assisted Positioning as CDS

Figure 2.3 illustrates the block diagram of a cognitive localization and tracking system with a triple layered structure:

- *First Layer*: Defines (i) the direct Bayesian state estimation $p\big(\mathbf{x}_n\big|r_{1:n}^{(j)}(t)\big)$ at the CP, where $\mathbf{x}_n = [\mathbf{p}_n^{\mathrm{T}}, \mathbf{v}_n^{\mathrm{T}}]^{\mathrm{T}}$ holds the agent position and its velocity, and (ii) the waveform adaptation at the CC based on the feedback information of the Bayesian state space filter.
- *Second Layer*: Represents (i) the memory for the GPEM described by the VAs $\mathcal{A}_n^{(j)} = \big\{\mathbf{a}_{k,n}^{(j)}\big\}_{k=1}^{K^{(j)}}$ with marginal PDFs $p\big(\mathcal{A}_n^{(j)}|r_{1:n}^{(j)}(t)\big)$ and the memory for the GSCM described by the $\mathrm{SINR}_{k,n}^{(j)}$ of the MPCs at the CP and (ii) the memory of VA specific signal parameters $\boldsymbol{\Theta}_{\mathrm{control},n} = \{\boldsymbol{\theta}_n^{(j,m)}\}$, e.g. the pulse duration T_{p} and/or carrier frequency f_c, at the CC.
- *Third Layer*: It represents the highest layer and is different from the two layers below in the sense that it defines the application driven by the cognitive localization/tracking system. The CP memory of applications holds abstract parameters or structures of the specified application and the CC enables the motor control for realizing higher goal planning [92].

The first and second layers describe the signal and information processing of the model parameters of the surrounding physical environment and the radio channel. On the other hand, the third layer holds higher goal parameters, i.e. motor-control input to fulfill navigation goals, that are based on the physical-related parameters [92–94]. As discussed in Chapter 1, this thesis is focused on the first and the second layers and excludes the tasks of the third layer.

The control parameter vector $\boldsymbol{\Theta}_{\text{control},n+1}$ of the next sensing cycle is chosen in order to gain the most "valuable" position-related information from the new received signal $r_{n+1}(t, \boldsymbol{\Theta}_{\text{control},n})$ using the predicted posterior $p\big(\mathbf{p}_{n+1}, \mathcal{A}_{n+1} | \tilde{r}_{n+1}(t, \boldsymbol{\Theta}_{\text{control},n})\big)$. This goal can be reached by minimizing an expected cost-to-go function, yielding

$$\hat{\boldsymbol{\Theta}}_{\text{control},n+1} = \underset{\boldsymbol{\Theta}_{\text{control},n}}{\arg\min} \quad \mathcal{C}(p\big(\mathbf{p}_{n+1}, \mathcal{A}_{n+1} | \tilde{r}_{n+1}(t, \boldsymbol{\Theta}_{\text{control},n})\big)), \tag{2.12}$$

where $\mathcal{C}(\cdot)$ is the expected cost-to-go function for optimal control [94, 95] of the environmental information contained in the predicted received signals $\tilde{r}_{n+1}(t, \boldsymbol{\Theta}_{\text{control},n})$ that depends on the chosen signal model. The expected cost-to-go function is based on an information-theoretic measure that should depend on the environment parameters, like the VA specific $\text{SINR}_{k,n}^{(j)}$, and serves as feedback information in the CDS. In general, estimation and control problems have to deal with probabilistic states and observations. As a consequence, also the control has to be probabilistic, i.e. the cost function or utility must handle uncertainties. Based on covering the uncertainty of the state with a PDF, a measure of informativeness of measurements has to be defined on the posterior state distribution. Two commonly used information measures of an RV are the entropy [96] and the Fisher information [14].

2.4.2 Information Measures

Entropy

For a continuous-valued vector RV $\mathbf{p} \in \mathbb{R}^L$, the entropy is given as [97]

$$h(\mathbf{p}) \doteq -\mathbb{E}_{\mathbf{p}} \left\{ \ln p(\mathbf{p}) \right\} = -\int_{-\infty}^{\infty} \cdots \int_{-\infty}^{\infty} p(\mathbf{p}) \ln p(\mathbf{p}) \mathrm{d}\mathbf{p}, \tag{2.13}$$

The entropy is directly related to the uncertainty of the according RV. For a multivariate Gaussian RV $\mathcal{N}\left(\mathbf{m}_{\mathbf{p}}, \mathbf{C}_{\mathbf{p}}\right)$ this means that the entropy is directly related to the covariance matrix $\mathbf{C}_{\mathbf{p}}$, yielding

$$h(\mathbf{p}) = \frac{1}{2} \ln \left((2\pi e)^L \mathbf{C}_{\mathbf{p}} \right), \tag{2.14}$$

where $\det(\cdot)$ defines the determinant of a matrix. The connection to information one could see in determinate of the covariance matrix $\mathbf{C}_{\mathbf{p}}$, which is a measure of the "volume" of the RV $\mathbf{p}$. The more compact the volume is, the smaller is the entropy $h(\mathbf{p})$ and consequently the more informative is the distribution $p(\mathbf{p})$.

Fisher Information

The FIM of a RV $\mathbf{r}$, dependent on the deterministic parameter $\mathbf{p}$, can also be used as a measure of information. Using the likelihood function $\ln f(\mathbf{r};\mathbf{p})$, it is defined as

$$\boldsymbol{\mathcal{I}}_{\mathbf{p}} = \mathbb{E}_{\mathbf{r};\mathbf{p}} \left\{ \left[\frac{\partial}{\partial \mathbf{p}} \ln f(\mathbf{r};\mathbf{p}) \right] \left[\frac{\partial}{\partial \mathbf{p}} \ln f(\mathbf{r};\mathbf{p}) \right]^{\mathrm{T}} \right\}. \tag{2.15}$$

The inverse of the FIM is a lower bound on the covariance $\mathbf{C}_{\hat{\mathbf{p}}} \succeq \boldsymbol{\mathcal{I}}_{\mathbf{p}}^{-1}$ of the deterministic parameter $\mathbf{p}$ of an estimator $\hat{\mathbf{p}}$ [14]. Looking at the entropy of the estimator's distribution $\mathcal{N}\left(\hat{\mathbf{p}}, \mathbf{C}_{\hat{\mathbf{p}}}\right)$, the explicit relationship between the FIM $\boldsymbol{\mathcal{I}}_{\mathbf{p}}$ of $\mathbf{r}$ (dependent on $\mathbf{p}$) and the entropy $h(\hat{\mathbf{p}})$ is given as

$$h(\hat{\mathbf{p}}) = \frac{1}{2} \log\left((2\pi e)^L \det\left(\mathbf{C}_{\hat{\mathbf{p}}} \right) \right) \geq -\frac{1}{2} \log\left((2\pi e)^L \det\left(\boldsymbol{\mathcal{I}}_{\mathbf{p}} \right) \right). \tag{2.16}$$

As the relationship in (2.16) shows, one can connect the FIM of a parameter vector with the entropy, resulting in a scalar measure of information that is valuable for choosing optimal waveform parameters, as it is needed for a cognitive positioning system. As it is shown in Section 3, the FIM $\boldsymbol{\mathcal{I}}_{\mathbf{p}}$ contains the environment and signal parameters, e.g. VA positions and according the SINRs. With this, a direct relationship between the environment, the feedback information and the control of the sensing is given, closing the PAC (Figure 2.3). In the same manner, the system can also be expanded to information-based control of the agent state to increase the informativeness in the measurements [93, 98, 99]. Before continuing with the formulation of the cognitive positioning system in Section 7, we have to derive the FIM on the position error (Section 3) and to introduce the algorithms for MINT (Sections 4-6). In Section 5 the posterior CRLB will be introduced, as information theoretic measure, to describe the time recursive behavior of the Bayesian filters used for MINT.

The conceptual block diagram illustrated in Figure 2.3, depicts the basic nature of the optimal behavior of a *robust* and *accurate* indoor positioning and tracking system. It combines attributes as **optimal** state space filtering, **optimal** sensing of the environment and **consistent** building of an environment and a control memory. In the follow up sections, we will always refer to the specific layer of Figure 2.3, which holds the according perceptive and control parameters that are described in these sections.

3

Cramér Rao Lower Bound (CRLB) for Multipath-Assisted Localization

In this chapter, the CRLB on the position error is derived and analyzed for MINT. For the measurement setups explained in Section 2.1.1, the following scenarios are used to get insights on different effects of interest: (i) Multipath-Sync with known clock-offset between anchors and agents, (ii) Multipath-NSync unknown clock-offsets between anchors and agents and optionally also between the individual anchors, and (iii) Multipath-Coop with cooperation between the agents, monostatic measurements, and possibly additional fixed anchors. Clock-synchronization for impulse radio UWB has shown to achieve a synchronization accuracy in order of 1 ns, which results still in large localization errors [100]. As a consequence, we estimate the clock-offset jointly, based on the received signal and the a-priori known floor plan. Only the differences between the arrival times of MPCs carry position-related information in this case, not the ToAs as in the synchronized case.

As it was already stated, the goal of multipath-assisted indoor positioning is to estimate the agent's position $\mathbf{p}$ from the received signal model (2.1), exploiting the knowledge of the VA positions $\{\mathbf{a}_k\}$, in presence of DM and AWGN. Hence, this parameters represent the environment, observed via the transmitted signal, the CRLB pinpoints the connection between the environment model parameters and the agent position estimation, i.e. it emphasizes the importance of a consistent environment memory of the CDS, as shown on the right hand-side of second layer in Figure 2.3. This Section is based on the work of [O7].

3.1 Problem Formulation

Let $\hat{\boldsymbol{\theta}}$ denote the estimate of the position-related deterministic unknown parameter vector $\boldsymbol{\theta} = [\mathbf{p}^{\mathrm{T}}\ \Re\boldsymbol{\alpha}^{\mathrm{T}}\ \Im\boldsymbol{\alpha}^{\mathrm{T}}]^{\mathrm{T}} \in \mathbb{R}^{D_{\boldsymbol{\theta}}}$ of dimension $D_{\boldsymbol{\theta}} = 2 + 2K$, where $\Re\boldsymbol{\alpha} = [\Re\alpha_1, \ldots, \Re\alpha_K]^{\mathrm{T}}$ and $\Im\boldsymbol{\alpha} =$

$[\Im\alpha_1, \ldots, \Im\alpha_K]^{\mathrm{T}}$ are the real and imaginary parts of the complex amplitudes $\boldsymbol{\alpha}$, respectively, which are nuisance parameters. According to the information inequality, the error covariance matrix of $\boldsymbol{\theta}$ is bounded by [14]

$$\mathbb{E}_{\mathbf{r};\boldsymbol{\theta}}\left\{\left(\hat{\boldsymbol{\theta}}-\boldsymbol{\theta}\right)\left(\hat{\boldsymbol{\theta}}-\boldsymbol{\theta}\right)^{\mathrm{H}}\right\} \succeq \boldsymbol{\mathcal{I}}_{\boldsymbol{\theta}}^{-1}, \tag{3.1}$$

where $\boldsymbol{\mathcal{I}}_{\boldsymbol{\theta}} \in \mathbb{R}^{D_{\boldsymbol{\theta}}\times D_{\boldsymbol{\theta}}}$ is the FIM of the position-related parameter vector $\boldsymbol{\theta}$ and its inverse represents the CRLB of $\boldsymbol{\theta}$. We apply the chain rule to derive this CRLB (cf. [42,46,48]), i.e., the FIM $\boldsymbol{\mathcal{I}}_{\boldsymbol{\theta}}$ is computed from the FIM of the signal parameter vector $\boldsymbol{\psi} = \left[\boldsymbol{\tau}^{\mathrm{T}}, \Re\boldsymbol{\alpha}^{\mathrm{T}}, \Im\boldsymbol{\alpha}^{\mathrm{T}}\right]^{\mathrm{T}} \in \mathbb{R}^{D_{\boldsymbol{\psi}}}$ of dimension $D_{\boldsymbol{\psi}} = 3K$, where $\boldsymbol{\tau} = [\tau_1, \ldots, \tau_K]^{\mathrm{T}}$ represents the vector of position-related delays. Based on $f(\mathbf{r};\boldsymbol{\theta}) = f(\mathbf{r};\boldsymbol{\alpha},\boldsymbol{\tau})f(\boldsymbol{\alpha},\boldsymbol{\tau};\mathbf{p};\mathcal{A}) = f(\mathbf{r};\boldsymbol{\psi})f(\boldsymbol{\alpha},\boldsymbol{\tau};\mathbf{p};\mathcal{A})$, we get

$$\boldsymbol{\mathcal{I}}_{\boldsymbol{\theta}} = \mathbf{J}^{\mathrm{T}}\boldsymbol{\mathcal{I}}_{\boldsymbol{\psi}}\mathbf{J} \tag{3.2}$$

with the Jacobian

$$\mathbf{J} = \frac{\partial\boldsymbol{\psi}}{\partial\boldsymbol{\theta}} \in \mathbb{R}^{D_{\boldsymbol{\psi}}\times D_{\boldsymbol{\theta}}} \tag{3.3}$$

that represents a affine parameter transformation. The FIM $\boldsymbol{\mathcal{I}}_{\boldsymbol{\psi}} \in \mathbb{R}^{D_{\boldsymbol{\psi}}\times D_{\boldsymbol{\psi}}}$ of the signal model parameters can be computed from the likelihood function $f(\mathbf{r};\boldsymbol{\psi})$ in (3.5) of the received signal $\mathbf{r}$ conditioned on parameter vector $\boldsymbol{\psi}$ [14],

$$\boldsymbol{\mathcal{I}}_{\boldsymbol{\psi}} = \mathbb{E}_{\mathbf{r};\boldsymbol{\psi}}\left\{\left[\frac{\partial}{\partial\boldsymbol{\psi}}\ln f(\mathbf{r};\boldsymbol{\psi})\right]\left[\frac{\partial}{\partial\boldsymbol{\psi}}\ln f(\mathbf{r};\boldsymbol{\psi})\right]^{\mathrm{T}}\right\}. \tag{3.4}$$

3.2 Likelihood Function

The likelihood function $f(\mathbf{r};\boldsymbol{\psi})$ is defined for the sampled received signal vector $\mathbf{r} = [\, r(0),\, r(T_{\mathrm{s}}),\, \ldots,\, r((N-1)T_{\mathrm{s}})\,]^{\mathrm{T}} \in \mathbb{C}^N$, containing N samples at rate $1/T_{\mathrm{s}}$. Using the assumption that the AWGN and the DM are both Gaussian, the likelihood function is given by

$$\begin{aligned} f(\mathbf{r};\boldsymbol{\psi}) = f(\mathbf{r};\boldsymbol{\alpha},\boldsymbol{\tau}) &= \frac{1}{\pi^N\det(\mathbf{C_r})}\exp\big\{-(\mathbf{r}-\mathbf{S}\boldsymbol{\alpha})^{\mathrm{H}}{\mathbf{C_r}}^{-1}(\mathbf{r}-\mathbf{S}\boldsymbol{\alpha})\big\} \\ &= \frac{1}{\pi^N\det(\mathbf{C_r})}\exp\big\{2\Re\left\{\mathbf{r}^{\mathrm{H}}{\mathbf{C_r}}^{-1}\mathbf{S}\boldsymbol{\alpha}\right\} - \boldsymbol{\alpha}^{\mathrm{H}}\mathbf{S}^{\mathrm{H}}{\mathbf{C_r}}^{-1}\mathbf{S}\boldsymbol{\alpha} - \mathbf{r}^{\mathrm{H}}{\mathbf{C_r}}^{-1}\mathbf{r}\big\} \\ &= \frac{1}{\pi^N\det(\mathbf{C_r})}\exp\big\{2\Re\left\{\mathbf{r}^{\mathrm{H}}{\mathbf{C_r}}^{-1}\mathbf{r}_{\mathrm{det},\boldsymbol{\psi}}\right\} - \mathbf{r}_{\mathrm{det},\boldsymbol{\psi}}^{\mathrm{H}}{\mathbf{C_r}}^{-1}\mathbf{r}_{\mathrm{det},\boldsymbol{\psi}} - \mathbf{r}^{\mathrm{H}}{\mathbf{C_r}}^{-1}\mathbf{r}\big\} \end{aligned} \tag{3.5}$$

where $\mathbf{r}_{\mathrm{det},\boldsymbol{\psi}} = \mathbf{S}\boldsymbol{\alpha}$ and $\mathbf{S}$ is the signal matrix given by

$$\mathbf{S} = \begin{bmatrix} \mathbf{s}_{\tau_1}^{\mathrm{H}} \\ \vdots \\ \mathbf{s}_{\tau_K}^{\mathrm{H}} \end{bmatrix}^{\mathrm{H}} = \begin{bmatrix} s(T_{\mathrm{s}}-\tau_1) & \ldots & s(T_{\mathrm{s}}-\tau_K) \\ s(2T_{\mathrm{s}}-\tau_1) & \ldots & s(2T_{\mathrm{s}}-\tau_K) \\ \vdots & & \vdots \\ s(NT_{\mathrm{s}}-\tau_1) & \ldots & s(NT_{\mathrm{s}}-\tau_K) \end{bmatrix} \tag{3.6}$$

containing delayed versions $\mathbf{s}_{\tau_k} = [s(-\tau_k), s(T_\mathrm{s}-\tau_k), \ldots, s((N-1)T_\mathrm{s}-\tau_k)]^\mathrm{T}$ of the sampled transmit pulse. The covariance matrix $\mathbf{C_r}$ is written as (see Appendix A.1.2)

$$\mathbf{C_r} = {\sigma_\mathrm{n}}^2\mathbf{I}_N + \mathbf{C_c} = {\sigma_\mathrm{n}}^2\mathbf{I}_N + \bar{\mathbf{S}}^\mathrm{H}\mathbf{S}_\nu\bar{\mathbf{S}} \tag{3.7}$$

where ${\sigma_\mathrm{n}}^2 = N_0/T_\mathrm{s}$ is the variance of the vector of AWGN samples and $\bar{\mathbf{S}} = [\mathbf{s}_0, \cdots, \mathbf{s}_{N-1}]^\mathrm{T} \in \mathbb{R}^{N\times N}$ is the *full* signal matrix with $\mathbf{s}_i = \Big[s((-i) \mod NT_\mathrm{s}), \ldots, s((N-1-i) \mod NT_\mathrm{s})\Big]^\mathrm{T}$, defined as a circulant matrix and the diagonal matrix $\mathbf{S}_\nu$ represents the sampled DM PDP $\mathbf{s}_\nu = [S_\nu(0), \ldots, S_\nu(T_\mathrm{s}(N-1))]^\mathrm{T}$. The covariance matrix of DM $\mathbf{C_c}$ is given by

$$[\bar{\mathbf{S}}^\mathrm{H}\mathbf{S}_\nu\bar{\mathbf{S}}]_{n,m} = \sum_{i=0}^{N-1} T_\mathrm{s}S_\nu(iT_\mathrm{s})s((n-i) \mod NT_\mathrm{s})s((m-i) \mod NT_\mathrm{s}). \tag{3.8}$$

3.3 Fisher Information Matrix (FIM) for the Signal Model Parameters

3.3.1 General Case

he FIM $\boldsymbol{\mathcal{I}}_{\boldsymbol{\psi}}$ is obtained from (3.4) with (3.5). As (3.5) describes a general Gaussian multivariate vector RV, the FIM for the complex signal $\mathbf{r}_{\mathrm{det},\boldsymbol{\psi}}$ is given as [14]

$$\big[\boldsymbol{\mathcal{I}}(\boldsymbol{\psi})\big]_{i,j} = 2\Re\left\{\left(\frac{\partial\mathbf{r}_{\mathrm{det},\boldsymbol{\psi}}}{\partial\psi_i}\right)^\mathrm{H}{\mathbf{C_r}}^{-1}\left(\frac{\partial\mathbf{r}_{\mathrm{det},\boldsymbol{\psi}}}{\partial\psi_j}\right)\right\}, \tag{3.9}$$

assuming that the noise covariance matrix $\mathbf{C_r}$ is known. Following the notation of [59], it is decomposed according to the subvectors of $\boldsymbol{\psi}$ into

$$\boldsymbol{\mathcal{I}}_{\boldsymbol{\psi}} = \begin{bmatrix} \boldsymbol{\Lambda}_\mathrm{A} & \Re\boldsymbol{\Lambda}_\mathrm{B} & \Im\boldsymbol{\Lambda}_\mathrm{B} \\ (\Re\boldsymbol{\Lambda}_\mathrm{B})^\mathrm{T} & \boldsymbol{\Lambda}'_\mathrm{C} & \boldsymbol{\Lambda}''_\mathrm{C} \\ (\Im\boldsymbol{\Lambda}_\mathrm{B})^\mathrm{T} & \boldsymbol{\Lambda}''_\mathrm{C} & \boldsymbol{\Lambda}'_\mathrm{C} \end{bmatrix} = \begin{bmatrix} \boldsymbol{\Lambda}_\mathrm{A} & \boldsymbol{\Lambda}_\mathrm{B} \\ \boldsymbol{\Lambda}_\mathrm{B}^\mathrm{T} & \boldsymbol{\Lambda}_\mathrm{C} \end{bmatrix} \tag{3.10}$$

with $\boldsymbol{\Lambda}_\mathrm{A} \in \mathbb{R}^{K\times K}$, $\boldsymbol{\Lambda}_\mathrm{B} \in \mathbb{R}^{K\times 2K}$ and $\boldsymbol{\Lambda}_\mathrm{C} \in \mathbb{R}^{2K\times 2K}$. As shown in Appendix A.1.1 and using $\dot{\mathbf{s}}_{\tau_k} = \frac{\partial\mathbf{s}_{\tau_k}}{\partial\tau_k}$, its elements are written as

$$[\boldsymbol{\Lambda}_\mathrm{A}]_{k,k'} = \mathbb{E}_{\mathbf{r};\boldsymbol{\psi}}\left\{-\frac{\partial^2\ln f(\mathbf{r};\boldsymbol{\psi})}{\partial\tau_k\partial\tau_{k'}}\right\} = 2\Re\left\{\alpha_k\alpha_{k'}^*\big(\dot{\mathbf{s}}_{\tau_{k'}}\big)^\mathrm{H}{\mathbf{C_r}}^{-1}\dot{\mathbf{s}}_{\tau_k}\right\} \tag{3.11}$$

$$[\Re\boldsymbol{\Lambda}_\mathrm{B}]_{k,k'} = \mathbb{E}_{\mathbf{r};\boldsymbol{\psi}}\left\{-\frac{\partial^2\ln f(\mathbf{r};\boldsymbol{\psi})}{\partial\tau_k\partial\Re\alpha_{k'}}\right\} = 2\Re\left\{\alpha_k\big(\mathbf{s}_{\tau_{k'}}\big)^\mathrm{H}{\mathbf{C_r}}^{-1}\dot{\mathbf{s}}_{\tau_k}\right\} \tag{3.12}$$

$$[\Im\boldsymbol{\Lambda}_\mathrm{B}]_{k,k'} = \mathbb{E}_{\mathbf{r};\boldsymbol{\psi}}\left\{-\frac{\partial^2\ln f(\mathbf{r};\boldsymbol{\psi})}{\partial\tau_k\partial\Im\alpha_{k'}}\right\} = 2\Im\left\{\alpha_k\big(\mathbf{s}_{\tau_{k'}}\big)^\mathrm{H}{\mathbf{C_r}}^{-1}\dot{\mathbf{s}}_{\tau_k}\right\} \tag{3.13}$$

$$\begin{aligned}[\boldsymbol{\Lambda}'_\mathrm{C}]_{k,k'} &= \mathbb{E}_{\mathbf{r};\boldsymbol{\psi}}\left\{-\frac{\partial^2\ln f(\mathbf{r};\boldsymbol{\psi})}{\partial\Re\alpha_k\partial\Re\alpha_{k'}}\right\} = \mathbb{E}_{\mathbf{r};\boldsymbol{\psi}}\left\{-\frac{\partial^2\ln f(\mathbf{r};\boldsymbol{\psi})}{\partial\Im\alpha_k\partial\Im\alpha_{k'}}\right\} \\ &= 2\Re\left\{\big(\mathbf{s}_{\tau_{k'}}\big)^\mathrm{H}{\mathbf{C_r}}^{-1}\mathbf{s}_{\tau_k}\right\}\end{aligned} \tag{3.14}$$

$$[\mathbf{\Lambda}''_{\mathrm{C}}]_{k,k'} = \mathbb{E}_{\mathbf{r}|\boldsymbol{\psi}} \left\{ -\frac{\partial^2 \ln f(\mathbf{r}|\boldsymbol{\psi})}{\partial \Im\alpha_k \partial \Re\alpha_{k'}} \right\} = \mathbb{E}_{\mathbf{r}|\boldsymbol{\psi}} \left\{ -\frac{\partial^2 \ln f(\mathbf{r}|\boldsymbol{\psi})}{\partial \Re\alpha_k \partial \Im\alpha_{k'}} \right\} = 0 \tag{3.15}$$

These equations can be used to numerically evaluate the FIM without further assumptions. The CRLB can thus be evaluated, but the inverse of the covariance matrix $\mathbf{C}_{\mathbf{r}}$, which is needed as a whitening operator [13] to account for the non-stationary DM process, limits the insight it can possibly provide. Applying the Schur complement yields, the elements of FIM of the MPC delays

$$\begin{aligned} \left[\boldsymbol{\mathcal{I}}_{\boldsymbol{\tau}}\right]_{k,k'} &= \left[\mathbf{\Lambda}_{\mathrm{A}} - \mathbf{\Lambda}_{\mathrm{B}}\left(\mathbf{\Lambda}_{\mathrm{C}}\right)^{-1}\mathbf{\Lambda}_{\mathrm{B}}^{\mathrm{T}}\right]_{k,k'} \\ &= 2\alpha_k^*\alpha_{k'} \left(\left(\dot{\mathbf{s}}_{\tau_k}\right)^{\mathrm{H}} \mathbf{C}_{\mathbf{r}}{}^{-1} \dot{\mathbf{s}}_{\tau_{k'}} - \frac{\left(\left(\mathbf{s}_{\tau_k}\right)^{\mathrm{H}} \mathbf{C}_{\mathbf{r}}{}^{-1} \dot{\mathbf{s}}_{\tau_{k'}} \right)^2}{\left(\mathbf{s}_{\tau_k}\right)^{\mathrm{H}} \mathbf{C}_{\mathbf{r}}{}^{-1} \mathbf{s}_{\tau_{k'}}} \right) \end{aligned} \tag{3.16}$$

More insight can be gained under the assumption that the received deterministic MPCs $\{\alpha_k s(t-\tau_k)\}$ are orthogonal, which occurs in practice when MPCs are non-overlapping.

3.3.2 Orthogonal Multipath Components (MPCs): Stationary Stationary Power Delay Profile (PDP)

As it is derived in Appendix A.1.2 in detail, the desired properties of $s(t)$—a large bandwidth and favorable autocorrelation properties—imply that the nonstationary PDP is sampled at time τ_k and we can replace $\mathbf{S}_\nu$ for each summand by a stationary PDP $\mathbf{S}_\nu^{(\tau_k)} = T_{\mathrm{s}} S_\nu(\tau_k)\mathbf{I}_N$.

In this case, the columns of the signal matrix $\mathbf{S}$ are orthogonal and $\mathbf{\Lambda}_{\mathrm{A}}$ becomes diagonal. Furthermore, $[\mathbf{\Lambda}_{\mathrm{B}}]_{k,k'}$ is zero (due to the symmetry of the ACF of $s(t)$ and the stationary of the PDP), which is also reflected by (3.22) in Section 3.3.3, thus for on diagonal values ($\tau_k = \tau_{k'}$) $\sin\left(2\pi f(\tau_k - \tau_k)\right) = 0$. As a consequence $[\mathbf{\Lambda}_{\mathrm{C}}]_{k,k'}$ is not needed. The elements of $\boldsymbol{\mathcal{I}}_{\boldsymbol{\tau}}$ are defined by $\mathbf{\Lambda}_{\mathrm{A}}$ and can then be written as (see Appendix A.1.2)

$$\left[\boldsymbol{\mathcal{I}}_{\boldsymbol{\tau}}\right]_{k,k} = [\mathbf{\Lambda}_{\mathrm{A}}]_{k,k} = 8\pi^2\beta^2 \mathrm{SINR}_k \gamma_k \tag{3.17}$$

where $\beta^2 = \int_f f^2 |S(f)|^2 \mathrm{d}f$ is the effective (mean square) bandwidth of the energy-normalized transmit pulse $s(t) \overset{\mathcal{F}}{\longleftrightarrow} S(f)$,

$$\mathrm{SINR}_k := \frac{\left|\alpha_k\right|^2}{N_0 + T_{\mathrm{p}} S_\nu(\tau_k)} \tag{3.18}$$

is the SINR of the k-th MPC, and γ_k is the so-called bandwidth extension factor. The product of these three factors quantifies the delay information provided by the k-th MPC. It hence provides the following insight for the investigated estimation problem: The interference term $T_{\mathrm{p}} S_\nu(\tau_k)$ is determined by the PDP of DM $S_\nu(\tau_k)$ at the delay τ_k of the MPC. It scales with the effective pulse duration T_{p} of the pulse $s(t)$, the reciprocal of its equivalent Nyquist bandwidth $B_{\mathrm{N}} = 1/T_{\mathrm{p}}$. An increased bandwidth is hence beneficial to suppress DM.

The bandwidth extension quantifies the SINR-gain due to the whitening operation. It is

defined as $\gamma_k = \beta_k^2/\beta^2$, where β_k^2 is the mean square bandwidth of the whitened pulse,

$$\beta_k^2 = \int_f f^2 |\mathrm{S}(f)|^2 \frac{N_0 + T_\mathrm{p} S_\nu(\tau_k)}{N_0 + S_\nu(\tau_k)|\mathrm{S}(f)|^2} \mathrm{d}f. \tag{3.19}$$

If the pulse has a block spectrum, we have (due to the energy normalization of $s(t)$) $|S(f)|^2 = T_\mathrm{p}$ for $|f| \leq B_\mathrm{N}/2$, hence $\beta_k^2 = \beta^2$ and $\gamma_k = 1$. I.e., in this case, there is *no* bandwidth extension due to whitening[16]. The same holds if DM is negligible, i.e. $N_0 \gg T_\mathrm{p} S_\nu(\tau_k)$. For the asymptotic case that AWGN is negligible, i.e. $S_\nu(\tau_k)|\mathrm{S}(f)|^2 \gg N_0$, we drop N_0 in (3.19) and get a block spectrum that corresponds to the *absolute* bandwidth of $S(f)$, hence $\gamma_k > 1$.

In general, γ_k is a function of the interference-plus-noise-ratio (INR) $T_\mathrm{p} S_\nu(\tau_k)/N_0$ and can be evaluated numerically. Closed-form results can be given for special cases. E.g. for a root-raised-cosine pulse with roll-off factor β_R, we have $\beta^2 = B_\mathrm{N}^2(\frac{1}{12} + \frac{\pi^2-8}{4\pi^2}\beta_\mathrm{R}^2)$ which scales slightly with β_R. In the asymptotic case where DM dominates, we get $\beta_k^2 = \frac{(1+\beta_\mathrm{R})^3}{12} B_\mathrm{N}^2$. Hence the bandwidth extension due to the whitening operation can result in an SINR gain of up to about 7 dB at $\beta_\mathrm{R} = 1$. Numerical evaluation shows a γ_k of 4 dB at $\beta_\mathrm{R} = 0.6$ and an INR of 15 dB.

For further analysis, we define the effective SINR

$$\widetilde{\mathrm{SINR}}_k = \mathrm{SINR}_k \gamma_k \tag{3.20}$$

which quantifies the delay information provided by MPC k as a function of the signal, interference, and noise levels.

3.3.3 Path Overlap between MPCs: PDP

For deriving the FIM for orthogonal MPCs, we assume that for high bandwidth almost all DM power is concentrated at delay τ_k, so that we can use a stationary PDP $\mathbf{S}_\nu^{(\tau_k)} = T_\mathrm{s} S_\nu(\tau_k)\mathbf{I}_N$ (see Appendix A.1.2). If clusters of MPCs are present, i.e. path-overlap between the MPCs occurs, the influence of the DM on the MPCs can not be seen as separated. We assume that the DM of the MPCs at delays τ_k and $\tau_{k'}$ is described by a joint DM PDP $\mathbf{S}_\nu^{(\tau_k,\tau_{k'})} = T_\mathrm{s} S_\nu(\tau_k, \tau_{k'})\mathbf{I}_N$. Following the derivation in (A.10), (A.11) and (A.12), one get

$$[\boldsymbol{\alpha}^\mathrm{H}\mathbf{S}^\mathrm{H}{\mathbf{C}_\mathbf{r}}^{-1}\mathbf{S}\boldsymbol{\alpha}]_{k,k'} \approx \int_f \frac{\alpha_k^* \alpha_{k'} |\mathrm{S}(f)|^2}{N_0 + S_\nu(\tau_k, \tau_{k'})|\mathrm{S}(f)|^2} \exp\left\{-j2\pi f(\tau_k - \tau_{k'})\right\} \mathrm{d}f. \tag{3.21}$$

With this, the FIM of the MPC delays are given as

$$\begin{aligned}\left[\boldsymbol{\mathcal{I}}_{\boldsymbol{\tau}}\right]_{k,k'} &= \left[\boldsymbol{\Lambda}_\mathrm{A} - \boldsymbol{\Lambda}_\mathrm{B}\left(\boldsymbol{\Lambda}_\mathrm{C}\right)^{-1}\boldsymbol{\Lambda}_\mathrm{B}^\mathrm{T}\right]_{k,k'} \approx 8\pi^2 \int_f f^2 |\mathrm{S}(f)|^2 \\ &\times \left(\frac{(\Re\alpha_k \Re\alpha_{k'} + \Im\alpha_k \Im\alpha_{k'}) \cos\left(2\pi f(\tau_k - \tau_{k'})\right)}{N_0 + S_\nu(\tau_k, \tau_{k'})|\mathrm{S}(f)|^2} - \frac{2\Im\alpha_k \Re\alpha_{k'} \sin\left(2\pi f(\tau_k - \tau_{k'})\right)}{N_0 + S_\nu(\tau_k, \tau_{k'})|\mathrm{S}(f)|^2} \right) \mathrm{d}f,\end{aligned} \tag{3.22}$$

where $\Re\alpha_k$ and $\Im\alpha_k$ are the real and imaginary part of the k-th amplitude. This result shows that it is not possible anymore to separate the equation into an SINR and the effective (root mean square) bandwidth of the pulse. But loosely speaking one could interpret the first summand

[16] This specialization was assumed in our previous paper [59].

of (3.22) as a reduced SINR value (over the pulse bandwidth) and the second summand as reduction of information due to the "power" of the overlapping area in a cluster of two MPCs.

3.3.4 Orthogonal MPCs: Nonstationary PDP

If the DM PDP is nonstationary, correlations and cross-correlations between the received signal samples due to the transmit pulse are considered per MPC and as a consequence the second term of the Schur compliment in (3.22) is not zero. The matrices $\Re\boldsymbol{\Lambda}_\mathrm{B}$ and $\Im\boldsymbol{\Lambda}_\mathrm{B}$ then are diagonal matrices. This accounts for the information loss due to the estimation of the nuisance parameters $\{\alpha_k\}$. Using the definition of the effective square bandwidth in time domain $\beta^2 = 1/(4\pi^2)\|\dot{\mathbf{s}}_{\tau_k}\|^2/\|\mathbf{s}_{\tau_k}\|^2$, where $\|\mathbf{s}_{\tau_k}\|^2 = \mathbf{s}_{\tau_k}^\mathrm{H}\mathbf{s}_{\tau_k}$, the FIM of the MPC delays is written as

$$\begin{aligned}\boldsymbol{\mathcal{I}}_{\boldsymbol{\tau}} &= \boldsymbol{\Lambda}_\mathrm{A} - \boldsymbol{\Lambda}_\mathrm{B}\big(\boldsymbol{\Lambda}_\mathrm{C}\big)^{-1}\boldsymbol{\Lambda}_\mathrm{B}^\mathrm{T} = 2|\alpha_k|^2\left(\big(\dot{\mathbf{s}}_{\tau_k}\big)^\mathrm{H}\mathbf{C}_\mathbf{r}{}^{-1}\dot{\mathbf{s}}_{\tau_k} - \frac{\Big(\big(\mathbf{s}_{\tau_k}\big)^\mathrm{H}\mathbf{C}_\mathbf{r}{}^{-1}\dot{\mathbf{s}}_{\tau_k}\Big)^2}{\big(\mathbf{s}_{\tau_k}\big)^\mathrm{H}\mathbf{C}_\mathbf{r}{}^{-1}\mathbf{s}_{\tau_k}}\right) \\ &= 8\pi^2\beta^2|\alpha_k|^2\left(\frac{\|\mathbf{s}_{\tau_k}\|^2}{\|\dot{\mathbf{s}}_{\tau_k}\|^2}\left(\big(\dot{\mathbf{s}}_{\tau_k}\big)^\mathrm{H}\mathbf{C}_\mathbf{r}{}^{-1}\dot{\mathbf{s}}_{\tau_k} - \frac{\Big(\big(\mathbf{s}_{\tau_k}\big)^\mathrm{H}\mathbf{C}_\mathbf{r}{}^{-1}\dot{\mathbf{s}}_{\tau_k}\Big)^2}{\big(\mathbf{s}_{\tau_k}\big)^\mathrm{H}\mathbf{C}_\mathbf{r}{}^{-1}\mathbf{s}_{\tau_k}}\right)\right) \\ &= 8\pi^2\beta^2\widehat{\mathrm{SINR}}_k,\end{aligned} \tag{3.23}$$

where $\widehat{\mathrm{SINR}}_k$ is the effective SINR of the k-th MPC that considers bandwidth extension and also the nonstationarity of the PDP.

3.3.5 Position Error Bound

The FIM $\boldsymbol{\mathcal{I}}_{\boldsymbol{\psi}}$ of the signal model parameters quantifies the information gained from the measurement $\mathbf{r}$. The position-related part of this information lies in the MPC delays $\boldsymbol{\tau}$, which are a function of the position $\mathbf{p}$. To compute the position error bound (PEB), the square-root of the trace of the CRLB covariance $\mathbf{C}_\mathbf{p} = \boldsymbol{\mathcal{I}}_\mathbf{p}^{-1}$ on the position error, we need the upper left 2×2 submatrix of the inverse of FIM $\boldsymbol{\mathcal{I}}_{\boldsymbol{\theta}}$,

$$\mathcal{P}\{\mathbf{p}\} = \sqrt{\mathrm{tr}\left\{\big[\boldsymbol{\mathcal{I}}_{\boldsymbol{\theta}}^{-1}\big]_{2\times 2}\right\}} = \sqrt{\mathrm{tr}\left\{\boldsymbol{\mathcal{I}}_\mathbf{p}^{-1}\right\}} = \sqrt{\mathrm{tr}\left\{\mathbf{C}_\mathbf{p}\right\}}, \tag{3.24}$$

which can be obtained with (3.2) and (3.3) using the blockwise inversion lemma. This results in the so-called *equivalent* FIM (EFIM) $\boldsymbol{\mathcal{I}}_\mathbf{p}$ [46],

$$\boldsymbol{\mathcal{I}}_\mathbf{p} = \mathbf{H}^\mathrm{T}\big(\boldsymbol{\Lambda}_\mathrm{A} - \boldsymbol{\Lambda}_\mathrm{B}\big(\boldsymbol{\Lambda}_\mathrm{C}\big)^{-1}\boldsymbol{\Lambda}_\mathrm{B}^\mathrm{T}\big)\mathbf{H} = \mathbf{H}^\mathrm{T}\boldsymbol{\mathcal{I}}_{\boldsymbol{\tau}}\mathbf{H},$$

which represents the information relevant for the position error bound. Matrix $\mathbf{H} = \partial\boldsymbol{\tau}/\partial\mathbf{p}$ is the submatrix of Jacobian (3.3) that relates to the position-related information, the derivatives of the delay vector $\boldsymbol{\tau}$ w.r.t. position $\mathbf{p}$. It describes the variation of the signal parameters w.r.t. the position and can assume different, scenario-dependent forms, depending on the roles of anchors and agents. General expressions for these *spatial delay gradients* are derived in the next Section.

Regularity Condition

To guarantee the existence of the FIM, i.e. the CRLB on the position error, the likelihood function on the agent position $f(\mathbf{r};\boldsymbol{\theta})$ needs to satisfy a regularity condition $\mathbb{E}_{\mathbf{r};\boldsymbol{\theta}}\left\{\frac{\partial \ln f(\mathbf{r};\boldsymbol{\theta})}{\partial \boldsymbol{\theta}}\right\} = 0$ [14]. Since the likelihood functions on the position and the channel parameters are just coupled via the Jacobian matrix $\mathbf{J}$ that is an affine parameter transformation, the regularity condition just has to hold for the signal model likelihood function described in (3.5), i.e. $\mathbb{E}_{\mathbf{r};\boldsymbol{\psi}}\left\{\frac{\partial \ln f(\mathbf{r};\boldsymbol{\psi})}{\partial \boldsymbol{\psi}}\right\} = 0$. If we assume that the support of the delay domain is given as $-\infty < \tau < \infty$, the derivative of the likelihood function e.g. w.r.t. τ_k yields

$$\begin{aligned}
\mathbb{E}_{\mathbf{r};\boldsymbol{\psi}}\left\{\frac{\partial \ln f(\mathbf{r};\boldsymbol{\psi})}{\partial \tau_k}\right\} &= \mathbb{E}_{\mathbf{r};\boldsymbol{\psi}}\left\{2\Re\Big\{\sum_k \alpha_k^* \alpha_{k'} \big(\mathbf{s}_{\tau_k}\big)^{\mathrm{H}} {\mathbf{C}_{\mathbf{r}}}^{-1} \dot{\mathbf{s}}_{\tau_{k'}}\Big\} - 2\Re\Big\{\mathbf{r}^{\mathrm{H}} {\mathbf{C}_{\mathbf{r}}}^{-1} \dot{\mathbf{s}}_{\tau_{k'}}\Big\}\right\} \\
&= \mathbb{E}_{\mathbf{r};\boldsymbol{\psi}}\left\{-2\Re\Big\{\Big(\mathbf{r}_{\mathrm{diff}} + \mathbf{w}\Big)\dot{\mathbf{s}}_{\tau_{k'}} \alpha_{k'}\Big\}\right\} \\
&= -2\Re\Big\{\mathbb{E}_{\mathbf{r};\boldsymbol{\psi}}\left\{\mathbf{r}_{\mathrm{diff}} + \mathbf{w}\right\} \dot{\mathbf{s}}_{\tau_{k'}} \alpha_{k'}\Big\} \\
&\vdots \qquad \rightarrow \mathbb{E}_{\mathbf{r};\boldsymbol{\psi}}\left\{\mathbf{r}_{\mathrm{diff}} + \mathbf{w}\right\} = 0 \\
&= 0.
\end{aligned} \tag{3.25}$$

This also holds for the real and imaginary part of the complex MPC amplitudes α_k, thus the regularity condition is fulfilled.

3.4 Spatial Delay Gradients

The following notations are used to find the elements of matrix $\mathbf{H}$: $\mathbf{p}^{(m)} \in \mathbb{R}^2$ is the position of the m-th agent, where $m \in \mathcal{N}_m = \{1, 2, \ldots, M\}$. $\mathbf{a}_1^{(j)} \in \mathbb{R}^2$ is the position of the j-th fixed anchor, $j \in \mathcal{N}_j = \{M+1, \ldots, M+J\}$, with VAs at positions $\mathbf{a}_k^{(j)} \in \mathbb{R}^2$. In the cooperative scenario, we replace j with an arbitrary index ξ to cover fixed anchors as well as agents which act as anchors. The corresponding VAs are at $\mathbf{a}_k^{(\xi)} \in \mathbb{R}^2$. To describe gradients w.r.t. anchor or agent position, we use an index η, introducing $\mathbf{p}^{(\eta)} \in \mathbb{R}^2$.

The delay of the k-th MPC is defined by the distance between the k-th VA and the m-th agent,

$$\tau_k^{(\xi,m)} = \frac{1}{c}\big\|\mathbf{p}^{(m)} - \mathbf{a}_k^{(\xi)}\big\| = \frac{1}{c}\sqrt{\big(x^{(m)} - x_k^{(\xi)}\big)^2 + \big(y^{(m)} - y_k^{(\xi)}\big)^2}. \tag{3.26}$$

The angle of vector $(\mathbf{p}^{(m)} - \mathbf{a}_k^{(\xi)})$ is written as $\phi_k^{(\xi,m)}$. To describe the relation between the signal parameter $\tau_k^{(\xi,m)}$ and the geometry, we need to analyze the spatial delay gradient, the derivative of the delay $\tau_k^{(\xi,m)}$ w.r.t. position $\mathbf{p}^{(\eta)}$,

$$\begin{aligned}
\mathbf{h}_k^{(\xi,\eta,m)} &= \frac{\partial \tau_k^{(\xi,m)}}{\partial \mathbf{p}^{(\eta)}} = \frac{1}{c}\frac{\partial \big\|\mathbf{p}^{(m)} - \mathbf{a}_k^{(\xi)}\big\|}{\partial \mathbf{p}^{(\eta)}} \\
&= \frac{1}{c}\frac{\partial\big(x^{(m)} - x_k^{(\xi)}\big)}{\partial \mathbf{p}^{(\eta)}} \frac{x^{(m)} - x_k^{(\xi)}}{\big\|\mathbf{p}^{(m)} - \mathbf{a}_k^{(\xi)}\big\|} + \frac{1}{c}\frac{\partial\big(y^{(m)} - y_k^{(\xi)}\big)}{\partial \mathbf{p}^{(\eta)}} \frac{y^{(m)} - y_k^{(\xi)}}{\big\|\mathbf{p}^{(m)} - \mathbf{a}_k^{(\xi)}\big\|}
\end{aligned}$$

$$= \frac{1}{c}\Big(\delta_{m,\eta}\mathbf{I}_2 - \delta_{\eta,\xi}\frac{\partial \mathbf{a}_k^{(\xi)}}{\partial \mathbf{p}^{(\xi)}}\Big)^{\mathrm{T}}\mathbf{e}\Big(\phi_k^{(\xi,m)}\Big) \tag{3.27}$$

where $\mathbf{e}(\phi) := [\cos(\phi), \sin(\phi)]^{\mathrm{T}}$ is a unit vector in direction of the argument angle and $\delta_{m,\eta}$ is the Kronecker delta. Using (A.29) from Appendix A.2 for the Jacobian $\mathbf{a}_k^{(\xi)}/\mathbf{p}^{(\xi)}$ of a VA position w.r.t. its respective anchor's position, we get

$$\mathbf{h}_k^{(\xi,\eta,m)} = \frac{1}{c}\Big[\delta_{m,\eta}\mathbf{e}\Big(\phi_k^{(\xi,m)}\Big) - \delta_{\eta,\xi}\mathbf{e}\Big((-1)^{Q_k^{(\xi)}}\phi_k^{(\xi,m)} + 2\bar{\zeta}_k^{(\xi)}\Big)\Big], \tag{3.28}$$

where the first summand represents the influence of the agent position while the second summand is linked to the anchor position. The parameter $\bar{\zeta}_k^{(\xi)}$ (see Appendix A.2) describes the effective wall angle of the k-th MPC w.r.t. to the η-th anchor (or agent) and $Q_k^{(\xi)}$ represents the according VA order. We stack the transposed gradient vectors (3.28) for the entire set of multipath components in the gradient matrix $\mathbf{H}^{(\xi,\eta,m)} \in \mathbb{R}^{K^{(\xi,m)}\times 2}$ and the matrices for all the agents' derivatives into matrix $\mathbf{H}^{(\xi,m)} \in \mathbb{R}^{K^{(\xi,m)}\times 2M}$. The following specializations are interesting for further derivations:

3.4.1 Bistatic scenario

Here the size of the VA set is given by $k = 1, \ldots, K^{(\xi,m)}$.

The gradient with respect to the agent: This case describes the derivatives of delay $\tau^{(\xi,m)}$ w.r.t. the agent position, i.e. $\eta = m$, yielding the gradient

$$\mathbf{h}_k^{(\xi,m,m)} = \frac{\partial \tau^{(\xi,m)}}{\partial \mathbf{p}^{(m)}} = \frac{1}{c}\mathbf{e}\Big(\phi_k^{(\xi,m)}\Big). \tag{3.29}$$

This is a vector pointing from an agent to the k-th VA of the according anchor. We define the gradient matrix $\mathbf{H}_{\mathrm{Ag}}^{(\xi,m)} = \mathbf{H}^{(\xi,m,m)} \in \mathbb{R}^{K^{(\xi,m)}\times 2}$.

The gradient with respect to the anchor: In this case, the derivatives w.r.t. the anchor position are described, i.e. $\eta = \xi$. For the k-th MPC, the gradient is expressed as

$$\mathbf{h}_k^{(\xi,\xi,m)} = \frac{\partial \tau_k^{(\xi,m)}}{\partial \mathbf{p}^{(\xi)}} = -\frac{1}{c}\mathbf{e}\Big((-1)^{Q_k^{(\xi)}}\phi_k^{(\xi,m)} + 2\bar{\zeta}_k^{(\xi)}\Big) = \frac{1}{c}\mathbf{e}\Big(\phi_k^{(m,\xi)}\Big) \tag{3.30}$$

which in this case is a vector pointing from an agent acting as anchor to the k-th VA of a cooperating agent. The proof for the final equality can be obtained graphically. The gradient matrix is $\mathbf{H}_{\mathrm{An}}^{(\xi,m)} = \mathbf{H}_{\mathrm{Ag}}^{(m,\xi)} = \mathbf{H}^{(\xi,\xi,m)} \in \mathbb{R}^{K^{(\xi,m)}\times 2}$.

3.4.2 Monostatic scenario

Here we restrict the VA set to $k = 2, \ldots, K^{(m,m)}$, the agent is as well the anchor, $\xi = m$, and both move synchronously, $\eta = m$, i.e., the two terms in (3.28) interact with each other. The

gradient

$$\mathbf{h}_k^{(m,m,m)} = \frac{\partial \tau_k^{(m,m)}}{\partial \mathbf{p}^{(m)}} = \frac{1}{c}\left(\mathbf{e}\Big(\phi_k^{(m,m)}\Big) - \mathbf{e}\Big((-1)^{Q_k^{(m)}}\phi_k^{(m,m)} + \Big)\right)$$
$$= \begin{cases} \frac{2}{c}\sin\left(\bar{\zeta}_k^{(m)}\right)\mathbf{e}\Big(\phi_k^{(m,m)} + \bar{\zeta}_k^{(m)} - \frac{\pi}{2}\Big) & \text{If } Q_k^{(m)}\text{is even} \\ \frac{2}{c}\sin\Big(\bar{\zeta}_k^{(m)} - \phi_k^{(m,m)}\Big)\mathbf{e}\Big(\bar{\zeta}_k^{(m)} - \frac{\pi}{2}\Big) & \text{If } Q_k^{(m)}\text{is odd} \end{cases} \tag{3.31}$$

has been decomposed—as shown in Appendix A.3—into a magnitude term $0 \leq \left\|\mathbf{h}_k^{(m,m,m)}\right\| \leq \frac{2}{c}$ and a resulting direction vector. Both depend on the angle $\phi_k^{(m,m)}$, the VA order, and the angles of all contributing walls comprised in $\bar{\zeta}_k^{(m)}$. The gradient matrix is $\mathbf{H}_{\text{Mo}}^{(m)} = \mathbf{H}^{(m,m,m)} \in \mathbb{R}^{(K^{(m,m)}-1)\times 2}$.

The following interpretations apply for the monostatic case: Single reflections ($Q_k^{(m)} = 1$, $\bar{\zeta}_k^{(m)} = \phi_k^{(m,m)} \pm \frac{\pi}{2}$) and reflections on rectangular corners ($Q_k^{(m)} = 2$, $\bar{\zeta}_k^{(m)} = \pm\frac{\pi}{2}$) constitute important types of monostatic VAs. Both have $\partial\tau_k^{(m,m)}/\partial\mathbf{p}^{(m)} = \frac{2}{c}\mathbf{e}(\phi_k^{(m,m)})$, which is twice as much spatial sensitivity of delays as in the bistatic cases (3.29) and (3.30), thus providing higher ranging information. The simplest case of a vanishing gradient (magnitude zero) is a second-order reflection between parallel walls ($Q_k^{(m)} = 2$, $\bar{\zeta}_k^{(m)} = 0$).

3.5 CRLB on the Position Error

In this Section, the CRLB on the position error is derived for the three scenarios Multipath-Sync, Multipath-NSync, and Multipath-Coop.

Using a stack vector $\mathbf{\Psi} = [\mathbf{T}^{\mathrm{T}}, \Re\mathbf{A}^{\mathrm{T}}, \Im\mathbf{A}^{\mathrm{T}}]^{\mathrm{T}}$ of the signal parameters for all relevant nodes, with $\mathbf{T}$ combining the delays and $\mathbf{A}$ combining the amplitudes, the Jacobian (3.3) has the following general structure.

$$\mathbf{J} = \frac{\partial\mathbf{\Psi}}{\partial\mathbf{\Theta}} = \begin{bmatrix} \mathbf{H} & \mathbf{L} & \mathbf{0} \\ \mathbf{0} & \mathbf{0} & \mathbf{I} \end{bmatrix} = \begin{bmatrix} \partial\mathbf{T}/\partial\mathbf{P} & \partial\mathbf{T}/\partial\boldsymbol{\epsilon} & \partial\mathbf{T}/\partial\Re\mathbf{A} & \partial\mathbf{T}/\partial\Im\mathbf{A} \\ \partial\Re\mathbf{A}/\partial\mathbf{P} & \partial\Re\mathbf{A}/\partial\boldsymbol{\epsilon} & \partial\Re\mathbf{A}/\partial\Re\mathbf{A} & \partial\Re\mathbf{A}/\partial\Im\mathbf{A} \\ \partial\Im\mathbf{A}/\partial\mathbf{P} & \partial\Im\mathbf{A}/\partial\boldsymbol{\epsilon} & \partial\Im\mathbf{A}/\partial\Re\mathbf{A} & \partial\Im\mathbf{A}/\partial\Im\mathbf{A} \end{bmatrix} \tag{3.32}$$

Vector $\mathbf{\Theta} = [\mathbf{P}^{\mathrm{T}}, \boldsymbol{\epsilon}^{\mathrm{T}}, \Re\mathbf{A}^{\mathrm{T}}, \Im\mathbf{A}^{\mathrm{T}}]^{\mathrm{T}}$, spatial delay gradient $\mathbf{H} = \partial\mathbf{T}/\partial\mathbf{P}$, and gradient $\mathbf{L} = \partial\mathbf{T}/\partial\boldsymbol{\epsilon}$ are specifically defined for the different cases in the following subsections.

3.5.1 Derivation of the CRLB for Multipath-Sync

Assuming that only one agent is present in Multipath-Sync and Multipath-NSync, we drop the agent index m so that $\mathbf{P} = \mathbf{p}$, and define $\mathcal{N}_j = \{1, 2, \ldots, J\}$. We use the geometry for the bistatic scenario, i.e. the first case in Section 3.4.1. The clock-offset $\boldsymbol{\epsilon}$ is considered to be known and zero. Using a suitable signaling scheme[17], measurements $\mathbf{r}^{(j)}$ from all J anchors are

[17] E.g. conventional multiple access schemes, like time division multiple access (TDMA).

independent. Hence, the log-likelihood function is defined as

$$\ln f(\mathbf{R};\boldsymbol{\Psi}) = \sum_{j\in\mathcal{N}_j} \ln f\big(\mathbf{r}^{(j)};\boldsymbol{\tau}^{(j)};\boldsymbol{\alpha}^{(j)}\big), \tag{3.33}$$

where $\mathbf{R} = \big[\big(\mathbf{r}^{(1)}\big)^{\mathrm{T}},\dots,\big(\mathbf{r}^{(J)}\big)^{\mathrm{T}}\big]^{\mathrm{T}}$ combines all measurements and $\boldsymbol{\tau}^{(j)}$ and $\boldsymbol{\alpha}^{(j)}$ are the delay and amplitude vectors respectively, corresponding to measurement $\mathbf{r}^{(j)}$. The Jacobian $\mathbf{J}$ has the following structure,

$$\mathbf{J} = \begin{bmatrix} \mathbf{H}^{(1)}_{K^{(1)}\times 2} & & \\ \vdots & & \\ \mathbf{H}^{(J)}_{K^{(J)}\times 2} & & \\ & & \mathbf{I}_{D_{\mathbf{I}}\times D_{\mathbf{I}}} \end{bmatrix}, \tag{3.34}$$

where zero-matrices in the off-diagonal blocks are skipped for clarity and $D_{\mathbf{I}} = 2\sum_{j=1}^{J} K^{(j)}$. The subblocks $\mathbf{H}^{(j)} = \mathbf{H}^{(j,1)}_{\mathrm{Ag}}$ account for the geometry as described in Section 3.4. Due to the independence of the measurements $\mathbf{r}^{(j)}$, the EFIMs $\boldsymbol{\mathcal{I}}^{(j)}_{\mathbf{p}}$ from the J different anchors are additive. Using Equation (3.2), we can write the EFIMs as

$$\boldsymbol{\mathcal{I}}_{\mathbf{p}} = \sum_{j\in\mathcal{N}_j} \big(\mathbf{H}^{(j)}\big)^{\mathrm{T}}\Big(\boldsymbol{\Lambda}^{(j)}_{\mathrm{A}} - \boldsymbol{\Lambda}^{(j)}_{\mathrm{B}}\big(\boldsymbol{\Lambda}^{(j)}_{\mathrm{C}}\big)^{-1}\big(\boldsymbol{\Lambda}^{(j)}_{\mathrm{B}}\big)^{\mathrm{T}}\Big)\mathbf{H}^{(j)} \tag{3.35}$$

where $\boldsymbol{\Lambda}^{(j)}_{\mathrm{A}}$, $\boldsymbol{\Lambda}^{(j)}_{\mathrm{B}}$, and $\boldsymbol{\Lambda}^{(j)}_{\mathrm{C}}$ are subblocks of $\boldsymbol{\mathcal{I}}^{(j)}_{\boldsymbol{\psi}}$ defined in (3.10). Expression (3.35) simplifies when we assume no path overlap (i.e. orthogonality) between signals from different VAs. In this case, $\boldsymbol{\Lambda}_{\mathrm{B}} = \mathbf{0}$ and $\boldsymbol{\Lambda}_{\mathrm{A}}$ will be diagonal, as discussed in Section 3.3.2, and we can write

$$\boldsymbol{\mathcal{I}}_{\mathbf{p}} = \sum_{j\in\mathcal{N}_j} \big(\mathbf{H}^{(j)}\big)^{\mathrm{T}}\boldsymbol{\Lambda}^{(j)}_{\mathrm{A}}\mathbf{H}^{(j)} \approx \frac{8\pi^2\beta^2}{c^2}\sum_{j\in\mathcal{N}_j}\sum_{k=1}^{K^{(j)}} \widetilde{\mathrm{SINR}}^{(j)}_k \mathbf{D}_{\mathrm{r}}(\phi^{(j)}_k) \tag{3.36}$$

where $\widetilde{\mathrm{SINR}}^{(j)}_k$ is the extended SINR (3.20) for the j-th anchor and

$$\mathbf{D}_{\mathrm{r}}(\phi^{(j)}_k) = \mathbf{e}(\phi^{(j)}_k)\mathbf{e}(\phi^{(j)}_k)^{\mathrm{T}} \tag{3.37}$$

is called ranging direction matrix (cf. [46]), a rank-one matrix with an eigenvector in direction of $\phi^{(j)}_k$. Valuable insight is gained from (3.36) and (3.18). In particular,

- Each VA (i.e. each deterministic MPC) adds some positive term to the equivalent Fisher information matrix (EFIM) in direction of $\phi^{(j)}_k$ and hence reduces the position error bound (PEB) in direction of $\phi^{(j)}_k$.
- The $\widetilde{\mathrm{SINR}}^{(j)}_k$ determines the magnitude of this contribution as discussed in Section 3.3.2 (cf. ranging intensity information (RII) in [46]). It is limited by diffuse multipath—an effect that reduces with increased bandwidth—and it can show a significant gain due to the interference whitening if the interference-to-noise ratio is large.
- The effective bandwidth β scales the EFIM. Any increase corresponds to a decreased PEB.

- The according PDF is described by a Gaussian multivariate RV with PDF $\mathcal{N}\left(\mathbf{p}, \boldsymbol{\mathcal{I}}_{\mathbf{p}}^{-1}\right)$
- Each geometrically modeled (deterministic) MPC delay $d_k^{(j)} = d(\mathbf{p}, \mathbf{a}_k^{(j)})$ yields additional position-related information which is quantified by its SINR value. In fact, the range $\hat{d}_k$ estimated from the k-th MPC has an error variance bounded by the inverse Fisher information of the corresponding distance [O6]

$$\mathrm{var}\left\{\hat{d}_k^{(j)}\right\} = \left(\sigma_{d,k}^{(j)}\right)^2 \geq \mathrm{J}_r^{-1}\left(d_k^{(j)}\right) = \frac{c^2}{\left(8\pi^2\beta^2\widetilde{\mathrm{SINR}}_k^{(j)}\right)}, \tag{3.38}$$

  i.e. the SINRs indicate the uncertainties of the MPC ranges described by the Gaussian RVs with PDF $\mathcal{N}\left(d_k^{(j)}, \mathrm{J}_r^{-1}\left(d_k^{(j)}\right)\right)$.

Discussion of *path overlap* (cf. (3.22)):

- $\tau_k - \tau_{k'} \ll T_\mathrm{p}$: In this case the MPCs can not be distinguished and the position-related information is entirely lost.
- $\tau_k - \tau_{k'} \approx T_\mathrm{p}$: In this case the MPCs are correlated, but the position-related information can still partly be used. The discrete-time formulation of the CRLB based on the likelihood function (3.5) can quantify this information gain. The FIM of the MPC delays described in (3.16) and (3.22) consider overlapping components. Obviously, the amount of information from these components is reduced by path overlap, but nevertheless they contribute position-related information.
- $\tau_k - \tau_{k'} \gg T_\mathrm{p}$: If this holds, the MPCs are considered to be orthogonal and (3.36) can be used if it holds for all $k \neq k'$.

3.5.2 Derivation of the CRLB for Multipath-NSync

Next we consider the same setup as before, but assume the clock offsets $\boldsymbol{\epsilon}$ to be unknown parameters. The differences between arrival times still provide position information in this case. When using multiple anchors, we distinguish two different scenarios where either the clocks of all anchors are synchronized among each other, or alternatively no synchronization is present at all. While this does not affect the signal parameter FIM, we need to take it into account when performing the parameter transformation. Apart from the partial derivatives $\mathbf{L} = \partial\mathbf{T}/\partial\boldsymbol{\epsilon}$, the terms of the Jacobian are identical for Multipath-Sync and Multipath-NSync, resulting in

$$\mathbf{J} = \begin{bmatrix} \mathbf{H}_{K^{(1)}\times 2}^{(1)} & \mathbf{L}_{K^{(1)}\times D_{\boldsymbol{\epsilon}}}^{(1)} & \\ \vdots & \vdots & \\ \mathbf{H}_{K^{(J)}\times 2}^{(J)} & \mathbf{L}_{K^{(J)}\times D_{\boldsymbol{\epsilon}}}^{(J)} & \\ & & \mathbf{I}_{D_\mathbf{I}\times D_\mathbf{I}} \end{bmatrix}, \tag{3.39}$$

where $\mathbf{L}^{(j)} = \partial\boldsymbol{\tau}^{(j)}/\partial\boldsymbol{\epsilon}$ and $D_{\boldsymbol{\epsilon}}$ is the length of $\boldsymbol{\epsilon}$.

Synchronized anchors: When assuming $\epsilon^{(1)} = \cdots = \epsilon^{(J)} = \epsilon$, the vector $\boldsymbol{\epsilon}$ reduces to $\boldsymbol{\epsilon} = \epsilon$. The derivatives of the arrival times with respect to the clock offset are then given by $\mathbf{L}_{\text{syn}}^{(j)} = \mathbf{l}^{(j)} = [1, \ldots, 1]^{\text{T}}$. Applying the parameter transformation and computing the block inverse similarly as in (3.35) leads to additivity of the 3×3 EFIMs $\boldsymbol{\mathcal{I}}_{\mathbf{p},\epsilon}^{(j)}$ for the extended parameter vector $[\mathbf{p}^{\text{T}}, \epsilon]^{\text{T}}$ (see Appendix A.4). When neglecting path overlap this expression simplifies to

$$\boldsymbol{\mathcal{I}}_{\mathbf{p},\epsilon} = \sum_{j \in \mathcal{N}_j} \boldsymbol{\mathcal{I}}_{\mathbf{p},\epsilon}^{(j)} = 8\pi^2 \beta^2 \sum_{j \in \mathcal{N}_j} \sum_{k=1}^{K^{(j)}} \widetilde{\text{SINR}}_k^{(j)} \mathbf{D}_{\text{r},\epsilon}(\phi_k^{(j)}), \tag{3.40}$$

with

$$\mathbf{D}_{\text{r},\epsilon}(\phi_k^{(j)}) = \mathbf{v}\mathbf{v}^{\text{T}}, \ \mathbf{v} = \left[\frac{1}{c}\cos(\phi_k^{(j)}), \ \frac{1}{c}\sin(\phi_k^{(j)}), \ 1\right]^{\text{T}}.$$

The inner sum in (3.40) reveals that the 3×3 EFIMs $\boldsymbol{\mathcal{I}}_{\mathbf{p},\epsilon}^{(j)}$ are in canonical form. Since $\mathbf{D}_{r,\epsilon}$ is a positive semidefinite matrix, it highlights that each VA adds information for the estimation of $\mathbf{p}$ and ϵ, scaled by its extended $\widetilde{\text{SINR}}_k$ and β.

The EFIM $\boldsymbol{\mathcal{I}}_{\mathbf{p}}$ can be computed from $\boldsymbol{\mathcal{I}}_{\mathbf{p},\epsilon}$ by again applying the blockwise inversion lemma. When neglecting path overlap, the expression for $\boldsymbol{\mathcal{I}}_{\mathbf{p}}$ becomes

$$\boldsymbol{\mathcal{I}}_{\mathbf{p}} = \frac{8\pi^2\beta^2}{c^2} \left[\sum_{j \in \mathcal{N}_j} \sum_{k=1}^{K^{(j)}} \widetilde{\text{SINR}}_k^{(j)} \mathbf{D}_{\text{r}}(\phi_k^{(j)}) - \boldsymbol{\mathcal{C}} \right], \tag{3.41}$$

where $\boldsymbol{\mathcal{C}}$ accounts for the (negative) influence of the clock offset estimation with

$$\boldsymbol{\mathcal{C}} = \frac{1}{\sum_{j \in \mathcal{N}_j} \sum_{k=1}^{K^{(j)}} \widetilde{\text{SINR}}_k^{(j)}} \mathbf{c}\mathbf{c}^{\text{T}},$$
$$\mathbf{c} = \sum_{j \in \mathcal{N}_j} \sum_{k=1}^{K^{(j)}} \widetilde{\text{SINR}}_k^{(j)} \mathbf{e}(\phi_k^{(j)}).$$

Note that Multipath-NSync can theoretically achieve equal performance as Multipath-Sync under the (rather unlikely) condition $\mathbf{c} = \mathbf{0}$. Otherwise $\boldsymbol{\mathcal{C}}$ reduces the information, and thereby increases the PEB.

Asynchronous anchors: When having $\epsilon^{(i)} \neq \epsilon^{(j)}$, $\forall i \neq j$, $i, j \in \mathcal{N}_j$, we stack all clock offsets in the vector $\boldsymbol{\epsilon} = [\epsilon^{(1)}, \ldots, \epsilon^{(J)}]^{\text{T}}$. The derivatives of the arrival times with respect to the clock offsets are then given by a gradient matrix $\mathbf{L} = \partial\mathbf{T}/\partial\boldsymbol{\epsilon}$ of size $\sum_{j \in \mathcal{N}_j} J^{(j)} \times J$ which stacks submatrices $\mathbf{L}_{\text{asyn}}^{(j)}$ with one nonzero column $[\mathbf{L}_{\text{asyn}}^{(j)}]_{i,j} = 1$, $i = 1, \ldots, J^{(j)}$. This leads to an additivity of the 2×2 EFIMs as shown in Appendix A.4, i.e. $\boldsymbol{\mathcal{I}}_{\mathbf{p}} = \sum_{j \in \mathcal{N}_j} \boldsymbol{\mathcal{I}}_{\mathbf{p}}^{(j)}$. When neglecting path overlap, $\boldsymbol{\mathcal{I}}_{\mathbf{p}}$ takes the form of (3.41), but with

$$\boldsymbol{\mathcal{C}} = \sum_{j \in \mathcal{N}_j} \frac{1}{\sum_{k=1}^{K^{(j)}} \widetilde{\text{SINR}}_k^{(j)}} \mathbf{c}^{(j)} \left(\mathbf{c}^{(j)}\right)^{\text{T}}, \tag{3.42}$$

$$\mathbf{c}^{(j)} = \sum_{k=1}^{K^{(j)}} \widetilde{\mathrm{SINR}}_k^{(j)} \mathbf{e}(\phi_k^{(j)}).$$

Again, equality with Multipath-Sync is obtained if each $\mathbf{c}^{(j)} = \mathbf{0}$, otherwise the PEB is increased.

3.5.3 Derivation of the CRLB for Multipath-Coop

We assume M agents $m \in \mathcal{N}_m = \{1, 2, \ldots, M\}$ and J fixed anchors $j \in \mathcal{N}_j = \{M+1, \ldots, M+J\}$, which cooperate with one another. As outlined in the introduction, every agent conducts a monostatic measurement, meaning it emits a pulse and receives the multipath signal reflected by the environment, and conventional bistatic measurements with all other agents and the fixed anchors. All measurements are distributed such that every agent is able to exploit information from any of its received and/or transmitted signals. The clock-offsets $\boldsymbol{\epsilon}$ are considered to be zero.

The signal parameter vectors for the (j,m)-th received signal $\mathbf{r}^{(j,m)}$ are defined as $\boldsymbol{\tau}^{(j,m)} = \left[\tau_1^{(j,m)}, \ldots, \tau_{K^{(j,m)}}^{(j,m)}\right]^{\mathrm{T}}$ and $\boldsymbol{\alpha}^{(j,m)} = \left[\alpha_1^{(j,m)}, \ldots, \alpha_{K^{(j,m)}}^{(j,m)}\right]^{\mathrm{T}}$. For deriving the cooperative EFIM, we stack positions $\mathbf{p}^{(m)}$ of the M agents into the vector

$$\mathbf{P} = \left[\left(\mathbf{p}^{(1)}\right)^{\mathrm{T}}, \ldots, \left(\mathbf{p}^{(M)}\right)^{\mathrm{T}}\right]^{\mathrm{T}} \in \mathbb{R}^{2M \times 1} \tag{3.43}$$

and all measurements $\mathbf{r}^{(j,m)}$ in the vector

$$\mathbf{R} = \left[\left(\mathbf{r}^{(1,1)}\right)^{\mathrm{T}}, \ldots, \left(\mathbf{r}^{(1,M)}\right)^{\mathrm{T}}, \ldots, \left(\mathbf{r}^{(M,M)}\right)^{\mathrm{T}}, \left(\mathbf{r}^{(M+1,1)}\right)^{\mathrm{T}}, \ldots, \left(\mathbf{r}^{(M+J,M)}\right)^{\mathrm{T}}\right]^{\mathrm{T}} \in \mathbb{C}^{D_{\mathbf{R}} \times 1}, \tag{3.44}$$

where $D_{\mathbf{R}} = NM(M+J)$. Further, we stack the signal parameters correspondingly in the vectors

$$\mathbf{T} = \left[\left(\boldsymbol{\tau}^{(1,1)}\right)^{\mathrm{T}}, \ldots, \left(\boldsymbol{\tau}^{(1,M)}\right)^{\mathrm{T}}, \ldots, \left(\boldsymbol{\tau}^{(M+J,M)}\right)^{\mathrm{T}}\right]^{\mathrm{T}} \tag{3.45}$$

and

$$\mathbf{A} = \left[\left(\boldsymbol{\alpha}^{(1,1)}\right)^{\mathrm{T}}, \ldots, \left(\boldsymbol{\alpha}^{(1,M)}\right)^{\mathrm{T}}, \ldots, \left(\boldsymbol{\alpha}^{(M+J,M)}\right)^{\mathrm{T}}\right]^{\mathrm{T}} \tag{3.46}$$

which have length $D_{\mathbf{T}} = D_{\mathbf{A}} = \sum_{j \in (\mathcal{N}_m \cup \mathcal{N}_j)} \sum_{m \in \mathcal{N}_m} K^{(j,m)}$ to construct vector $\boldsymbol{\Psi} = [\mathbf{T}^{\mathrm{T}}, \Re\mathbf{A}^{\mathrm{T}}, \Im\mathbf{A}^{\mathrm{T}}]^{\mathrm{T}}$. The corresponding joint log-likelihood function, assuming independent measurements $\mathbf{r}^{(j,m)}$ between the cooperating nodes, is defined as

$$\ln f(\mathbf{R}; \boldsymbol{\Psi}) = \sum_{j \in (\mathcal{N}_m \cup \mathcal{N}_j)} \sum_{m \in \mathcal{N}_m} \ln f\left(\mathbf{r}^{(j,m)}; \boldsymbol{\tau}^{(j,m)}; \boldsymbol{\alpha}^{(j,m)}\right). \tag{3.47}$$

The EFIM $\boldsymbol{\mathcal{I}}_{\mathbf{P}}$ is described by (see Appendix A.5)

$$\boldsymbol{\mathcal{I}}_{\mathbf{P}} = \sum_{j \in (\mathcal{N}_m \cup \mathcal{N}_j)} \sum_{m \in \mathcal{N}_m} \left(\mathbf{H}^{(j,m)}\right)^{\mathrm{T}} \boldsymbol{\Lambda}^{(j,m)} \mathbf{H}^{(j,m)} \tag{3.48}$$

where

$$\mathbf{\Lambda}^{(j,m)} = \mathbf{\Lambda}_{\mathrm{A}}^{(j,m)} - \mathbf{\Lambda}_{\mathrm{B}}^{(j,m)} \big(\mathbf{\Lambda}_{\mathrm{C}}^{(j,m)}\big)^{-1} \big(\mathbf{\Lambda}_{\mathrm{B}}^{(j,m)}\big)^{\mathrm{T}} \tag{3.49}$$

yields the sub-blocks $\boldsymbol{\mathcal{I}}_{\boldsymbol{\psi}}^{(j,m)}$ of the FIM for the likelihood function (3.47), for independent measurements, and $\mathbf{H}^{(j,m)}$ are the spatial delay gradients[18] of the Jacobian

$$\mathbf{J} = \begin{bmatrix} \mathbf{H}_{K^{(1,1)}\times 2M}^{(1,1)} & & \\ \vdots & & \\ \mathbf{H}_{K^{(1,M)}\times 2M}^{(1,M)} & & \\ \vdots & & \\ \mathbf{H}_{K^{(M+J,M)}\times 2M}^{(M+J,M)} & & \\ & & \mathbf{I}_{D_{\mathbf{I}}\times D_{\mathbf{I}}} \end{bmatrix}, \tag{3.50}$$

where $D_{\mathbf{I}} = 2D_{\mathbf{A}}$.[19] As shown in Appendix A.5, one gets the following final result for the EFIM $\boldsymbol{\mathcal{I}}_{\mathbf{p}}$ for all agents

$$\boldsymbol{\mathcal{I}}_{\mathbf{P}} = \begin{bmatrix} \boldsymbol{\mathcal{I}}_{\mathrm{Mo}}^{(1)} + 2\boldsymbol{\mathcal{I}}_{\mathrm{Ag}}^{(1)} + \boldsymbol{\mathcal{I}}_{\mathrm{An}}^{(1)} & 2\boldsymbol{\mathcal{I}}_{\mathrm{C}}^{(1,2)} & \dots & 2\boldsymbol{\mathcal{I}}_{\mathrm{C}}^{(1,M)} \\ 2\boldsymbol{\mathcal{I}}_{\mathrm{C}}^{(2,1)} & \ddots & & \\ \vdots & & & \\ 2\boldsymbol{\mathcal{I}}_{\mathrm{C}}^{(M,1)} & & \boldsymbol{\mathcal{I}}_{\mathrm{Mo}}^{(M)} + 2\boldsymbol{\mathcal{I}}_{\mathrm{Ag}}^{(M)} + \boldsymbol{\mathcal{I}}_{\mathrm{An}}^{(M)} \end{bmatrix}. \tag{3.51}$$

The diagonal blocks $\boldsymbol{\mathcal{I}}_{\mathrm{Ag}}^{(\eta)} = \sum_{m\in\mathcal{N}_m\setminus\{\eta\}} \big(\mathbf{H}_{\mathrm{Ag}}^{(m,\eta)}\big)^{\mathrm{T}} \mathbf{\Lambda}^{(m,\eta)} \mathbf{H}_{\mathrm{Ag}}^{(m,\eta)}$ account for the bistatic measurements between agent η and all other agents, $\boldsymbol{\mathcal{I}}_{\mathrm{An}}^{(\eta)} = \sum_{j\in\mathcal{N}_j} \big(\mathbf{H}_{\mathrm{Ag}}^{(j,\eta)}\big)^{\mathrm{T}} \mathbf{\Lambda}^{(j,\eta)} \mathbf{H}_{\mathrm{Ag}}^{(j,\eta)}$ account for the bistatic measurements between agent η and all fixed anchors, and $\boldsymbol{\mathcal{I}}_{\mathrm{Mo}}^{(\eta)} = \big(\mathbf{H}_{\mathrm{Mo}}^{(\eta)}\big)^{\mathrm{T}} \mathbf{\Lambda}^{(\eta,\eta)} \mathbf{H}_{\mathrm{Mo}}^{(\eta)}$ account for the monostatic measurement of agent η.
The off-diagonal blocks $\boldsymbol{\mathcal{I}}_{\mathrm{C}}^{(\eta,\eta')} = \big(\mathbf{H}_{\mathrm{Ag}}^{(\eta',\eta)}\big)^{\mathrm{T}} \mathbf{\Lambda}^{(\eta',\eta)} \mathbf{H}_{\mathrm{Ag}}^{(\eta,\eta')}$ account for the uncertainty about the cooperating agents in their role as anchors (cf. (A.39) and (A.40)). This has a negative effect on the localization performance of the agents. The factors of two in (3.51), related to the EFIM of measurements inbetween agents, results from the fact that those measurements are performed twice. This simplifies the notations in this section. If such repeated measurements are avoided, the same result would apply but with these factors removed. Finally, the PEB of agent η at position $\mathbf{p}^{(\eta)}$ is given as

$$\mathcal{P}\{\mathbf{p}^{(\eta)}\} = \sqrt{\mathrm{tr}\left\{ \big[\boldsymbol{\mathcal{I}}_{\mathbf{P}}^{-1}\big]_{2\times 2}^{(\eta,\eta)} \right\}}. \tag{3.52}$$

[18] Multipath-Coop can be seen as the most general setup, if clock offset issues are also included. This can be done by combining the results of Multipath-NSync and Multipath-Coop by replacing $\mathbf{H}^{(j,m)}$ with $\mathbf{G}^{(j,m)} = [\mathbf{H}^{(j,m)}, \mathbf{L}^{(j,m)}]$ (see Appendix A.4), which accounts for the geometry and clock offset. For monostatic measurements $\mathbf{L}^{m,m} = \mathbf{0}$.

[19] Assuming no path overlap, (3.49) can be simplified as in (3.36), using the result from Appendix A.1.2.

3.6 Additional Analyses

3.6.1 Derivation of the Bayesian Cramér Rao Lower Bound (BCRLB) considering Anchors and VAs with Uncertainties

Again, the Multipath-Sync scenario is studied in this section. In order to understand the effect of uncertainty of the VA positions on the CRLB of the agent position, it is helpful to look at (2.10). One can observe that the uncertainty in the VA positions have to be marginalized out, in order to study the uncertainty of the agent position. That means in the context of the Bayesian Cramér Rao lower bound (BCRLB) that after taking the expectation over the measured data and the probabilistic parameter vector, the proper sub-Fisher information matrix (FIM) has to be considered. The position-related parameter vector now also contains the anchors and the according VAs $\boldsymbol{\theta} = [\mathbf{p}^{\mathrm{T}},\ \mathcal{A}^{\mathrm{T}}\ , \Re\mathbf{A}^{\mathrm{T}},\ \Im\mathbf{A}^{\mathrm{T}}]^{\mathrm{T}}$, where the agent position $\mathbf{p}$, the anchor positions $\mathbf{a}_1^{(j)}$ and the VA positions $\mathbf{a}_k^{(j)}$ are RVs. For notational convenience, the anchors and the according VAs are comprised in the set $\mathcal{A} = \left\{\mathcal{A}^{(j)}\right\}_{j=1}^{J} = \left\{\mathbf{a}_k^{(j)}\right\}_{k=1}^{K^{(j)}}$. The dimension of the parameter vector $\boldsymbol{\theta}$ is defined as $D_{\boldsymbol{\theta}} = 2 + 2\sum_{j=1}^{J} K^{(j)} + 2K$. The corresponding Bayesian FIM $\boldsymbol{\mathcal{I}}_{\boldsymbol{\theta}}$ of $\boldsymbol{\theta}$ is computed from the joint posterior PDF,

$$\begin{aligned} p\big(\mathbf{p}, \mathcal{A}|\mathbf{R}\big) &\propto p\big(\mathbf{R}|\mathbf{p}, \mathcal{A}; \mathbf{A}; \mathbf{T}\big) p\big(\mathbf{p}, \mathcal{A}\big) \\ &= \prod_{j=1}^{J} p\big(\mathbf{r}^{(j)}|\mathbf{p}, \mathcal{A}^{(j)}; \boldsymbol{\alpha}^{(j)}; \boldsymbol{\tau}^{(j)}\big) p\big(\mathbf{p}, \mathcal{A}^{(j)}\big) \end{aligned} \tag{3.53}$$

where $\mathbf{R}$, $\mathbf{A}$ and $\mathbf{T}$ are the stacked vector of the received signals $\mathbf{r}^{(j)}$ and of the according complex MPC amplitudes and delays, respectively. The received signals $\mathbf{r}^{(j)}$ from different anchors are supposed to be statistically independent. The Bayesian FIM is given as

$$\begin{aligned} \boldsymbol{\mathcal{I}}_{\boldsymbol{\theta}} &= \mathbb{E}_{\mathbf{r},\boldsymbol{\theta}} \left\{ \left[\frac{\partial}{\partial \boldsymbol{\theta}} \ln p\big(\mathbf{p}, \mathcal{A}|\mathbf{R}\big) \right] \left[\frac{\partial}{\partial \boldsymbol{\theta}} \ln p\big(\mathbf{p}, \mathcal{A}|\mathbf{R}\big) \right]^{\mathrm{T}} \right\} \\ &= \mathbb{E}_{\mathbf{r},\boldsymbol{\theta}} \left\{ \left[\frac{\partial}{\partial \boldsymbol{\theta}} \ln p\big(\mathbf{R}|\mathbf{p}, \mathcal{A}; \mathbf{A}; \mathbf{T}\big) \right] \left[\frac{\partial}{\partial \boldsymbol{\theta}} \ln p\big(\mathbf{R}|\mathbf{p}, \mathcal{A}; \mathbf{A}; \mathbf{T}\big) \right]^{\mathrm{T}} \right\} \\ &\quad + \mathbb{E}_{\boldsymbol{\theta}} \left\{ \left[\frac{\partial}{\partial \boldsymbol{\theta}} \ln p\big(\mathbf{p}, \mathcal{A}\big) \right] \left[\frac{\partial}{\partial \boldsymbol{\theta}} \ln p\big(\mathbf{p}, \mathcal{A}\big) \right]^{\mathrm{T}} \right\}. \end{aligned} \tag{3.54}$$

With the Jacobian (3.3), again a affine transformation can be done from the channel parameters to the position-related parameters, yielding

$$\boldsymbol{\mathcal{I}}_{\boldsymbol{\theta}} = \mathbb{E}_{\boldsymbol{\theta}} \left\{ \mathbf{J}^{\mathrm{T}} \boldsymbol{\mathcal{I}}_{\boldsymbol{\psi}} \mathbf{J} \right\} + \boldsymbol{\mathcal{I}}_{\boldsymbol{\theta}}^{\mathrm{prior}} = \bar{\boldsymbol{\mathcal{I}}}_{\mathbf{p},\mathcal{A}} + \boldsymbol{\mathcal{I}}_{\boldsymbol{\theta}}^{\mathrm{prior}}, \tag{3.55}$$

where the difference to (3.2) is that also the expectation over the probabilistic parameters $\mathbf{p}$ and $\mathbf{a}_k^{(j)}$ in $\boldsymbol{\theta}$ has to be computed. The first summand defines the relation between the channel parameters $\boldsymbol{\psi}$ and the positions of the agent and the anchors with according VAs. The second summand $\boldsymbol{\mathcal{I}}_{\boldsymbol{\theta}}^{\mathrm{prior}}$ is the FIM of the prior PDFs of the agent and the anchors with according VAs. It is a block diagonal matrix, where the first 2×2 block holds the prior FIM of agent position $\boldsymbol{\mathcal{I}}_{\mathbf{p}}^{\mathrm{prior}}$ and the next K 2×2 blocks hold the prior FIMs of the j-th anchor and the according VA

positions $\boldsymbol{\mathcal{I}}_{\mathcal{A}^{(j)}}^{\text{prior}}$, yielding

$$\boldsymbol{\mathcal{I}}_{\boldsymbol{\theta}}^{\text{prior}} = \text{diag}\Big(\boldsymbol{\mathcal{I}}_{\mathbf{p}}^{\text{prior}},\, \boldsymbol{\mathcal{I}}_{\mathcal{A}^1}^{\text{prior}},\, \ldots,\, \boldsymbol{\mathcal{I}}_{\mathcal{A}^J}^{\text{prior}},\, \mathbf{0}_{2K\times 2K}\Big). \tag{3.56}$$

The Jacobian $\mathbf{J}$ is define as

$$\mathbf{J} = \begin{bmatrix} \mathbf{H}_{\text{Ag}}^{(1,1)} & \mathbf{H}_{\text{An}}^{(1,1)} & & & \\ \vdots & & \ddots & & \\ \mathbf{H}_{\text{Ag}}^{(J,1)} & & & \mathbf{H}_{\text{An}}^{(J,1)} & \\ & & & & \mathbf{I}_{D_{\mathbf{I}}\times D_{\mathbf{I}}} \end{bmatrix}, \tag{3.57}$$

where $D_{\mathbf{I}} = 2\sum_{j=1}^{J} K^{(j)}$ and $\mathbf{H}_{\text{Ag}}^{(j,1)} \in \mathbb{R}^{K^{(j)}\times 2}$ and $\mathbf{H}_{\text{An}}^{(j,1)} \in \mathbb{R}^{K^{(j)}\times 2}$ comprise the delay gradients of the j-th anchor w.r.t. the agent position and w.r.t. the anchor and VA positions. When neglecting path overlap, the Bayesian FIM $\bar{\boldsymbol{\mathcal{I}}}_{\mathbf{p},\mathcal{A}}$ (without the prior FIMs) of the agent and the anchors with VA positions become

$$\begin{aligned} \bar{\boldsymbol{\mathcal{I}}}_{\mathbf{p},\mathcal{A}} &= \mathbb{E}_{\boldsymbol{\theta}}\left\{ \begin{bmatrix} \mathbf{A}_{2\times 2} & \mathbf{B}_{2\times 2J} \\ \mathbf{B}_{2\times 2J}^{\text{T}} & \mathbf{C}_{2J\times 2J} \end{bmatrix} \right\} \\ &= \mathbb{E}_{\boldsymbol{\theta}}\left\{ \begin{bmatrix} \sum_{j\in\mathcal{N}_j} \left(\mathbf{H}_{\text{Ag}}^{j,1}\right)^{\text{T}} \boldsymbol{\Lambda}_{\text{A}}^{(j)} \mathbf{H}_{\text{Ag}}^{j,1} & \left(\mathbf{H}_{\text{Ag}}^{(1,1)}\right)^{\text{T}} \boldsymbol{\Lambda}_{\text{A}}^{(1)} \mathbf{H}_{\text{An}}^{(1,1)} & \cdots & \left(\mathbf{H}_{\text{Ag}}^{(J,1)}\right)^{\text{T}} \boldsymbol{\Lambda}_{\text{A}}^{(J)} \mathbf{H}_{\text{An}}^{(J,1)} \\ \left(\mathbf{H}_{\text{An}}^{(1,1)}\right)^{\text{T}} \boldsymbol{\Lambda}_{\text{A}}^{(1)} \mathbf{H}_{\text{Ag}}^{(1,1)} & \left(\mathbf{H}_{\text{An}}^{(1,1)}\right)^{\text{T}} \boldsymbol{\Lambda}_{\text{A}}^{(1)} \mathbf{H}_{\text{An}}^{(1,1)} & & \\ \cdots & & \ddots & \\ \left(\mathbf{H}_{\text{An}}^{(J,1)}\right)^{\text{T}} \boldsymbol{\Lambda}_{\text{A}}^{(J)} \mathbf{H}_{\text{Ag}}^{(J,1)} & & & \left(\mathbf{H}_{\text{An}}^{(J,1)}\right)^{\text{T}} \boldsymbol{\Lambda}_{\text{A}}^{(J)} \mathbf{H}_{\text{An}}^{(J,1)} \end{bmatrix} \right\}. \end{aligned} \tag{3.58}$$

Using the Schur complement the EFIM of the agent position yields

$$\begin{aligned} \boldsymbol{\mathcal{I}}_{\mathbf{p}} &= \boldsymbol{\mathcal{I}}_{\mathbf{p}}^{\text{prior}} + \mathbf{A}_{2\times 2} - \mathbf{B}_{2\times 2J}\mathbf{C}_{2J\times 2J}^{-1}\mathbf{B}_{2\times 2J}^{\text{T}} = \boldsymbol{\mathcal{I}}_{\mathbf{p}}^{\text{prior}} + \mathbb{E}_{\boldsymbol{\theta}}\left\{ \sum_{j\in\mathcal{N}_j} \underbrace{\left(\mathbf{H}_{\text{Ag}}^{j,1}\right)^{\text{T}} \boldsymbol{\Lambda}_{\text{A}}^{(j)} \mathbf{H}_{\text{Ag}}^{j,1}}_{(I)} \right\} \\ &\quad - \mathbb{E}_{\boldsymbol{\theta}}\left\{ \sum_{j\in\mathcal{N}_j} \underbrace{\left(\mathbf{H}_{\text{Ag}}^{(j,1)}\right)^{\text{T}} \boldsymbol{\Lambda}_{\text{A}}^{(j)} \mathbf{H}_{\text{An}}^{(j,1)}}_{(II)} \left(\boldsymbol{\mathcal{I}}_{\mathcal{A}^{(j)}}^{\text{prior}} + \underbrace{\left(\mathbf{H}_{\text{An}}^{(j,1)}\right)^{\text{T}} \boldsymbol{\Lambda}_{\text{A}}^{(j)} \mathbf{H}_{\text{An}}^{(j,1)}}_{(III)} \right)^{-1} \underbrace{\left(\mathbf{H}_{\text{An}}^{(j,1)}\right)^{\text{T}} \boldsymbol{\Lambda}_{\text{A}}^{(j)} \mathbf{H}_{\text{Ag}}^{(j,1)}}_{(VI)} \right\} \\ &\overset{(a)}{=} \boldsymbol{\mathcal{I}}_{\mathbf{p}}^{\text{prior}} + \mathbb{E}_{\boldsymbol{\theta}}\left\{ \sum_{j\in\mathcal{N}_j} \left(\mathbf{H}_{\text{Ag}}^{j,1}\right)^{\text{T}} \boldsymbol{\Lambda}_{\text{A}}^{(j)} \mathbf{H}_{\text{Ag}}^{j,1} \right\} \\ &\quad - \mathbb{E}_{\boldsymbol{\theta}}\left\{ \sum_{j\in\mathcal{N}_j} \left(\mathbf{H}_{\text{Ag}}^{j,1}\right)^{\text{T}} \boldsymbol{\Lambda}_{\text{A}}^{(j)} \mathbf{H}_{\text{Ag}}^{j,1} \left(\boldsymbol{\mathcal{I}}_{\mathcal{A}^{(j)}}^{\text{prior}} + \left(\mathbf{H}_{\text{Ag}}^{j,1}\right)^{\text{T}} \boldsymbol{\Lambda}_{\text{A}}^{(j)} \mathbf{H}_{\text{Ag}}^{j,1} \right)^{-1} \left(\mathbf{H}_{\text{Ag}}^{j,1}\right)^{\text{T}} \boldsymbol{\Lambda}_{\text{A}}^{(j)} \mathbf{H}_{\text{Ag}}^{j,1} \right\} \end{aligned} \tag{3.59}$$

where $\boldsymbol{\mathcal{I}}_{\mathcal{A}^{(j)}}^{\text{prior}}$ is the joint prior FIM of the j-th anchor with according VAs. The identity (a) holds because (i) the geometry cross terms $\mathbf{H}_{\text{Ag}}^{(j,1)}$ and $\mathbf{H}_{\text{An}}^{(j,1)}$ in (II) and (IV) between agent and anchor/VAs just differ in the sign to (I), and (ii) the anchor geometry terms in (III) are the same as in (I). The first two summands in (3.59) describe the overly optimistic lower bound when there are no uncertainties in the anchor and VA positions. This position-related information is

reduced by the amount of information that is needed to estimate the anchor and VA positions as it is comprised in the second summand. As one can see, when the prior information of the VA positions $\boldsymbol{\mathcal{I}}_{\mathbf{a}_k^{(j)}}^{\text{prior}}$ is increased, the position-related information loss is reduced.

To gain better insights into (3.59), we assume that all anchors in $\mathcal{N}^{(j)}$ have exactly known positions. Since, the floor plan geometry is supposed to be imprecise, all VAs have to have uncertainties in their positions $\mathbf{a}_k^{(j)}$. Using the Woodbury identity[20] and assuming no path overlap as for the Multipath-Sync scenario in Section 3.5, the EFIM in (3.59) can be rewritten as

$$\boldsymbol{\mathcal{I}}_{\mathbf{p}} = \underbrace{\boldsymbol{\mathcal{I}}_{\mathbf{p}}^{\text{prior}}}_{(I)} + \underbrace{\sum_{j\in\mathcal{N}^{(j)}} \mathbb{E}_{\mathbf{p}}\left\{\frac{8\pi^2\beta^2}{c^2}\widetilde{\text{SINR}}_1^{(j)}\mathbf{D}_{\text{r}}(\phi_1^{(j)})\right\}}_{(II)} + \underbrace{\sum_{j\in\mathcal{N}^{(j)}}\sum_{k=2}^{K^{(j)}}\left(\left(\boldsymbol{\mathcal{I}}_{\mathbf{a}_k^{(j)}}^{\text{prior}}\right)^{-1} + \mathbb{E}_{\boldsymbol{\theta}}\left\{\frac{8\pi^2\beta^2}{c^2}\widetilde{\text{SINR}}_k^{(j)}\mathbf{D}_{\text{r}}(\phi_k^{(j)})\right\}^{-1}\right)^{-1}}_{(III)}, \tag{3.60}$$

where $\boldsymbol{\mathcal{I}}_{\mathbf{a}_k^{(j)}}^{\text{prior}}$ is the FIM for the k-th VA of the j-th anchor. To wrap up the final findings, we describe the individual terms of (3.60): (I) holds the prior FIM of the agent, (II) defines the EFIM of the anchors, hence the expectation $\mathbb{E}_{\boldsymbol{\theta}}\{\cdot\}$ has to be evaluated just for the agent PDF $p(\mathbf{p})$ and (III) comprises the EFIMs of the VAs. In this case the expectation $\mathbb{E}_{\boldsymbol{\theta}}\{\cdot\}$ has to be computed for the joint PDF $p(\mathbf{p}, \mathcal{A}^{(j)})$ of the agent and the VAs of all anchors. Equation (3.60) shows also nicely what is happening when the floor plan again is assumed to be precisely known. If so, the EFIMs $\boldsymbol{\mathcal{I}}_{\mathbf{a}_k^{(j)}}^{\text{prior}} \to \infty$ and hence (II) and (III) fuse to one term again. The expectation $\mathbb{E}_{\boldsymbol{\theta}}\{\cdot\}$ again has to be evaluated just for the agent PDF $p(\mathbf{p})$. Assuming further an uniform PDF over the floor plan for the prior of the agent, (3.60) reduces to (3.36), the EFIM of the "classical" Multipath-Sync setup.

3.6.2 CRLB with unknown Noise Covariance Matrix

If it is assumed that the noise covariance matrix is unknown, the parameters of the PDP and the AWGN have also to be estimated. We call this measurement setup from now on *MultipathPDP-Sync*. The according FIM for the complex signal $\mathbf{r}_{\text{det},\widetilde{\boldsymbol{\psi}}}$ is then given as [14]

$$\left[\boldsymbol{\mathcal{I}}(\widetilde{\boldsymbol{\psi}})\right]_{ij} = \underbrace{2\Re\left\{\left(\frac{\partial \mathbf{r}_{\text{det},\widetilde{\boldsymbol{\psi}}}}{\partial\widetilde{\psi}_i}\right)^{\text{H}}\mathbf{C}_{\mathbf{r}}(\widetilde{\boldsymbol{\psi}})^{-1}\left(\frac{\partial \mathbf{r}_{\text{det},\widetilde{\boldsymbol{\psi}}}}{\partial\widetilde{\psi}_j}\right)\right\}}_{(I)} + \underbrace{\text{tr}\left[\mathbf{C}_{\mathbf{r}}(\widetilde{\boldsymbol{\psi}})^{-1}\frac{\partial\mathbf{C}_{\mathbf{r}}(\widetilde{\boldsymbol{\psi}})}{\partial\widetilde{\psi}_i}\mathbf{C}_{\mathbf{r}}(\widetilde{\boldsymbol{\psi}})^{-1}\frac{\partial\mathbf{C}_{\mathbf{r}}(\widetilde{\boldsymbol{\psi}})}{\partial\widetilde{\psi}_j}\right]}_{(II)}, \tag{3.61}$$

[20] $(A+UCV)^{-1} = A^{-1} - A^{-1}U\left(C^{-1}+VA^{-1}U\right)^{-1}VA^{-1}$

where $\widetilde{\boldsymbol{\psi}} = [\boldsymbol{\psi}^{\mathrm{T}}, {\sigma_{\mathrm{n}}}^2, \boldsymbol{\Gamma}_{\nu}^{\mathrm{T}}]^{\mathrm{T}}$ is the extended parameter vector and $\mathbf{C}_{\mathbf{r}}(\widetilde{\boldsymbol{\psi}}) = {\sigma_{\mathrm{n}}}^2\mathbf{I}_N + \mathbf{C}_{\mathbf{c}}(\widetilde{\boldsymbol{\psi}})$ is the parametrized noise co-variance matrix. The covariance matrix of DM $\mathbf{C}_{\mathbf{c}}(\widetilde{\boldsymbol{\psi}})$ is defined using a parametrized DM PDP $S_{\nu}(\tau, \widetilde{\boldsymbol{\psi}})$. Thus, the parameter vector $\boldsymbol{\Gamma}_{\nu}$ depends on the used PDP model. The first term (I) in (3.61) is described by (3.10), accounting for the deterministic model parameters, only that it is filled up with additional zeros to account for the dimensions of ${\sigma_{\mathrm{n}}}^2 \in \mathbb{R}^1$ and $\boldsymbol{\Gamma}_{\nu} \in \mathbb{R}^{D_{\boldsymbol{\Gamma}_{\nu}}}$. The second term (II) holds the FIM of the DM PDP and the AWGN parameters. Hence, the overall FIM is described by

$$\begin{aligned}\boldsymbol{\mathcal{I}}_{\widetilde{\boldsymbol{\psi}}} &= \begin{bmatrix} \boldsymbol{\Lambda}_{\mathrm{A}} & \boldsymbol{\Lambda}_{\mathrm{B}} & \mathbf{0} \\ \boldsymbol{\Lambda}_{\mathrm{B}}^{\mathrm{T}} & \boldsymbol{\Lambda}_{\mathrm{C}} & \mathbf{0} \\ \mathbf{0} & \mathbf{0} & \mathbf{0} \end{bmatrix} + \begin{bmatrix} \boldsymbol{\Gamma}_A & \mathbf{0} & \boldsymbol{\Gamma}_B \\ \mathbf{0} & \mathbf{0} & \mathbf{0} \\ \boldsymbol{\Gamma}_B^{\mathrm{T}} & \mathbf{0} & \boldsymbol{\Gamma}_C \end{bmatrix} = \begin{bmatrix} \bar{\boldsymbol{\Lambda}}_A + \boldsymbol{\Gamma}_A & \begin{bmatrix} \boldsymbol{\Lambda}_B & \boldsymbol{\Gamma}_B \end{bmatrix} \\ \begin{bmatrix} \boldsymbol{\Lambda}_B \\ \boldsymbol{\Gamma}_B \end{bmatrix} & \begin{bmatrix} \boldsymbol{\Lambda}_{\mathrm{C}} & \mathbf{0} \\ \mathbf{0} & \boldsymbol{\Gamma}_C \end{bmatrix} \end{bmatrix} \\ &= \begin{bmatrix} \bar{\boldsymbol{\Lambda}}_{\mathrm{A}} & \bar{\boldsymbol{\Lambda}}_{\mathrm{B}} \\ (\bar{\boldsymbol{\Lambda}}_{\mathrm{B}})^{\mathrm{T}} & \bar{\boldsymbol{\Lambda}}_{\mathrm{C}} \end{bmatrix} \end{aligned} \tag{3.62}$$

where matrix elements $\boldsymbol{\Gamma}_A \in \mathbb{R}^{K\times K}$ contains the derivatives w.r.t. the MPC delays, $\boldsymbol{\Gamma}_B \in \mathbb{R}^{1+K\times D_{\boldsymbol{\Gamma}_{\nu}}}$ the cross derivatives w.r.t. the MPC delays and the DM/AWGN parameters and $\boldsymbol{\Gamma}_C \in \mathbb{R}^{D_{\boldsymbol{\Gamma}_{\nu}}+1\times D_{\boldsymbol{\Gamma}_{\nu}}+1}$ w.r.t. the DM/AWGN parameters, written as

$$[\boldsymbol{\Gamma}_A]_{k,k'} = \mathrm{tr}\left[{\mathbf{C}_{\mathbf{r}}}^{-1}\bar{\mathbf{S}}^{\mathrm{H}}\frac{\partial \mathbf{S}_{\nu}}{\partial \tau_k}\bar{\mathbf{S}}{\mathbf{C}_{\mathbf{r}}}^{-1}\bar{\mathbf{S}}^{\mathrm{H}}\frac{\partial \mathbf{S}_{\nu}}{\partial \tau_{k'}}\bar{\mathbf{S}}\right] \tag{3.63}$$

$$[\boldsymbol{\Gamma}_B]_{k,1} = \mathrm{tr}\left[{\mathbf{C}_{\mathbf{r}}}^{-1}\bar{\mathbf{S}}^{\mathrm{H}}\frac{\partial \mathbf{S}_{\nu}}{\partial \tau_k}\bar{\mathbf{S}}{\mathbf{C}_{\mathbf{r}}}^{-1}\right] \tag{3.64}$$

$$[\boldsymbol{\Gamma}_B]_{k,1+j} = \mathrm{tr}\left[{\mathbf{C}_{\mathbf{r}}}^{-1}\bar{\mathbf{S}}^{\mathrm{H}}\frac{\partial \mathbf{S}_{\nu}}{\partial \tau_k}\bar{\mathbf{S}}{\mathbf{C}_{\mathbf{r}}}^{-1}\bar{\mathbf{S}}^{\mathrm{H}}\frac{\partial \mathbf{S}_{\nu}}{\partial \theta_{\nu,j}}\bar{\mathbf{S}}\right] \tag{3.65}$$

$$[\boldsymbol{\Gamma}_C]_{1,1} = \mathrm{tr}\left[{\mathbf{C}_{\mathbf{r}}}^{-2}\right] \tag{3.66}$$

$$[\boldsymbol{\Gamma}_C]_{1,1+i} = \mathrm{tr}\left[{\mathbf{C}_{\mathbf{r}}}^{-1}{\mathbf{C}_{\mathbf{r}}}^{-1}\bar{\mathbf{S}}^{\mathrm{H}}\frac{\partial \mathbf{S}_{\nu}}{\partial \theta_{\nu,i}}\bar{\mathbf{S}}\right] \tag{3.67}$$

$$[\boldsymbol{\Gamma}_C]_{1+i,1+j} = \mathrm{tr}\left[{\mathbf{C}_{\mathbf{r}}}^{-1}\bar{\mathbf{S}}^{\mathrm{H}}\frac{\partial \mathbf{S}_{\nu}}{\partial \theta_{\nu,i}}\bar{\mathbf{S}}{\mathbf{C}_{\mathbf{r}}}^{-1}\bar{\mathbf{S}}^{\mathrm{H}}\frac{\partial \mathbf{S}_{\nu}}{\partial \theta_{\nu,j}}\bar{\mathbf{S}}\right], \tag{3.68}$$

where the derivatives of $S_{\nu}(\tau)$ w.r.t. the channel parameters that are needed for computing the different blocks of the FIMs in (3.63)-(3.68) can be found in Appendix A.1.4. The EFIM for MultipathPDP-Sync on the position error is defined as

$$\boldsymbol{\mathcal{I}}_{\mathbf{p}} = \sum_{j\in\mathcal{N}_j}\left(\mathbf{H}^{(j)}\right)^{\mathrm{T}}\Big(\bar{\boldsymbol{\Lambda}}_{\mathrm{A}}^{(j)} - \bar{\boldsymbol{\Lambda}}_{\mathrm{B}}^{(j)}\big(\bar{\boldsymbol{\Lambda}}_{\mathrm{C}}^{(j)}\big)^{-1}\big(\bar{\boldsymbol{\Lambda}}_{\mathrm{B}}^{(j)}\big)^{\mathrm{T}}\Big)\mathbf{H}^{(j)}. \tag{3.69}$$

If orthogonality between the MPCs—but a nonstationary PDP—is assumed, $\boldsymbol{\Lambda}_{\mathrm{A}}$ of Multipath-Sync is defined by (3.23). Using a DM PDP model with one cluster that starts at LOS delay τ_1 and neglecting all other noise parameter, only $[\boldsymbol{\Gamma}_A]_{1,1}$ remains. As described in Appendix A.1.3 $[\boldsymbol{\Gamma}_A]_{1,1}$ is approximated by (A.15) and thus the EFIM on the position error in (3.69) can be rewritten as

$$\boldsymbol{\mathcal{I}}_{\mathbf{p}} \approx \frac{8\pi^2\beta^2}{c^2}\sum_{k=1}^{K}\widehat{\mathrm{SINR}}_k\mathbf{D}_{\mathrm{r}}(\phi_k) + {T_{\mathrm{s}}}^2{S_{\nu}(\tau_1)}^2\big\|\mathbf{s}_{\tau_1}\big\|^4\mathrm{tr}\left[{\mathbf{C}_{\mathbf{r}}}^{-2}\right]\mathbf{D}_{\mathrm{r}}(\phi_1), \tag{3.70}$$

where second summand accounts for information gained by estimating the onsets of the DM PDP that starts at τ_1. As argued in Appendix A.1.3, the approximation in (3.70) is reasonable when assuming a large signal bandwidth and that the PDP is almost constant after the onset. Hence the PDP can be approximated by a scaled Heaviside function $S_\nu(\tau_1)u(\tau - \tau_1)$, where $S_\nu(\tau_1)$ is given by (A.16) in Appendix A.1.4.

3.7 Results

Table 3.1: Channel parameters for numerical evaluations.

	Param.	Value for Room		Description
		Valid.	Synth.	
Deterministic MPCs		2		max. VA order
		3 dB		attenuation per reflection
Signal parameters	f_c	8 GHz	7 GHz	carrier freq.
	T_p	1 ns, (0.5 ns,2 ns)		pulse duration
		RRC		pulse shape
	β_R	0.6		roll-off factor
PDP of diffuse multipath	Ω_1	$2.67\mathrm{e}^{-6}$	$1.16\mathrm{e}^{-6}$	norm. power
	γ_1	10 ns	20 ns	
	γ_rise	3 ns	5 ns	shape param.
	χ	0.98		
$\mathrm{E}_\mathrm{LOS}/N_0$		29.5 dB (at 1 m)		LOS SNR

Computational results are presented in this section for two environments. We first validate the theoretical results using experimental data for a room illustrated in Fig. 3.1 and then discuss in detail the trade-offs of different measurement scenarios for a synthetic room shown in Fig. 3.2.

For the transmit signal $s(t)$, we use a root raised cosine (RRC) pulse with unit energy and a roll-off factor $\beta_\mathrm{R} = 0.6$, modulated on a carrier at $f_\mathrm{c} = 7\,\mathrm{GHz}$. The computations are done for pulse durations of $T_\mathrm{p} = 0.5\,\mathrm{ns}$, $T_\mathrm{p} = 1\,\mathrm{ns}$ and $T_\mathrm{p} = 2\,\mathrm{ns}$. In the synthetic environments, we assume for all antennas isotropic radiation patterns in the azimuth plane and gains of 0 dB. The free-space pathloss has been modeled by the Friis equation. To account for the material impact, we assume 3 dB attenuation per reflection. As in our previous paper [59], the PDP of the DM is considered to be a fixed double-exponential function (cf. (A.16) in Appendix A.1.4), as introduced by [58, eq. (9)]. This choice reflects the common assumption of an exponential decay of the DM power and also the fact that the LOS component is not impaired by DM as severely as MPCs arriving later [101]. The model has been fitted in [58] to measurements collected in an industrial environment. We have used $\chi = 0.98$ as in [58] to describe the impact of DM on the LOS component and adapted γ_rise and γ_1 to reflect the smaller dimensions of our environments. Table 3.1 summarizes the parameters of the channel and signal models.

We would like to emphasize that this parametric model was introduced for simplicity and reproducibility, to analyze the impact of DM on the PEB in various scenarios. In practice,

Table 3.2: MPC SINRs for the validation environment, estimated from measured signals and computed from the channel model.

	SINR (measurem.) / SINR (model) [dB]		
MPC	$T_\mathrm{p} = 0.5\,\mathrm{ns}$	$T_\mathrm{p} = 1\,\mathrm{ns}$	$T_\mathrm{p} = 2\,\mathrm{ns}$
LOS Anchor 1	23.1 / 25.8	24.7 / 24.7	23.2 / 23.7
lower wall	11.1 / 18.3	5.4 / 15.9	4.1 / 13.7
right window	13.5 / 12.6	7.6 / 10.2	6.9 / 7.7
upper wall	2.2 / 11.7	-0.6 / 9.5	5.2 / 7.1
lower wall – right win.	9.5 / 7.3	7.6 / 4.9	4.9 / 2.4
LOS Anchor 2	25.9 / 26.4	26.0 / 25.3	26.5 / 24.2
right window	11.9 / 12.6	10.5 / 10.8	9.3 / 8.8
upper window	10.1 / 14.0	8.2 / 11.6	5.1 / 9.1
left wall	3.1 / 14.4	4.2 / 11.9	5.5 / 9.4
upper wall – right win.	10.6 / 5.7	11.7 / 3.9	3.5 / 1.8
upper win. – left wall	7.2 / 9.7	4.8 / 7.3	2.1 / 4.8

the SINR values can be estimated from channel measurements and used with the results from Section 3.5 to compute the PEB for real environments. This approach is used next to validate the theoretical results and the parametric channel model.

3.7.1 Validation with Measurement Data: Multipath-Sync

The validation is conducted in an example environment shown in Fig. 3.1, c.f. [O5]. The MPC SINRs (3.18) are estimated from channel measurement data as discussed in [O6], [45], using fixed positions for two anchors and a set of "estimation points" for the agent as illustrated in the figure. Table 3.2 shows the obtained values for selected MPCs. It also lists the corresponding SINRs computed from the parametric channel model, with parameters given in Table 3.1. The choice of the parameters of the double exponential PDP of the DM has been made to account for the smaller room dimensions in comparison to the synthetic environment used below.

The *estimated SINRs* in Table 3.2 show the relevance of the corresponding MPCs. The LOS is the most significant one. Its SINR is approximately constant over all bandwidths used, indicating that it is only slightly influenced by DM. The reflections at the windows and at the lower wall also provide significant position-related information. A scaling with bandwidth—as suggested by (3.18)—is observable reasonably well. Other MPCs provide less information, such as the left wall (plasterboard) and the upper wall. This is caused by a reduced reflection coefficient, increased interference by DM, and increased variance of the MPC amplitude over the estimation points. Reference [1] contains further results supporting the presented findings based on measurement data from other environments [102].

Table 3.2 also shows that the *parametric channel model* yields realistic SINRs in many cases and therefore valid performance bounds. It has to be stressed that the global PDP model as used

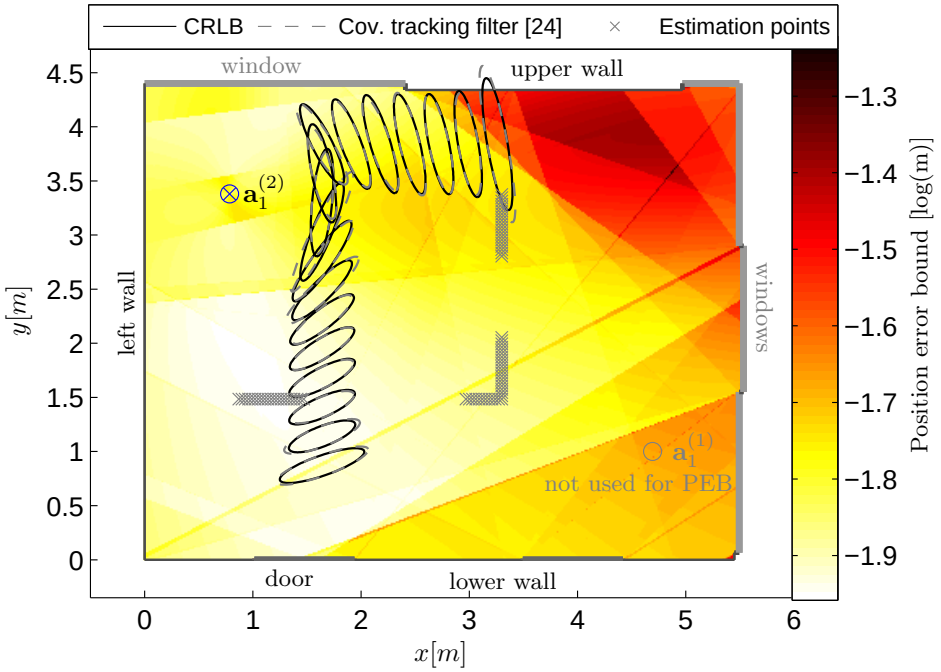

Figure 3.1: Logarithmic PEB (3.24) for estimated SINRs in the validation environment using measured signals with $T_p = 0.5\,ns$ and $f_c = 8\,GHz$ and only MPCs corresponding to the anchor at $\mathbf{a}_1^{(2)}$. 30-fold standard deviation ellipses are shown for the CRLB and a tracking algorithm.

here cannot describe the local behavior of DM. However, based on the provided framework, it is straightforward to introduce more realism by fitting separate parameterized or sampled models to any appropriate local area.

Figure 3.1 shows the logarithmic PEB for the validation environment using the estimated SINRs from Table 3.2 for Anchor 2 and $T_\mathrm{p} = 0.5\,\mathrm{ns}$. Equation (3.36) has been employed to compute the PEB, i.e. path overlap has been neglected and synchronization assumed. Clearly, one can observe from this figure the visibility regions and the relative importance (c.f. Table 3.2) of specific MPCs. The PEB is better than 10 cm at almost the entire area. The ellipses encode the geometrically decomposed PEB with 30-fold standard deviation, computed from (3.24). Dashed ellipses are for a multipath-assisted tracking algorithm as discussed in Section 5 and [O6] that makes use of the estimated SINRs for properly weighting the information from MPCs. It can be observed that both results match closely.

3.7.2 Synthetic Environment

The synthetic environment shown in Fig. 3.2 is used to compare different measurement scenarios. The PEB is evaluated across the entire room, assuming one or two fixed anchors at positions $\mathbf{a}_1^{(1)} = [10, 7]^\mathrm{T}$ and $\mathbf{a}_1^{(2)} = [2, 1]^\mathrm{T}$. We use a point grid with a resolution of 2 cm, resulting in $180,000$ points. VAs up to order two are considered, unless otherwise specified.

Multipath-Sync

Fig. 3.2 shows the PEB over the floor plan for Multipath-Sync and $T_\mathrm{p} = 1\,\mathrm{ns}$. Figs. 3.2(a) and (b) compare the simplified PEB neglecting path-overlap (cf. (3.36)) with the full PEB considering

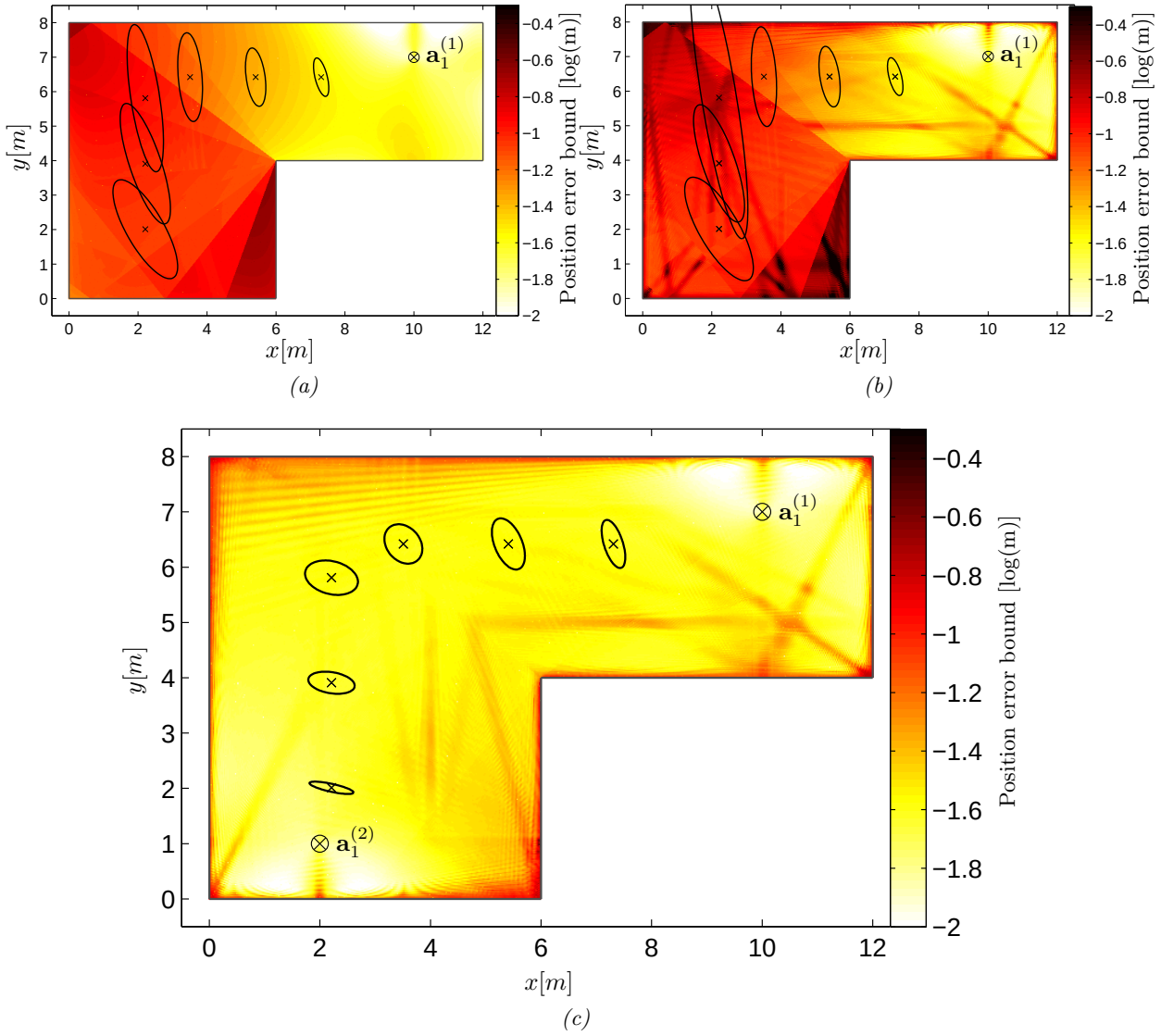

Figure 3.2: Logarithmic PEB (3.24) for Multipath-Sync with $T_p = 1$ ns over the example room for VAs up to order two. (a) One anchor at $\mathbf{a}_1^{(1)}$; path overlap neglected. (b) same as (a) but considering the influence of path overlap. (c) a second anchor has been introduced at $\mathbf{a}_1^{(2)}$; path overlap included. At some sample points, 20-fold standard deviation ellipses are shown.

it (cf. (3.35)). A single anchor is employed in both cases at position $\mathbf{a}_1^{(1)}$, yielding a PEB below 10 cm for most of the area. One can clearly see the visibility regions of different VA-modeled MPCs encoded by the level of the PEB. A valid PEB is obtained over the entire room even though the anchor is partly not visible from the agent positions. If path-overlap is considered in the computation of the CRLB (Fig. 3.2(b)), the adverse effect of room symmetries is observable, corresponding to regions where deterministic MPCs overlap. In case of *unresolvable* path overlap, i.e. the delay difference of two MPCs is less than the pulse duration $\tau_k - \tau_{k'} \ll T_\mathrm{p}$, the information of the components is entirely lost (see Section 3.5.1). The ellipses illustrate the geometrically decomposed PEB with 20-fold standard-deviation.

Fig. 3.2(c) shows the PEB with path-overlap for the same parameters but for two anchors. The error ellipses clearly indicate that the PEB is much smaller and the impact of path overlap has been reduced.

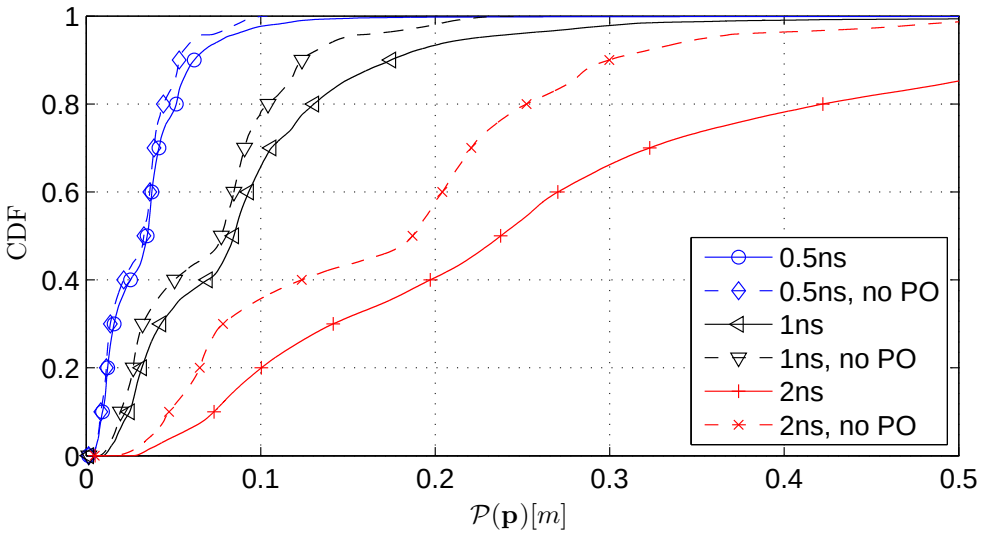

Figure 3.3: CDFs of the PEB (3.24) for Multipath-Sync, pulse durations $T_p = 0.5\,ns$, $T_p = 1\,ns$ and $T_p = 2\,ns$, and one anchor at $\mathbf{a}_1^{(1)}$. Path overlap is neglected in results marked by dashed lines.

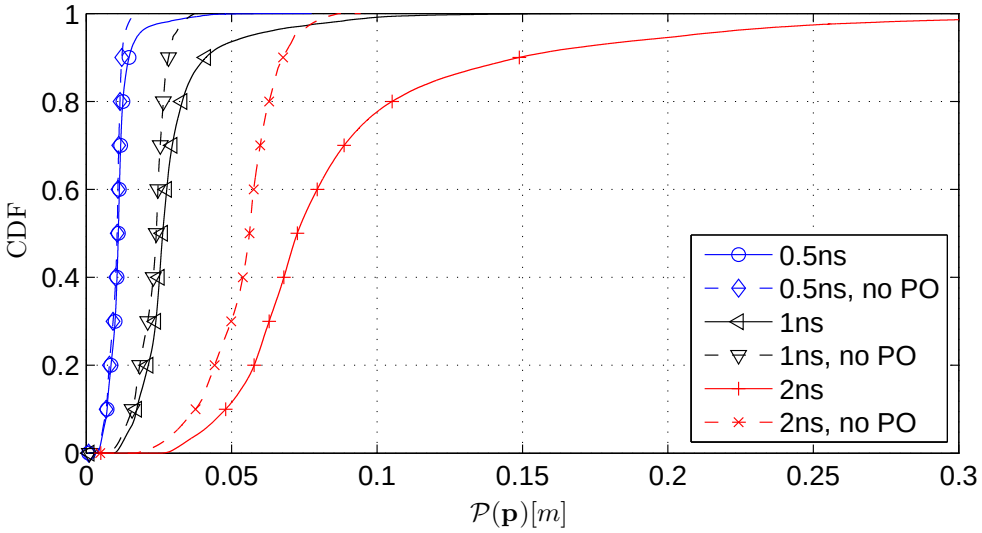

Figure 3.4: CDFs of the PEB (3.24) for Multipath-Sync, pulse durations $T_p = 0.5\,ns$, $T_p = 1\,ns$ and $T_p = 2\,ns$, and two anchors at $\mathbf{a}_1^{(1)}$ and $\mathbf{a}_1^{(2)}$. Path overlap is neglected in results marked by dashed lines.

A quantitative assessment of this scenarios is given in Figs. 3.3 and 3.4, showing the CDFs of the PEB for different pulse durations ($T_\mathrm{p} = 0.5\,\mathrm{ns}$, $T_\mathrm{p} = 1\,\mathrm{ns}$ and $T_\mathrm{p} = 2\,\mathrm{ns}$). One can observe that the PEB increases vastly w.r.t. this parameter. The "no PO" results account for the proportional scaling of Fisher information with bandwidth and additionally for the increased interference power due to DM, both of which are clearly seen in approximation (3.36). The influence of path overlap, which is neglected by (3.36), magnifies this effect even further because its occurrence becomes more probable. It almost diminishes—on the other hand—for the shortest pulse $T_\mathrm{p} = 0.5\,\mathrm{ns}$. Over all, the error magnitude scales by a factor of almost ten, while the bandwidth is scaled by a factor of four.

Fig. 3.5 shows the comparison of the PEB over the floor plan for Multipath-Sync (red lines with

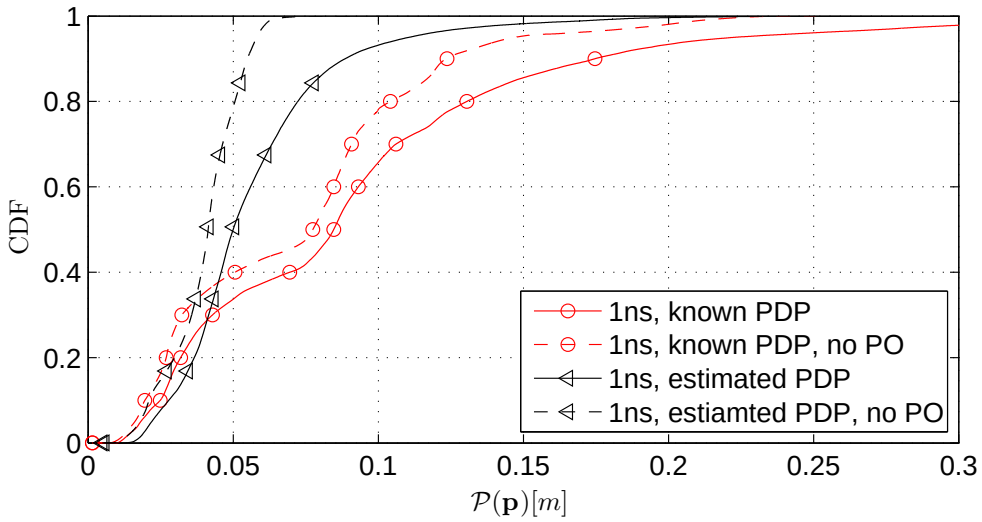

(a) Anchor $\mathbf{a}_1^{(1)}$

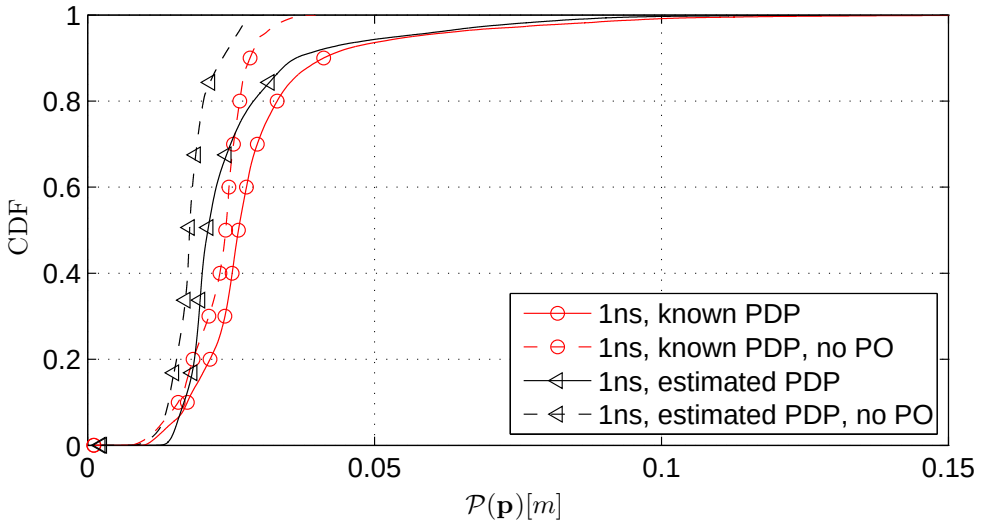

(b) Anchor $\mathbf{a}_1^{(1)}$ and $\mathbf{a}_1^{(2)}$

Figure 3.5: CDFs of the PEB (3.24) for Multipath-Sync with unknown noise and DM statistics, pulse durations $T_p = 1\,ns$ and anchors at $\mathbf{a}_1^{(1)}$ and $\mathbf{a}_1^{(2)}$. Path overlap is neglected in results marked by dashed lines.

circle markers) and for MultipathPDP-Sync[21] (black lines with triangular markers). Figs. 3.5a and 3.5a illustrate the PEB using a single anchor at $\mathbf{a}_1^{(1)}$ and two anchors at $\mathbf{a}_1^{(1)}$ and $\mathbf{a}_1^{(2)}$ for pulse duration $T_\mathrm{p} = 1\,\mathrm{ns}$ and VAs up to order 2. Both figures contain the PEBs for the "PO" case (cf. (3.69)) and "no PO" (c.f. (3.70)), illustrated by solid and dashed lines, respectively. For both cases the estimation of the PDP's onset τ_1 results in a reduction of the PEB. This obvious from (3.69), thus path overlap is neglected and also the PDP model parameters, beside τ_1, are assumed to be known. More interesting is that this reduction can be also seen for the "PO" case, even the estimation of nuisance parameters reduces the amount of information gained by estimating the onset.

Section 5 and [O4–O6, O8] present algorithms based on the presented signal model that can closely approach these bounds. I.e. cm-level accuracy is obtained for 90 % of the estimates.

[21] Again, the DM PDP model is given in (A.16) in Appendix A.1.4.

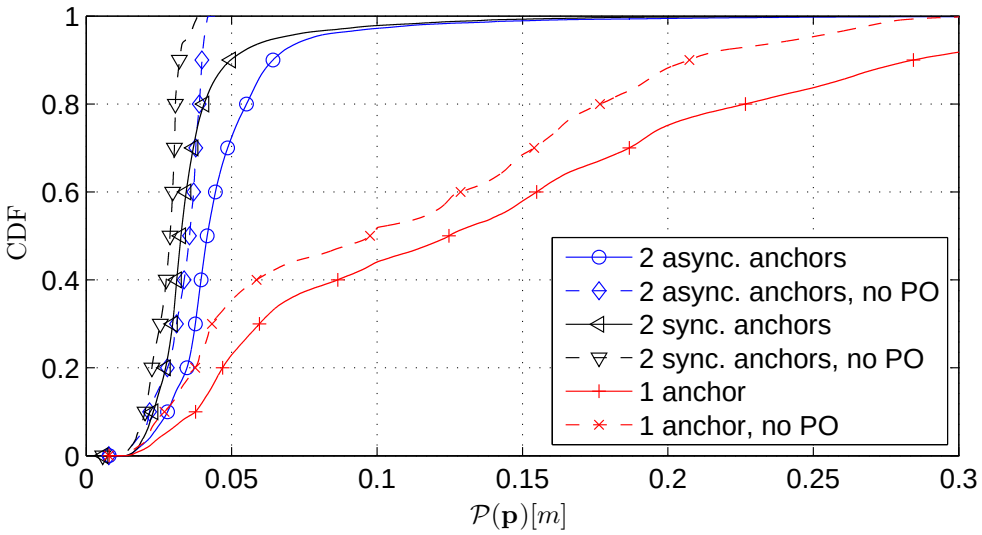

Figure 3.6: CDFs of the PEB (3.24) for Multipath-NSync and different synchronization states at pulse duration $T_p = 1\,ns$. Either two anchors are used at $\mathbf{a}_1^{(1)}$ and $\mathbf{a}_1^{(2)}$, which can be synchronized or not, or just the first anchor.

Multipath-NSync

Fig. 3.6 compares the CDFs of the PEB for Multipath-NSync and different synchronization states inbetween anchors, obtained from (3.41). The CDFs are shown for either two anchors at $\mathbf{a}_1^{(1)}$ and $\mathbf{a}_1^{(2)}$ which can be synchronized or not, or just the first anchor. A pulse duration of $T_\mathrm{p} = 1\,\mathrm{ns}$ is used. The performance deteriorates w.r.t. the Multipath-Sync case in Figs. 3.3 and 3.4, which can be explained by the fact that some of the delay information is used for clock-offset estimation, resulting in a loss of *position*-related information. A second anchor helps to counteract this effect. Here, one can recognize an additional gain of information if the two anchors are synchronized. The impact of path overlap is smaller if two anchors are used and even less pronounced if the anchors are synchronized.

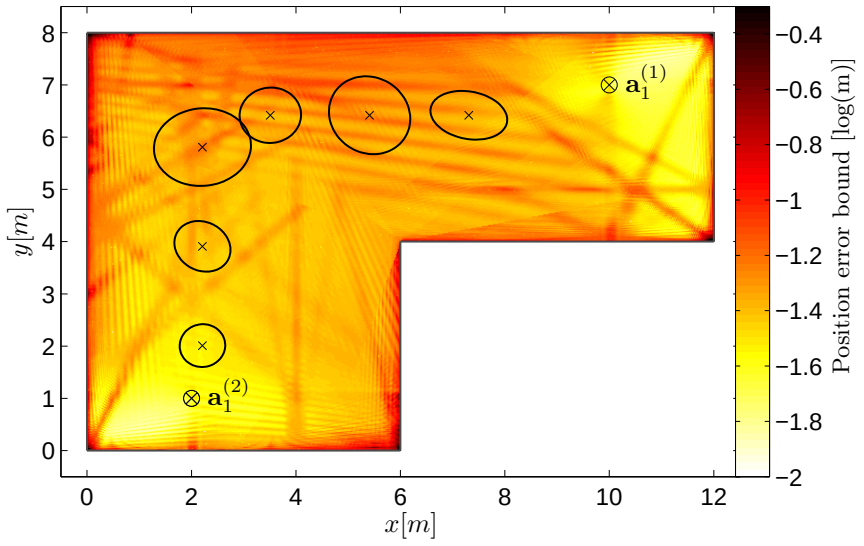

Figure 3.7: Logarithmic PEB (3.24) for Multipath-NSync over the example room with $T_p = 1\,ns$, using two asynchronous anchors at $\mathbf{a}_1^{(1)}$ and $\mathbf{a}_1^{(2)}$. 20-fold standard deviation ellipses are shown at some sample points.

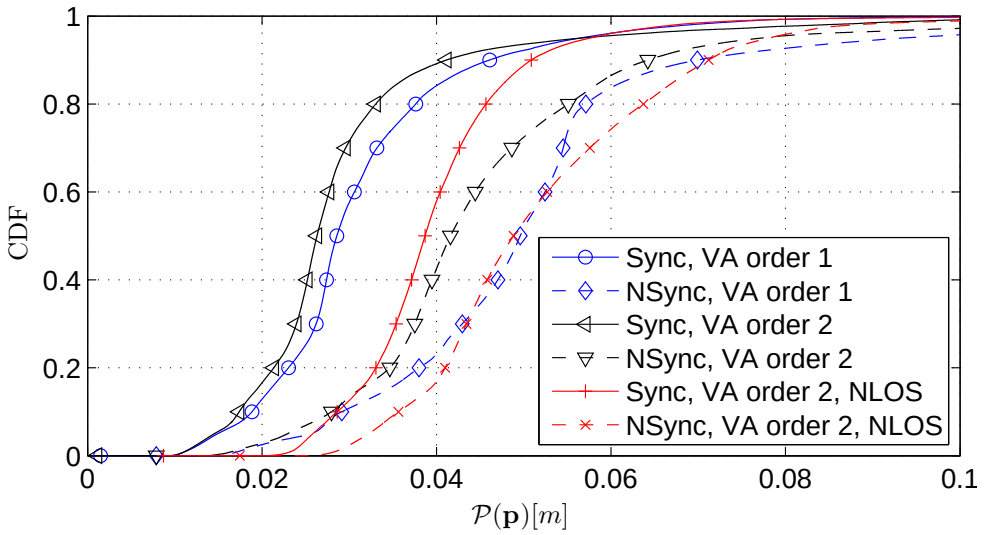

Figure 3.8: CDFs of the PEB in (3.24) for Multipath-Sync and Multipath-NSync and $T_p = 1\,ns$ with two anchors at $\mathbf{a}_1^{(1)}$ and $\mathbf{a}_1^{(2)}$. VAs of order one or two are considered; for the latter case also for an artificial NLOS situation over the whole room.

A qualitative representation of the PEB is shown in Fig. 3.7 for Multipath-NSync over the example room, with two anchors at $\mathbf{a}_1^{(1)}$ and $\mathbf{a}_1^{(2)}$, and $T_\mathrm{p} = 1\,\mathrm{ns}$. Comparing this result with the synchronized case shown in Fig. 3.2(c), one can observe an increase due to the need of extracting syncronization information. Also, the impact of path overlap has increased.

Fig. 3.8 compares Multipath-Sync and Multipath-NSync for the two-anchors case and $T_\mathrm{p} = 1\,\mathrm{ns}$, considering VAs of order one or two and an NLOS scenario where the LOS component has been set to zero across the entire room. One can observe the importance of the LOS component which usually has a significantly larger SINR and provides thus more position-related information than MPCs arriving later. Increasing the VA order leads in general also to an information gain. However, in a few cases this trend is reversed since a larger VA-order can lead to more positions with unresolvable path overlap. This occurs especially at locations close to walls and in corners.

Multipath-Coop

Fig. 3.9 contains 2D-plots of the different contributions to the PEB in (3.52) for the cooperative case. The PEB has been evaluated for Agent 3 across the entire room with two resting, cooperating agents at $\mathbf{p}^{(1)}$ and $\mathbf{p}^{(2)}$. In Fig. 3.9(a), only the monostatic measurements of Agent 3 are considered, illustrating the adverse effect of room symmetries and resulting unresolvable path overlap. In particular, areas close to the walls are affected as well as the diagonals of the room. Fig. 3.9(b) shows the information provided by the agents at $\mathbf{p}^{(1)}$ and $\mathbf{p}^{(2)}$ in their role as anchors. Their contribution is similar to the fixed-anchor case analyzed in Fig. 3.2(c), but due to uncertainties in their own positions, this information is not fully accessible. A robust, infrastructure-free positioning system is obtained if these two components can complement one another. Indeed Fig. 3.9(c) indicates excellent performance across the entire area. The distinction between the parts of the position-related information is further highlighted by the CRLB ellipses in Fig. 3.9(c), which also include the fixed-anchor (bistatic) case of Fig. 3.2(c). It shows

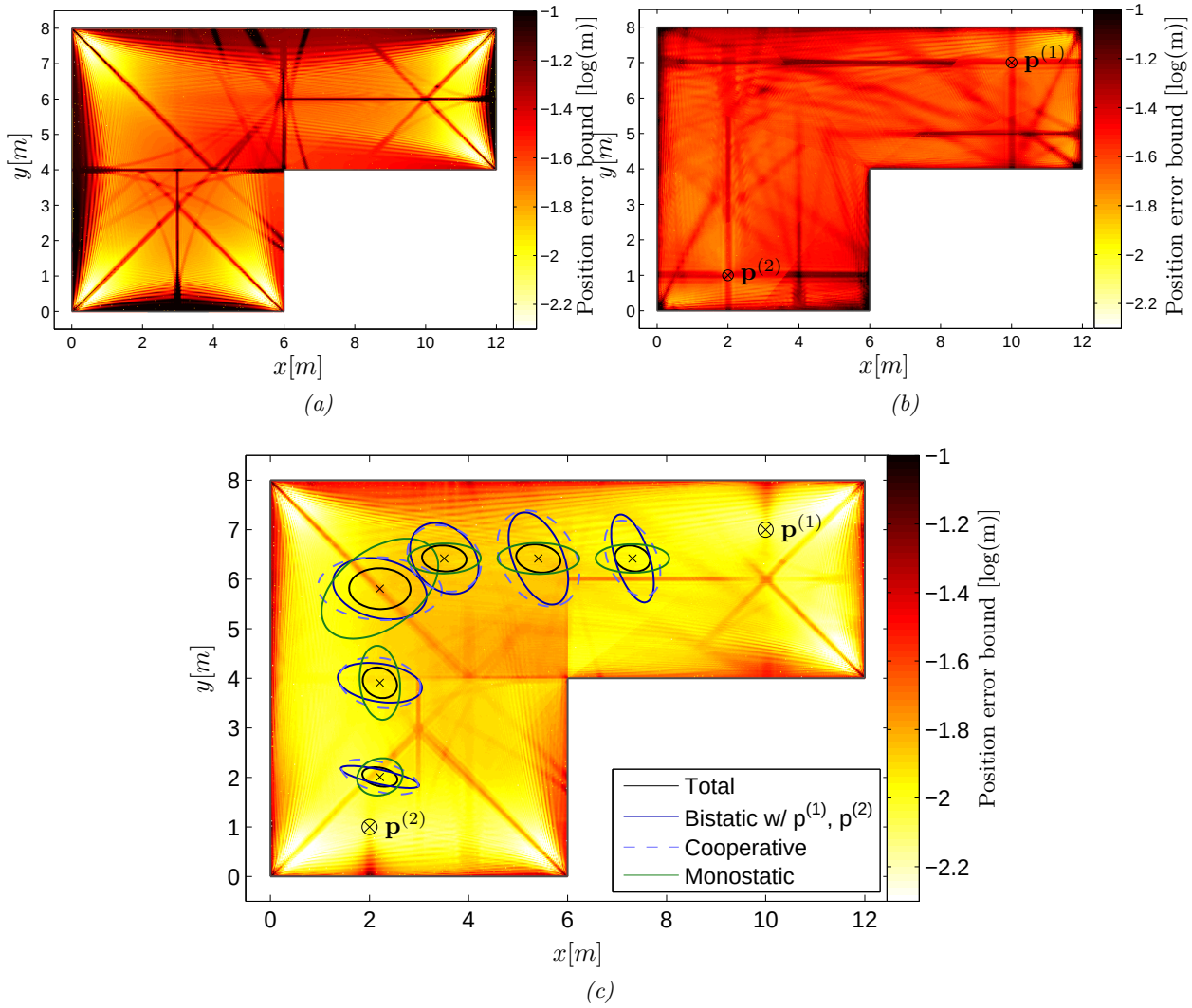

Figure 3.9: Logarithmic PEB (3.52) with $T_p = 1\,ns$ over the example room for three cooperating agents, two of which are resting at positions $\mathbf{p}^{(1)}$ and $\mathbf{p}^{(2)}$. The PEB is decomposed into its (a) monostatic and (b) cooperative components. Plot (c) shows the total PEB for Multipath-Coop. In (c), also the 40-fold standard deviation ellipses are shown at some sample points for these three cases and—in addition—for the (bistatic) case with fixed anchors.

the decreased information of the cooperative part in comparison to the bistatic case with fixed anchors. The monostatic ellipses are mostly oriented towards the nearest wall, where the most significant information comes from. In many cases, this information is nicely complemented by the cooperative contribution.

Fig. 3.10 shows the CDFs of the PEB in (3.52) for $T_\mathrm{p} = 1\,\mathrm{ns}$ and VAs of order one and two. It is interesting to note that Multipath-Coop does not benefit from taking into account second-order MPCs. This is explained by the large influence of the monostatic measurements, for which second-order reflections cause many regions with unresolvable path overlap (c.f. Fig. 3.9(a)). For cooperative measurements, increasing the VA order is still beneficial.

Fig. 3.11 illustrates the influence of bandwidth on Multipath-Coop, using $T_\mathrm{p} = 0.5\,\mathrm{ns}$ and $T_\mathrm{p} = 2\,\mathrm{ns}$ for VAs of order two. Especially for the monostatic measurements, the occurrence of unresolvable path overlap is significantly reduced, leading to an advantage of a larger bandwidth.

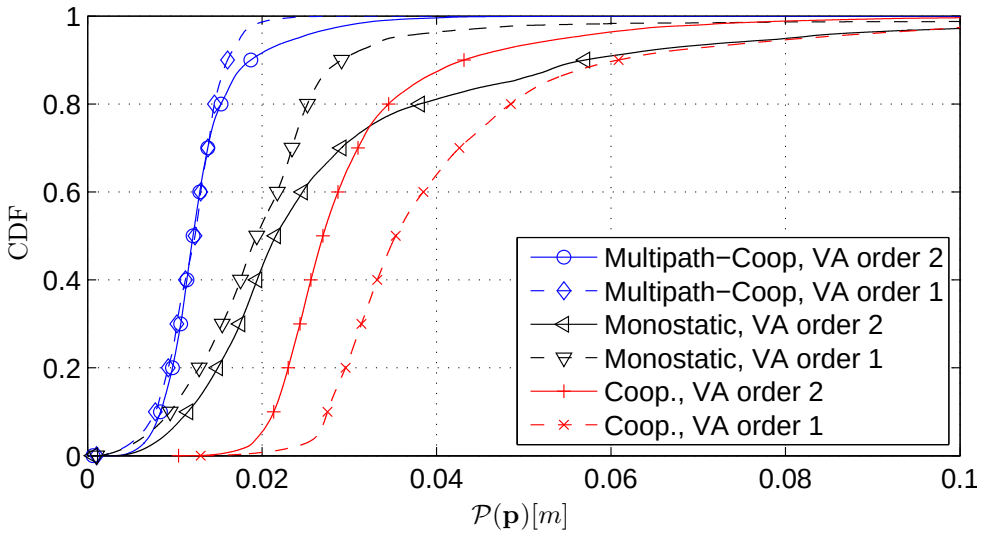

Figure 3.10: CDFs of the PEB (3.52) for Multipath-Coop with $T_p = 1\,ns$, for VAs of order one and two, analyzing contributions of different measurements.

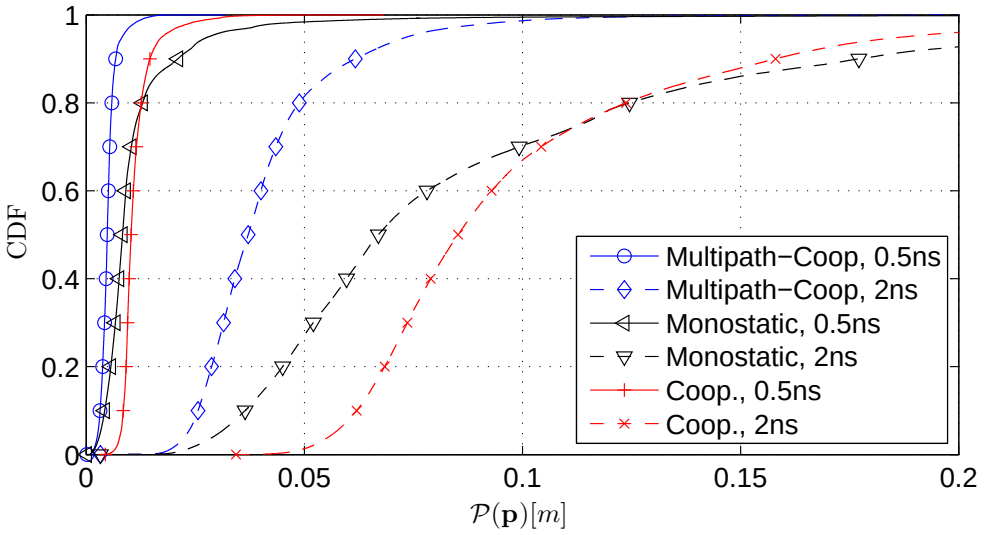

Figure 3.11: CDFs of the PEB in (3.52) for Multipath-Coop with $T_p = 0.5\,ns$ and $T_p = 2\,ns$ for VAs of order two, showing contributions of different measurements types.

3.8 Chapter Summary and Conclusions

In this Chapter, we have introduced and validated a unified framework for evaluating the accuracy of radio-based indoor-localization methods that exploit geometric information contained in deterministic multipath components (MPCs). The analysis shows and quantifies fundamental relationships between environment properties and the position-related information that can potentially be acquired. This is due to two mechanisms: (i) diffuse multipath (DM), which is related to physical properties of the propagation environment, acts as interference to useful specular MPCs. (ii) Path overlap, which relates to system design choices as the placement of agents but also to the given geometry of an environment, may render deterministic components useless. An increased signal bandwidth allows to counteract those effects since it improves the time-resolution of the measurements: The power of DM thus decreases and path overlap becomes

less likely.

The framework allows for the analysis of different measurement setups: For instance, (i) in absence of synchronization, position information can be extracted from the time-difference between MPCs. The need for clock-offset estimation reduces thereby the positioning accuracy in comparison to a synchronized setup. (ii) Cooperation between agents increases the available position-related information, but the uncertainty of the unknown positions of agents *acting* as anchors partly levels this effect. (iii) With monostatic measurements, the VAs move synchronously with the agents, which leads to a scaling of the information provided by MPCs. These MPC-geometry-dependent scaling factors lie between zero and two w.r.t. a conventional bistatic measurement.

The quantification of position-related information, as provided by the presented framework, can be used for designing positioning and tracking algorithms introduced in Sections 4-7 and also [O4–O6, O8]. The proper parametrization of the underlying geometric-stochastic channel model optimizes such algorithms and provides valuable insight for system design choices such as antenna placements and signal parameters. Algorithms that can learn and extract these environmental parameters online from measurements may achieve such optimization without the need for manual system optimization and are thus an important topic for further research on robust indoor localization.

4 Positioning using Multipath Channel Information

This chapter is based on the work of [O4] and introduces a positioning algorithm using multipath channel information and prior floor plan knowledge. The method can be applied to find the initial position of an agent for the tracking algorithms described in Chapter 5 and Chapter 6. The computation of the likelihood function can be interpreted as a position dependent channel estimation problem with prior floorplan information. Using the floorplan knowledge, the sets of VAs are computed for every anchor using optical ray-tracing [1]. To find the actual position of an agent, both the deterministic and DM and the AWGN noise parameters are estimated for agent position hypotheses.

In realistic scenarios, the floorplan has uncertainties that are taking into account by using a probabilistic formulation of the VA positions as described in Section 2.3 in (2.10). Hence, the uncertainties of the VAs should be considered by marginalization. In this chapter, the uncertainty in the VA positions is neglected. It will be re-introduced in Section 5.1.4 in the context of tracking filter.

4.1 Maximum Likelihood (ML) Estimator of the Agent Position

The maximum a-posteriori (MAP) estimator of the agent position is formulated for deterministic known VA positions by using (2.11), yielding

$$\begin{aligned}\hat{\mathbf{p}}_{\mathrm{MAP}} &= \arg\max_{\mathbf{p}} \prod_{j\in\mathcal{N}_j} p\big(\mathbf{p}|\mathbf{r}^{(j)}\big) \\ &= \arg\max_{\mathbf{p}} \prod_{j\in\mathcal{N}_j} p\big(\mathbf{r}^{(j)}|\boldsymbol{\alpha}^{(j)},\boldsymbol{\tau}^{(j)}\big)p\big(\boldsymbol{\alpha}^{(j)},\boldsymbol{\tau}^{(j)}|\mathbf{p};\mathcal{A}^{(j)}\big)p\big(\mathbf{p}\big)\end{aligned}$$

$$= \arg\max_{\mathbf{p}} \prod_{j \in \mathcal{N}_j} p\big(\mathbf{r}^{(j)}|\boldsymbol{\alpha}^{(j)}, \boldsymbol{\tau}^{(j)}\big) p\big(\boldsymbol{\alpha}^{(j)}|\boldsymbol{\tau}^{(j)}\big) p(\boldsymbol{\tau}^{(j)}|\mathbf{p}; \mathcal{A}^{(j)}) p\big(\mathbf{p}\big)$$

$$= \arg\max_{\mathbf{p}} \prod_{j \in \mathcal{N}_j} p\big(\mathbf{r}^{(j)}|\boldsymbol{\alpha}^{(j)}, \boldsymbol{\tau}^{(j)}\big) p\big(\boldsymbol{\alpha}^{(j)}|\boldsymbol{\tau}^{(j)}\big) \prod_{k=1}^{K^{(j)}} p(\tau_k^{(j)}|\mathbf{p}; \mathbf{a}_k^{(j)}) p\big(\mathbf{p}\big). \tag{4.1}$$

With the assumption of known VA positions and additionally that the channel parameters are deterministic unknowns, the marginal PDFs of the MPC delays are described by

$$p\big(\tau_k^{(j)}|\mathbf{p}, \mathbf{a}_k^{(j)}\big) = \delta\big(\tau_k^{(j)} - \frac{1}{c} d\big(\mathbf{a}_k^{(j)}, \mathbf{p}\big)\big) \tag{4.2}$$

and the PDF of the according MPC complex amplitudes is described by

$$p(\boldsymbol{\alpha}^{(j)}|\boldsymbol{\tau}^{(j)}) = \delta\big(\boldsymbol{\alpha}^{(j)} - \hat{\boldsymbol{\alpha}}_{\mathrm{LS}}^{(j)}\big(\boldsymbol{\tau}^{(j)}\big)\big). \tag{4.3}$$

The least-square estimate of the complex amplitude vector $\hat{\boldsymbol{\alpha}}_{\mathrm{LS}}^{(j)}$ as in (4.7), describes the relation between the received signal $\mathbf{r}^{(j)}$ and the delay vector $\boldsymbol{\tau}^{(j)}$ at the agent position hypothesis $\mathbf{p}$. Considering a uniform prior distribution over the floor plan for the agent position

$$p(\mathbf{p}) = \begin{cases} 1/\mathcal{M}_{\mathcal{F}} & \mathbf{p} \in \mathcal{F} \\ 0 & \text{elsewhere} \end{cases}, \tag{4.4}$$

where $\mathcal{M}_{\mathcal{F}}$ is the area of the floor plan on the 2-D support $\mathcal{F}$ of agent position hypothesis $\mathbf{p}$, the MAP estimator in (4.1) reduces to an ML estimator. Using the likelihood function in (3.5) results in

$$\hat{\mathbf{p}}_{\mathrm{ML}} = \arg\max_{\mathbf{p}} \prod_{j \in \mathcal{N}_j} f\big(\mathbf{r}^{(j)}; \boldsymbol{\alpha}^{(j)}; \boldsymbol{\tau}^{(j)}; \mathbf{p}; \mathcal{A}^{(j)}\big). \tag{4.5}$$

4.1.1 Evaluation of the Likelihood Function

The actual ML estimation algorithm is described in Section 4.1.2. Independent of the used algorithm, the likelihood function has to be evaluated by applying the following steps:

1. To reduce the uncertainties in the geometry, a MAP estimator has to be used to refine the VAs positions, employing a set of training data at known locations, yielding $\hat{\mathbf{a}}_k^{(j)}$. For detailed information about the VA position refinement process, please refer to [O6], [45].

2. With the set of VAs, the position dependent set of expected delays $\hat{\tau}_k^{(j)}(\mathbf{p}) = \frac{1}{c} d(\hat{\mathbf{a}}_k^{(j)}, \mathbf{p})$ is used to construct the signal matrix $\hat{\mathbf{S}}^{(j)}$ as in (3.6). The expected delays $\hat{\tau}_k^{(j)}(\mathbf{p})$ are refined by searching for the actual amplitude maxima in the received signal vector $\mathbf{r}^{(j)}$ in a window $[\hat{\tau}_k^{(j)}(\mathbf{p}) - T_{\mathrm{p}}, \hat{\tau}_k^{(j)}(\mathbf{p}) + T_{\mathrm{p}}]$ with the length of the main lobe of the transmitted signal $s(t)$.

3. Since the DM plus AWGN statistic is usually unknown, the covariance $\mathbf{C_r}^{(j)}$ has to be estimated from a sufficient large set of measured signals $\{\mathbf{r}_l^{(j)}\}_{l=1}^{L}$ around the actual agent position. Constructing the signal matrix $\hat{\mathbf{S}}^{(j)}$ for the position hypothesis $\mathbf{p}_l$ of the l-th

measurement, the template signal $\mathbf{r}_{\mathrm{det},l}^{(j)}$ is computed and further the covariance matrix is estimated by

$$\hat{\mathbf{C}}_{\mathbf{r}}^{(j)} = \frac{1}{L}\sum_{l=1}^{L}\left(\mathbf{r}_l^{(j)} - \mathbf{r}_{\mathrm{det},l}^{(j)}\right)\left(\mathbf{r}_l^{(j)} - \mathbf{r}_{\mathrm{det},l}^{(j)}\right)^{\mathrm{H}}. \tag{4.6}$$

Note, that the LOS propagation delay $\hat{\tau}_{1,l}$ differences between the measurements have to be compensated to be able to average over the set of measurements $\{\mathbf{r}_l^{(j)}\}$ of the spatially close agent positions.

4. Using $\hat{\mathbf{S}}$ and (4.6), the ML estimation of the complex amplitudes $\boldsymbol{\alpha}$ reduces to a linear estimation problem. This means, the complex amplitudes are computed by the weighted least square solution in the following form

$$\hat{\boldsymbol{\alpha}}_{\mathrm{LS}}^{(j)} = \left(\hat{\mathbf{S}}^{(j)}\left(\hat{\mathbf{C}}_{\mathbf{r}}^{(j)}\right)^{-1}\left(\hat{\mathbf{S}}^{(j)}\right)^{\mathrm{H}}\right)^{-1}\hat{\mathbf{S}}^{(j)}\left(\hat{\mathbf{C}}_{\mathbf{r}}^{(j)}\right)^{-1}\mathbf{r}^{(j)}. \tag{4.7}$$

The steps 2 to 4 have to be iterated until a defined convergence criterion is reached, replacing $\mathbf{r}^{(j)}$ by $\mathbf{r}_w^{(j)} = \left(\hat{\mathbf{C}}_{\mathbf{r}}^{(j)}\right)^{-1}\mathbf{r}^{(j)}$. The likelihood function is evaluated by inserting the estimated parameter $\hat{\mathbf{S}}^{(j)}$, $\hat{\mathbf{C}}_{\mathbf{r}}^{(j)}$ and $\hat{\boldsymbol{\alpha}}_{\mathrm{LS}}^{(j)}$ into equation (3.5).

4.1.2 Implementation of the ML Estimator

Due to the fact that the likelihood function is highly multi-modal, non-Gaussian in $\mathbf{p}$ and the measurement model is non-linear, a straight-forward ML estimation is not applicable. Hence, a hybrid probabilistic-heuristic approach is used which combines an SIR PF with the concept of PSO in order to find the global maximum in the parameter space. In [103] probability model-based methods for global optimization are presented. To explore the entire search space and find new candidate solutions, randomness has to be introduced in the maximization method. This can be realized: (i) in the re-sampling step of the PF by generating also new values for the particles instead of conventional re-sampling with replacement or (ii) via a state-space model which induces the exploration.

The introduced approach, uses a dynamic state-space model to explore the search-space. The state equation consists of two parts, the first one is described by a constant-velocity random walk model and the second part is responsible for the particle swarm behavior [104].

Sequential Monte Carlo Methods – SIR Particle Filters

Particle filters represent a sub-optimal sequential Monte Carlo method for solving non-linear and non-Gaussian sequential Bayesian state estimation problems which can not be computed in a closed form. This method allows for a complete representation of the state distribution also for arbitrary PDFs with no restricted assumptions of the form of the density. In general, the Bayesian tracking problem is the recursive computation of a degree of belief of a hidden state, e.g. position and velocity $\mathbf{x}_n = [\mathbf{p}_n^{\mathrm{T}}, \mathbf{v}_n^{\mathrm{T}}]^{\mathrm{T}}$, using measurement $\mathbf{r}_n$ at time-index n. Hence, this Bayesian approach is used for ML localization, not tracking, the index n describes in this Section

the evolution of the distribution as a function of time until convergence is reached. In every iteration the new received signal vector $\mathbf{r}_n$ is accumulated in $\mathbf{r}_{1:n}$. In the case there is just one measurement for each anchor per iteration (i.e. a set of measurements in the vicinity of $\mathbf{p}$ to be able to estimate the noise covariance matrix) $\mathbf{r}_{1:n} = \mathbf{r}_n = \mathbf{r} \ \forall\, n$. The state estimation is done in two consecutive stages using a first-order hidden Markov model (HMM): (i) the prediction step obtains the predicted posterior PDF $p(\mathbf{x}_n|\mathbf{r}_{1:n})$ using the Chapman-Kolmogorv equation [105]

$$p(\mathbf{x}_n|\mathbf{r}_{1:n-1}) = \int_{\mathbf{x}_{n-1}} p(\mathbf{x}_n|\mathbf{x}_{n-1}) p(\mathbf{x}_{n-1}|\mathbf{r}_{1:n-1}) \mathrm{d}\mathbf{x}_{n-1}, \tag{4.8}$$

where $p(\mathbf{x}_n|\mathbf{x}_{n-1})$ is the state evolution probability, and (ii) the update step which is solved via Bayes'rule

$$p(\mathbf{x}_n|\mathbf{r}_{1:n}) = \frac{p(\mathbf{r}_n|\mathbf{x}_n) p(\mathbf{x}_n|\mathbf{r}_{1:n-1})}{\int_{\mathbf{x}_n} p(\mathbf{r}_n|\mathbf{x}_n) p(\mathbf{x}_n|\mathbf{r}_{1:n-1}) \mathrm{d}\mathbf{x}_n}, \tag{4.9}$$

where $p(\mathbf{r}_n|\mathbf{x}_n) = \prod_{j\in\mathcal{N}_j} f(\mathbf{r}_n^{(j)}|\boldsymbol{\tau}^{(j)}; \boldsymbol{\alpha}^{(j)}; \mathbf{p}_n; \mathcal{A}^{(j)})$ is the measurement likelihood function (3.5) dependent on the position $\mathbf{p}_n$.

For solving (4.8) and (4.9), particle filters use a finite set of weighted samples, i.e. particles $\{\mathbf{x}_n^{(i)}, a_n^{(i)}\}_{i=1}^I$, to approximate the involved PDFs. The particles are sampled from an importance distribution $\mathbf{x}_n^{(i)} \sim \mathrm{q}(\mathbf{x}_n^{(i)}|\mathbf{x}_{n-1}^{(i)}, \mathbf{r}_n)$ and their weights $a_n^{(i)}$ are computed in each iteration with

$$a_n^{(i)} = a_{n-1}^{(i)} \frac{p(\mathbf{r}_n|\mathbf{x}_n^{(i)}) p(\mathbf{x}_n^{(i)}|\mathbf{x}_{n-1}^{(i)})}{q(\mathbf{x}_n^{(i)}|\mathbf{x}_{n-1}^{(i)}, \mathbf{r}_n)}, \qquad \sum_{i=1}^{I} a_n^{(i)} = 1, \tag{4.10}$$

using the weight $a_{n-1}^{(i)}$ from the previous time step and the new measured data $\mathbf{r}_n$. A simple choice of importance distribution is the state evolution probability $q(\mathbf{x}_n^{(i)}|\mathbf{x}_{n-1}^{(i)}, \mathbf{r}_n) = p(\mathbf{x}_n^{(i)}|\mathbf{x}_{n-1}^{(i)})$. To reduce the degeneration[22] of the particles, a re-sampling step is introduced after every iteration. In this step, particles are drawn according to their weights which means that particle states $\mathbf{x}_n^{(i)}$ with high weight $a_n^{(i)}$ are duplicated more often than particles with lower weights. The particle weights after every re-sampling step are set to $a_n^{(i)} = 1/N$. A commonly used re-sampling method is systematic re-sampling [106]. So, the computation of the weights simplifies to $a_n^{(i)} \propto p(\mathbf{r}_n|\mathbf{x}_n^{(i)}) = \prod_{j\in\mathcal{N}_j} f(\mathbf{r}_n^{(j)}|\boldsymbol{\tau}^{(j)}; \boldsymbol{\alpha}^{(j)}; \mathbf{p}_n^{(i)}; \mathcal{A}^{(j)})$. The posterior PDF can be approximated as

$$p(\mathbf{x}_n|\mathbf{r}_{1:n}) \approx \sum_{i=1}^{I} a_n^{(i)} \delta(\mathbf{x}_n - \mathbf{x}_n^{(i)}), \tag{4.11}$$

where for $I \to \infty$, (4.11) approaches the true posterior.

Concerning the re-sampling step another issue is the "particle collapse", the degenerated particle representation of the state space, where all particles occupy the same point in the state space. A remedy against this is to use a regularization Kernel $K(\cdot)$ after re-sampling to draw

[22] This means that after some iterations almost all particles except one have negligible weights leading to a poor approximation of the posterior PDF.

new samples [105] yielding (4.11) to

$$p(\mathbf{x}_n|\mathbf{r}_{1:n}) \approx \sum_{i=1}^{I} a_n^{(i)} K(\mathbf{x}_n - \mathbf{x}_n^{(i)}) \tag{4.12}$$

that represents the smoothed posterior PDF. As described in [105], an optimal choice of Kernel is the Epanechnikov Kernel with Kernel bandwidth that minimizes the mean square error (MSE) between the true posterior and the regularized posterior PDF. In practice, the empirical covariance S_n of the particle distribution is computed before the re-sampling step. This empirical covariance S_n is then used to compute the Kernel bandwidth to obtain the regularized posterior PDF.

PF-PSO

In PSO the particles are generated randomly and by iterative updates of the positions using a cost function. The particles learn from their own cost-measure and the cost-measure of the other particles introducing swarm behavior. In our case, the particles in the swarm gain a velocity in direction of the global maximum, so that the PSO is able to jump out of local maxima and find the global optimum. This swarm behavior is integrated in the PF by the state transition equation [104] which is described by

$$\mathbf{x}_n^{(i)} = \mathbf{F}\mathbf{x}_{n-1}^{(i)} + u_1 \begin{bmatrix} \mathbf{p}_{n-1}^{i\text{best}} - \mathbf{p}_{n-1}^{(i)} \\ \Delta T(\mathbf{p}_{n-1}^{i\text{best}} - \mathbf{p}_{n-1}^{(i)}) \end{bmatrix} + u_2 \begin{bmatrix} \mathbf{p}_{n-1}^{g} - \mathbf{p}_{n-1}^{(i)} \\ \Delta T(\mathbf{p}_{n-1}^{g} - \mathbf{p}_{n-1}^{(i)}) \end{bmatrix} + \mathbf{G}\mathbf{n}_{\text{acc}}. \tag{4.13}$$

Here,

$$\mathbf{F} = \begin{bmatrix} 1 & 0 & \Delta T & 0 \\ 0 & 1 & 0 & \Delta T \\ 0 & 0 & \Delta T & 0 \\ 0 & 0 & 0 & \Delta T \end{bmatrix} \quad \text{and} \quad \mathbf{G} = \begin{bmatrix} \frac{\Delta T^2}{2} & 0 \\ 0 & \frac{\Delta T^2}{2} \\ \Delta T & 0 \\ 0 & \Delta T \end{bmatrix} \tag{4.14}$$

are the state transition matrix and the noise weighting matrix, and ΔT is the discrete time step between two time instances, which represents in the case of positioning a weighting factor of the velocity and can not be seen as a "real" time difference measure. The weights u_1 and u_2 are random control factors drawn from a uniform distribution $\mathcal{U}(0,1)$, $\mathbf{n}_{\text{acc}}$ is a zero-mean Gaussian driving acceleration noise with co-variance matrix $\sigma_{\text{acc}}^2\mathbf{I}_2$. $\mathbf{p}_n^{i\text{best}}$ and $\mathbf{p}_n^g$ denote the maximum of the set of particles in the current iteration n and the global maximum of the past iterations, respectively. The algorithm starts with uniformly distributed particles over the entire search space. For these candidates the likelihood function is evaluated and the global maximum of the likelihood function L_n^g and the corresponding position $\mathbf{p}_n^g = \arg\max_{\mathbf{p}_n^{(i)}} \prod_{j\in\mathcal{N}_j} f(\mathbf{r}_n^{(j)}|\boldsymbol{\tau}^{(j)}, \boldsymbol{\alpha}^{(j)}, \mathbf{p}_n^{(i)}; \mathcal{A}^{(j)})$ are computed. Further, the current maximum of the particles $\mathrm{L}_n^{i\text{best}} = \mathrm{L}_n^g$ and also the corresponding position $\mathbf{p}_n^{i\text{best}} = \mathbf{p}_n^g$ are set to the global values. Then, the state $\mathbf{x}_n^{(i)}$ (prediction step) and the according weights $a_n^{(i)}$ (measurement update) of the particles are evaluated iteratively for a defined number of iterations. After each measurement update and before the re-sampling step is executed, the maximum of the current particles $\mathrm{L}_n^{i\text{best}}$ at position $\mathbf{p}_n^{i\text{best}}$ is computed and

accepted as new global maximum if $\mathrm{L}_n^{i\mathrm{best}} > \mathrm{L}_n^g$.

Estimation of the DM plus AWGN Covariance

As for every particle at position $\mathbf{p}_n^{(i)}$ the deterministic MPCs are estimated, also the covariance $\mathbf{C}_\mathrm{r}^{(i)}$ given in (4.6) has to be estimated for the i-th particle. If the set of measurement with which the $\mathbf{C}_\mathrm{r}^{(i)}$ is estimated are from very closely spaced agent positions $\mathbf{p}_1 \approx \mathbf{p}_2 \approx \cdots \approx \mathbf{p}_L$, it is a proper assumption to estimate the deterministic MPCs for all measurements using the same agent position hypothesis $\mathbf{p}$ and to align all measurements to the same first delay. This simplification is exploited when estimating the DM plus AWGN covariance $\mathbf{C_r}$.

The estimation of the covariance matrix $\mathbf{C_r}$ for every particle is computationally very demanding and time consuming. Possible simplifications are the following:

- Estimate the covariance matrix $\mathbf{C}_\mathrm{r}^g$ for the actual global maximum of the likelihood function L_n^g at position $\mathbf{p}_n^g$ of n-th iteration step.

- Estimate the covariance matrices $\{\mathbf{C}_\mathrm{r}^{i\mathrm{best}}\}$ for a certain number N_lhf of highest peaks of the likelihood function at positions $\{\mathbf{p}_n^{i\mathrm{best}}\}_{i\mathrm{best}=1}^{N_\mathrm{lhf}}$ of n-th iteration step. For all particles which are not at the location of these maxima, the distances to this maxima are computed. In the next iteration step $n+1$, the evaluation of the likelihood function is performed for a particle with the $\mathbf{C}_\mathrm{r}^{i\mathrm{best}}$ which is computed for the nearest past maximum of the likelihood function $\mathrm{L}_n^{i\mathrm{best}}$.

Initialization of PF

A straightforward initialization of the PF is to draw the particle state uniformly from $p(\mathbf{p})$ described in (4.4). However, for a satisfying convergence rate of the particle-based positioning algorithm, a high initial number of particle is needed. To reduce the computation demands and time, one possibility to overcome this issue is to draw the prior particle state from a "simpler" likelihood function than the one given by (3.5). This likelihood function uses a certain number N_meas of estimated MPC distances $\hat{d}_{i,n}^{(j)}$ comprised in the set $\mathcal{Z}_n$ and the VAs at positions $\mathbf{a}_k^{(j)}$, yielding [107]

$$f(\mathcal{Z}_n|\mathbf{p}_n;\mathcal{A}) = \prod_{i=1}^{N_\mathrm{meas}} P_\mathrm{VA} \prod_{j\in\mathcal{N}_j} \frac{1}{\sum_{k=1}^{K_n^{(j)}} v_k^{(j)}} \sum_{k=1}^{K_n^{(j)}} v_k^{(j)} \mathcal{N}\Big(\hat{d}_{i,n}^{(j)} | d(\mathbf{a}_k^{(j)}, \mathbf{p}_n), \big(\sigma_{d,k}^{(j)}\big)^2\Big) + (1 - P_\mathrm{VA}) f_{\overline{\mathrm{VA}}}(\mathcal{Z}_n|\mathbf{p}_n;\mathcal{A}), \quad (4.15)$$

where P_VA is the probability that the estimated MPC distance $\hat{d}_{i,n}^{(j)}$ corresponds to a certain VA $\mathbf{a}_k^{(j)}$, $v_k^{(j)}$ is a weighting factor that describes the relevance of this VA and $\sigma_{d,k}^{(j)}$ defines the ranging standard deviation. If prior knowledge of the position-related information of the VAs is available, both, $v_k^{(j)}$ and $\sigma_{d,k}^{(j)}$ can be computed using the SINRs from Section 3.3.2. If there is no prior knowledge, $v_k^{(j)}$ can be defined by the VA order, i.e. VAs with higher order have a lower weight, and the range standard deviations can be defined using the pulse duration T_p.

The likelihood function $f_{\overline{\text{VA}}}(\mathcal{Z}_n|\mathbf{p}_n, \mathcal{A})$ represents measurements that are falsely detected. It can be selected as a uniform distribution between zero and a maximum range that depends on the floor plan size and the used maximum VA order. More details can be found in [107].

4.2 Performance Evaluation

4.2.1 Measurement Setup

Measurements

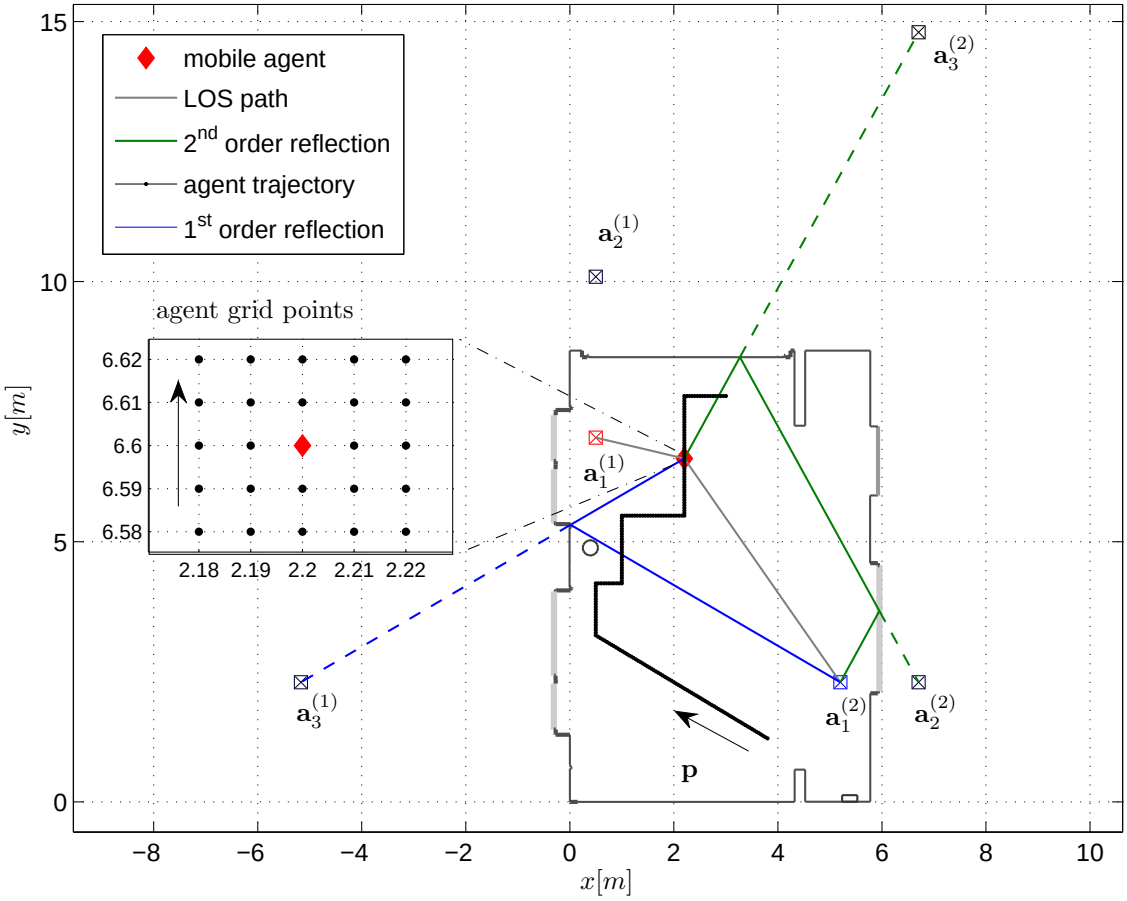

Figure 4.1: Floor-plan of an empty seminar room with a 5 cm-spaced trajectory (black line) of agent positions. The close-up shows that for every agent position $\mathbf{p}$ (magenta dot), a set of 25 measurements has been recorded in a rectangular grid with a 1 cm spacing. Furthermore, two physical anchors $j = \{1, 2\}$ are illustrated and a few of the expected VAs.

For the evaluation of this positioning approach, we use the seminar room scenario of the MeasureMINT database [102]. We use an agent trajectory as shown in Fig. 4.1, consisting of 220 points spaced by 5 cm. At each position, ultra-wideband (UWB) measurements are available of the channel between the agent and the two anchors at the positions $\mathbf{p}_1^{(1)} = [0.5, 7]^{\text{T}}$ and $\mathbf{p}_1^{(2)} = [5.2, 3.2]^{\text{T}}$. The measurements allow for 25 quasi-parallel trajectories, as in total 25×220 points have been measured at a 1 cm grid spacing [O6], [1]. The grid measurements in the vicinity of the agent's actual position serve for the estimation of DM. The measurements have

been performed using an M-sequence correlative channel sounder developed by *Ilmsens*. This sounder provides measurements over approximately the FCC frequency range, from $3 - 10\,\mathrm{GHz}$. On anchor and agent sides, dipole-like antennas made of Euro-cent coins have been used. They have an approximately uniform radiation pattern in azimuth plane and zeroes in the directions of floor and ceiling. Out of this range, we select the desired frequency band using filtering with a raised cosine pulse $s(t)\mathrm{e}^{2\pi f_c t}$ with a pulse duration $T_\mathrm{p} = 0.5\,\mathrm{ns}$ (corresponding to a bandwidth of $2\,\mathrm{GHz}$) at a center frequency of $f_\mathrm{c} = 7\,\mathrm{GHz}$. To get the complex-valued baseband signal, a down conversion is performed.

Estimation

To evaluate the likelihood function in (3.5), we used two approaches: (i) Grid based maximum a-posteriori (MAP) given in (4.1): The likelihood function is evaluated over a $40 \times 40\,\mathrm{cm}$ rectangle around the true agent position with resolution of $1\mathrm{x}1\,\mathrm{cm}^2$ and the highest mode corresponds to the estimated maximum of the likelihood function given in (4.5); (ii) PF-PSO: A sufficiently large number of particles, i.e. $N = 2000$, is uniformly distributed over the whole room. The likelihood function is evaluated for $N_\mathrm{iter} = 8$ iterations following the description given in Sec. 4.1.2, where the initial acceleration process noise $\sigma_\mathrm{acc} = 8\,\mathrm{cm/s}^2$ and the initial velocity weight $\Delta T = 0.0125\,\mathrm{s}$. Since the likelihood function has very narrow modes, the weights $a_n^{(i)}$ are compressed with a roughening factor which means that the exponent of the likelihood function was divided by this factor. The initial value of the roughening factor was set to a value of 100. During the iterations of the PF-PSO filter, σ_acc and ΔT parameters were linearly decreased down to zero to simulate an annealing process and the roughening factor was decreased until it reaches 1. To enhance the robustness of the point-estimate $\hat{\mathbf{p}}$ of the ML estimator, we computed the median over the entire set of particles at each trajectory point. To generate the error CDFs we performed Monte-Carlo simulations averaged over 30 dynamic model noise realizations[23].

4.2.2 Discussion of Performance Results

Measurements, Position Likelihood, and CRLB

In Fig. 4.2, the likelihood function (3.5) is shown in log-domain evaluated for the whole room for a measured CIR $\mathbf{r}^{(j)}$ between the agent located at position $\mathbf{p} = [2.2, 6.6]^\mathrm{T}$ and the two anchors. In the figure, the multi-modality of the likelihood function is clearly visible. The global maximum at $\hat{\mathbf{p}} = [2.19, 6.6]^\mathrm{T}$ matches the true position of the agent very well. The radii of the arcs with a high likelihood correspond to the delays of the LOS and VAs visible in the measurements. In the figure, we also plot the estimated positions and co-variances (estimated from particles) for a few trajectory points together with the computed CRLB of the position error. Both error ellipses are plotted with hundred-fold standard deviation. The orientation of the error ellipses depends on the geometry of the room and the positions of the anchors and the agent involved. We observe that the orientation and size of the CRLB error ellipses fit well with the estimated co-variance ellipses. Small deviations can be explained by the fact that the co-variance has to

[23] We observed that this number of used Monte-Carlo simulations leads to a steady state outcome suggesting that it is sufficiently high.

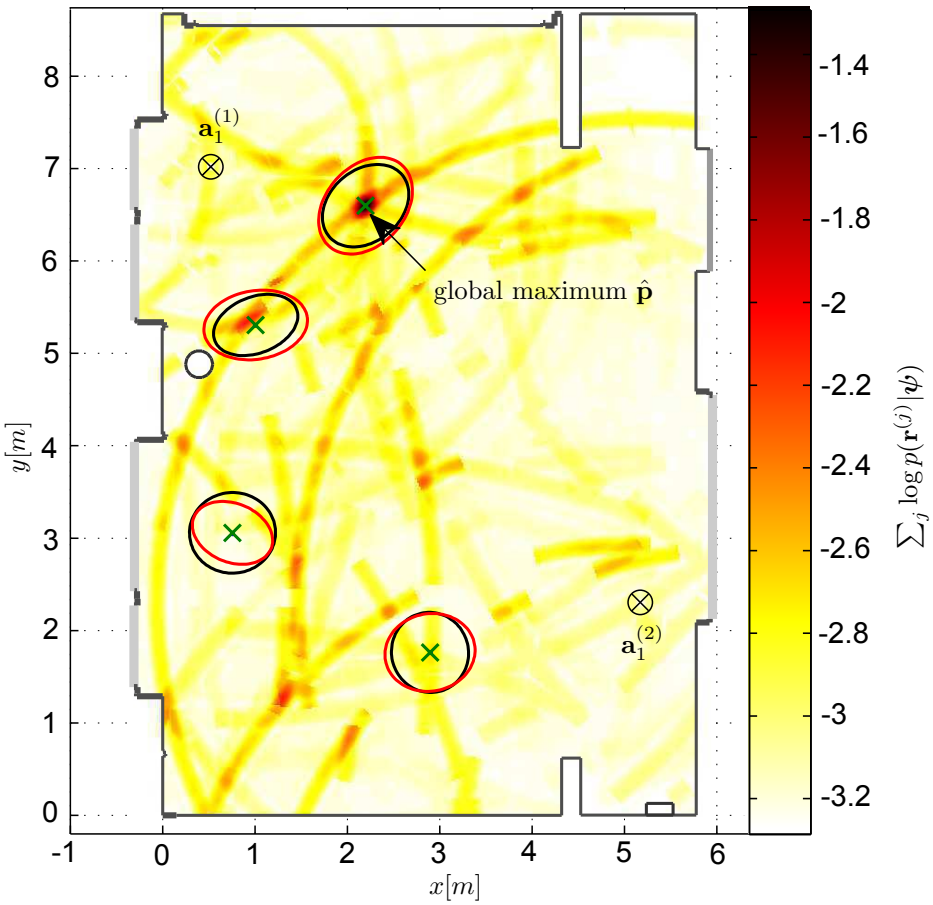

Figure 4.2: Likelihood evaluated over the whole room. The anchors are placed at $\mathbf{a}_1^{(1)}$ and $\mathbf{a}_1^{(2)}$, the agent is placed at $\mathbf{p} = [2.2, 6.6]^{\mathrm{T}}$. The global maximum at position $\hat{\mathbf{p}} = [2.19, 6.6]^{\mathrm{T}}$ matches well with the true agent position. Additionally, the estimated agent position, the co-variance and the CRLB are shown with hundred-fold standard deviation for a few other agent positions.

be estimated from a set of measurements rather than from a single measurement. The same holds for the estimation of parameters needed for the computation of the CRLB, c.f. (3.36). So, this comparison gives just an approximate comparison between the CRLB and the co-variance of the position estimate.

Positioning performance

In Fig. 4.3, the CDFs of the position error are shown for the grid-based MAP and PF-based ML estimation methods. These CDFs include data from all 220 agent positions using only Anchors 1 and 2 individually and in combination (top to bottom). The CDF plots *"without DM"* neglect the knowledge of DM, i.e. $\mathbf{C_r}^{(j)} = N_0^{(j)}\mathbf{I}_M$ in the likelihood (3.5). Then the signal model reduces to the deterministic MPCs plus additional AWGN. We observe that for both methods, the knowledge of DM results in a reduction of the position errors. Also, the occurrence of outliers is reduced when considering DM, which demonstrates the benefit of the suggested signal model and can be seen as a measure of higher *robustness*.

If only Anchor 2 is active, the position error is below 2.5 cm in 90 % of the estimates for the grid based MAP method considering DM and 5.5 cm without DM knowledge. The ML estimation with DM knowledge is also below 2.5 cm in 90 % of the estimates while it reaches a

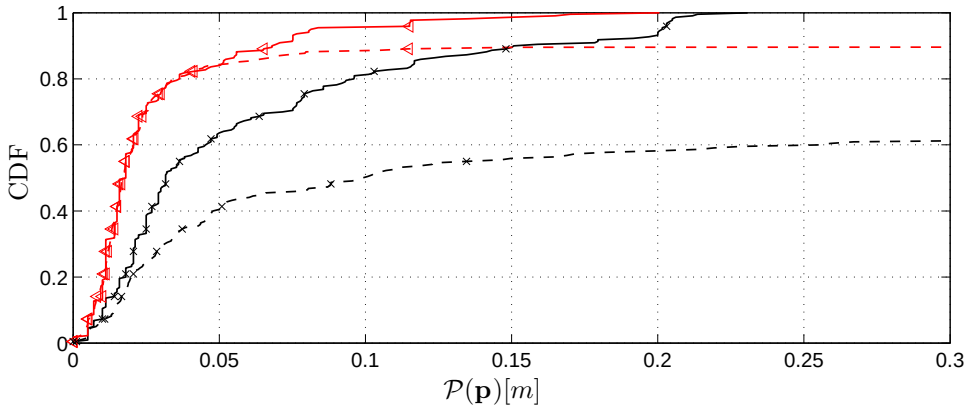

(a) Anchor $\mathbf{a}_1^{(1)}$

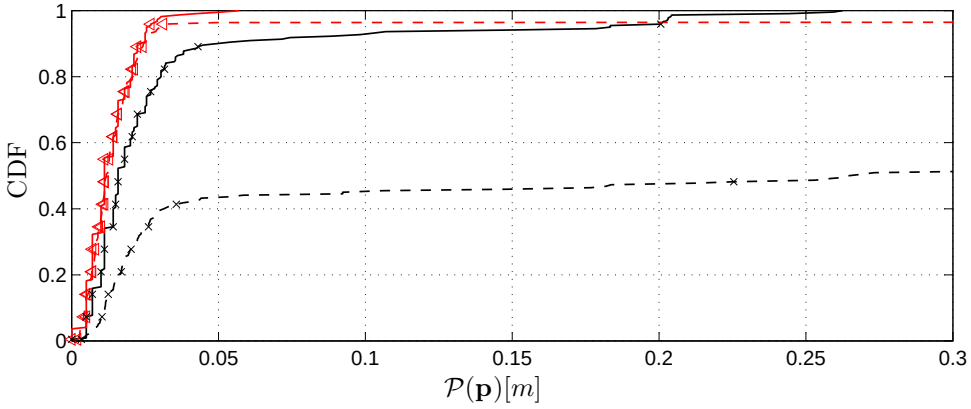

(b) Anchor $\mathbf{a}_1^{(2)}$

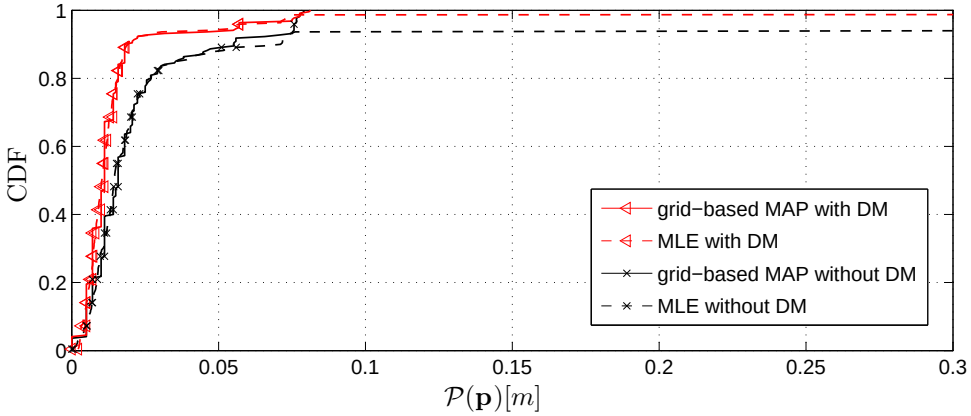

(c) Anchor $\mathbf{a}_1^{(1)}$ and $\mathbf{a}_1^{(2)}$

Figure 4.3: CDFs for the grid-based MAP and ML estimation methods, with and without considering DM in the likelihood function considering only $\mathbf{a}_1^{(1)}$ *(a),* $\mathbf{a}_1^{(2)}$ *(b) or the combination of both (c).*

similar accuracy in only 40 % of the cases without DM. The same holds for all combinations of the involved anchors: the performance of the ML estimation is much worse, without DM knowledge. The reasons for this are twofold: First, the model is less accurate, thus modes of the likelihood function at the wrong position are too optimistic which leads more often to a convergence of the ML estimation in the wrong mode. The second issue is of numerical nature. Due to the more probable model-mismatch of the signal model, the values of the log-likelihood function are even (much) smaller and also exhibit a larger dynamic range. Hence, the likelihood

function is more skewed which leads to the requirement of more particles for the ML estimation.

If Anchor 1 is active, the positioning error shows the same tendency, but the values are increased. This suggests that the location of Anchor 1 is less suited for positioning along the agent trajectory compared to the location of Anchor 2. Since information available through measurements never increases the uncertainty, the error is the smallest when both anchors are active. This is independent of the signal model used (with or without DM). The lowest error is achieved if DM is taken into account. Then the resulting error remains below 1.9 cm for both methods in 90 % of the position estimates. Note that the bandwidth used is 2 GHz, yielding a delay resolution of 15 cm.

4.3 Chapter Summary and Conclusions

In this chapter it was shown that the proposed maximum likelihood (ML) estimation algorithm for multipath-assisted indoor positioning is working with real channel measurement in a *robust* and *accurate* sense. Due to the rich geometric information contained in the MPCs, positioning is possible with only one anchor. Depending on the environment this is also true for NLOS scenarios, in principle. However, in a LOS scenario considering DM, a position error of less than 2.5 cm in 90 % of the estimates was achieved for only one active anchor. The results show that the knowledge of DM leads to significant improvement of robustness *and* accuracy of the estimation scheme. The proposed algorithm can be employed as an efficient scheme for initialization of multipath-assisted indoor navigation and tracking (MINT).

5

Position Tracking using Multipath Channel Information

In this chapter different state space estimators are presented for position tracking using multipath channel information. These state space estimators can be subdivided into the following groups:

1. Estimators that conduct DA between the expected delays (between agent and VAs) and the estimated MPC delays. Assuming a Gaussian state space and measurement noise, but a non-linear measurement equation $d(\mathbf{a}_{n,k}^{(j)}, \mathbf{p}_n)$, Kalman filters, like the extended Kalman filter (EKF) or the unscented Kalman filter (UKF), are proper choices of state space filters.

2. Estimators that using the likelihood function (3.5) of the entire received signal vectors $\mathbf{r}^{(j)}$, without doing explicitly DA. To cope with the non-linear and non-Gaussian likelihood model a PF is used as described in Section 4. These estimators are more robust in comparison to the EKF or UKF [108, 109], however on the other hand they have much higher computational complexity.

3. To preserve the *robustness* of PF-based methods, but with the additional benefit of low computational complexity, a hybrid filter is used that combines a PF-approach with an EKF or UKF (and DA) [110]. This hybrid approach needs much less particles to represent the posterior distribution of the state space.

Further, the state space (agent state) is extended to the positions of the VAs to set the stage for probabilistic MINT.

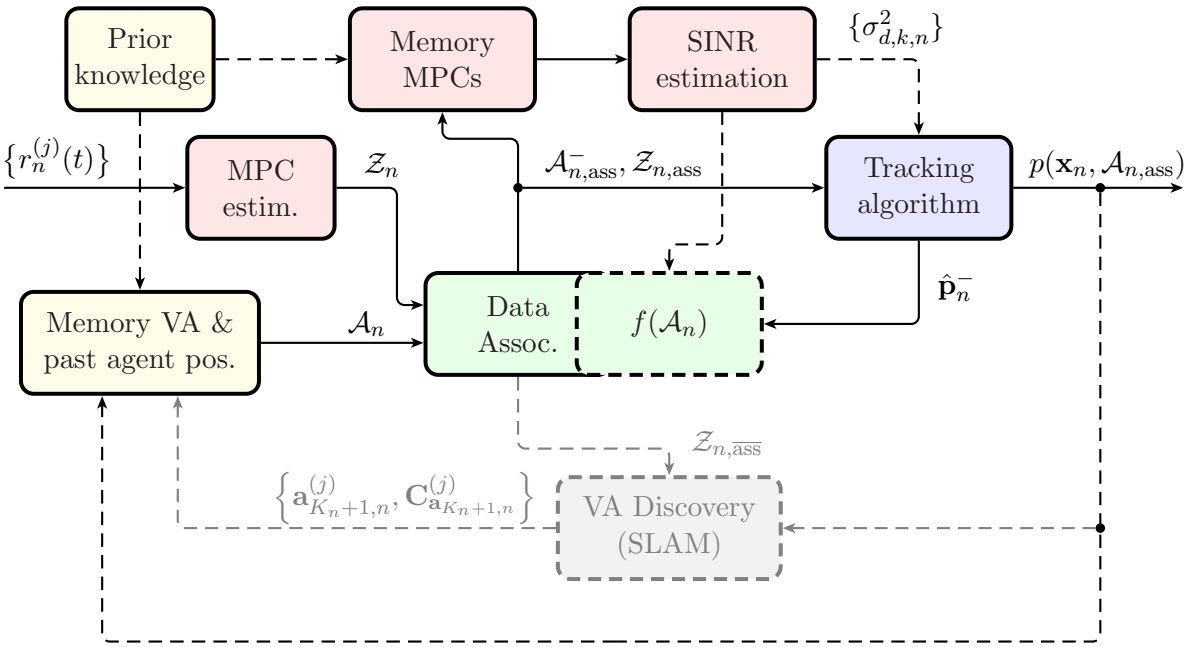

Figure 5.1: Block diagram of MINT using data association (DA). The gray blocks will be introduced in Chapter 6.

5.1 Multipath-assisted Indoor Navigation and Tracking (MINT) using Data Association (DA)

Parts of Section 5.1.1 are based on [O6], [1] and can be seen as a recap for the sake of completeness. Fig. 5.1 illustrates the schematics of the entire algorithm. Sub-blocks that executing the DA are depicted in green. All sets shown in Fig. 5.1, already represent the union sets for all J anchors (see for Section 2.2.1).

5.1.1 Data Association

The set of expected MPC delays $\mathcal{D}_n^{(j)}$ at time step n contains the distances of each VA in $\mathcal{A}_n^{(j)}$ to the predicted position (see Section 5.1.2)

$$\mathcal{D}_n^{(j)} = \left\{ d_{k,n}^{(j)} : \ \forall \ \mathbf{a}_{n,k}^{(j)} \in \mathcal{A}_n^{(j)} \right\}, \tag{5.1}$$

where $d_{k,n}^{(j)} = d(\mathbf{a}_{n,k}^{(j)}, \mathbf{p}_n)$ are the expected distances between the agent at position $\mathbf{p}_n$ and the k-th VA at position $\mathbf{a}_{n,k}^{(j)}$. The set of estimated distances of anchor j is given as $\mathcal{Z}_n^{(j)} = \{\hat{d}_{k,n}^{(j)}\}_{k=1}^{\hat{K}_n^{(j)}}$ as described in Section 2.2.1. As $\mathcal{D}_n^{(j)}$ and the set of estimated delays $\mathcal{Z}_n^{(j)}$ are sets of usually different cardinality, i.e. $|\mathcal{Z}_n^{(j)}| = \hat{K}_n^{(j)} \neq |\mathcal{D}_n^{(j)}| = K_n^{(j)}$, no conventional distance measure is defined and therefore there is no straightforward way of an association. We employ a well-known multi-target miss-distance, the *optimal sub-pattern assignment* (OSPA) metric [111].

For $\hat{K}_n^{(j)} \geq K_n^{(j)}$, which can be ensured by filling up $\mathcal{Z}_n^{(j)}$ with dummy clutter, it is defined as

$$d_{\mathrm{OSPA}}(\mathcal{D}_n^{(j)}, \mathcal{Z}_n^{(j)}) = \left[\frac{1}{\hat{K}_n^{(j)}} \left(\min_{\boldsymbol{\pi} \in \Pi_{\hat{K}_n^{(j)}}} \sum_{i=1}^{K_n^{(j)}} \left[d^{(d_\mathrm{c})}(d_{i,n}^{(j)}, \hat{d}_{\boldsymbol{\pi}_i,n}^{(j)}) \right]^p + d_\mathrm{c}^p (\hat{K}_n^{(j)} - K_n^{(j)}) \right) \right]^{\frac{1}{p}}, \quad (5.2)$$

where Π_N is defined as the set of permutations of positive integers up to N and $\boldsymbol{\pi}_i$ is a vector which elements represents the i-th ordering of positive integers. The function $d^{(d_\mathrm{c})}(x, y) = \min(d_\mathrm{c}, d(x, y))$, i.e. an arbitrary distance metric $d(\cdot)$ that is cut off at a $d_\mathrm{c} > 0$, the so-called *cut-off distance*, which is a design parameter. The metric order is denoted as p. The first sum in the metric is the cumulative distance over the optimal sub-pattern assignment of $\mathcal{Z}_n^{(j)}$ to $\mathcal{D}_n^{(j)}$, i.e. where $K_n^{(j)}$ entries of $\mathcal{Z}_n^{(j)}$ are assigned optimally to the entries of $\mathcal{D}_n^{(j)}$. The Hungarian or Munkres algorithm can be used for this assignment [111, 112]. For the remaining $\hat{K}_n^{(j)} - K_n^{(j)}$ entries of $\mathcal{Z}_n^{(j)}$, d_c is assigned as penalty distance. For performing the data association (DA), we introduce a set $\mathcal{C}_n^{(j)}$ of correspondence variables [113], whose i-th entry $c_{n,i}^{(j)}$ is defined as

$$c_{n,i}^{(j)} = \begin{cases} k, & \text{if } \hat{d}_{i,n}^{(j)} \text{ corresponds to VA } \mathbf{a}_k^{(j)} \\ 0, & \text{if } \hat{d}_{i,n}^{(j)} \text{ corresponds to clutter.} \end{cases} \quad (5.3)$$

The optimal sub-pattern assignment between $\mathcal{D}_n$ and $\mathcal{Z}_n$ is reflected by the first part of (5.2)

$$\boldsymbol{\pi}_\mathrm{opt} = \arg \min_{\boldsymbol{\pi} \in \Pi_{\hat{K}_n^{(j)}}} \sum_{i=1}^{K_n^{(j)}} d^{(d_\mathrm{c})}(d_{i,n}^{(j)}, \hat{d}_{\boldsymbol{\pi}_i,n}^{(j)})^p. \quad (5.4)$$

With this, the correspondence variables are set as

$$c_{n,i}^{(j)} = \begin{cases} k, & \text{if } [\boldsymbol{\pi}_\mathrm{opt}]_k = i \text{ and } d^{(d_\mathrm{c})}(d_{n,k}^{(j)}, \hat{d}_{n,i}^{(j)}) < d_\mathrm{c} \\ 0, & \text{else.} \end{cases} \quad (5.5)$$

Where, $[\boldsymbol{\pi}_\mathrm{opt}]_k$ denotes the k-th entry of the optimal sub-pattern assignment. After the DA was applied for all anchors, the following union sets are defined:

- The set of associated discovered (and optionally a-priori known) VAs $\mathcal{A}_{n,\mathrm{ass}} = \bigcup_j \mathcal{A}_{n,\mathrm{ass}}^{(j)}$.
- The according set of associated measurements $\mathcal{Z}_{n,\mathrm{ass}} = \bigcup_j \mathcal{Z}_{n,\mathrm{ass}}^{(j)}$.
- The set of remaining measurements $\mathcal{Z}_{n,\overline{\mathrm{ass}}} = \bigcup_j \mathcal{Z}_{n,\overline{\mathrm{ass}}}^{(j)}$, which are not associated to VAs of $\mathcal{A}_n$. As shown in Fig. 5.1 (yellow parts), these not associated delays are used for the discovery of new VAs as described in Section 6.

Ongoing work: The DA can also be performed probabilistically [114, 115], i.e. for a set of particles, the likelihood function (4.15) is evaluated for each association pair between the measured delays and the expected delays to the VAs at the agent position $\mathbf{p}_n$. For each particle with the according set of associations $\mathcal{A}_{n,\mathrm{ass}}^{(i)}$, the equations (5.7) and (5.6) are evaluated using e.g. a UKF as it will be described in the following subsections. The posterior distribution of the state space is then estimated from all weighted UKF posterior states that belong to the

particles of the DA. An algorithm based on belief propagation on a factor graph is presented in [116], which involves target-related and measurement-related data association. The algorithms' complexity scales only quadratically in the number of targets, i.e. in our case the number of VAs, and linearly in the number of measurements, i.e. the number of sensors. It also outperforms state-of-the-art methods, like the Joint probabilistic data association filter (JPDA) [114] whose complexity scales exponentially with the number of targets (VAs).

5.1.2 State Space and Measurement Model

The distance estimates for all anchors $\mathcal{Z}_n$ are stacked in the measurement input vector and modeled as

$$\mathbf{z}_n = \left[\dots,\ d(\mathbf{a}_{n,k}^{(j)}, \mathbf{p}_n),\ \dots\right]^T + \mathbf{n}_{\mathrm{z},n}, \qquad \mathbf{a}_{k,n}^{(j)} \in \mathcal{A}_{n,\mathrm{ass}}. \tag{5.6}$$

The cardinality of the VA set $\mathcal{A}_{n,\mathrm{ass}}$ is defined as $K_n = \sum_j K_n^{(j)}$. The vector $\mathbf{n}_{\mathrm{z},n}$ contains Gaussian measurement noise with covariance matrix $\mathbf{R}_{\mathrm{z},n}$. The choice of $\mathbf{R}_{\mathrm{z},n}$ depends on the amount of prior information about the range uncertainties (3.38) and will be explained in Section 5.1.3. As state space model for the agent, a simple linear Gaussian constant-velocity motion model is used

$$\begin{aligned}\mathbf{x}_n &= \mathbf{A}(\mathbf{x}_{n-1}, \mathbf{n}_{\mathrm{a},n}) = \mathbf{F}\mathbf{x}_{n-1} + \mathbf{G}\mathbf{n}_{\mathrm{a},n} \\ &= \begin{bmatrix} 1 & 0 & \Delta T & 0 \\ 0 & 1 & 0 & \Delta T \\ 0 & 0 & 1 & 0 \\ 0 & 0 & 0 & 1 \end{bmatrix} \mathbf{x}_n + \begin{bmatrix} \frac{\Delta T^2}{2} & 0 \\ 0 & \frac{\Delta T^2}{2} \\ \Delta T & 0 \\ 0 & \Delta T \end{bmatrix} \mathbf{n}_{\mathrm{a},n}.\end{aligned} \tag{5.7}$$

The state vector of the agent is $\mathbf{x}_n = [\mathbf{p}_n, \mathbf{x}_n]^{\mathrm{T}}$, and ΔT is the discrete time update rate. The driving acceleration noise term $\mathbf{n}_{\mathrm{a},n}$ is zero-mean, circular symmetric with variance σ_{a}^2 and models motion changes that deviate from the constant-velocity assumption. The transformed noise covariance matrix is given as $\mathbf{R}_{\mathrm{a}} = \sigma_{\mathrm{a}}^2 \mathbf{G}\mathbf{G}^{\mathrm{T}}$. Possible state space filters in combination with DA with low computational demand are the following:

The EKF for MINT [O6], [1]: Uses a first-order Taylor approximation of the measurement equations $d(\mathbf{a}_{n,k}^{(j)}, \mathbf{p}_n)$ for the j-th anchor, yielding

$$\mathbf{H}_n^{(j)} = \begin{bmatrix} \frac{\partial d(\mathbf{a}_{1,n}, \mathbf{p}_n)}{\partial x_n} & \frac{\partial d(\mathbf{a}_{1,n}, \mathbf{p}_n)}{\partial y_n} & 0 & 0 \\ \vdots & \vdots & \vdots & \vdots \\ \frac{\partial d(\mathbf{a}_{K_n,n}, \mathbf{p}_n)}{\partial x_n} & \frac{\partial d(\mathbf{a}_{K_n,n}, \mathbf{p}_n)}{\partial y_n} & 0 & 0 \end{bmatrix}, \tag{5.8}$$

where for the sake of simplicity the anchor index j has been dropped from the VAs $\mathbf{a}_{k,n}^{(j)}$ and the number of VAs $K_n^{(j)}$. Stacking the linearized measurement matrices of the J anchors yields $\mathbf{H}_n = \left[\left(\mathbf{H}_n^1\right)^{\mathrm{T}}, \dots, \left(\mathbf{H}_n^J\right)^{\mathrm{T}}\right]^{\mathrm{T}}$. After the prediction step (5.9) of the EKF, the DA is performed. Then, the linearized measurement matrix (5.8) and the covariance matrix $\mathbf{R}_{\mathrm{z},n}$ are computed

and the EKF update (5.10) can be performed. The principle algorithm scheme is depicted in Fig. 5.1.

- Prediction step:

$$\mathbf{x}_n^- = \mathbf{A}(\mathbf{x}_{n-1}) = \mathbf{F}\mathbf{x}_{n-1} \tag{5.9a}$$

$$\mathbf{C}_{\mathbf{x}_n}^- = \mathbf{F}\mathbf{C}_{\mathbf{x}_{n-1}}\mathbf{F}^{\mathrm{T}} + \mathbf{R}_{\mathrm{a}} \tag{5.9b}$$

- Update step:

$$\mathbf{z}_n^- = \big[\,\ldots,\; d(\mathbf{a}_{n,k}^{(j)}, \mathbf{p}_n^-),\; \ldots\big]^T, \qquad \mathbf{a}_{k,n}^{(j)} \in \mathcal{A}_{n,\mathrm{ass}} \tag{5.10a}$$

$$\mathbf{K}_n = \mathbf{C}_{\mathbf{x}_n}^- \mathbf{H}_n^{\mathrm{T}} \big(\mathbf{H}_n \mathbf{C}_{\mathbf{x}_n}^- \mathbf{H}_n^{\mathrm{T}} + \mathbf{R}_{z,n}\big)^{-1} = \mathbf{C}_{\mathbf{x}_n^- \mathbf{z}_n^-} \mathbf{C}_{\mathbf{z}_n^- \mathbf{z}_n^-}^{-1} \tag{5.10b}$$

$$\mathbf{x}_n = \mathbf{x}_n^- + \mathbf{K}_n \big(\mathbf{z}_n - \mathbf{z}_n^-\big) \tag{5.10c}$$

$$\mathbf{C}_{\mathbf{x}_n} = (\mathbf{I} - \mathbf{K}_n \mathbf{H}_n)\mathbf{C}_{\mathbf{x}_n}^- = \mathbf{C}_{\mathbf{x}_n}^- - K_n \mathbf{C}_{\mathbf{z}_n^- \mathbf{z}_n^-} \mathbf{K}_n^{\mathrm{T}} \tag{5.10d}$$

The unscented Kalman filter (UKF) for MINT: The UKF uses a so-called unscented transformation (UT) [108] that is a method for calculating the statistics of a RV $\mathbf{x} \in \mathbb{R}^I$ with dimension I, which undergoes a nonlinear transformation. This method is based on deterministically chosen sample points, the so-called sigma points (SPs) [108,109]. These SPs can be directly inserted into non-linear prediction and update equations, instead of using a first-order Taylor approximation of the nonlinearity as it is done for EKF. The first-order approximation can induce large errors in the mean $\boldsymbol{\mu}_{\mathbf{x}} = \mathbb{E}\{\mathbf{x}\}$ and the covariance matrix $\mathbf{C}_{\mathbf{x}} = \mathbb{E}\big\{(\mathbf{x} - \boldsymbol{\mu}_{\mathbf{x}})(\mathbf{x} - \boldsymbol{\mu}_{\mathbf{x}})^{\mathrm{T}}\big\}$ of the transformed RV $\mathbf{x} \in \mathbb{R}^I$. This may lead to an underestimation of the covariance and a bias in the estimated mean, so that the filter may tend even to diverge from the agent track. This can be prevented by using the UKF[24].

The SPs of the RV $\mathbf{x}$ are $\mathcal{X} = \big\{\mathbf{x}^{(i)}\big\}_{i=0}^{2I}$ and their corresponding "mean" weights $\big\{w_{\mathrm{m}}^{(i)}\big\}_{i=0}^{2I}$ and "covariance" weights $\big\{w_{\mathrm{c}}^{(i)}\big\}_{i=0}^{2I}$ are chosen such that the sample mean estimate $\hat{\boldsymbol{\mu}}_{\mathbf{x}} = \sum_{i=0}^{2I} w_{\mathrm{m}}^{(i)} \mathbf{x}^{(i)}$ and the sample covariance matrix estimate $\hat{\mathbf{C}}_{\mathbf{x}} = \sum_{i=0}^{2I} w_{\mathrm{c}}^{(i)} (\mathbf{x}^{(i)} - \hat{\boldsymbol{\mu}}_{\mathbf{x}})(\mathbf{x}^{(i)} - \hat{\boldsymbol{\mu}}_{\mathbf{x}})^{\mathrm{T}}$ are exactly the same as the true mean $\boldsymbol{\mu}_{\mathbf{x}}$ and covariance matrix $\mathbf{C}_{\mathbf{x}}$ of the exemplary RV. The closed-form expression of the SP, the weights and the tuning parameters can be found in [108,109]. The UKF is described by the following set of equations:

[24] The differences between the means and the covariance matrices after first-order Taylor approximation and UT are illustrated very well in Fig. 2 in [109].

- Form a matrix $\mathcal{X}_{n-1}$ with $2I+1$ SPs:

$$\mathcal{X}_{n-1,0} = \mathbf{x}_{n-1} \tag{5.11}$$

$$\mathcal{X}_{n-1,i} = \mathbf{x}_{n-1} + \left[\gamma\sqrt{\mathbf{C}_{\mathbf{x}_{n-1}}}\right]_i \qquad i = 1,\ldots,I \tag{5.12}$$

$$\mathcal{X}_{n-1,i} = \mathbf{x}_{n-1} - \left[\gamma\sqrt{\mathbf{C}_{\mathbf{x}_{n-1}}}\right]_i \qquad i = I+1,\ldots,2I, \tag{5.13}$$

where for every row of the covariance matrix $\mathbf{C}_{\mathbf{x}_{n-1}}$ a set of I SPs is computed and $\gamma = \sqrt{I+\lambda}$ with λ as scaling factor, chosen as in [109].

- Prediction step:

$$\mathcal{X}_n^- = \mathbf{A}(\mathcal{X}_{n-1}) \tag{5.14a}$$

$$\mathbf{x}_n^- = \sum_{i=0}^{2I} w_{\mathrm{m}}^{(i)} \mathcal{X}_{i,n}^- \tag{5.14b}$$

$$\mathbf{C}_{\mathbf{x}_n}^- = \sum_{i=0}^{2I} w_{\mathrm{c}}^{(i)} (\mathcal{X}_{i,n}^- - \mathbf{x}_n^-)(\mathcal{X}_{i,n}^- - \mathbf{x}_n^-)^{\mathrm{T}} + \mathbf{R}_{\mathrm{a}} \tag{5.14c}$$

- Redraw $2I+1$ SPs $\mathcal{X}_n^{*-}$ from predicted mean $\mathbf{x}_n^-$ and covariance matrix $\mathbf{C}_{\mathbf{x}_n}^-$

- Update step:

$$\mathcal{Z}_n^{\mathrm{SP}} = \left[\ldots,\ d(\mathbf{a}_{n,k}^{(j)}, \mathbf{x}_n^{*-}),\ \ldots\right]^T, \qquad \forall\ \mathbf{a}_{k,n}^{(j)} \in \mathcal{A}_{n,\mathrm{ass}},\ \forall \mathbf{x}_n^{*-} \in \mathcal{X}_n^{*-} \tag{5.15a}$$

$$\mathbf{z}_n^- = \sum_{i=0}^{2I} w_{\mathrm{m}}^{(i)} \mathcal{Z}_{i,n}^{\mathrm{SP}} \tag{5.15b}$$

$$\mathbf{C}_{\mathbf{z}_n^-\mathbf{z}_n^-} = \sum_{i=0}^{2I} w_c^{(i)} (\mathcal{Z}_{i,n}^{\mathrm{SP}} - \mathbf{z}_n^-)(\mathcal{Z}_{i,n}^{\mathrm{SP}} - \mathbf{z}_n^-)^{\mathrm{T}} + \mathbf{R}_{\mathrm{z},n} \tag{5.15c}$$

$$\mathbf{C}_{\mathbf{x}_n^-\mathbf{z}_n^-} = \sum_{i=0}^{2I} w_c^{(i)} (\mathcal{X}_n^{*-} - \mathbf{x}_n^-)(\mathcal{Z}_{i,n}^{\mathrm{SP}} - \mathbf{z}_n^-)^{\mathrm{T}} \tag{5.15d}$$

With these equations, the Kalman gain $\mathbf{K}_n$ (5.10b), the posterior mean $\mathbf{x}_n$ in (5.10c) and the posterior covariance matrix $\mathbf{C}_{\mathbf{x}_n}$ in (5.10d) can be computed.

5.1.3 SINR and Range Uncertainty Estimation

For the measurement noise model of the tracking filter, the range estimation uncertainties $\mathrm{var}\left\{\hat{d}_{k,n}^{(j)}\right\}$ to the associated VAs are used to build the measurement noise covariance matrix as

$$\mathbf{R}_{\mathrm{z},n} = \mathrm{diag}\left\{\mathrm{var}\left\{\hat{d}_{k,n}^{(j)}\right\}\right\} = \mathrm{diag}\left\{\left(\sigma_{\mathrm{d},k,n}^{(j)}\right)^2\right\} \qquad \forall\, k,j : \mathbf{a}_{k,n}^{(j)} \in \mathcal{A}_{n,\mathrm{ass}}. \tag{5.16}$$

Hence, the measurement noise covariance matrix is directly coupled with the position-related information that is based on SINRs. As described in (3.38) the MPC range uncertainty is related to the SINR_k of the k-th VA at agent position $\mathbf{p}_n$ via the inverse Fisher information of the corresponding distance. The SINRs are estimated with a method of moments estimator [O6] using a set of MPC complex amplitudes, associated k-th VA. The estimator is defined as

$$\mathrm{SINR}_{k,\mathrm{moments}}^{(j)} = \left(\frac{\hat{\mu}_1}{\left(\hat{\mu}_1^2 - \hat{\mu}_2\right)^{1/2}} - 1\right)^{-1}, \tag{5.17}$$

where $\hat{\mu}_1$ and $\hat{\mu}_2$ are the mean and the variance of a set of estimated complex amplitudes $\left\{|\hat{\alpha}_k^{(j)}|^2\right\}$, respectively. According to (2.1) the estimated complex amplitudes $\hat{\alpha}_k^{(j)} = \hat{\alpha}_{\mathrm{det},k}^{(j)} + \hat{\alpha}_{\mathrm{diff},k}^{(j)} + \hat{\alpha}_{\mathrm{noise},k}$ comprise the deterministic, the DM and the AWGN parts of the k-th MPC. Hence, the method of moments estimator estimates the Rician K-factor of the k-th MPC which represents the according SINR_k. Appendix C provides insights about the estimator's connection to the signal model in (2.1).

This estimation can be done either from offline training data or online over a window of past estimated agent positions with the according set of associated amplitudes $\left\{\hat{\alpha}_{k,i}^{(j)}\right\}_{i=n_0}^{n}$. All blocks in Fig 5.1 that are responsible for estimating the range variances are drawn in red. The online estimation is started once an initial window size of measurements is available for the respective newly associated VA. Until then, a default value $\sigma_{\mathrm{d,init}}^2$ is assigned. The VA-filter block in Fig. 5.1 (in green) allows to exclude VAs with too unreliable position information, i.e. too large ranging standard deviation, from the DA, using a threshold value $\sigma_{\mathrm{d,max}}^2$. For a VA without associated measurements at time step n, the previous value of the estimated range variance is assigned.

5.1.4 Integrate VAs into the State Space

As it has been discussed in Section 2.1, for a proper description of the environment the uncertainties in the floor plan have to be considered, captured by the uncertainty of the VAs as described in (2.9). That means the VAs have to be represented by RVs within a joint probabilistic space with the agent's probabilistic state. With the online estimation of the SINRs of the k-th VA as described in Section 5.1.3 and the recursive estimation of the VA position marginals, the next step towards a "fully" cognitive positioning system is accomplished. The interrelation between the Bayesian state estimator and the GPEM memory at the perceptor-side of the CDS are indicated by the up- and downwards arrows in Fig. 2.3. To reference to this new method, we use the term *probabilistic MINT*. The according Bayesian FIM for the agent and the VA positions are given in (3.58) and the marginal Bayesian FIM for the agent in (3.60). The last

term of equation (3.60) illustrates the information loss due to the uncertainties in the VAs in comparison to (3.36).

To incorporate the associated VAs $\mathcal{A}_{n,\text{ass}}$ into the state space of $\mathbf{x}_n$, the model (5.7) is extended to

$$\tilde{\mathbf{x}}_n = \tilde{\mathbf{F}}_n \tilde{\mathbf{x}}_{n-1} + \tilde{\mathbf{G}}_n \mathbf{n}_{\text{a},n} = \begin{bmatrix} \mathbf{F} & \mathbf{0}_{4\times 2K_n} \\ \mathbf{0}_{2K_n\times 4} & \mathbf{I}_{2K_n\times 2K_n} \end{bmatrix} \tilde{\mathbf{x}}_{n-1} + \begin{bmatrix} \mathbf{G} \\ \mathbf{0}_{2K_n\times 2} \end{bmatrix} \mathbf{n}_{\text{a},n}, \tag{5.18}$$

where $\tilde{\mathbf{x}}_n = [\mathbf{x}_n^{\text{T}}, \mathbf{a}_{2,n}^{\text{T}}, \ldots, \mathbf{a}_{K_n,n}^{\text{T}}]^{\text{T}}$ represents the stacked state vector, where $\{\mathbf{a}_{k,n}^{(j)}\} \in \mathcal{A}_{n,\text{ass}}$. The covariance matrix of $\tilde{\mathbf{x}}_n$ is defines as

$$\tilde{\mathbf{C}}_n = \begin{bmatrix} \mathbf{C}_{\mathbf{x}_n} & \begin{bmatrix} \mathbf{C}_{\mathbf{x}_n,\mathbf{a}_{2,n}} & \cdots & \mathbf{C}_{\mathbf{x}_n,\mathbf{a}_{K_n,n}} \end{bmatrix} \\ \begin{bmatrix} \mathbf{C}_{\mathbf{x}_n,\mathbf{a}_{2,n}}^{\text{T}} \\ \vdots \\ \mathbf{C}_{\mathbf{x}_n,\mathbf{a}_{K_n,n}}^{\text{T}} \end{bmatrix} & \begin{bmatrix} \mathbf{C}_{\mathbf{a}_{2,n}} & \cdots & \mathbf{C}_{\mathbf{a}_{2,n},\mathbf{a}_{K_n,n}} \\ \vdots & \ddots & \vdots \\ \mathbf{C}_{\mathbf{a}_{2,n},\mathbf{a}_{K_n,n}}^{\text{T}} & \cdots & \mathbf{C}_{\mathbf{a}_{K_n,n}} \end{bmatrix} \end{bmatrix}, \tag{5.19}$$

where $\mathbf{C}_{\mathbf{x}_n,\mathbf{a}_{k,n}}$ are the cross-covariances between the agent state $\mathbf{x}_n$ and the VAs at positions $\mathbf{a}_{k,n}$, $\mathbf{C}_{\mathbf{a}_{k,n},\mathbf{a}_{k',n}}$, with $k \neq k'$, are the cross-covariances between VAs and $\mathbf{C}_{\mathbf{a}_{k,n}}$ are the covariances of the VAs. The measurement model is defined as

$$\tilde{\mathbf{z}}_n = \tilde{\mathbf{h}}_n(\tilde{\mathbf{x}}_n) + \tilde{\mathbf{n}}_{z,n} = \tilde{\mathbf{H}}_n \tilde{\mathbf{x}}_n + \tilde{\mathbf{n}}_{z,n}, \tag{5.20}$$

where $\tilde{\mathbf{z}}_n = [\mathbf{z}_n^{\text{T}}, \mathbf{z}_{2,\mathcal{P}_{2,n}}^{\text{T}}, \ldots, \mathbf{z}_{K_n,\mathcal{P}_{K_n,n}}^{\text{T}}]^{\text{T}}$ is the stacked measurement vector. The vector $\mathbf{z}_{k,\mathcal{P}_{k,n}}$ represents a set of measurements over time (past measurements) that have been associated with the k-th VA, where $\mathcal{P}_{k,n}$ defines the according set of time indices at which the DA was possible. The stack vector $\tilde{\mathbf{n}}_{z,n}$ contains the according measurement noise. The measurement model $\tilde{\mathbf{h}}_n$ contains all distance equations from the VA positions to the agent position $d(\mathbf{a}_{n,k}^{(j)}, \mathbf{p}_n)\ \forall\, \mathbf{a}_{n,k}^{(j)} \in \mathcal{A}_{n,\text{ass}}$ and from the actual and past agent positions to the VA positions $d(\mathbf{p}_n, \mathbf{a}_{timestepsym,k}^{(j)})\ \forall\, \mathbf{a}_{n,k}^{(j)} \in \mathcal{A}_{n,\text{ass}}$ to update the agent and the VAs, respectively.

In case an EKF is used as state space estimator, the linearized measurement matrix $\tilde{\mathbf{H}}_n = \left[\left(\tilde{\mathbf{H}}_n^1\right)^{\text{T}}, \ldots, \left(\tilde{\mathbf{H}}_n^J\right)^{\text{T}}\right]^{\text{T}}$ is needed as illustrated in Equation (5.21). Note that (5.21) shows the general structure of the fully occupied measurement matrix, but for time instance n just columns are present for which the corresponding VAs are in $\mathcal{A}_{n,\text{ass}}$, and rows for which measurements of $\mathbf{z}_n$ and $\mathbf{z}_{k,\mathcal{P}_{k,n}}^{\text{T}}\ \forall \mathbf{a}_{n,k}^{(j)} \in \mathcal{A}_{n,\text{ass}}$ are available. To compute all distance equations in $\tilde{\mathbf{h}}_n$ and derivatives in $\tilde{\mathbf{H}}_n$, also past agent positions $\mathbf{p}_i$ with $i \in \mathcal{P}_{k,n}\ \forall\, k$ are used. The measurement covariance matrix $\mathbf{R}_{\text{z},n}$ contains the according past range variances that are based on the estimated SINRs.

In (5.21) all anchor indices j are dropped for $\mathbf{a}_{k,n}^{(j)}$ and for $K_n^{(j)}$, for the sake of simplicity. The upper left block in (5.21) comprises the linearized measurement equations for the agent position $\mathbf{p}_n$. The other K_n blocks of linearized measurement equations are for the VA positions $\{\mathbf{a}_{k,n}^{(j)}\} \in \mathcal{A}_{n,\text{ass}}$. The upper right diagonal matrix holds the linearized measurement equations for the actual delay measurements to the VAs and the lower right block-diagonal matrix the linearized measurement equations for the past measurements to VAs that were associated with the according delay. As shown in Figure 5.1, the tracking filter (blue block) feeds the newly estimated agent position $\mathbf{p}$ and the VA positions $\{\mathbf{a}_{k,n}^{(j)}\}_{k=1}^{K^{(j)}}$ back to the VAs/agent position

memory (yellow block). These relations between the tracking filter and the memory are reflected by the interconnection between the Bayesian state filter block and environment model memory block of the perception side of the cognitive positioning system, shown in Figure 2.3.

The additional past states and measurements are incorporated to improve the updates of the VA positions and can be interpreted as an extension of the measurement model. Considering also the uncertainties of the past agent positions in a "fully" Bayesian approach, one would need to incorporate the agent's past positions and covariances into the state space to pass the uncertainties onto the actual position of the agent. With this the cross-covariances between the past states itself and the VAs have to be considered in the state space model and measurement model equations. The concept of using past agent states for estimating features, in our case the VAs, was termed in [117] as delayed mapping. An optimal smoothing tracking filter [118] that propagates the uncertainty back and forth in time (message passing over time) is beneficial to further improving the agent positions. The state space in (5.18) and measurement model in (5.20) set the stage for SLAM which will be discussed in Section 6.

$$
\tilde{\mathbf{H}}_n^{(j)} = \begin{bmatrix}
\frac{\partial d(\mathbf{a}_{1,n},\mathbf{p}_n)}{\partial x_n} & \frac{\partial d(\mathbf{a}_{1,n},\mathbf{p}_n)}{\partial y_n} & 0 & 0 & 0 & 0 & \dots \\
\frac{\partial d(\mathbf{a}_{2,n},\mathbf{p}_n)}{\partial x_n} & \frac{\partial d(\mathbf{a}_{2,n},\mathbf{p}_n)}{\partial y_n} & 0 & 0 & \frac{\partial d(\mathbf{a}_{2,n},\mathbf{p}_n)}{\partial x_{2,n}} & \frac{\partial d(\mathbf{a}_{2,n},\mathbf{p}_n)}{\partial y_{2,n}} & \dots \\
\vdots & \vdots & \vdots & \vdots & \vdots & \vdots & \vdots \\
\frac{\partial d(\mathbf{a}_{K_n,n},\mathbf{p}_n)}{\partial x_n} & \frac{\partial d(\mathbf{a}_{K_n,n},\mathbf{p}_n)}{\partial y_n} & 0 & 0 & 0 & 0 & \dots \\
0 & 0 & 0 & 0 & \frac{\partial d(\mathbf{a}_{2,n},\mathbf{p}_{n-1})}{\partial x_{2,n}} & \frac{\partial d(\mathbf{a}_{2,n},\mathbf{p}_{n-1})}{\partial y_{2,n}} & \dots \\
\vdots & \vdots & \vdots & \vdots & \vdots & \vdots & \vdots \\
0 & 0 & 0 & 0 & \frac{\partial d(\mathbf{a}_{2,n},\mathbf{p}_1)}{\partial x_{2,n}} & \frac{\partial d(\mathbf{a}_{2,n},\mathbf{p}_1)}{\partial y_{2,n}} & \dots \\
0 & 0 & 0 & 0 & 0 & 0 & \dots \\
\vdots & \vdots & \vdots & \vdots & \vdots & \vdots & \vdots \\
0 & 0 & 0 & 0 & 0 & 0 & \dots
\end{bmatrix}
\begin{bmatrix}
\dots & 0 & 0 \\
\dots & 0 & 0 \\
\vdots & \vdots & \vdots \\
\dots & \frac{\partial d(\mathbf{a}_{K_n,n},\mathbf{p}_n)}{\partial x_{K_n,n}} & \frac{\partial d(\mathbf{a}_{K_n,n},\mathbf{p}_n)}{\partial y_{K_n,n}} \\
\dots & 0 & 0 \\
\vdots & \vdots & \vdots \\
\dots & 0 & 0 \\
\dots & \frac{\partial d(\mathbf{a}_{K_n,n},\mathbf{p}_{n-1})}{\partial x_{K_n,n}} & \frac{\partial d(\mathbf{a}_{K_n,n},\mathbf{p}_{n-1})}{\partial y_{K_n,n}} \\
\vdots & \vdots & \vdots \\
\dots & \frac{\partial d(\mathbf{a}_{K_n,n},\mathbf{p}_1)}{\partial x_{K_n,n}} & \frac{\partial d(\mathbf{a}_{K_n,n},\mathbf{p}_1)}{\partial y_{K_n,n}}
\end{bmatrix}. \quad (5.21)
$$

5.2 MINT without DA

In this section, again the VA positions $\mathbf{a}_{k,n}^{(j)}$ are assumed to be known exactly. Hence, the state space vector $\tilde{\mathbf{x}}_n = \mathbf{x}_n$ includes only the state of the agent.

5.2.1 Sequential Monte Carlo Methods using the entire received Signal

The SIR PF introduced in Section 4.1.2 is used in the same manner for tracking of the agent's marginal PDF $p(\mathbf{p}_n)$. The posterior state distribution of the agent is described by a finite set of weighted particles $\{\mathbf{x}_n^{(i)}, a_n^{(i)}\}_{i=1}^{I}$ for every time instance n to describe the temporal evolution of the PDF. In contrast to methods described above, no DA is needed which means that the Bayesian state estimator uses the information of the entire received signal $r(t)$ by evaluating the likelihood function $p(\mathbf{r}_n|\mathbf{p}_n, \boldsymbol{\psi}_n)$ in (3.5).

Online estimation of the Noise Covariance Matrix

As the SINRs of the VAs are estimated in an online manner, also the noise covariance matrix of DM and AWGN $\hat{\mathbf{C}}_{\mathrm{r},n}$ is estimated during the tracking over a certain window of past received signals $\left\{\mathbf{r}_i^{(j)}\right\}_{i=n_0}^{n}$. The past measurements are aligned to the actual measurement $\mathbf{r}_n^{(j)}$ with which the time variant covariance matrix $\hat{\mathbf{C}}_{\mathrm{r},n}$ expressed with (4.6) is computed by applying the steps of Section 4.1.1 using the sets of expected VAs at all past agent positions $\left\{\mathbf{p}_i\right\}_{i=n_0}^{n}$.

5.2.2 Low Complexity Method: EKF/UKF Particle Filtering

As described in [110], the "basic" SIR PF can be improved in terms of its MSE by using a proposal density based on an EKF or UKF. Most importantly, these filters achieve almost the same MSE performance as the conventional PFs with a much lower number of particles, i.e. lower computational demand. The KF method generates a Gaussian approximation of the proposal density for every particle that also incorporates the actual measured signals, yielding

$$q(\mathbf{x}_n^{(i)}|\mathbf{x}_{n-1}^{(i)}, \mathbf{r}_{1:n}) = \mathcal{N}(\mathbf{x}_{n-1}^{(i)}, \bar{\mathbf{x}}_n^{(i)}, \mathbf{C}_{\bar{\mathbf{x}}_n}^{(i)}), \tag{5.22}$$

where $\bar{\mathbf{x}}_n^{(i)}$ and $\mathbf{C}_{\bar{\mathbf{x}}_n}^{(i)}$ are the posterior mean and covariance of the EKF/UKF filter, respectively. Applying DA as described in Section 5.1 for the predicted states of the particles and using the EKF/UKF equations described in Section 5.1.2, the Gaussian proposal density for each particle is computed and new samples are drawn from the proposal density

$$\mathbf{x}_n^{(i)} \sim q(\mathbf{x}_n^{(i)}|\mathbf{x}_{n-1}^{(i)}, \mathbf{r}_{1:n}). \tag{5.23}$$

In the case, the proposal density is based on a UKF, the resulting sequential state estimator is called unscented PF [110].

5.3 Derivation of the Posterior Cramér Rao Lower Bound (PCRLB) for Multipath-Sync

The general form of the posterior Cramér Rao lower bound (PCRLB) for a discrete-time non-linear filtering problem was derived in [119]. Applying the Schur-Complement, the posterior FIM of a state vector $\mathbf{x}_n$ can be computed recursively, given as

$$\boldsymbol{\mathcal{I}}_{\mathbf{x}_n} = \mathbf{B}^{22}_{\mathbf{x}_{n-1}} - \mathbf{B}^{21}_{\mathbf{x}_{n-1}} \left(\boldsymbol{\mathcal{I}}_{\mathbf{x}_{n-1}} + \mathbf{B}^{11}_{\mathbf{x}_{n-1}} \right)^{-1} \mathbf{B}^{12}_{\mathbf{x}_{n-1}}, \tag{5.24}$$

where the general forms of the recursive sub-matrices $\mathbf{B}^{11}_{\mathbf{x}_n}$, $\mathbf{B}^{22}_{\mathbf{x}_n}$, $\mathbf{B}^{12}_{\mathbf{x}_n}$ and $\mathbf{B}^{21}_{\mathbf{x}_n}$ that are defined as [119]

$$\mathbf{B}^{11}_{\mathbf{x}_{n-1}} = \mathbb{E}\left\{ -\Delta^{\mathbf{x}_{n-1}}_{\mathbf{x}_{n-1}} \log p(\mathbf{x}_n|\mathbf{x}_{n-1}) \right\} \tag{5.25}$$

$$\mathbf{B}^{12}_{\mathbf{x}_{n-1}} = \mathbb{E}\left\{ -\Delta^{\mathbf{x}_{n}}_{\mathbf{x}_{n-1}} \log p(\mathbf{x}_n|\mathbf{x}_{n-1}) \right\} \tag{5.26}$$

$$\mathbf{B}^{21}_{\mathbf{x}_{n-1}} = \mathbb{E}\left\{ -\Delta^{\mathbf{x}_{n-1}}_{\mathbf{x}_{n}} \log p(\mathbf{x}_n|\mathbf{x}_{n-1}) \right\} = \left(\mathbf{B}^{12}_{\mathbf{x}_{n-1}} \right)^{\mathrm{T}} \tag{5.27}$$

$$\mathbf{B}^{22}_{\mathbf{x}_{n-1}} = \mathbb{E}\left\{ -\Delta^{\mathbf{x}_{n}}_{\mathbf{x}_{n}} \log p(\mathbf{x}_n|\mathbf{x}_{n-1}) \right\} + \mathbb{E}\left\{ -\Delta^{\mathbf{x}_{n}}_{\mathbf{x}_{n}} \log p(\mathbf{r}_n|\mathbf{x}_{n-1}) \right\}, \tag{5.28}$$

where $\Delta^{\mathbf{x}_{n-1}}_{\mathbf{x}_n} = \frac{\partial^2(\cdot)}{\partial \mathbf{x}_n \partial \mathbf{x}_{n-1}}$ defines the second order partial derivative w.r.t. $\mathbf{x}_n$ and $\mathbf{x}_{n-1}$. Using (5.25), (5.9) and (3.36) result in

$$\mathbf{B}^{11}_{\mathbf{x}_{n-1}} = \mathbf{F}^{\mathrm{T}} \left(\sigma_a^2 \mathbf{G}\mathbf{G}^{\mathrm{T}} \right)^{-1} \mathbf{F} \tag{5.29}$$

$$\mathbf{B}^{12}_{\mathbf{x}_{n-1}} = \left(\mathbf{B}^{21}_{\mathbf{x}_{n-1}} \right)^{\mathrm{T}} = -\mathbf{F}^{\mathrm{T}} \left(\sigma_a^2 \mathbf{G}\mathbf{G}^{\mathrm{T}} \right)^{-1} \tag{5.30}$$

$$\mathbf{B}^{22}_{\mathbf{x}_{n-1}} = \left(\sigma_a^2 \mathbf{G}\mathbf{G}^{\mathrm{T}} \right)^{-1} + \mathbb{E}_{\mathbf{p}_n}\left\{ \boldsymbol{\mathcal{I}}_{\mathbf{p}_n} \right\}, \tag{5.31}$$

where $\boldsymbol{\mathcal{I}}_{\mathbf{p}_n}$ is the EFIM of the actual agent position $\mathbf{p}_n$ defined in (3.35). Using an EKF or UKF, $\mathbf{B}^{22}_{\mathbf{x}_{n-1}} = (\sigma_{\mathrm{a}}^2 \mathbf{G}\mathbf{G}^{\mathrm{T}})^{-1} + \boldsymbol{\mathcal{I}}_{\mathbf{p}_n}$, which shows that the FIM on the state vector error depends on the state space model and the position-related channel information of the n-th time instance. One important point to stress is that if the information contained in the measurements is overwhelming in comparison to information gained by the state space model, the EFIM can be approximated by $\boldsymbol{\mathcal{I}}_{\mathbf{x}_n} \approx \boldsymbol{\mathcal{I}}_{\mathbf{p}_n}$. The PCRLB is defined as $\mathbf{C}_{\mathbf{x}_n} = \boldsymbol{\mathcal{I}}^{-1}_{\mathbf{x}_n}$.

5.4 Ongoing work: Probabilistic MINT with Bayesian Channel Estimation

At this stage of the algorithm, the uncertainties of measurements are not directly connected with the uncertainties of the agent and the VA positions. Hence, a next step is to intertwine the probabilistic model of state with the MPC parameter estimation. An algorithm is suggested that performs DA between unreliably estimated MPC distances and expected agent-VA distances. For "dominant" MPCs that can easily be associated with corresponding VAs, the channel parameters are estimated probabilistically using the predicted state of the agent and the VAs instead of applying DA (the number of used VAs is already restricted using the SINRs

of the previous state as it is described in Section 5.1.3). This means that the uncertainties in the VA positions and the agent position are considered in the estimation of $\hat{\boldsymbol{\tau}}_k^{(j)}$ and $\hat{\boldsymbol{\alpha}}_k^{(j)}$, hence the individual MPC delay and complex amplitude estimates are described by RVs. The subsequent UKF update itself just utilizes the means of the MPC delays $\mathbb{E}\left\{\hat{\boldsymbol{\tau}}_k^{(j)}\right\}$, however the method of moment estimator for computing the corresponding SINRs (5.17), considers the PDFs of the complex amplitudes, thus the uncertainties in the estimated delays are properly considered in the UKF update.

A possible implementation would be a particle-based Bayesian channel estimator. Particles are drawn from VAs and agent marginal distributions. For every agent-VA particle pair, the distances are computed and collected in the sets $\left\{\hat{\boldsymbol{\tau}}_{k,i}^{(j)}\right\}_{i=1}^{I}$. Further, the corresponding complex amplitudes $\left\{\hat{\boldsymbol{\alpha}}_{k,i}^{(j)}\right\}_{i=1}^{I}$ are estimated. Using these sets of complex amplitudes per time instance n, the SINRs are estimated over the window of past estimated agent positions (Section 5.1.3).

5.5 Results

5.5.1 Measurement Setup

For analyzing the tracking methods discussed above, we use the same measurements as described in Section 4.2.1 coming from the MeasureMINT database [102]. Again, out of measured band, we select the desired frequency band using filtering with a raised cosine pulse $s(t)\mathrm{e}^{2\pi f_c t}$. If not stated differently, the pulse duration is $T_\mathrm{p} = 0.5\,\mathrm{ns}$ (corresponding to a bandwidth of $2\,\mathrm{GHz}$) and the center frequency is $f_\mathrm{c} = 7\,\mathrm{GHz}$. All simulations in this section have been conducted for the scenario shown in Fig. 5.2. Using optical ray-tracing based on the floor-plan [1], the VAs were computed a-priori up to order 2 for both anchors (at positions $\mathbf{a}_1^{(1)} = [0.5, 7]^\mathrm{T}$ and $\mathbf{a}_1^{(2)} = [5.2, 3.2]^\mathrm{T}$). The experiments have been done for 25×220-point and 5 1000-point quasi-parallel trajectories, with a spacing of $\Delta p = 5\,\mathrm{cm}$ and $\Delta p = 1\,\mathrm{cm}$, respectively.

5.5.2 Discussion of Performance Results

The process noise variance in the motion models (5.7) and (5.18) are obtained as in [83] based on selecting a maximum velocity as $v_\mathrm{max} = |\mathbf{v}_\mathrm{max}|$, which defines the 3σ point of the noise in velocity domain. The corresponding process noise variance in the acceleration domain is then $\sigma_\mathrm{a}^2 = (v_\mathrm{max}/(3\Delta T))^2$ with $v_\mathrm{max} = \Delta p/\Delta T$ and $\Delta T = 1\,\mathrm{s}$. For state space tracker that use DA, a cutoff distance of $d_\mathrm{c} = 0.1\,\mathrm{m}$ has been chosen.

The sets of MPC delays $\left\{\tau_{k,n}^{(j)}\right\}$ and complex amplitudes $\left\{\alpha_{k,n}^{(j)}\right\}$ were estimated from the sampled received signal vector $\mathbf{r}_n^{(j)}$ using an oversampling factor of 5. For the estimation of the SINRs, the method of moments estimator in (5.17) was applied on the set of the k-th VA's complex amplitudes $\left\{\alpha_{k,i}^{(j)}\right\}_{i=n-w_{past}}^{n}$ for a window $w_{past} = 40$ of past agent positions. For "conventional" MINT, the visibilities of the VAs are precomputed over entire floor plan using optical ray-tracing [O6]. In the case of probabilistic MINT, the visibilities are computed via the SINRs.

MINT with a-priori known Floor Plan – exactly known VA positions

Fig. 5.2 shows an example tracking result (220 agent positions with 5 cm spacing) obtained by the UKF state space tracker, assuming "perfect" knowledge of the floor plan. I.e. the VAs (indicated with black square-crosses) are computed using optical-ray-tracing for the two anchors at the positions $\mathbf{a}_1^{(1)}$ and $\mathbf{a}_1^{(2)}$. The VA positions are corrected using a MAP estimator introduced in [O6]. The agent tracking result is shown in black with some corresponding covariance error ellipses (in black; enlarged by a factor of 100) and (estimated) PCRLB error ellipses (in red; also enlarged by a factor of 100). The excellent match between the UKF and the PCRLB covariance ellipses confirms the usefulness of the measurement noise covariance matrix (5.16) that depends on the multipath channel parameters, i.e. the SINRs, as described in (3.38). If a VA's ranging standard deviation exceeds a defined threshold of $\sigma_{\mathrm{d,max}} = 4.34\,\mathrm{cm}$, corresponding to an SINR of 2 dB at $T_\mathrm{p} = 0.5\,\mathrm{ns}$, c.f. (3.38), the VA is not considered in the tracking process. Nevertheless the SINR of the according VA is still estimated, thus the VA is able to rejoin the set of tracked VAs. The VA is not used until the past window of complex amplitudes has reached a certain size, so that the SINRs can be estimated properly.

Fig. 5.3 illustrates a few estimated ranging standard deviations $\sigma_{\mathrm{d},k,n}$ of the VAs marked in Fig 5.2, over 5 1000-point trajectories. The thin blue curves represent the standard deviations for the 5 individual trajectory runs and the bold blue curves represent the median values. The initial default values assigned to the VAs, $\sigma_{\mathrm{d},k,n} = 5\,\mathrm{cm}$, is shown by black line, the threshold $\sigma_{\mathrm{d,max}}$ by dashed gray line. In case that the ranging standard deviation can not be estimated properly anymore due to lack of measured data, the ranging standard deviation is again set to the initial default value $\sigma_{\mathrm{d},k,n}$, hence the according VA is not used anymore for tracking. The estimation of the according SINR needs to recover. As Fig. 5.3a and 5.3b show, the ranging variance of the direct LOS paths to the anchors are almost along the entire trajectory very small and thus useable for tracking. In the expected region where MPCs should be invisible (gray areas), the uncertainties, i.e. standard deviation, raises, indicating the decrease of position-related information in the according MPCs. The reason why the value of the SINRs increases that steeply in the NLOS region, although the SINRs are estimated over the window of past measurements, is because the visibilities are considered in the computation of the expected set of VAs.

Figs. 5.3c and 5.3d indicate that the blackboard is nicely detectable and also useable for tracking, both for Anchors 1 and 2. As expected, in the NLOS region, the standard deviation is increasing until the component is not detectable anymore. For the right window, the estimated ranging standard deviations are shown in Fig. 5.3e and 5.3f. For Anchor 1 this VA is visible just at the end of the trajectory and after the VA has been detected, the standard deviation is rather high and unstable. For Anchor 2 the VA is indeed visible along the entire trajectory, however the estimated value is very unreliable, reflected in the large variance of the individual runs. This can be partly explained by the overlap, i.e. interference, of a few MPCs, coming from the door, the wall and the window on the right hand-side consisting all of different materials and showing all a different profile depth.

Figs. 5.4a and 5.4b show the overall CDFs of the position error of the agent for the trajectories with 220 and 1000 points, respectively. The black and the red curves represent the overall CDFs for the EKF and UKF tracking filters, whereas the light and dark gray lines represent the CDFs

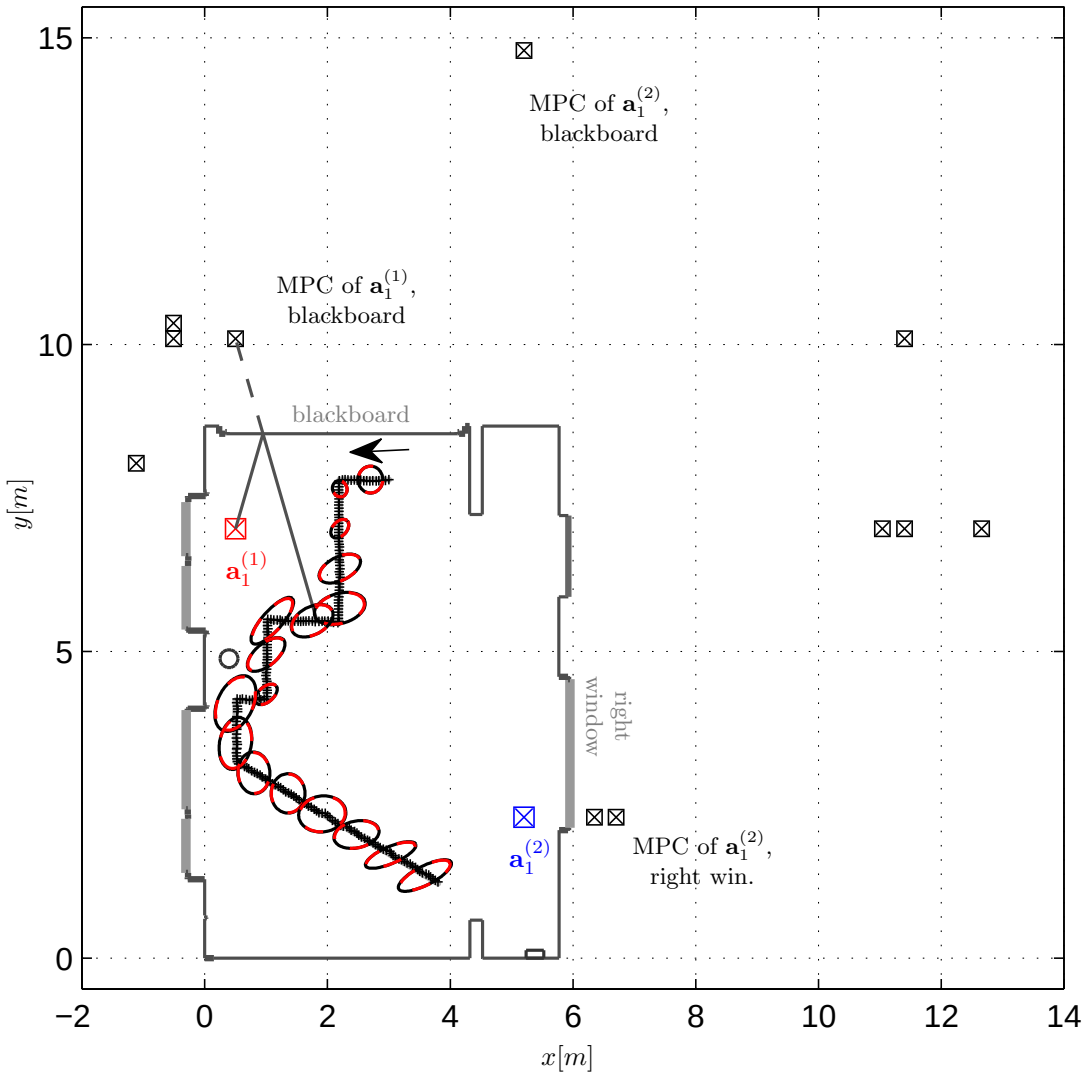

Figure 5.2: Floor plan of the evaluation scenario and a tracking example of the 5 cm-spaced trajectory using the UKF state space tracker. The anchors are at positions $\mathbf{a}_1^{(1)}$ and $\mathbf{a}_1^{(2)}$, respectively. The agent position is estimated using specular multipath, for which one example path is shown in dark gray. An agent tracking result is shown in black with some corresponding covariance error ellipses (black, 100-fold standard deviation) and PCRLB ellipses (dashed red, 100-fold standard deviation). The black arrow indicates the direction the agent is moving.

of the individual trajectory runs. The reason why both curves are almost identical lies in the fact that the nonlinearity of the measurement model w.r.t. the agent position is not that influential, thus a UKF implementation is not necessarily needed. However, the computational complexity is the same for both and the UKF is superior for higher nonlinearity and has a smaller bias than the EKF, thus the UKF is used in further experiments. Obviously, the performance is better for the trajectory with smaller spacing, but the difference is rather small.

Fig. 5.5 illustrates overall agent position error CDFs for the UKF, the PF and the low complexity UKF-PF tracking filters[25] along the 5 1000-point trajectories. As expected the particle filter tracking filter (red, black, gray curves) show higher accuracy than the UKF filter, especially for a high number of particle, but with the drawback of high computational demand. Whatsoever, also the UKF tracking filter shows already high level of accuracy very robustly. A

[25] For particle-based methods 30 Monte Carlo runs were conducted.

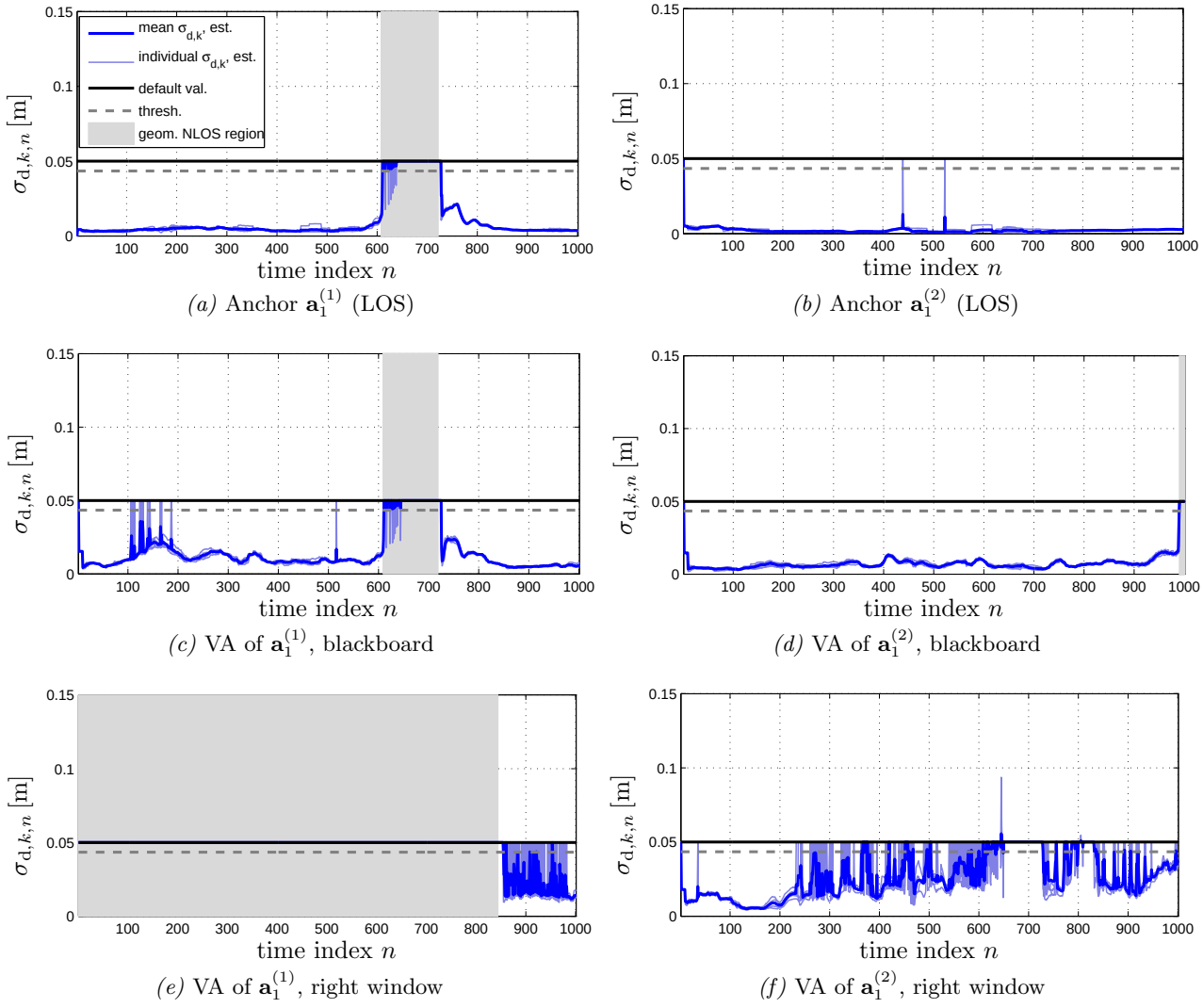

(a) Anchor $\mathbf{a}_1^{(1)}$ (LOS)

(b) Anchor $\mathbf{a}_1^{(2)}$ (LOS)

(c) VA of $\mathbf{a}_1^{(1)}$, blackboard

(d) VA of $\mathbf{a}_1^{(2)}$, blackboard

(e) VA of $\mathbf{a}_1^{(1)}$, right window

(f) VA of $\mathbf{a}_1^{(2)}$, right window

Figure 5.3: Estimated standard deviations of the ranging to selected VAs, i.e. (a) the LOS to Anchor 1*, (b) the LOS to Anchor* 2*, (c) the reflections w.r.t. the blackboard and Anchor 1 (c) as well as (d) Anchor* 2*, (e) the right window and Anchor* 1*, and (f) the right window and Anchor* 2*. Gray regions indicate geometrically computed regions where the corresponding MPC is not visible. Blue lines denote the estimated ranging uncertainty, and black lines the initial default value. The SINRs are estimated for a window $w_{past} = 40$ of past agent positions. Precomputed visibilities are considered.*

reasonable trade-off between less computational demand and high accuracy and robustness is guaranteed, is given by the UKF-PF tracking filter. It also has quasi real-time computation and increased robustness in comparison to the UKF tracking filter in severe tracking situations.

Probabilistic MINT with uncertain a-priori Floor Plan – VAs as RVs

Fig. 5.6 shows an exemplary tracking result for one of the 1000-point trajectories obtained by the UKF state space tracker with VAs included into the state space, so that floor plan uncertainties can be considered. The size and the orientation of the VAs' covariance ellipses depend on the geometry and the agent's uncertainty ellipse and vice versa. There are two major reasons why a probabilistic representation of the environment is beneficial, (i) uncertainties in the floor plan

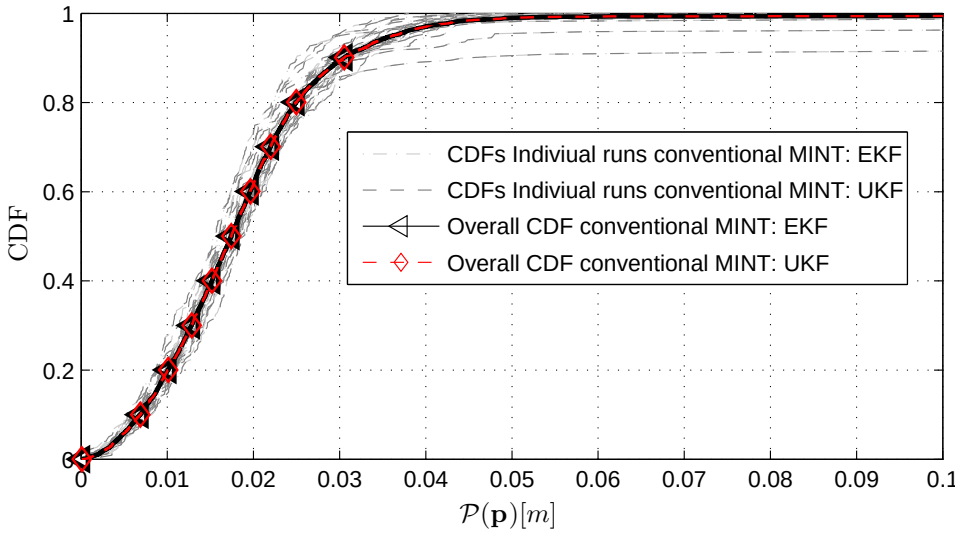

(a) 25 220-point trajectories with 5 cm spacing

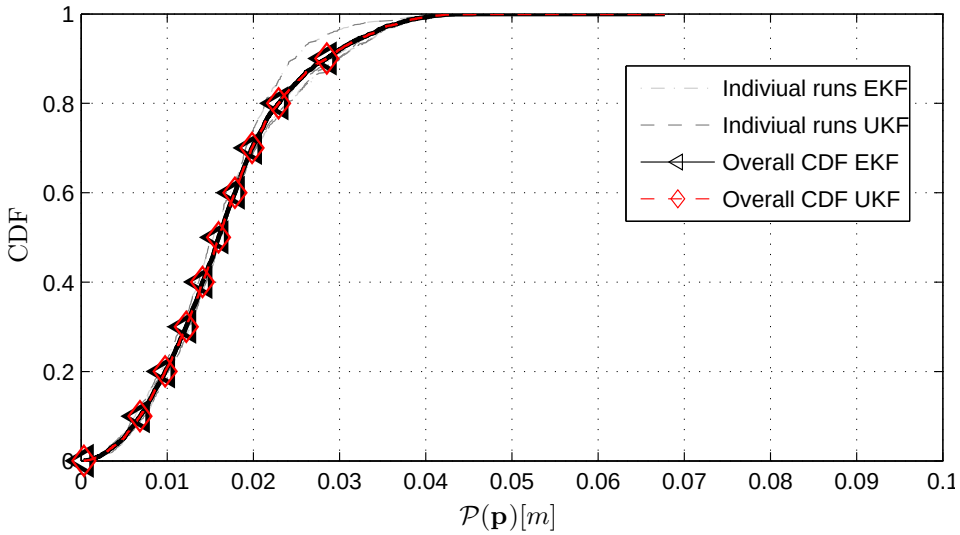

(b) 5 1100-point trajectories with 1 cm spacing

Figure 5.4: Performance CDFs for $T_p = 0.5\,ns$ and $f_c = 7\,GHz$. The light and dark gray CDFs indicate the tracking error of "conventional" MINT using the EKF and UKF approaches, respectively. The black and red lines denote the respective overall CDFs. The tracking algorithms use VAs up to second order with a-priori known positions and online tracking of their range variances.

that are somehow inevitable can be included into the state estimator, and (ii) data association errors or "bad" measurements are not that severe in sense of divergence of the estimator, thus the overall joint PDF of the VA positions is able to compensate such errors so that the filter is able to overcome such situations. For probabilistic MINT, the visibilities of VAs are always computed using the SINRs.

Fig 5.7 shows a comparison of probabilistic MINT and "conventional" MINT for the 5 1000-point trajectories. The black curve denotes the overall CDF for probabilistic MINT and the red line for "conventional" MINT, without considering the precomputed visibilities of VAs. In this case the visibilities of VAs are computed using the SINRs. The blue line shows "conventional" MINT with precomputed visibilities. The results reveal that an accurate given floor plan and a prior computed visibilities lead to the best accuracy. Nevertheless, the difference to probabilistic

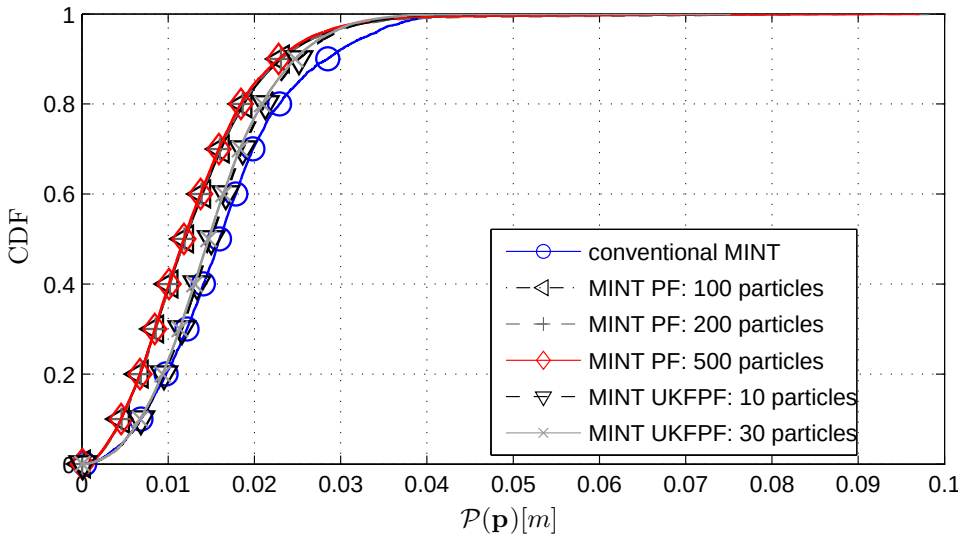

Figure 5.5: Performance CDFs for the UKF (blue), the PF (red line) and the UKF-PF with signal parameters $T_p = 0.5\,ns$ and $f_c = 7\,GHz$. The tracking algorithms use VAs up to second order with a-priori known positions and online tracking of their ranging variances.

MINT is rather small and the same robustness is given, although the visibilities are computed based on the SINR values. Most importantly is that "conventional" MINT loses robustness in comparison to probabilistic MINT when the information about the floor plan is reduces (no visibilities), as the red line in Fig 5.7 indicates.

In Fig 5.8 the overall position error CDFs are depicted for the 5 1000-point trajectories for different levels of noise in the initial geometrically computed VA positions $\mathbf{a}_{k,\text{geom}}^{(j)}$. This means every initial mean position of the VAs is sampled from a two dimension Gaussian RV $\mathbf{a}_{k,n=1}^{(j)} \propto \mathcal{N}\big(\mathbf{a}_{k,\text{geom}}^{(j)}, \mathbf{\Sigma}_{\mathbf{a}_k}\big)$, where $\mathbf{\Sigma}_{\mathbf{a}_k} = \text{diag}(\sigma_k^2)$ is the initial covariance matrix and σ_k defines the standard deviation in x- and y-directions. For evaluating the algorithm's performance considering initial noise, 30 Monte Carlo runs were conducted. The black curve in Fig 5.8 denotes the overall CDF for all 5 1000-point trajectories without considering noisy initial VA positions, meaning that $\sigma_k = 0\,\text{cm}$. An increase of the standard deviation to $\sigma_k = 5\,\text{cm}$ and even to $\sigma_k = 10\,\text{cm}$ just slightly decreases the performance indicated by the red and the gray curves, respectively, meaning that the algorithm shows an excellent robustness. Only, an increase to $\sigma_k = 20\,\text{cm}$ decreases the performance noticeably. A close inspection has shown that 2 out of 30×5 Monte Carlo runs along the 5 1000-point trajectories have diverged, resulting in a maximum error of approximately 1 m.

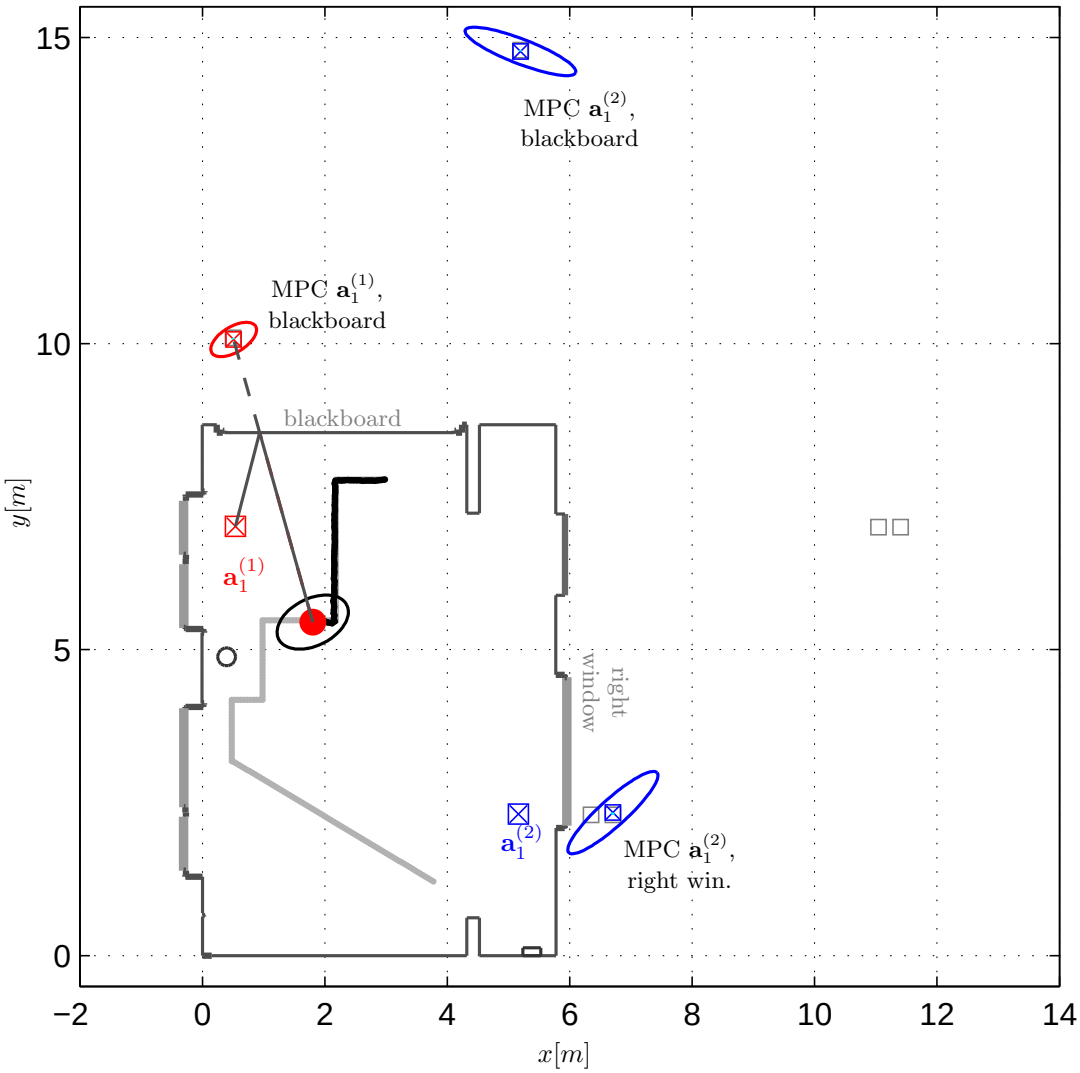

Figure 5.6: Illustration of the environment map obtained by the UKF tracking algorithm that includes VAs into the state space for one of the 1000*-point trajectories. Two anchors at* $\mathbf{a}_1^{(1)}$ *and* $\mathbf{a}_1^{(2)}$ *represent the infrastructure. Gray squares indicate geometrically expected VAs, black square markers with uncertainty ellipses in red and blue (*40*-fold standard deviations) represent tracked VAs for anchor 1 and 2, respectively. An agent tracking result is shown in black and its corresponding error ellipse (*100*-fold standard deviation).*

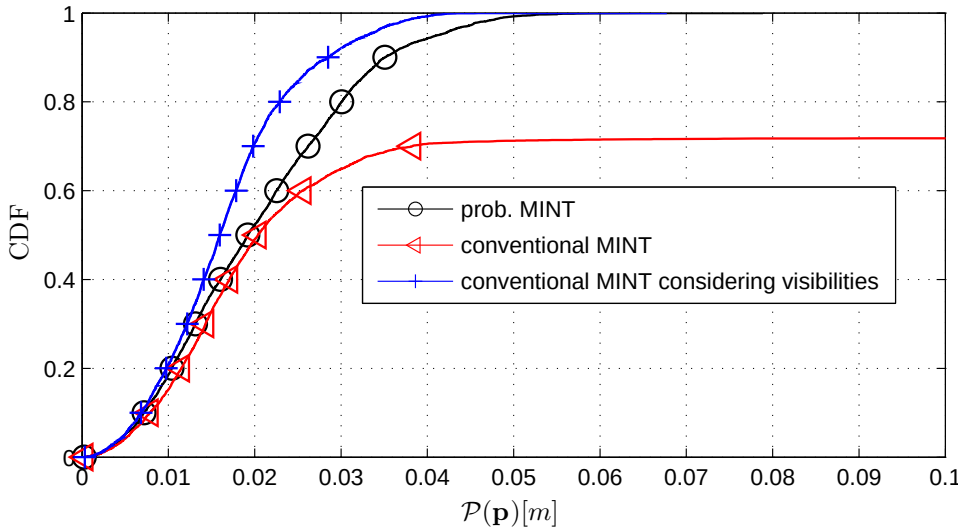

Figure 5.7: Performance comparison of probabilistic MINT and "conventional" MINT ($T_p = 0.5\,ns$ and $f_c = 7\,GHz$). The black curve denotes the overall CDF for probabilistic MINT and the red line for "conventional" MINT, without considering the precomputed visibilities of VAs. The blue line shows "conventional" MINT with precomputed visibilities.

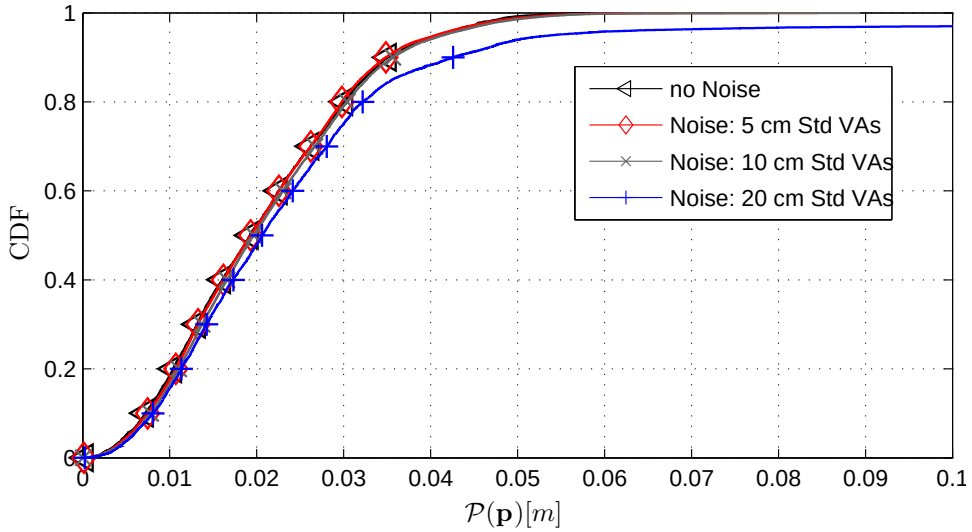

Figure 5.8: Performance CDFs of the UKF tracking algorithm for different noise levels in the initial VA mean positions ($T_p = 0.5\,ns$ and $f_c = 7\,GHz$). The black curve denotes the overall CDF without initial noise for the 5 1000-point trajectories. The red, gray and blue curves denote the CDFs for 5 cm, 10 cm and 20 cm standard deviation in the initial position of the VAs.

5.6 Chapter Summary and Conclusions

In this chapter different algorithms for MINT have been analyzed. Starting with "conventional" MINT algorithms that take the a priori known floor plan for granted and do not consider uncertainties, we moved to a "fully" probabilistic approach by modeling also the VAs and optionally the anchors as RVs. Is was shown that "conventional" MINT algorithms based on data association (DA) and Kalman filter (KF) as well as those based on the entire received signal and particle filter (PF) have excellent performance in sense of *accuracy* and *robustness*, if the underlying floor plan is sufficiently accurate and side information as the precomputed visibilities are available.

In the case there are no visibilities available, the "conventional" MINT algorithms already start to struggle or entirely fail when the floor plan information is imprecisely known. For such situation probabilistic MINT provides again the needed level of robustness (and also accuracy) that is vital for positioning system. The features that only a roughly known floor plan is needed for initializing the system and no precomputed visibilities are needed, provide the wanted flexibility for setting up the system in new indoor environments.

6

Simultaneous Localization and Mapping using Multipath Channel Information

The extended state space model in (5.18) and measurement model in (5.20) are a formulation of probabilistic environment model in (2.9) that considers floor plan uncertainties. However, it has not been discussed yet if the floor plan can be learned online from the present and past measurements, i.e. how to design an algorithm that needs no a-priori floor plan knowledge at all. This Section focuses on probabilistic feature-based simultaneous localization and mapping (SLAM) with VAs of the according anchors as representative features of floor plans. Naturally, this represents the next step from probabilistic MINT towards a "fully" cognitive positioning system by at first learning the surrounding environment and building up the GPEM and GSCM memories. The work presented in this Section is partly based on [O8].

6.1 General SLAM Formulation

As stated, the VAs at position $\mathbf{a}_{k,n}^{(j)}$ are the mirror images of the anchors at position $\mathbf{a}_{1,n}^{(j)}$ at flat surfaces (e.g. walls) of the surrounding environment and thus they are a parametric representation of the environment. Starting with the positions of the anchors $\mathbf{a}_{1,n}^{(j)}$ and optionally a small set of precomputed VAs (using optical ray-tracing [O6]), *channel-information-assisted* SLAM is a method to find new VAs and also to estimate an according reliability measure, the $\mathrm{SINR}_{k,n}^{(j)}$ described in Equation (3.20), for those features. For this problem, we introduced the term *MINT-SLAM*. When using additionally IMU data, the initial criteria can be even more relaxed by also assuming the anchor positions to be unknown.

Bayesian feature-based SLAM allows to compute the joint posterior $p(\mathbf{x}_n, \mathcal{A}_n | \mathcal{Z}_{1:n})$ of the state vector of the agent $\mathbf{x}_n = [\mathbf{p}_n, \mathbf{v}_n]^{\mathrm{T}}$, where $\mathbf{p}_n$ is the position and $\mathbf{v}_n$ the velocity of the agent, respectively, and the finite set $\mathcal{A}_n = \bigcup_j \mathcal{A}_n^{(j)}$, which represents all VA positions at time

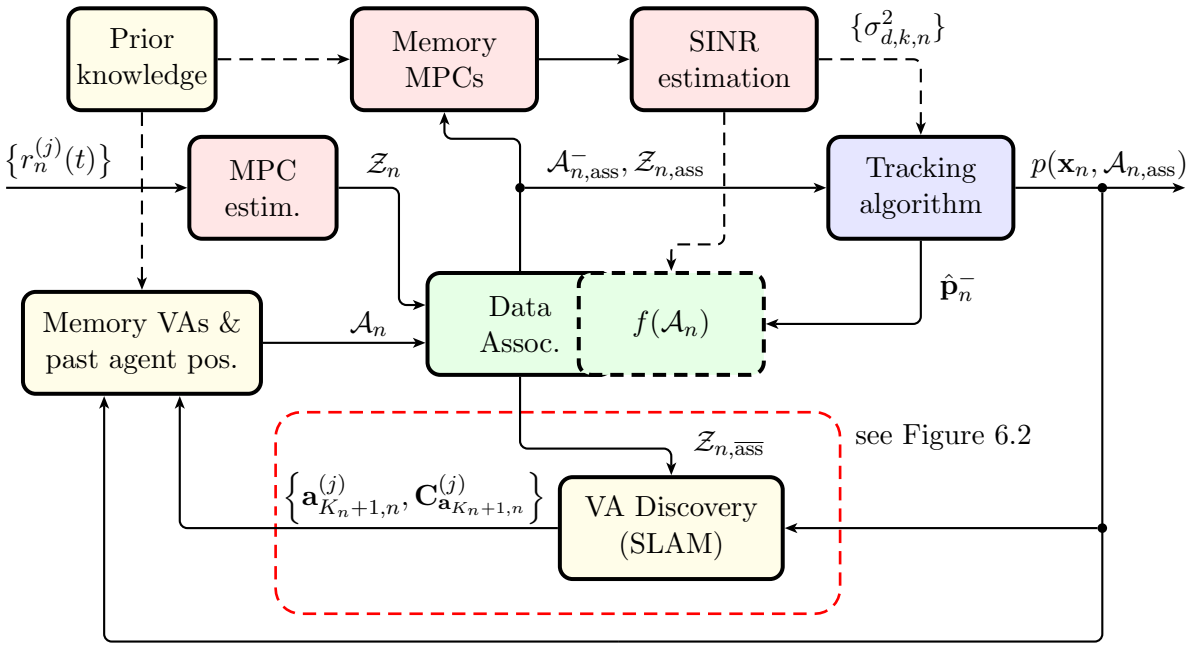

Figure 6.1: Block diagram of MINT SLAM using data association (DA).

instance n that are associated with measured distances (see Section 5.1.1). As a consequence of using just a single antenna at the anchors- and the agent, and the partial observability of the VAs, delayed mapping [117] has to be applied, which means that a set of past measurements $\mathcal{Z}_{1:n}$ and the according estimated states of the agent $\mathbf{x}_{1:n}$ are needed to initialize new possible VAs. In the most generic form, the prediction equation for a feature map and an agent state, can be written as, using the Markovian assumption,

$$p(\mathbf{x}_n, \mathcal{A}_n|\mathcal{Z}_{1:n-1}) = \int\limits_{\mathbf{x}_{n-1},\mathcal{A}_{n-1}} p(\mathbf{x}_{n-1}, \mathcal{A}_{n-1}|\mathcal{Z}_{1:n-1}) p(\mathbf{x}_n|\mathbf{x}_{n-1}) p(\mathcal{A}_n|\mathcal{A}_{n-1}) d\{\mathbf{x}_{n-1}, \mathcal{A}_{n-1}\} \quad (6.1)$$

where $p(\mathbf{x}_n|\mathbf{x}_{n-1})$ and $p(\mathcal{A}_n|\mathcal{A}_{n-1})$ are the state transition probability distribution functions of the agent and the VAs, respectively. The latter can be represented by an identity function. The update equation is then

$$p(\mathbf{x}_n, \mathcal{A}_n|\mathcal{Z}_{1:n}) = \frac{p(\mathcal{Z}_n|\mathbf{x}_n, \mathcal{A}_n) p(\mathbf{x}_n, \mathcal{A}_n|\mathcal{Z}_{1:n-1})}{p(\mathcal{Z}_{1:n}|\mathcal{Z}_{1:n-1})} \quad (6.2)$$

where $p(\mathcal{Z}_n|\mathbf{x}_n, \mathcal{A}_n)$ is the likelihood function of the current measurements. The equations (6.1) and (6.2) are a time recursive version of Equation (2.9), without explicitly considering the MPC channel parameter vectors $\boldsymbol{\alpha}$ and $\boldsymbol{\tau}$. The set of VAs and anchors $\mathcal{A}_n$ is not just changing with time due to the association process, but also due to the detection of newly discovered VAs. After discovering a new VA, its distribution can be described in the joint state space with already detected VAs and the agent as stated in (6.1) and (6.2). Fig. 6.1 illustrates the general scheme of the MINT-SLAM algorithm, where the red box comprises the VA discovery process that is shown in detail in Fig. 6.2.

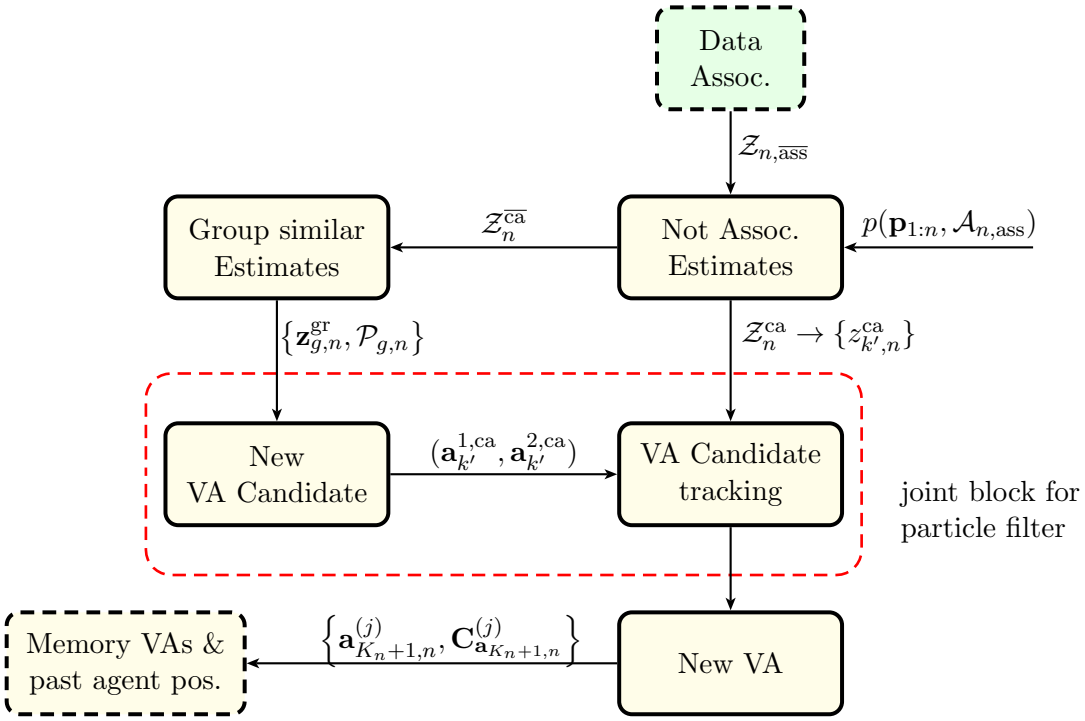

Figure 6.2: Block Diagram of VA discovery

6.2 Feature Detection: VA Discovery

The set of measurements $\mathcal{Z}_{n,\overline{\text{ass}}}$ that are not associated to known VAs is used for discovering new VAs. In principle, the MINT-SLAM algorithm tries to associate these measurements with candidates for new VAs at different stages.

6.2.1 General Scheme

This process is illustrated in Figure 6.2 and is summarized in the following way:

- The potential subset $\mathcal{Z}_n^{\text{ca}} \subset \mathcal{Z}_{n,\overline{\text{ass}}}$ of the non-associated measurements contains measurements that can be associated with already existing VA candidates $\mathbf{a}_{k'}^{\text{ca}}$, $k' = 1, \ldots, K'_n$, which have not yet been estimated unambiguously[26]. The VA-candidate-associated measurements $\{z_{1,n}^{\text{ca}}, \ldots, z_{K'_n,n}^{\text{ca}}\}$ and the current agent position $\mathbf{p}_n$ are used to improve the position estimate of the corresponding VA candidates and to resolve the ambiguity in their positions.

- As soon as the position ambiguity is resolved, a new VA is initialized at position $\mathbf{p}_{K_n+1,n}$[27], with covariance matrix $\mathbf{C}_{\mathbf{p}_{K_n+1,n}}$ and added to the geometry data-base. This new VA can be used in the next time step.

[26] A reason for ambiguity in the position of a newly estimated VA is that the circles spanned by the measured distances around the according agent positions may intersect in two points (e.g. due to agent movement on a straight line).

[27] The symbol K_n defines the number of all discovered VA—until time instance n—that are stored in the geometry memory (see Figure 6.2).

- Measurements that have not yet been associated with a VA candidate are comprised in $\mathcal{Z}_n^{\overline{\text{ca}}}$ and further grouped into vectors of similar distances $\mathbf{z}_{g,n}^{\text{gr}}$, $g \in \mathcal{P}_{g,n}$ with $g = 1, \ldots, G_n$, where $\mathcal{P}_{g,n}$ represents the set of time-indices of distances associated with the g-th group and G_n is the current number of groups. If the size of a group reaches a certain threshold, a new VA candidate is estimated with the grouped distances and according agent positions $\mathbf{p}_{\mathcal{P}_{g,n}}$.

6.2.2 Range-Bancroft Approach

- *Estimate new VA candidate pairs*: In the case that a vector of similar distances $\mathbf{z}_{g,n}^{\text{gr}}$ has reached a certain number of entries, a new VA candidate pair $(\mathbf{a}_{k'}^{1,\text{ca}}, \mathbf{a}_{k'}^{2,\text{ca}})$ is estimated with this vector of distances and the according agent positions $\mathbf{p}_n \in \mathbf{p}_{\mathcal{P}_{g,n}}$ using the range-Bancroft algorithm [120]. This pair $(\mathbf{a}_{k'}^{1,\text{ca}}, \mathbf{a}_{k'}^{2,\text{ca}})$ of VA candidates is given by the two possible solutions of the range-Bancroft method.

- *Tracking of VA candidate pairs*: Already found VA candidate pairs $(\mathbf{a}_{k'}^{1,\text{ca}}, \mathbf{a}_{k'}^{2,\text{ca}})$ are then updated with a tracking filter (RLS, EKF or UKF) using the new associated distance measurements $\{z_{1,n}^{\text{ca}}, \ldots, z_{K'_n,n}^{\text{ca}}\}$ and the measurement model based distances $d(\mathbf{p}_n, \mathbf{a}_{k'}^{c,\text{ca}})$ with the current agent position $\mathbf{p}_n$ and the VA candidate position $\mathbf{a}_{k'}^{c,\text{ca}}$, $c \in \{1, 2\}$, until the above described ambiguities are resolved.

6.2.3 Particle Filter Approach

In the case that the vector of similar distances $\mathbf{z}_{g,\mathcal{P}_{g,n}}^{\text{gr}}$ has reached a certain number of entries, an SIR PF kernel is initialized with particles $\left\{\mathbf{a}_{k'}^{(i),\text{ca}}, w_i\right\}_{i=1}^{I}$ representing the state of the according new VA candidate distribution. The measurement update of the particles is based on the likelihood function defined in (4.15), which is evaluated using the vector measurements $\mathbf{z}_{g,n}^{\text{gr}}$, $g \in \mathcal{P}_{g,n}$ and the measurement model based distances $d(\mathbf{p}_n, \mathbf{a}_{k'}^{(i),\text{ca}})$ for all particles and agent positions $\mathbf{p}_n \in \mathbf{p}_{\mathcal{P}_{g,n}}$. After each measurement update and re-sampling step, the particles are regularized using an Epanechnikov Kernel as described in Section 4.1.2. The update, re-sampling and regularization steps are iterated until the particle are sufficiently converged to the initial state of the new VA at position $\mathbf{a}_{K_n+1,n}$ and covariance $\mathbf{C}_{\mathbf{a}_{K_n+1,n}}$. In some parts this method has similarities with [121, 122].

6.2.4 Ongoing work: An Alternative Approach

For further improvement of the algorithm's robustness, a Rao-Blackwellized PF method would be a proper choiceas in [73,123]. For MINT SLAM this means that probabilistic DA is performed (as described in Section 5.1) for the grouping process described in Section 6.2.1. Already detected VAs are tracked using the method described in Section 5.4. All other non-associated MPCs are used again for finding new VAs, but with the difference that particle-based probabilistic DA is utilized. This means that the set of not associated delays $\mathcal{Z}_{n,\overline{\text{ass}}}$ is grouped into vectors of similar

distances $\{\mathbf{z}_{1,\mathcal{P}_{1,n}}^{(i),\mathrm{gr}},\ldots,\mathbf{z}_{G_n,\mathcal{P}_{G_n,n}}^{(i),\mathrm{gr}}\}_{i=1}^{I}$ for every particle with weighting computed by (4.15). To reduce the computational complexity, only the most probable grouping combinations are used. For every group, one of the algorithms for VA discovery (described in Sections 6.2.2 or 6.2.3) is applied. After some iterations, groups will survive that have higher chances for discovering new VAs.

6.2.5 Initializing new VAs

Resolved VAs are stored in the geometry memory and further used in the state space model. The update of the RLS, EKF or UKF algorithm or the PF, after a defined convergence criterion is reached, provides the initial position $\mathbf{a}_{K_n+1,n}$ and covariance matrix $\mathbf{C}_{\mathbf{a}_{K_n+1,n}}$ of the newly found VA. The cross-covariance $\mathbf{C}_{\mathbf{x}_n,\mathbf{a}_{K_n+1,n}}$ between the new VA and the agent position and the covariances $\mathbf{C}_{\mathbf{a}_{K_n+1,n},\mathbf{a}_{k,n}}$ between the new VA and all other VAs are initialized with zero matrices. Analysis of the state covariance matrix has shown that these cross-covariances get plausible values after a few time steps.

6.3 Results of SLAM Algorithm

6.3.1 Measurement Setup

Real measured Data

For analyzing the tracking methods discussed above, we use the same measurements as described in Section 4.2.1 [102]. Again, out of the measured band, we select the desired frequency band using filtering with a raised cosine pulse. If not stated differently, the pulse duration is $T_\mathrm{p} = 0.5\,\mathrm{ns}$ (corresponding to a bandwidth of 2 GHz) and the center frequency is $f_\mathrm{c} = 7\,\mathrm{GHz}$. The scenario has been illustrated in Figs 4.1 and 6.8. Using optical ray-tracing based on the floor-plan [1], the VAs for both anchors (at the positions $\mathbf{a}_1^{(1)} = [0.5, 7]^\mathrm{T}$ and $\mathbf{a}_1^{(2)} = [5.2, 3.2]^\mathrm{T}$) were computed a-priori up to order two. This set of VAs is used for comparison with discovered and further tracked VAs. The past window of agent positions for the SINR estimation is again chosen to be $w_\mathrm{past} = 40$. For all simulations, 30 Monte Carlo runs were conducted.

Synthetic Data

A synthetic environment and measurements are used to evaluate the general performance of the introduced MINT-SLAM algorithm regarding correct feature detectability.

Fig. 6.3 illustrates an example of the synthetic signals exchanged between the agent and Anchors 1 and 2, generated using the signal model in (2.1) and parameters listed in Table 3.1. The AWGN level is chosen to be quite small ($E_\mathrm{LOS}/N_0 \approx 25\,\mathrm{dB}$), but even for much higher levels the algorithm is not that strongly influenced, thus ML channel estimation algorithm averages over a sufficient large number of noisy signal samples along the time delay axis. Much more impairing is the interference due to DM. Only because the position-related channel information, in form of the SINRs associated to the VAs, is used in an efficient manner, the algorithm is able

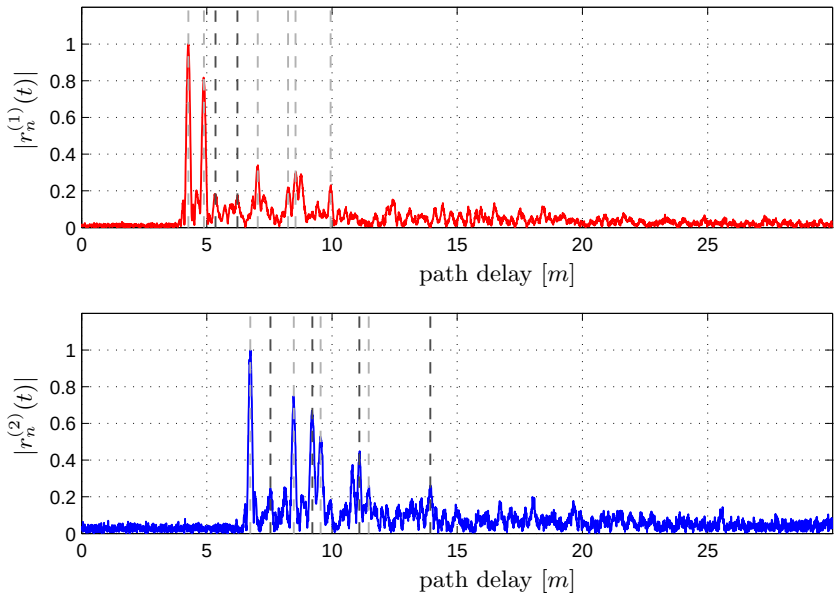

Figure 6.3: Synthetic signals generated according to signal model (2.1) with $T_p = 0.5\,ns$ and $f_c = 7\,GHz$. The signals exchanged between the agent and Anchor 1 and Anchor 2 are depicted in red and blue, respectively. The dashed black lines represent the estimated delays of the MPCs and the gray ones represent those that are already associated with detected VAs.

to handle the strongly cluttered received signals. Only the ranging estimates (without using e.g. angle-of-arrival (AoA) estimates) are used to detect and estimate VAs.

6.3.2 Discussion of Performance Results

Synthetic Data

Fig. 6.4 shows the floor plan with an tracking example used for analyzing synthetic signals. It is readily noticeable that the algorithm estimates very well VAs that correspond to the a-priori geometrically computed VAs. At this agent position only two of all expected VAs are not detected and no "clutter" VAs have been estimated. Fig. 6.5 shows the overall CDFs for the MINT SLAM algorithm with PF and range-Bancroft initialization in black and blue, respectively. As "ground truth" comparison, the dashed red line shows the overall CDF, assuming all VAs up to second order as known a-priori and tracking online their positions and range variances. Both initialization methods perform very well, considering the quite non-linear moving behavior of the agent. Using the particle initialization there is a performance gain, although it is small. However, the more important consequence can be observed in Fig. 6.6 that illustrates the number of estimated features, i.e. VAs, along the trajectory for the synthetic measurements. Here, the dashed red line denotes the number of VAs for probabilistic MINT using the UKF to mark the "ground truth" for the scenario. The before mentioned performance gain of the PF-based initialization is also reflected in the number of estimated features that matches excellently with the ground truth. Nevertheless, also with range-Bancroft-based initialization, the estimated number of targets of the algorithm is already quite close to the true number of geometric features.

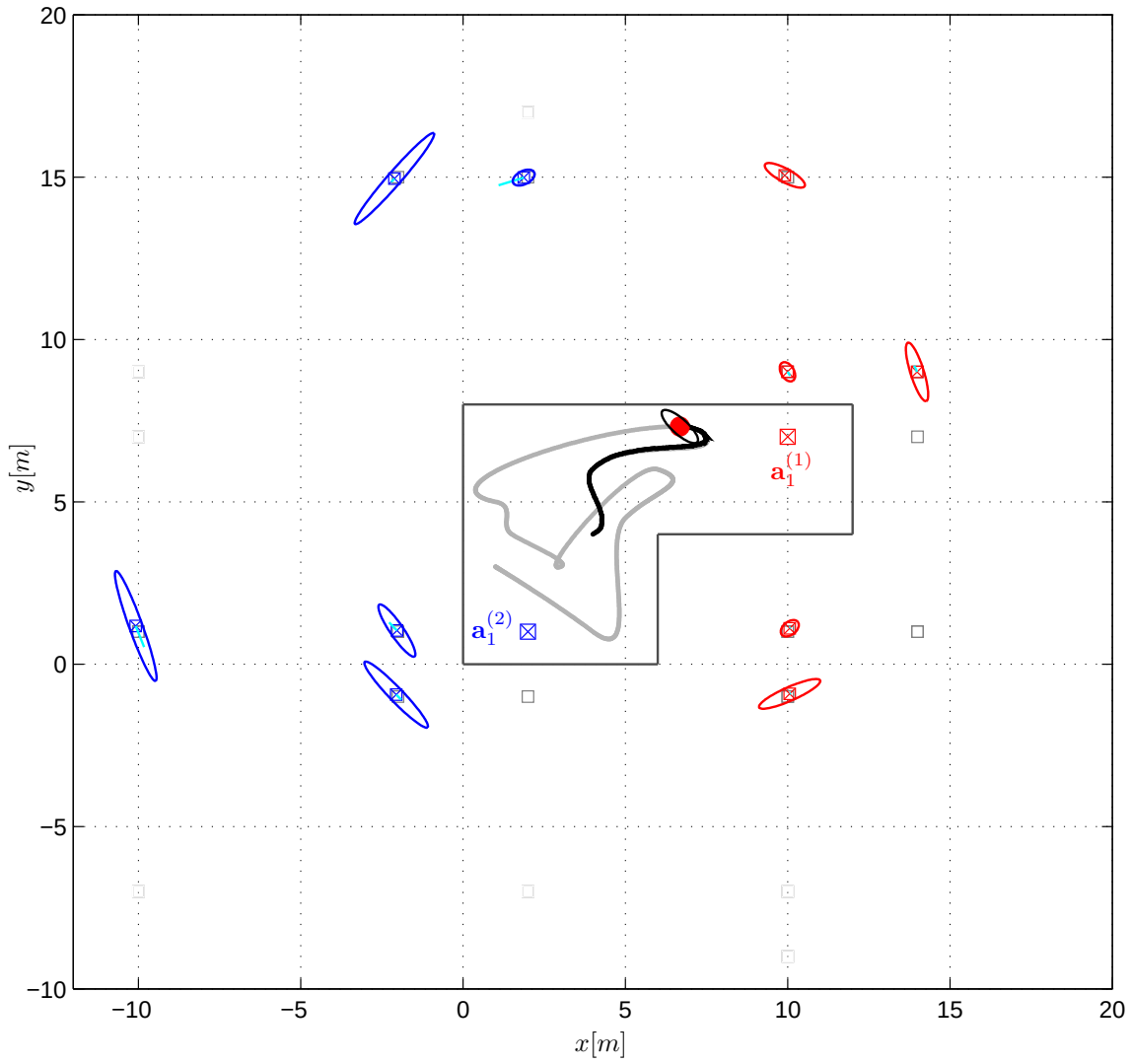

Figure 6.4: Illustration of the environment map obtained by the PF MINT-SLAM algorithm in a synthetic scenario with synthetic measurements. Two anchors at $\mathbf{a}_1^{(1)}$ and $\mathbf{a}_1^{(2)}$ represent the infrastructure. Gray squares indicate geometrically expected VAs, blue and red square-cross markers with uncertainty ellipses (40-fold) represent discovered VAs. An agent tracking result is shown in black with some corresponding error ellipses (150-fold).

Remark: "Bad" geometry: The results that are used to analyze the geometric effects, shown in Fig. 6.7, are generated using real measured data. In the case the agent moves along straight lines, the detection of VAs is rather difficult for the following reasons: (i) geometry dependent ambiguities of the VAs' positions may arise and (ii) position changes of the agent lead to rather flat intersection (glancing intersection) of the ToA circles used for positioning of a VA. Therefore the geometric delusion of precision (GDOP) of the VA localization (detection) is rather high. The PF initialization is able to cope with such "weak" geometry for positioning, although the convergence behavior is negatively influenced. The initialization process is illustrated Fig. 6.7 using the PF (with likelihood function in (4.15)). The figure indicates quite clearly that an unambiguous detection needs several tracking steps until the particles (blue cross marker) have converged. The number of particles used for this simulation is 1000.

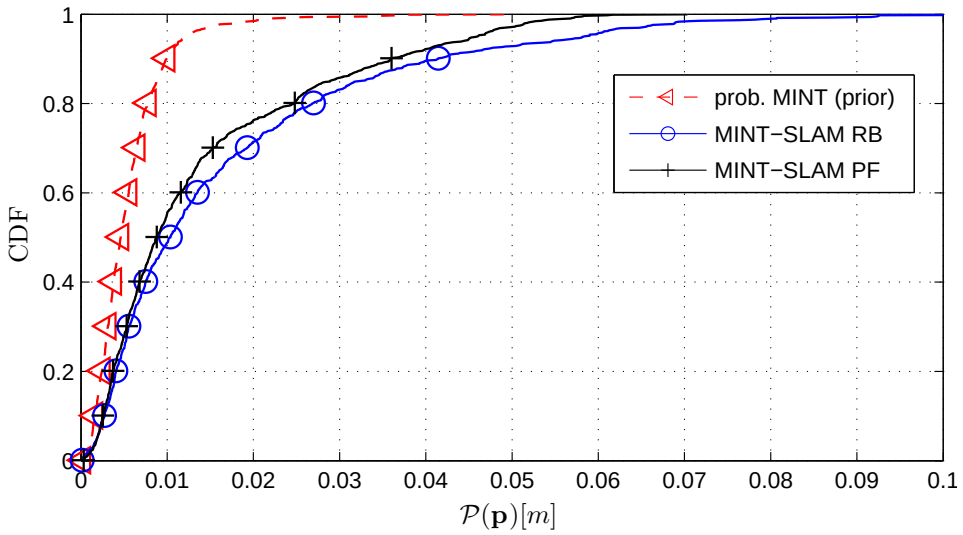

Figure 6.5: Performance CDFs of MINT-SLAM for synthetic measurements. Only the anchor coordinates are known. The black line denotes the overall CDF of the PF initialization and the blue one of range-Bancroft initialization. The red dashed line shows the overall CDF using all VAs up to second order as a-priori known and online tracking of their positions and range variances.

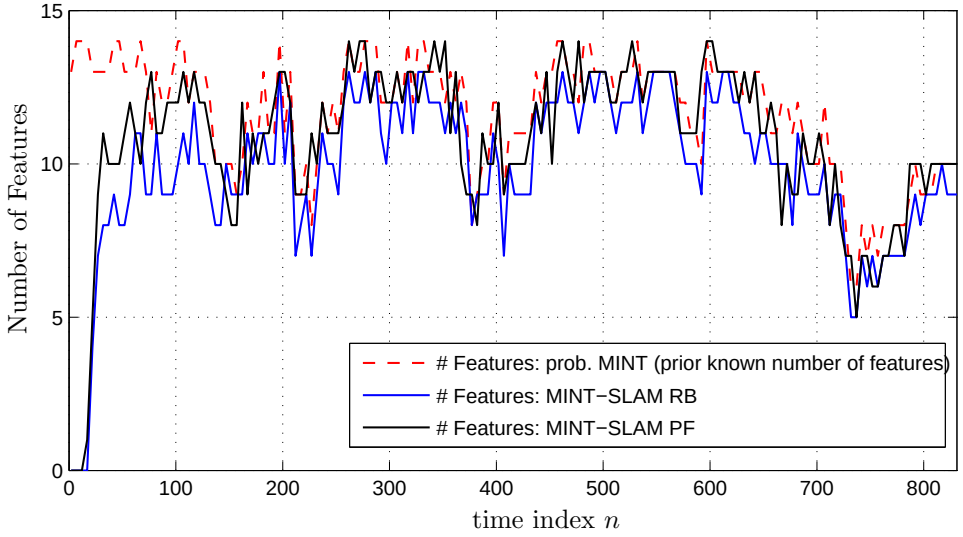

Figure 6.6: Number of estimated features, i.e. VAs, along the trajectory for SLAM using multipath information for synthetic measurements. The dashed red line denotes the number of VAs for probabilistic MINT using the UKF, which is considered as ground truth. The blue and the red lines show the number of estimated VAs for range-Bancroft and PF initialization, respectively.

Real measured Data

It has been demonstrated in [O8] that a 2D-map can be constructed with no prior information about the scenario other than the absolute positions of two fixed anchors. Fig. 6.8 shows an illustrative example of this SLAM approach. Grey squares indicate the positions of some "expected" VAs computed from the floor plan. Discovered VAs are shown by red (Anchor 1) and blue (Anchor 2) square-cross markers; their marginal position covariance matrices are indicated by standard deviation ellipses (enlarged by a factor of 40 for better visibility). The according true agent trajectory is indicated in gray. The current estimated agent position is shown by the red dot; its standard deviation ellipse is in black (enlarged by a factor of 100).

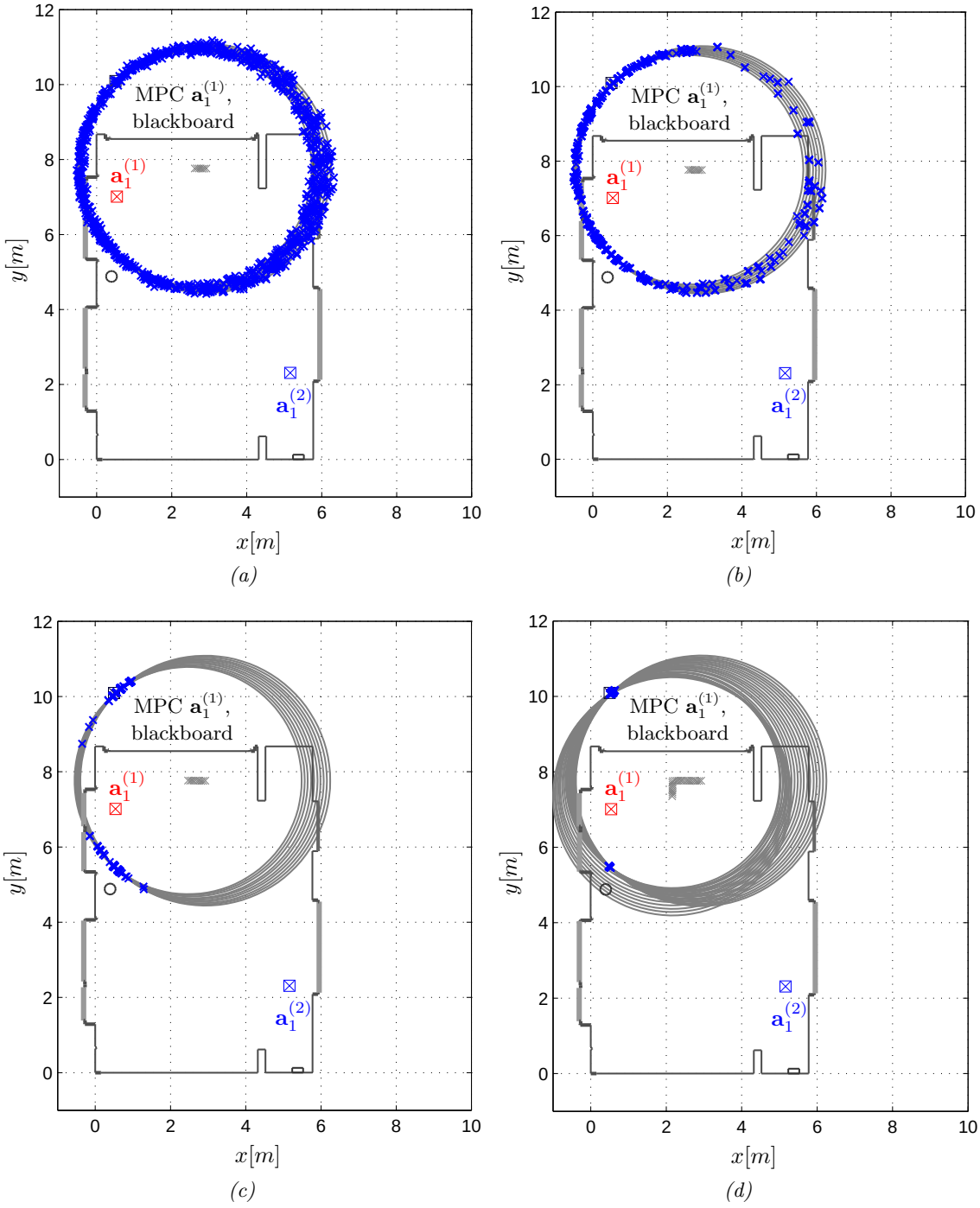

Figure 6.7: Illustration of the VA detection process over time using the PF initialization. Two anchors at $\mathbf{a}_1^{(1)}$ and $\mathbf{a}_1^{(2)}$ represent the infrastructure (in blue and red, respectively). The gray and the blue crosses represent, respectively, the estimated positions of the agent and the particles for estimating the new VA (corresponding to the blackboard). The number of particles used for this simulation is 1000. The gray circles illustrate the measurement model with the agent at center and radius determined by the VA positions.

As shown in the figure—after 68 time steps—a number of relevant VAs have been identified that match very well with the geometrically computed VAs. Some of these VAs have only been associated for a few time steps, corresponding to rather large variances due to large geometric delusion of precision and/or low SINR values (e.g. MPC "$\mathbf{a}_1^{(1)}$ door and left window"). On

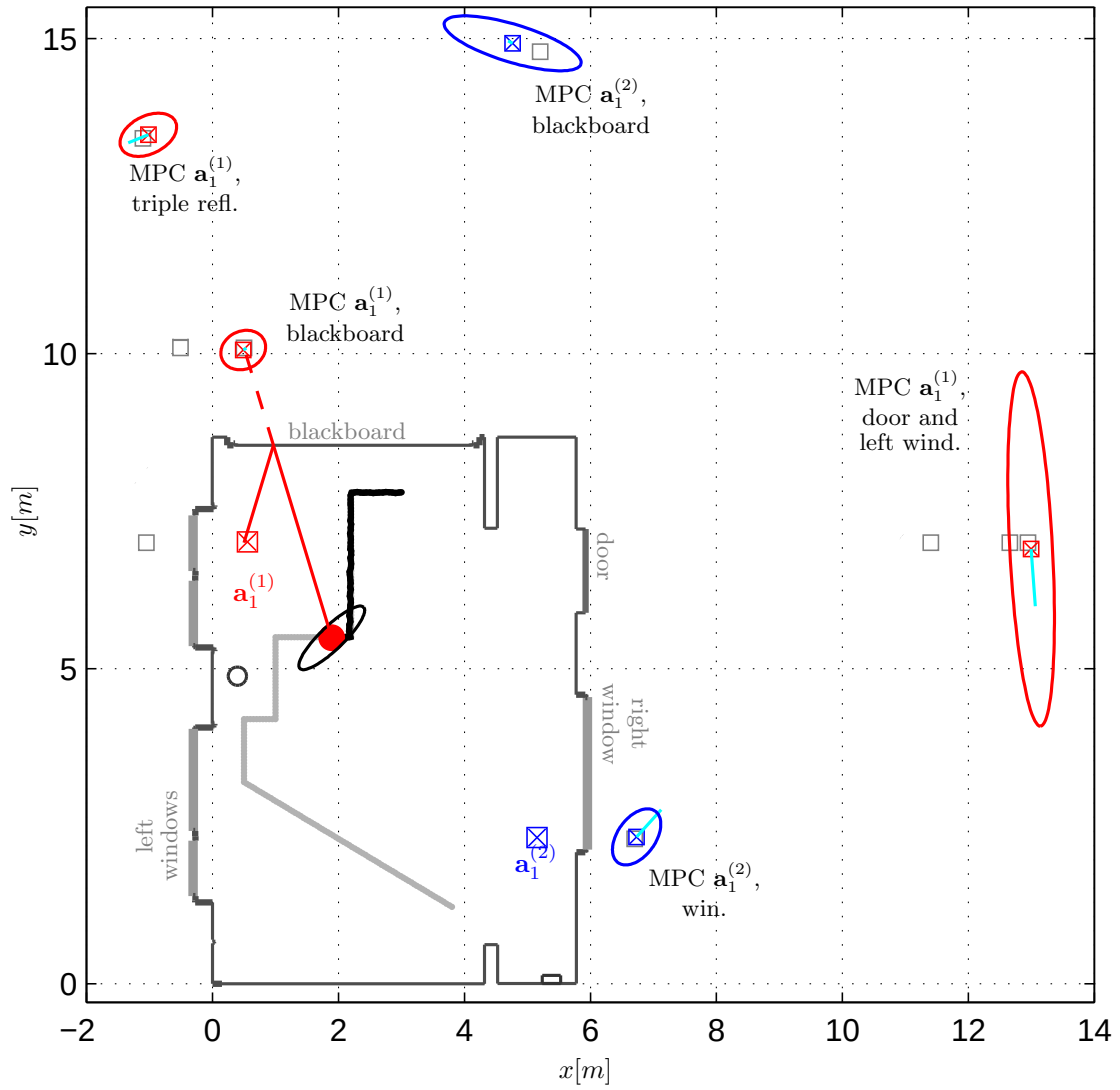

Figure 6.8: Illustration of the environment map obtained by the PF MINT-SLAM algorithm. Two anchors at $\mathbf{a}_1^{(1)}$ and $\mathbf{a}_1^{(2)}$ represent the infrastructure. Gray squares indicate geometrically expected VAs, blue and red plus markers with uncertainty ellipses (40-fold) represent discovered VAs. An agent tracking result is shown in black with some corresponding error ellipses (100-fold).

the other hand, some VAs already have converged to their true location precisely (e.g. MPC "$\mathbf{a}_1^{(1)}$ blackboard"). Some detected VAs, e.g. the one at approximately $\mathbf{a}_k^{(1)} = [-1.4, 13.4]^{\mathrm{T}}$, correspond to VAs of even order three, meaning that in spite of the low energy of the triple reflections, the MPCs have a sufficiently high SINR value, as this specific component shows. Falsely discovered VAs often show a very large variance of their associated amplitudes, leading to low SINRs, which allows to discard them when the ranging variance exceeds a threshold as described in Section 5.5.2. The threshold standard deviation $\sigma_{\mathrm{d,max}} = 5.47\,\mathrm{cm}$, corresponding to a SINR of 0 dB. Some of the detected VAs do not correspond to any geometrically explainable positions, i.e. they represent clutter. This may correspond to scattering objects that are visible for a significant time span. It does not comply to the geometric model of VAs and will be mapped to erroneous positions. However, for many of these false detections, the variance in the position domain is large, in principle allowing for a treatment of these errors on a higher layer. In total, their influence on the tracking process remains limited. 90 % of the errors are within

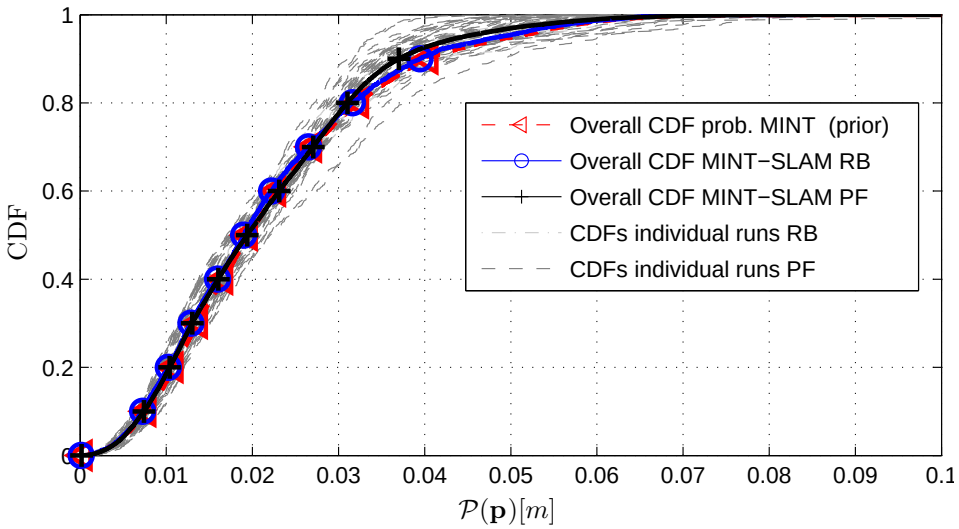

Figure 6.9: Performance CDFs of SLAM using multipath information for $T_p = 0.5\,ns$ and $f_c = 7\,GHz$. Only the anchor coordinates are known. The light and dark gray CDFs indicates the tracking error of the agent using the presented SLAM approach over the 5 trajectories with 1000 agent positions for the range-Bancroft and PF initialization, respectively. The black line denotes the overall CDF for the PF initialization and the blue one for range-Bancroft initialization. The red dashed line shows the overall CDF for probabilistic MINT using all VAs up to second order as a-priori known and online tracking of their positions and range variances.

4.4 cm. Assuming the availability of side information from an inertial measurement unit (IMU), we expect that the robustness of this SLAM algorithm against divergence gets even higher.

Fig. 6.9 shows CDFs of the position error of the agent. The light and dark gray CDFs indicates the tracking error of the agent using the presented SLAM approach over the 5 individual trajectory runs (5 1000-pint trajectories) for the range-Bancroft and PF initialization, respectively. Only the two anchor positions $\mathbf{a}_1^{(1)}$ and $\mathbf{a}_1^{(2)}$ are used as prior knowledge. It can be seen that no run diverges and thus the overall performance is excellent. 90 % of the errors are within 3.5 cm for the PF and the range-Bancroft initialization. As a comparison, the dashed red line shows the overall performance over the 5 runs for probabilistic MINT using all VAs up to order two as prior knowledge. The corresponding VA positions are tracked using the UKF, and their range variances are estimated online based on the estimated positions of the agent as described in Section 5.5.2. This provides a performance of 90 % within 3.5 cm, i.e. the same than for MINT-SLAM. A reason for the good performance of the MINT-SLAM approach is that in the VA discovery process, many unreliable MPCs are not detected and thus do not impair the localization. In the case of probabilistic MINT with a-priori known VAs, these MPCs will be associated to the signal features and may cause errors. Due to the variance tracking, they will be weighted down after some time, but until then, they influence the tracking.

Fig. 6.10 contains (as Fig. 5.3 for probabilistic MINT) the estimated standard deviations of the ranging to the selected VAs marked in Fig. 6.8. The default value assigned to newly detected VAs, 0.07 m, is shown by a black line and the threshold $\sigma_{\mathrm{d,max}}$ that is used to select VAs to become candidates for the data association by a gray line. As in Fig 5.3, the Figs. 6.10a and 6.10b show that the ranging variances of the direct LOS paths are very small along almost the entire trajectory and thus useable for tracking. Figs. 6.10c and 6.10d show, the blackboard is (as expected) again nicely detectable for Anchor 1, whereas for Anchor 2 for a few trajectories

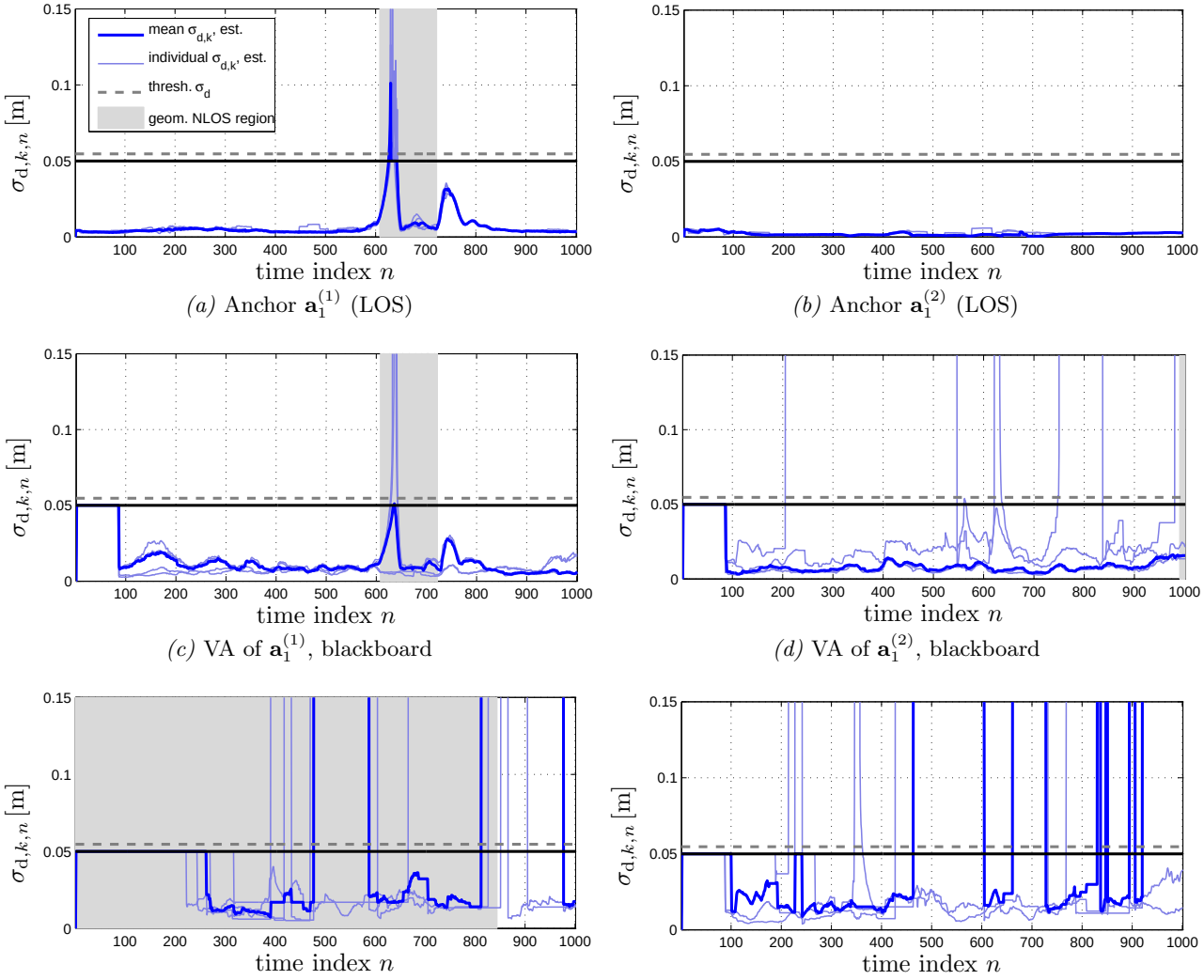

(a) Anchor $\mathbf{a}_1^{(1)}$ (LOS)

(b) Anchor $\mathbf{a}_1^{(2)}$ (LOS)

(c) VA of $\mathbf{a}_1^{(1)}$, blackboard

(d) VA of $\mathbf{a}_1^{(2)}$, blackboard

(e) VA of $\mathbf{a}_1^{(1)}$, right window

(f) VA of $\mathbf{a}_1^{(2)}$, right window

Figure 6.10: Estimated standard deviations of the ranging to selected VAs, i.e. (a) the LOS to Anchor 1, (b) the LOS to Anchor 2, (c) the reflections w.r.t. the blackboard and Anchor 1 (c) as well as (d) Anchor 2, (e) the right window and Anchor 1, and (f) the right window and Anchor 2. Gray regions indicate geometrically computed regions where the corresponding MPC is not visible. Blue lines denote the estimated ranging uncertainty, and black lines the initial default value. The SINRs are estimated for a window $w_{past} = 40$ of past agent positions. Precomputed visibilities are considered.

the detectability is not given anymore. The variances for the right window seem to be again rather large, as depicted in Figs. 6.10e and 6.10f. This confirms, the results of Section 5.5.2 shown in Fig. 5.3e and 5.3f.

In the expected regions where the MPCs should be invisible, the uncertainty raises, indicating the decrease in position information. For the direct path and blackboard reflection of Anchor 1, Figs. 6.10a and 6.10c show that the corresponding uncertainty can again decrease. Interestingly, the estimation continues to yield good values also in the NLOS region. This means that in this region, still a measurement is associated to the discovered VA, otherwise only the previous SINR value is reused.

6.4 Chapter Summary and Conclusions

In this chapter it was shown that *probabilistic* MINT algorithm is also able to operate without any prior floor plan information. The proposed *MINT-SLAM* algorithm is able to efficiently learn a feature-based representation of the environment using VAs, while tracking the agent position.

As in *probabilistic* MINT, a key component of the algorithm is the efficient learning of the underlying uncertainty model of the channel. With the knowledge of the SINR values of the discovered VAs, the proposed MINT-SLAM algorithm is able to mask miss-detected VAs and suppress clutter. The simulation results have shown that the performance of the MINT-SLAM algorithm is the same or even slightly better than for that *probabilistic* MINT algorithm, which needs prior floor plan information. A reason for the slightly better performance of the SLAM approach is that in the VA discovery process, many VAs which are associated with unreliable MPCs are not detected and thus do not impair the tracking.

In this operating mode the tracking system is able to be set-up without any prior knowledge about the indoor environment. It is very often the case that just a very rough or even no floor plan is available, thus a system that robustly learns its surrounding environment model during the tracking is inevitable.

7

Cognitive Tracking using Multipath Channel Information

Looking back at the previous chapters, one can observe that we already have almost all ingredients for a cognitive MINT system as introduced in Section 2.4. Fig. 7.1 illustrates the schematics of this cognitive tracking/localization algorithm. The system is able to adapt online its behavior to the environment, i.e. perceptual attention is given, through the following principles:

- At the cognitive perceptor (CP) side, the GSCM and GPEM memories are updated using the received signal $r_n(t, \boldsymbol{\theta}_{\text{control},n})$ with waveform parameters chosen by the cognitive controller (CC).

- In the actual sensing cycle the attention is put through the cognitive controller (CC) using the control parameters $\boldsymbol{\theta}_{\text{control},n}$ on the potential set of VAs and their parameters memorized in the GSCM and GPEM. These model parameters are seen at the cognitive perceptor (CP) side of Fig. 7.1.

Now the question is, "*How to control the environment information flow through the received signal and put cognitive attention on the relevant features in the following sensing cycle?*" The answer to this lies in the CC and the feed-back and feed-forward information between the perceptor and the controller as illustrated in Fig. 7.1. The cognitive control algorithm introduced in this section is based on [79]. In there, the derivation of the so-called cognitive reinforcement learning (RL) algorithm and the proof that the algorithm obtains Bellman optimality are presented.

As already stated in Section 2.4, the control parameters should be chosen in order to optimize the expected cost-to-go function $\mathcal{C}(\cdot)$ of the predicted posterior PDF as defined in (2.12) in Section 2.4. In general, the expected cost-to-go function for a Bayesian state space filter can be

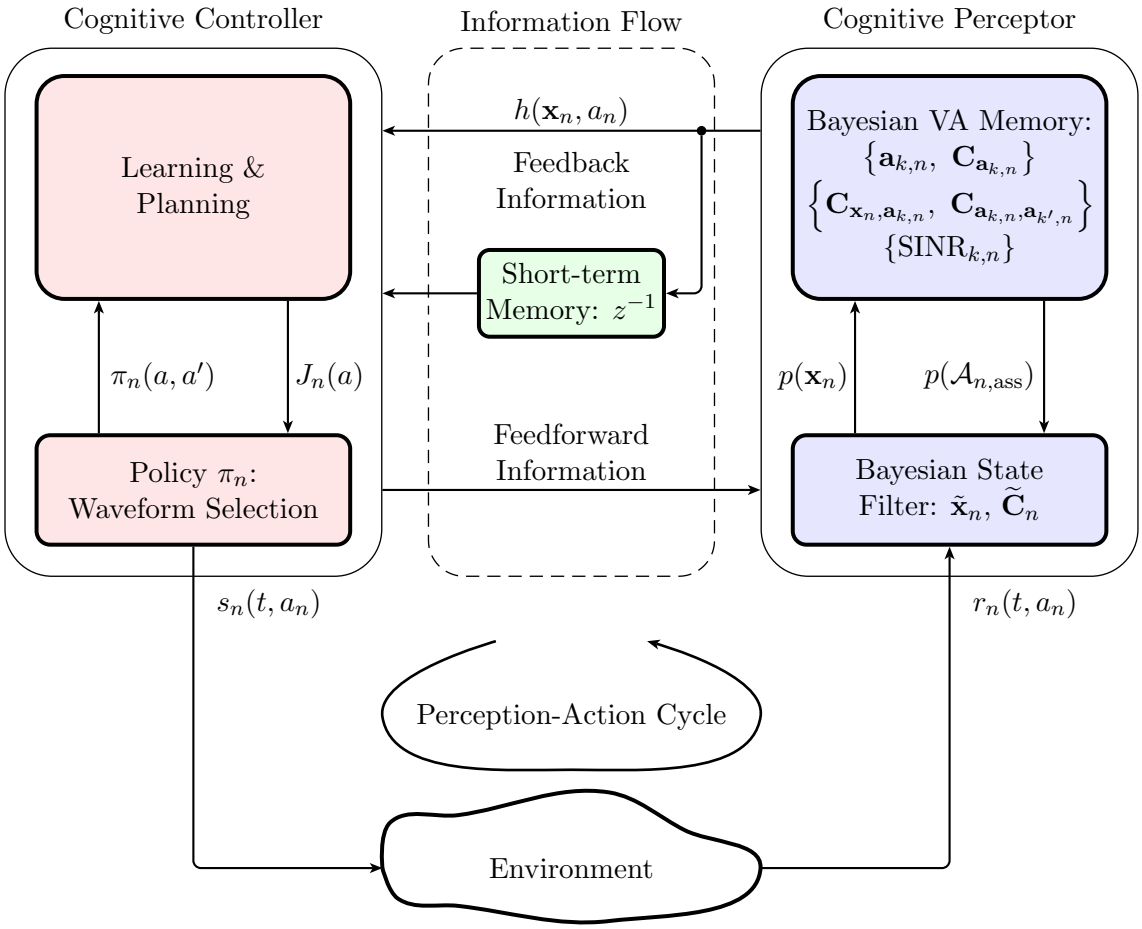

Figure 7.1: Block diagram of the cognitive tracking system.

written as

$$\mathcal{C}\left(p(\mathbf{x}_{n+1}, \mathcal{A}_{n+1}|\tilde{\mathbf{r}}_{n+1}(t, \boldsymbol{\Theta}_{\mathrm{control},n})\right) = \bar{g}\left(\boldsymbol{\epsilon}_{n+1|n+1}(\boldsymbol{\Theta}_{\mathrm{control},n})\right), \tag{7.1}$$

where $\boldsymbol{\epsilon}_{n+1|n+1}(\boldsymbol{\Theta}_{\mathrm{control},n})$ is the predicted posterior state-estimation error depend on the control parameters and $\bar{g}(\cdot)$ defines the cost-to-go function of the transmitter. In Section 2.4, the Shannon entropy was discussed as a possible information measure for the feedback, thus a possible cost-to-go function $\bar{g}(\cdot)$ of the transmitter is the Shannon entropy of the predicted posterior state-estimation error $\boldsymbol{\epsilon}_{n+1|n+1}(\boldsymbol{\Theta}_{\mathrm{control},n})$, given as [97, 124]

$$\bar{g}\left(\boldsymbol{\epsilon}_{n+1|n+1}(\boldsymbol{\Theta}_{\mathrm{control},n})\right) = h\left(\boldsymbol{\epsilon}_{n+1|n+1}(\boldsymbol{\Theta}_{\mathrm{control},n})\right). \tag{7.2}$$

This entropy is directly coupled with the posterior covariance matrix of the Bayesian tracking filter that is lower bounded by the inverse of the EFIM in (3.36) through (5.24). The entropy of the predicted posterior state-estimation error (when assuming a Gaussian approximation) is given as

$$\begin{aligned} h\left(\boldsymbol{\epsilon}_{n+1|n+1}(\boldsymbol{\Theta}_{\mathrm{control},n})\right) &= \frac{1}{2}\log\left((2\pi e)^L \det\left(\widetilde{\mathbf{C}}_{\mathbf{x}_{n+1}}(\boldsymbol{\Theta}_{\mathrm{control},n})\right)\right) \\ &\propto \det\left(\widetilde{\mathbf{C}}_{\mathbf{x}_{n+1}}(\boldsymbol{\Theta}_{\mathrm{control},n})\right) \geq -\det\left(\boldsymbol{\mathcal{I}}_{\mathbf{x}_{n+1}}(\boldsymbol{\Theta}_{\mathrm{control},n})\right), \end{aligned} \tag{7.3}$$

where $\widetilde{\mathbf{C}}_{\mathbf{x}_{n+1}}(\boldsymbol{\Theta}_{\text{control},n})$ and $\boldsymbol{\mathcal{I}}_{\mathbf{x}_{n+1}}(\boldsymbol{\Theta}_{\text{control},n})$, respectively, are the predicted state covariance matrix as in (5.19) and the according predicted posterior FIM as in (5.24) of the state vector provided from the Bayesian state space filter (e.g. UKF or PF)[28], dependent on the control parameter vector $\boldsymbol{\Theta}_{\text{control},n}$. Thus, the entropy in (7.3) is directly coupled with the position-related information that is contained in the measurement noise covariance matrix $\mathbf{R}_{\text{z},n}$ described by (5.16) in Section 5.1.3. When using a UKF this is reflected by measurement update equations in (5.15), especially by (5.15c) (see Section 5.1.2). How the introduced algorithm is using the state space and measurement model equations of the Bayesian state space estimator is described in more detail in Sections 7.2.2 and 7.3.

7.1 Reinforcement Learning (RL)

For readability of the following derivations of the control optimization algorithm, the cost-to-go of the CC (7.3) is rewritten as

$$\bar{g}\left(\boldsymbol{\epsilon}_{n+1|n+1}(\boldsymbol{\Theta}_{\text{control},n})\right) = h\left(\mathbf{x}_{n+1}, a_n\right), \tag{7.4}$$

where $a_n = \boldsymbol{\Theta}_{\text{control},n}$ are the selected actions (the control parameters) over time, with $a_n \in \mathcal{A}$, where $\mathcal{A}$ is the space of cognitive action with size $|\mathcal{A}|$ that represents the waveform library in our case. Consequently, the next set of waveform parameters has to be chosen in order to minimize the cost-to-go of the next posterior entropy. As elaborated in [125], dynamic programming represents an optimal solution for such problems, but unfortunately it is based on the assumption that the state to be controlled is "perfectly" perceivable. Hence, methods have been introduced that are capable of handling imperfect state information [126] with the drawback that they are computational complex. In [74,124] approximate dynamic programming was used for optimal control. In there, the trace of the posterior covariance matrix was used as cost-to-go function to reduce the computational complexity. The policy for control parameter selection in the transmitter at time instance n is seeking to find the set of waveform parameters, for which the cost-to-go function $\bar{g}(\boldsymbol{\epsilon}_{n+1|n+1}(a_n)) \approx \text{tr}[\widetilde{\mathbf{C}}_{\mathbf{x}_{n+1}}(a_n)]$ is minimized for a rolling future horizon of l_{future} predicted states. In practice, it is difficult to construct all state transition probabilities from one state to another that are conditioned on the selected actions, including their cost incurred as a result of each transition. reinforcement learning (RL)[29] [127] represents an approximation of dynamic programming [125,126] for solving such optimal control and future planning task with high computationally efficiency. In RL literature the cost-to-go function is termed value-to-go function $J_n(a_n)$ that is updated online for every PAC based on the immediate rewards r_n. The immediate rewards r_n is a measure of "quality" of an action a_n taken on the environment. Using the Markovian assumption and following the way in [79], it is given by

$$r_n = g_n\left(h(\mathbf{x}_{n-1}, a_{n-1}) - h(\mathbf{x}_n, a_n)\right) \tag{7.5}$$

[28] In general, the feedback information can also be computed for a non-Gaussian Bayesian state space filter using a PF as described in [93], where information-seeking control is used to find the optimal sensing positions of agents in cooperative networks.

[29] RL represents an intermediate learning procedure that lies between supervised and unsupervised learning as stated in [124].

where $h(\mathbf{x}_n, a_n) \propto \det\left(\mathbf{C}_{\mathbf{x}_n}(a_n)\right)$ and $g_n(\cdot)$ is an arbitrary scalar operator that in its most general form could also depend on the time instance n [79]. A reasonable function for the reward is the scaled change in the posterior entropy from one PAC to the next, i.e.

$$r_n = \text{sign}\left(\Delta h(\mathbf{x}_n, a_n)\right) \left|\log\left(\left|\Delta h(\mathbf{x}_n, a_n)\right|\right)\right|. \tag{7.6}$$

A positive reward will be favoring the current action a_n for the future action a_{n+1} and conversely a negative one will lead to a penalty for these actions. As described in [79], the cognitive RL algorithm has to find the optimal future action a_{n+1} for the next PAC based on the immediate reward r_n and the learned value-to-go function $J_n(a_n)$.

For computing the expected costs of future actions as it is done in dynamic programming, RL divides the computation of the value-to-go function into two parts, (i) the learning phase that incorporates the actual measured reward into the value-to-go function based on actions a_n and a_{n-1}, and (ii) the planning phase that incorporates predicted future rewards into the value-to-go function. Whereas for learning a "real" reward is perceived from the environment, for planning just model-based predicted rewards are perceived from the internal perceptor memory using the feedforward link. A faster convergence to the optimal control policy can be achieved in this way.

7.2 Learning and Planning: Algorithm

The value-to-go function that is used in the cognitive controller is defined as [79]

$$J_n(a) = \mathbb{E}_{\pi_n}\left\{r_n + \gamma r_{n+1} + \gamma^2 r_{n+2} + \cdots | a_n = a\right\}, \quad a \in \mathcal{A}, \tag{7.7}$$

where r_n is the actual reward, r_{n+l} are the predicted future rewards that are based on the GPEM and GSCM parameter that are used by the Bayesian filter, $0 < \gamma \leq 1$ is the discount factor for future rewards based on action $a_n \in \mathcal{A}$ and the expected value is calculated using the cognitive policy

$$\pi_n(a, a') = \mathbb{P}\left[a_{n+1} = a' | a_n = a\right], \quad a, a' \in \mathcal{A}, \tag{7.8}$$

where $\mathbb{P}[\cdot|\cdot]$ defines a conditional probability mass function (PMF) that describes the transition probabilities of all action $a \in \mathcal{A}$ over time instances n. Following the derivations in [79], the value-to-go function can be reformulated in an incremental recursive manner, yielding

$$J_n(a) \leftarrow J_n(a) + \alpha\left[\mathcal{R}(a) + \gamma \sum_{a'} \pi_n(a, a') J_n(a') - J_n(a)\right], \quad \forall\, a \in \mathcal{A}, \tag{7.9}$$

where $\mathcal{R}(a) = \mathbb{E}_{\pi_n}\{r_n | a_n = a\}$ denotes the expected immediate reward and $\alpha > 0$ is the learning rate. The algorithm for updating the value-to-go function can be found in Appendix D as Algorithm 1. The incremental recursive update in (7.9) means that for all actions $a \in \mathcal{A}$ the value-to-go function is updated using the expected immediate reward and the policy $\pi_n(a, a')$ for all these actions.

7.2.1 Learning from applied Actions

With the value of the immediate reward r_n, a new value is learned for the value-to-go function for the currently selected action a_n using $J_n(a_n) \leftarrow (1-\alpha)J_n(a_n) + \alpha\mathcal{R}(a_n)$ of (7.9). This accounts for the "real" physical action on the environment. Hence, only one parameter set can be chosen as an action for the perception-action cycle (PAC) at a time; it would take at least $|\mathcal{A}|T$ seconds for applying all actions on the environment and collecting the according immediate rewards, where T is the time period of a PAC. Unfortunately, this results in a poor convergence rate of the algorithm and unacceptable behavior for time-variant environments. A possible remedy against this is the planning of future actions based on the state space and measurement model of the Bayesian state estimator.

7.2.2 Planning for Improving Convergence Behavior

Planning is defined as predicting expected future rewards using the state and measurement model of the Bayesian state space filter to improve the convergence rate of the RL algorithm. As depicted in Fig. 7.1, the feedforward link is used to connect the controller with the perceptor. The feedforward information is a hypothesized future action, which is selected for a future planning stage. Inspecting (7.9) and the Algorithm 1 in Appendix D, one can observe that for every action $a \in \mathcal{M}$, where $\mathcal{M} \subset \mathcal{A}$ is a subset of $\mathcal{A}$ depending on the actual policy π_n, the predicted posterior covariance matrices $\widetilde{\mathbf{C}}_{n+l}(a)$ and the according predicted future rewards r_{n+l}, are computed with decreasing discount factor γ^l for predicted future rewards, for $l = 1, \ldots, l_{\text{future}}$, where l_{future} is the future horizon. The predicted covariance matrices $\widetilde{\mathbf{C}}_{n+l}(a)$ for a specific future action a is computed using the state space (e.g. (5.18)) and measurement model (e.g. (5.20)) of the Bayesian state space estimator and the according GPEM and GSCM parameters stored in the perceptors' memory as shown in Fig. 7.1. After the planning process is finished, the value-to-go function is updated for all actions $a \in \mathcal{M}$. Finally, the actual PAC is closed by updating the policy to π_{n+1} using the value-to-go function J_{n+1} and choosing the new action, i.e. the waveform parameters, for the next PAC according to this new policy. This means that the value-to-go function $J_n(a_n)$ and the policy π_n are updated iteratively from one another from one PAC to the next PAC, with one important detail which is discussed below.

Explore/Exploit trade-off: As one can observe from Algorithm 2 in Appendix D, both the planning process and choosing new actions are based on the policy. In planning, the chosen action-subset $\mathcal{M}$ is defined by sampling from the policy π_n and new actions are selected based on the updated policy π_{n+1}. Hence, the policy is responsible for the explore/exploit trade-off in the action space. A widely used method for balancing the exploration of new actions and exploiting the already learned value-to-go function $J_n(a_n)$ is the ϵ-greedy strategy, meaning that with a small probability of ϵ a random action is selected, representing pure exploration, and with probability of $1-\epsilon$ the action is chosen according to the maximum of the value-to-go function, representing a pure exploitation. The random selection of a new action and the action in the subspace $\mathcal{M}$ can either be selected from a uniform distribution over the action space $\mathcal{A}$ or from

the policy π_n. The policy and the selection of an action are described by

$$\pi_{n+1}(a_{n+1}, a_n) = \begin{cases} \text{random action from } \mathcal{A} & \text{if } \xi < \epsilon \\ \arg\max_{a \in \mathcal{A}} J_n(a) & \text{otherwise} \end{cases}, \tag{7.10}$$

where $0 \leq \xi \leq 1$ is a uniform random number drawn at each time step n. As we have said, from the policy in (7.10) the new action a_{n+1} is selected and applied on the environment so that the next PAC can start. The important concept of *attention* at the perceptor as well as the actuator side in the cognitive dynamic system can be argued with the following:

- **Perceptual attention:** Is given by the fact that the environment dependent parameters, i.e. the marginal PDFs of the VAs $p(\mathbf{a}_{k,n})$ and their multipath channel dependent reliability measures, $\text{SINR}_{k,n}$, are learned and updated online, so that the perceptual Bayesian state space filter puts its attention on the relevant position-related information in the received signal.

- **Control attention:** Is given by the fact that the policy π_n that is learned over time and the according subset of actions $\mathcal{M}$ put focus on the "more relevant" actions. These action in turn focus on the relevant position-related information in the received signal.

7.3 Waveform Library

The general form of the waveform library contains the control parameters $\boldsymbol{\Theta}^{(j)}_{\text{control},n} = \{\boldsymbol{\theta}^{(j)}_n\}^J_{j=1}$ $= \{T^{(j)}_{\text{p},n}, f^{(j)}_{\text{c},n}\}^J_{j=1}$ for the j-th anchor consisting of carrier frequencies and pulse durations. Hence, the VA specific channel MPC parameters using specific sub-bands of the radio channel spectrum defined by the parameter pair $T^{(j)}_{\text{p},n}$ and $f^{(j)}_{\text{c},n}$ can be chosen in an "optimal" manner. Optimal in this case means that the position-related information for the agent position $\mathbf{p}$ is maximized (see (3.36) in Section 3.5.1).

Equations (3.18) and (3.20) in Section 3.3.2, which describe the parameters $\widetilde{\text{SINR}}^{(j)}_{k,n}$, show the relation between the pulse parameter pair $T^{(j)}_{\text{p},n}$ and $f^{(j)}_{\text{c},n}$ and the position-related information contained in the channel. The pulse duration $T^{(j)}_{\text{p},n}$ scales the amount of DM and is directly proportional to the effective root mean square bandwidth β. The relation to $f^{(j)}_{\text{c},n}$ is not that obvious, since it describes the frequency dependency of the environment parameters and thus the GSCM parameters as the complex amplitudes of the MPCs and the DM PDP. The set of selected VAs should lead to the highest overall SINR values (and accordingly the smallest range variances $\text{var}\left\{\hat{d}^{(j)}_{k,n}\right\}$) and the smallest possible GDOP footnoteThe GDOP the ratio between position variance and the range variance [24]. For positioning a small value indicates a high level of confidence that high precision can be reached. Hence, the GDOP indicates a "good " geometry for positioning, i.e. a good geometric placement of the anchors., i.e. geometric optimal constellation of VA positions which is reflected by the ranging direction matrix described in (3.37) in Section 3.5.1. In a cognitive sense this means that the actions $a \in \mathcal{A}$ are chosen to reduce the posterior entropy over time under quasi-stationary environment conditions.

7.4 Results

7.4.1 Measurement Setup

For analyzing the tracking methods, discussed above, we use the same measurements as described in Section 5.5.1 [102]. The chosen initial pulse duration is $T_\mathrm{p} = 0.5\,\mathrm{ns}$ (corresponding to a bandwidth of 2 GHz) and the center frequency is $f_\mathrm{c} = 7\,\mathrm{GHz}$. The scenario is same as in Section 5.5.1 illustrated in Fig 5.2. The VAs for the anchors at the positions $\mathbf{a}_1^{(1)}$ and $\mathbf{a}_1^{(2)}$ were computed a-priori up to order 2. The past window of agent positions for the SINR estimation is again chosen to be $w_\mathrm{past} = 40$. For all simulations 30 Monte Carlo runs were conducted.

7.4.2 Initial Experiment Setup

For the sake of simplicity, we reduce the control parameters to just the carrier frequency $\mathbf{\Theta}_{\mathrm{control},n} = f_{\mathrm{c},n}$ for each PAC for all anchors and we fix the pulse duration T_p. This means that the cognitive MINT system adaptively finds the carrier frequency $f_{\mathrm{c},n}$ from PAC to PAC that yields the highest reward from the environment by maximizing the position-related information. Starting from the initial value $f_{\mathrm{c},1} = 7\,\mathrm{GHz}$ (which represents the center of the measured bandwidth), the carrier frequency is adapted over time using the posterior entropy in (7.3).

The finite space of cognitive actions $\mathcal{A}$ contains the discrete frequency values bounded by the measured bandwidth, i.e. $f_{\mathrm{c},n,i} \in \mathcal{A}$, where $i = 1, \ldots, |\mathcal{A}|$. The frequency spacing between the frequency bins is equidistant, $\Delta f_\mathrm{c} = f_{\mathrm{c},n,i+1} - f_{\mathrm{c},n,i}$. For the experiments, we haven chosen $\Delta f_\mathrm{c} = 50\,\mathrm{MHz}$, considering the large signal bandwidth of 2 GHz. The starting policy is defined as a uniform distribution $\pi_1(a, a) = \mathcal{U}(f_{\mathrm{c},n,1}, f_{\mathrm{c},n,|\mathcal{A}|})$ and the cost-to-go function is chosen to be $J_1(a) = 0\ \forall a$. The size of the planning subspace is $|\mathcal{M}| = 20$; the size of $\mathcal{A}$ is $|\mathcal{A}| = 40$.

7.4.3 Discussion of Performance Results

Conventional MINT

Fig. 7.2 shows the overall position error CDFs for "conventional" MINT (which assumes perfect floor plan knowledge) with and without cognitive waveform adaptation. To show the advantage of the cognitive MINT algorithm, a restricted set of VAs is chosen and as in Section 5.5.2 the visibilities of the VAs are computed using the SINRs instead of optical ray-tracing. As the CDF of "conventional" MINT indicates (blue line with circle marker), the tracking algorithm tends to diverge since too little position-related information is available. The black and the red lines show the overall position error CDFs for cognitive MINT for a future horizon window of $l = 1$ and $l = 5$, respectively. As one can observe, the performance is significantly increased due to the cognitive waveform adaptation. This means that the cognitive MINT algorithm is able to increase the amount of position-related information by changing the sensing spectrum via the carrier frequency $f_{\mathrm{c},n,i} \in \mathcal{A}$ to bands that carry more geometry-dependent information in the MPC. Another interesting observation of Fig. 7.2 is that an increase of the planning horizon results in an increased performance, confirming the correct functionality of the cognitive algorithm.

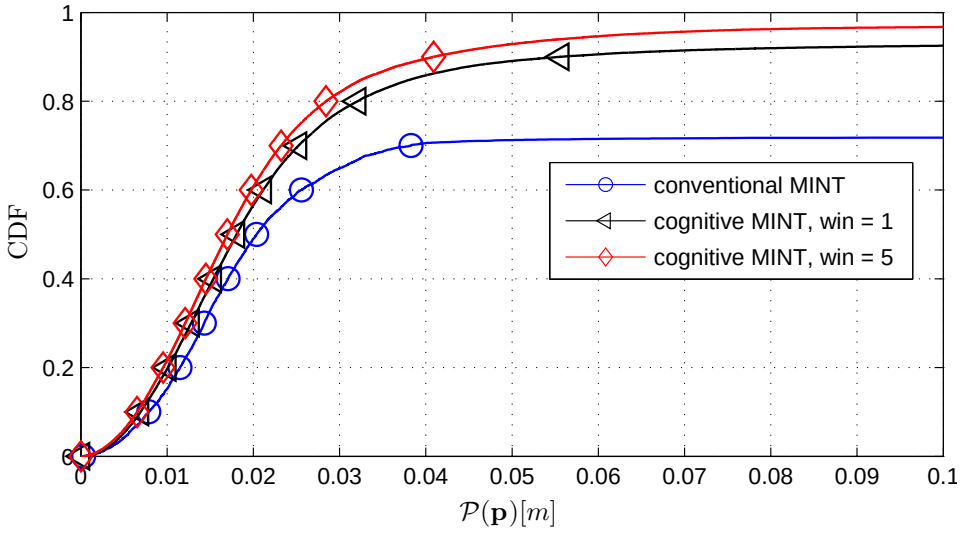

Figure 7.2: Performance CDFs of the cognitive MINT algorithm using a smaller restricted set of VAs. Visibilities of VAs are computed using the SINRs instead of optical ray-tracing.

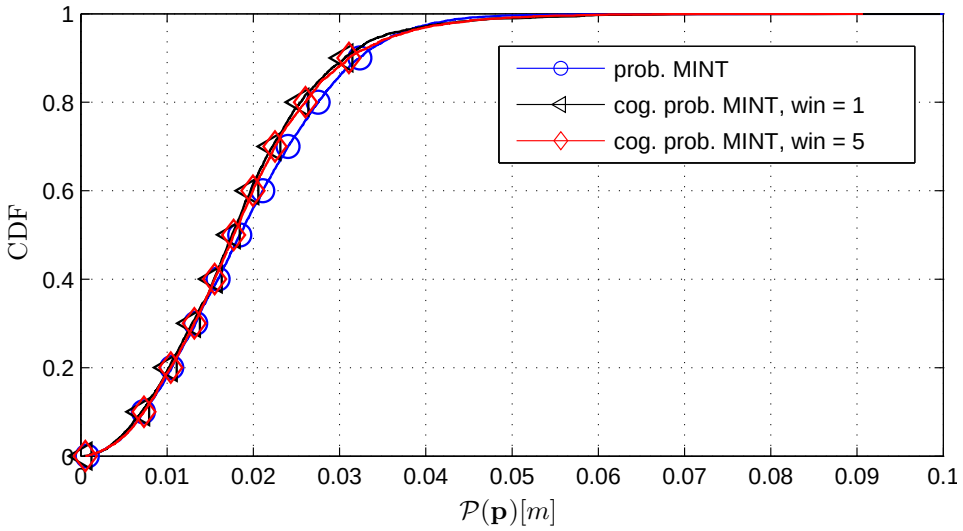

Figure 7.3: Performance CDFs of cognitive probabilistic MINT using a smaller restricted set of VAs. For probabilistic MINT, the visibilities of VAs are always computed using the SINRs.

Probabilistic MINT

Fig. 7.3 shows the overall position error CDFs for probabilistic MINT with and without cognitive waveform adaptation. As we have already discussed in Section 5.5.2, uncertainties in the floor plan and wrong associations can be robustly handled due to the probabilistic treatment of VAs and thus none of the individual trajectory runs diverges. The already achieved high accuracy and robustness of probabilistic MINT are the reasons that cognitive sensing leads to only a minor additional performance gain for this scenario. It is suspected that for lower bandwidth the performance gain induced by the cognitive probabilistic MINT should be much more distinct.

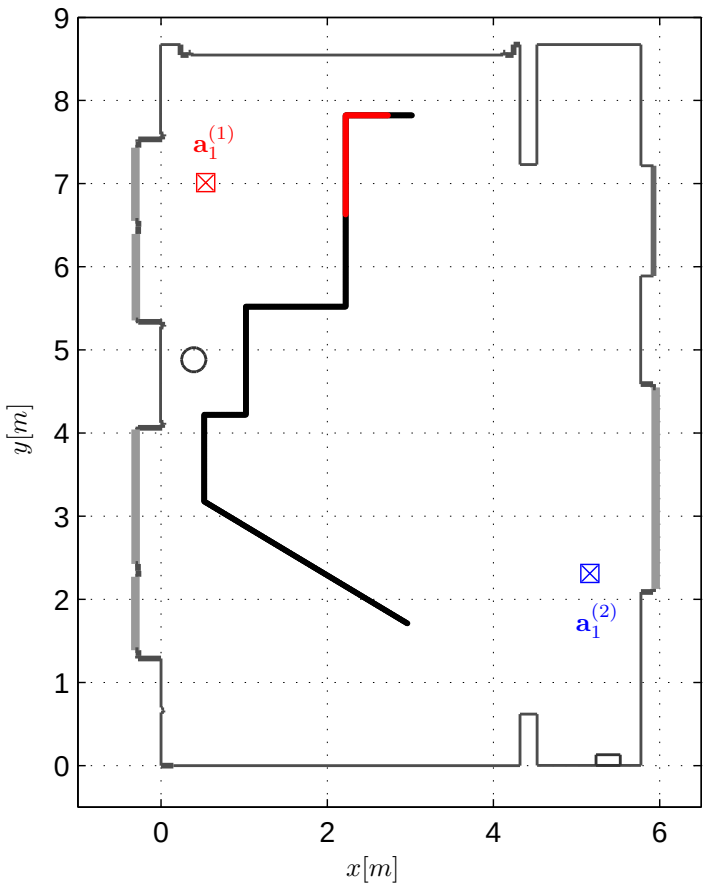

Figure 7.4: Scenario for probabilistic MINT using cognitive sensing in presence of additional DM interference. The anchors are at the positions $\mathbf{a}_1^{(1)}$ and $\mathbf{a}_1^{(2)}$. The black line represents the agent trajectory and the red part of the line indicates the agent positions, where the DM interference is activated.

Probabilistic MINT with additional DM Interference

In the last setup, we additionally have added synthetic DM interference filtered at a carrier frequency $f_c = 7\,\text{GHz}$, with a bandwidth of $2\,\text{GHz}$. The DM parameters are chosen according to Table 3.1 except for the DM power. The experiments were conducted with three levels of DM power, $\Omega_1 = 1.1615 * 10^{-9}$, $\Omega_1 = 5.8076 * 10^{-9}$ and $\Omega_1 = 1.1615 * 10^{-8}$.

Fig. 7.4 illustrates the scenario used for the experiment. The black line represents the agent trajectory and the red part of it indicates the agent positions, where the DM interference is activated. Fig. 7.5 shows the signals exchanged between the agent and the Anchors 1 and 2 for one sample position. The "clean" signals are shown in Fig. 7.5a, the noisy signal for DM power of $\Omega_1 = 1.1615 * 10^{-9}$ in Fig. 7.5b. Looking at Fig. 7.5b it is quite obvious that this level of DM represents already a severe interference. The justification of using such a interference noise model lies in the fact that it can describe many kinds of measurement modeling mismatches, e.g. if the anisotropy of the antenna pattern for different angle of arrivals is not considered.

Fig. 7.6 illustrates the mean values of the cognitively adapted carrier frequency along one of the trajectories at DM power $\Omega_1 = 1.1615 * 10^{-8}$. The mean is computed using the 30 Monte Carlo simulations of the experiment. The black line denotes the initial carrier frequency $f_{\text{c},1}$ and the blue one the mean of the cognitively adapted carrier $f_{\text{c},n}$. The blue dashed lines show a few

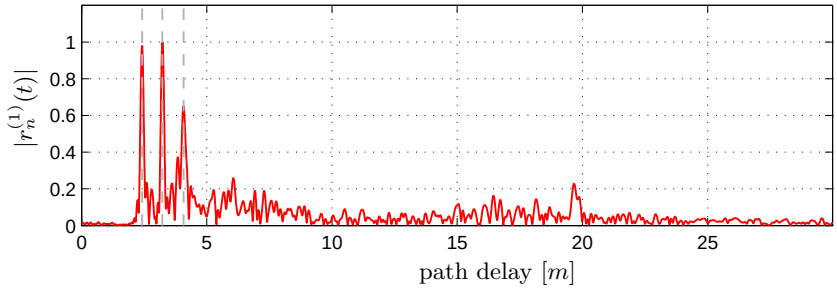

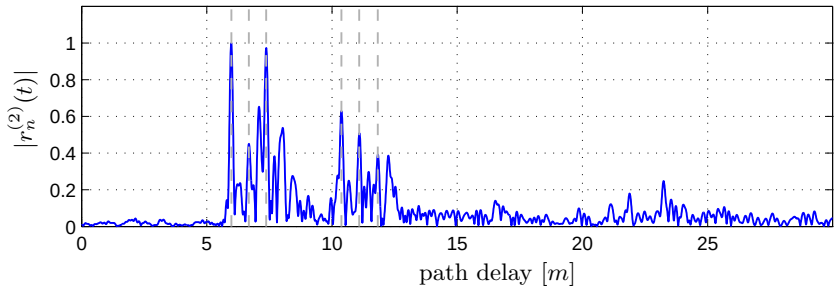

(a) Clean signals

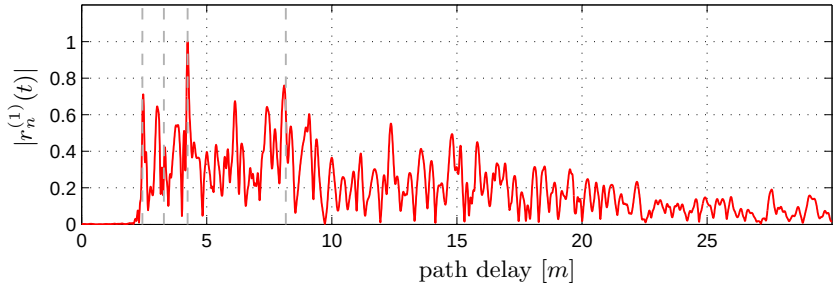

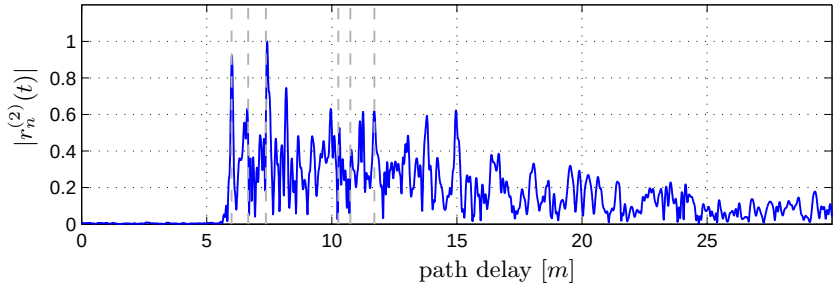

(b) Noisy signal with DM power of $\Omega_1 = 1.1615 * 10^{-8}$

Figure 7.5: Signals exchanged between agent and Anchors 1 and 2 for an example agent position. The gray lines represent the estimated delays of the MPCs. Fig. 7.5a shows the "clean" signal and Fig. 7.5b the noisy signal.

example realizations of cognitively adapted carrier frequencies along different trajectories and for different Monte Carlo runs. The figure shows quite clearly that the cognitive probabilistic MINT algorithm is avoiding (almost at all agent positions, where additional DM interference is present) carrier frequencies $f_{c,n}$ near to the carrier of DM.

Fig. 7.7 shows the according mean entropy values of probabilistic MINT (red line with diamond markers) and cognitive probabilistic MINT (black line with triangle markers) over time instances n for DM power $\Omega_1 = 1.1615 * 10^{-8}$. The red and black dashed lines show a few example entropy realizations along different trajectories and for different Monte Carlo runs. Before the noise disturbance starts the entropy of the probabilistic MINT algorithm is almost the same as of

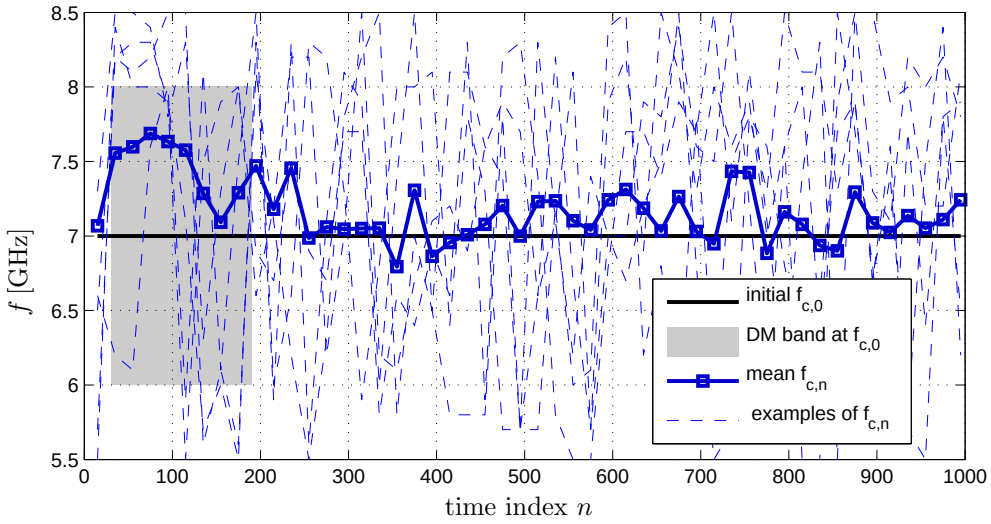

Figure 7.6: Mean carrier frequency for DM power $\Omega_1 = 1.1615 * 10^{-8}$. The black line denotes for the initial carrier frequency $f_{c,1}$ and the blue one the mean of the cognitively adapted carrier frequency $f_{c,n}$. The blue dashed lines show a few example realizations of cognitively adapted carrier frequencies along different trajectories and for different Monte Carlo runs.

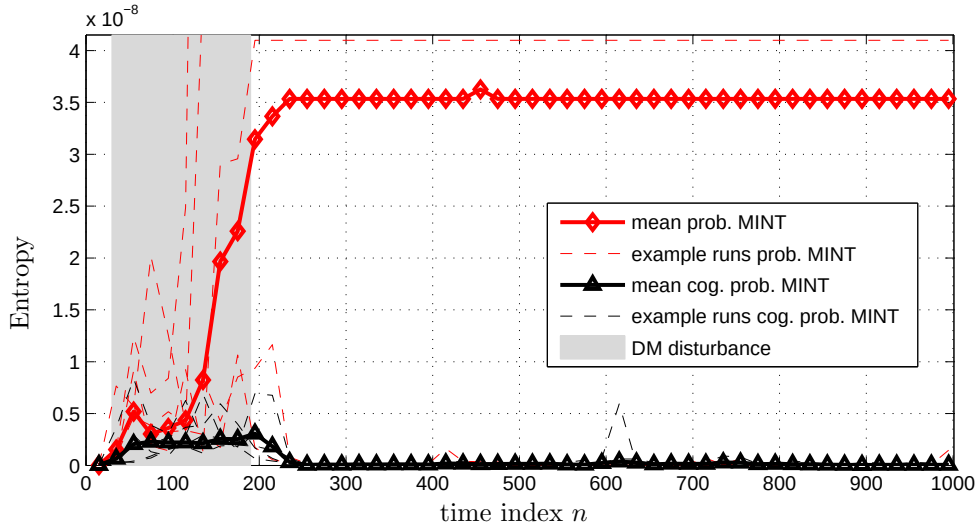

Figure 7.7: Mean entropy of probabilistic MINT and cognitive probabilistic MINT over time instances n for DM power $\Omega_1 = 1.1615 * 10^{-8}$. The red and black dashed lines show a few example entropy realizations along different trajectories and for different Monte Carlo runs.

the cognitive probabilistic MINT algorithm. In the moment the disturbance is introduced, the entropy of the posterior increases. The cognitive probabilistic MINT algorithm then starts to change its carrier frequency $f_{c,n}$ (as shown in Fig. 7.6) until the entropy is again reduced. This leads to an almost constant or even decreasing entropy even in the presence of a tremendous noise level (black line with triangle markers in Fig. 7.7). In contrast to that the probabilistic MINT algorithm without cognitive waveform adaptation starts to diverge after the disturbance is introduced and is not able to recover. This is indicated by the rapid increase of the entropy and stagnation at a large value shown in Fig. 7.7 by the red line with diamond markers.

This result is confirmed by looking at the performance CDFs of the agent position error shown in Fig. 7.8. This comparison between probabilistic MINT and cognitive probabilistic MINT illustrates the powerful property of the cognitive algorithm to separate relevant from irrelevant

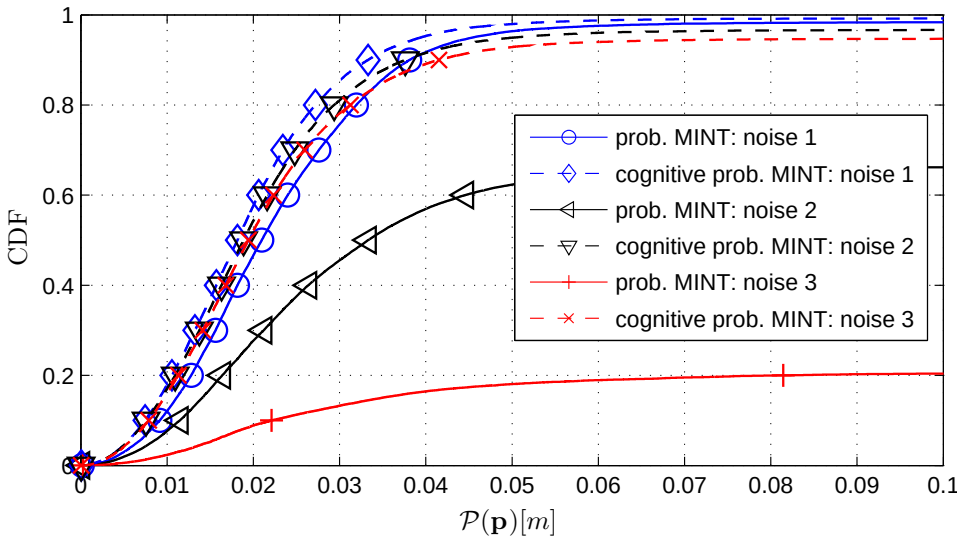

Figure 7.8: Performance CDFs of the cognitive probabilistic MINT algorithm with introducing a disturbance at three different noise levels along a certain part of the trajectory. Noise 1 *corresponds to DM with* $\Omega_1 = 1.1615{*}10^{-9}$*, Noise* 2 *with power* $\Omega_1 = 5.8076{*}10^{-9}$ *and with power* $\Omega_1 = 1.1615{*}10^{-8}$

information using adaptation of the control parameter $f_{c,n}$ to avoid the noisy frequency band of the signal. The probabilistic MINT algorithm without waveform adaptation tends to diverge under such harsh conditions as depicted by CDFs drawn with solid lines. In contrast to this, the cognitive MINT algorithm overcomes these impairments, leading again to a *robust* behavior as depicted by CDFs drawn with dashed lines.

7.5 Chapter Summary and Conclusions

In this chapter a "fully" cognitive localization system has been established and analyzed which intertwines *probabilistic* MINT with a cognitive dynamic system (CDS). The resulting *cognitive probabilistic* MINT algorithm adapts the waveform parameters in order to enhance the representation of the posterior PDF of the state vector.

Using real data it has been shown that the *cognitive probabilistic* MINT algorithm is able to increase the amount of *position-related* information by changing the sensed frequency band via the carrier frequency. This can be explained by the fact that by changing the sensed frequency band, new statistical samples of the channel are gained so that efficient learning of the channel model parameters (and also marginal PDFs of the VA positions) is supported. Another experiment has shown that severe additional interference noise is suppressed and thus *robustness* is controlled by cognitively changing the waveform parameters. The cognitive controller (CC) combined with probabilistic MINT can also be combined straight forwardly with probabilistic MINT-SLAM.

8 Conclusions

As stated at the beginning of this thesis, *accurate* and *robust* positioning in indoor environments is a challenging task, especially due to dense multipath. With our prior work, we have shown that both attributes can be achieved satisfyingly even with minimal infrastructural requirements. *Position-related information* is used in this approach, which is based on insights gained by a CRLB analysis and prior floor plan knowledge. However, still accurate floor plan knowledge is needed, which is in practice not always available. Hence, it was inevitable (i) to remove the requirement of a precisely known a-priori floor plan and (ii) to cope with uncertainties in the environment representation, i.e. the floor plan features. These goals are inherently coupled with relevant channel information and hence, (iii) efficient online learning of *position-related information* (embedded in the multipath channel) is also essential for a proper probabilistic consideration of the observed features of the floor plan (the VAs). To improve the separation between relevant and irrelevant channel information in situations of high noise levels, it has been hypothesized that *cognitive control of the waveform parameters* can provide the final ingredient for *robust* positioning and tracking.

This thesis confirms with theoretical results and extensive simulation results using real measurements that all of these aims can be achieved. Based on the rigorous mathematical analysis of the GSCM and GPEM, an algorithmic proof has been given that *simultaneous localization and mapping* is feasible with *high accuracy* using *multipath channel information*. Hence, the research question stated in Section 1.4 has been answered:

- Spatially consistent information about the geometric features of the environment contained in the multipath channel components gathered over time, can be used to infer a probabilistic model of the features of a floor plan (the VAs) and to learn online the VAs' corresponding reliability measure. This can be achieved starting **without any prior knowledge of the floor plan**.

- Active sensing of the environment, i.e. Tx-side waveform adaptation, is an efficient instrument to **increase the amount of relevant information**, (i.e. position-related multipath information) and to **focus the algorithms' attention on relevant environment features (a specific set of VAs)**.

The resulting **Cognitive Multipath-assisted Simultaneous Localization and Mapping algorithm** has the following detailed characteristics:

- Robust online learning of the *geometric-probabilistic environment model (GPEM)*
- Robustness against outliers in the measurements and false data associations facilitated by probabilistic modeling of the VAs
- Local adaptation to the channel characteristics enabled by online learning of the parameters of the *geometric-stochastic channel model (GSCM)*
- Focusing the perceptive attention to relevant channel features enabled by *cognitive control (CC) of the transmitted waveform*

The experiments have shown that there are different levels of uncertainties that have to be treated properly. Firstly, the system has to put its focus on relevant perceived information based on the underlying physical channel and environment model, leading to *perceptive attention*.

This leads us to the following final conclusion:

All concepts—GPEM, GSCM and CC—intertwined facilitate the desired level of robustness and accuracy of the positioning and tracking system in harsh indoor environments.

A Derivations of the CRLB

A.1 FIM for MPCs

A.1.1 General Case of MPCs delays

$\mathbf{\Lambda}_{\mathrm{A}} \in \mathbb{R}^{K\times K}$ contains the second-order derivatives of the log-likelihood function w.r.t. the delays of the MPCs.

$$
\begin{aligned}
[\mathbf{\Lambda}_{\mathrm{A}}]_{k,k'} &= \mathbb{E}_{\mathbf{r};\boldsymbol{\psi}}\left\{-\frac{\partial^2 \ln f(\mathbf{r};\boldsymbol{\psi})}{\partial\tau_k\partial\tau_{k'}}\right\} \\
&= \mathbb{E}_{\mathbf{r};\boldsymbol{\psi}}\left\{-\frac{\partial^2\left\{2\Re\left\{\mathbf{r}^{\mathrm{H}}{\mathbf{C}_{\mathbf{r}}}^{-1}\mathbf{S}\boldsymbol{\alpha}\right\}-\boldsymbol{\alpha}^{\mathrm{H}}\mathbf{S}^{\mathrm{H}}{\mathbf{C}_{\mathbf{r}}}^{-1}\mathbf{S}\boldsymbol{\alpha}-\mathbf{r}^{\mathrm{H}}{\mathbf{C}_{\mathbf{r}}}^{-1}\mathbf{r}\right\}}{\partial\tau_k\partial\tau_{k'}}\right\} \\
&= \mathbb{E}_{\mathbf{r};\boldsymbol{\psi}}\left\{-\frac{\partial^2\left\{2\Re\left\{\mathbf{r}^{\mathrm{H}}{\mathbf{C}_{\mathbf{r}}}^{-1}\mathbf{S}\boldsymbol{\alpha}\right\}\right\}}{\partial\tau_k\partial\tau_{k'}}\right\}+\frac{\partial^2\left\{\boldsymbol{\alpha}^{\mathrm{H}}\mathbf{S}^{\mathrm{H}}{\mathbf{C}_{\mathbf{r}}}^{-1}\mathbf{S}\boldsymbol{\alpha}\right\}}{\partial\tau_k\partial\tau_{k'}} \\
&= \underbrace{\mathbb{E}_{\mathbf{r};\boldsymbol{\psi}}\left\{-2\Re\left\{\alpha_k\mathbf{r}^{\mathrm{H}}{\mathbf{C}_{\mathbf{r}}}^{-1}\frac{\partial^2\mathbf{s}_{\tau_k}}{\partial\tau_k\partial\tau_{k'}}\right\}\right\}}_{(I)} \\
&+\frac{\partial\left\{\alpha_k\boldsymbol{\alpha}^{\mathrm{H}}\mathbf{S}^{\mathrm{H}}{\mathbf{C}_{\mathbf{r}}}^{-1}\frac{\partial\mathbf{s}_{\tau_k}}{\partial\tau_k}\right\}}{\partial\tau_{k'}}+\frac{\partial\left\{\alpha_k^*\left(\frac{\partial\mathbf{s}_{\tau_k}}{\partial\tau_k}\right)^{\mathrm{H}}{\mathbf{C}_{\mathbf{r}}}^{-1}\mathbf{S}\boldsymbol{\alpha}\right\}}{\partial\tau_{k'}} \\
&+\underbrace{2\Re\left\{\alpha_k\boldsymbol{\alpha}^{\mathrm{H}}\mathbf{S}^{\mathrm{H}}{\mathbf{C}_{\mathbf{r}}}^{-1}\frac{\partial^2\mathbf{s}_{\tau_k}}{\partial\tau_k\partial\tau_{k'}}\right\}}_{(II)} \\
\vdots \qquad &\rightarrow \mathbb{E}_{\mathbf{r};\boldsymbol{\psi}}\left\{\mathbf{r}^{\mathrm{H}}\right\}=\boldsymbol{\alpha}^{\mathrm{H}}\mathbf{S}^{\mathrm{H}} \quad\rightarrow\quad (I)+(II)=0
\end{aligned}
\tag{A.1}
$$

$$= \alpha_k \alpha_{k'}^* \left(\frac{\partial \mathbf{s}_{\tau_{k'}}}{\partial \tau_{k'}} \right)^{\mathrm{H}} \mathbf{C_r}^{-1} \frac{\partial \mathbf{s}_{\tau_k}}{\partial \tau_k} + \alpha_k^* \alpha_{k'} \left(\frac{\partial \mathbf{s}_{\tau_k}}{\partial \tau_k} \right)^{\mathrm{H}} \mathbf{C_r}^{-1} \frac{\partial \mathbf{s}_{\tau_{k'}}}{\partial \tau_{k'}}$$
$$= 2\Re \left\{ \alpha_k \alpha_{k'}^* \left(\frac{\partial \mathbf{s}_{\tau_{k'}}}{\partial \tau_{k'}} \right)^{\mathrm{H}} \mathbf{C_r}^{-1} \frac{\partial \mathbf{s}_{\tau_k}}{\partial \tau_k} \right\}$$

All other sub-matrix elements of the channel FIM can be derived in the same manner. Thus, we neglect the equivalent terms to (I) and (II) in the further derivations. $\Re\mathbf{\Lambda}_{\mathrm{B}} \in \mathbb{R}^{K \times K}$ contains the derivatives of the log-likelihood function w.r.t. the delays and the real part of the complex complex amplitudes of the MPCs.

$$[\Re\mathbf{\Lambda}_{\mathrm{B}}]_{k,k'} = \mathbb{E}_{\mathbf{r};\boldsymbol{\psi}} \left\{ -\frac{\partial^2 \ln f(\mathbf{r};\boldsymbol{\psi})}{\partial \tau_k \partial \Re \alpha_{k'}} \right\} \tag{A.2}$$
$$= \frac{\partial \left\{ \alpha_k \boldsymbol{\alpha}^{\mathrm{H}} \mathbf{S}^{\mathrm{H}} \mathbf{C_r}^{-1} \frac{\partial \mathbf{s}_{\tau_k}}{\partial \tau_k} \right\}}{\partial \Re \alpha_{k'}} + \frac{\partial \left\{ \alpha_k^* \left(\frac{\partial \mathbf{s}_{\tau_k}}{\partial \tau_k} \right)^{\mathrm{H}} \mathbf{C_r}^{-1} \mathbf{S}\boldsymbol{\alpha} \right\}}{\partial \Re \alpha_{k'}}$$
$$= \alpha_k \left(\mathbf{s}_{\tau_{k'}} \right)^{\mathrm{H}} \mathbf{C_r}^{-1} \frac{\partial \mathbf{s}_{\tau_k}}{\partial \tau_k} + \alpha_k^* \left(\frac{\partial \mathbf{s}_{\tau_k}}{\partial \tau_k} \right)^{\mathrm{H}} \mathbf{C_r}^{-1} \mathbf{s}_{\tau_{k'}}$$
$$= 2\Re \left\{ \alpha_k \left(\mathbf{s}_{\tau_{k'}} \right)^{\mathrm{H}} \mathbf{C_r}^{-1} \frac{\partial \mathbf{s}_{\tau_k}}{\partial \tau_k} \right\}$$

$\Im\mathbf{\Lambda}_{\mathrm{B}} \in \mathbb{R}^{K \times K}$ contains the derivatives of the log-likelihood function w.r.t. the delays and the imaginary part of the complex complex amplitudes of the MPCs.

$$[\Im\mathbf{\Lambda}_{\mathrm{B}}]_{k,k'} = \mathbb{E}_{\mathbf{r};\boldsymbol{\psi}} \left\{ -\frac{\partial^2 \ln f(\mathbf{r};\boldsymbol{\psi})}{\partial \tau_k \partial \Im \alpha_{k'}} \right\} \tag{A.3}$$
$$= \frac{\partial \left\{ \alpha_k \boldsymbol{\alpha}^{\mathrm{H}} \mathbf{S}^{\mathrm{H}} \mathbf{C_r}^{-1} \frac{\partial \mathbf{s}_{\tau_k}}{\partial \tau_k} \right\}}{\partial \Im \alpha_{k'}} + \frac{\partial \left\{ \alpha_k^* \left(\frac{\partial \mathbf{s}_{\tau_{k'}}}{\partial \tau_k} \right)^{\mathrm{H}} \mathbf{C_r}^{-1} \mathbf{S}\boldsymbol{\alpha} \right\}}{\partial \Im \alpha_{k'}}$$
$$= -j\alpha_k \left(\mathbf{s}_{\tau_{k'}} \right)^{\mathrm{H}} \mathbf{C_r}^{-1} \frac{\partial \mathbf{s}_{\tau_k}}{\partial \tau_k} + j\alpha_k^* \left(\frac{\partial \mathbf{s}_{\tau_k}}{\partial \tau_k} \right)^{\mathrm{H}} \mathbf{C_r}^{-1} \mathbf{s}_{\tau_{k'}}$$
$$= 2\Im \left\{ \alpha_k \left(\mathbf{s}_{\tau_{k'}} \right)^{\mathrm{H}} \mathbf{C_r}^{-1} \frac{\partial \mathbf{s}_{\tau_k}}{\partial \tau_k} \right\}$$

$\mathbf{\Lambda}'_{\mathrm{C}} \in \mathbb{R}^{K \times K}$ contains the second derivatives of the log-likelihood function w.r.t. the real and imaginary part of the complex complex amplitudes of the MPCs.

$$[\mathbf{\Lambda}'_{\mathrm{C}}]_{k,k'} = \mathbb{E}_{\mathbf{r};\boldsymbol{\psi}} \left\{ -\frac{\partial^2 \ln f(\mathbf{r};\boldsymbol{\psi})}{\partial \Re \alpha_k \partial \Re \alpha_{k'}} \right\} = \mathbb{E}_{\mathbf{r};\boldsymbol{\psi}} \left\{ -\frac{\partial^2 \ln f(\mathbf{r};\boldsymbol{\psi})}{\partial \Im \alpha_k \partial \Im \alpha_{k'}} \right\} \tag{A.4}$$
$$= \frac{\partial \left\{ \boldsymbol{\alpha}^{\mathrm{H}} \mathbf{S}^{\mathrm{H}} \mathbf{C_r}^{-1} \mathbf{s}_{\tau_k} \right\}}{\partial \Re \alpha_{k'}} + \frac{\partial \left\{ \left(\mathbf{s}_{\tau_k} \right)^{\mathrm{H}} \mathbf{C_r}^{-1} \mathbf{S}\boldsymbol{\alpha} \right\}}{\partial \Re \alpha_{k'}}$$
$$= \left(\mathbf{s}_{\tau_{k'}} \right)^{\mathrm{H}} \mathbf{C_r}^{-1} \mathbf{s}_{\tau_k} + \left(\mathbf{s}_{\tau_k} \right)^{\mathrm{H}} \mathbf{C_r}^{-1} \mathbf{s}_{\tau_{k'}}$$
$$= 2\Re \left\{ \left(\mathbf{s}_{\tau_{k'}} \right)^{\mathrm{H}} \mathbf{C_r}^{-1} \mathbf{s}_{\tau_k} \right\}$$

$\mathbf{\Lambda}''_{\mathrm{C}} \in \mathbb{R}^{K\times K}$ contains the cross derivatives of the log-likelihood function w.r.t. the real and imaginary part of the complex complex amplitudes of the MPCs.

$$\begin{aligned}[\mathbf{\Lambda}''_{\mathrm{C}}]_{k,j} &= \mathbb{E}_{\mathbf{r};\boldsymbol{\psi}}\left\{-\frac{\partial^2 \ln f(\mathbf{r};\boldsymbol{\psi})}{\partial\Im\alpha_k \partial\Re\alpha_{k'}}\right\} = \mathbb{E}_{\mathbf{r};\boldsymbol{\psi}}\left\{-\frac{\partial^2 \ln f(\mathbf{r};\boldsymbol{\psi})}{\partial\Re\alpha_k \partial\Im\alpha_{k'}}\right\} \\ &= \frac{\partial\Big\{\boldsymbol{\alpha}^{\mathrm{H}}\mathbf{S}^{\mathrm{H}}{\mathbf{C}_{\mathbf{r}}}^{-1}\mathbf{s}_{\tau_k}\Big\}}{\partial\Im\alpha_{k'}} + \frac{\partial\Big\{\left(\mathbf{s}_{\tau_k}\right)^{\mathrm{H}}{\mathbf{C}_{\mathbf{r}}}^{-1}\mathbf{S}\boldsymbol{\alpha}\Big\}}{\partial\Im\alpha_{k'}} \\ &= -j\left(\mathbf{s}_{\tau_{k'}}\right)^{\mathrm{H}}{\mathbf{C}_{\mathbf{r}}}^{-1}\mathbf{s}_{\tau_k} + j\left(\mathbf{s}_{\tau_k}\right)^{\mathrm{H}}{\mathbf{C}_{\mathbf{r}}}^{-1}\mathbf{s}_{\tau_{k'}} \\ &= 2\Im\Big\{\left(\mathbf{s}_{\tau_{k'}}\right)^{\mathrm{H}}{\mathbf{C}_{\mathbf{r}}}^{-1}\mathbf{s}_{\tau_k}\Big\} \end{aligned} \tag{A.5}$$

In the case that the baseband signal $s(t)$ has symmetric spectrum (and for the non-coherent channel model), $\mathbf{\Lambda}''_{\mathrm{C}} = \mathbf{0}$.

A.1.2 Orthogonal MPCs

For a sampled received signal, the covariance matrix of AWGN and the DM is written as

$$\mathbf{C}_{\mathbf{r}} = {\sigma_{\mathrm{n}}}^2\mathbf{I}_N + \mathbf{C}_{\mathbf{c}} = {\sigma_{\mathrm{n}}}^2\mathbf{I}_N + \bar{\mathbf{S}}^{\mathrm{H}}\mathbf{S}_\nu\bar{\mathbf{S}} \tag{A.6}$$

where $\bar{\mathbf{S}} = [\mathbf{s}_0, \cdots, \mathbf{s}_{N-1}]^{\mathrm{T}} \in \mathbb{R}^{N\times N}$ is the *full* signal matrix with $\mathbf{s}_i = \Big[s((-i) \mod NT_{\mathrm{s}}), \ldots, s((N-1-i) \mod NT_{\mathrm{s}})\Big]^{\mathrm{T}}$, defined as a circulant matrix and the diagonal matrix $\mathbf{S}_\nu$ represents the sampled DM PDP $\mathbf{s}_\nu = [S_\nu(0), \ldots, S_\nu(T_{\mathrm{s}}(N-1))]^{\mathrm{T}}$. The covariance matrix of DM is given by

$$[\bar{\mathbf{S}}^{\mathrm{H}}\mathbf{S}_\nu\bar{\mathbf{S}}]_{n,m} = \sum_{i=0}^{N-1} T_{\mathrm{s}}S_\nu(iT_{\mathrm{s}})s((n-i) \mod NT_{\mathrm{s}})s((m-i) \mod NT_{\mathrm{s}}). \tag{A.7}$$

Using the Woodbury matrix identity, the inverse of $\mathbf{C}_{\mathbf{r}}$ can be written as

$${\mathbf{C}_{\mathbf{r}}}^{-1} = \frac{1}{{\sigma_{\mathrm{n}}}^2}\Big[\mathbf{I}_N - \bar{\mathbf{S}}^{\mathrm{H}}\big({\sigma_{\mathrm{n}}}^2\mathbf{S}_\nu^{-1} + \bar{\mathbf{S}}\bar{\mathbf{S}}^{\mathrm{H}}\big)^{-1}\bar{\mathbf{S}}\Big]. \tag{A.8}$$

In (3.5), this inverse is multiplied from the right by $\mathbf{S}\boldsymbol{\alpha}$, which can be re-written as

$${\mathbf{C}_{\mathbf{r}}}^{-1}\mathbf{S}\boldsymbol{\alpha} = \sum_{k=1}^{K}\alpha_k{\mathbf{C}_{\mathbf{r}}}^{-1}\mathbf{s}_{\tau_k} = \frac{1}{{\sigma_{\mathrm{n}}}^2}\sum_{k=1}^{K}\alpha_k\Big[\mathbf{I}_N - \bar{\mathbf{S}}^{\mathrm{H}}\big({\sigma_{\mathrm{n}}}^2\mathbf{S}_\nu^{-1} + \bar{\mathbf{S}}\bar{\mathbf{S}}^{\mathrm{H}}\big)^{-1}\bar{\mathbf{S}}\Big]\mathbf{s}_{\tau_k}$$

where the factor $\bar{\mathbf{S}}\mathbf{s}_{\tau_k}$ on the very right is an autocorrelation vector of the transmitted signal shifted to delay time τ_k. The desired properties of $s(t)$—a large bandwidth and favorable autocorrelation properties—imply that this autocorrelation has most of its energy concentrated at delay τ_k. It hence samples the nonstationary PDP at time τ_k and we can replace $\mathbf{S}_\nu$ for each summand by a stationary PDP $\mathbf{S}_\nu^{(\tau_k)} = T_{\mathrm{s}}S_\nu(\tau_k)\mathbf{I}_N$. Using this assumption, we define

$$\big[{\mathbf{C}_{\mathbf{r}}}^{(\tau_k)}\big]^{-1} = \big[{\sigma_{\mathrm{n}}}^2\mathbf{I}_N + T_{\mathrm{s}}S_\nu(\tau_k)\bar{\mathbf{S}}^{\mathrm{H}}\bar{\mathbf{S}}\big]^{-1} \tag{A.9}$$

which involves the inverse of a cyclic matrix that can be diagonalized by a discrete Fourier transform (DFT). We introduce a unitary DFT matrix $\mathbf{W}$, $\mathbf{W}^{\mathrm{H}}\mathbf{W} = \mathbf{W}\mathbf{W}^{\mathrm{H}} = \mathbf{I}_N$, and use $\bar{\mathbf{S}} = \mathbf{W}\widetilde{\mathbf{S}}\mathbf{W}^{\mathrm{H}}$, where $\widetilde{\mathbf{S}} = \mathrm{diag}\sqrt{N}\mathbf{W}\mathbf{s}_0$ is a diagonal matrix containing the DFT of $\mathbf{s}_0^{\mathrm{T}}$ (the first row of $\bar{\mathbf{S}}$), to obtain

$$\begin{aligned}\left[\mathbf{C_r}^{(\tau_k)}\right]^{-1} &= \left[\mathbf{W}\left({\sigma_\mathrm{n}}^2\mathbf{I}_N + T_\mathrm{s}S_\nu(\tau_k)\widetilde{\mathbf{S}}^{\mathrm{H}}\widetilde{\mathbf{S}}\right)\mathbf{W}^{\mathrm{H}}\right]^{-1} \\ &= \mathbf{W}\left({\sigma_\mathrm{n}}^2\mathbf{I}_N + T_\mathrm{s}S_\nu(\tau_k)\widetilde{\mathbf{S}}^{\mathrm{H}}\widetilde{\mathbf{S}}\right)^{-1}\mathbf{W}^{\mathrm{H}}. \end{aligned} \tag{A.10}$$

With this, we can approximate the second summand of likelihood function (3.5) by

$$\begin{aligned}[\boldsymbol{\alpha}^{\mathrm{H}}\mathbf{S}^{\mathrm{H}}{\mathbf{C_r}}^{-1}\mathbf{S}\boldsymbol{\alpha}]_{k,k'} &\approx \alpha_k\alpha_{k'}^*\mathbf{s}_{\tau_{k'}}^{\mathrm{H}}\left[\mathbf{C_r}^{(\tau_k)}\right]^{-1}\mathbf{s}_{\tau_k} \\ &= \sum_{i=0}^{N-1}\frac{\alpha_k\alpha_{k'}^*|\mathrm{S}_f[i]|^2}{{\sigma_\mathrm{n}}^2 + T_\mathrm{s}S_\nu(\tau_k)|\mathrm{S}_f[i]|^2}\exp\left\{\frac{-j2\pi i(\tau_k-\tau_{k'})}{N}\right\} \end{aligned} \tag{A.11}$$

where $\mathrm{S}_f[i]$ are samples of the DFT of $\mathbf{s}_0$ and the exponential accounts for the delays τ_k and $\tau_{k'}$. Approximating the sum by an integral yields

$$[\boldsymbol{\alpha}^{\mathrm{H}}\mathbf{S}^{\mathrm{H}}{\mathbf{C_r}}^{-1}\mathbf{S}\boldsymbol{\alpha}]_{k,k'} \approx \int_f \frac{\alpha_k^*\alpha_{k'}|\mathrm{S}(f)|^2}{N_0 + S_\nu(\tau_k)|\mathrm{S}(f)|^2}\exp\left\{-j2\pi f(\tau_k-\tau_{k'})\right\}\mathrm{d}f. \tag{A.12}$$

With this expression, the diagonal elements of submatrix $\boldsymbol{\Lambda}_\mathrm{A}$ of the FIM can be written as

$$\begin{aligned}[\boldsymbol{\Lambda}_\mathrm{A}]_{k,k} &= \mathbb{E}_{\mathbf{r};\boldsymbol{\psi}}\left\{-\frac{\partial^2\ln f(\mathbf{r};\boldsymbol{\psi})}{\partial\tau_k\partial\tau_k}\right\} \\ &\approx 8\pi^2|\alpha_k|^2\int_f f^2\frac{|\mathrm{S}(f)|^2}{N_0 + S_\nu(\tau_k)|\mathrm{S}(f)|^2}\mathrm{d}f \\ &= 8\pi^2\mathrm{SINR}_k\int_f f^2|\mathrm{S}(f)|^2\frac{N_0 + T_\mathrm{p}S_\nu(\tau_k)}{N_0 + S_\nu(\tau_k)|\mathrm{S}(f)|^2}\mathrm{d}f \\ &= 8\pi^2\beta^2\mathrm{SINR}_k\gamma_k \end{aligned} \tag{A.13}$$

where $\beta^2 = \int_f f^2|S(f)|^2\mathrm{d}f$ is the mean square bandwidth of $s(t)$, $\mathrm{SINR}_k = |\alpha_k|^2/(N_0+T_\mathrm{p}S_\nu(\tau_k))$ is the SINR of the k-th MPC, and $\gamma_k = \beta_k^2/\beta^2$ is called bandwidth extension factor, expressing the influence of the whitening. The latter relates the mean square bandwidth of the *whitened* pulse $\beta_k^2 = \int_f f^2|\mathrm{S}(f)|^2\frac{N_0+T_\mathrm{p}S_\nu(\tau_k)}{N_0+S_\nu(\tau_k)|\mathrm{S}(f)|^2}\mathrm{d}f$ to β^2. Its value is a function of the INR $T_\mathrm{p}S_\nu(\tau_k)/N_0$. Note that $s(t)$ is assumed to be normalized to unit energy, hence we have $|S(f)|^2 = T_\mathrm{p}$ for $|f| \le 1/(2T_\mathrm{p})$ if $s(t)$ has a block spectrum.

A.1.3 Considering unknown Noise Statistics

Assuming orthogonality of the MPCs, but a non stationary DM PDP that just depends on its onset parameter τ_1, only the FIM block $[\boldsymbol{\Gamma}_A]_{1,1}$ is non zero, resulting in

$$\begin{aligned}[\boldsymbol{\Gamma}_A]_{1,1} &= \mathrm{tr}\left[{\mathbf{C_r}}^{-1}\bar{\mathbf{S}}^{\mathrm{H}}\frac{\partial\mathbf{S}_\nu}{\partial\tau_1}\bar{\mathbf{S}}{\mathbf{C_r}}^{-1}\bar{\mathbf{S}}^{\mathrm{H}}\frac{\partial\mathbf{S}_\nu}{\partial\tau_1}\bar{\mathbf{S}}\right] \\ &= \mathrm{tr}\left[{\mathbf{C_r}}^{-1}\bar{\mathbf{S}}^{\mathrm{H}}\mathrm{diag}\left(\frac{\partial\mathbf{s}_\nu}{\partial\tau_1} + T_\mathrm{s}S_\nu(\tau_1)\boldsymbol{\delta}(\tau_1)\right)\bar{\mathbf{S}}{\mathbf{C_r}}^{-1}\bar{\mathbf{S}}^{\mathrm{H}}\mathrm{diag}\left(\frac{\partial\mathbf{s}_\nu}{\partial\tau_1} + T_\mathrm{s}S_\nu(\tau_1)\boldsymbol{\delta}(\tau_1)\right)\bar{\mathbf{S}}\right], \end{aligned} \tag{A.14}$$

where the derivative of the PDP w.r.t. the delay τ_1 is given as in (A.17) and $\boldsymbol{\delta}(\tau_1)$ represents the derivative of the unit step function $u(\tau-\tau_1)$ in the discrete time domain, so that $\bar{\mathbf{S}}^{\mathrm{H}}\boldsymbol{\delta}(\tau_1)\bar{\mathbf{S}} = \mathbf{s}_{\tau_1}^{\mathrm{H}}\mathbf{s}_{\tau_1}$. Assuming a large signal bandwidth and that the PDP is almost constant after the onset, the PDP can be approximated by a scaled Heaviside function $S_\nu(\tau_1)u(\tau-\tau_1)$, thus $\partial\mathbf{s}_\nu/\partial\tau_1 \approx 0$ and (A.14) can be rewritten as

$$\begin{aligned}
[\mathbf{\Gamma}_A]_{1,1} &\approx \mathrm{tr}\left[{\mathbf{C_r}}^{-1}\mathbf{s}_{\tau_1}^{\mathrm{H}}T_{\mathrm{s}}S_\nu(\tau_1)\mathbf{s}_{\tau_1}{\mathbf{C_r}}^{-1}\mathbf{s}_{\tau_1}^{\mathrm{H}}T_{\mathrm{s}}S_\nu(\tau_1)\mathbf{s}_{\tau_1}\right] \\
&\vdots \qquad \rightarrow \text{Using the invariance property of the trace under cyclic permutations} \\
&= {T_{\mathrm{s}}}^2 S_\nu(\tau_1)^2 \mathrm{tr}\left[\mathbf{s}_{\tau_1}^{\mathrm{H}}\mathbf{s}_{\tau_1}{\mathbf{C_r}}^{-1}\mathbf{s}_{\tau_1}^{\mathrm{H}}\mathbf{s}_{\tau_1}{\mathbf{C_r}}^{-1}\right] \\
&= {T_{\mathrm{s}}}^2 S_\nu(\tau_1)^2 \left\|\mathbf{s}_{\tau_1}\right\|^4 \mathrm{tr}\left[{\mathbf{C_r}}^{-2}\right].
\end{aligned} \tag{A.15}$$

A.1.4 Derivatives of Diffuse Multipath (DM) PDP w.r.t. its Parameters

The double exponential PDP has the following form [58, eq. (9)]

$$S_\nu(\tau) = \frac{\Omega_1(\gamma_1+\gamma_{rise})}{\gamma_1(\gamma_1+\gamma_{rise}(1-\chi))}\left(1-\chi \mathrm{e}^{-\frac{\tau-\tau_1}{\gamma_{rise}}}\right)\mathrm{e}^{-\frac{\tau-\tau_1}{\gamma_1}}u(\tau-\tau_1), \tag{A.16}$$

where $u(\tau)=1$ for $\tau\in[0,\infty[$ defines the Heaviside function.

The derivative w.r.t. the first arrival delay τ_1:

$$\begin{aligned}
\frac{\partial S_\nu(\tau)}{\partial\tau_1} = \frac{\Omega_1(\gamma_1+\gamma_{rise})}{\gamma_1(\gamma_1+\gamma_{rise}(1-\chi))}&\left(\frac{1}{\gamma_1}-\left(\frac{\chi}{\gamma_1}+\frac{\chi}{\gamma_{rise}}\right)\mathrm{e}^{-\frac{\tau-\tau_1}{\gamma_{rise}}}\right) \\
&\times \mathrm{e}^{-\frac{\tau-\tau_1}{\gamma_1}}u(\tau-\tau_1) - S_\nu(\tau)\delta(\tau-\tau_1).
\end{aligned} \tag{A.17}$$

The derivative w.r.t. the normalized DM power Ω_1:

$$\frac{\partial S_\nu(\tau)}{\partial\Omega_1} = \frac{\gamma_1+\gamma_{rise}}{\gamma_1(\gamma_1+\gamma_{rise}(1-\chi))}\left(1-\chi \mathrm{e}^{-\frac{\tau-\tau_1}{\gamma_{rise}}}\right)\mathrm{e}^{-\frac{\tau-\tau_1}{\gamma_1}}u(\tau-\tau_1). \tag{A.18}$$

The derivative w.r.t. the decay time γ_1:

$$\begin{aligned}
\frac{\partial S_\nu(\tau)}{\partial\gamma_1} \approx \frac{\Omega_1}{\gamma_1(\gamma_1+\gamma_{rise}(1-\chi))}&\left(\frac{\gamma_1+\gamma_{rise}}{\gamma_1^2}(\tau-\tau_1)-\left(1+2\frac{\gamma_{rise}}{\gamma_1}\right)\right) \\
&\times\left(1-\chi \mathrm{e}^{-\frac{\tau-\tau_1}{\gamma_{rise}}}\right)\mathrm{e}^{-\frac{\tau-\tau_1}{\gamma_1}}u(\tau-\tau_1).
\end{aligned} \tag{A.19}$$

The derivative w.r.t. the rise time γ_{rise}:

$$\begin{aligned}
\frac{\partial S_\nu(\tau)}{\partial\gamma_{rise}} \approx \frac{\Omega_1}{\gamma_1(\gamma_1+\gamma_{rise}(1-\chi))}&\left(\left(1-\chi \mathrm{e}^{-\frac{\tau-\tau_1}{\gamma_{rise}}}\right)-\frac{\gamma_1+\gamma_{rise}}{\gamma_{rise}^2}\right. \\
&\left.\times(\tau-\tau_1)\mathrm{e}^{-\frac{\tau-\tau_1}{\gamma_{rise}}}\chi\right)\mathrm{e}^{-\frac{\tau-\tau_1}{\gamma_1}}u(\tau-\tau_1).
\end{aligned} \tag{A.20}$$

The derivative w.r.t. first arrival delay power χ:

$$\frac{\partial S_\nu(\tau)}{\partial \chi} \approx \frac{\Omega_1}{\gamma_1(\gamma_1+\gamma_{rise}(1-\chi))}\left(\left(\frac{1}{\gamma_1}+\frac{\gamma_{rise}^2}{\gamma_1^2}\right)\left(1-\chi \mathrm{e}^{-\frac{\tau-\tau_1}{\gamma_{rise}}}\right)- \times(\gamma_1+\gamma_{rise})\,\mathrm{e}^{-\frac{\tau-\tau_1}{\gamma_{rise}}}\right)\mathrm{e}^{-\frac{\tau-\tau_1}{\gamma_1}}u(\tau-\tau_1). \tag{A.21}$$

A.2 Jacobian of VA Position w.r.t. Anchor Position

We want to find a simple expression for the delay gradient $\partial \mathbf{p}_k^{(\xi)}/\partial \mathbf{p}^{(\xi)}$. We restrict our derivation to a single VA of a specific node without loss of generality, so we drop all ξ, k-indexing and use a simpler notation $\partial \mathbf{p}_{\mathrm{VA}}/\partial \mathbf{p}$. As explained in Section 2.1, $\mathbf{p}_{\mathrm{VA}}$ is obtained by mirroring $\mathbf{p}$ on walls Q times where Q is the VA order. We use index q for this iteration and refer to the intermediate positions as $\tilde{\mathbf{p}}_q$ where $\tilde{\mathbf{p}}_0 = \mathbf{p}$ and $\tilde{\mathbf{p}}_Q = \mathbf{p}_{\mathrm{VA}}$. We need to express $\mathbf{p}_{\mathrm{VA}}$ as a function of $\mathbf{p}$ and room geometry. We account for the latter by considering walls with line equations

$$y - y_q = \tan(\zeta_q)(x - x_q) \tag{A.22}$$

where ζ_q is the wall angle and $\mathbf{d}_q = (x_q, y_q)^{\mathrm{T}}$ is an offset vector. We obtain the q-th position by mirroring position $q-1$ on the q-th wall, or more formally

$$\tilde{\mathbf{p}}_q = \mathbf{Mir}(\tilde{\mathbf{p}}_{q-1}, \zeta_q, \mathbf{d}_q)\ . \tag{A.23}$$

where **Mir** is defined as the mirroring operator. Starting at $q = Q$ and using recursive substitution down to $q = 0$, we get

$$\mathbf{p}_{\mathrm{VA}} = \mathbf{Mir}(\ldots\mathbf{Mir}(\mathbf{Mir}(\mathbf{p}, \zeta_1, \mathbf{d}_1), \zeta_2, \mathbf{d}_2)\ldots, \zeta_Q, \mathbf{d}_Q)\ . \tag{A.24}$$

The mirroring operation is given by

$$\begin{aligned}\mathbf{Mir}(\tilde{\mathbf{p}}_{q-1}, \zeta_q, \mathbf{d}_q) &= \mathbf{M}(\zeta_q)(\tilde{\mathbf{p}}_{q-1} - \mathbf{d}_q) + \mathbf{d}_q \\ &= \mathbf{M}(\zeta_q)\tilde{\mathbf{p}}_{q-1} + \big(\mathbf{I} - \mathbf{M}(\zeta_q)\big)\mathbf{d}_q\end{aligned} \tag{A.25}$$

where we use a mirror matrix that acts w.r.t. a line through the origin at angle ζ_q,

$$\mathbf{M}(\zeta_q) = \begin{bmatrix} \cos(2\zeta_q) & \sin(2\zeta_q) \\ \sin(2\zeta_q) & -\cos(2\zeta_q) \end{bmatrix} = \mathbf{Rot}(2\zeta_q)\begin{bmatrix} 1 & 0 \\ 0 & -1 \end{bmatrix} = \mathbf{Rot}(2\zeta_q)\mathbf{F}$$

and can be decomposed into a rotation by $2\zeta_q$, $\mathbf{Rot}(2\zeta_q)$ and a sign-flip $\mathbf{F}$ in the second dimension. $\mathbf{M}(\zeta_q)$ has eigenvalues $\{-1, +1\}$ and bears analogies to rotation. For breaking down (A.24), we prefer the latter form of (A.25) because of the separated $\tilde{\mathbf{p}}_{q-1}$-summand. By carefully repeated application, we obtain a formula

$$\mathbf{p}_{\mathrm{VA}} = \mathbf{M}(\zeta_Q) \cdot \tilde{\mathbf{p}}_{Q-1} + \big(\mathbf{I} - \mathbf{M}(\zeta_Q)\big)\mathbf{d}_Q$$

$$
\begin{aligned}
&= \mathbf{M}(\zeta_Q)\mathbf{M}(\zeta_{Q-1}) \cdot \tilde{\mathbf{p}}_{Q-2} + \\
&\quad \mathbf{M}(\zeta_Q)\big(\mathbf{I} - \mathbf{M}(\zeta_{Q-1})\big)\mathbf{d}_{Q-1} + \big(\mathbf{I} - \mathbf{M}(\zeta_Q)\big)\mathbf{d}_Q \\
&= \ \ldots \ = \left(\prod_{q=0}^{Q-1} \mathbf{M}(\zeta_{Q-q}) \right)\mathbf{p} \ + \sum_{q=1}^{Q} \left(\prod_{\tilde{q}=1}^{Q-q} \mathbf{M}(\zeta_{Q+1-\tilde{q}}) \right) \left(\mathbf{I} - \mathbf{M}(\zeta_q)\right) \mathbf{d}_q
\end{aligned} \tag{A.26}
$$

where the derivative w.r.t. $\mathbf{p}$ is just the leading product of mirror matrices. Transposition reverses multiplication order

$$
\left(\frac{\partial \mathbf{p}_{\mathrm{VA}}}{\partial \mathbf{p}} \right)^{\mathrm{T}} = \prod_{q=1}^{Q} \mathbf{M}(\zeta_q) \ . \tag{A.27}
$$

To resolve this product, we derive a pseudo-homomorphism property of the mirror matrix. We note that both $\mathbf{F}$ and $\mathbf{M}(\zeta)$ are symmetric, orthogonal, and self-inverse. Thus, $\mathbf{M}(\zeta) = \mathbf{Rot}(2\zeta)\mathbf{F}$ implies $\mathbf{M}(\zeta)\mathbf{F} = \mathbf{Rot}(2\zeta)$. We rearrange the product of two mirror matrices

$$
\begin{aligned}
\mathbf{M}(\zeta_a)\mathbf{M}(\zeta_b) &= \mathbf{M}(\zeta_a)\mathbf{M}(\zeta_b)^{\mathrm{T}} = \mathbf{Rot}(2\zeta_a)\mathbf{F}\mathbf{F}^{\mathrm{T}}\mathbf{Rot}(2\zeta_b)^{\mathrm{T}} \\
&= \mathbf{Rot}(2\zeta_a)\mathbf{I}\ \mathbf{Rot}(-2\zeta_b) = \mathbf{Rot}(2(\zeta_a - \zeta_b))
\end{aligned}
$$

and obtain the property

$$
\mathbf{M}(\zeta_a)\mathbf{M}(\zeta_b) = \mathbf{M}(\zeta_a - \zeta_b)\mathbf{F} \ . \tag{A.28}
$$

Applying (A.28) to (A.27) $(Q-1)$-times the Jacobian of a VA position w.r.t. its respective anchor's position yields

$$
\left(\frac{\partial \mathbf{p}_{\mathrm{VA}}}{\partial \mathbf{p}} \right)^{\mathrm{T}} = \mathbf{M}(\bar{\zeta})\mathbf{F}^{Q-1} = \mathbf{Rot}(2\bar{\zeta})\mathbf{F}^{Q} \tag{A.29}
$$

where we refer to $\bar{\zeta} := \zeta_1 - \zeta_2 + \ldots + (-1)^{Q-1}\zeta_Q = \sum_{q=1}^{Q}(-1)^{q-1}\zeta_q$ as the effective wall angle, where index q iterates the order of occurrence of walls during MPC reflection or VA construction.

A.3 Delay Gradient for the Monostatic Setup

We transform the initial gradient from Appendix A.2 into a magnitude-times-unit-vector form by component-wise application of basic trigonometric identities. This yields an insightful expression for the monostatic case, cf. (3.31). We consider

$$
\begin{aligned}
\mathbf{e}(\phi) - \mathbf{e}((-1)^Q\phi + 2\bar{\zeta}) &= \begin{bmatrix} \cos(\phi) - \cos((-1)^Q\phi + 2\bar{\zeta}) \\ \sin(\phi) - \sin((-1)^Q\phi + 2\bar{\zeta}) \end{bmatrix} \\
&= \begin{bmatrix} 2\sin\left(\frac{\left((-1)^Q+1\right)\phi+2\bar{\zeta}}{2}\right)\sin\left(\frac{\left((-1)^Q-1\right)\phi+2\bar{\zeta}}{2}\right) \\ 2\cos\left(\frac{\left((-1)^Q+1\right)\phi+2\bar{\zeta}}{2}\right)\sin\left(-\frac{\left((-1)^Q-1\right)\phi+2\bar{\zeta}}{2}\right) \end{bmatrix}.
\end{aligned}
$$

By defining symbols for the arguments that contain ϕ depending on the even/odd parity of Q

$$O := \frac{(-1)^Q - 1}{2}\phi + \bar{\zeta} = \begin{cases} \bar{\zeta} & \text{If } Q \text{ is even} \\ \bar{\zeta} - \phi & \text{If } Q \text{ is odd} \end{cases}$$
$$E := \frac{(-1)^Q + 1}{2}\phi + \bar{\zeta} = \begin{cases} \bar{\zeta} + \phi & \text{If } Q \text{ is even} \\ \bar{\zeta} & \text{If } Q \text{ is odd} \end{cases}$$

we further get

$$\begin{aligned} &\mathbf{e}(\phi) - \mathbf{e}((-1)^Q\phi + 2\bar{\zeta}) = 2\sin(O) \begin{bmatrix} \sin(E) \\ -\cos(E) \end{bmatrix} \\ &= 2\sin(O)\ \mathbf{e}\Big(E - \frac{\pi}{2}\Big) = \begin{cases} 2\sin(\bar{\zeta})\mathbf{e}(\phi + \bar{\zeta} - \frac{\pi}{2}) & \text{If } Q \text{ is even} \\ 2\sin(\bar{\zeta} - \phi)\mathbf{e}(\bar{\zeta} - \frac{\pi}{2}) & \text{If } Q \text{ is odd} \end{cases} . \end{aligned} \tag{A.30}$$

A.4 Derivation of the Multipath-NSync CRLB

Synchronized anchors: In order to derive the 3×3 EFIM $\boldsymbol{\mathcal{I}}_{\mathbf{p},\epsilon}$ we need to repartition the transformation matrix $\mathbf{J}$ by combining the submatrices $\mathbf{H}^{(j)}$ and $\mathbf{L}^{(j)} = \mathbf{l}_{\text{syn}}^{(j)}$ to $\mathbf{G}^{(j)} = [\mathbf{H}^{(j)}, \mathbf{l}_{\text{syn}}^{(j)}]$. Applying the transformation leads to

$$\boldsymbol{\mathcal{I}}_{\mathbf{P}} = \mathbf{J}^{\mathrm{T}}\boldsymbol{\mathcal{I}}_{\boldsymbol{\psi}}\mathbf{J} = \begin{bmatrix} \sum\limits_{j\in\mathcal{N}_j} \big(\mathbf{G}^{(j)}\big)^{\mathrm{T}}\boldsymbol{\Lambda}_{\mathrm{A}}^{(j)}\mathbf{G}^{(j)} & \big(\mathbf{G}^{(1)}\big)^{\mathrm{T}}\boldsymbol{\Lambda}_{\mathrm{B}}^{(1)} & \cdots & \big(\mathbf{G}^{(J)}\big)^{\mathrm{T}}\boldsymbol{\Lambda}_{\mathrm{B}}^{(J)} \\ \big(\boldsymbol{\Lambda}_{\mathrm{B}}^{(1)}\big)^{\mathrm{T}}\mathbf{G}^{(1)} & \boldsymbol{\Lambda}_{\mathrm{C}}^{(1)} & & \\ \vdots & & \ddots & \\ \big(\boldsymbol{\Lambda}_{\mathrm{B}}^{(J)}\big)^{\mathrm{T}}\mathbf{G}^{(J)} & & & \boldsymbol{\Lambda}_{\mathrm{C}}^{(J)} \end{bmatrix}. \tag{A.31}$$

The 3×3 EFIM is then given as the sum over the EFIMs of the corresponding anchors

$$\boldsymbol{\mathcal{I}}_{\mathbf{p},\epsilon} = \sum_{j\in\mathcal{N}_j} \big(\mathbf{G}^{(j)}\big)^{\mathrm{T}}\Big[\boldsymbol{\Lambda}_{\mathrm{A}}^{(j)} - \boldsymbol{\Lambda}_{\mathrm{B}}^{(j)}\big(\boldsymbol{\Lambda}_{\mathrm{C}}^{(j)}\big)^{-1}\big(\boldsymbol{\Lambda}_{\mathrm{B}}^{(j)}\big)^{\mathrm{T}}\Big]\mathbf{G}^{(j)}. \tag{A.32}$$

When neglecting path overlap, this reduces to

$$\boldsymbol{\mathcal{I}}_{\mathbf{p},\epsilon} = \sum_{j\in\mathcal{N}_j} \big(\mathbf{G}^{(j)}\big)^{\mathrm{T}}\boldsymbol{\Lambda}_{\mathrm{A}}^{(j)}\mathbf{G}^{(j)}, \tag{A.33}$$

which leads finally to (3.40).

Asynchronous anchors: The result for $\boldsymbol{\mathcal{I}}_{\boldsymbol{\theta}}$ (A.31) is also valid when considering asynchronous anchors, provided that we respect $\mathbf{L}^{(j)} = \mathbf{L}_{\text{asyn}}^{(j)}$ and $\mathbf{G}^{(j)} = [\mathbf{H}^{(j)}, \mathbf{L}_{\text{asyn}}^{(j)}]$. We apply the blockwise inversion lemma twice, first to derive the EFIM $\boldsymbol{\mathcal{I}}_{\mathbf{p},\boldsymbol{\epsilon}}$ (note that now $\boldsymbol{\epsilon}$ is a vector), and then again to proof the additivity of the EFIMs $\boldsymbol{\mathcal{I}}_{\mathbf{p}}^{(j)}$. The EFIM $\boldsymbol{\mathcal{I}}_{\mathbf{p},\boldsymbol{\epsilon}}$ is now a square matrix of order $2 + J$. It can be expressed as in (A.32), but taking account of the changed definition of $\mathbf{G}^{(j)}$.

We can write its structure as

$$\boldsymbol{\mathcal{I}}_{\mathbf{p},\boldsymbol{\epsilon}} = \sum_{j\in\mathcal{N}_j} \begin{bmatrix} \boldsymbol{\mathcal{I}}_A^{(j)} & \boldsymbol{\mathcal{I}}_B^{(j)} \\ \left(\boldsymbol{\mathcal{I}}_B^{(j)}\right)^{\mathrm{T}} & \boldsymbol{\mathcal{I}}_D^{(j)} \end{bmatrix}, \tag{A.34}$$

with $\boldsymbol{\mathcal{I}}_A^{(j)} \in \mathbb{R}^{2\times 2}$, $\boldsymbol{\mathcal{I}}_B^{(j)} \in \mathbb{R}^{2\times J}$ and $\boldsymbol{\mathcal{I}}_D^{(j)} \in \mathbb{R}^{J\times J}$. Further evaluation yields, that only the j-th column of $\boldsymbol{\mathcal{I}}_B^{(j)}$ is nonzero, and the sum over $\boldsymbol{\mathcal{I}}_B^{(j)}$ can be written as

$$\sum_{j\in\mathcal{N}_j} \boldsymbol{\mathcal{I}}_B^{(j)} = \left[\mathbf{b}^{(1)}, \ldots, \mathbf{b}^{(J)}\right],\ \mathbf{b}^{(j)} \in \mathbb{R}^2, \tag{A.35}$$

meaning that each column is determined by the contribution of a different anchors.Similarly, $\boldsymbol{\mathcal{I}}_D^{(j)}$ has only one nonzero entry $\left[\boldsymbol{\mathcal{I}}_D^{(j)}\right]_{j,j}$, leading to

$$\sum_{j\in\mathcal{N}_j} \boldsymbol{\mathcal{I}}_D^{(j)} = \operatorname{diag}\left(\left[\boldsymbol{\mathcal{I}}_D^{(1)}\right]_{1,1}, \ldots, \left[\boldsymbol{\mathcal{I}}_D^{(J)}\right]_{J,J}\right). \tag{A.36}$$

Rewriting $\boldsymbol{\mathcal{I}}_{\mathbf{p},\boldsymbol{\epsilon}}$ (A.34) and again applying the blockwise inversion lemma yields the additivity of the EFIMs $\boldsymbol{\mathcal{I}}_{\mathbf{p}}^{(j)}$:

$$\boldsymbol{\mathcal{I}}_{\mathbf{p}} = \sum_{j\in\mathcal{N}_j} \boldsymbol{\mathcal{I}}_A^{(j)} - \frac{1}{\left[\boldsymbol{\mathcal{I}}_D^{(j)}\right]_{j,j}} \mathbf{b}^{(j)} \left(\mathbf{b}^{(j)}\right)^{\mathrm{T}} = \sum_{j\in\mathcal{N}_j} \boldsymbol{\mathcal{I}}_{\mathbf{p}}^{(j)}. \tag{A.37}$$

The involved terms are defined by

$$\boldsymbol{\mathcal{I}}_A^{(j)} = \left(\mathbf{H}^{(j)}\right)^{\mathrm{T}} \left(\boldsymbol{\Lambda}_{\mathrm{A}}^{(j)} - \boldsymbol{\Lambda}_{\mathrm{B}}^{(j)} \left(\boldsymbol{\Lambda}_{\mathrm{C}}^{(j)}\right)^{-1} \left(\boldsymbol{\Lambda}_{\mathrm{B}}^{(j)}\right)^{\mathrm{T}}\right) \mathbf{H}^{(j)},$$

$$\left[\boldsymbol{\mathcal{I}}_D^{(j)}\right]_{j,j} = \sum_{u=1}^{K^{(j)}} \sum_{v=1}^{K^{(j)}} \left[\boldsymbol{\Lambda}_{\mathrm{A}}^{(j)} - \boldsymbol{\Lambda}_{\mathrm{B}}^{(j)} \left(\boldsymbol{\Lambda}_{\mathrm{C}}^{(j)}\right)^{-1} \left(\boldsymbol{\Lambda}_{\mathrm{B}}^{(j)}\right)^{\mathrm{T}}\right]_{u,v},$$

and

$$\mathbf{b}^{(j)} = \left(\mathbf{H}^{(j)}\right)^{\mathrm{T}} \left(\boldsymbol{\Lambda}_{\mathrm{A}}^{(j)} - \boldsymbol{\Lambda}_{\mathrm{B}}^{(j)} \left(\boldsymbol{\Lambda}_{\mathrm{C}}^{(j)}\right)^{-1} \left(\boldsymbol{\Lambda}_{\mathrm{B}}^{(j)}\right)^{\mathrm{T}}\right) [1 \ldots 1]_{1\times K^{(J)}}^{\mathrm{T}}.$$

A.5 Derivation of the Multipath-Coop CRLB

The EFIM for the cooperative setup is defined as

$$\boldsymbol{\mathcal{I}}_{\mathbf{P}} = \mathbf{H}^{\mathrm{T}} \operatorname{diag}\left(\boldsymbol{\Lambda}^{(1,1)}, \ldots, \boldsymbol{\Lambda}^{(1,M)}, \ldots, \boldsymbol{\Lambda}^{(M+J,M)}\right) \mathbf{H},$$

being of size $2M \times 2M$. It can be written with subblock $\mathbf{H}$ from (3.50) in the canonical form (3.48). Matrix $\boldsymbol{\Lambda}^{(j,m)}$ is defined in (3.49). The canonical form decomposes the EFIM $\boldsymbol{\mathcal{I}}_{\mathbf{P}}$ into contributions from independent transmissions inbetween the agents or between agents and fixed

anchors. Matrix $\boldsymbol{\mathcal{I}}_{\mathbf{P}}$ consists of the following subblocks for $\eta, \eta' \in \mathcal{N}_m = \{1, \ldots, M\}$,

$$[\boldsymbol{\mathcal{I}}_{\mathbf{P}}]_{2\times 2}^{\eta,\eta'} = \sum_{j\in(\mathcal{N}_m \cup \mathcal{N}_j)} \sum_{m\in\mathcal{N}_m} \big(\mathbf{H}^{(j,\eta,m)}\big)^{\mathrm{T}} \boldsymbol{\Lambda}^{(j,m)} \mathbf{H}^{(j,\eta',m)} \tag{A.38}$$

where $\mathbf{H}^{(j,\eta,m)}$ stacks the spatial delay gradients (3.28) as defined in Section 3.4. Considering that only summand (j, m) of (A.38) contributes to a block, for which either index j or index m equals η or η', we get the following subblocks:

Off-diagonal blocks: $\eta \neq \eta'$

$$\begin{aligned}
[\boldsymbol{\mathcal{I}}_{\mathbf{P}}]_{2\times 2}^{(\eta,\eta')} &= \big(\mathbf{H}^{(j,\eta,m)}\big)^{\mathrm{T}} \boldsymbol{\Lambda}^{(j,m)} \mathbf{H}^{(j,\eta',m)}\Big|_{j=\eta,m=\eta'} + \big(\mathbf{H}^{(j,\eta,m)}\big)^{\mathrm{T}} \boldsymbol{\Lambda}^{(j,m)} \mathbf{H}^{(j,\eta',m)}\Big|_{j=\eta',m=\eta} \\
&= \big(\mathbf{H}_{\mathrm{An}}^{(\eta,\eta')}\big)^{\mathrm{T}} \boldsymbol{\Lambda}^{(\eta,\eta')} \mathbf{H}_{\mathrm{Ag}}^{(\eta',\eta)} + \big(\mathbf{H}_{\mathrm{Ag}}^{(\eta',\eta)}\big)^{\mathrm{T}} \boldsymbol{\Lambda}^{(\eta',\eta)} \mathbf{H}_{\mathrm{An}}^{(\eta',\eta)},
\end{aligned}$$

using the definitions for $\mathbf{H}_{\mathrm{An}}^{(\eta,\eta')}$ and $\mathbf{H}_{\mathrm{Ag}}^{(\eta,\eta')}$ from Section 3.4.1. With $\mathbf{H}_{\mathrm{An}}^{(\eta,\eta')} = \mathbf{H}_{\mathrm{Ag}}^{(\eta',\eta)}$ (Section 3.4.1) and $\boldsymbol{\Lambda}^{(\eta,\eta')} = \boldsymbol{\Lambda}^{(\eta',\eta)}$ we get

$$[\boldsymbol{\mathcal{I}}_{\mathbf{P}}]_{2\times 2}^{(\eta,\eta')} = 2\boldsymbol{\mathcal{I}}_{\mathrm{C}}^{(\eta,\eta')} = 2\big(\mathbf{H}_{\mathrm{Ag}}^{(\eta',\eta)}\big)^{\mathrm{T}} \boldsymbol{\Lambda}^{(\eta',\eta)} \mathbf{H}_{\mathrm{Ag}}^{(\eta,\eta')}. \tag{A.39}$$

Diagonal blocks: $\eta = \eta'$

$$\begin{aligned}
[\boldsymbol{\mathcal{I}}_{\mathbf{P}}]_{2\times 2}^{\eta,\eta} &= \big(\mathbf{H}^{(\eta,\eta,\eta)}\big)^{\mathrm{T}} \boldsymbol{\Lambda}^{(\eta,\eta)} \mathbf{H}^{(\eta,\eta,\eta)} + \sum_{\substack{j\in\mathcal{N}_m\setminus\{\eta\} \\ m=\eta}} \big(\mathbf{H}^{(j,\eta,m)}\big)^{\mathrm{T}} \boldsymbol{\Lambda}^{(j,m)} \mathbf{H}^{(j,\eta,m)} \\
&\quad + \sum_{\substack{m\in\mathcal{N}_m\setminus\{\eta\} \\ j=\eta}} \big(\mathbf{H}^{(j,\eta,m)}\big)^{\mathrm{T}} \boldsymbol{\Lambda}^{(j,m)} \mathbf{H}^{(j,\eta,m)} + \sum_{j\in\mathcal{N}_j} \Big(\mathbf{H}^{(j,\eta,\eta)}\Big)^{\mathrm{T}} \boldsymbol{\Lambda}^{(j,\eta)} \mathbf{H}^{(j,\eta,\eta)} \\
&= \big(\mathbf{H}_{\mathrm{Mo}}^{(\eta)}\big)^{\mathrm{T}} \boldsymbol{\Lambda}^{(\eta,\eta)} \mathbf{H}_{\mathrm{Mo}}^{(\eta)} + \sum_{j\in\mathcal{N}_m\setminus\{\eta\}} \big(\mathbf{H}_{\mathrm{Ag}}^{(j,\eta)}\big)^{\mathrm{T}} \boldsymbol{\Lambda}^{(j,\eta)} \mathbf{H}_{\mathrm{Ag}}^{(j,\eta)} \\
&\quad + \sum_{m\in\mathcal{N}_m\setminus\{\eta\}} \big(\mathbf{H}_{\mathrm{An}}^{(\eta,m)}\big)^{\mathrm{T}} \boldsymbol{\Lambda}^{(\eta,m)} \mathbf{H}_{\mathrm{An}}^{(\eta,m)} \sum_{j\in\mathcal{N}_j} \big(\mathbf{H}_{\mathrm{Ag}}^{(j,\eta)}\big)^{\mathrm{T}} \boldsymbol{\Lambda}^{(j,\eta)} \mathbf{H}_{\mathrm{Ag}}^{(j,\eta)}
\end{aligned}$$

using again $\mathbf{H}_{\mathrm{An}}^{(\eta,\eta')}$ and $\mathbf{H}_{\mathrm{Ag}}^{(\eta,\eta')}$ from Section 3.4.1 and $\mathbf{H}_{\mathrm{Mo}}^{(\eta)}$ from Section 3.4.2. With $\mathbf{H}_{\mathrm{An}}^{(\eta,m)} = \mathbf{H}_{\mathrm{Ag}}^{(m,\eta)}$ and $\boldsymbol{\Lambda}^{(j,m)} = \boldsymbol{\Lambda}^{(m,j)}$ due to reciprocity, we get

$$[\boldsymbol{\mathcal{I}}_{\mathbf{P}}]_{2\times 2}^{(\eta,\eta)} = \boldsymbol{\mathcal{I}}_{\mathrm{Mo}}^{(\eta)} + 2\sum_{m\in\mathcal{N}_m\setminus\{\eta\}} \boldsymbol{\mathcal{I}}_{\mathrm{Ag}}^{(m,\eta)} + \sum_{j\in\mathcal{N}_j} \boldsymbol{\mathcal{I}}_{\mathrm{An}}^{(j,\eta)} = \boldsymbol{\mathcal{I}}_{\mathrm{Mo}}^{(\eta)} + 2\boldsymbol{\mathcal{I}}_{\mathrm{Ag}}^{(\eta)} + \boldsymbol{\mathcal{I}}_{\mathrm{An}}^{(\eta)} \tag{A.40}$$

which implicitly defines the contributions from monostatic measurements, bistatic measurements inbetween agents, and bistatic measurements between agents and fixed anchors.

B

Simulation Results Multipath-Coop

B.1 Problem Formulation

We assume M agents at positions $\mathbf{p}_1^{(m)}$ with $m \in \mathcal{N}_m = \{1, 2, \ldots, M\}$, which cooperate with one another. As outlined in the introduction, every agent conducts a monostatic measurement, meaning it emits a pulse and receives the multipath signal reflected by the environment, and conventional bistatic measurements with all other agents and the fixed anchors. All bistatic and monostatic measurements are distributed such that every agent is able to exploit information from any of its received and/or transmitted signals.

Fig. 2.1 illustrates the geometric model for multipath-assisted positioning. A signal exchanged between an agent at position $\mathbf{p}_1^{(m')}$ and an agent at $\mathbf{p}_1^{(m)}$ contains specular reflections at the room walls, indicated by the black lines.[30] These reflections can be modeled geometrically using VAs $\mathbf{p}_k^{(m')}$, mirror images of the anchor w.r.t. walls that can be computed from the floor plan [1,31]. We call this the *bistatic* setup, where the fixed anchors and the floor plan constitute the available infrastructure. In a *cooperative* setup, agents localize themselves using bistatic measurements inbetween them. Here, the node at $\mathbf{p}_k^{(m')}$ is an agent that plays the role of an anchor (and thus provides a set of VAs) for the agent at $\mathbf{p}_1^{(m)}$. If the agents are equipped accordingly, they can use *monostatic* measurements, indicated by the gray lines. Here, the node at $\mathbf{p}_k^{(m')}$ acts as anchor for itself with its own set of VAs.

B.2 State Space and Measurement Model

The state dynamics are characterized by a linear, constant-velocity motion model. Each agent $\mathbf{x}_n^{(m)}$ is discribed by its position $\mathbf{p}_{1,n}^{(m)}$ and velocity $\mathbf{v}_{1,n}^{(m)}$ according to $\mathbf{x}_n^{(m)} = [(\mathbf{p}_{1,n}{}^{(m)})^{\mathrm{T}}, (\mathbf{v}_{1,n}{}^{(m)})^{\mathrm{T}}]^{\mathrm{T}}$.

[30] Since the radio channel is reciprocal, the assignment of transmitter and receiver roles to anchors and agents is arbitrary and this choice can be made according to higher-level considerations.

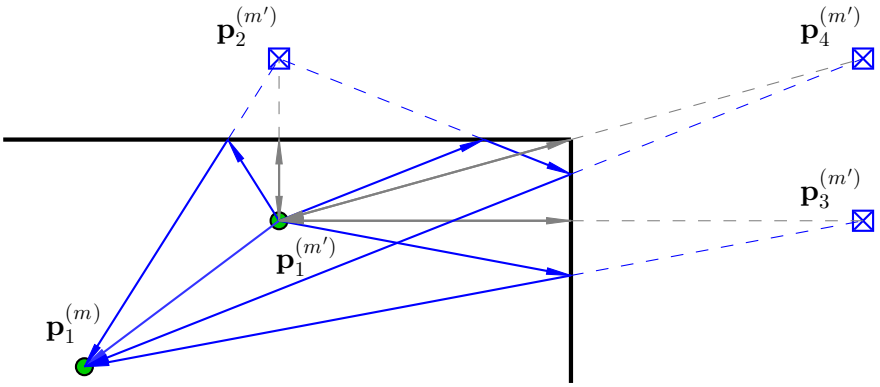

Figure B.1: Illustration of multipath geometry using VAs for (i) bistatic transmissions (blue) between an agent at $\mathbf{p}_1^{(m')}$ and an agent at $\mathbf{p}_1^{(m)}$ and for (ii) a monostatic measurement (gray) by an agent at $\mathbf{p}_1^{(m')}$.

The position of the agent is mirrored at a each wall segment in order to obtain the positions of the corresponding VAs $\mathbf{p}_{k,n}^{(m)}$. The orientation of the wall segments determine the relation between the movement gradients of the agent and the corresponding VAs. We describe this relation by introducing a VA transition matrix $\mathbf{P}_k^{(m)}$ [O7]. The state space model for agent m is characterized by

$$\tilde{\mathbf{x}}_n^{(m)} = \underbrace{\begin{bmatrix} \mathbf{F} & & \mathbf{0}_{4\times 2K_n} \\ \mathbf{0}_{2K_n\times 2} & \mathbf{P}^{(m)} & \mathbf{I}_{2K_n\times 2K_n} \end{bmatrix}}_{\tilde{\mathbf{F}}^{(m)}} \tilde{\mathbf{x}}_{n-1}^{(m)} + \underbrace{\begin{bmatrix} \mathbf{G} \\ \mathbf{0}_{2K_n\times 2} \end{bmatrix}}_{\tilde{\mathbf{G}}^{(m)}} \mathbf{n}_{\mathrm{a},n}, \tag{B.1}$$

with

$$\mathbf{F} = \begin{bmatrix} 1 & 0 & \Delta T & 0 \\ 0 & 1 & 0 & \Delta T \\ 0 & 0 & 1 & 0 \\ 0 & 0 & 0 & 1 \end{bmatrix} \quad \mathbf{G} = \begin{bmatrix} \frac{\Delta T^2}{2} & 0 \\ 0 & \frac{\Delta T^2}{2} \\ \Delta T & 0 \\ 0 & \Delta T \end{bmatrix}$$

and $\tilde{\mathbf{x}}_n^{(m)} = [\mathbf{x}^{\mathrm{T}(m)}{}_n, \mathbf{p}^{\mathrm{T}(m)}{}_{2,n}, \ldots \mathbf{p}^{\mathrm{T}(m)}{}_{K,n}]^{\mathrm{T}}$ and $\mathbf{P}^{(m)} = [\mathbf{P}^{\mathrm{T}(m)}{}_2, \ldots, \mathbf{P}^{\mathrm{T}(m)}{}_{K_n}]^{\mathrm{T}}$ with dimensions $(2K_n \times 2)$. Under the assumption of independent movement of the agents, the motion model finally results in

$$\underbrace{\begin{bmatrix} \tilde{\mathbf{x}}_n^{(1)} \\ \vdots \\ \tilde{\mathbf{x}}_n^{(M)} \end{bmatrix}}_{\hat{\mathbf{x}}_n} = \begin{bmatrix} \tilde{\mathbf{F}}^{(1)} & & \mathbf{0} \\ & \ddots & \\ \mathbf{0} & & \tilde{\mathbf{F}}^{(M)} \end{bmatrix} \underbrace{\begin{bmatrix} \tilde{\mathbf{x}}_{n-1}^{(1)} \\ \vdots \\ \tilde{\mathbf{x}}_{n-1}^{(M)} \end{bmatrix}}_{\tilde{\mathbf{x}}_{n-1}} + \begin{bmatrix} \tilde{\mathbf{G}}_n^{(1)} \\ \\ \tilde{\mathbf{G}}_n^{(M)} \end{bmatrix} \mathbf{n}_{\mathrm{a},n}. \tag{B.2}$$

The according linearized measurement model is defined as

$$\begin{bmatrix} \tilde{\mathbf{z}}_n^{(1)} \\ \vdots \\ \tilde{\mathbf{z}}_n^{(M)} \end{bmatrix} = \begin{bmatrix} \tilde{\mathbf{H}}_n^{(1)} & & \mathbf{0} \\ & \ddots & \\ \mathbf{0} & & \tilde{\mathbf{H}}_n^{(M)} \end{bmatrix} \begin{bmatrix} \tilde{\mathbf{x}}_n^{(1)} \\ \vdots \\ \tilde{\mathbf{x}}_n^{(M)} \end{bmatrix} + \tilde{\mathbf{n}}_{z,n}. \tag{B.3}$$

where $\tilde{\mathbf{z}}_n^{(m)}$ stacks the monostatic measurements from the m-th agent and the bistatic measurements to all other agents. The stack vector $\tilde{\mathbf{n}}_{z,n}$ contains the according measurement noise with covariance matrix $\mathbf{R}_n$ described in Section 5.1.3 in (5.16). The linearized column-wise stacked measurement matrices $\tilde{\mathbf{H}}_n^{(m)} = [(\tilde{\mathbf{H}}_n^{(\eta=1,m)})^{\mathrm{T}}, \ldots, (\tilde{\mathbf{H}}_n^{(\eta=M,m)})^{\mathrm{T}}]^{\mathrm{T}}$ described in (B.4), with $m, \eta \in \mathcal{N}_m$ and $m \neq \eta$. The matrix $\mathbf{H}_{\xi,\mu,n}^{(\eta,\eta,m)} = [\frac{\partial d(\mathbf{p}_{\mu,n}^{(\eta)}, \mathbf{p}_{1,n}^{(m)})}{\partial x_{\xi,n}^{(\eta)}}, \frac{\partial d(\mathbf{p}_{\mu,n}^{(\eta)}, \mathbf{p}_{1,n}^{(m)})}{\partial y_{\xi,n}^{(\eta)}}]$ defines the derivatives of the measurement equation w.r.t. the x- and y-position coordinates. The upper-left sub-block of (B.4) holds the derivatives of the monostatic measurement equations w.r.t. the m-th agent position and upper diagonal sub-block the according derivatives w.r.t. to the monostatic VA positions of the m-th agent. The lower-left sub-block holds derivatives of the bistatic measurement equations to all other agent positions and according VA positions ($\eta = 1 \ldots M$ and $m \neq \eta$) w.r.t. the m-th agent position. The lower-right diagonal sub-block holds the equivalent derivatives w.r.t. to the according bistatic VA positions.

$$\tilde{\mathbf{H}}_n^{(\eta,m)} = \begin{bmatrix} \mathbf{H}_{1,2,n}^{(m,m,m)} & 0 & 0 & \mathbf{H}_{2,2,n}^{(m,m,m)} & \ldots & \mathbf{0} & \ldots & \mathbf{0} & \ldots & \mathbf{0} \\ \vdots & \vdots & \vdots & \vdots & \vdots & \vdots & \vdots & \vdots & \vdots & \vdots \\ \mathbf{H}_{1,K_n,n}^{(m,m,m)} & 0 & 0 & \mathbf{0} & \ldots & \mathbf{H}_{K_n,K_n,n}^{(m,m,m)} & \ldots & \mathbf{0} & \ldots & \mathbf{0} \\ \mathbf{H}_{1,1,n}^{(\eta,m,m)} & 0 & 0 & \mathbf{0} & \ldots & \mathbf{0} & \ldots & \mathbf{H}_{1,1,n}^{(\eta,\eta,m)} & \ldots & \mathbf{0} \\ \vdots & \vdots & \vdots & \vdots & \vdots & \vdots & \vdots & \vdots & \vdots & \vdots \\ \mathbf{H}_{1,K_n,n}^{(\eta,m,m)} & 0 & 0 & \mathbf{0} & \ldots & \mathbf{0} & \ldots & \mathbf{0} & \ldots & \mathbf{H}_{K_n,K_n,n}^{(\eta,\eta,m)} \end{bmatrix} \tag{B.4}$$

B.3 Results

We evaluate the performance of the proposed algorithm in terms of localization error and computational time using synthetic data in a two-dimensional space. The transmit signal consists of a raised-cosine pulse with a roll-off factor of $R = 0.6$, a pulse duration of $T_{\mathrm{p}} = 0.5\,\mathrm{ns}$ and unit energy. The received signals of the *monostatic* and *bistatic* measurements are modeled according to (2.1). Each reflection attenuates the pulse by 3 dB. The free-space loss is modeled according to Friis' transmission equation. The parameters of the DM are set according to [O7] and the power of the additive white noise is set to $N_0 = 2 \cdot 10^{-16}\,\mathrm{W/Hz}$. In order to achieve a fair comparison to the proposed method in [O3] we choose the same parameter setup and simulation scenario (c.f. Figure B.2). Three agents move independently along trajectories under partly non-line-of-sight conditions where we assume a given start position. Figure B.2 shows an example of the estimated agent positions $\hat{\mathbf{p}}_{1,n}$, $\hat{\mathbf{p}}_{2,n}$ and $\hat{\mathbf{p}}_{3,n}$ using the proposed EKF-based algorithm are indicated for every 5-th position. At each time step n the agents run *monostatic* and *bistatic* measurements to the neighboring agents. The utilized likelihood function of [O3, eq. (8)] simplifies the proposed system model (Sec. III in [O3]). We accounted for this by

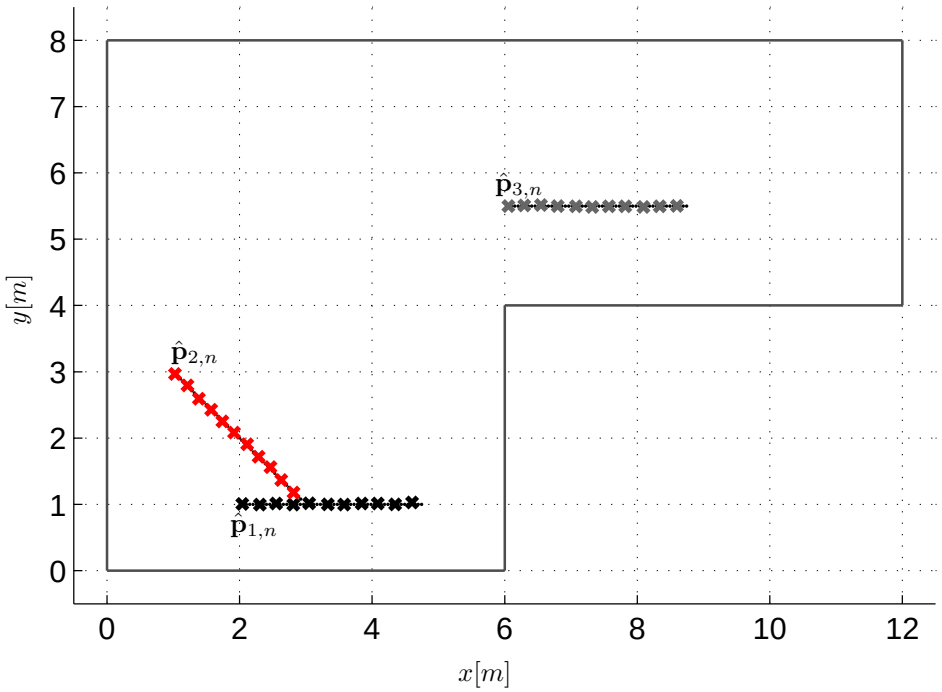

Figure B.2: Simulation scenario as in Froehle2013 with three agents moving along different trajectories. Further, an example of the estimated agent positions $\hat{\mathbf{p}}_{1,n}$, $\hat{\mathbf{p}}_{2,n}$ and $\hat{\mathbf{p}}_{3,n}$ using the proposed EKF-based algorithm are indicated for every 5-th position.

changing the likelihood function to (7) of [O3]. Further, [O3] undermines the uncertainty of the neighboring beliefs by reducing the size of the neighboring particles to the mean value (see Sec. V-B of [O3]). We omit this simplification.

The maximum number of extracted MPCs is limited to $K_n^{(.,.)} = 12, \forall n$ (see 2.2.1). The initial position of each VA $\mathbf{p}_{k,n}^{(m)}$ as well as the corresponding VA transition matrix $\mathbf{P}_k^{(m)}$ are calculated in advance. Figure B.3 illustrates the cumulative distribution function (CDF) of the localization error of the proposed algorithm (CoMINT EKF) compared to [O3] of ten trajectory realizations—each evaluated with 50 Monte Carlo runs. The comparison reveals the strong influence on performance of localization error and computational demand [O3] regarding its implementation scheme of message passing (i.e. particle or parametric message representation and scheduling). Choosing a sample-based message representation the localization error reduces with increasing number of particles on the cost of computational complexity. Denoting N as the number of particles representing the message passing scheme, [O3] faces a complexity of $\mathcal{O}(MN^2)$. The proposed method has a complexity of $\mathcal{O}(M^2K_n^3)$ determined by the data association stage [111]. Since the number of particles N is much higher compared to the number of extracted MPC $K_n^{(.,.)}$ the proposed method outperforms [O3] in terms of computational complexity. We proof this claim by comparison of the average computational time for localization scaled to the proposed method. Depending on the number of particles the average computational time of the proposed method speeds up by a factor of approximately 217, 756 and 2355 for 100, 250 and 500 particles, respectively.

The gain in terms of computational time is established by the assumption of Gaussian distance errors. Figure B.3 indicates the influence of this assumption by comparison to [O3] with different number of particles of 100, 250 and 500. The proposed method reaches a performance

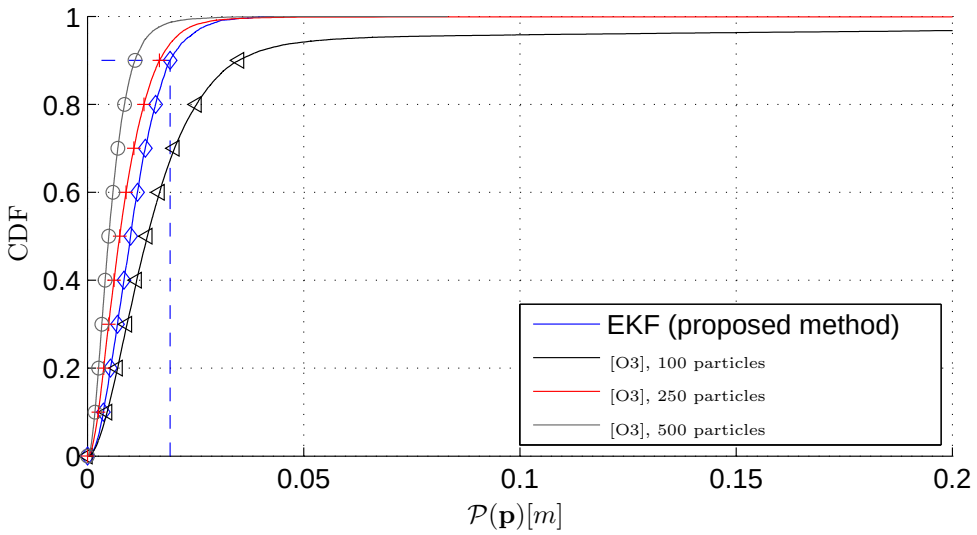

Figure B.3: Cumulative distribution function of the localization error of the proposed algorithm (CoMINT EKF) (blue) compared to [O3] with a different size of 500 (gray), 250 (red) and 100 (black) particles of each agent.

comparable to [O3] with a number of particles from $100 - 250$ where $90\,\%$ of the errors are located within $2\,\mathrm{cm}$.

C

Insights in Method of Moments Estimator of the SINRs

The estimated complex amplitudes are computed using (2.5) resulting in $\hat{\alpha}_k = \alpha_k e^{j\psi_k} + x_k$, where $x_k \propto C\mathcal{N}\left(0, 2\sigma^2\right)$ denotes contributions from DM and AWGN with variance σ^2. Correcting the estimated complex amplitude by the phase ψ_k denoting $\hat{\alpha}_k e^{-j\psi_k}$, so that the real and imaginary parts are Gaussian RV defined as $X_1 \propto \mathcal{N}\left(\Re\alpha_k, \sigma^2\right)$ and $X_2 \propto \mathcal{N}\left(\Im\alpha_k, \sigma^2\right)$, respectively. Hence, $|\hat{\alpha}_k|^2$ is described by a noncentral chi-squared distribution with two degrees of freedom. In general, the mean and the variance of a RV $X = X_1^2 + X_2^2$, where X_1 and X_2 are Gaussian, are defined as [128]

$$\mu_1 = \mathbb{E}\{X\} = r^2 + 2\sigma^2 \tag{C.1}$$

$$\mu_2 = \mathbb{E}\left\{(X-\mu)^2\right\} = 4\sigma^4 + 2\sigma^2 r^2, \tag{C.2}$$

where $r = \mathbb{E}\{X_1\}^2 + \mathbb{E}\{X_2\}^2 = |\alpha_k|^2$. The resulting method of moment estimator is defined as [45]

$$\mathrm{SINR}_{k,\mathrm{moments}} = \left(\frac{\hat{\mu}_{1,k}}{\left(\hat{\mu}_{1,k}^2 - \hat{\mu}_{2,k}\right)^{1/2}} - 1 \right)^{-1}, \tag{C.3}$$

where $\hat{\mu}_{1,k} = \mathbb{E}\left\{|\hat{\alpha}_k|^2\right\}$ is the mean and $\hat{\mu}_{2,k} = \mathbb{E}\left\{\left||\hat{\alpha}_k|^2 - \hat{\mu}_{1,k}\right|^2\right\}$ is the variance of the squared absolute value of the estimated MPC amplitudes. Using the projection onto the received signal (2.5), the mean is

$$\begin{aligned} \hat{\mu}_{1,k} &= \mathbb{E}\left\{|\hat{\alpha}_k|^2\right\} \\ &= |\alpha_k|^2 \|\mathbf{s}_{\tau_k}\|^2 + \mathbf{s}_{\tau_k}^{\mathrm{H}} \bar{\mathbf{S}}^{\mathrm{H}} \mathbf{S}_\nu \bar{\mathbf{S}} \mathbf{s}_{\tau_k} + N_0 \|\mathbf{s}_{\tau_k}\|^2 \end{aligned} \tag{C.4}$$

and the variance is

$$\begin{aligned}\hat{\mu}_{2,k} &= \mathbb{E}\left\{\left|\left|\hat{\alpha}_k\right|^2 - \hat{\mu}_{1,k}\right|^2\right\} \\ &= \left(\mathbf{s}_{\tau_k}^{\mathrm{H}}\bar{\mathbf{S}}^{\mathrm{H}}\mathbf{S}_\nu\bar{\mathbf{S}}\mathbf{s}_{\tau_k}\right)^2 + 2\mathbf{s}_{\tau_k}^{\mathrm{H}}\bar{\mathbf{S}}^{\mathrm{H}}\mathbf{S}_\nu\bar{\mathbf{S}}\mathbf{s}_{\tau_k}N_0\|\mathbf{s}_{\tau_k}\|^2 \\ &\quad + N_0^2\|\mathbf{s}_{\tau_k}\|^4 + 2|\alpha_k|^2\|\mathbf{s}_{\tau_k}\|^2\left(\mathbf{s}_{\tau_k}^{\mathrm{H}}\bar{\mathbf{S}}^{\mathrm{H}}\mathbf{S}_\nu\bar{\mathbf{S}}\mathbf{s}_{\tau_k} + N_0\|\mathbf{s}_{\tau_k}\|^2\right).\end{aligned} \tag{C.5}$$

With this, (C.3) can be rewritten as

$$\begin{aligned}\mathrm{SINR}_{k,\mathrm{moments}} &= \frac{|\alpha_k|^2\|\mathbf{s}_{\tau_k}\|^2}{\mathbf{s}_{\tau_k}^{\mathrm{H}}\left(N_0 + \bar{\mathbf{S}}^{\mathrm{H}}\mathbf{S}_\nu\bar{\mathbf{S}}\right)\mathbf{s}_{\tau_k}} \\ &= \frac{|\alpha_k|^2}{N_0 + T_{\mathrm{s}}\mathbf{s}_{\tau_k}^{\mathrm{H}}\bar{\mathbf{S}}^{\mathrm{H}}\mathbf{S}_\nu\bar{\mathbf{S}}\mathbf{s}_{\tau_k}},\end{aligned} \tag{C.6}$$

where $\|\mathbf{s}_{\tau_k}\|^2 = 1/T_{\mathrm{s}}$. This result shows that the method of moments estimator computes the ratio between the energy of the deterministic MPCs $|\alpha_k|^2$ to the noise power density of AWGN N_0 and of DM $\bar{\mathbf{S}}^{\mathrm{H}}\mathbf{S}_\nu\bar{\mathbf{S}}$ projected onto the transmit pulse shifted to the MPC delays τ_k.

D

Cognitive Reinforcement Learning Algorithms

The algorithms in the Tables 1 and 2 can be found in [79] and are put into this appendix of the thesis just for the sake of completeness, so that the interested reader can take a look onto them without searching for the literature.

Variables:
$\mathcal{A}$:= set of all actions
J := value-to-go function
γ := discount factor $0 < \gamma \leq 1$
α := learning rate, $\alpha > 0$
Inputs:
$\mathcal{R}(a)$:= expected reward of action a ;
π_n := learning policy ;
for *all cognitive actions* $a \in \mathcal{A}$ **do**
$\quad J_n(a) \leftarrow J_n(a) + \alpha \left[\mathcal{R}(a) + \gamma \sum_{a'} \pi_n(a, a') J_n(a') - J_n(a)\right]$;
end

Algorithm 1: Algorithm for updating value-to-go function

Variables:

$\mathcal{A}$:= set of all actions

$\mathcal{M}$:= subset of actions for planning

J := value-to-go function

γ := discount factor $0 < \gamma \leq 1$

π_n := learning policy

a_n selected action

r_n computed reward

h_{learnmem} := entropy memory for learning

h_{planmem} := entropy memory for planning

l_{future} := future horizon

Initialization:

$a_0 \leftarrow$ random action ;

$h_{\text{learnmem}} \leftarrow h(\mathbf{x}_0)$;

Act on environment with a_0 ;

for *all times instances* n **do**

  $h(\mathbf{x}_n, a_n) \leftarrow$ input from perceptor $\widetilde{\mathbf{C}}_n(a_n)$;

  Learning:

  $r_n \leftarrow g_n(h_{\text{learnmem}} - h(\mathbf{x}_n, a_n))$;

  Update value-to-go: $J_n(a_n) \leftarrow (1-\alpha)J_n(a_n) + \alpha r_n$;

  $h_{\text{learnmem}} \leftarrow h(\mathbf{x}_n, a_n)$;

  Planning:

  Sample from π_n or uniform distribution to get $\mathcal{M} \subseteq \mathcal{A}$;

  for *all cognitive actions* $a \in \mathcal{M}$ **do**

    for $i = 1$ *to* l_{future} **do**

      $h_{\text{planmem}} \leftarrow h(\mathbf{x}_{n+i-1}, a)$;

      Use Bayesian filter to compute the predicted and the prediced measurement covariance matrix $\widetilde{\mathbf{C}}_{n+i}(a)$;

      $h(\mathbf{x}_{n+i}, a) \leftarrow$ input from perceptor $\widetilde{\mathbf{C}}_{n+i}(a)$;

      $r_n \leftarrow g_n(h_{\text{planmem}} - h(\mathbf{x}_{n+i}, a))$;

      Update value-to-go function:

      $J_n(a) \leftarrow J_n(a) + \alpha\left[\mathcal{R}(a) + \gamma \sum_{a'} \pi_n(a, a') J_n(a') - J_n(a)\right]$;

    end

  end

  $J_{n+1} \leftarrow J_n(a)$;

  Update π_n using J_{n+1} according to ϵ-greedy strategy: π_{n+1} ;

  Select action a_{n+1} based on π_{n+1} ;

  Act on environment with a_{n+1} ;

end

Algorithm 2: Entire algorithm for cognitive reinforcement learning

Part II

Included Papers

Cognitive Radar for the Localization of RFID Transponders in Dense Multipath Environments

Klaus Witrisal*, Erik Leitinger*, Paul Meissner*, and Daniel Arnitz†
*Graz University of Technology, Inffeldgasse 16c, A-8010 Graz, Austria, email: Witrisal@tugraz.at
†Duke University, Durham, NC, USA

***Abstract*—High-accuracy localization remains a much desired but elusive feature for passive radio transponders as used in radio-frequency identification (RFID). We believe that the principle of cognitive radar can overcome the fundamental physical limitations hindering its implementation. We propose to jointly employ a narrowband radio to interrogate the transponders and an adaptive (ultra) wideband backscatter radio for the target tracking and for actuating, sensing, and learning the radio environment. This paper explores system model and key processing steps of such a cognitive secondary radar. At its core is a perception-action cycle, which consists of transmitter and receiver-side environment models for representing radio channel conditions and Bayesian trackers for the target states. Multipath is exploited to improve the robustness and to make optimum use of the radar's sensing capabilities. Feedback information is derived from the Cramér-Rao lower bound on the position error. Initial results are presented as a basic proof of principle.**

***Index Terms*—Ultra-wideband, Cramér-Rao lower bound, localization, multipath-assisted indoor positioning, channel modeling**

I. Introduction

Recent seminal work by S. Haykin and co-workers described Cognitive Radar (CR) as a "step toward bridging the gap between neuroscience and engineering" [1]. The information processing in the visual brain, which has been extensively studied in neuroscience, gives valuable insight in the unparalleled capability of the brain of filtering out clutter and focusing attention on activity. In their earlier paper [2], a bat has been discussed as an example showing the efficiency of cognitive processing in nature, in a setting that closely resembles a multistatic radar. The bat adapts its emitted ultrasound pulses, e.g. while approaching its bait. In doing so, it acts on the environment in an adaptive fashion, its sonar comprises a closed perception-action cycle (PAC). *Memory* and *attention* are considered to be key facilitators of *"intelligence"*, both of which can be mapped to signal processing functionalities of a CR [1]–[3].

A cognitive tracking and identification system is described in this paper that allows high-definition localization of large numbers of passive radio transponders[1] (enhanced RFID tags) in indoor environments at decimeter accuracy. We assume that most tagged objects are static over significant time spans. The radar then learns an accurate model of the scenario including radio channel properties, based on which it assigns bandwidth and processing resources for real-time tracking of objects that are being moved. The proposed system aims at (pseudo) real-time tracking of up to hundreds objects per cubic meter as seen in warehouse or sales floor applications.

In this paper, we focus on the PAC having a central role in a CR. Dense multipath propagation is the dominating characteristics of the propagation environment that has to be taken into account [4]. Adaptive illumination of the environment can exploit known *deterministic* multipath components (MPCs) through a TX-side environment model that is learned at runtime. Time reversal (TR) processing [5], [6] is proposed, which is expected to be beneficial to overcome the degenerate pinhole channel of a backscatter radio system [7]. At the receiver side, deterministic MPCs can aid the target localization problem and overcome non-line-of-sight (NLOS) situations [8]. An RX-side environment model that is also learned at runtime provides the required channel information. This rigorous way of exploiting multipath is the key difference to the related work found in [9].

The paper is organized as follows. The system model is introduced in Section II, including channel model and position error bound. In Section III, the PAC is introduced, highlighting TX adaptation, RX signal processing, and feedback. Sections IV and V elaborate on the implementation of memory and attention. Experimental results are discussed in Section VI.

II. System Model and Position Error Bound

A. System concept and channel model

A network of transmitting and receiving radar nodes may be used in a final deployment of the proposed tracking system. However, for simplicity, we consider in this paper a single transmitting node only at position $\mathbf{a}_{\mathrm{TX}}$ and a single receiving node at $\mathbf{a}_{\mathrm{RX}}$. A large number of passive targets is present in the environment at locations $\{\mathbf{p}_\ell\}$, each of which can identify itself by modulating its radar cross section (RCS)[2].

All RF signals propagate in a multipath environment. We write the radio channel between radar node $m \in \{\mathrm{TX}, \mathrm{RX}\}$

This work was partly supported by the Austrian Science Fund (FWF) within the National Research Network SISE project S10610.

[1] "Passive" means that no battery is available for powering the transponder.

[2] In [10], a hybrid UHF and UWB interrogation system has been discussed for RFID. The UHF system is used for powering up and addressing individual RFID tags. While responding by UHF backscatter signaling, the tag will modulate its UWB-RCS simultaneously and synchronously. This known signature is used to separate the returns of RFID tags from one another and from clutter. The challenges of the UHF layer of this system are beyond the scope of this paper. However, it is noted that the UHF system can benefit from (channel) information gathered by the CR.

and target ℓ using a hybrid, deterministic-stochastic channel impulse response model

$$h_{\ell,m}(\tau,\mathbf{p}_\ell) = \sum_{k=1}^{K_m(\mathbf{p}_\ell)} \alpha_{k,m}^{(\ell)}\delta(\tau-\tau_{k,m}(\mathbf{p}_\ell)) + \nu_{\ell,m}(\tau) \quad (1)$$

where the sum accounts for a set of $K_m(\mathbf{p}_\ell)$ deterministic MPCs at delays $\{\tau_{k,m}(\mathbf{p}_\ell)\}$ and path amplitudes $\{\alpha_{k,m}^{(\ell)}\}$, while $\nu_{\ell,m}(\tau)$ represents diffuse multipath.

We assume a deterministic model for the delays related to the geometry of multipath components. For example, reflections (of arbitrary order) at plane surfaces can be attributed to virtual transceivers at fixed locations $\mathbf{a}_{k,m}$ that result from reflecting the physical transceiver in those planes. This yields $\tau_{k,m}(\mathbf{p}_\ell) = \frac{1}{c}\|\mathbf{a}_{k,m}-\mathbf{p}_\ell\|$, where c is denoted as propagation velocity.

The path amplitudes are factorized into a deterministic part $\gamma_{k,m}(\mathbf{p})|_{\mathbf{p}=\mathbf{p}_\ell}$ and a random component $\beta_{k,m}^{(\ell)}$. The former accounts for the path loss, deterministic phase shift, and visibility of some MPC and is equal for all targets if at location $\mathbf{p}$. The latter accounts for the differences between individual transponders and for model mismatches.

The backscatter channel is composed of down and uplink channels as in (1), connected by the differential RCS $T_\ell(f)$ (cf. [11]) that represents the RCS difference between the binary modulation states. It will differ for individual transponders due to de-tuning, tag orientation (polarization), and production variations. We assume that these variations can be approximated by the random variables $\{\beta_{k,m}^{(\ell)}\}$ of the channel model, akin to the concept of random antenna modeling in [12]. Any errors to this model are accounted for in $\nu_{\ell,m}(\tau)$.

B. Position Error Bound

The achievable precision of multilateration systems is quantified by the position error bound (PEB), the Cramér-Rao lower bound (CRLB) of the estimated position vector $\hat{\mathbf{p}}$. We define the PEB as $\sqrt{\mathrm{tr}\{\mathbf{J}_\mathbf{p}^{-1}\}}$, where $\mathbf{J}_\mathbf{p}$ is the equivalent Fisher information matrix (EFIM) for the position vector $\mathbf{p}$ [13]. Following [8], [13], the EFIM can be given as

$$\mathbf{J}_\mathbf{p} = \frac{8\pi^2\beta^2}{c^2}\sum_{k=1}^{K}\mathrm{SINR}_k\mathbf{J}_\mathbf{r}(\phi_k) \quad (2)$$

where β^2 is the effective (mean square) signal bandwidth,

$$\mathrm{SINR}_k := \frac{|\alpha_k|^2}{N_0 + T_\mathrm{s}S_\nu(\tau_k)} \quad (3)$$

is the signal-to-interference-plus-noise ratio (SINR) of the k-th deterministic signal component arriving at delay τ_k and angle ϕ_k, and $\mathbf{J}_\mathbf{r}(\phi_k)$ is the so-called ranging direction matrix (cf. [13]), a rank-one matrix with an eigenvector in direction of ϕ_k. "Interference" has been modeled as a Gaussian random process representing diffuse multipath [8]. Its effective power is $T_\mathrm{s}S_\nu(\tau_k)$, the product of an effective pulse duration T_s and the power delay profile $S_\nu(\tau_k)$ for the diffuse multipath at delay τ_k. This result holds for a scenario, where an active source is being localized. For backscatter channels, the PEB has a similar form, but the transceiver configuration now resembles a MIMO radar as in [14]. Furthermore, the model of the diffuse multipath has to account for the convolution of the diffuse and deterministic parts of the down and uplink channels. Initial result for this backscatter-channel PEB are presented in Section VI-B.

Equation (2) illustrates that each deterministic signal component contributes information to the localization problem[3], given that its source's geometry is known. This knowledge will be provided by the RX-side environment model of the CR. Equation (2) also indicates—through the SINR_k—*how much* information each signal component adds, which is needed for proper weighting of measurements. These weights can also be learned by the CR. Firm insight is thus provided how to employ the CR for efficiently and robustly estimating the target locations. Evaluating (2), it has been found in [8], [15] that bandwidths of at least 1 GHz are needed to achieve satisfying positioning performance in dense indoor channels.

III. Perception-Action Cycle

The PAC at the core of the CR consists of three main building blocks (cf. [1]), the Bayesian tracking filter for representing the target states, the system model library for receiver optimization, and the transmit waveform library for transmitter control. However, in contrast to [1], we propose to employ multiple Bayesian state-space trackers for representing environment and target states. The TX-side and RX-side environment models represent global information that is *common* to all targets, while the target state-space models represent *individual* information including the target positions.

A. Transmitter adaptation

Time-reversal transmitter beam forming is a well-known strategy for coping with clutter in MIMO radar systems (see e.g. [16]) but it has also been discussed for UWB (e.g. [5], [6]). Some intuitive arguments can be given, why TR processing can be a good choice for this CR, while a proof of optimality is out of scope of this paper. Most importantly, focusing the transmit power onto the target optimizes the link budget. The transmit waveform for TR processing reveals the information required at the TX[4]. It is written as

$$s_\ell(t;\boldsymbol{\theta}_\mathrm{TX}(\hat{\mathbf{p}}_\ell),\hat{\mathbf{x}}_\ell) = \sum_{k=1}^{\hat{K}_\mathrm{TX}}\left(\gamma_{k,\mathrm{TX}}(\hat{\mathbf{p}}_\ell)\hat{\beta}_{k,\mathrm{TX}}^{(\ell)}\right)^* p\big(t+\tau_{k,\mathrm{TX}}(\hat{\mathbf{p}}_\ell)\big) \quad (4)$$

where $\boldsymbol{\theta}_\mathrm{TX}(\hat{\mathbf{p}}_\ell)$ is the TX-side environment model that deterministically depends on the target position, while $\hat{\mathbf{x}}_\ell$ represents the current target state including the position estimate $\hat{\mathbf{p}}_\ell$. $\boldsymbol{\theta}_\mathrm{TX}(\hat{\mathbf{p}}_\ell)$ comprises the number of modeled deterministic

[3] References [8], [13] indicate that (2) holds only if path overlap is avoided. In other words, the deterministic components need to be orthogonal. For the time being, we assume this requirement to hold.

[4] The time index designating consecutive iterations of the PAC is skipped in these equations for notational simplicity. It is re-introduced in Section IV.

MPCs $\hat{K}_{\mathrm{TX}}$ and their parameters such as delay and amplitude. To achieve a deterministic relation to $\hat{\mathbf{p}}_\ell$, we propose to compute these parameters from the (estimated) positions of virtual transmitters at locations $\hat{\mathbf{a}}_{k,\mathrm{TX}}$, e.g. $\tau_{k,\mathrm{TX}}(\hat{\mathbf{p}}_\ell) = \frac{1}{c}\|\hat{\mathbf{a}}_{k,\mathrm{TX}} - \hat{\mathbf{p}}_\ell\|$ and $\gamma_{k,\mathrm{TX}}(\hat{\mathbf{p}}_\ell) = \hat{A}_{k,\mathrm{TX}} \exp\big(j2\pi\tau_{k,\mathrm{TX}}(\hat{\mathbf{p}}_\ell) f_c\big)$, where $\hat{A}_{k,\mathrm{TX}}$ is an estimated MPC gain and f_c is the carrier frequency[5]. A deterministic channel model can never be accurate enough to achieve perfect TR for each (target) location $\mathbf{p}_\ell$. To account for mismatches, we incorporate in the state vector $\hat{\mathbf{x}}_\ell$ the previously introduced gain correction factors $\hat{\beta}^{(\ell)}_{k,\mathrm{TX}}$ for each MPC. Finally, $p(t+\tau_{k,\mathrm{TX}}(\hat{\mathbf{p}}_\ell))$ in (4) are transmit pulses shifted to a-causal TX times (for simplicity of notation).

The transmitter-side environment model $\boldsymbol{\theta}_{\mathrm{TX}}(\mathbf{p})$ will be learned considering the *joint feedback* from the receiver for an *ensemble of targets*, as explained in Section IV.

B. Measurement Model

The received signal, when interrogating tag ℓ, is obtained from convolution of (4) by the up and down-link channels (1) for $m = \mathrm{TX}, \mathrm{RX}$ and the addition of WGN $w(t)$,

$$\begin{aligned}
z_\ell(t) =& s_\ell(t; \boldsymbol{\theta}_{\mathrm{TX}}(\hat{\mathbf{p}}_\ell), \hat{\mathbf{x}}_\ell) * h_{\ell,\mathrm{TX}}(t, \mathbf{p}_\ell) * h_{\ell,\mathrm{RX}}(t, \mathbf{p}_\ell) + w(t) \\
=& \Big[\sum_{k=1}^{\hat{K}_{\mathrm{TX}}} \gamma^*_{k,\mathrm{TX}}(\hat{\mathbf{p}}_\ell)\gamma_{k,\mathrm{TX}}(\mathbf{p}_\ell)\big(\hat{\beta}^{(\ell)}_{k,\mathrm{TX}}\big)^* \beta^{(\ell)}_{k,\mathrm{TX}} \\
& \times p\big(t + \tfrac{1}{c}\|\hat{\mathbf{a}}_{k,\mathrm{TX}} - \hat{\mathbf{p}}_\ell\| - \tfrac{1}{c}\|\mathbf{a}_{k,\mathrm{TX}} - \mathbf{p}_\ell\|\big) \\
& + \sum_{k=1}^{\hat{K}_{\mathrm{TX}}} \sum_{k'=1, k'\neq k}^{K_{\mathrm{TX}}(\mathbf{p}_\ell)} \gamma^*_{k,\mathrm{TX}}(\hat{\mathbf{p}}_\ell)\gamma_{k',\mathrm{TX}}(\mathbf{p}_\ell)\big(\hat{\beta}^{(\ell)}_{k,\mathrm{TX}}\big)^* \beta^{(\ell)}_{k',\mathrm{TX}} \\
& \times p\big(t + \tfrac{1}{c}\|\hat{\mathbf{a}}_{k,\mathrm{TX}} - \hat{\mathbf{p}}_\ell\| - \tfrac{1}{c}\|\mathbf{a}_{k',\mathrm{TX}} - \mathbf{p}_\ell\|\big) \\
& + s_\ell(t; \boldsymbol{\theta}_{\mathrm{TX}}(\hat{\mathbf{p}}_\ell), \hat{\mathbf{x}}_\ell) * \nu_{\ell,\mathrm{TX}}(t) \Big] * h_{\ell,\mathrm{RX}}(t, \mathbf{p}_\ell) + w(t) \\
\approx& \Big[\sum_{k=1}^{\hat{K}_{\mathrm{TX}}} \big|\gamma_{k,\mathrm{TX}}(\mathbf{p}_\ell)\beta^{(\ell)}_{k,\mathrm{TX}}\big|^2 \Big] p(t) * h_{\ell,\mathrm{RX}}(t, \mathbf{p}_\ell) \\
& + w(t; \boldsymbol{\theta}_{\mathrm{TX}}(\hat{\mathbf{p}}_\ell), \hat{\mathbf{x}}_\ell). \qquad (5)
\end{aligned}$$

The final approximation (5) assumes accurate environment models and target state estimates, i.e. we have $\hat{\mathbf{p}}_\ell \approx \mathbf{p}_\ell$ and $\hat{\mathbf{a}}_{k,\mathrm{TX}} \approx \mathbf{a}_{k,\mathrm{TX}}$ and $\gamma_{k,\mathrm{TX}}(\hat{\mathbf{p}}_\ell)\hat{\beta}^{(\ell)}_{k,\mathrm{TX}} \approx \gamma_{k,\mathrm{TX}}(\mathbf{p}_\ell)\beta^{(\ell)}_{k,\mathrm{TX}}$, $\forall k$, such that the deterministic MPCs add up coherently at the target. It comprises an additive noise component $w(t; \boldsymbol{\theta}_{\mathrm{TX}}(\hat{\mathbf{p}}_\ell), \hat{\mathbf{x}}_\ell)$ which depends on the TX waveform parameters $\boldsymbol{\theta}_{\mathrm{TX}}(\hat{\mathbf{p}}_\ell)$ and $\hat{\mathbf{x}}_\ell$. By this dependence, the transmitter controls the accuracy of the state estimation in the RX, an essential property of a CR [1].[6]

C. Receiver processing

Assuming the approximation (5) to hold, we can exploit the insight obtained in Section II-B to design the receiver-side signal processing. The measurement log-likelihood function is approximated as the inner product of the received signal and a hypothesized channel response (cf. [8, (14)]),

$$\begin{aligned}
&\ln \mathrm{p}(z_\ell(t)|\boldsymbol{\psi}_{\mathrm{RX}}(\mathbf{p}), \hat{\mathbf{x}}_\ell) \\
&\quad \approx \frac{2}{N_0}\Big\langle z_\ell(t), \sum_{k=1}^{\hat{K}_{\mathrm{RX}}} \hat{w}^2_k(\mathbf{p})\hat{\alpha}^{(\ell)}_{k,\mathrm{RX}} p(t - \hat{\tau}_{k,\mathrm{RX}}(\mathbf{p}))\Big\rangle \\
&\qquad - \frac{E_p}{N_0}\sum_{k=1}^{\hat{K}_{\mathrm{RX}}} \hat{w}^2_k(\mathbf{p})|\hat{\alpha}^{(\ell)}_{k,\mathrm{RX}}|^2 \qquad (6)
\end{aligned}$$

where E_p is the energy of pulse $p(t)$. The hypothesis is parametrized by the vector $\boldsymbol{\psi}_{\mathrm{RX}}(\mathbf{p})$, whose entries comprise the RX-side environment model. In particular, we again relate the path delays to virtual receivers at fixed positions, obtaining $\hat{\tau}_{k,\mathrm{RX}}(\mathbf{p}) = \frac{1}{c}\|\hat{\mathbf{a}}_{k,\mathrm{RX}} - \mathbf{p}\|$. These virtual receiver locations will be estimated by analyzing the *combined measurements* of an ensemble of targets, see Section IV. The environment model also provides the weights $\hat{w}^2_k(\mathbf{p})$, which quantify the power of diffuse multipath interfering with the k-th deterministic component (cf. Section II-B and [8]). The path gains $\{\hat{\alpha}^{(\ell)}_{k,\mathrm{RX}}\}$ are nuisance parameters to the location estimation.[7]

In case the environment models and/or the target state estimates are not *exact*, the following extended likelihood function can be employed

$$\begin{aligned}
&\ln \mathrm{p}(z_\ell(t)|\boldsymbol{\psi}_{\mathrm{RX}}(\mathbf{p}), \boldsymbol{\theta}_{\mathrm{TX}}(\mathbf{p}), \hat{\mathbf{x}}_\ell) \\
&\quad \approx \frac{2}{N_0}\Big\langle z_\ell(t), \sum_{k=1}^{\hat{K}_{\mathrm{TX}}}\sum_{i=1}^{\hat{K}_{\mathrm{RX}}} \hat{w}^2_i(\mathbf{p})\hat{\alpha}^{(\ell)}_{k,\mathrm{TX}}\hat{\alpha}^{(\ell)}_{i,\mathrm{RX}} \\
&\qquad s_\ell(t - \hat{\tau}_{k,\mathrm{RX}}(\mathbf{p}) - \hat{\tau}_{i,\mathrm{TX}}(\mathbf{p}); \boldsymbol{\theta}_{\mathrm{TX}}(\hat{\mathbf{p}}_\ell), \hat{\mathbf{x}}_\ell)\Big\rangle \\
&\quad - \frac{1}{N_0}\int \Big| \sum_{k=1}^{\hat{K}_{\mathrm{TX}}}\sum_{i=1}^{\hat{K}_{\mathrm{RX}}} \hat{w}_i(\mathbf{p})\hat{\alpha}^{(\ell)}_{k,\mathrm{TX}}\hat{\alpha}^{(\ell)}_{i,\mathrm{RX}} \\
&\qquad s_\ell(t - \hat{\tau}_{k,\mathrm{RX}}(\mathbf{p}) - \hat{\tau}_{i,\mathrm{TX}}(\mathbf{p}); \boldsymbol{\theta}_{\mathrm{TX}}(\hat{\mathbf{p}}_\ell), \hat{\mathbf{x}}_\ell)\Big|^2 \mathrm{d}t. \qquad (7)
\end{aligned}$$

Hence, a mismatch between the *real* and estimated target position $\hat{\mathbf{p}}_\ell$, which results in choosing the wrong TR processing parameter $\boldsymbol{\theta}_{\mathrm{TX}}(\hat{\mathbf{p}}_\ell)$ for the transmitter adaptation, can be accounted for. Otherwise, the likelihood function would have a systematic error, which means that its maximum were not on the target's real position.

D. Feedback information

The (posterior) CRLB is a suitable measure for feedback information within the PAC [1]. Suitable approximations of this quantity are subject of ongoing research. However, the

[5] Note that a path-loss model is not included in this example.

[6] It is noted that the noise component $w(t; \boldsymbol{\theta}_{\mathrm{TX}}(\hat{\mathbf{p}}_\ell), \hat{\mathbf{x}}_\ell)$ also represents the cross-terms $k \neq k'$ from the intermediate convolution result.

[7] In noncoherent processing, the path gains are estimated individually from the measurements. Coherent processing assumes knowledge of the complex-valued path gains. It has been shown in [14] that in this case the target localization error will depend on the carrier frequency of the radio signal rather than the bandwidth. This finding promises huge potential for a CR-based passive tag tracking system, because it suggests that, after an initial learning phase, the environment may be monitored very efficiently using narrowband signals instead of UWB signals. Therefore, bandwidth and carrier frequency should be incorporated in the PAC of the proposed CR, but this has been left for future work.

available CRLB (2) and the measurement model (5) already indicate the type of feedback information that may be used.

- The accuracy of the TX-side TR processing determines the signal energy, noise power, and effective bandwidth of the tag reflection, cf. (5): The signal energy is proportional to the energy sum of all correctly resolved MPCs; non-resolved MPCs contribute to the noise process; incorrectly resolved pulse delays lead to a broadening of the effective transmit pulse, equivalent to decreased effective bandwidth.
- With appropriate RX-side processing, proper weighting of the MPCs is feasible. This requires the estimation of the signal-to-interference ratios of the MPCs, cf. (2).

This completes the discussion of the PAC for the proposed system. The following sections outline the roles of memory and attention.

IV. Memory

We split the memory in two parts, the target states on the one hand (including the random part of the channel state information) and the environment model on the other hand. When tracking either part of the memory, we consider the other part as fixed. We proceed by describing these two estimation steps, respectively, highlighting their interdependencies.

1) State space tracking: The state of the ℓ-th RFID tag at time step n is given as $\mathbf{x}_{\ell,n} = [\mathbf{p}; \mathbf{v}; \boldsymbol{\beta}_{\mathrm{TX}}; \boldsymbol{\beta}_{\mathrm{RX}}]$, where $\mathbf{p} = [x; y]$ is the position, $\mathbf{v} = [v_x; v_y]$ is the velocity, and $\boldsymbol{\beta}_{\mathrm{TX}}$ and $\boldsymbol{\beta}_{\mathrm{RX}}$ are the random parts of the MPC amplitudes. At this stage of our work, we consider perfect environment models and neglect the randomness of the channels of individual tags. I.e., the entries of $[\boldsymbol{\beta}_{\mathrm{TX}}; \boldsymbol{\beta}_{\mathrm{RX}}]$ are considered to be all ones. The implementation of this random model component will be an important topic for future work.

The measurement received from the ℓ-th tag is denoted as $\mathbf{z}_{\ell,n}$. As the states can only be observed through the measurements, we can model the tracking problem as a hidden Markov model. The posterior PDF at the $(n-1)$-th step is given by $\mathrm{p}(\mathbf{x}_{\ell,n-1}|\mathbf{z}_{\ell,1:n-1}, \boldsymbol{\theta}_{\mathrm{TX}}, \boldsymbol{\psi}_{\mathrm{RX}})$. Due to the fact that conditioned on the state at the previous time step, the current state is independent of all previous measurements, we can use the state-space transition PDF $\mathrm{p}(\mathbf{x}_{\ell,n}|\mathbf{x}_{\ell,n-1}, \mathbf{z}_{\ell,1:n-1}) = \mathrm{p}(\mathbf{x}_{\ell,n}|\mathbf{x}_{\ell,n-1})$ to obtain the prior PDF of the target state $\mathbf{x}^-_{\ell,n}$ using the Chapman-Kolmogorov equation

$$\mathrm{p}(\mathbf{x}_{\ell,n}|\mathbf{z}_{\ell,1:n-1}, \boldsymbol{\theta}_{\mathrm{TX}}, \boldsymbol{\psi}_{\mathrm{RX}}) = \int \mathrm{p}(\mathbf{x}_{\ell,n}|\mathbf{x}_{\ell,n-1}) \mathrm{p}(\mathbf{x}_{\ell,n-1}|\mathbf{z}_{\ell,1:n-1}, \boldsymbol{\theta}_{\mathrm{TX}}, \boldsymbol{\psi}_{\mathrm{RX}}) \mathrm{d}\mathbf{x}_{\ell,n-1}. \quad (8)$$

As mentioned above, the TX-side environment model $\boldsymbol{\theta}_{\mathrm{TX}}(\mathbf{p})$ is used for the TR processing. The feedback information of the PAC for choosing the optimal TR parameters can be extracted from the prior PDF (8), using the criteria discussed in Section III-D. The most simple way to obtain a specific instance of feedback information is to use the position estimate $\hat{\mathbf{p}}_{\ell,n}$ of the predicted target state $\mathbf{x}^-_{\ell,n}$ to adapt the transmitted signal in (4), i.e.

$$\boldsymbol{\theta}_{\mathrm{TX}}(\hat{\mathbf{p}}_{\ell,n}) = \boldsymbol{\theta}_{\mathrm{TX}}\big(\mathbb{E}\{\mathbf{p}^-_{\ell,n}\}\big). \quad (9)$$

Hence, the new measurement $\mathbf{z}_{\ell,n}$ to be used in the update step of the state-space filter depends on the TR processing parameters $\boldsymbol{\theta}_{\mathrm{TX}}(\hat{\mathbf{p}}_{\ell,n})$. The prior PDF (8) is updated with the measurement $\mathbf{z}_{\ell,n}$ using the Bayesian theorem, so that the posterior PDF of the updated state $\mathbf{x}^+_{\ell,n}$ can be written as

$$\mathrm{p}(\mathbf{x}_{\ell,n}|\mathbf{z}_{\ell,n}, \boldsymbol{\theta}_{\mathrm{TX}}, \boldsymbol{\psi}_{\mathrm{RX}}) = \frac{\mathrm{p}(\mathbf{z}_{\ell,n}|\mathbf{x}_{\ell,n}, \boldsymbol{\theta}_{\mathrm{TX}}, \boldsymbol{\psi}_{\mathrm{RX}}) \mathrm{p}(\mathbf{x}_{\ell,n}|\mathbf{z}_{\ell,1:n-1}, \boldsymbol{\theta}_{\mathrm{TX}}, \boldsymbol{\psi}_{\mathrm{RX}})}{\mathrm{p}(\mathbf{z}_{\ell,n}|\mathbf{z}_{\ell,1:n-1}, \boldsymbol{\theta}_{\mathrm{TX}}, \boldsymbol{\psi}_{\mathrm{RX}})} \quad (10)$$

whose denominator is given by

$$\mathrm{p}(\mathbf{z}_{\ell,n}|\mathbf{z}_{\ell,1:n-1}, \boldsymbol{\theta}_{\mathrm{TX}}, \boldsymbol{\psi}_{\mathrm{RX}}) = \int \mathrm{p}(\mathbf{z}_{\ell,n}|\mathbf{x}_{\ell,n}, \boldsymbol{\theta}_{\mathrm{TX}}, \boldsymbol{\psi}_{\mathrm{RX}}) \mathrm{p}(\mathbf{x}_{\ell,n}|\mathbf{z}_{\ell,1:n-1}, \boldsymbol{\theta}_{\mathrm{TX}}, \boldsymbol{\psi}_{\mathrm{RX}}) \mathrm{d}\mathbf{x}_{\ell,n}. \quad (11)$$

2) Environment Memory: The second part of the memory is also implemented using a Bayesian estimator. For this step, the posterior PDFs of the state vectors $\mathbf{x}_{\ell,n}$ of the RFID tags are considered to be known. The measurements of an ensemble of RFID tags at time step n are stacked into a vector $\mathbf{Z} = [\mathbf{z}_{1,n}; \mathbf{z}_{2,n}; \ldots; \mathbf{z}_{L,n}]$, where L is the number of tags. Also, the known state parameters for time step n of the ensemble of tags are stacked in a vector $\mathbf{X} = [\mathbf{x}_{1,n}; \mathbf{x}_{2,n}; \ldots; \mathbf{x}_{L,n}]$. Using Bayes' theorem, one can then write the posterior PDF of the TX-side and RX-side environment models as

$$\mathrm{p}(\boldsymbol{\theta}_{\mathrm{TX}}, \boldsymbol{\psi}_{\mathrm{RX}}|\mathbf{Z}, \mathbf{X}) = \frac{\mathrm{p}(\mathbf{Z}|\boldsymbol{\theta}_{\mathrm{TX}}, \boldsymbol{\psi}_{\mathrm{RX}}, \mathbf{X}) \mathrm{p}(\boldsymbol{\theta}_{\mathrm{TX}}, \boldsymbol{\psi}_{\mathrm{RX}}|\mathbf{X}) \mathrm{p}(\mathbf{X})}{\int \mathrm{p}(\mathbf{Z}|\boldsymbol{\theta}_{\mathrm{TX}}, \boldsymbol{\psi}_{\mathrm{RX}}, \mathbf{X}) \mathrm{p}(\boldsymbol{\theta}_{\mathrm{TX}}, \boldsymbol{\psi}_{\mathrm{RX}}|\mathbf{X}) \mathrm{p}(\mathbf{X}) \mathrm{d}\boldsymbol{\theta}_{\mathrm{TX}} \mathrm{d}\boldsymbol{\psi}_{\mathrm{RX}}}. \quad (12)$$

Eq. (12) illustrates the interaction of the joint feedback and joint measurements. The former yields position-resolved instances of the TX-side environment model. These are useful for the latter, as they enable an observation of the RX-side environment model through the ensemble of tags.

Due to these two separated steps, the Bayesian state-space tracking filtering and the Bayesian estimation of the TX-side and RX-side environment models can be executed in an iterative manner to get both the state of the RFID tags and the environment parameters. At this stage of our work, we focus on the first step, the tracking problem, and assume the environment as perfectly known. The modeling of the environment is part of ongoing work.

On top of these state-space models, we envision additional layers of memory that can implement large-scale models of the environment and the tag population. For instance, the changing visibility of MPCs throughout the observation area and specific characteristics of various transponders may be represented. And, when considering changing the bandwidth and carrier frequency of the TX signal, adaptations of the environment models need to be made.

V. Attention

We assume availability of a static propagation environment over extended periods of time. In such phases, the CR can repeatedly probe the environment and thereby incrementally learn the environment models, interrogating the targets in a round-robin fashion until convergence.

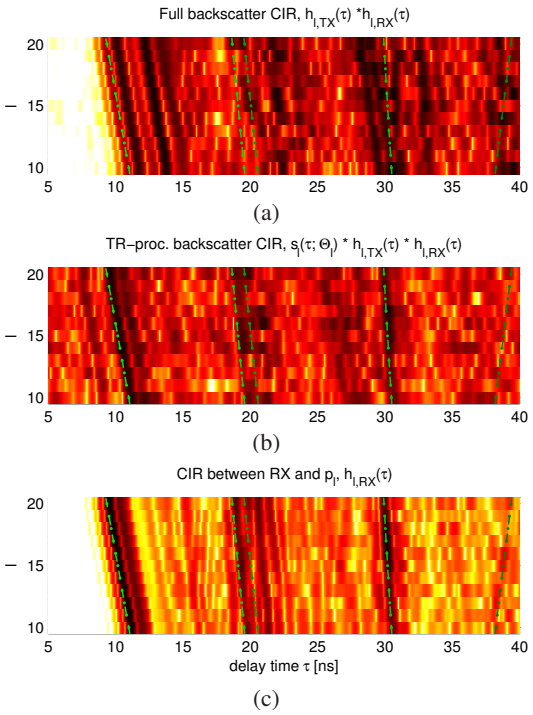

Fig. 1. Illustration of TR processing over an NLOS uplink channel. Deterministic components of the (LOS) downlink channel are indicated. (a) CIRs for the backscatter channel, the concatenation of up and downlink channels; (b) RX signals with TR processing; (c) CIRs for the downlink.

The key role of attention is providing fast and accurate response to changes within the environment. Ideally, the CR will respond by assigning additional resources for tracking those moving targets. Here, an adaptive signal bandwidth can be exploited again. Less bandwidth implies less accuracy but also a lower resolution of the search space. The latter will benefit the convergence of the PAC when re-localizing targets that moved "suddenly". Remember that we propose to monitor thousands of targets, hence a continuous high-rate monitoring of all targets is not feasible. Thus it is very likely that the state-space trackers have to respond to "large" movements.

VI. Initial Results

A. Time-reversal Processing – Experimental Results

The performance of TR processing is demonstrated in Fig. 1, based on measurement data. The up and downlink channels have been measured separately (but simultaneously) using a vector network analyzer in the 6–8 GHz frequency range, connected to three antennas for TX, RX, and transponder. The transponder antenna was moved along a straight line in 5 cm steps. For this illustration, the TX and RX-side environment models have been extracted from the geometry of the environment as discussed in [15]. An NLOS situation was chosen for the uplink to demonstrate the full potential of TR. The downlink was LOS.

Fig. 1(a) illustrates the impulse response of the "full" backscatter channel, the concatenation of the up and downlink channels, without TR processing. A series of 11 measurements is depicted, allowing the eye to distinguish deterministic components from diffuse multipath. The expected MPCs of the downlink channel—corresponding to the RX-side environment model—are superimposed as dashed lines with bullet markers. It is clearly seen that this model does not match the measurement data. Any localization algorithm employing this information would fail.

Fig. 1(b) includes the TR signal according to (4). Now a good match is seen between the measurement and the expected MPCs, in particular at 10 and 30 ns but also at 20 ns. For comparison, the pure downlink channel is shown in Fig. 1(c). The latter reveils the same components. It shows less pronounced diffuse multipath but the information bearing timing is equivalent. Another difference is the appearance of artifacts from the TR processing in Fig. 1(b), such as spurious components arriving prior to the LOS.

B. Target Tracking, Time-reversal, and PAC

We next illustrate the impact of TR processing for waveform adaptation in the PAC on the tracking performance. The TX-side and RX-side environment models are assumed to be perfectly known at this stage. A computer simulation model has been implemented, consisting of one TX node and two RX nodes to track one mobile target (MT) along a trajectory as shown in Fig. 2(a). The trajectory consists of 35 target positions, which represent 35 time steps. For the motion model we used a linear and constant velocity state-space propagation model with Gaussian process noise.

The multipath channels from the transmitter to the RFID tag and the channel from the tag to the receiver are modeled by (1). The deterministic part of the channels comprises the LOS path and first and second-order specular reflections. The transmitted pulse $\mathrm{p}(t)$ is modeled as root-raised cosine pulse, with a roll-off factor of $\beta_{roll} = 0.6$ and a pulse duration of $T_p = 0.5$ ns. The carrier frequency f_c of the pulse is 7 GHz and similar to [8], we used a free-space path-loss model for the MPC gains. The diffuse part of one single channel is modeled as double-exponential function cf. (eq. (9) in [17]). Its parameters are the total power of the diffuse multipath $\Omega_1 = 2.32 \times 10^{-7}$, $\gamma_1 = 20$ ns, $\gamma_{rise} = 5$ ns and $\chi = 0.98$. The *effective* SNR of the LOS components are 30 dB (at the first trajectory point).

A particle based method was used for the Bayesian state-space filter. We used an auxiliary sampling importance resampling particle filter as described in [18]. The PDFs are represented by 100 particles. The particles are perfectly initialized with the first trajectory point of the MT. Fig. 2(a) illustrates the evolution of the particles along the trajectory. The CDFs of the obtained position estimation errors are shown in Fig. 2(b), averaged over 60 runs.

To better understand the impact of TR employed for transmitter adaptation, the CRLB has been evaluated numerically for a single backscatter link of this scenario. Fig. 3 shows a clear advantage for the TR method. Without TR, path overlap occurs to a vast extent, due to the very large number of deterministic components in the backscatter channel (approx. 120). Path overlap leads to information loss for the overlapping

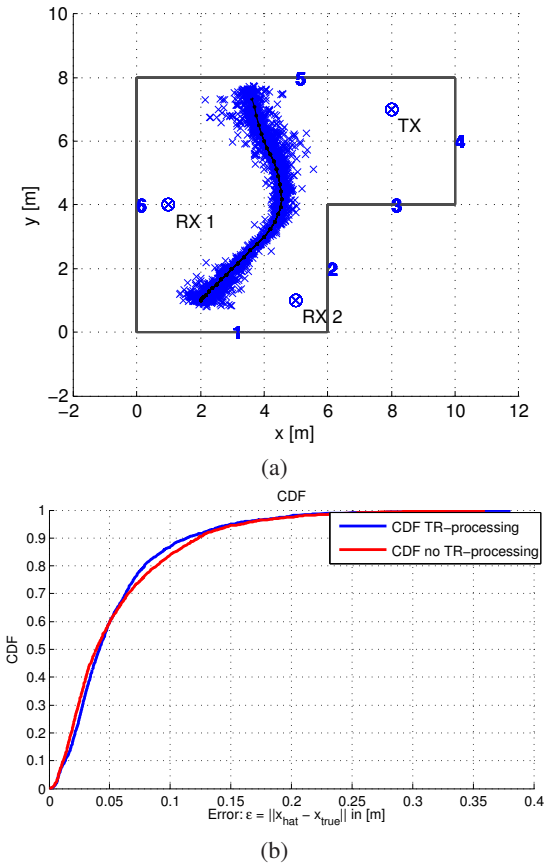

Fig. 2. (a) Simulation scenario and particles representing the target state along the trajectory. (b) Tracking performance.

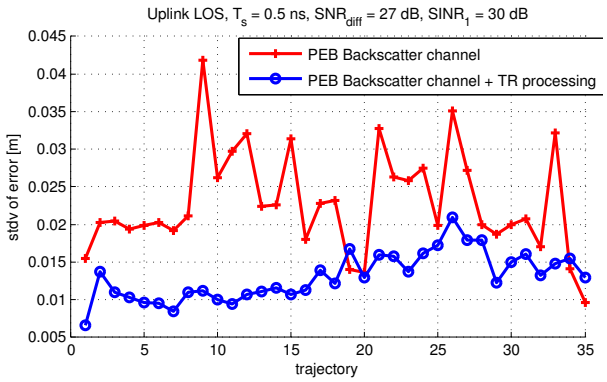

Fig. 3. CRLB of the position estimate along the trajectory shown in Fig. 2(a). The CRLB has been numerically evaluated for a single backscatter link (TX-RX1).

deterministic components, which is evident in Fig. 3 in form of peaks in the PEB. Path overlap is greatly lowered with TR, seen in a smoother PEB at significantly lower level.

Fig. 2(b) also compares two experiments, where one does and the other does not employ TR. Here surprisingly little difference is seen between the two cases. Reason is the availability of the additional RX node. It creates two stable backscatter links, both at LOS, which yields a robust configuration for location tracking, with and without TR.

VII. Conclusions

This paper proposes cognitive radar for tracking passive backscatter transponders (RFID tags) in dense multipath environments. Deterministic multipath components are exploited to overcome robustness issues in non-LOS situations. The radar learns TX and RX-side models of the radio channel for this purpose. Time reversal processing yields a focusing of the TX power onto the target location, which helps overcoming the tight link budget. Initially, a UWB radar is needed to be able to distinguish MPCs. However, once the environment models are known, the radar may reduce its signal bandwidth, yielding reduced processing demands and improved response times.

References

[1] S. Haykin, Y. Xue, and P. Setoodeh, "Cognitive radar: Step toward bridging the gap between neuroscience and engineering," *Proc. IEEE*, vol. PP, no. 99, pp. 1 –29, 2012.

[2] S. Haykin, "Cognitive radar: a way of the future," *IEEE Signal Processing Mag.*, vol. 23, pp. 30–40, Jan. 2006.

[3] ——, "Cognitive dynamic systems: Radar, control, and radio [point of view]," *Proc. IEEE*, vol. 100, no. 7, pp. 2095 –2103, Jul. 2012.

[4] A. Molisch, "Ultra-wide-band propagation channels," *Proc. IEEE*, vol. 97, no. 2, pp. 353–371, Feb. 2009.

[5] T. Strohmer, M. Emami, J. Hansen, G. Papanicolaou, and A. Paulraj, "Application of time-reversal with mmse equalizer to uwb communications," in *IEEE Global Telecommun. Conf., GLOBECOM*, vol. 5, nov.-3 dec. 2004, pp. 3123 – 3127 Vol.5.

[6] N. Guo, B. Sadler, and R. Qiu, "Reduced-complexity UWB time-reversal techniques and experimental results," *IEEE Trans. Wireless Commun.*, vol. 6, no. 12, pp. 4221 –4226, Dec. 2007.

[7] D. Arnitz, U. Muehlmann, and K. Witrisal, "Wideband characterization of backscatter channels: Derivations and theoretical background," *IEEE Trans. Antennas Propagat.*, vol. 60, no. 1, pp. 257–266, Jan. 2012.

[8] K. Witrisal and P. Meissner, "Performance bounds for multipath-assisted indoor navigation and tracking (MINT)," in *IEEE International Conference on Communications, ICC*, Ottawa, Canada, Jun. 2012.

[9] Y. Chen and P. Rapajic, "Ultra-wideband cognitive interrogator network: adaptive illumination with active sensors for target localisation," vol. 4, no. 5, pp. 573–584, 26 2010.

[10] D. Arnitz, U. Muehlmann, and K. Witrisal, "UWB ranging in passive UHF RFID: A proof of concept," *IET Electronics Letters*, vol. 46, no. 20, pp. 1401–1402, Sep. 2010.

[11] ——, "Multi-frequency continuous-wave radar approach to ranging in passive UHF RFID," *IEEE Trans. Microwave Theory Tech.*, vol. 57, no. 5, pp. 1398–1405, May 2009.

[12] A. Sibille, M. Sacko, Z. Mhanna, F. Guidi, and C. Roblin, "Joint antenna-channel statistical modelling of UWB backscattering RFID," in *IEEE Intern. Conf. on Ultra-Wideband, ICUWB*, Bologna, Italy, Sep. 2011.

[13] Y. Shen and M. Win, "Fundamental limits of wideband localization; Part I: A general framework," *IEEE Trans. Inform. Theory*, vol. 56, no. 10, pp. 4956–4980, Oct. 2010.

[14] H. Godrich, A. Haimovich, and R. Blum, "Target localization accuracy gain in MIMO radar-based systems," *IEEE Trans. Inform. Theory*, vol. 56, no. 6, pp. 2783–2803, Jun. 2010.

[15] P. Meissner and K. Witrisal, "Analysis of Position-Related information in measured UWB indoor channels," in *European Conf. on Antennas and Propagation, EuCAP*, Prague, Czech Republic, Mar. 2012.

[16] J. Moura and Y. Jin, "Time reversal imaging by adaptive interference canceling," *IEEE Trans. Signal Processing*, vol. 56, no. 1, pp. 233 –247, Jan. 2008.

[17] J. Karedal, S. Wyne, P. Almers, F. Tufvesson, and A. F. Molisch, "A measurement-based statistical model for industrial ultra-wideband

channels," *IEEE Trans. Wireless Commun.*, vol. 6, no. 8, pp. 3028–3037, Aug. 2007.

[18] M. Arulampalam, S. Maskell, N. Gordon, and T. Clapp, "A tutorial on particle filters for online nonlinear/non-gaussian bayesian tracking," *IEEE Trans. Signal Processing*, no. 2, pp. 174 –188, feb 2002.

Performance Bounds for Multipath-assisted Indoor Localization on Backscatter Channels

Erik Leitinger*, Paul Meissner*, Markus Fröhle+, and Klaus Witrisal*
* Email: erik.leitinger@tugraz.at, Graz University of Technology, Austria
+ Email: frohle@chalmers.se, Chalmers University of Technology, Sweden

***Abstract*—In this paper, we derive the Cramér-Rao lower bound (CRLB) on the position error for an RFID tag localization system exploiting multipath on backscatter radio channels. The backscatter channel is modeled with a hybrid deterministic/stochastic channel model. In this way, both the geometry of the deterministic multipath components (MPCs) and the interfering diffuse multipath are taken into account. Computational results show the influence of the room geometry on the bound and the impact of the diffuse multipath. Time reversal (TR) processing on the uplink channel is analyzed using the deterministic MPCs to overcome the degenerate nature of the backscatter channel. The CRLB shows the potential gain obtained from TR processing as well as its strong dependence on the geometry. Such TR processing has been proposed for TX waveform adaptation in the perception-action cycle of a cognitive radar. The results of this paper illustrate that it can indeed influence beneficially the measurement noise of the received signal, yielding control over the localization system.**

I. Introduction

Ultra-wideband signals are promising candidates for localization in harsh indoor multipath environments, due to fine time-resolution enabled by large bandwidth. Nevertheless, indoor positioning is still a challenging task, in particular due to errors caused by non-line-of-sight (NLOS) propagation conditions. These problems are even stronger on backscatter channels employed by RFID systems.

Performance bounds such as the Cramér-Rao lower bound (CRLB) can yield valuable insights on the influence of the channel parameters on the localization accuracy. In [1], [2] the CRLB given by the information inequality is derived directly from the received signal rather than from specific features extracted from the signal. Multipath components (MPCs) associated to strong reflections can increase accuracy of the position estimation, if prior floor-plan knowledge is available [3]. These MPCs can be seen as originating from so-called virtual anchors (VAs) as shown in Fig. 1, hence a deterministic model is available for these MPCs. A key difference of [3], compared to [1], [2], is the stochastic modeling of the diffuse multipath (DM) which acts as interference for these useful geometry-related components. The theoretical results from [3] were verified using data from an extensive indoor measurement campaign [4]. For conventional "non-backscatter" channels, the feasibility of multipath-assisted tracking algorithms was demonstrated in [5] for real channel measurements.

This work was partly supported by the Austrian Science Fund (FWF) within the National Research Network SISE project S10610.

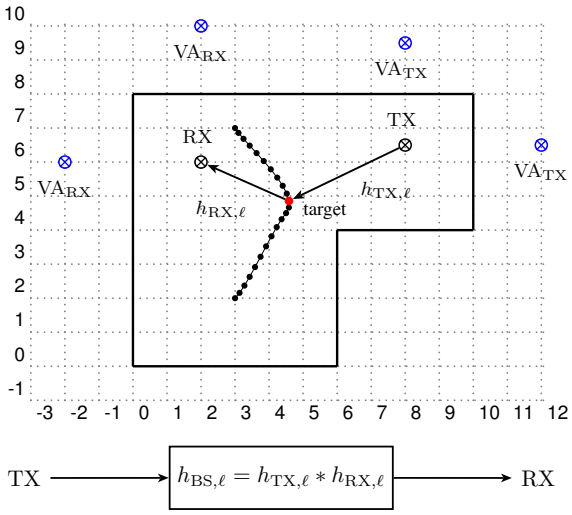

Fig. 1. Top: Floorplan with a transmitter (TX) and receiver (RX) radar node and a subset of corresponding VAs. The up-link is the channel between TX and the target at position ℓ along a trajectory, the down-link is the channel between the target and RX. Bottom: Backscatter model as concatenation of up- and down-link channels.

The contribution of this paper is the extension of the theoretical framework in [3] to the localization error bound of a radar target using a backscatter channel model. It is well-known that the channel in backscatter radio systems is a degenerate pinhole channel [6], formed by the concatenation of the channels from the transmitter (TX) to the target and from the target to the receiver (RX). In our work we assume that the signal received through the RFID tag can be distinguished from the signal coming directly from the environment, due to the modulation of the RFID tag.

Time-reversal processing (TR) [7], [8] for backscatter channels has been motivated in [9], to focus the energy onto RFID tags at certain positions and to separate the up- and down-link channels from one another. We analyze the impact of TR processing on the CRLB for multipath-assisted RFID localization in this paper. Common TR processing uses the entire reversed complex conjugate channel. This is not resilient w.r.t. imperfect channel knowledge, as any errors cause incoherent summation of paths and thereby loss of focusing of the energy. Therefore, we only use a limited set of deterministic MPCs that can be modeled geometrically, as these have been shown to carry a large fraction of the channel energy [4]. Such TR processing has been proposed for TX processing in the

perception-action cycle of a cognitive radar [9]. Quantifying its impact on the CRLB provides a way to close this feedback loop.

This paper is organized as follows: The signal and channel models are given in Section II. The derivation of the CRLB and the evaluation of the influence of TR processing are provided in Section III. Results are discussed in Section IV. Finally, conclusions are drawn.

II. Signal and Channel Models

In order to give a mathematical description of the received signal $r(t)$, which is needed to compute the CRLB, we first introduce a model for a hybrid, deterministic/stochastic channel [3] and secondly for a backscatter channel as the concatenation of the former ones.

A. Hybrid Deterministic/Stochastic Channel

The hybrid deterministic/stochastic complex baseband radio channel $h_{m,\ell}(\tau)$ between a radar node $m \in \{\mathrm{TX}, \mathrm{RX}\}$ located at position $\mathbf{p}_{1,m}$ and a target at position $\mathbf{p}_\ell$ is defined as

$$h_{m,\ell}(\tau) = \sum_{k=1}^{K_{m,\ell}} \alpha_{k,m,\ell}\delta(\tau - \tau_{k,m,\ell}) + \nu_{m,\ell}(\tau) \qquad (1)$$

where the first term consists of $K_{m,\ell}$ deterministic MPCs with complex amplitudes $\alpha_{k,m,\ell} \in \mathbb{C}$ and delays $\tau_{k,m,\ell} = \frac{1}{c}||\mathbf{p}_\ell - \mathbf{p}_{k,m}||$, where c is the speed of light. The delays of deterministic MPCs, i.e. strong specular reflections on walls, can be modeled geometrically, if the floor-plan is known. Fig. 1 shows the locations $\left\{\mathbf{p}_{k,m} = [x_{k,m}, y_{k,m}]^T\right\}_{k=1}^{K_{m,\ell}}$ of a subset of VAs in the considered environment. The second term $\nu_{m,\ell}(\tau)$ denotes the diffuse multipath (DM) and is modeled with a stochastic process. We assume uncorrelated scattering (US), so that the ACF of the DM is given as

$$K_\nu(\tau, u) = \mathbb{E}\left\{\nu_{m,\ell}(\tau)\nu_{m,\ell}(u)^*\right\} = S_{\nu,m,\ell}(\tau)\delta(\tau - u). \quad (2)$$

$S_{\nu,m,\ell}(\tau)$ is the power delay profile (PDP), where $S_{\nu,m,\ell}(\tau) = 0$ for $\tau < \tau_{1,m,\ell}$, which implies that the DM does not exist until the first deterministic MPC excites the channel. For a specific radar node m and a well-defined "local area" around the target position $\mathbf{p}_\ell$ (several wavelengths), DM is assumed to be quasi-stationary, which means that the channel's first- and second-order statistics do not change noticeably in the spatial domain [10].

B. Backscatter Channel

For brevity, we drop the tag position index ℓ in further derivations. The backscatter channel impulse response (CIR) is obtained by the convolution of the up- and down-link channels both modeled with (1) yielding

$$\begin{aligned} h_{\mathrm{BS}}(\tau) &= h_{\mathrm{TX}}(\tau) * h_{\mathrm{RX}}(\tau) \\ &= \sum_{k=1}^{K_{\mathrm{TX}}}\sum_{l=1}^{K_{\mathrm{RX}}} \alpha_{k,\mathrm{TX}}\alpha_{l,\mathrm{RX}}\delta(\tau - \tau_{k,\mathrm{TX}} - \tau_{l,\mathrm{RX}}) \\ &+ \sum_{k=1}^{K_{\mathrm{TX}}} \alpha_{k,\mathrm{TX}}\nu_{\mathrm{RX}}(\tau - \tau_{k,\mathrm{TX}}) + \sum_{l=1}^{K_{\mathrm{RX}}} \alpha_{l,\mathrm{RX}}\nu_{\mathrm{TX}}(\tau - \tau_{l,\mathrm{RX}}) \\ &+ \nu_{\mathrm{TX}}(\tau) * \nu_{\mathrm{RX}}(\tau). \end{aligned} \qquad (3)$$

Here, the first term represents the deterministic part of the backscatter channel. The second and third terms are the convolution of the DM of the up-link channel with the deterministic components of the down-link channel, and vice versa. The last term constitutes the convolution of the DM of the up- and down-link channels. In the following, we denote the sum of the last three terms of (3) that comprise the DM as $\nu_{\mathrm{BS}}(\tau) = \nu_{\mathrm{TX},\mathrm{DM}_{\mathrm{RX}}}(\tau) + \nu_{\mathrm{RX},\mathrm{DM}_{\mathrm{TX}}}(\tau) + \nu_{\mathrm{DM}_{\mathrm{TX}},\mathrm{DM}_{\mathrm{RX}}}(\tau)$. From (3) it is seen that the backscatter channel can be decomposed into a deterministic and a diffuse part, in the same way as the up- and down-links in (1).

With the quasi-stationarity, US assumption and that $\nu_{\mathrm{TX}}(\tau)$ and $\nu_{\mathrm{RX}}(\tau)$ are assumed to be independent, the PDP of the backscatter channel is the second central moment of the DM process

$$\begin{aligned} S_{\nu,\mathrm{BS}}(\tau) &= \mathbb{E}\left\{\nu_{\mathrm{BS}}(\tau)\nu_{\mathrm{BS}}^*(\tau)\right\} \\ &= \mathbb{E}\left\{\sum_{k=1}^{K_{\mathrm{TX}}}\sum_{k'=1}^{K_{\mathrm{TX}}} \alpha_{k,\mathrm{TX}}\alpha_{k',\mathrm{TX}}^*\nu_{\mathrm{RX}}(\tau - \tau_{k,\mathrm{TX}})\nu_{\mathrm{RX}}^*(\tau - \tau_{k',\mathrm{TX}})\right\} \\ &+ \mathbb{E}\left\{\sum_{l=1}^{K_{\mathrm{RX}}}\sum_{l'=1}^{K_{\mathrm{RX}}} \alpha_{l,\mathrm{RX}}\alpha_{l',\mathrm{RX}}^*\nu_{\mathrm{TX}}(\tau - \tau_{l,\mathrm{RX}})\nu_{\mathrm{TX}}^*(\tau - \tau_{l',\mathrm{RX}})\right\} \\ &+ \mathbb{E}\left\{\nu_{\mathrm{TX}}(\tau) * \nu_{\mathrm{RX}}(\tau)(\nu_{\mathrm{TX}}(\tau) * \nu_{\mathrm{RX}}(\tau))^*\right\}. \end{aligned} \qquad (4)$$

We assume a zero-mean Gaussian model for the DM, thus first and second moments give a complete description of the random process. The validity of the US assumption for a backscatter channel constituted by two US-channels has been proven in the appendix of [6], which leads to

$$\begin{aligned} S_{\nu,\mathrm{BS}}(\tau) &= \sum_{k=1}^{K_{\mathrm{TX}}} |\alpha_{k,\mathrm{TX}}|^2 S_{\nu,\mathrm{RX}}(\tau - \tau_{k,\mathrm{TX}}) \\ &+ \sum_{l=1}^{K_{\mathrm{RX}}} |\alpha_{l,\mathrm{RX}}|^2 S_{\nu,\mathrm{TX}}(\tau - \tau_{l,\mathrm{RX}}) + S_{\nu,\mathrm{TX}}(\tau) * S_{\nu,\mathrm{RX}}(\tau). \end{aligned} \qquad (5)$$

In Fig. 2(a) the deterministic MPCs and the PDPs of the DM of some exemplary up- and down-link channels are shown. Fig. 2(b) shows the deterministic components $h_{\mathrm{BS,det}}(\tau)$ and the individual terms of the PDP $S_{\nu,\mathrm{BS}}(\tau)$ of the backscatter channel.

C. Transmitted Signal – Time-Reversal Processing

We assume that the TX transmits a signal $s(t) \in \mathbb{C}$. On the one hand, this can be a single pulse $p(t)$ with pulse duration T_p, e.g. a commonly used root raised cosine pulse. Hence, the received signal represents the backscatter channel convolved with this pulse $p(t)$. On the other hand, the transmitted signal $s(t)$ can be a sum of complex weighted and time-shifted copies of this pulse $p(t)$ in order to obtain a TR signal.

TR processing is one promising candidate to overcome the degenerate pinhole nature of the backscatter channel, because it optimizes the link-budget between the TX and RX by focusing the energy onto the target. This is done by using the VAs, which are a geometric model for the deterministic

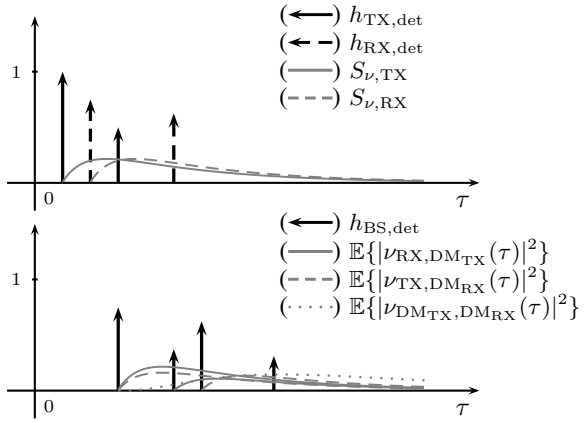

Fig. 2. (a) Up- and down-link channel. Solid lines denote the up-link channel, with deterministic components in black and the PDPs of the DM in gray. Dashed lines indicate the down-link channel. (b) Backscatter channel. Solid black lines denote the deterministic components. The gray lines indicate the different summands of the PDP.

MPCs of $h_{\mathrm{TX}}(\tau)$ in (1), as a virtual antenna array for spatial focusing. The TX signal becomes

$$s(t) = \Big[\sum_{k=1}^{\hat{K}_{\mathrm{TX}}} \hat{\alpha}^*_{k,\mathrm{TX}}\delta\big(t+\hat{\tau}_{k,\mathrm{TX}}\big)\Big] * p(t) \tag{6}$$

where $\{\hat{\alpha}_{k,\mathrm{TX}},\ \hat{\tau}_{k,\mathrm{TX}}\}$ is the set of $\hat{K}_{\mathrm{TX}}(\tau)$ estimated MPC parameters of the up-link channel h_{TX} for a position $\hat{\mathbf{p}}$. The complex amplitudes are normalized s.t. $\int_{-\infty}^{\infty}|s(t)|^2\mathrm{d}t = E_{\mathrm{TR}}$. The received signal at radar node RX can be obtained by the convolution of (3) with the transmit waveform (6) and AWGN $n(t)$ with a two-sided power spectral density of $N_0/2$, given as

$$\begin{aligned} r(t) &= s(t) * h_{\mathrm{BS}}(t) + n(t) \qquad (7)\\ &= \Big[\sum_{k=1}^{K_{\mathrm{TX}}}\sum_{l=1}^{K_{\mathrm{RX}}}\sum_{k'=1}^{\hat{K}_{\mathrm{TX}}} \alpha_{k,\mathrm{TX}}\alpha_{l,\mathrm{RX}}\hat{\alpha}^*_{k',\mathrm{TX}} \\ &\qquad \times \delta(t-\tau_{k,\mathrm{TX}}-\tau_{l,\mathrm{RX}}+\hat{\tau}_{k',\mathrm{TX}}) \\ &+ \sum_{k=1}^{K_{\mathrm{TX}}}\sum_{k'=1}^{\hat{K}_{\mathrm{TX}}} \alpha_{k,\mathrm{TX}}\hat{\alpha}^*_{k',\mathrm{TX}}\nu_{\mathrm{RX}}(t-\tau_{k,\mathrm{TX}}+\hat{\tau}_{k',\mathrm{TX}}) \\ &+ \sum_{l=1}^{K_{\mathrm{RX}}}\sum_{k'=1}^{\hat{K}_{\mathrm{TX}}} \alpha_{l,\mathrm{RX}}\hat{\alpha}^*_{k',\mathrm{TX}}\nu_{\mathrm{TX}}(t-\tau_{l,\mathrm{RX}}+\hat{\tau}_{k`,\mathrm{TX}}) \\ &+ \int\sum_{k'=1}^{\hat{K}_{\mathrm{TX}}} \hat{\alpha}^*_{k',\mathrm{TX}}\nu_{\mathrm{TX}}(\lambda)\nu_{\mathrm{RX}}(t+hat\tau_{k',\mathrm{TX}}-\lambda)\mathrm{d}\lambda\Big] * p(t)+n(t). \end{aligned}$$

The first term comprises deterministic components of the received signal $r(t)$, and the remaining terms constitute the DM arriving at the RX. Eq. (7) again shows that the channel described by the convolution of $h_{\mathrm{BS}}(\tau)$ and $h_{\mathrm{TR}}(\tau)$ can be decomposed into deterministic and diffuse parts. Assuming perfect TR parameters are available, (7) gives additional insights in the TR processing: First, the energy is concentrated on the deterministic MPCs of the down-link channel $h_{\ell,\mathrm{RX}}(\tau)$. Second, again the structure of an equivalent deterministic channel and DM can be observed. The PDP of the received DM can be obtained as

$$\begin{aligned} &S_{\nu,\mathrm{TR}}(\tau) = \qquad (8)\\ &= \sum_{k=1}^{K_{\mathrm{TX}}}\sum_{k'=1}^{\hat{K}_{\mathrm{TX}}} |\alpha_{k,\mathrm{TX}}|^2|\hat{\alpha}_{k',\mathrm{TX}}|^2 S_{\nu,\mathrm{RX}}(\tau-\tau_{k,\mathrm{TX}}+\hat{\tau}_{k',\mathrm{TX}}) \\ &+ \sum_{l=1}^{K_{\mathrm{RX}}}\sum_{k'=1}^{\hat{K}_{\mathrm{TX}}} |\alpha_{l,\mathrm{RX}}|^2|\hat{\alpha}_{k',\mathrm{TX}}|^2 S_{\nu,\mathrm{TX}}(\tau-\tau_{l,\mathrm{RX}}+\hat{\tau}_{k',\mathrm{TX}}) \\ &+ \sum_{k'=1}^{\hat{K}_{\mathrm{TX}}} |\hat{\alpha}_{k',\mathrm{TX}}|^2 \int_{-\infty}^{\infty} S_{\nu,\mathrm{TX}}(\lambda)S_{\nu,\mathrm{RX}}(\tau+\hat{\tau}_{k',\mathrm{TX}}-\lambda)\mathrm{d}\lambda. \end{aligned}$$

III. Error Bound on the Position Estimation

In this section, we derive the equivalent Fisher information matrix (EFIM) [1] for the target localization problem via the backscatter channel. The derivation and the notation follow closely [2] and [3]. Additionally, the influence of TR processing on the bound is analyzed.

A. Problem Formulation

Our goal is to estimate the position $\mathbf{p}$ of the target from the received signal $r(t)$ in the presence of DM and AWGN, using the TX and RX nodes at positions $\mathbf{p}_{1,\mathrm{TX}}$ and $\mathbf{p}_{1,\mathrm{RX}}$. With a-priori known floor-plan information, the TX and RX span two corresponding sets of VAs at positions $\{\mathbf{p}_{k,\mathrm{TX}}\}$ and $\{\mathbf{p}_{l,\mathrm{RX}}\}$. For the sake of simplicity, we introduce for the backscatter channel the equivalent propagation delays $\tau_{k,l} = \tau_{k,\mathrm{TX}}+\tau_{l,\mathrm{RX}} = \frac{1}{c}||\mathbf{p}-\mathbf{p}_{k,\mathrm{TX}}||+\frac{1}{c}||\mathbf{p}-\mathbf{p}_{l,\mathrm{RX}}||$, which are related to the geometry. Their corresponding complex amplitudes $\alpha_{k,l} = \alpha_{k,\mathrm{TX}}\alpha_{l,\mathrm{RX}}$ are nuisance parameters for the position estimation. We collect the delays $\tau_{k,l}$ and the real and imaginary parts of the amplitudes $\alpha_{k,l}$ in vectors $\boldsymbol{\tau}$, $\boldsymbol{\alpha}^{\mathrm{R}}$, and $\boldsymbol{\alpha}^{\mathrm{I}}$ respectively.

The CRLB on the position error is a lower bound for the MSE of an unbiased estimator and is computed as the inverse of the Fisher information matrix (FIM) $\mathbf{J}(\boldsymbol{\theta})$ [11]. The vector of unknown parameters for position estimation is defined as $\boldsymbol{\theta} = \big[\mathbf{p}^{\mathrm{T}}\ (\boldsymbol{\alpha}^{\mathrm{R}})^{\mathrm{T}}\ (\boldsymbol{\alpha}^{\mathrm{I}})^{\mathrm{T}}\big]^{\mathrm{T}}$ (cf. [1]–[3]) and a transformed parameter vector related to the received signal $r(t)$ is $\boldsymbol{\psi} = \big[\boldsymbol{\tau}^{\mathrm{T}}\ (\boldsymbol{\alpha}^{\mathrm{R}})^{\mathrm{T}}\ (\boldsymbol{\alpha}^{\mathrm{I}})^{\mathrm{T}}\big]^{\mathrm{T}}$. The FIM of the transformed parameter vector $\boldsymbol{\psi}$ is defined as

$$\mathbf{J}(\boldsymbol{\psi}) = \mathbb{E}_{\mathbf{r}|\boldsymbol{\psi}}\left\{-\frac{\partial^2}{\partial\boldsymbol{\psi}\partial\boldsymbol{\psi}}\ln \mathrm{p}(\mathbf{r}|\boldsymbol{\psi})\right\} \tag{9}$$

where the observation vector $\mathbf{r}$ is obtained from the Karhunen-Loéve expansion of the received signal $r(t)$ [11]. The FIM for position estimation is computed by applying the chain rule

$$\mathbf{J}(\boldsymbol{\theta}) = \mathbf{P}\mathbf{J}(\boldsymbol{\psi})\mathbf{P}^{\mathrm{T}} \tag{10}$$

where $\mathbf{P} = \partial\boldsymbol{\psi}/\partial\boldsymbol{\theta}$ is the the Jacobian of the transformation.

B. Likelihood Function of the Received Signal

The likelihood function we use is adopted from [3]. Due to the fact that the DM $\nu_{\mathrm{BS}}(\tau)$ is a colored non-stationary Gaussian noise process, a whitening operation has to be applied to the received signal $r(t)$ to obtain a tractable form. Given that the backscatter channel and the TR processed backscatter channel are both composed the same way as the channel used in [3], the framework to derive the likelihood function can be extended to backscatter channels. Using the Karhunen-Loéve expansion and integral equations [11], we can write

$$\begin{aligned}\ln \mathrm{p}(\mathbf{r}|\boldsymbol{\psi}) \propto \\ \frac{2}{N_0}\int_0^{T_{\mathrm{ob}}} \Re\Big\{r(t)\sum_{k=1}^{K_{\mathrm{TX}}}\sum_{l=1}^{K_{\mathrm{RX}}} w_{k,l}^2\alpha_{k,l}^* s^*(t-\tau_{k,l})\Big\}\mathrm{d}t \\ -\frac{1}{N_0}\int_0^{T_{\mathrm{ob}}}\Big|\sum_{k=1}^{K_{\mathrm{TX}}}\sum_{l=1}^{K_{\mathrm{RX}}} w_{k,l}\alpha_{k,l}s(t-\tau_{k,l})\Big|^2\mathrm{d}t \end{aligned} \tag{11}$$

where T_{ob} is the observation time and $w_{k,l} = \sqrt{N_0/(N_0+T_pS_\nu(\tau_{k,l}))}$ are the weighting factors accounting for DM. $S_\nu(\tau_{k,l})$ denotes the PDP of the DM alone or with TR-processing. The term $T_pS_\nu(\tau_{k,l})$ constitutes the inference power of the DM. The signal $s(t)\in\mathbb{C}$ either represents the TR waveform or the pulse waveform $p(t)$.

C. EFIM and Position Error Bound (PEB)

The PEB represents the CRLB on the position error at position $\mathbf{p}$ and is defined as

$$\mathcal{P}(\mathbf{p}) \equiv \sqrt{\mathrm{tr}\{[\mathbf{J}(\boldsymbol{\theta})_{2\times2}]^{-1}\}} \tag{12}$$

where $\mathrm{tr}\{\cdot\}$ is the trace of a square matrix. $\mathbf{J}(\boldsymbol{\theta})_{2\times2}$ is the upper left submatrix, which comprises the information on the position estimation and is called EFIM [1]. It leads to a reduction of the dimensionality of the FIM. The matrix $\mathbf{P}$ for the parameter transformation in (10) is

$$\mathbf{P} = \begin{bmatrix}\mathbf{H}_{2\times K_{\mathrm{TX}}K_{\mathrm{RX}}} & \mathbf{0}_{2\times 2K_{\mathrm{TX}}K_{\mathrm{RX}}} \\ \mathbf{0}_{2K_{\mathrm{TX}}K_{\mathrm{RX}}\times 2} & \mathbf{I}_{2K_{\mathrm{TX}}K_{\mathrm{RX}}\times 2K_{\mathrm{TX}}K_{\mathrm{RX}}}\end{bmatrix} \tag{13}$$

where $\mathbf{0}$ is the zero matrix, $\mathbf{I}$ denotes the identity matrix and $\mathbf{H}$ incorporates the geometry. The columns of $\mathbf{H}$ are of the form $-\frac{1}{c}[\cos\phi_{k,\mathrm{TX}}+\cos\phi_{l,\mathrm{RX}},\ \sin\phi_{k,\mathrm{TX}}+\sin\phi_{l,\mathrm{RX}}]^{\mathrm{T}}$, where $\phi_{k,\mathrm{TX}}$ and $\phi_{l,\mathrm{RX}}$ are the angles between VAs of the TX- and RX-radar node and the target. For example on the TX side, this angle is defined as $\phi_{k,\mathrm{TX}} = \tan^{-1}((y-y_{k,\mathrm{TX}})/(x-x_{k,\mathrm{TX}}))$. The EFIM on the position error can be written as [3]

$$\mathrm{EFIM} \equiv \mathbf{J}(\boldsymbol{\theta})_{2\times2} = \mathbf{H}\boldsymbol{\Lambda}_{\mathrm{A}}\mathbf{H}^{\mathrm{T}} - \mathbf{H}\boldsymbol{\Lambda}_{\mathrm{B}}\boldsymbol{\Lambda}_{\mathrm{C}}^{-1}\boldsymbol{\Lambda}_{\mathrm{B}}^{\mathrm{T}}\mathbf{H}^{\mathrm{T}} \tag{14}$$

where the block matrices $\boldsymbol{\Lambda}_{\mathrm{A}}$, $\boldsymbol{\Lambda}_{\mathrm{B}}$ and $\boldsymbol{\Lambda}_{\mathrm{C}}$ are defined in the appendix. If there is no path overlap, which means that signals coming from different VAs do not intersect in the time-domain, $\boldsymbol{\Lambda}_{\mathrm{A}}$ is a diagonal matrix and $\boldsymbol{\Lambda}_{\mathrm{B}}$ is zero. According to [3], the EFIM can then be written in a canonical form a

$$\mathbf{J}(\boldsymbol{\theta})_{2\times2} = \frac{8\pi^2\beta^2}{c^2}\sum_{k=1}^{K_{\mathrm{TX}}}\sum_{l=1}^{K_{\mathrm{RX}}}\mathrm{SINR}_{k,l}\mathbf{J}_{\mathrm{r}}(\phi_k,\phi_l) \tag{15}$$

where β^2 is the effective mean squared bandwidth of the pulse $p(t)$,

$$\mathrm{SINR}_{k,l} = w_{k,l}^2\frac{|\alpha_{k,l}|^2}{N_0} = \frac{|\alpha_{k,l}|^2}{N_0+T_pS_\nu(\tau_{k,l})} \tag{16}$$

is the signal-to-interference-plus-noise ratio of the k,l-th backscatter MPC and

$$\mathbf{J}_{\mathrm{r}}(\phi_k,\phi_l) = \begin{bmatrix}\mathrm{A}^2 & \mathrm{AB}\\ \mathrm{AB} & \mathrm{B}^2\end{bmatrix} \tag{17}$$

is the 2×2 ranging direction matrix accounting for the geometry, where $\mathrm{A} = \cos\phi_{k,\mathrm{TX}}+\cos\phi_{l,\mathrm{RX}}$ and $\mathrm{B} = \sin\phi_{k,\mathrm{TX}}+\sin\phi_{l,\mathrm{RX}}$. Note that (15) in general does not hold for backscatter channels with TR processing, due to additional generated overlap of signal paths.

This analytical result was comprehensively analyzed for the single-channel MINT scenario in [3]. There, the main findings which also are evident in (15) are the following: First, any increase of the effective bandwidth decreases the PEB. Second, each additional VA increases the EFIM and consequently decreases the PEB, and third, the gain of each VA is determined by the corresponding SINR.

D. Influence of TR Processing on the Position Error Bound

One impact of TR processing on the CRLB is that the weights $w_{k,l}$ accounting for the DM change according to the PDP $S_{\nu,\mathrm{TR}}$. Furthermore, TR processing influences the signal correlation function, which appears in the block matrices of the EFIM (c.f. appendix), the following way

$$\begin{aligned}\mathrm{R}_s(\tau_{k,l}-\tau_{k',l'}) &= \int_{-\infty}^{\infty} s(t-\tau_{k,l})s(t-\tau_{k',l'})\mathrm{d}t \\ &= \int_{-\infty}^{\infty}\sum_{m=1}^{\hat{K}_{\mathrm{TX}}}\sum_{m'=1}^{\hat{K}_{\mathrm{TX}}}\left|\hat{\alpha}_{m,\mathrm{TX}}\right|^2\left|\hat{\alpha}_{m',\mathrm{TX}}\right|^2 \\ &\qquad p(t-\tau_{k,l}+\hat{\tau}_{m,\mathrm{TX}})p(t-\tau_{k',l'}+\hat{\tau}_{m',\mathrm{TX}})\mathrm{d}t \\ &= \sum_{m=1}^{\hat{K}_{\mathrm{TX}}}\sum_{m'=1}^{\hat{K}_{\mathrm{TX}}}\left|\hat{\alpha}_{m,\mathrm{TX}}\right|^2\left|\hat{\alpha}_{m',\mathrm{TX}}\right|^2 \\ &\qquad \mathrm{R}_p((\tau_{k,l}-\hat{\tau}_{m,\mathrm{TX}})-(\tau_{k',l'}-\hat{\tau}_{m',\mathrm{TX}})).\end{aligned} \tag{18}$$

where $\mathrm{R}_p(\tau_{k,l}-\tau_{k',l'}) = \int_{-\infty}^{\infty}p(t-\tau_{k,l})p(t-\tau_{k',l'})\mathrm{d}t$ is the ACF of the transmitted pulse $p(t)$. Eq. (18) illustrates the additional generated path overlap by TR processing.

IV. Results

1) Simulation Setup: A computational analysis has been performed for the scenario illustrated in Fig. 1 for a target that moves along a trajectory consisting of 24 target positions. The TX radar node is located at position $\mathbf{p}_{1,\mathrm{TX}} = [8,\ 7.5]^{\mathrm{T}}$ and the RX radar node at position $\mathbf{p}_{1,\mathrm{RX}} = [2,\ 6]^{\mathrm{T}}$. Deterministic MPCs of the up- and down-link channels $h_{\mathrm{TX}}(\tau)$ and $h_{\mathrm{RX}}(\tau)$ have been generated using VAs for first- and second-order reflections and the LOS components. A similar path-loss model has been used for the MPC gain as in [3], assuming a carrier frequency of 7 GHz and adding 3 dB of attenuation for each reflection order. The transmitted pulse $p(t)$ is modeled

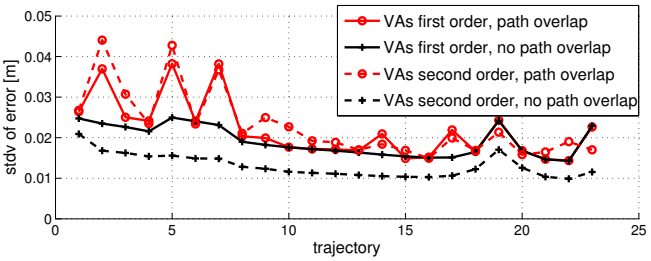

Fig. 3. PEB along a trajectory for backscatter channel for VA order 1 and 2, with and without path overlap, $T_p = 0.5$ ns.

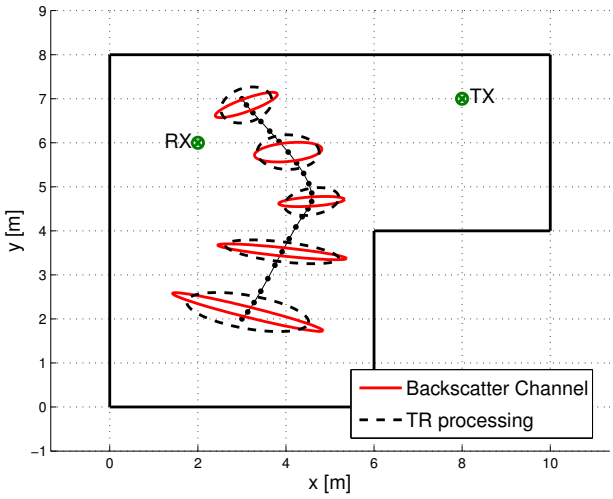

Fig. 4. Simulation scenario. Position error ellipses of the forty-fold standard deviation, $T_p = 0.5$ ns.

as root raised cosine pulse with roll-off factor $\beta_{\text{roll}} = 0.6$ and pulse duration of $T_p = 0.5$ ns corresponding to a bandwidth of 2 GHz. The PDPs of the diffuse part of both channels are modeled as double-exponential functions cf. [12, (9)]. Their parameters are the total power of the diffuse multipath $\Omega_1 = 1.16 \times 10^{-6}$, the decay time $\gamma_1 = 20$ ns, the rise time $\gamma_{\text{rise}} = 5$ ns and the shape parameter $\chi = 0.98$, which were kept fixed over the entire trajectory. However, due to the concatenation of the up- and down-link channels, the resulting PDP of the DM for the backscatter channel depends on the deterministic channel parts, and thus on the target position. The SNR of DM varies along the trajectory between 25 dB and 31 dB. The SINR of the LOS component at the first trajectory position $\mathbf{p} = [3, 2]$ is 21 dB for the backscatter channel and 15 dB for the backscatter channel with TR processing.

2) CRLB and Influence of TR Processing: We first analyze the CRLB for backscatter channels without TR processing. Due to the fact that in a backscatter channel more MPCs appear than in a conventional channel, path-overlap is more probable, which causes stronger degradation of the PEB. This is illustrated in Fig. 3, where the PEB is computed from the complete EFIM (14) and from the canonical form of the EFIM that neglects path-overlap. First-order reflections (solid lines) and second-order reflections (dashed lines) are analyzed. We

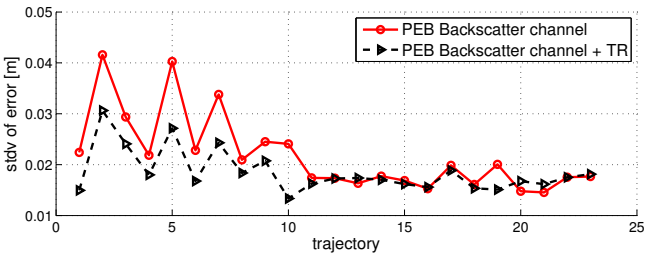

(a) LOS, VA order 1 for TR processing

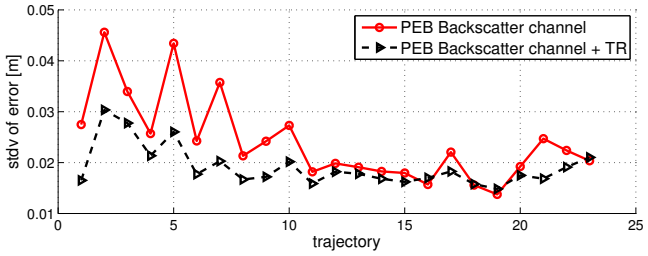

(b) NLOS, VA order 1 for TR processing

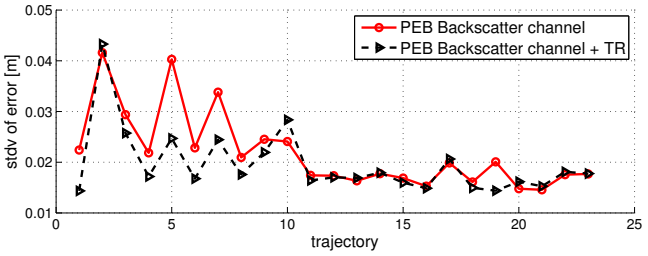

(c) LOS, VA order 2 for TR processing

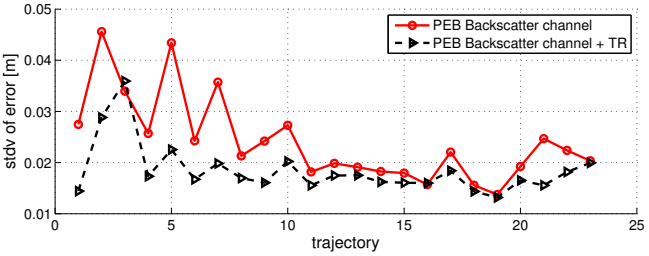

(d) NLOS, VA order 2 for TR processing

Fig. 5. PEB along a trajectory for LOS and NLOS scenarios with VA order of 1 for TR processing (path overlap considered), $T_p = 0.5$ ns.

can see that the PEB neglecting path overlap is decreased with increasing order of MPCs, since more information can be exploited. On the other hand, the PEB considering path-overlap is partly increased since path-overlap makes this information unusable.

Fig. 4 shows the impact of TR processing using VA order of 2. Position error ellipses are given in terms of the forty-fold standard deviation for several trajectory positions. Red (solid) stands for the backscatter channel alone and black (dashed) includes TR processing. One can first see that the error depends on the geometry. It is lower in the direction of the radar nodes, because MPCs from other directions are more

impaired by DM. An interesting fact is that TR processing partly levels this imbalance. It improves the information from reflected MPCs, while reducing information from the LOS component that gets affected by DM more significantly, due which is a fundamental requirement for a cognitive radar to gain control over the environment sensing in its perception-action cycle [13]. The overall PEB is decreased by TR processing for most positions, but the gain depends strongly on the geometry.

Figs. 5(a)-(d) show the PEB of the backscatter channel with TR processing along the trajectory for the LOS and NLOS cases (path overlap considered), where the latter means that the first component of the TX channel has been set to zero. Figs. 5(a) and (b) illustrate TR processing with MPCs coming from VAs of first-order. One can see that TR processing results in a performance gain, especially for NLOS scenarios. As Figs. 5(c) and (d) show, the inclusion of second-order reflections in TR parameter set does not automatically yields in a performance gain. This can be explained by the fact that the impairment of additional DM is higher than the gain caused by energy focusing. The results illustrate again that the performance gain through TR processing is strongly dependent on the geometry of the room.

V. Conclusions

Using a channel model that explicitly models the diffuse multipath, a unified likelihood model for the localization on backscatter channels has been introduced. The impact of TR processing can be evaluated as well. Results show the detrimental effect of path overlap and DM in backscatter channels. Using geometrically modeled deterministic MPCs for TR processing does not automatically imply large performance gains. The special structure of DM in the backscatter channel suggest a careful usage of a subset of the uplink paths for TR, which is supported by our derivations and results. TR processing yields a closed control loop for optimal sensing of the environment as it is required in a cognitive radar system. The CRLB can be used as feedback information as it quantifies the performance gain.

Appendix

A. Derivation of the Subblocks of the FIM

The FIM $\mathbf{J}(\boldsymbol{\psi})$ of the transformed parameter vector $\boldsymbol{\psi} = \left[\tau^{\mathrm{T}}\ (\boldsymbol{\alpha}^{\mathrm{R}})^{\mathrm{T}}\ (\boldsymbol{\alpha}^{\mathrm{I}})^{\mathrm{T}}\right]^{\mathrm{T}}$ can be calculated from (9) the following way

$$\mathbf{J}(\boldsymbol{\psi}) = \begin{bmatrix} \boldsymbol{\Lambda}_{\mathrm{A}} & \boldsymbol{\Lambda}_{\mathrm{B}}^{\mathrm{R}} & \boldsymbol{\Lambda}_{\mathrm{B}}^{\mathrm{I}} \\ (\boldsymbol{\Lambda}_{\mathrm{B}}^{\mathrm{R}})^{\mathrm{T}} & \boldsymbol{\Lambda}_{\mathrm{C}}' & \boldsymbol{\Lambda}_{\mathrm{C}}'' \\ (\boldsymbol{\Lambda}_{\mathrm{B}}^{\mathrm{I}})^{\mathrm{T}} & \boldsymbol{\Lambda}_{\mathrm{C}}'' & \boldsymbol{\Lambda}_{\mathrm{C}}' \end{bmatrix}_{3K_{\mathrm{TX}}K_{\mathrm{RX}} \times 3K_{\mathrm{TX}}K_{\mathrm{RX}}} \tag{19}$$

where $\boldsymbol{\Lambda}_{\mathrm{B}} = [\boldsymbol{\Lambda}_{\mathrm{B}}^{\mathrm{R}}\ \boldsymbol{\Lambda}_{\mathrm{B}}^{\mathrm{I}}]$ and $\boldsymbol{\Lambda}_{\mathrm{C}} = [\boldsymbol{\Lambda}_{\mathrm{C}}'\ \boldsymbol{\Lambda}_{\mathrm{C}}''; \boldsymbol{\Lambda}_{\mathrm{C}}''\ \boldsymbol{\Lambda}_{\mathrm{C}}']$. The sub-blocks are derived as

$$\begin{aligned}
[\boldsymbol{\Lambda}_{\mathrm{A}}]_{kl,k'l'} &= \mathbb{E}_{\mathbf{r}|\boldsymbol{\psi}}\left\{\frac{\partial^2 \ln \mathrm{p}(\mathbf{r}|\boldsymbol{\psi})}{\partial\tau_{k,l}\partial\tau_{k',l'}}\right\} \\
&= \frac{2}{N_0} w_{k,l} w_{k',l'} \Re\left\{\alpha_{k,l}\alpha_{k',l'}^{*} \frac{\partial^2 \mathrm{R}_s(\tau_{k,l}-\tau_{k',l'})}{\partial\tau_{k,l}\partial\tau_{k',l'}}\right\} \\
[\boldsymbol{\Lambda}_{\mathrm{B}}^{\mathrm{R}}]_{kl,k'l'} &= \mathbb{E}_{\mathbf{r}|\boldsymbol{\psi}}\left\{\frac{\partial^2 \ln \mathrm{p}(\mathbf{r}|\boldsymbol{\psi})}{\partial\tau_{k,l}\partial\alpha_{k',l'}^{\mathrm{R}}}\right\} \\
&= \frac{2}{N_0} w_{k,l} w_{k',l'} \Re\left\{\alpha_{k,l} \frac{\partial \mathrm{R}_s(\tau_{k,l}-\tau_{k',l'})}{\partial\tau_{k,l}}\right\} \\
[\boldsymbol{\Lambda}_{\mathrm{B}}^{\mathrm{I}}]_{kl,k'l'} &= \mathbb{E}_{\mathbf{r}|\boldsymbol{\psi}}\left\{\frac{\partial^2 \ln \mathrm{p}(\mathbf{r}|\boldsymbol{\psi})}{\partial\tau_{k,l}\partial\alpha_{k',l'}^{\mathrm{I}}}\right\} \\
&= \frac{2}{N_0} w_{k,l} w_{k',l'} \Im\left\{\alpha_{k,l} \frac{\partial \mathrm{R}_s(\tau_{k,l}-\tau_{k',l'})}{\partial\tau_{k,l}}\right\} \\
[\boldsymbol{\Lambda}_{\mathrm{C}}']_{kl,k'l'} &= \mathbb{E}_{\mathbf{r}|\boldsymbol{\psi}}\left\{\frac{\partial^2 \ln \mathrm{p}(\mathbf{r}|\boldsymbol{\psi})}{\partial\alpha_{k,l}^{\mathrm{R}}\partial\alpha_{k',l'}^{\mathrm{R}}}\right\} = \mathbb{E}_{\mathbf{r}|\boldsymbol{\psi}}\left\{\frac{\partial^2 \ln \mathrm{p}(\mathbf{r}|\boldsymbol{\psi})}{\partial\alpha_{k,l}^{\mathrm{I}}\partial\alpha_{k',l'}^{\mathrm{I}}}\right\} \\
&= \frac{2}{N_0} w_{k,l} w_{k',l'} \Re\left\{\mathrm{R}_s(\tau_{k,l}-\tau_{k',l'})\right\} \\
[\boldsymbol{\Lambda}_{\mathrm{C}}'']_{kl,k'l'} &= \mathbb{E}_{\mathbf{r}|\boldsymbol{\psi}}\left\{\frac{\partial^2 \ln \mathrm{p}(\mathbf{r}|\boldsymbol{\psi})}{\partial\alpha_{k,l}^{\mathrm{R}}\partial\alpha_{k',l'}^{\mathrm{I}}}\right\} \\
&= \frac{2}{N_0} w_{k,l} w_{k',l'} \Im\left\{\mathrm{R}_s(\tau_{k,l}-\tau_{k',l'})\right\}
\end{aligned}$$

where $\mathrm{R}_s(\tau_{k,l}-\tau_{k',l'}) = \int_{-\infty}^{\infty} s(t-\tau_{k,l})s(t-\tau_{k',l'})\mathrm{d}t$ is the signal correlation function.

References

[1] Y. Shen and M. Win, "Fundamental limits of wideband localization; part I: A general framework," *Information Theory, IEEE Transactions on*, vol. 56, no. 10, pp. 4956 –4980, Oct. 2010.

[2] H. Godrich, V. Chiriac, A. Haimovich, and R. Blum, "Target tracking in mimo radar systems: Techniques and performance analysis," in *Radar Conference, 2010 IEEE*, 2010, pp. 1111–1116.

[3] K. Witrisal and P. Meissner, "Performance bounds for multipath-assisted indoor navigation and tracking (MINT)," in *Communications (ICC), 2012 IEEE International Conference on*, June 2012, pp. 4321 –4325.

[4] P. Meissner and K. Witrisal, "Analysis of position-related information in measured UWB indoor channels," in *Antennas and Propagation (EUCAP), 2012 6th European Conference on*, March 2012, pp. 6 –10.

[5] P. Meissner, E. Leitinger, M. Froehle, and K. Witrisal, "Accurate and robust indoor localization systems using ultra-wideband signals," in *European Conference on Navigation (ENC)*, Vienna, 2013.

[6] D. Arnitz, U. Muehlmann, and K. Witrisal, "Wideband characterization of backscatter channels: Derivations and theoretical background," *Antennas and Propagation, IEEE Transactions on*, vol. 60, no. 1, pp. 257 –266, Jan. 2012.

[7] T. Strohmer, M. Emami, J. Hansen, G. Papanicolaou, and A. Paulraj, "Application of time-reversal with mmse equalizer to UWB communications," in *Global Telecommunications Conference, 2004. GLOBECOM '04. IEEE*, vol. 5, Nov. 2004, pp. 3123 – 3127 Vol.5.

[8] N. Guo, B. Sadler, and R. Qiu, "Reduced-complexity uwb time-reversal techniques and experimental results," *Wireless Communications, IEEE Transactions on*, vol. 6, no. 12, pp. 4221 –4226, Dec. 2007.

[9] K. Witrisal, E. Leitinger, P. Meissner, and D. Arnitz, "Cognitive radar for the localization of RFID transponders in dense multipath environments," in *Radar (RadarCon), 2013 IEEE International Conference on*, April 2013.

[10] A. Molisch, "Ultra-wide-band propagation channels," *Proceedings of the IEEE*, vol. 97, no. 2, pp. 353 –371, Feb. 2009.

[11] H. L. Van Trees, *Detection, Estimation and Modulation, Part I.* Wiley Press, 1968.

[12] J. Karedal, S. Wyne, P. Almers, F. Tufvesson, and A. Molisch, "A measurement-based statistical model for industrial ultra-wideband channels," *Wireless Communications, IEEE Transactions on*, vol. 6, no. 8, pp. 3028–3037, Aug.

[13] S. Haykin, Y. Xue, and P. Setoodeh, "Cognitive radar: Step toward bridging the gap between neuroscience and engineering," *Proceedings of the IEEE*, vol. 100, no. 11, pp. 3102 –3130, nov. 2012.

Cooperative Multipath-Assisted Indoor Navigation and Tracking (Co-MINT) Using UWB Signals

Markus Froehle, Erik Leitinger, Paul Meissner, and Klaus Witrisal
Graz University of Technology, Austria.
Email: {froehle, erik.leitinger, paul.meissner, witrisal}@tugraz.at

***Abstract*—In multipath-assisted indoor navigation and tracking (MINT), explicit use is made of multipath propagation in the ultra-wideband channel. With the help of floorplan information, localization is possible with only one reference node. In this work, we introduce MINT among cooperating users in order to omit the need of any known reference nodes. The received signal is modeled as a combination of deterministic multipath components, diffuse multipath represented by a random process and AWGN. In a mixed line-of-sight (LOS)/non-LOS (NLOS) indoor scenario, we show how information from mono-static and bi-static measurements of cooperating users can be merged for localization and tracking. The problem is formulated with a factor graph and solved via belief propagation on the factor graph. Simulation results show that localization and tracking of a mobile agent is possible: (i) independent of LOS or NLOS, (ii) without the need for further infrastructure.**

I. Introduction

Ultra-wideband (UWB) signals are of special interest for indoor localization. Their large available frequency range offers a fine delay resolution and robustness w.r.t. propagation conditions in harsh environments [1], [2], [3]. In indoor environments multipath propagation is prevalent. The benefit of the UWB channel is that many of the multipath components (MPCs) are recognizable and resolvable in the measurements. This is especially important in dense indoor environments.
Many traditional localization methods rely on tri- or multilateration of at least three known reference anchors to infer the position of a mobile agent. This works well in line-of-sight (LOS) situations. To cope with non-LOS (NLOS) situations between anchor and agent, methods for either NLOS detection or NLOS mitigation have been developed, e.g. [4]. The first approach allows to discard NLOS measurements while the second one is used to mitigate the NLOS-induced range bias. However, both methods make no use of the geometric structure and the position-related information of MPCs [5], [6].
In [7], cooperation between mobile agents (MS) allows to determine the user's position in situations where the number of visible anchors is less than three. With this, the position estimate is updated with measurements to neighbor mobile nodes within communication range. In [8], we have explicitly made use of the multipath propagation in the UWB channel. This allows to reduce the number of known reference anchors to one with the help of a-priori known floorplan information. Signals that are reflected at e.g. a wall, can be seen as being emitted by a virtual source located behind the reflecting surface [5]. The floor plan allows to associate this virtual source to a known so-called virtual anchor (VA) for localization. In Fig. 1, the position of an anchor node marked

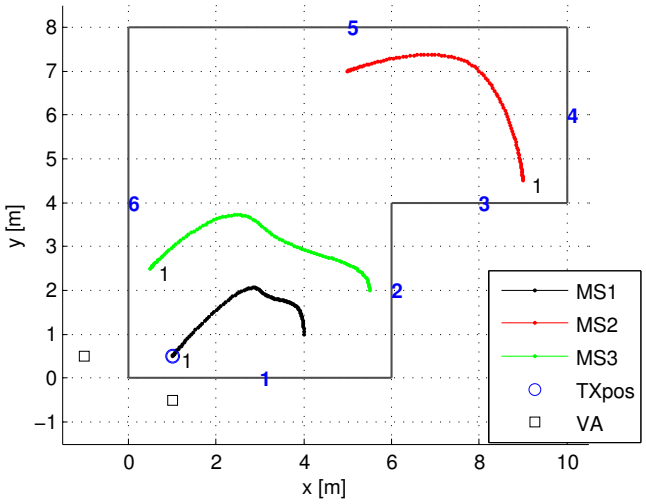

Fig. 1. Floorplan with trajectories of $I = 3$ mobile stations (MSs). The trajectories have a length of 100 time-steps each. The virtual anchors (VAs) of the first-order specular reflections at the wall segments no. 1 and 6 are illustrated for a transmitter located at TXpos.

with TXpos is shown together with its corresponding VAs for walls no. 1 and 6. The usage of VAs for localization allows to determine the position of a target with only one physical anchor node [8]. This approach of localization has been called multipath-assisted indoor navigation and tracking (MINT) [6]. In addition to the MINT approach, cooperation among users was introduced in [9] to overcome the problem of a multimodal likelihood due to data-association ambiguities. Distance measurements between cooperating users are employed additionally to non-cooperative MINT measurements to a known anchor node.

In this paper, we consider an anchor-less two-phase cooperative localization scenario. In the first phase, each mobile performs mono-static measurements. In this *mono-static* measurement setup, the mobile is both transmitter (TX) and receiver (RX). Localization with only this type of measurements alone would not be possible due to ambiguities in the likelihood-function caused by the room geometry. In the second phase, each mobile performs cooperative measurements with its neighbors which are within communication range. In this *bi-static* measurement setup, the neighbor node acts as TX for the RX node. Cooperative measurements are useful only if the TX position is known. Hypotheses for this are taken from the mono-static measurement. It is therefore possible to de-

termine the position of each cooperating mobile node without the help of a known reference anchor. The contributions of this work are:

- Anchor-less indoor localization of mobile users. Floor-plan information is the only prior knowledge used.
- Non-cooperative mono- and cooperative bi-static measurements are combined using a statistical model.
- An algorithm for cooperative localization and tracking of mobile users, e.g. emergency personnel, is presented and its performance is evaluated.

The remainder of the paper is structured as follows: A statistical description of the localization approach is given in Section II, the system model is given in Section III, and Section IV describes the localization algorithm. Finally, Section V is devoted to the simulation results.

II. Statistical Description

The state of the i-th mobile station (MS) at time-step k is denoted as $\mathbf{x}_k^i = [(\mathbf{p}_k^i)^{\mathrm{T}}, (\mathbf{v}_k^i)^{\mathrm{T}}]^{\mathrm{T}}$ with position $\mathbf{p}_k^i = [\mathrm{p}_{\mathrm{x},k}^i, \mathrm{p}_{\mathrm{y},k}^i]^{\mathrm{T}}$ and velocity $\mathbf{v}_k^i = [\mathrm{v}_{\mathrm{x},k}^i, \mathrm{v}_{\mathrm{y},k}^i]^{\mathrm{T}}$. Our goal is to infer the state $\mathbf{x}_k^i$ of all MSs $i = 1, \ldots, I$ in time-step k, given all past and current self (mono-static) measurements $\mathbf{z}_{\mathrm{self},1:k} = [(\mathbf{z}_{\mathrm{self},1}^1)^{\mathrm{T}}, \ldots, (\mathbf{z}_{\mathrm{self},1}^I)^{\mathrm{T}}, \ldots, (\mathbf{z}_{\mathrm{self},k}^I)^{\mathrm{T}}]^{\mathrm{T}}$ and all past and current relative (bi-static) measurements $\mathbf{z}_{\mathrm{rel},1:k} = [(\mathbf{z}_{\mathrm{rel},1}^{1,1})^{\mathrm{T}}, \ldots, (\mathbf{z}_{\mathrm{rel},1}^{1,J_1(1)})^{\mathrm{T}}, \ldots, (\mathbf{z}_{\mathrm{rel},1}^{I,J_1(I)})^{\mathrm{T}}, \ldots, (\mathbf{z}_{\mathrm{rel},k}^{I,J_k(I)})^{\mathrm{T}}]^{\mathrm{T}}$, where $J_k(i)$ is the number of cooperating MSs for the i-th MS at time-step k. Similarly, we stack the individual states $\mathbf{x}_k^i$ of all MS into one state vector $\mathbf{x}_k = [(\mathbf{x}_k^1)^{\mathrm{T}}, \ldots, (\mathbf{x}_k^I)^{\mathrm{T}}]^{\mathrm{T}}$. The posterior PDF of the system state $\mathbf{x}_{k-1}$ at time-step $k-1$ is given by $p(\mathbf{x}_{k-1}|\mathbf{z}_{\mathrm{self},1:k-1}, \mathbf{z}_{\mathrm{rel},1:k-1})$. Predicting it to the next time-step k yields the prior PDF [10], [11]

$$p(\mathbf{x}_k|\mathbf{z}_{\mathrm{self},1:k-1}, \mathbf{z}_{\mathrm{rel},1:k-1}) = \int p(\mathbf{x}_k|\mathbf{x}_{k-1}) p(\mathbf{x}_{k-1}|\mathbf{z}_{\mathrm{self},1:k-1}, \mathbf{z}_{\mathrm{rel},1:k-1}) d\mathbf{x}_{k-1}, \quad (1)$$

where the assumption of a first order Markov process $p(\mathbf{x}_k|\mathbf{x}_{k-1:1}) = p(\mathbf{x}_k|\mathbf{x}_{k-1})$ is made. The update of the prior PDF with the measurement received at time-index k yields the posterior PDF and is calculated using Bayes' rule

$$p(\mathbf{x}_k|\mathbf{z}_{\mathrm{self},1:k}, \mathbf{z}_{\mathrm{rel},1:k}) \propto p(\mathbf{z}_{\mathrm{self},k}, \mathbf{z}_{\mathrm{rel},k}|\mathbf{x}_k) p(\mathbf{x}_k|\mathbf{z}_{\mathrm{self},1:k-1}, \mathbf{z}_{\mathrm{rel},1:k-1}). \quad (2)$$

We assume self and relative measurements to be independent of each other conditioned on the state:

$$p(\mathbf{z}_{\mathrm{self},k}, \mathbf{z}_{\mathrm{rel},k}|\mathbf{x}_k) = p(\mathbf{z}_{\mathrm{self},k}|\mathbf{x}_k) p(\mathbf{z}_{\mathrm{rel},k}|\mathbf{x}_k). \quad (3)$$

Further, we assume that the states of the mobiles and their measurements are independent, which are similar assumptions as in [7]. Then, the posterior PDF can be factorized using (1) and (3) with (2) into

$$p(\mathbf{x}_k|\mathbf{z}_{\mathrm{self},1:k}, \mathbf{z}_{\mathrm{rel},1:k}) \propto \prod_{i=1}^{I} p(\mathbf{z}_{\mathrm{self},k}^i|\mathbf{x}_k^i) \prod_{j \in \mathcal{N}_{\to i}} p(\mathbf{z}_{\mathrm{rel},k}^{i,j}|\mathbf{x}_k^i, \mathbf{x}_k^j) \int p(\mathbf{x}_k^i|\mathbf{x}_{k-1}^i) p(\mathbf{x}_{k-1}^i|\mathbf{z}_{\mathrm{self},1:k-1}^i, \mathbf{z}_{\mathrm{rel},1:k-1}^{i,j}) d\mathbf{x}_{k-1}^i, \quad (4)$$

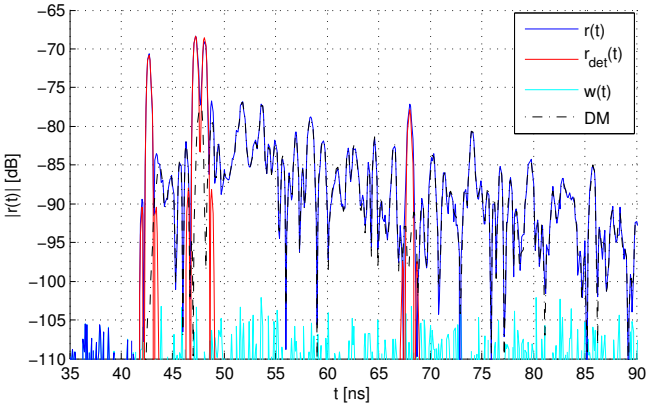

Fig. 2. Example of the received UWB signal $r(t)$ generated with (5). The deterministic multipath, which corresponds to the template signal $\hat{r}_{\mathrm{det}}(t)$, is superimposed by diffuse multipath (DM) and AWGN noise $w(t)$.

where $\mathcal{N}_{\to i}$ denotes the set of all neighbors of agent $\mathbf{x}_k^i$ within communication range. The following observations can be made: (i) (2) describes a recursive propagation of the posterior PDF; (ii) the predicted system state is updated by the self measurements $\mathbf{z}_{\mathrm{self},k}$ and the cooperative measurements $\mathbf{z}_{\mathrm{rel},k}$; (iii) the posterior PDF contains all I nodes.

III. System Model

Similar to [6], we assume a base-band signal $s(t)$ being transmitted from the TX located at $\mathbf{p}_1$. Due to multipath propagation, it experiences scattering and reflection by the environment, where deterministic reflections are mapped to VAs located at $\{\mathbf{p}_l\}, l = 2, \ldots, L$. The receiver located at $\mathbf{p}$ receives the signal

$$r(t) = \sum_{l=1}^{L} \alpha_l s(t - \tau_l) + \int_{-\infty}^{\infty} s(\lambda) \nu(t - \lambda) d\lambda + w(t), \quad (5)$$

where the first term considers deterministic MPCs. The transmitted signal $s(t)$ is scaled by the complex gains $\alpha_l \in \mathbb{C}$ and delayed by $\tau_l = \frac{1}{c}||\mathbf{p} - \mathbf{p}_l||$ on each transmission path $l = 1, \ldots, L$. The propagation velocity is denoted by c. The second term in (5) models diffuse multipath (DM). It is described as a stochastic process $\nu(t)$ convolved with the transmitted signal $s(t)$ [6]. It is characterized by the auto correlation function $E\{\nu(\tau)\nu^*(u)\} = S_\nu(\tau)\delta(\tau - u)$ with power delay profile $S_\nu(\tau)$. Finally, $w(t)$ denotes AWGN with double-sided power spectral density (PSD) of $N_0/2$. An example of the received UWB signal generated with the system model (5) is shown in Fig. 2.

A. Measurement Model: State-measurement Likelihood

Assume we have an ideal noise and DM-free template signal $\hat{r}_{\mathrm{det}}(t)$. It can be constructed based on the positions of the L VA locations $\{\mathbf{p}_l\}$, $l = 1, \ldots, L$, the receiver position $\mathbf{p}$, and the known geometry,

$$\hat{r}_{\mathrm{det}}(t) = \sum_{l=1}^{L} A(\tau_l) \exp(-j2\pi f_c \tau_l) s(t - \tau_l), \quad (6)$$

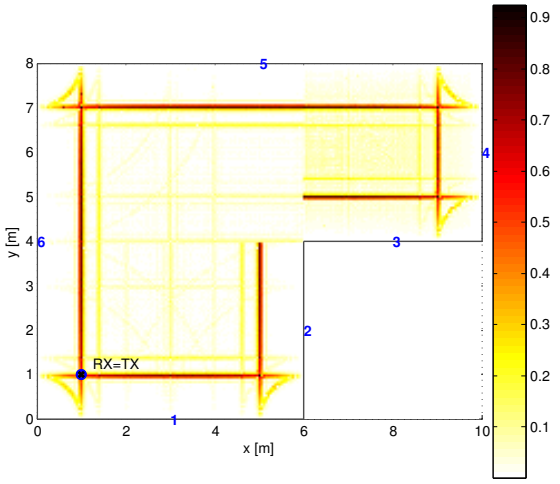

Fig. 3. Mono-static state-measurement log-likelihood according to (8). TX and RX are co-located. Specular reflections up to the second order have been considered. The distance between the wall and the likelihood peaks parallel to the walls corresponds with the path-length of the strongest MPC.

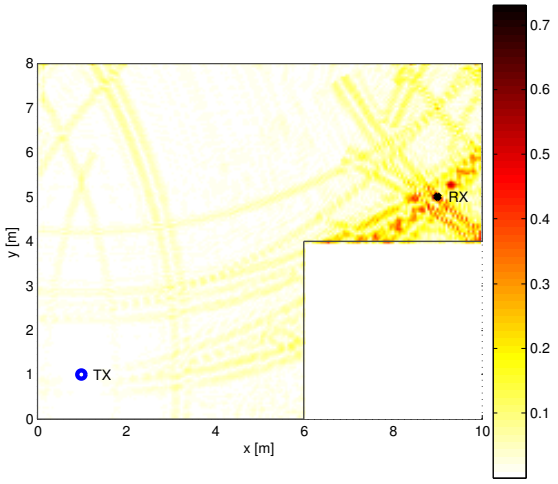

Fig. 4. Bi-static state-measurement log-likelihood according to (8). TX and RX are placed such that a NLOS condition is present. Specular reflections up to the second order have been considered. The highest likelihood is located at the RX position. In the surrounding area are still some high valued peaks due to symmetries caused by the room geometry.

where $A(\tau_l)$ denotes the signal attenuation described by a path-loss model and f_c denotes the carrier frequency of the transmitted signal $s(t)$. With the signal model in (5) and the known template signal (6) we can state a standard AWGN likelihood function (LHF) [12]

$$p(\mathbf{z}|\mathbf{x}) \propto \exp\left\{-\frac{1}{N_0}\int_0^{T_0} |r(t) - \hat{r}_{\mathrm{det}}(t)|^2\, dt\right\}, \qquad (7)$$

where the measurement vector $\mathbf{z}$ represents the received signal $r(t)$. The template signal $\hat{r}_{\mathrm{det}}(t)$ is constructed according to (6) using the state vector $\mathbf{x}$ and the known floorplan information. To properly account for DM present in (5), we would need to incorporate the signal-to-noise-plus-interference ratio (SINR) of the deterministic MPCs into (7), cf. with [6]. However, for the sake of simplicity, we use in this work a heuristic correlation metric to describe the likelihood between state and measurement. It has the form

$$p(\mathbf{z}|\mathbf{x}) \propto \exp\left\{\left|\left\langle \frac{r(t)}{||r(t)||}, \frac{\hat{r}_{\mathrm{det}}(t)}{||\hat{r}_{\mathrm{det}}(t)||}\right\rangle\right|\right\}, \qquad (8)$$

where $\langle\cdot,\cdot\rangle$ denotes the dot product and $||\cdot||$ is the norm. With the metric in (8) neither DM nor the SNR is accounted for. Future work will consider this by incorporating the LHF of [6] in order to model both of them.

In our case, there are two types of measurements $\mathbf{z}^i_{\mathrm{self},k}$ and $\mathbf{z}^{i,j}_{\mathrm{rel},k}$. We use the same LHF for both of them. They differ only in how the template signal $\hat{r}_{\mathrm{det}}(t)$ is constructed. For $\mathbf{z}^i_{\mathrm{self},k}$, only the local MS state $\mathbf{x}^i_k$ is needed, whereas for $\mathbf{z}^{i,j}_{\mathrm{rel},k}$ both involved MS states $\mathbf{x}^i_k$ and $\mathbf{x}^j_k$ are needed. Next, we take a closer look on the individual LHFs.

1) Mono-static Measurement Likelihood: In the mono-static case, the mobile at position $\mathbf{p}$ is both TX and RX. The likelihood $p(\mathbf{z}^i_{\mathrm{self},k}|\mathbf{x}^i_k)$ only depends on the current state $\mathbf{x}^i_k$. In Fig. 3, the log-likelihood for a received measurement $\mathbf{z}^i_{\mathrm{self},k}$ at $\mathbf{p} = [1,1]^{\mathrm{T}}$ is plotted over the whole room. The LOS, first and second-order VAs are considered. The likelihood does not have one significant global maximum. Rather it has a ridge parallel to the walls. The distance from the wall to the ridge corresponds to the path-length of the strongest deterministic MPC present in $\mathbf{z}^i_{\mathrm{self},k}$. Seeing this, it becomes obvious that localization with this measurement likelihood alone will fail, because of its ambiguities parallel to the walls. Despite this it provides us with a high resolution in the direction perpendicular to the walls.

2) Bi-static Measurement Likelihood: In the bi-static case, one MS acts as TX, whereas the other cooperating MS acts as RX. The likelihood $p(\mathbf{z}^{i,j}_{\mathrm{rel},k}|\mathbf{x}^i_k, \mathbf{x}^j_k)$ depends on the states of both involved mobile nodes, the receiver node $\mathbf{x}^i_k$ and the transmitter node $\mathbf{x}^j_k$. In Fig. 4, the log-likelihood is plotted. The TX is located at $\mathbf{p}_1 = [1,1]^{\mathrm{T}}$ and the RX at $\mathbf{p} = [9,5]^{\mathrm{T}}$. VAs up to the second order have been considered. In this NLOS scenario, the global maximum is correctly located at the position of the RX. Due to geometric ambiguities, there are areas with high likelihood in the neighborhood of the RX position. The combination of all mono- and bi-static measurements in the likelihood yields the joint likelihood given in (3).

B. State Propagation Model

We use a simple constant-velocity state propagation model to predict the target state in the next time-step

$$p(\mathbf{x}^i_k|\mathbf{x}^i_{k-1}) = \mathcal{N}(\mathbf{x}^i_k; \mathbf{F}\mathbf{x}^i_{k-1}, \sigma_a^2\mathbf{G}\mathbf{G}^{\mathrm{T}}) \qquad (9)$$

With

$$\mathbf{F} = \begin{bmatrix} 1 & 0 & \Delta T & 0 \\ 0 & 1 & 0 & \Delta T \\ 0 & 0 & 1 & 0 \\ 0 & 0 & 0 & 1 \end{bmatrix} \qquad (10)$$

and

$$\mathbf{G} = \begin{bmatrix} \frac{\Delta T^2}{2} & 0 \\ 0 & \frac{\Delta T^2}{2} \\ \Delta T & 0 \\ 0 & \Delta T \end{bmatrix}, \qquad (11)$$

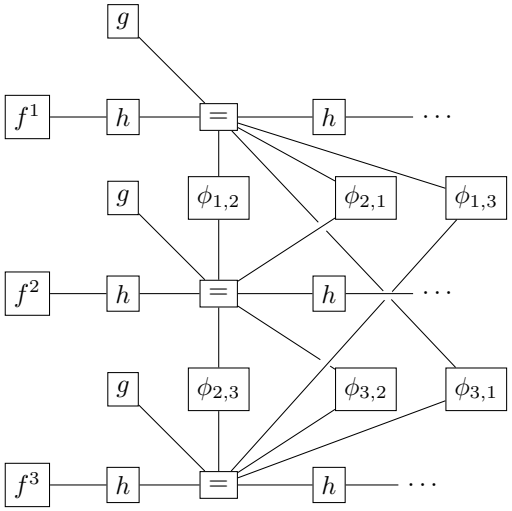

Fig. 5. Factor-graph of $p(\mathbf{x}_1|\mathbf{z}_{\text{self},1}, \mathbf{z}_{\text{rel},1})$ with abbreviations: $f^i(\mathbf{x}_0^i) = p(\mathbf{x}_0^i)$, $h(\mathbf{x}_{k-1}^i, \mathbf{x}_k^i) = p(\mathbf{x}_k^i|\mathbf{x}_{k-1}^i)$, $\phi_{i,j}(\mathbf{x}_k^i, \mathbf{x}_k^j) = p(\mathbf{z}_{\text{rel},k}^{i,j}|\mathbf{x}_k^i, \mathbf{x}_k^j)$, and $g(\mathbf{x}_k^i) = p(\mathbf{z}_{\text{self},k}^i|\mathbf{x}_k^i)$.

where $\mathcal{N}(\cdot; \mu, \Sigma)$ denotes a Normal distribution with mean μ and covariance matrix Σ. σ_a is the standard deviation of acceleration and ΔT is the time between two successive measurements.

IV. Localization Algorithm

A. Factor Graph Representation

The graphical model of (4) is illustrated in Fig. 5 for the first two time-steps with $I = 3$ MSs. Edges represent random variables, whereas squares represent factors. In the first time-step the prior of the i-th MS is given by the factor $f^i(\mathbf{x}_0^i)$. The factor $h(\mathbf{x}_{k-1}^i, \mathbf{x}_k^i)$ connects the state $\mathbf{x}_{k-1}^i$ with the state $\mathbf{x}_k^i$ via the underlying state-propagation model. The factors of the mono-static measurement $g(\mathbf{x}_k^i)$ and the bi-static measurement $\phi_{i,j}(\mathbf{x}_k^i, \mathbf{x}_k^j)$ are connected via an edge corresponding to state $\mathbf{x}_k^i$. To infer the posterior PDF on a cycle free FG the sum-product-algorithm (SPA) is used [10]. In our case, the FG has cycles and approximate inference methods, such as loopy belief propagation (BP), need to be used [7]. Then, the posterior PDF, given by (4), is represented by beliefs which are approximations of the exact posterior PDF $b_{\mathbf{X}_k}(\mathbf{x}_k) \approx p(\mathbf{x}_k|\mathbf{z}_{\text{self},1:k}, \mathbf{z}_{\text{rel},1:k})$.

B. Implementation

We used a particle-based implementation of belief propagation, also known as non-parametric BP [13]. Therefore, we adapted the SPAWN algorithm of [7] to the cooperative MINT indoor localization scenario. This is outlined in Algorithm 1. In contrast to [7] and [14], the non-cooperative state-measurement likelihood $p(\mathbf{z}_{\text{self},k}^i|\mathbf{x}_k^i)$ depends only on the current state $\mathbf{x}_k^i$ and not also on the previous state $\mathbf{x}_{k-1}^i$. Additionally, we consider the whole received signal in the measurement vector $\mathbf{z}_k$ and not only an extracted distance estimate from the LOS path. The initialization step sets the belief of the own state equal to the prior PDF using M particles with weights $w_0^{i,m}$. Then, for all K time-steps a non-cooperative and a

Algorithm 1 Cooperative MINT

initialization:

$m_{\mathbf{X}_0^i \to h}(\mathbf{x}_0^i) = f^i(\mathbf{x}_0^i) = \left\{w_0^{i,m}, \mathbf{x}_0^{i,m}\right\}_{m=1}^{M}, i = 1, \ldots, I$

for $k = 1, \ldots, K$ **do**

  non-cooperative part: ▷ prediction operation

  for $i = 1, \ldots, I$ **do** ▷ use (9)

$$m_{h \to \mathbf{X}_k^i}(\mathbf{x}_k^i) = \int h(\mathbf{x}_k^i, \mathbf{x}_{k-1}^i) m_{\mathbf{X}_k^i \to h}(\mathbf{x}_{k-1}^i) d\mathbf{x}_{k-1}^i \tag{12}$$

    $m_{g \to \mathbf{X}_k^i}(\mathbf{x}_k^i) = g(\mathbf{x}_k^i)$ ▷ non-cooperative belief

    set: $b_{\mathbf{X}_k^i}^0(\mathbf{x}_k^i) \propto m_{g \to \mathbf{X}_k^i}(\mathbf{x}_k^i) m_{h \to \mathbf{X}_k^i}(\mathbf{x}_k^i)$

  end for

  cooperative part: ▷ correction operation

  for $l = 1, \ldots, N_{\text{iter}}; i = 1, \ldots, I; j \in \mathcal{N}_{\to i}$ **do**

    broadcast own belief: $b_{\mathbf{X}_k^i}^{l-1}(\mathbf{x}_k^i)$

    receive neighbor belief: $b_{\mathbf{X}_k^j}^{l-1}(\mathbf{x}_k^j)$

    compute message from cooperation:

$$m_{\phi_{i,j} \to \mathbf{X}_k^i}(\mathbf{x}_k^i) \propto \int \phi_{i,j}(\mathbf{x}_k^i, \mathbf{x}_k^j) b_{\mathbf{X}_k^j}^{l-1}(\mathbf{x}_k^j) d\mathbf{x}_k^j \approx \phi_{i,j}(\mathbf{x}_k^i, \overline{\mathbf{x}}_k^j) \tag{13}$$

    with the sample mean: ▷ set TX position to $\overline{\mathbf{x}}_k^j$

$$\overline{\mathbf{x}}_k^j = \sum_{m=1}^{M} w_{k,l}^{j,m} \mathbf{x}_k^{j,m} \tag{14}$$

    update own belief:

$$b_{\mathbf{X}_k^i}^l(\mathbf{x}_k^i) \propto m_{g \to \mathbf{X}_k^i}(\mathbf{x}_k^i) m_{h \to \mathbf{X}_k^i}(\mathbf{x}_k^i) \prod_{j \in \mathcal{N}_{\to i}} m_{\phi_{i,j} \to \mathbf{X}_k^i}(\mathbf{x}_k^i) \tag{15}$$

  end for

  determine outgoing message:

$$m_{\mathbf{X}_k^i \to h}(\mathbf{x}_k^i) = b_{\mathbf{X}_k^i}^{N_{\text{iter}}}(\mathbf{x}_k^i) = \left\{w_{k,N_{\text{iter}}}^{i,m}, \mathbf{x}_k^{i,m}\right\}_{m=1}^{M} \tag{16}$$

  normalize and re-sample to get:

$$m_{\mathbf{X}_k^i \to h}(\mathbf{x}_k^i) = \left\{\frac{1}{M}, \mathbf{x}_k^{i,m}\right\}_{m=1}^{M} \tag{17}$$

  report: $\hat{\mathbf{x}}_k^i = \overline{\mathbf{x}}_k^i$ ▷ sample mean to extract MS state

end for

cooperative belief update is performed. In the non-cooperative part the time-propagation of state $\mathbf{x}_{k-1}^i$ to $\mathbf{x}_k^i$ is performed via the state-propagation model $h(\cdot, \cdot)$. Based on the new state $\mathbf{x}_k^i$ the outgoing message from $m_{g \to \mathbf{X}_k^i}(\mathbf{x}_k^i)$ is computed. There, the mono-static measurement $\mathbf{z}_{\text{self},k}^i$ is used. Next, the cooperative part is performed. The own belief is initialized with the product of the messages from state prediction and the non-cooperative correction. This belief is updated with the messages received from the neighbors in an iterative manner. Therefore, the own belief is broadcast to the neighbors. The received belief $b_{\mathbf{X}_k^j}^{l-1}(\mathbf{x}_k^j)$ represents the PDF of the TX position. For computing complexity reasons, we estimate only one TX position out of $b_{\mathbf{X}_k^j}^{l-1}(\mathbf{x}_k^j)$ by taking its sample mean $\overline{\mathbf{x}}_k^j$. Future work needs to address this simplification in order to benefit

from the whole received information through cooperation. The mean $\overline{\mathbf{x}}_k^j$ thus defines the TX position and allows to compute the message $m_{\phi\to\mathbf{x}_k^i}(\mathbf{x}_k^i)$. Having this, the own belief $b^l_{\mathbf{x}_k^i}(\mathbf{x}_k^i)$ can be computed with the messages from the non-cooperative part and the messages from all neighbors $\mathcal{N}_{\to i}$ of node i. After N_{iter} iterations or after sufficient convergence the own belief is reported. To avoid degeneracy it is normalized and resampled with sequential importance resampling [11]. Finally, we compute the sample mean of $m_{\mathbf{x}_k^i\to h}(\mathbf{x}_k^i)$ to extract the MS state.

V. Simulation Results

A. Setup

The state-propagation model has been given in (9). The time between two successive measurements is $\Delta T = 0.25$s and $\Delta L_{\max} = 0.1$m leading to a position variance of $\sigma^2_{\mathbf{p}} \approx (0.02)^2$ and a velocity variance of $\sigma^2_{\mathbf{v}} \approx (0.15)^2$ in x, y-direction[1].
The measurements follow the model given in (5). Deterministic MPCs correspond to the LOS path and specular reflections of first and second order. We used a free-space propagation model for $A(\tau_l)$ similar to [6]. The carrier frequency is 7GHz and each reflection attenuates the signal additionally by 3dB. We used a relatively low amount of DM modeled by a double exponential function in [15, Eq. (9)] with parameters $\Omega_1 = 11.6\cdot 10^{-9}$, $\gamma_1 = 20$ns, $\gamma_{\text{rise}} = 5$ns, and $\chi = 0.98$. Ω_1 denotes the total power of DM. The transmitted signal $s(t)$ is modeled by a raised cosine pulse with roll-off factor $\alpha = 0.6$ and pulse duration $T = 0.5$ns corresponding to a bandwidth of 2GHz. The noise PSD has been set to $N_0 = 10^{-12}$W/Hz.
In the simulation we have used $I = 3$ MSs moving along the trajectories illustrated in Fig. 1. Each trajectory consists of 100 MS positions, corresponding to $K = 100$ time-steps. In each time-step k all MSs perform a mono-static measurement $\mathbf{z}^i_{\text{self},k}$ and a relative measurement $\mathbf{z}^{i,j}_{\text{rel},k}$ to their neighbors, where we assumed that all MSs are within communication range. The particles have been initialized perfectly with the true MS positions. The belief of every MS is represented by 1000 particles. The number of iterations in the cooperative update step has been set to $N_{\text{iter}} = 3$ (see Alg. 1).

B. Discussion of Simulation Results

The cumulative distribution functions (CDFs) of the individual error of each mobile are shown in Fig. 6. The CDFs where averaged over 80 individual runs. In 90% of the cases, the estimated target positions of all 3 MS are within 40cm. The reasons for the attained error performance of the three MSs in this scenario are discussed next.

1) LOS vs. NLOS: Between MS1 and MS3, the LOS path exists for the whole trajectory. This is not the case for the trajectory of MS2, where the LOS path to both other mobiles is shadowed at some MS positions along the trajectory. Due to the fact that most of the signal energy is contained in the LOS component, the value of the LHF in the NLOS case is worse compared to the LOS case. Fig. 4 illustrates the deteriorated value of the LHF in the NLOS case. Although

[1] In the same manner as in [9], we assume $3\sigma_a$ equals the maximum acceleration within time ΔT. We define $\sigma_a = \frac{\Delta L_{\max}}{3}\frac{1}{\Delta T^2}$, where $\Delta L_{\max}$ is the maximum travel distance of an MS within time period ΔT.

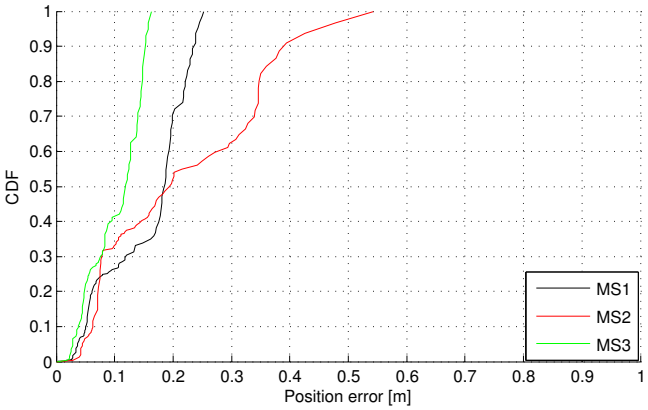

Fig. 6. Localization error CDFs for $I = 3$ cooperating MSs. 90% of the position estimates are within 40cm. MS2 performs worse compared to MS1 and MS3, because its trajectory is partly in NLOS to the cooperating MSs.

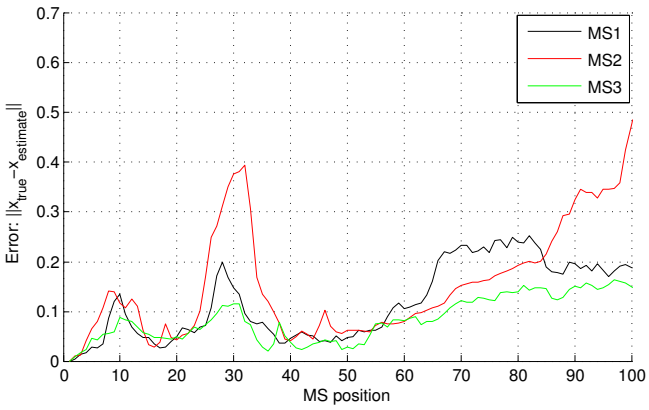

Fig. 7. Mean localization error at each MS position along the measurement trajectory for $I = 3$ cooperating MSs. MS2 performs worst due to its NLOS situation. This also negatively affects the performance of the other cooperating MSs.

the global maximum over the whole room is located at the correct RX position, it is crossed by smaller peaks close to the true RX position due to multipath. This leads to an uncertainty in position information (see Fig. 6). The reader is referred to [6] for an analysis of the position error bound with bi-static measurements for MINT.

2) Ambiguities in the Likelihood: The likelihood function given in (8) is only a cross-correlation at zero time lag with the template signal. The template signal itself is constructed based on the prevalent geometry, which leads to ambiguities. Such ambiguities are directly reflected in the LHF. On the one hand, this behavior can be seen clearly in the mono-static LHF shown in Fig. 3. The likelihood has a peak value parallel to the room walls. The distance corresponds to the delay of the strongest specular reflection. With this information it is clear that localization is not possible with only the mono-static measurements $\mathbf{z}_{\text{self}}$ in our scenario. The ambiguity in the mono-static LHF drags the targets into the wrong direction. On the other hand, the bi-static LHF delivers us with a maximum at the true position as long as the TX position is known. The drawback of this is that if localization is performed only with the bi-static measurements $\mathbf{z}_{\text{rel}}$, the errors in each

time-step are accumulated. This behavior is similar to inertial measurement units, e.g. a pedometer, because no measurement is employed to a known anchor point. Therefore, we need the conjunction of both, the mono- and bi-static measurement to achieve the desired localization effect in our mobile node-only scenario. The conjunction of both LHFs overwhelms to a great extend the drawbacks of the individual LHFs. The mono-static measurement delivers the connection to the known reference, i.e. the wall, and the bi-static measurement resolves most of the ambiguity in the mono-static LHF set by the room geometry.

3) Target propagation model mismatch: In the constant velocity state-propagation model, the system dynamics is modeled by the process noise. We assumed the process noise to be normal distributed (compare with (9)). Therefore, the state-propagation model is only accurate in cases with close-to-linear target motion. To cope with slight violations between target motion and propagation model the process noise variance σ_a^2 may be increased. But then, also the number of used particles need to be increased significantly in the implementation in order to support the underlying PDF with enough samples. Fig. 7 contains the target estimation error for the MSs in every time-step along the trajectory. If we compare the MS positions with high estimation error with the MS trajectories given in Fig. 1, we observe a higher error at MS positions where the movement direction of the MSs changes. This behavior can be observed for instance at $k = 65$ for MS $i = 1$. Unfortunately, it also affects the performance of the other cooperating MSs and leads to a degradation of the overall performance. A more accurate state-propagation model might lower the present model mismatch and lead to a better performance.

4) Implementation based error: The FG given in Fig. 5 has loops and exact inference is not possible. Using belief propagation the beliefs are only approximations of the true PDFs. This is the first step where an error is introduced compared to the statistical description given in (4). A second step concerns the estimation of the TX position out of the received neighbor belief. With the likelihood given in (8), it is not possible to sample from it by knowing only one input. This is in contrast to the likelihood in [7], [9], [13], [14]. To limit computing complexity, we have extracted the mean value out of the received belief as the TX position. This only works well if the mean value is a good approximation of the true position of $\mathbf{x}_k^j$. Future work will address this issue.

VI. Conclusion and Outlook

This work introduced the usage of MINT for UWB among cooperating users to solve the localization task. Compared to the non-cooperative MINT approach the need for a known anchor node is omitted completely, which lowers the requirement in infrastructure to only the floorplan information. It is enabled by a combination of non-cooperative mono-static self-measurements of each agent and cooperative bi-static measurements between the agents. In the simulations, diffuse multipath has been modeled in addition to the present noise, as it has been shown to be a major factor impairing performance. Simulation results showed the applicability of this approach in a mixed LOS and NLOS scenario. Future work will address the employed simplification of the LHF, uncertain floorplan information and the state initialization.

Acknowledgment

We gratefully acknowledge fruitful discussions with Florian Meyer and Franz Hlawatsch of Vienna University of Technology. This work was supported by the Austrian Science Fund (FWF) within the National Research Network SISE project S10610 and by the Austrian Research Promotion Agency (FFG) within KIRAS PL3, grant no. 832335 “LOBSTER”.

References

[1] S. Gezici, Z. Tian, G. Giannakis, H. Kobayashi, A. Molisch, H. Poor, and Z. Sahinoglu, “Localization via ultra-wideband radios: a look at positioning aspects for future sensor networks,” *Signal Processing Magazine, IEEE*, vol. 22, no. 4, pp. 70–84, Jul. 2005.

[2] A. Molisch, “Ultra-Wide-Band Propagation Channels,” *Proceedings of the IEEE*, vol. 97, no. 2, pp. 353–371, Feb. 2009.

[3] J. Kunisch and J. Pamp, “An ultra-wideband space-variant multipath indoor radio channel model,” in *Ultra Wideband Systems and Technologies, 2003 IEEE Conference on*, Nov. 2003, pp. 290–294.

[4] S. Marano, W. Gifford, H. Wymeersch, and M. Win, “NLOS identification and mitigation for localization based on UWB experimental data,” *Selected Areas in Communications, IEEE Journal on*, vol. 28, no. 7, pp. 1026–1035, Sep. 2010.

[5] Y. Shen and M. Win, “On the Use of Multipath Geometry for Wideband Cooperative Localization,” in *Global Telecommunications Conference, 2009. GLOBECOM 2009. IEEE*, Dec. 2009, pp. 1–6.

[6] K. Witrisal and P. Meissner, “Performance bounds for multipath-assisted indoor navigation and tracking (MINT),” in *Communications (ICC), 2012 IEEE International Conference on*, Jun. 2012, pp. 4321–4325.

[7] H. Wymeersch, J. Lien, and M. Win, “Cooperative Localization in Wireless Networks,” *Proceedings of the IEEE*, vol. 97, no. 2, pp. 427–450, Feb. 2009.

[8] P. Meissner and K. Witrisal, “Multipath-assisted single-anchor indoor localization in an office environment,” in *Systems, Signals and Image Processing (IWSSIP), 2012 19th International Conference on*, Apr. 2012, pp. 22–25.

[9] S. Van de Velde, H. Wymeersch, P. Meissner, K. Witrisal, and H. Steendam, “Cooperative multipath-aided indoor localization,” in *Wireless Communications and Networking Conference (WCNC), 2012 IEEE*, Apr. 2012, pp. 3107–3111.

[10] C. M. Bishop, *Pattern Recognition and Machine Learning*. Springer, 2006.

[11] M. Arulampalam, S. Maskell, N. Gordon, and T. Clapp, “A tutorial on particle filters for online nonlinear/non-Gaussian Bayesian tracking,” *Signal Processing, IEEE Transactions on*, vol. 50, no. 2, pp. 174–188, Feb. 2002.

[12] H. Godrich, A. Haimovich, and R. Blum, “Target Localization Accuracy Gain in MIMO Radar-Based Systems,” *Information Theory, IEEE Transactions on*, vol. 56, no. 6, pp. 2783–2803, Jun. 2010.

[13] A. Ihler, I. Fisher, J.W., R. Moses, and A. Willsky, “Nonparametric belief propagation for self-localization of sensor networks,” *Selected Areas in Communications, IEEE Journal on*, vol. 23, no. 4, pp. 809–819, Apr. 2005.

[14] J. Lien, U. Ferner, W. Srichavengsup, H. Wymeersch, and W. MZ, “A Comparison of Parametric and Sample-Based Message Representation in Cooperative Localization,” *International Journal of Navigation and Observation*, vol. 2012, pp. 843–854, 2012.

[15] J. Karedal, S. Wyne, P. Almers, F. Tufvesson, and A. Molisch, “A Measurement-Based Statistical Model for Industrial Ultra-Wideband Channels,” *Wireless Communications, IEEE Transactions on*, vol. 6, no. 8, pp. 3028–3037, Aug. 2007.

Multipath-Assisted Maximum-Likelihood Indoor Positioning using UWB Signals

Erik Leitinger*†, Markus Fröhle+†, Paul Meissner*, and Klaus Witrisal*
* Email: erik.leitinger@tugraz.at, Graz University of Technology, Austria
+ Email: frohle@chalmers.se, Chalmers University of Technology, Sweden, †equal contribution

***Abstract*—Multipath-assisted indoor positioning (using ultra-wideband signals) exploits the geometric information contained in deterministic multipath components. With the help of a-priori available floorplan information, robust localization can be achieved, even in absence of a line-of-sight connection between anchor and agent. In a recent work, the Cramér-Rao lower bound has been derived for the position estimation variance using a channel model which explicitly takes into account diffuse multipath as a stochastic noise process in addition to the deterministic multipath components. In this paper, we adapt this model for position estimation via a measurement likelihood function and evaluate the performance for real channel measurements. Performance results confirm the applicability of this approach. A position accuracy better than 2.5 cm has been obtained in 90 % of the estimates using only one active anchor at a bandwidth of 2 GHz and robustness against non-line-of-sight situations has been demonstrated.**

I. Introduction

Ultra-wideband (UWB) signals are promising candidates for indoor positioning. Their large frequency range offers a fine delay resolution and robustness in harsh propagation environments such as indoors [1]. The benefit of the UWB channel is that many of the multipath components (MPCs) are recognizable and resolvable in the measurements.

Deterministic MPCs, having parameters that can be modeled as a function of the surrounding geometry, can be used for localization and tracking [2]–[5]. The transmitted signal which is reflected at e.g. a wall, can be seen as being emitted from a virtual source located behind the reflecting surface. With the help of a floorplan, it is possible to calculate the position of these virtual sources and use them as so-called virtual anchors (VAs) for localization. Fig. 1 illustrates an exemplary floor-plan with two fixed anchors and a small subset of corresponding VAs. In this way, localization is possible with only a single anchor node independent of a line-of-sight (LOS) or non-LOS (NLOS) situation. We call this approach multipath-assisted indoor navigation and tracking (MINT). In [5], the Cramér-Rao Lower Bound (CRLB) has been derived for this problem. Diffuse multipath (DM), e.g. scattered signals which are not covered by the deterministic model, impairs the detection of the useful deterministic components. This interfering part of the channel is modeled as an additive stochastic process.

This work was supported by the Austrian Science Fund (FWF) within the National Research Network SISE project S10610, by the Austrian Research Promotion Agency (FFG) within KIRAS PL3, grant no. 832335 “LOBSTER”, and by EU FP7 Marie Curie Initial Training Network MULTI-POS (Multi-technology Positioning Professionals) under grant nr. 316528.

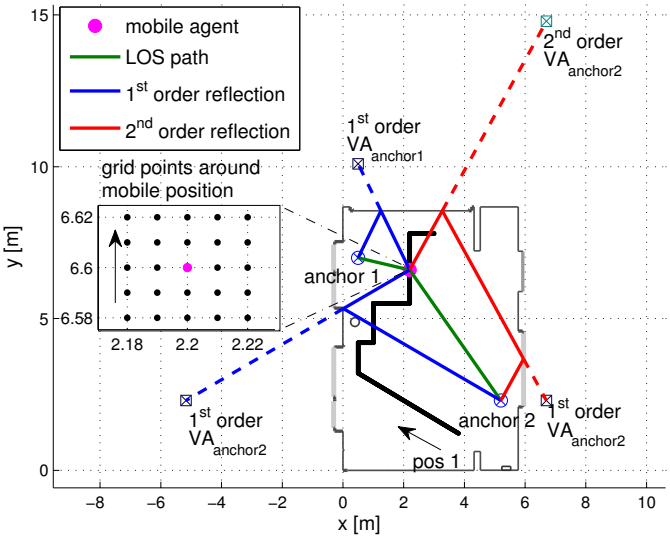

Fig. 1. Floor-plan of an empty seminar room with a 5-cm-spaced trajectory (black line) of agent positions. The close-up shows that for every agent position $\mathbf{p}$ (magenta dot), a set of 25 measurements has been recorded in a rectangular grid with 1 cm spacing. Furthermore, two physical anchors $j = \{1, 2\}$ are illustrated and a few of the expected virtual anchors (VAs).

In this paper, we adapt the model of [5] to formulate the maximum likelihood estimator (MLE) of the agent position. We also evaluate the localization performance with real measurements, where we analyze in particular the impact of considering DM in the likelihood function (LHF). The LHF is highly multi-modal and the MLE problem is non-convex, meaning that methods such as gradient descent are not useful for finding the global maximum. We thus apply particle filter methods [6] with swarm behavior [7]. The contributions of this work are:

- Formulation of MLE for the channel model given in [5]
- Localization performance evaluation of the MLE with real indoor channel measurements
- Characterization of the DM, i.e. estimation of its power delay profile (PDP), and analysis of its impact on the MLE, and
- Comparison between the MLE co-variance and the estimated CRLB.

II. Problem Overview

A. Signal Model

A UWB baseband signal $s(t) \in \mathbb{R}$ with effective pulse duration T_p, is transmitted from an anchor $j = 1 \dots N_\mathrm{A}$, located at position $\mathbf{p}_\mathrm{I}^{(j)} \in \mathbb{R}^2$, where N_A is the number of physical anchors considered. The received signal at the agent position $\mathbf{p}$ is modeled as [5]

$$\begin{aligned} r^{(j)}(t) &= r_\mathrm{det}^{(j)}(t) + r_\mathrm{diff}^{(j)}(t) + w(t) \\ &= \sum_{k=1}^{K^{(j)}} \alpha_k^{(j)} s(t-\tau_k^{(j)}) + s * \nu^{(j)}(t) + w(t), \end{aligned} \quad (1)$$

where the first term comprises a sum of $K^{(j)}$ deterministic MPCs with complex amplitudes $\alpha_k^{(j)} \in \mathbb{C}$ and delays $\tau_k^{(j)} = \frac{1}{c}||\mathbf{p}-\mathbf{p}_k^{(j)}||_2$, where c is the speed of light. Due to the knowledge of the floorplan, we can associate these MPCs to specular reflections at surfaces, i.e. they are modeled by VAs at positions $\mathbf{p}_k^{(j)}$, with $k = 2 \dots K^{(j)}$, where $K^{(j)}$ is the number of expected VAs at position $\mathbf{p}$ (c.f. Fig. 1). The second term $r_\mathrm{diff}^{(j)}(t)$ denotes the convolution $(*)$ of the transmitted signal $s(t)$ with the DM $\nu^{(j)}(t)$ which is modeled as a zero-mean Gaussian random process. We assume uncorrelated scattering along the delay axis τ. Hence, the auto-correlation function (ACF) of $\nu^{(j)}(t)$ is given by $K_\nu^{(j)}(\tau, u) = S_\nu^{(j)}(\tau)\delta(\tau - u)$, where $S_\nu^{(j)}(\tau)$ is the PDP of the DM for the j-th anchor at the agent position $\mathbf{p}$. According to this model, the DM is quasi-stationary in the spatial domain, which means that $S_\nu^{(j)}(\tau)$ does not change in the vicinity of position $\mathbf{p}$ [1]. Note that $r_\mathrm{diff}^{(j)}(t)$ is non-stationary in the delay domain. Finally, the last term $w(t)$ denotes AWGN with a double-sided power spectral density (PSD) of N_0.

In Fig. 2, a set of measured signals $\{r_i^{(j)}(t)\}_{i=1}^{25}$ is shown for anchor 2 (colored thin lines). The measurements $r_i^{(j)}(t)$ are from the direct vicinity of the agent's actual position $\mathbf{p}$ to guarantee a quasi-stationary behavior in the spatial domain, as illustrated in Fig. 1. Further, the correlation function of the DM plus AWGN is illustrated and given by $C^{(j)}(t,u) = N_0\delta(t-u) + \int_{-\infty}^{\infty} S_\nu^{(j)}(\tau)s(t-\tau)s(u-\tau)\mathrm{d}\tau$ (bold dashed red line). The received signal $r^{(j)}(t)$ at the agent's actual position $\mathbf{p}$ (i.e. at the center of the grid) is illustrated by the bold dashed black line.

B. Likelihood Function (LHF)

The LHF is defined for the channel parameter vector $\boldsymbol{\psi} = \left[\boldsymbol{\tau}^\mathrm{T}, (\boldsymbol{\alpha}^\mathrm{R})^\mathrm{T}, (\boldsymbol{\alpha}^\mathrm{I})^\mathrm{T}\right]^\mathrm{T}$, where $\boldsymbol{\tau} = [\tau_1, \dots, \tau_K]^\mathrm{T}$ represents the vector with the geometry-related delays and $(\boldsymbol{\alpha}^\mathrm{R}) = [\alpha_1^R, \dots, \alpha_K^R]^\mathrm{T}$, $(\boldsymbol{\alpha}^\mathrm{I}) = [\alpha_1^I, \dots, \alpha_K^I]^\mathrm{T}$ are the real and imaginary parts of the corresponding complex amplitudes $\boldsymbol{\alpha}$. An approximation of this LHF, using a whitening operation as

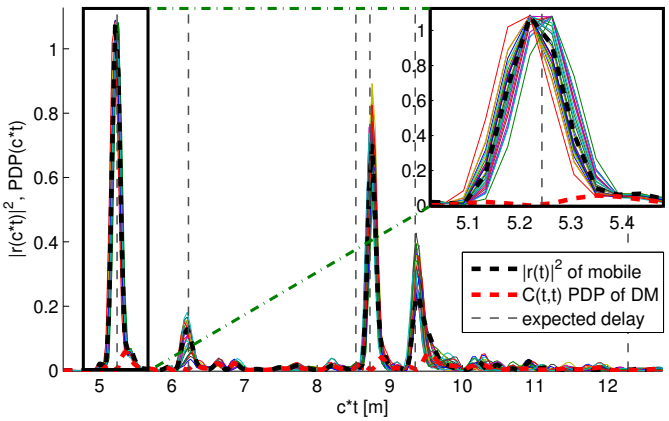

Fig. 2. A set of received $\{r_i^{(j)}(t)\}_{i=1}^{25}$ measurements recorded at grid positions illustrated in Fig. 1 (thin solid colored lines), including the actual agent position $\mathbf{p} = [2.2, 6.6]^\mathrm{T}$ (bold dashed black line). Anchor 2 is used. Also, the corresponding DM correlation function $C^{(j)}(t,t)$ is shown (bold dashed red line). Expected delays to VAs visible at the agent's position are illustrated by dashed gray vertical lines.

described in [5], is given by

$$\begin{aligned} \mathrm{p}(r^{(j)}(t)|\boldsymbol{\psi}) \propto \exp\Bigg(&\frac{2}{N_0}\int_0^{T_0} \Re\{r^{(j)}(t)\sum_{k=1}^{K} w_k^2 \alpha_k^* s(t-\tau_k)\}\mathrm{d}t \\ &- \frac{1}{N_0}\int_0^{T_0} \Big|\sum_{k=1}^{K} w_k \alpha_k s(t-\tau_k)\Big|^2 \mathrm{d}t\Bigg), \end{aligned} \quad (2)$$

where T_0 is the observation time and $w_k^2 = N_0/(N_0 + T_p S_\nu(\tau_k))$ are weighting factors accounting for the DM [5]. The term $T_p S_\nu(\tau_k)$ represents the equivalent power of the DM. For the sake of brevity, we have dropped the anchor index j for the channel parameters, but we will use it in situations where we emphasize the explicit anchor dependence.

The LHF for the sampled received signal, where T_s represents the sampling time, is described by

$$\begin{aligned} \mathrm{p}(\mathbf{r}^{(j)}|\boldsymbol{\psi}) = \mathrm{p}(\mathbf{r}^{(j)}|\boldsymbol{\tau}, \boldsymbol{\alpha}) \propto \\ \exp\Big(-\frac{1}{2}(\mathbf{r}^{(j)} - \mathbf{S}^\mathrm{H}\boldsymbol{\alpha})^\mathrm{H}\mathbf{C}^{-1}(\mathbf{r}^{(j)} - \mathbf{S}^\mathrm{H}\boldsymbol{\alpha})\Big) \end{aligned} \quad (3)$$

where $\mathbf{r}^{(j)} = [r^{(j)}(T_s), \dots, r^{(j)}(MT_s)]^\mathrm{T} \in \mathbb{R}^M$ denotes the sampled received signal vector and $(\cdot)^\mathrm{H}$ is the Hermitian conjugate. The signal matrix $\mathbf{S} \in \mathbb{R}^{K\times M}$ is given by

$$\mathbf{S} = \begin{bmatrix} s(T_s-\tau_1) & s(2T_s-\tau_1) & \dots & s(MT_s-\tau_1) \\ \vdots & & & \vdots \\ s(T_s-\tau_K) & s(2T_s-\tau_K) & \dots & s(MT_s-\tau_K) \end{bmatrix} \quad (4)$$

containing delayed versions of the transmitted pulse $s(nT_s - \tau_k)$. In (3), the matrix $\mathbf{C} = N_0\mathbf{I}_M + \mathbf{K}_\mathrm{c} \in \mathbb{R}^{M\times M}$ denotes the co-variance matrix of white noise and DM. The DM co-variance matrix is given by $[\mathbf{K}_\mathrm{c}]_{n,m} = T_s\sum_{i=1}^{M} S_\nu(iT_s)s(nT_s - iT_s)s(mT_s - iT_s)$, where $[\cdot]_{n,m}$ is the (n,m)-th matrix element. $\mathbf{I}_M$ is the identity matrix of size M.

With the ideal assumptions that the delayed versions of the transmit-pulse $s(nT_s - \tau_k)$ are orthogonal to one another, which implies that $\tau_k = mT_s$, and T_s is at Nyquist rate, the co-variance matrix $\mathbf{C}$ results in a diagonal matrix and the rows of the signal matrix $\mathbf{S}$ are orthogonal. So, the LHF is simplified to

$$\mathrm{p}(\mathbf{r}^{(j)}|\boldsymbol{\psi}) \propto \exp\{\frac{1}{N_0}\Re\{\mathbf{r}^{(j)\mathrm{H}}\mathbf{S}^{\mathrm{H}}\mathbf{W}\boldsymbol{\alpha}\} - \frac{1}{2N_0}\boldsymbol{\alpha}^{\mathrm{H}}\mathbf{W}^{\frac{1}{2}}\mathbf{S}\mathbf{S}^{\mathrm{H}}\mathbf{W}^{\frac{1}{2}}\boldsymbol{\alpha}\} \quad (5)$$

where $\mathbf{W}^{(j)} \in \mathbb{R}^{K\times K}$ is a diagonal matrix which contains the whitening weights of the orthogonal pulses. Its diagonal elements are defined as $[\mathbf{W}]_{k.k} = N_0(N_0\mathbf{I}_K + T_s[\mathbf{K}_{\mathrm{c}}]_{\lfloor\frac{\tau_k}{T_s}\rfloor})^{-1}$, where $[\cdot]_{k,k}$ is the (k,k)-th matrix element and $\lfloor\cdot\rfloor$ is the round down (floor) operator. Note that (5) can be interpreted as the sampled version of the continuous likelihood represented by (2).

C. Cramér-Rao Lower Bound (CRLB)

As a performance measure and lower bound we use the CRLB of the position error defined by the inequality $\mathbb{E}\{||\mathbf{p} - \hat{\mathbf{p}}||_2^2\} \geq \mathrm{tr}\{\mathbf{J}_{\mathbf{p}}^{-1}\}$, where $\mathbf{J}_{\mathbf{p}}$ is the equivalent Fisher information matrix (EFIM) [4] for the position vector and $\mathrm{tr}\{\cdot\}$ is the trace operator. In [5], the CRLB has been derived for the signal model in (2). The CRLB shows the influence of the VA positions, i.e. the room geometry, and of the power ratio between the modeled "information carrying" deterministic MPCs and detrimental DM, on the precision of the position estimator. With the assumption that the signals received from different propagation paths are orthogonal to one another, the EFIM $\mathbf{J}_{\mathbf{p}}$ is formulated for a set of anchors in a canonical form by

$$\mathbf{J}_{\mathbf{p}} = \frac{8\pi^2\beta^2}{c^2}\sum_{j=1}^{N_{\mathrm{A}}}\sum_{k=1}^{K^{(j)}}\mathrm{SINR}_k^{(j)}\mathbf{J}_{\mathrm{r}}(\phi_k^{(j)}), \quad (6)$$

where β denotes the effective signal bandwidth and $\mathbf{J}_{\mathrm{r}}(\phi_k^{(j)})$ the ranging direction matrix, which has an eigenvector in direction $\phi_k^{(j)}$ from the agent to the k-th VA. $\mathrm{SINR}_k^{(j)}$ represents the signal-to-interference-plus-noise ratio of the k-th MPC and is defined as

$$\mathrm{SINR}_k^{(j)} = (w_k^{(j)})^2\frac{|\alpha_k^{(j)}|^2}{N_0} = \frac{|\alpha_k^{(j)}|^2}{N_0 + T_p S_\nu^{(j)}(\tau_k)}. \quad (7)$$

The value of the SINR shows the importance of the knowledge of the DM statistics in order to accurately estimate the information gained by a MPC.

D. MLE of the agent's position

The computation of the LHF can be seen as a position dependent channel estimation problem with prior floorplan information. Using the floorplan knowledge, the sets of VAs are computed for every anchor using optical ray-tracing [2]. In realistic scenarios, the floorplan has uncertainties which we take into account by using a probabilistic formulation of the VA positions. The maximum a-posteriori (MAP) estimator of the agent's position can then be formulated as

$$\begin{aligned}\hat{\mathbf{p}}_{\mathrm{MAP}} &= \underset{\mathbf{p},\mathbf{p}_{\mathrm{VA}}^{(j)},\boldsymbol{\tau},\boldsymbol{\alpha}}{\arg\max}\prod_{j=1}^{N_{\mathrm{A}}}\mathrm{p}(\mathbf{p},\mathbf{p}_{\mathrm{VA}}^{(j)},\boldsymbol{\tau},\boldsymbol{\alpha}|\mathbf{r}^{(j)}) \\ &= \underset{\mathbf{p},\mathbf{p}_{\mathrm{VA}}^{(j)},\boldsymbol{\tau},\boldsymbol{\alpha}}{\arg\max}\prod_{j=1}^{N_{\mathrm{A}}}\mathrm{p}(\mathbf{r}^{(j)}|\boldsymbol{\tau},\boldsymbol{\alpha})\mathrm{p}(\boldsymbol{\alpha}|\boldsymbol{\tau})\mathrm{p}(\boldsymbol{\tau}|\mathbf{p},\mathbf{p}_{\mathrm{VA}}^{(j)}) \\ &\quad\times\mathrm{p}(\mathbf{p},\mathbf{p}_{\mathrm{VA}}^{(j)})\mathrm{p}(\boldsymbol{\alpha})\mathrm{p}(\boldsymbol{\tau}) \quad (8)\end{aligned}$$

where $\mathbf{p}_{\mathrm{VA}}^{(j)} = [\mathbf{p}_1^{(j)},\ldots,\mathbf{p}_{K^{(j)}}^{(j)}]^{\mathbf{T}}$ is the set of VAs to compute the delay paths $\boldsymbol{\tau}$ of the MPCs for the agent's position $\mathbf{p}$. If we assume that the VA positions are exactly known and that the channel parameters are unknown deterministic parameters then $\mathrm{p}(\boldsymbol{\tau}|\mathbf{p},\mathbf{p}_{\mathrm{VA}}^{(j)}) = \delta(\boldsymbol{\tau} - \frac{1}{c}||\mathbf{p} - \mathbf{p}_{\mathrm{VA}}^{(j)}||_2)$ and $\mathrm{p}(\boldsymbol{\alpha}|\boldsymbol{\tau}) = \delta(\boldsymbol{\alpha} - \hat{\boldsymbol{\alpha}}_{\mathrm{LS}})$, where $\hat{\boldsymbol{\alpha}}_{\mathrm{LS}}$ is the least-square solution describing the relation between complex amplitudes $\boldsymbol{\alpha}$ and the vector of delays $\boldsymbol{\tau}$ at the agent position $\mathbf{p}$ (see (12)). $\delta(\cdot)$ denotes the Dirac-delta distribution. Assuming a uniform distribution for $\mathrm{p}(\mathbf{p})$, the estimation problem accounting for all anchors reduces to a MLE using (3) which is formulated as

$$\hat{\mathbf{p}}_{\mathrm{ML}} = \underset{\mathbf{p},\boldsymbol{\tau},\boldsymbol{\alpha}}{\arg\max}\prod_{j=1}^{N_{\mathrm{A}}}\mathrm{p}(\mathbf{r}^{(j)}|\boldsymbol{\tau},\boldsymbol{\alpha},\mathbf{p}). \quad (9)$$

The actual MLE algorithm is described in section II-E. Independent of the used estimator, the likelihood has to be evaluated by applying the following steps: noitemsep,nolistsep

1) To reduce the uncertainties in the geometry, a re-localization of the VA positions to $\hat{\mathbf{p}}_k^{(j)}$ of the j-th anchor is done beforehand by using a set of measurements with known agent positions. For detailed information about the re-localization process we refer the reader to [2].
2) With the pre-computed or re-localized set of VAs, the position dependent set of expected delays $\hat{\tau}_k^{(j)}(\mathbf{p}) = \frac{1}{c}||\mathbf{p} - \hat{\mathbf{p}}_k^{(j)}||_2$, is used to construct the signal matrix (4) by
$$\hat{\mathbf{S}} = \begin{bmatrix} s(T_s - \hat{\tau}_1^{(j)}(\mathbf{p})) & \ldots & s(MT_s - \hat{\tau}_1^{(j)}(\mathbf{p})) \\ \vdots & & \vdots \\ s(T_s - \hat{\tau}_{K^{(j)}}^{(j)}(\mathbf{p})) & \ldots & s(MT_s - \hat{\tau}_{K^{(j)}}^{(j)}(\mathbf{p})) \end{bmatrix}. \quad (10)$$
The expected delays $\tau_k^{(j)}(\mathbf{p})$ are refined by searching for the actual amplitude maximum in the received signal vector $\mathbf{r}^{(j)}$ in the window $[\hat{\tau}_k^{(j)}(\mathbf{p}) - T_p, \hat{\tau}_k^{(j)}(\mathbf{p}) + T_p]$.
3) Since the DM statistics are usually unknown, the covariance $\mathbf{C}$ has to be estimated from a sufficiently large set of measured signals $\{\mathbf{r}_i^{(j)}\}_{i=1}^L$ around the actual agent position. Using the signal matrix of (10) for the position hypothesis $\mathbf{p}_i$ of the i-th measurement, the template signal $\mathbf{r}_{\mathrm{det},i}$ is constructed and further the covariance matrix is estimated by
$$\hat{\mathbf{C}} = \frac{1}{L}\sum_{i=1}^{L}(\mathbf{r}_i^{(\mathrm{al},j)} - \mathbf{r}_{\mathrm{det},i})(\mathbf{r}_i^{(\mathrm{al},j)} - \mathbf{r}_{\mathrm{det},i})^{\mathrm{H}}. \quad (11)$$

Note, that the LOS propagation delay $\tau_{1,i}$ differences between the measurements has to be compensated to be able to average over the set of aligned measurements $\{\mathbf{r}_i^{(\mathrm{al},j)}\}$ of the spatially close agent positions. In order to get a benchmark for the induced improvement of robustness and accuracy due to consideration of DM, we assume for the DM estimation known positions on a measurement grid around the actual agent position. In a realistic positioning application, this estimation has to be performed based on estimated positions and the corresponding signals hypotheses. However, this is considered as out of scope of this paper.

4) Using (10) and (11), the MLE of the complex amplitudes $\boldsymbol{\alpha}$ reduces to a linear estimation problem. This means that using the complex derivative the estimation is formulated as a weighted least square solution in the following form

$$\hat{\boldsymbol{\alpha}}_{\mathrm{LS}} = (\hat{\mathbf{S}}\hat{\mathbf{C}}^{-1}\hat{\mathbf{S}}^{\mathrm{H}})^{-1}\hat{\mathbf{S}}\hat{\mathbf{C}}^{-1}\mathbf{r}^{(j)}. \tag{12}$$

The LHF is evaluated by inserting the estimated parameter $\hat{\mathbf{S}}$, $\hat{\mathbf{C}}$ and $\hat{\boldsymbol{\alpha}}_{\mathrm{LS}}$ into equation (3).

E. Implementation of the MLE

Due to the fact that the LHF is highly multi-modal, non-Gaussian and the measurement model is non-linear, a straightforward ML estimation is not applicable. Hence, we present a hybrid probabilistic-heuristic approach which combines a sequential importance re-sampling (SIR) particle filter (PF) with the concept of particle swarm global optimization (PSO) which is able to find the global maximum in the parameter space. In [8] probability model-based methods for global optimization are presented. A SIR particle filtering is suggested as a proper method for finding the global maximum. To explore the entire search space and find new candidate solutions, randomness has to be introduced in the maximization method. This can be realized: (i) in the re-sampling step of the PF by generating also new values for the particles instead of conventional re-sampling with replacement or (ii) via a state-space model which induces the exploration.

In our approach, we use a dynamic state-space model to explore the search-space. The state equation consists of two parts, the first one is described by a constant-velocity random walk model and the second part is responsible for the particle swarm behavior [7].

1) SIR Particle Filter: Particle filters represent a sub-optimal sequential Monte Carlo method for solving non-linear and non-Gaussian sequential Bayesian state estimation problems which can not be computed in a closed form. In general, the Bayesian tracking problem is the recursive computation of a degree of belief of a hidden state, e.g. position and velocity $\mathbf{x}_n = [\mathbf{p}_n, \mathbf{v}_n]^T$, using measurement $\mathbf{r}_n$ at time-index n. Due to the fact that this paper deals with ML localization, not tracking, the index n describes the evolution of the distribution as a function of time until convergence is reached, i.e. iterations use just one measurement, i.e. $\mathbf{r}_{1:n} = \mathbf{r}_n = \mathbf{r} \quad \forall n$. The state estimation is done in two consecutive stages using a first-order hidden Markov model (HMM): (i) the prediction step which obtains the predicted posterior PDF $\mathrm{p}(\mathbf{x}_n|\mathbf{r}_n)$ using the Chapman-Kolmogorv equation [6]

$$\mathrm{p}(\mathbf{x}_n|\mathbf{r}_{1:n-1}) = \int \mathrm{p}(\mathbf{x}_n|\mathbf{x}_{n-1})\mathrm{p}(\mathbf{x}_{n-1}|\mathbf{r}_{1:n-1})\mathrm{d}\mathbf{x}_{n-1}, \tag{13}$$

where $\mathrm{p}(\mathbf{x}_n|\mathbf{x}_{n-1})$ is the state evolution probability, and (ii) the update step which is solved via Bayes' rule

$$\mathrm{p}(\mathbf{x}_n|\mathbf{r}_{1:n}) = \frac{\mathrm{p}(\mathbf{r}_n|\mathbf{x}_n)\mathrm{p}(\mathbf{x}_n|\mathbf{r}_{1:n-1})}{\int \mathrm{p}(\mathbf{r}_n|\mathbf{x}_n)\mathrm{p}(\mathbf{x}_n|\mathbf{r}_{1:n-1})\mathrm{d}\mathbf{x}_n}, \tag{14}$$

where $\mathrm{p}(\mathbf{r}_n|\mathbf{x}_n) = \mathrm{p}(\mathbf{r}_n|\boldsymbol{\tau}, \boldsymbol{\alpha}, \mathbf{p}_n)$ is the measurement LHF (3) dependent on the position $\mathbf{p}_n$. For solving (13) and (14), particle filters use a finite set of weighted samples, i.e. particles $\{\mathbf{x}_n^i, a_n^i\}_{i=1}^N$, to approximate the involved PDFs. The particles are sampled from an importance distribution $\mathbf{x}_n^i \sim \mathrm{q}(\mathbf{x}_n|\mathbf{x}_{n-1}, \mathbf{r}_n)$ and their weights a_n^i are computed in each iteration with

$$a_n^i = a_{n-1}^i \frac{\mathrm{p}(\mathbf{r}_n|\mathbf{x}_n^i)\mathrm{p}(\mathbf{x}_n^i|\mathbf{x}_{n-1}^i)}{\mathrm{q}(\mathbf{x}_n^i|\mathbf{x}_{n-1}^i, \mathbf{r}_n)}, \qquad \sum_{i=1}^{N} a_n^i = 1. \tag{15}$$

A simple choice of importance distribution is to take the state evolution probability $\mathrm{q}(\mathbf{x}_n|\mathbf{x}_{n-1}, \mathbf{r}_n) = \mathrm{p}(\mathbf{x}_n|\mathbf{x}_{n-1})$. To reduce the degeneration of the particles, a re-sampling step is introduced after every iteration. In this step, particles are drawn according to their weight which means that particle states $\mathbf{x}_n^i$ with high weight a_n^i are duplicated more often than particles with lower weights. The particle weights after every re-sampling step are set to $a_n^i = 1/N$. So, the computation of the weights simplifies to $a_n^i \propto \mathrm{p}(\mathbf{r}_n|\mathbf{x}_n) = \mathrm{p}(\mathbf{r}_n|\boldsymbol{\tau}, \boldsymbol{\alpha}, \mathbf{p}_n)$.

2) PF-PSO: In PSO the particles are generated randomly and by iterative updates of the positions using a cost function. The particles learn from their own cost-measure and the cost-measure of the other particles introducing swarm behavior. In our case, the particles in the swarm gain a velocity in direction of the global maximum, so that the PSO is able to jump out of local maxima and find the global optimum. This swarm behavior is integrated in the PF by the state transition equation [7] which is described by

$$\begin{aligned}\mathbf{x}_n = \mathbf{F}\mathbf{x}_{n-1} &+ u_1 \begin{bmatrix} \mathbf{p}_{\mathrm{b}}^{i\mathrm{best}} - \mathbf{p}_{n-1} \\ w_v(\mathbf{p}_{\mathrm{b}}^{i\mathrm{best}} - \mathbf{p}_{n-1}) \end{bmatrix} \\ &+ u_2 \begin{bmatrix} \mathbf{p}_{\mathrm{b}}^{\mathrm{g}} - \mathbf{p}_{n-1} \\ w_v(\mathbf{p}_{\mathrm{b}}^{\mathrm{g}} - \mathbf{p}_{n-1}) \end{bmatrix} + \mathbf{G}\mathbf{n}_{\mathrm{acc}}.\end{aligned} \tag{16}$$

Here,

$$\mathbf{F} = \begin{bmatrix} 1 & 0 & w_v & 0 \\ 0 & 1 & 0 & w_v \\ 0 & 0 & w_v & 0 \\ 0 & 0 & 0 & w_v \end{bmatrix} \quad \text{and} \quad \mathbf{G} = \begin{bmatrix} \frac{w_v^2}{2} & 0 \\ 0 & \frac{w_v^2}{2} \\ w_v & 0 \\ 0 & w_v \end{bmatrix} \tag{17}$$

are the state transition matrix and the noise weighting matrix, w_v is the velocity weight, u_1 and u_2 are random control factors drawn from a uniform distribution $\mathcal{U}(0,1)$, $\mathbf{n}_{\mathrm{acc}}$ is a zero-mean Gaussian driving acceleration noise with co-variance

matrix $\sigma_{\text{acc}}^2\mathbf{I}_2$. $\mathbf{p}_{\text{b}}^{i\text{best}}$ and $\mathbf{p}_{\text{b}}^{\text{g}}$ denote the maximum of the set of particles in the current iteration n and the global maximum of the past iterations, respectively. The algorithm starts with uniformly distributed particles over the entire search space. For these candidates the likelihood function is evaluated and the global maximum of the LHF L_{g} and the corresponding position $\mathbf{p}_{\text{b}}^{\text{g}} = \arg\max_{\mathbf{p}_n^i} \text{p}(\mathbf{r}|\boldsymbol{\tau}, \boldsymbol{\alpha}, \mathbf{p}_n^i)$ are computed. Further, the current maximum of the particles $\text{L}^{i\text{best}} = \text{L}_{\text{g}}$ and also the corresponding position $\mathbf{p}_{\text{b}}^{i\text{best}} = \mathbf{p}_{\text{b}}^{\text{g}}$ are set to the global values. Then, the state $\mathbf{x}_n^i$ (prediction step) and the according weights a_n^i (measurement update) of the particles are evaluated iteratively for a defined number of iterations. After each measurement update and before the re-sampling step is executed, the maximum of the current particles $\text{L}^{i\text{best}}$ at position $\mathbf{p}_{\text{b}}^{i\text{best}}$ is computed and accepted as new global maximum if $\text{L}^{i\text{best}} > \text{L}_{\text{g}}$.

III. Performance Evaluation

A. Setup

1) Measurement: The measurement scenario is illustrated in Fig. 1. We have used an M-sequence UWB channel sounder from Ilmsens (See: www.ilmsens.com) to record the UWB channel impulse responses (CIRs). The device is equipped with one TX and two RXs channels. We have used self made dipole antennas having an almost isotropic radiation pattern in the horizontal plane. In the measurement scenario, the anchors correspond to the RX and the agent to the TX. The anchors are placed at positions $\mathbf{p}_1^{(1)} = [0.5, 7]^{\text{T}}$ and $\mathbf{p}_1^{(2)} = [5.2, 3.2]^{\text{T}}$, respectively. The measurement trajectory of the agent consists of 220 points spaced by 5 cm. In addition to this, for every agent position on the trajectory, 25 measurements have been recorded with the agent placed according to the grid shown in Fig. 1. These additional measurements serve for the estimation of DM in the vicinity of the agent trajectory point. To obtain the UWB-CIR, the received signal and the transmitted M- sequence are cross-correlated. The bandwidth of the channel sounder corresponds to the FCC UWB range from $3.1 - 10.6$ GHz. A raised cosine filter $s(t)$ with roll-off factor $\beta_{\text{r}} = 0.5$ and an effective pulse duration of $T_P = 1/B$ is used to select a specific sub-band with bandwidth $B = 2$ GHz at center-frequency $f_c = 7$ GHz. To get the complex-valued baseband signal, a down conversion is performed.

2) Estimation: To evaluate the LHF in (2), we used two approaches: (i) Grid based MAP: The LHF is evaluated over a 40×40 cm rectangle around the true agent position with resolution of $1\text{x}1\,\text{cm}^2$ and the highest mode corresponds to the MLE given in (9); (ii) PF-PSO: A sufficiently large number of particles, i.e. $N = 2000$, is uniformly distributed over the whole room. The LHF is evaluated for $N_{\text{iter}} = 8$ iterations following the description given in Sec. II-E1, where the initial acceleration process noise $\sigma_{\text{acc}} = 8\,\frac{\text{cm}}{\text{s}^2}$ and the initial velocity weight $w_v = 0.0125$. Since the LHF has very narrow modes, the weights a_n^i are compressed with a roughening factor which means that the exponent of the LHF was divided by this factor. The initial value of the roughening factor was set to value of 100. During the iterations of the PF-PSO filter, these three parameters were linear decreased to simulate an annealing process, whereas the roughening factor was decreased until it reaches 1. To enhance robustness of the point-estimate $\hat{\mathbf{p}}$ of the MLE, we computed the median over the entire set of particles at each trajectory point. To generate the error CDFs we performed Monte-Carlo simulations averaged over 30 [1] dynamic model noise realizations.

B. Discussion of Performance Results

1) UWB-CIR measurements and DM estimate: In Fig. 2 the CIR of the signal received at anchor 2 and agent position $\mathbf{p} = [2.2, 6.6]^{\text{T}}$ is shown. The direct LOS path is clearly visible together with MPCs corresponding to specular reflections of first and second order. Their expected delays are illustrated in the figure as dashed gray vertical lines. One can observe that they fit the model quite well. The amplitude and phase of the emitted wave change according to the reflection coefficient of the wall. This is not modeled by the VA and we observe that not all expected VAs have a significant contribution.

2) Measurements, Position Likelihood, and CRLB: In Fig. 3, the likelihood (3) is shown in log-domain evaluated for the whole room for a measured CIR $\mathbf{r}^{(j)}$ between the agent located at position $\mathbf{p} = [2.2, 6.6]^{\text{T}}$ and the two anchors. In the figure, the multi-modality of the LHF is clearly visible. The global maximum at $\hat{\mathbf{p}} = [2.189, 6.599]^{\text{T}}$ matches the true position of the agent very well. The radii of the arcs with a high likelihood correspond to the delays of the LOS and VAs visible in the measurements. In the figure, we also plot the estimated positions and co-variances (estimated from particles) for a few trajectory points together with the computed CRLB of the position error. Both error ellipses are plotted with hundred-fold standard deviation. The orientation of the error ellipses depends on the geometry of the room and the positions of the anchors and the agent involved. We observe that the orientation and size of the CRLB error ellipses fit well with the estimated co-variance ellipses. Small deviations can be explained by the fact that the co-variance has to be estimated from a set of measurements rather than from a single measurement. The same holds for the estimation of parameters needed for the computation of the CRLB, c.f. (6). So, this comparison gives just an approximate comparison between the CRLB and the co-variance of the position estimate.

3) Positioning performance: In Fig. 4, the cumulative distribution functions (CDFs) of the position error are shown for the grid-based MAP and the MLE (PF-PSO method). These CDFs include data from all 220 agent positions using only anchors 1 and 2 individually and in combination (top to bottom). The CDF plots for grid-based MAP and MLE *"without DM"* neglect the knowledge of DM, i.e. $\mathbf{C}^{(j)} = N_0^{(j)}\mathbf{I}_M$ in the likelihood (3). Then the signal model reduces to the deterministic MPC plus additional AWGN (c.f. (1)). We observe that for both methods, the knowledge of DM results in a reduction of the position errors. Also, the occurrence of

[1] We observed that this number of used Monte-Carlo simulations leads to a steady state outcome suggesting that it is sufficiently high.

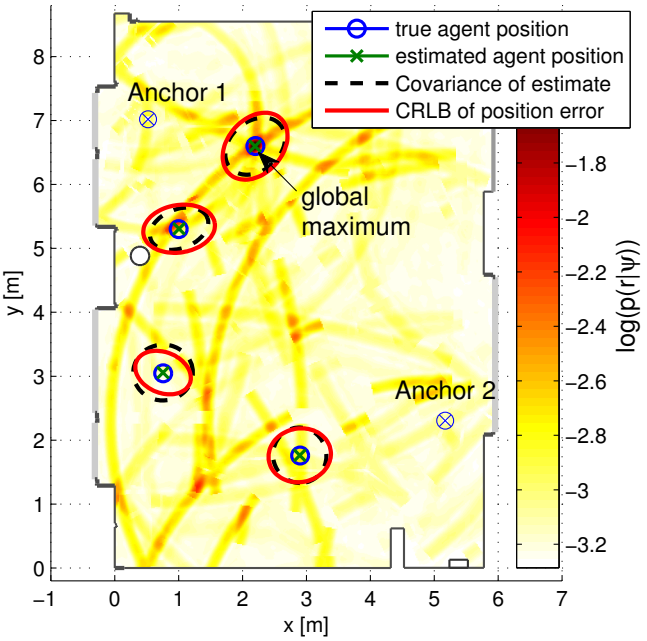

Fig. 3. Likelihood evaluated over the whole room. The anchors are placed at $\mathbf{p}_1^{(1)} = [0.5, 7]^{\mathrm{T}}$ and $\mathbf{p}_1^{(2)} = [5.2, 3.2]^{\mathrm{T}}$, the agent is placed at $\mathbf{p} = [2.2, 6.6]^{\mathrm{T}}$. The global maximum at position $\hat{\mathbf{p}} = [2.189, 6.599]^{\mathrm{T}}$ matches well with the true agent position. Additionally, the estimated agent position, the co-variance and the CRLB are shown with hundred-fold standard deviation for a few other agent positions.

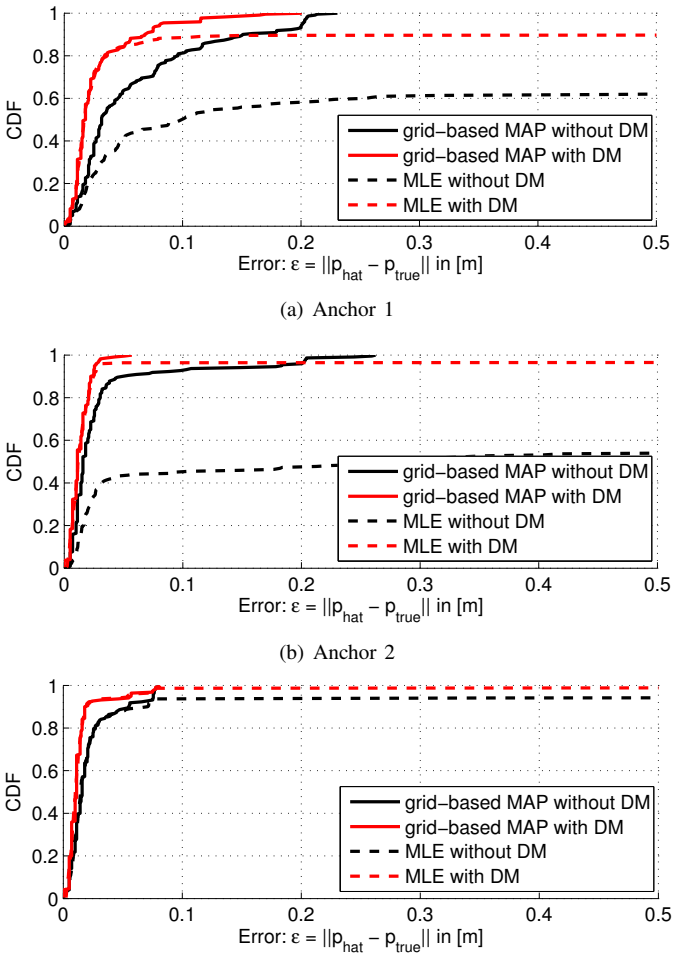

(a) Anchor 1

(b) Anchor 2

(c) Anchor 1 and 2

Fig. 4. CDFs for the grid-based MAP and MLE methods, with and without considering DM in the LHF considering only anchor 1 (a), anchor 2 (b) or the combination of both (c).

outliers is reduced when considering DM, which demonstrates the benefit of the suggested signal model and can be seen as a measure of higher *robustness*. If only anchor 2 is active, the position error is below 2.5 cm in 90 % of the estimates for the grid based MAP method considering DM and 5.5 cm without DM knowledge.

The MLE with DM knowledge is also below 2.5 cm in 90 % of the estimates while it reaches a similar accuracy in only 40 % of the cases without DM. For all combinations of the involved anchors without DM knowledge, the performance of the MLE is much worse. The reasons for this are twofold: First, the model is less accurate, thus modes of the LHF at the wrong position are too optimistic which leads more often to a convergence of the MLE in the wrong mode. The second issue is of numerical nature. Due to the more probable model-mismatch of the signal model, the values of the log-LHF are even (much) smaller and also exhibit a larger dynamic range. Hence, the LHF is more skewed which leads to the requirement of more particles for the MLE. If anchor 1 is active, the positioning error shows the same tendency, but the values are increased. This suggests that the location of anchor 1 is less suited for positioning along the agent trajectory compared to the location of anchor 2.

Since information available through measurements never increases the uncertainty, the error is the smallest when both anchors are active. This is independent of the signal model used (with or without DM). The lowest error is achieved if DM is taken into account. Then the resulting error remains below 1.9 cm for both methods in 90 % of the position estimates. Note that the bandwidth used is 2GHz, yielding a delay resolution of 15 cm.

IV. Conclusion and Outlook

In this paper we have shown that the proposed MLE algorithm for multipath-assisted indoor positioning is working with real channel measurement in a *robust* and *accurate* sense. Due to the rich geometric information contained in the MPCs, positioning is possible with only one anchor. Depending on the environment this is also true for non-LOS scenarios, in principle. In-depth verification of this is part of future work. However, in a LOS scenario considering DM we achieved a position error of less than 2.5 cm in 90 % of the estimates for only one active anchor. The results show that the knowledge of DM leads to significant improvement of robustness *and* accuracy of the estimation scheme. However, the demonstrated DM estimation from a set of measurements with optimal position knowledge has to be seen as an ideal benchmark for

the benefit of using DM. In ongoing work we learn the DM statistics during tracking of an agent moving through the room to establish a more practical estimator.

REFERENCES

[1] A. Molisch, "Ultra-wide-band propagation channels," *Proceedings of the IEEE*, vol. 97, no. 2, pp. 353–371, Feb. 2009.

[2] P. Meissner and K. Witrisal, "Analysis of position-related information in measured UWB indoor channels," in *Antennas and Propagation (EUCAP), 2012 6th European Conference on*, March 2012, pp. 6–10.

[3] ——, "Multipath-assisted single-anchor indoor localization in an office environment," in *Systems, Signals and Image Processing (IWSSIP), 2012 19th International Conference on*, April 2012, pp. 22–25.

[4] Y. Shen and M. Win, "Fundamental limits of wideband localization; part I: A general framework," *Information Theory, IEEE Transactions on*, vol. 56, no. 10, pp. 4956–4980, Oct. 2010.

[5] K. Witrisal and P. Meissner, "Performance bounds for multipath-assisted indoor navigation and tracking (MINT)," in *Communications (ICC), 2012 IEEE International Conference on*, June 2012, pp. 4321–4325.

[6] M. Arulampalam, S. Maskell, N. Gordon, and T. Clapp, "A tutorial on particle filters for online nonlinear/non-gaussian bayesian tracking," *Signal Processing, IEEE Transactions on*, vol. 50, no. 2, pp. 174–188, Feb 2002.

[7] G. Tong, Z. Fang, and X. Xu, "A particle swarm optimized particle filter for nonlinear system state estimation," in *Evolutionary Computation, 2006. CEC 2006. IEEE Congress on*, 2006, pp. 438–442.

[8] J. Hu, Y. Wang, E. Zhou, M. Fu, and S. Marcus, "A survey of some model-based methods for global optimization," in *Optimization, Control, and Applications of Stochastic Systems*, ser. Systems & Control: Foundations & Applications. Birkhäuser Boston, 2012, pp. 157–179.

Real-Time Demonstration of Multipath-Assisted Indoor Navigation and Tracking (MINT)

Paul Meissner, Erik Leitinger, Manuel Lafer, and Klaus Witrisal
Graz University of Technology, Austria; E-mail: paul.meissner@tugraz.at

***Abstract*—This paper presents an evaluation of a demonstration system for multipath-assisted indoor navigation and tracking (MINT). MINT overcomes the non-line-of-sight problems of range-based indoor localization systems by explicitly using location information of reflected signal components. With the real-time demonstration system, performance evaluations are possible without the need to rely on pre-recorded measurement trajectories or simulated radio channels. Hence, the robustness and accuracy of MINT in different environments can be tested easily and a proof-of-concept in close-to-practical conditions is obtained. Exemplary results in two different rooms highlight the following key findings: The excellent performance of MINT that we reported previously based on pre-recorded measurements can also be obtained with the real-time system, i.e. 5 cm accuracy for 90 % of the estimates at a bandwidth of 2 GHz. Furthermore, the covariance of the position error of the tracking filters matches well with the corresponding Cramér-Rao lower bound (CRLB).**

I. Introduction

Non-line-of-sight (NLOS) situations between anchors and agents are the main reason for errors for radio based indoor localization systems. Enclosed indoor scenarios cause strong specular reflections and also a large level of diffuse (often called dense) multipath (DM). Errors caused by multipath can be dealt with by detecting NLOS situations and mitigating the corresponding range errors [1], [2]. Using the previously introduced *multipath-assisted* indoor navigation and tracking (MINT) approach [3], [4], the specular reflections can be turned into an advantage. Assuming that the floor plan of the environment is known, the travel times of specular multipath-components (MPCs) can be matched to the geometry by introducing *virtual* anchors (VAs, see Fig. 1).

As such a scheme relies heavily on the propagation channel, we have obtained numerous position-resolved channel measurements [5] to evaluate its performance [4], [6]. However, channel measurement campaigns are tedious to perform. A real-time demonstration system, which is discussed in this paper, allows for flexible and rapid evaluation of e.g. novel algorithms for MINT in more realistic conditions. Issues like fast motion changes and signal obstructions can be tested realistically and easily. For indoor localization systems, experimentation is an important way to understand the limitations and implications of the often heterogeneous requirements and environments. A method for precise anchor-free positioning in a specific environment is presented in [7], requiring many closely spaced measurements. For the evaluation of cooperative methods, large-scale campaigns are often more appropriate [8], [9], but similarly tedious to perform.

This work was partly supported by the Austrian Science Fund (FWF) within the National Research Network SISE project S10610, and by the Austria Research Promotion Agency (FFG) within KIRAS PL3, grant nb. 832335 “LOBSTER”.

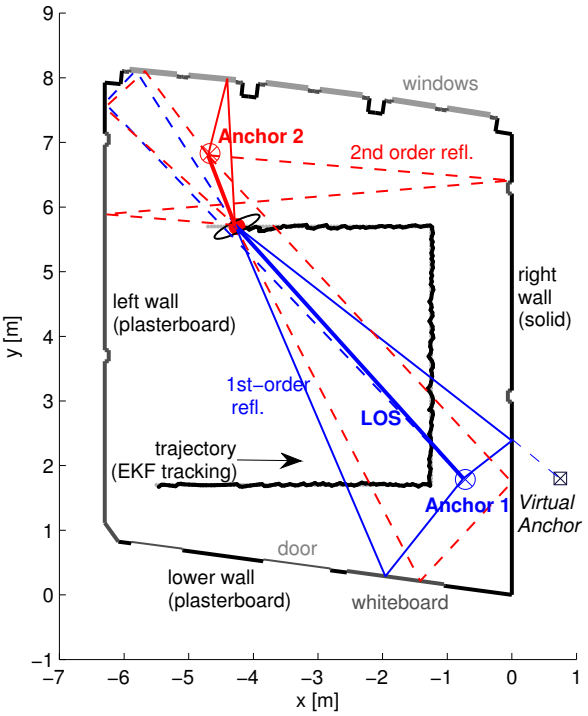

Fig. 1. Setup of the MINT demonstration system in Room 1. The tracking algorithm described in Sec. II is used on a known test trajectory to allow for error computation. Signal contributions from LOS-, first-order-, and second-order reflections are illustrated in bold, thin solid, and thin dashed lines, respectively. Color encodes the anchor number. On the right side, an example for a first-order VA is depicted for Anchor 1.

For the MINT demonstration system, it is desirable to compare the performance of different implementations in certain environments. Also, the localization accuracy can be compared to theoretical predictions given by performance bounds that include effects such as path overlap [3] and the DM [6]. The contributions of this paper are:

- We present a proof-of-concept for the MINT approach using a real-time demonstrator, showing excellent accuracy and robustness.
- Using tracking results obtained in two example rooms, we show how estimation of path parameters motivated by theory can be used to predict the performance of the system in an environment and also to improve the

performance.

In the remainder of this paper, Sec. II deals with the scenario, the models and the tracking algorithms, which is a recap from previous work. Section III briefly introduces the hardware of the demo system, while Sec. IV presents the prediction of the expected localization performance based on sample measurements. Finally, detailed results are presented and discussed in Sec. V.

II. Scenario, Model and Algorithms

The aim of this paper is to present a real-time demonstration system for the MINT approach [3]. We discussed the specific implementation and its evaluation based on pre-recorded channel measurements in [4] and [6] . In this paper, we therefore restrict the presentation of models and algorithms to a minimum and focus our attention on results obtained with the demonstration system in two exemplary scenarios.

Fig. 1 shows one of the two rooms used in this paper and illustrates the MINT approach itself, using a snapshot of the graphical output of the demonstration system during tracking. Up to $J = 2$ anchors at known positions are placed within a room to track a moving agent. As discussed in detail in [4] and references therein, we use the known floor plan to mirror the anchor coordinates with respect to each reflective surface to calculate the positions of the VAs [10]. The first-order VA corresponding to Anchor 1 and the right wall is illustrated in Fig. 1. The VA is a geometric model for the path delay of the corresponding MPC. Given that the MPC is detectable in the received signal, the VA can in principle be used as if it was a physically existing anchor.

The signal between the j-th anchor and the agent at the ℓ-th position $\mathbf{p}_\ell$, is written as [3]

$$r_\ell^{(j)}(t) = \sum_{k=1}^{K_\ell^{(j)}} \alpha_{k,\ell}^{(j)} s(t - \tau_{k,\ell}^{(j)}) + s(t) * \nu_\ell^{(j)}(t) + w(t) \quad (1)$$

where the $\alpha_{k,\ell}^{(j)}$ and $\tau_{k,\ell}^{(j)}$ are the complex amplitudes and delays of the k-th deterministic MPCs, respectively. The signal $s(t)$ denotes the transmitted pulse. The signals $\nu_\ell^{(j)}(t)$ and $w(t)$ denote DM and white Gaussian measurement noise, respectively [3]. Especially in indoor environments, DM plays a large role in the detectability of the deterministic MPCs, which will be discussed in more detail later.

The estimation of the arrival times of the deterministic MPCs is done as in [4] using an iterative search-and-subtract implementation of a maximum-likelihood estimator based on the assumption of separable paths, i.e.

$$\{\hat{\tau}_{k,\ell}^{(j)}\} = \arg\min_{\{\tau_{k,\ell}^{(j)}\}} \int_T \left| r_\ell^{(j)}(t) - \sum_{k=1}^{\hat{K}_\ell^{(j)}} \hat{\alpha}_{k,\ell}^{(j)} s(t - \tau_{k,\ell}^{(j)}) \right|^2 dt. \quad (2)$$

The path amplitudes are nuisance parameters and are estimated using the projection of the received signal on a unit energy pulse template shifted to the corresponding delay

$$\hat{\alpha}_{k,\ell}^{(j)} = \int_0^T [r_\ell^{(j)}(t)]^* s(t - \hat{\tau}_{k,\ell}^{(j)}) dt. \quad (3)$$

The number of estimated MPCs $\hat{K}_\ell^{(j)}$ should be chosen corresponding to the number of expected specular paths in an environment.

We focus on the influence of the measurement on the tracking and hence restrict the motion model of the agent to a simple linear Gaussian constant-velocity model

$$\begin{aligned} \mathbf{x}_{\ell+1} =& \mathbf{F}\mathbf{x}_\ell + \mathbf{G}\mathbf{n}_{\mathrm{a},\ell} \quad (4) \\ =& \begin{bmatrix} 1 & 0 & \Delta T & 0 \\ 0 & 1 & 0 & \Delta T \\ 0 & 0 & 1 & 0 \\ 0 & 0 & 0 & 1 \end{bmatrix} \mathbf{x}_\ell + \begin{bmatrix} \frac{\Delta T^2}{2} & 0 \\ 0 & \frac{\Delta T^2}{2} \\ \Delta T & 0 \\ 0 & \Delta T \end{bmatrix} \mathbf{n}_{\mathrm{a},\ell}. \end{aligned}$$

Here, ΔT denotes the sampling time[1] and the state vector $\mathbf{x}_\ell$ of the agent contains x- and y-position and velocity. The driving acceleration noise term $\mathbf{n}_{\mathrm{a},\ell}$ models motion changes that deviate from this model. The tracking is done as in [4] using an Extended Kalman Filter (EKF) with data association (DA), since the estimated MPC arrival times in (2) are not associated to the VAs. At the position predicted by the EKF, the expected VAs and the corresponding delays (those whose reflection paths are possible) are calculated using pre-computed ray-tracing results. The estimated arrival times from (2) are then matched to these such that the cumulative distance of estimated and expected delays is minimized, using the optimal subpattern assignment approach [11]. Associations at a distance higher than a given maximum ranging uncertainty, the so-called cut-off distance d_c are discarded. The remaining associated delays and corresponding VA positions are then passed to the EKF for the update step, in which a trilateration w.r.t. the associated VAs is performed. We refer the reader to [4] and references therein for a much more detailed description.

III. Hardware Setup and Signal Preprocessing

The receiving and transmitting device used for the real-time system is an M-sequence based UWB channel sounder developed by the German company *Ilmsens*. As there are two RX and one TX channels, the moving agent in the demonstration system is the TX and the anchors are the RXs, but from the view of the algorithms, these roles could also be reversed. The channel sounder is capable of sending and receiving up to 13 signals per channel per second, hence the lowest possible sampling time is $\Delta T = 0.077\,\mathrm{s}$. On TX and RX sides, self-made dipole-like antennas made of Euro-cent coins are used. They have an approximately uniform radiation pattern in azimuth domain and zeroes in the direction of floor and ceiling. The antennas are connected to the measurement device using cables, and are mounted on tripods. The tripod for the moving TX is equipped with wheels.

The received signal is cross-correlated with the used M-sequence to obtain an estimate of the bandpass channel impulse response $h_\ell^{(j)}(t)$. The channel sounder covers approximately the whole FCC UWB frequency range of $3.1 - 10.6\,\mathrm{GHz}$. To select any desired subband with center frequency f_c and bandwidth B within this range, we use a raised cosine filter with impulse response $s(t)$ with an

[1] The difference of time-steps at which measurements are performed.

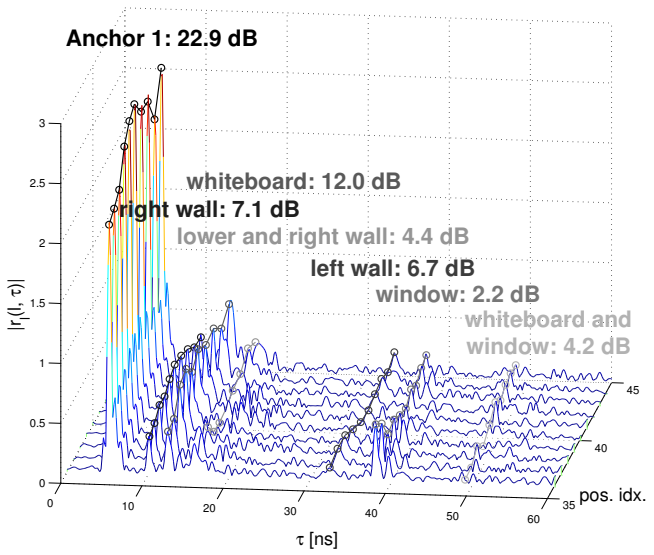

Fig. 2. Received signal from Anchor 1 in Room 1 over a short measurement trajectory (the corner part of the SINR estimation points shown in Fig. 4a) for $T_\mathrm{p} = 0.5\,\mathrm{ns}$ and $f_\mathrm{c} = 7\,\mathrm{GHz}$. The estimated SINRs of selected VAs (reflectors) are shown together with the evolution of their path amplitudes.

effective pulse duration $T_\mathrm{p} = 1/B$ and a fixed roll-off factor $\beta_\mathrm{R} = 0.5$. By downconversion, a received complex baseband signal according to (1) is obtained as

$$r_\ell^{(j)}(t) = \left[h_\ell^{(j)}(t) * s(t) e^{j2\pi f_\mathrm{c} t}\right] e^{-j2\pi f_\mathrm{c} t}. \tag{5}$$

All signal processing is done on a computer using Matlab, which allows for maximum flexibility. Different levels of graphical output are selectable by the user, such as the visualization of currently used MPCs and their propagation paths as shown in Fig. 1. After setting up the system in an environment, transfer functions of connectors and cables as well as the crosstalk between TX and RX channels are removed with a calibration procedure similar to [12].

IV. Prediction of Localization Performance

When setting up the demonstration system in an environment, it is beneficial to have a prediction of the expected localization performance available. This can be achieved e.g. using the Cramér-Rao lower bound (CRLB) on the position estimation for MINT, which was derived in [3]. Under the assumption of no path overlap (PO), i.e. the deterministic MPCs in (1) are orthogonal, the equivalent Fisher information matrix (EFIM) [13] on the position is given as

$$\mathbf{J}_{\mathbf{p}_\ell} = \frac{8\pi^2\beta^2}{c^2} \sum_{j=1}^{J} \sum_{k=1}^{K_\ell^{(j)}} \mathrm{SINR}_{k,\ell}^{(j)} \mathbf{J}_\mathbf{r}(\phi_{k,\ell}^{(j)}), \tag{6}$$

where β denotes the effective (RMS) bandwidth of $s(t)$ and $\mathrm{SINR}_{k,\ell}^{(j)}$ denotes the signal-to-interference-and-noise-ratio of the k-th deterministic MPC at the ℓ-th position. The ranging direction matrix $\mathbf{J}_\mathbf{r}(\phi_{k,\ell}^{(j)})$ [13] is defined as

$$\mathbf{J}_\mathbf{r}(\phi_{k,\ell}^{(j)}) = \begin{bmatrix} \cos^2(\phi_{k,\ell}^{(j)}) & \cos(\phi_{k,\ell}^{(j)})\sin(\phi_{k,\ell}^{(j)}) \\ \cos(\phi_{k,\ell}^{(j)})\sin(\phi_{k,\ell}^{(j)}) & \sin^2(\phi_{k,\ell}^{(j)}) \end{bmatrix}. \tag{7}$$

It indicates the geometric information of the k-th MPC, the angle from the k-th VA to the position $\mathbf{p}_\ell$, as it has one eigenvector pointing in the direction $\phi_{k,\ell}^{(j)}$. The $\mathrm{SINR}_{k,\ell}^{(j)}$, which weights this geometric information, is defined as

$$\mathrm{SINR}_{k,\ell}^{(j)} = \frac{|\alpha_{k,\ell}^{(j)}|^2}{N_0 + T_\mathrm{p} S_{\nu,\ell}^{(j)}(\tau_{k,\ell}^{(j)})}. \tag{8}$$

It is the ratio of the energy of the k-th MPC to the sum of the noise PSD N_0 and the effective power of the DM at the delay $\tau_{k,\ell}^{(j)}$. The latter is characterized by the power delay profile $S_{\nu,\ell}^{(j)}(\tau)$ of the DM [3].

We observe that the SINRs of deterministic MPCs require knowledge of the PDP of the DM at position ℓ. This requires many closely-spaced measurements around $\mathbf{p}_\ell$, which are usually not available. An alternative estimator of the SINR based on a Gaussian model for the DM was derived in [6] and is also used here. In short, it uses a few position-resolved measurements within a region, where the corresponding MPCs are visible. On these, non-overlapping MPCs are estimated as in (2) and corrected for deterministic effects such as path loss and also random effects such as uncertainties in the floor plan. Finally, the estimator is based on the ratio of the estimated deterministic MPC energy to the variations that still remain in the estimated amplitudes after the correction steps.

It is important to note that only position-averaged MPC SINRs can be estimated by this method since statistical moments of the estimated amplitudes need to be computed. We account for this fact by estimating SINR_k globally for each VA, which describes the reliability of the localization information of the respective MPC. Fig. 2 shows several received signals from Anchor 1 in Room 1, using $T_\mathrm{p} = 0.5\,\mathrm{ns}$ and $f_\mathrm{c} = 7\,\mathrm{GHz}$. Also shown is the evolution of the estimated amplitudes of selected deterministic MPCs and the estimated SINR values. The trajectory part covers a distance of $45\,\mathrm{cm}$ and is part of the SINR estimation points in Room 1 (see Fig. 4a). It can be observed that MPCs with low variations in their amplitudes, such as the LOS, whiteboard and right wall, in general have a large SINR. If there are large variations which cannot be attributed to deterministic effects, the SINR is considerably lower, such as for the window.

The estimated SINRs can be used with (6) to get an EFIM estimate $\hat{\mathbf{J}}_{\mathbf{p}_\ell}$. Note that the only location-dependent effect remaining is the geometry. The ranging direction matrices account for the direction of the information, while the room geometry defines which reflections are visible at $\mathbf{p}_\ell$ and contribute to the EFIM. The expected localization accuracy for an environment can be quantified by the position error bound (PEB)

$$\mathrm{E}\{\|\mathbf{p}_\ell - \hat{\mathbf{p}}_\ell\|\} \geq \mathrm{PEB}(\mathbf{p}_\ell) = \sqrt{\mathrm{Tr}\,(\mathbf{J}_{\mathbf{p}_\ell}^{-1})}. \tag{9}$$

V. Example Results

A. Evaluation Scenarios and Parameters

The two rooms used are shown together with indications of the building materials in Figs. 1 and 5a, respectively. To quantitatively evaluate robustness and accuracy of the MINT

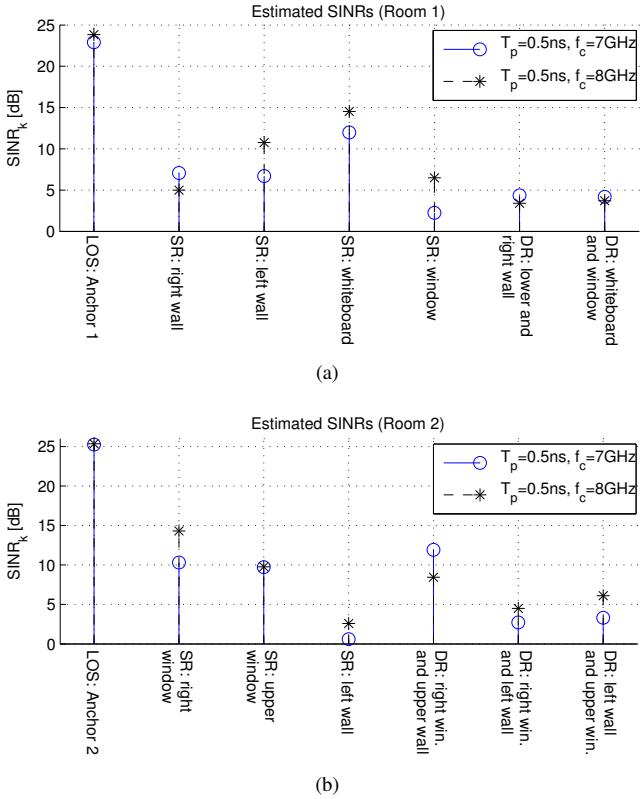

Fig. 3. Exemplary estimated SINRs of deterministic MPCs in Room 1 for Anchor 1 (a) and in Room 2 for Anchor 2 (b). A pulse duration $T_\mathrm{p} = 0.5\,\mathrm{ns}$ and two different center frequencies of $f_\mathrm{c} = 7\,\mathrm{GHz}$ and $f_\mathrm{c} = 8\,\mathrm{GHz}$ were used. SR and DR denote single- and double reflection, respectively.

implementation, one sample trajectory is used in each room, to enable calculation of a position error. The test trajectories consist of 235 points spaced by $\Delta_\mathbf{p} = 5\,\mathrm{cm}$ in Room 1, and of 154 points spaced by $\Delta_\mathbf{p} = 3\,\mathrm{cm}$ in Room 2. It should be noted that although the evaluation is done only on those trajectories, the results obtained are in close accordance with other results in different environments. As will be shown by the PEB results, they also cover challenging regions in these rooms and the performance accurately reflects the expectations provided by the bounds that are based on the estimated SINRs.

In the motion model, the process noise covariance matrix $\mathbf{Q} = \sigma_a^2 \mathbf{G}\mathbf{G}^\mathbf{T}$ is chosen to allow for motion at a given maximum velocity in x- or y-direction, say $v_{x,\max}$. This is obtained by selecting the process noise variance in the acceleration-domain as $\sigma_a^2 = (\frac{v_{x,\max}}{3\Delta T})^2$. During real-time operation, only $v_{x,\max}$ has to be chosen. ΔT is measured for every iteration and hence also σ_a^2 is updated, since depending on the chosen level of graphical output, the sampling time is not constant. For the quantitative performance evaluations, we set $v_{x,\max} = \Delta_\mathbf{p}/\Delta T$ at e.g. $\Delta T = 1$, to avoid errors that are due to the motion model.

The measurement uncertainty in the EKF can be determined using an approach discussed in [14]. Based on estimates of SINRs as described in Sec. IV, the tracking can be tuned to the reflection properties of the environment. The locations of these measurement points are illustrated in Figs. 4a and 5a. Of course MINT can be used without this information [4]. To

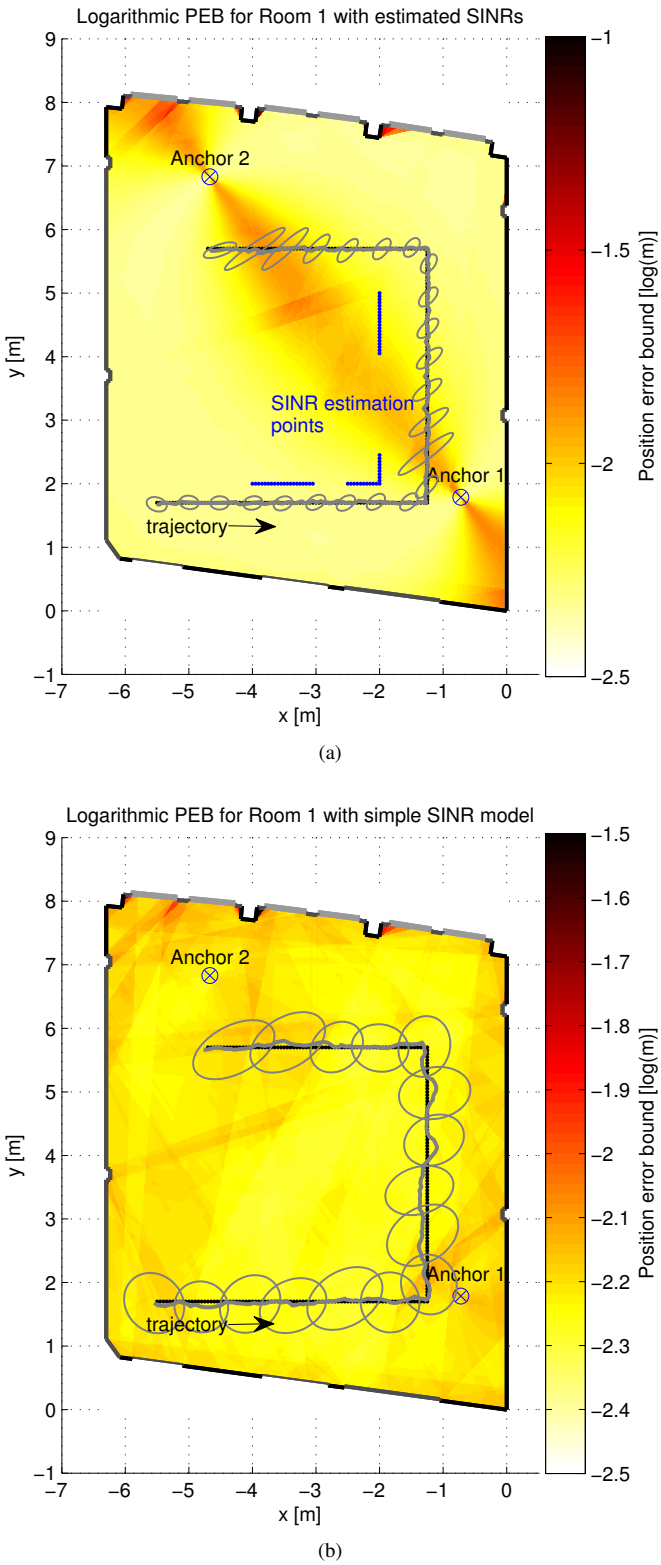

Fig. 4. Logarithmic CRLB for the position error over Room 1 for $T_\mathrm{p} = 0.5\,\mathrm{ns}$ and $f_\mathrm{c} = 8\,\mathrm{GHz}$. (a) SINRs are used which have been estimated at the points marked in blue. (b) No SINR knowledge is available, but the mean SINR equals the mean of the estimated ones. Gray lines indicate MINT tracking results (estimated tracks and 40-fold standard deviation ellipses) for the respective scenario. It is evident that the SINRs can be used to obtain a much more realistic performance prediction.

enable a fair comparison, the SINRs for this case are selected as the mean of the estimated ones. The cutoff distance has been chosen as $d_c = 0.12$ m. Initialization of the EKF is done with the true position and zero velocity, since the initialization problem is out of scope of this paper. However, it can be solved using maximization of the likelihood function that is also used to derive the CRLB [15] or with a bank of parallel EKFs.

B. Estimation of the MPC SINRs and the PEB

In both rooms, SINRs of the LOS-component and potential first- and second-order reflections are estimated using the method described in Sec. IV and [6], [14] using 60 position-resolved measurements per room, as indicated in Figs. 4a and 5a. A subset of the obtained SINR results is shown in Fig. 3 for a pulse duration of $T_p = 0.5$ ns and two different center frequencies of 7 and 8 GHz. It can be seen that especially the plasterboard walls provide more information at the higher frequencies. As they represent spatially extended reflectors with large visibility regions, they are potentially important for MINT. Hence, observing the SINRs can give important hints on the optimal frequency range for a given scenario.

Using the geometry, (6), and (9), the CRLB on the position error (neglecting path overlap) can be computed for a scenario. The resulting PEB is illustrated in Figs. 4 and 5 for both rooms, with and without estimated SINRs, but – to allow for a fair comparison – for the same sets of MPCs. In the latter case, a simple model for the SINR is used: For the sake of a fair comparison, the SINRs of (8) are chosen such that their mean equals the mean of the estimated ones. Also, each reflection order decreases the SINR by an example value of 3 dB.

For Room 1, the PEB is shown using MPCs from both anchors. Without knowledge of the MPC SINRs, the PEB mostly encodes the expected visibility regions of the reflections and as such gives only a rough indication of the expected performance. If estimated SINRs are used, we can clearly observe a dilution of precision around the room diagonal, where location information is mostly coming from similar directions. This case is also illustrated in Fig. 1, where the MPCs are shown that the EKF can use in this region. We conclude that awareness of the SINRs gives a clearer picture of the expected performance in a given scenario. It should be noted again that the detrimental effect of path overlap [3] is not reflected by this PEB.

In Room 2, we illustrate the PEB for using only a single anchor (Anchor 2). Exploiting multipath, localization is still possible with MINT. Also here, the SINRs give good performance indications. For example, the visibility regions corresponding to the middle right and the upper window (c.f. Fig. 3b) are visible, which have rather large SINRs.

C. Tracking Results

Fig. 6 shows CDFs of the position error along the trajectories for MINT in both rooms. The evaluations have again been performed with a pulse duration of 0.5 ns and the two center frequencies of 7 and 8 GHz, with and without estimated SINRs. A general advantage is visible in these two rooms at the higher frequency range. According to our experience with

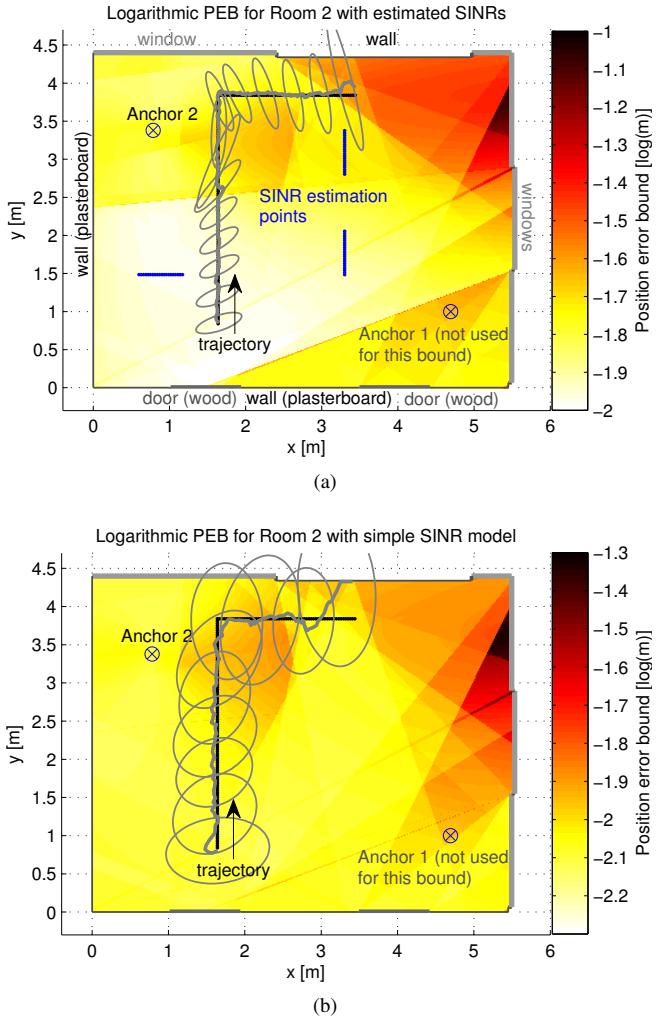

Fig. 5. Logarithmic CRLB for the position error over Room 2 for $T_p = 0.5$ ns and $f_c = 8$ GHz, if only Anchor 2 is used. (a) SINRs are used which have been estimated at the points marked in blue. (b) No SINR knowledge is available, but the mean SINR equals the mean of the estimated ones. Gray lines indicate single-anchor MINT tracking results (estimated tracks and 30-fold standard deviation ellipses).

the demonstration system, we attribute this effect mostly to the higher SINRs of the large plasterboard walls. For the case of no SINR knowledge, the MINT implementation achieves a performance of 13 cm for 90 % of the estimates in Room 1 and 21 cm for 90 % of the estimates in Room 2. With estimated SINRs, 90 % of the position errors are within approximately 5 cm in both rooms, in Room 1 even with the lower center frequency. In Room 2, using the SINRs allows for a similar performance using only a *single* anchor.

Figs. 4 and 5 also contain the tracking results shown in the CDFs in Fig. 6. Furthermore, the (significantly magnified) estimation error standard deviation ellipses of the EKF are indicated at some points. We observe an excellent tracking performance together with a largely reduced variance when estimated SINRs are used. In this case, the error ellipses follow well the predicted PEB and indicate the geometric dilution of precision, especially when the agent is between the two anchors.

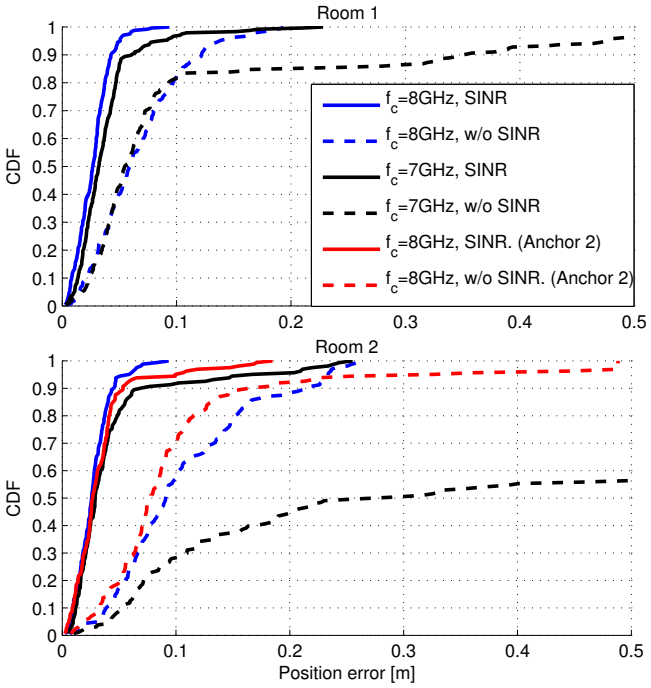

Fig. 6. CDFs of the position error for Room 1 (upper plot) and Room 2 (lower plot). Using the estimated SINRs, similar performance can be obtained in both rooms. Otherwise, the robustness can not always be achieved, especially in challenging environments such as Room 2. As predicted by the SINRs, the higher center frequency is beneficial there. For Room 2, results are also shown for using only a single anchor.

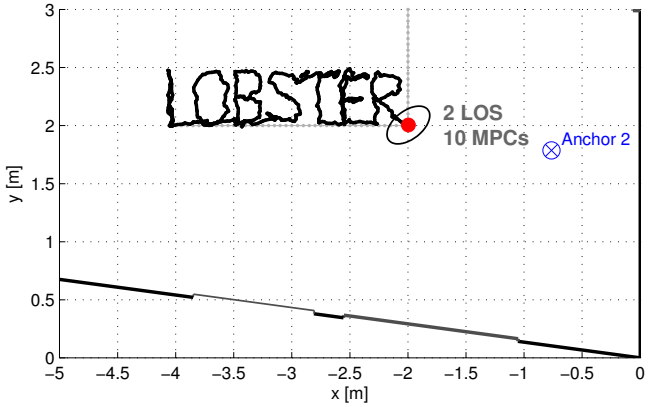

Fig. 7. Exemplary tracking results in Room 1, using estimated SINRs and $T_\mathrm{p} = 0.5\,\mathrm{ns}$ and $f_\mathrm{c} = 7\,\mathrm{GHz}$. About 900 time steps were used to write the funding project's name "LOBSTER". The letter height is roughly $0.5\,\mathrm{m}$, which demonstrates that an accuracy well within $10\,\mathrm{cm}$ can be achieved robustly.

An exemplary tracking result using SINR estimates is shown in Fig. 7, where the funding project's name "LOBSTER" has been written in letters with a height of approximately $0.5\,\mathrm{m}$. The legibility again demonstrates the good performance.

VI. Conclusions and Outlook

We have presented a real-time implementation of the MINT approach in the form of a demonstration system. This system can be used to examine the localization performance and to identify influences on it in different environments. The results show that the excellent performance of MINT that we have reported previously for measurement campaigns can be reproduced with the real-time implementation. Also, the CRLB on the position error can be estimated using a few measurements. This provides a detailed prediction of the achievable accuracy in some specific environment. The tracking algorithm also benefits from this additional channel awareness, as robustness and accuracy are improved.

The form of the position error bound used in this work is based on the simplifying assumption of no overlap in the deterministic MPCs. The extension of the measurement-based performance prediction to path overlap situations is a crucial step in ongoing research, since path overlap is an important and unavoidable performance impairment. In the current system, the MPC SINRs are estimated from position-resolved measurements that have been performed a-priori. Current work covers online learning of these estimates based on the results of the tracking algorithms.

References

[1] H. Wymeersch, S. Marano, W. Gifford, and M. Win, "A Machine Learning Approach to Ranging Error Mitigation for UWB Localization," *IEEE Transactions on Communications*, vol. 60, pp. 1719–1728, 2012.

[2] S. Marano and, W. Gifford, H. Wymeersch, and M. Win, "NLOS identification and mitigation for localization based on UWB experimental data," *IEEE Journal on Selected Areas in Communications*, vol. 28, no. 7, pp. 1026 –1035, 2010.

[3] K. Witrisal and P. Meissner, "Performance Bounds for Multipath-aided Indoor Navigation and Tracking (MINT)," in *International Conference on Communications (ICC)*, Ottawa, Canada, 2012.

[4] P. Meissner, E. Leitinger, M. Froehle, and K. Witrisal, "Accurate and Robust Indoor Localization Systems Using Ultra-wideband Signals," in *European Navigation Conference (ENC)*, Vienna, Austria, 2013. [Online]. Available: http://arxiv.org/abs/1304.7928

[5] P. Meissner, E. Leitinger, M. Lafer, and K. Witrisal, "MeasureMINT UWB database," 2013. [Online]. Available: www.spsc.tugraz.at/tools/UWBmeasurements

[6] P. Meissner and K. Witrisal, "Analysis of Position-Related Information in Measured UWB Indoor Channels," in *6th European Conference on Antennas and Propagation (EuCAP)*, Prague, Czech Repuplic, 2012.

[7] Y. Kuang, K. Astrom, and F. Tufvesson, "Single antenna anchor-free UWB positioning based on multipath propagation," in *Communications (ICC), 2013 IEEE International Conference on*, 2013.

[8] A. Conti, M. Guerra, D. Dardari, N. Decarli, and M. Win, "Network Experimentation for Cooperative Localization," *Selected Areas in Communications, IEEE Journal on*, vol. 30, no. 2, pp. 467–475, 2012.

[9] B. Denis, R. Raulefs, B. Fleury, B. Uguen, N. Amiot, L. de Celis, J. Dominguez, M. Koldsgaard, M. Laaraiedh, H. Noureddine, E. Staudinger, and G. Steinboeck, "Cooperative and heterogeneous indoor localization experiments," in *Communications Workshops (ICC), 2013 IEEE International Conference on*, 2013.

[10] J. Kunisch and J. Pamp, "An ultra-wideband space-variant multipath indoor radio channel model," in *Ultra Wideband Systems and Technologies, 2003 IEEE Conference on*, 2003, pp. 290 – 294.

[11] D. Schuhmacher, B.-T. Vo, and B.-N. Vo, "A Consistent Metric for Performance Evaluation of Multi-Object Filters," *IEEE Transactions on Signal Processing*, vol. 56, no. 8, pp. 3447 –3457, 2008.

[12] R. Cepeda, S. C. J. Parker, and M. Beach, "The Measurement of Frequency Dependent Path Loss in Residential LOS Environments using Time Domain UWB Channel Sounding," in *Ultra-Wideband, 2007. ICUWB 2007. IEEE International Conference on*, 2007.

[13] Y. Shen and M. Z. Win, "Fundamental Limits of Wideband Localization - Part I: A General Framework," *IEEE Transactions on Information Theory*, pp. 4956 –4980, Oct. 2010.

[14] P. Meissner, E. Leitinger, and K. Witrisal, "UWB for Robust Indoor Tracking: Weighting of Multipath Components for Efficient Estimation," *IEEE Wireless Communications Letters*, 2014, submitted.

[15] E. Leitinger, M. Froehle, P. Meissner, and K. Witrisal, "Multipath-Assisted Maximum-Likelihood Indoor Positioning using UWB Signals," in *IEEE ICC 2014 Workshop on Advances in Network Localization and Navigation (ANLN)*, 2014, accepted.

UWB for Robust Indoor Tracking: Weighting of Multipath Components for Efficient Estimation

Paul Meissner, Erik Leitinger, and Klaus Witrisal

***Abstract*—In a radio propagation channel, deterministic reflections carry important position-related information. With the help of prior knowledge such as a floor plan, this information can be exploited for indoor localization. This letter presents the improvement of a multipath-assisted tracking approach using information about the relevance of deterministic multipath components in an environment. This information is fed to a tracking filter as observation noise model. It is estimated from a few training signals between anchors and an agent at known positions. Tracking results are presented for measurements in a partial non-line-of-sight environment. At a bandwidth of 2 GHz, an accuracy of 4 cm can be achieved for over 90 % of the positions if additional channel information is available. Otherwise, this accuracy is only possible for about 45 % of the positions. The covariance of the estimation matches closely to the corresponding Cramèr-Rao Lower Bound.**

I. Introduction

Robustness and accuracy are key requirements of indoor localization systems. We define robustness as the percentage of cases in which a system can achieve its given potential accuracy. Due to their fine time resolution, range-based ultra-wideband (UWB) systems provide accurate distance estimates between anchors and the agent to be localized [1]. However, a non-line-of-sight (NLOS) situation can decrease the robustness due to biased range estimates. We have proposed an approach called multipath-assisted indoor navigation and tracking (MINT) to enhance the robustness [2], [3]. It makes use of the floor plan to associate multipath components (MPCs) to the surrounding geometry.

In this paper, we show how position-related information can be used efficiently as additional prior information. Channel parameters describing the reliability of the reflected MPCs [3], [4] are estimated from a few training signals with an agent at known positions and used in the tracking filter as measurement noise model. For a navigating agent, awareness to the uncertainty of the available information is crucial for the tracking performance both in theoretic [5] and in practical settings [6]. Taking into account diffuse multipath (DM) allows for much more realistic performance indications [7], especially in dense multipath environments.

The main contributions of this letter are:

- We show that a multipath-assisted tracking approach can be made aware of the relevance of specific deterministic MPCs in an environment.
- Using measurements, we show that centimeter-level accuracy can be achieved robustly also in NLOS conditions.

P. Meissner, E. Leitinger and K. Witrisal are with Graz University of Technology, Graz, Austria, email: paul.meissner@tugraz.at.

The authors thank Manuel Lafer for his help in performing the measurements.

Notation: The symbols $*$, $(\cdot)^T$, $(\cdot)^*$, $\mathbb{E}\{\cdot\}$, $\Re\{\cdot\}$, and $\mathbf{I}_N$ denote convolution, transposition, conjugation, expectation, real part, and an identity matrix of dimension N, respectively.

II. Tracking and Channel Estimation

A. Signal and Geometry Models

We aim at tracking a mobile agent in an environment with J anchors at known positions. The signal between the j-th anchor and the agent at the position $\mathbf{p}_\ell$ is modeled as [3]

$$r_\ell^{(j)}(t) = \sum_{k=1}^{K_\ell^{(j)}} \alpha_{k,\ell}^{(j)} s(t - \tau_{k,\ell}^{(j)}) + s(t) * \nu_\ell^{(j)}(t) + w(t). \quad (1)$$

The sets $\{\alpha_{k,\ell}^{(j)}\}$ and $\{\tau_{k,\ell}^{(j)}\}$ are the complex amplitudes and delays of the k-th deterministic MPC, respectively. The signal $s(t)$ denotes the transmitted pulse shape with effective pulse duration T_p. The random process $\nu_\ell^{(j)}(t)$ denotes DM and is modeled as a Gaussian process with auto-covariance $\mathbb{E}\{\nu_\ell^{(j)}(\tau)[\nu_\ell^{(j)}(u)]^*\} = S_{\nu,\ell}^{(j)}(\tau)\delta(\tau - u)$, where $S_{\nu,\ell}^{(j)}(\tau)$ is the power delay profile (PDP) of the DM. The signal $w(t)$ denotes white Gaussian measurement noise with double-sided power spectral density (PSD) of $N_0/2$.

The delays of the $K_\ell^{(j)}$ deterministic MPCs are modeled geometrically using mirror images of the j-th anchor with respect to the corresponding walls, introducing so-called virtual anchors (VAs) [2], [8]. Fig. 1 shows two examples of such VAs. It can be seen that the distance from the agent's position $\mathbf{p}_\ell$ to the k-th VA at $\mathbf{a}_k^{(j)}$ corresponds to the delay $\tau_{k,\ell}^{(j)} = \frac{1}{c} d_{k,\ell}^{(j)} = \frac{1}{c}\|\mathbf{p}_\ell - \mathbf{a}_k^{(j)}\|$ of the corresponding MPC, where c denotes the speed of light. For the whole scenario, a set $\mathcal{A}^{(j)}$ of all potential VAs of the j-th anchor can be constructed. Higher-order VAs are obtained by mirroring again lower-order VAs with respect to reflectors. Using optical ray-tracing, the set of visible VAs can be computed for position $\mathbf{p}_\ell$ as

$$\mathcal{A}_\ell^{(j)} = \{\mathbf{a}_{\ell,1}^{(j)}, \ldots, \mathbf{a}_{\ell,K_\ell^{(j)}}^{(j)}\} = \{\mathbf{a}_k^{(j)} : f_\mathrm{vis}(\mathbf{a}_k^{(j)}, \mathbf{p}_\ell) = 1\} \quad (2)$$

where the ray-tracing is expressed by the function

$$f_\mathrm{vis}(\mathbf{a}_k^{(j)}, \mathbf{p}) = \begin{cases} 1, & \text{if VA } \mathbf{a}_k^{(j)} \text{ is visible at } \mathbf{p} \\ 0, & \text{else.} \end{cases} \quad (3)$$

B. Tracking Algorithm

In a first step, the location-dependent parameters, i.e. the arrival times of the deterministic MPCs, are estimated from the received signal modeled by (1). The arrival time estimation

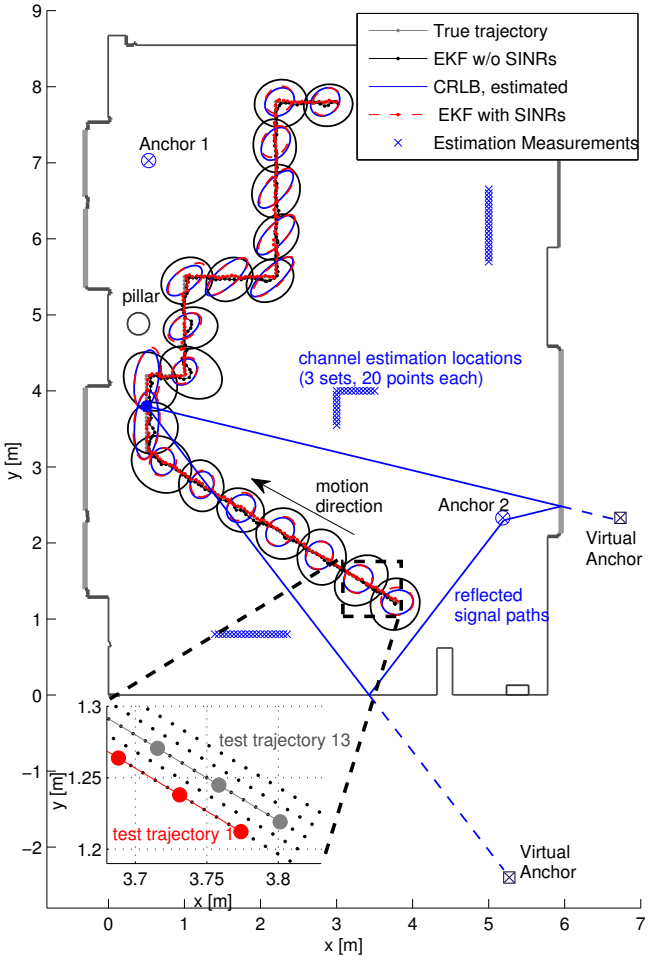

Fig. 1. Floor plan of the evaluation scenario, bold gray lines denote windows and other lines illustrate walls made of different materials. Examples for true and estimated agent trajectories are shown, the former is hidden beneath the others. The bottom contains a close-up of the trajectories, illustrating the 1-cm-spaced grid, out of which 25 5-cm-spaced trajectories are obtained. Two physical anchors are indicated with examples for virtual anchors modeling reflections from walls. Ellipses denote 20-fold standard deviations of the trackers as well as the respective 20-fold CRLB, as described in the text.

at position ℓ is realized as an iterative least-squares approximation of the received signal

$$\hat{\tau}_{k,\ell}^{(j)} = \arg\min_{\tau} \int_0^T \left| r_\ell^{(j)}(t) - \hat{r}_{\ell,k-1}^{(j)}(t) - \hat{\alpha}(\tau) s(t-\tau) \right|^2 dt \tag{4}$$

using a template signal $\hat{r}_{\ell,k}^{(j)}(t) = \sum_{k'=1}^{k} \hat{\alpha}_{k',\ell}^{(j)} s(t - \hat{\tau}_{k',\ell}^{(j)})$ for all MPCs up to the k-th. The path amplitudes are nuisance parameters, estimated using a projection of $r_\ell^{(j)}(t)$ onto a unit energy pulse $s(t)$ as

$$\hat{\alpha}(\tau) = \int_0^T [r_\ell^{(j)}(t)]^* s(t-\tau) dt; \quad \hat{\alpha}_{k,\ell}^{(j)} = \hat{\alpha}(\hat{\tau}_{k,\ell}^{(j)}). \tag{5}$$

The number of estimated MPCs $\hat{K}_\ell^{(j)}$ should be chosen according to the number of expected specular paths in an environment. With the assumptions of separable MPCs and white noise, (4) and (5) correspond to a maximum-likelihood (ML) estimation of the deterministic MPCs.

The tracking is done as in [2] using an EKF with data association (DA), which is necessary since the estimated MPC arrival times in (4) are not associated to the VAs. We choose a simple linear Gaussian constant-velocity motion model

$$\begin{aligned} \mathbf{x}_{\ell+1} &= \mathbf{F}\mathbf{x}_\ell + \mathbf{G}\mathbf{n}_{\mathrm{a},\ell} \\ &= \begin{bmatrix} 1 & 0 & \Delta T & 0 \\ 0 & 1 & 0 & \Delta T \\ 0 & 0 & 1 & 0 \\ 0 & 0 & 0 & 1 \end{bmatrix} \mathbf{x}_\ell + \begin{bmatrix} \frac{\Delta T^2}{2} & 0 \\ 0 & \frac{\Delta T^2}{2} \\ \Delta T & 0 \\ 0 & \Delta T \end{bmatrix} \mathbf{n}_{\mathrm{a},\ell}. \end{aligned} \tag{6}$$

The state vector $\mathbf{x}_\ell$ of the agent contains position $\mathbf{p}_\ell$ and the velocity vector, and ΔT is the update rate. The driving acceleration noise term $\mathbf{n}_{\mathrm{a},\ell}$ with zero mean and covariance matrix $\mathbf{Q} = \sigma_a^2 \mathbf{G}\mathbf{G}^T$ models motion changes that deviate from the constant-velocity assumption.

For the measurement update of the EKF, the set of expected VAs is calculated for the DA at the predicted position $\mathbf{p}_\ell^-$ using (2) for each anchor, yielding sets $\bar{\mathcal{A}}_\ell^{(j)}$. At this time, prior information such as a set $\tilde{\mathcal{A}}^{(j)}$ defining *relevant* VAs can be used to restrict the set of expected VAs, resulting in $\bar{\mathcal{A}}_\ell^{(j)} \cap \tilde{\mathcal{A}}^{(j)}$. The corresponding expected path delays are then matched to the estimated arrival times (4) such that the cumulative distance of estimated and expected delays is minimized, yielding sets of associated VAs $\mathcal{A}_{\ell,\mathrm{ass}}^{(j)}$. The association is done using a constrained optimal subpattern assignment approach [2], [9], where the constraint is that associations at a distance larger than a given maximum ranging uncertainty, the so-called cut-off distance d_c, are discarded.

After joining information from all anchors, $\mathcal{A}_{\ell,\mathrm{ass}} = \bigcup_j \mathcal{A}_{\ell,\mathrm{ass}}^{(j)}$, the corresponding distance estimates are stacked in the EKF's measurement input vector which is *modeled* as

$$\mathbf{z}_\ell = \left[\ldots, \ \|\mathbf{a}_k^{(j)} - \mathbf{p}_\ell\|, \ \ldots \right]^T + \mathbf{n}_{z,\ell}, \ \mathbf{a}_k^{(j)} \in \mathcal{A}_{\ell,\mathrm{ass}}. \tag{7}$$

The measurement noise $\mathbf{n}_{z,\ell}$ is assumed to be zero-mean multivariate Gaussian. The choice of the measurement noise covariance matrix $\mathbf{R}_\ell$ depends on the amount of prior information. If a-priori estimates of the range estimation uncertainties $\mathrm{var}\left\{\hat{d}_{k,\ell}^{(j)}\right\}$ are available for a set of VAs, then

$$\mathbf{R}_\ell = \mathrm{diag}\left\{ \mathrm{var}\left\{ \hat{d}_{k,\ell}^{(j)} \right\} \right\} \quad \forall\, k,j : \mathbf{a}_k^{(j)} \in \mathcal{A}_{\ell,\mathrm{ass}}. \tag{8}$$

Otherwise, an overall uncertainty σ_d^2 is used, i.e.

$$\mathbf{R}_\ell = \sigma_\mathrm{d}^2 \mathbf{I}_{|\mathcal{A}_{\ell,\mathrm{ass}}|}. \tag{9}$$

C. Position-Related Information and its Estimation

In [3], we have derived the Cramèr Rao Lower Bound (CRLB) for positioning based on the signal model (1) and the VAs. With the assumption of no path overlap, i.e. the MPCs are orthogonal, the equivalent Fisher information matrix (EFIM) for position $\mathbf{p}_\ell$ [10] is given as

$$\mathbf{J}_{\mathbf{p}_\ell} = \sum_{j=1}^{J} \sum_{k=1}^{K_\ell^{(j)}} \mathrm{J}_r(d_{k,\ell}^{(j)}) \mathbf{J}_r(\phi_{k,\ell}^{(j)}). \tag{10}$$

where the ranging direction matrix $\mathbf{J}_r(\phi_{k,\ell}^{(j)})$ determines the direction $\phi_{k,\ell}^{(j)}$ of the information of the k-th MPC, since it

is spanned by the outer product of the unit vector pointing from the k-th VA at $\mathbf{a}_k^{(j)}$ to the agent at $\mathbf{p}_\ell$ with itself [3]. It is scaled by the Fisher information contained in the signal $r_\ell^{(j)}(t)$ about the path length $d_{k,\ell}^{(j)}$. Its inverse is the CRLB for the variance of an unbiased range estimate $\hat{d}_{k,\ell}^{(j)}$

$$\mathrm{J}_r^{-1}(d_{k,\ell}^{(j)}) = \left(\frac{8\pi^2\beta^2}{c^2}\mathrm{SINR}_{k,\ell}^{(j)}\right)^{-1} \leq \mathrm{var}\left\{\hat{d}_{k,\ell}^{(j)}\right\}. \quad (11)$$

Here, β denotes the effective (root mean square) bandwidth of $s(t)$ and the signal-to-interference-and-noise-ratio (SINR) of the k-th MPC at $\mathbf{p}_\ell$ is defined as

$$\mathrm{SINR}_{k,\ell}^{(j)} = \frac{|\alpha_{k,\ell}^{(j)}|^2}{N_0 + T_\mathrm{p} S_{\nu,\ell}^{(j)}(\tau_{k,\ell}^{(j)})}. \quad (12)$$

In [4], we have derived an estimator for the average $\mathrm{SINR}_k^{(j)}$, averaged over positions within a confined spatial region in which propagation characteristics such as the PDP of the DM are assumed to be stationary. However, there is only a limited number of MPCs visible within such a region. To increase this number, we use measurements at N_s sets of points $\{\mathbf{p}_\ell : \ell \in \mathcal{P}_i\}$, where $\mathcal{P}_i,\ i = 1, \ldots, N_\mathrm{s}$, collects the indices of the points. Within each set, propagation characteristics are again assumed to be stationary and an $\widehat{\mathrm{SINR}}_k^{(j,i)}$ can be estimated. For this, we have to take into account the *observability* of the corresponding VA. We define the subsets

$$\begin{aligned}\mathcal{P}_k^{(j,i)} =& \{\ell \in \mathcal{P}_i : f_\mathrm{vis}(\mathbf{p}_\ell, \mathbf{a}_k^{(j)}) = 1 \wedge \\ & |\tau_{k,\ell}^{(j)} - \tau_{k',\ell}^{(j)}| > T_\mathrm{p}\ \forall\ k' \neq k,\ \mathbf{a}_{k'}^{(j)} \in \mathcal{A}_\ell^{(j)}\}\end{aligned} \quad (13)$$

with cardinality $N_k^{(j,i)}$. The conditions in (13) imply that the k-th VA is visible at $\mathbf{p}_\ell$ and there is no path overlap [3], [10] with any other VA-modeled MPC.

The overall aim is to take into account the uncertainty of the MPCs in an environment, both w.r.t. the path length estimation and also w.r.t. the position of the VAs, as these are subject to floor plan uncertainties. For the estimation of a *global* range uncertainty of a specific MPC, which is necessary to be useful as a location-independent noise model (8), we propose the weighted mean of the local uncertainties

$$\widehat{\mathrm{var}}\left\{\hat{d}_k^{(j)}\right\} = \frac{1}{\sum_{i=1}^{N_\mathrm{s}} N_k^{(j,i)}} \sum_{i=1}^{N_\mathrm{s}} N_k^{(j,i)} \widehat{\mathrm{var}}\left\{\hat{d}_{k,\ell}^{(j)} : \ell \in \mathcal{P}_k^{(j,i)}\right\}. \quad (14)$$

The $\widehat{\mathrm{var}}\left\{\hat{d}_{k,\ell}^{(j)}\right\}$ is obtained from an SINR estimate and (11). This and the use of (14) are motivated by assuming the range estimates $\hat{d}_{k,\ell}^{(j)}$ to be Gaussian distributed, which is justified by the fact that (4) is an approximation for the according ML estimator and as such is asymptotically efficient, i.e. $\hat{d}_{k,\ell}^{(j)} \sim \mathcal{N}\left(d_{k,\ell}^{(j)}; \mathrm{J}_r^{-1}(d_{k,\ell}^{(j)})\right)$.

The VA positions are corrected using a prior $p(\tilde{\mathbf{a}}_k^{(j)})$ for the k-th VA. This leads to the MAP estimate

$$\hat{\mathbf{a}}_k^{(j)} = \arg\max_{\tilde{\mathbf{a}}_k^{(j)}} \ln p(\mathbf{r}^{(j)}(t)|\tilde{\mathbf{a}}_k^{(j)}) + \ln p(\tilde{\mathbf{a}}_k^{(j)}) \quad (15)$$

with a likelihood function that evaluates the contribution of the k-th VA to all estimation signals $\mathbf{r}^{(j)}(t)$ (c.f. [3] but neglecting the whitening to account for the DM)

$$\begin{aligned}\ln p(\mathbf{r}^{(j)}(t)|\tilde{\mathbf{a}}_k^{(j)}) \propto & \frac{2}{N_0} \sum_{i=1}^{N_\mathrm{s}} \sum_{\ell \in \mathcal{P}_k^{(j,i)}} \int_0^T \Re\left\{[r_\ell^{(j)}(t)]^* \tilde{s}_{k,\ell}^{(j)}(t)\right\} dt \\ & - \frac{1}{N_0}\int_0^T |\tilde{s}_{k,\ell}^{(j)}(t)|^2 dt.\end{aligned} \quad (16)$$

Here, $\tilde{s}_{k,\ell}^{(j)}(t) = \tilde{\alpha}_{k,\ell}^{(j)} s(t - \tilde{\tau}_{k,\ell}^{(j)})$ is a template signal where $\tilde{\tau}_{k,\ell}^{(j)} = \frac{1}{c}\|\tilde{\mathbf{a}}_k^{(j)} - \mathbf{p}_\ell\|$ and the MPC amplitudes are again nuisance parameters and estimated using (5). The vector of received signals for the estimation is given as

$$\mathbf{r}^{(j)}(t) = [r_{\ell\in\mathcal{P}_1}^{(j)}(t),\ \ldots,\ r_{\ell\in\mathcal{P}_{N_\mathrm{s}}}^{(j)}(t)]^T. \quad (17)$$

With the signal model in (1) and $\hat{m}_{1,k}^{(j,i)}$ and $\hat{m}_{2,k}^{(j,i)}$ denoting estimates of the first and second central moments of the energy samples $|\tilde{\alpha}_{k,\ell}^{(j)}|^2$ for $\ell \in \mathcal{P}_k^{(j,i)}$, the corresponding average SINRs are estimated as [4]

$$\widehat{\mathrm{SINR}}_k^{(j,i)} = \left(\frac{\hat{m}_{1,k}^{(j,i)}}{\sqrt{\hat{m}_{1,k}^{(j,i)^2} - \hat{m}_{2,k}^{(j,i)}}} - 1\right)^{-1}. \quad (18)$$

Those can be used together with (11) and (14) to obtain a range uncertainty for the k-th VA for the given environment.

The SINR estimation described in [4] also performs a correction of deterministic factors such as distance-dependent path-loss. Overall, it leads to sets $\tilde{\mathcal{A}}^{(j)}$ of VAs with lower cardinality than $\mathcal{A}^{(j)}$, consisting of re-estimated VA locations obtained in (15).

III. Measurement Scenario

Measurements were obtained along a trajectory of 220 points, spaced by 5 cm, see Fig. 1. Around each point, 25 measurements were performed within a 5 x 5 cm grid, yielding in fact 25 parallel trajectories for the performance analysis.

The channel between the agent on the trajectory and two anchors (see Fig. 1) has been measured with an M-sequence based UWB channel sounder developed by *Ilmsens*, as also described in [11]. On anchor and agent sides, dipole-like antennas made of Euro-cent coins have been used. They have an approximately uniform radiation pattern in azimuth plane and zeroes in the directions of floor and ceiling. Out of the measured frequency range of $3.1 - 10.6$ GHz, a subband with center frequency f_c and bandwidth $B = 1/T_\mathrm{p}$ has been selected using filtering with a raised-cosine pulse $s(t)e^{j2\pi f_\mathrm{c} t}$ with pulse duration T_p, followed by a downconversion.

IV. Results

For the tracking along the 25 trajectories, a frequency range corresponding to $f_\mathrm{c} = 7$ GHz and $T_\mathrm{p} = 0.5$ ns has been chosen, which results in a bandwidth of 2 GHz. The process noise variance in the motion model (6) is obtained as in [2] based on selecting a maximum velocity in e.g. the x-direction $v_{x,\max}$, which defines the 3σ point of the noise in velocity domain. The corresponding process noise variance in the acceleration domain is then $\sigma_a^2 = (v_{x,\max}/(3\Delta T))^2$ with $v_{x,\max} = 1$ m/s and $\Delta T = 1$ s in this paper. The DA cutoff distance has been chosen as $d_\mathrm{c} = 0.12$ m. VAs up to order two

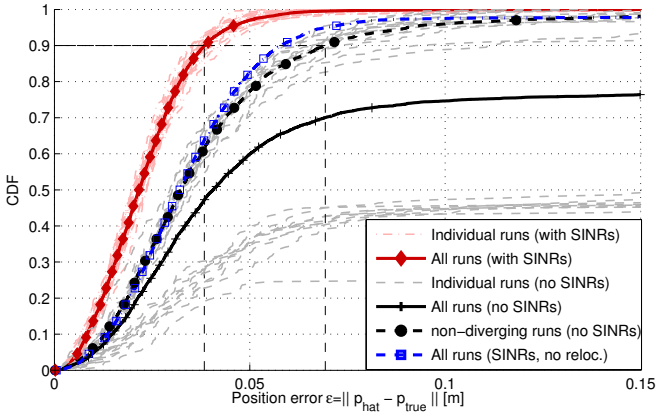

Fig. 2. Performance CDFs for $T_\mathrm{p} = 0.5\,\mathrm{ns}$ and $f_\mathrm{c} = 7\,\mathrm{GHz}$. Thin lines show the individual 25 runs over the trajectories in Fig. 1. Red and gray indicate the EKFs with and without estimated SINRs. Bold lines denote the total performance for all runs, the dashed black line indicates the performance without SINRs on all non-diverging runs (15 out of 25).

have been used, and SINR estimation was done using $N_\mathrm{s} = 3$ sets of 20 points (Fig. 1). The prior for the VA positions in (15) has been chosen as a uniform distribution within a circle of diameter $10\,\mathrm{cm}$ around the calculated VA position. The performance of the EKF is compared for the cases with estimated SINRs (8), and where no such information is available (9). To allow for a fair comparison in the latter case, the overall ranging uncertainty is selected as the mean of the estimated uncertainties, which is $\sigma_\mathrm{d} = 0.042\,\mathrm{m}$.

An exemplary tracking result is illustrated in Fig. 1. In this case, the EKF can track the agent with and without estimated MPC SINRs, also in the NLOS region with respect to Anchor 1 (caused by the concrete pillar on the left side of the room). At every 12-th position, the 20-fold estimation error standard deviation ellipse of the EKF is illustrated. The comparison with the estimated CRLB, given as the inverse of (10), shows a close match to the tracking performance when using the SINRs, which confirms the efficient use of the MPCs. It should be noted that the CRLB shown does not include the motion model, i.e. it is not the posterior CRLB. However, for the chosen process noise variance, which is deliberately larger than the measurement uncertainties, the motion prior does not add significant information, making (10) applicable.

Fig. 2 shows the position error CDFs. It is evident that the channel characterization (red) yields excellent robustness, as all 25 runs have similar performance with $90\,\%$ of the errors below $4\,\mathrm{cm}$. Without SINR information (black/gray), the robustness is affected, as 10 of 25 runs diverge, mostly in the NLOS region discussed before. The overall CDF for the 15 non-diverging runs (black bold dashed line, circle markers) shows the *potential* performance of MINT without channel information, where $90\,\%$ of the errors are within $7\,\mathrm{cm}$. The influence of the MAP-re-localization of the VA positions (15) is illustrated by the CDF indicated by the blue dash-dotted curve with square markers. All runs are included, SINRs used, but without the re-localized VA positions. SINR awareness provides robustness, while re-localization improves accuracy.

Fig. 3 illustrates the mean number of associated MPCs,

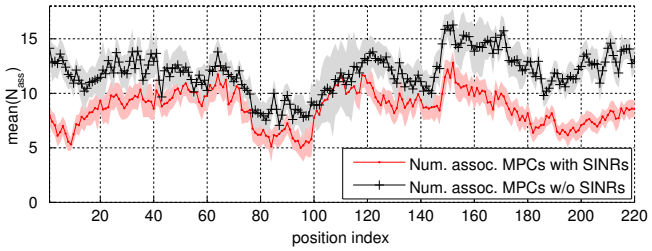

Fig. 3. Mean and standard deviation of the number of associated MPCs used for tracking. The 15 of 25 non-diverging runs are included for the case where no SINRs are available.

$\mathbb{E}\{|\mathcal{A}_{\ell,\mathrm{ass}}|\}$, over all runs using SINRs and the 15 non-diverging runs without SINRs, together with the standard deviation. The additional channel knowledge helps to substantially prune the set of potential VAs to the relevant ones. This leads to less erroneous associations of estimated MPCs to VAs and also reduces the computational complexity.

The results presented here match results in [11], which also includes quantitative results for the SINR estimation in different environments.

V. Conclusions

We have shown that channel knowledge quantifying the position-related information of deterministic MPCs is a key factor for obtaining accurate and robust indoor localization. By estimating the uncertainty of range estimates corresponding to deterministic MPCs and making this information available to a tracking filter, multipath propagation can be used efficiently. Experimental results have confirmed the advantage, demonstrating excellent performance.

References

[1] D. Dardari, A. Conti, U. Ferner, A. Giorgetti, and M. Z. Win, "Ranging With Ultrawide Bandwidth Signals in Multipath Environments," *Proceedings of the IEEE*, 2009.

[2] P. Meissner, E. Leitinger, M. Froehle, and K. Witrisal, "Accurate and Robust Indoor Localization Systems Using Ultra-wideband Signals," in *European Navigation Conference (ENC)*, Vienna, Austria, 2013.

[3] K. Witrisal and P. Meissner, "Performance bounds for multipath-assisted indoor navigation and tracking (MINT)," in *International Conference on Communications (ICC)*, Ottawa, Canada, 2012.

[4] P. Meissner and K. Witrisal, "Analysis of Position-Related Information in Measured UWB Indoor Channels," in *6th European Conference on Antennas and Propagation (EuCAP)*, Prague, Czech Repuplic, 2012.

[5] Y. Shen, S. Mazuelas, and M. Win, "Network Navigation: Theory and Interpretation," *IEEE Journal on Selected Areas in Communications*, 2012.

[6] A. Conti, D. Dardari, M. Guerra, L. Mucchi, and M. Win, "Experimental Characterization of Diversity Navigation," *IEEE Systems Journal*, 2014.

[7] N. Decarli, F. Guidi, and D. Dardari, "A Novel Joint RFID and Radar Sensor Network for Passive Localization: Design and Performance Bounds," *IEEE Journal of Selected Topics in Signal Processing*, 2014.

[8] J. Kunisch and J. Pamp, "An ultra-wideband space-variant multipath indoor radio channel model," in *IEEE Conference on Ultra Wideband Systems and Technologies*, 2003.

[9] D. Schuhmacher, B.-T. Vo, and B.-N. Vo, "A Consistent Metric for Performance Evaluation of Multi-Object Filters," *IEEE Transactions on Signal Processing*, 2008.

[10] Y. Shen and M. Z. Win, "Fundamental Limits of Wideband Localization - Part I: A General Framework," *IEEE Transactions on Information Theory*, Oct. 2010.

[11] P. Meissner, E. Leitinger, M. Lafer, and K. Witrisal, "Real-Time Demonstration System for Multipath-Assisted Indoor Navigation and Tracking (MINT)," in *IEEE ICC 2014 Workshop on Advances in Network Localization and Navigation (ANLN)*, Sydney, Australia, 2014.

Simultaneous Localization and Mapping using Multipath Channel Information

Erik Leitinger*,†, Paul Meissner*,†, Manuel Lafer* and Klaus Witrisal*
* Graz University of Technology, Austria
† The authors equally contributed to this work.

***Abstract*—Location awareness is one of the most important requirements for many future wireless applications. Multipath-assisted indoor navigation and tracking (MINT) is a possible concept to enable robust and accurate localization of an agent in indoor environments. Using a-priori knowledge of a floor plan of the environment and the position of the physical anchors, specular multipath components can be exploited, based on a geometric-stochastic channel model. So-called virtual anchors (VAs), which are mirror images of the physical anchors, are used as additional anchors for positioning. The quality of this additional information depends on the accuracy of the corresponding floor plan.**

In this paper, we propose a new simultaneous localization and mapping (SLAM) approach that allows to learn the floor plan representation and to deal with inaccurate information. A key feature is an online estimated channel characterization that enables an efficient combination of the measurements. Starting with just the known anchor positions, the proposed method includes the VA positions also in the state space and is thus able to adapt the VA positions during tracking of the agent. Furthermore, the method is able to discover new potential VAs in a feature-based manner. This paper presents a proof of concept using measurement data. The excellent agent tracking performance—90 % of the error lower than 5 cm—achieved with a known floor plan can be reproduced with SLAM.

I. Introduction

Simultaneous localization and mapping (SLAM) [1], [2] is all about using uncertain data that are obtained by an agent in some uncertain environment. The uncertainty presents itself on different levels: The measurement data may come from different sensors, giving rise to different measurement variances. When these data are processed by an algorithm, the algorithm needs to take into account this heterogeneity by (i) associating all measurements to their respective origin and (ii) weighting the measurements according to their respective (possibly a-priori unknown) uncertainty.

In classical SLAM implementations, much of the *measurement origin uncertainty*[1] is alleviated by using sensors that allow for a resolution of the measurement origin. In the popular example of laser scanners, distance estimates to features are obtained that are labelled with a corresponding angle w.r.t. the pose of the agent. To keep requirements on the agent simple, only single antenna terminals are used in the approach presented here. Hence, only a single signal per anchor (nodes at known positions in the environment) is available per time step. Using an online estimated channel characterization, measurements from past estimated agent positions are fused efficiently, giving rise to *channel information assisted* SLAM.

[1]As opposed to the *inaccuracy* of the measurements themselves [3].

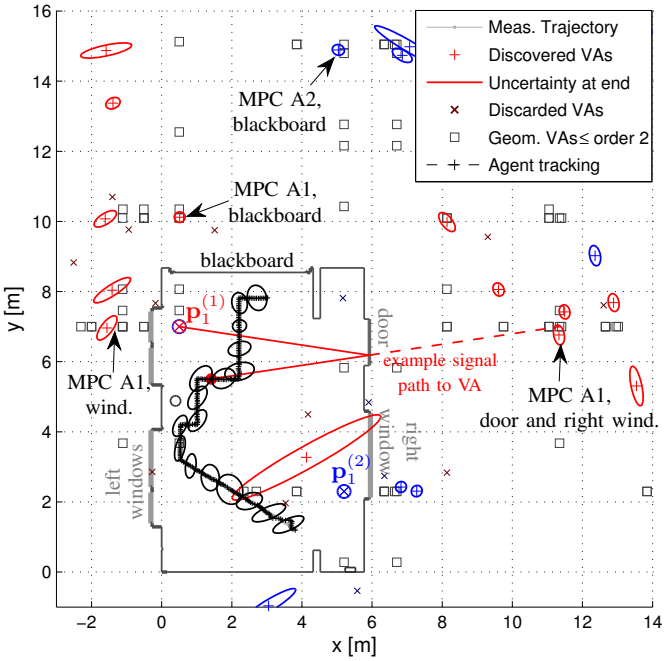

Fig. 1. Illustration of the SLAM approach followed in this paper. Two anchors at $\mathbf{p}_1^{(1)}$ and $\mathbf{p}_1^{(2)}$ represent the infrastructure. The agent position as well as the floor plan (represented by virtual anchors (VAs)) are estimated using specular multipath, for which one example path is shown. Black squares indicate geometrically expected VAs, blue and red plus markers with uncertainty ellipses (30-fold) represent discovered VAs. An agent tracking result is shown in black with some corresponding ellipses (50-fold). Selected VAs discussed in Section IV are indicated.

The required spatially consistent information about the environment is embedded in the multipath components (MPCs), i.e. the reflections of the signal occurring in the environment [4]. In our prior work [4]–[7], knowledge of the floor plan was assumed to make use of MPCs for localization. In SLAM, however, the floor plan is also subject to the estimation problem. Hence, the aims of this work are (i) to remove the requirement of a precisely a-priori known floor plan and (ii) to cope with uncertainties in the environment representation.

The floor plan is represented by virtual anchors (VAs), i.e. mirror images of the positions of the physically existing anchors in the environment [8]. These VAs allow for an efficient representation of the localization-relevant geometry [7]. Fig.

1 illustrates the concept of VAs. For the resulting localization approach, the term *multipath-assisted indoor navigation and tracking* (MINT) has been coined. Probabilistic MINT flavor is added to the SLAM problem by starting the tracking with just the anchor locations in the environment representation. The MPCs estimated from the received signals of the moving agent over time deliver the spatially consistent geometric data for tracking and for the update of the floor plan[2]. All other—not geometrically modelled—propagation effects included in the signals constitute interference to the useful position-related information and are called diffuse multipath (DM) [9]. An online estimation of the influence of the DM on the range uncertainties to the VAs allows for an efficient selection of the VAs that can reliably be updated and used for the agent tracking. This is a key difference to existing radio-based SLAM approaches like [10], [11]. The presented approach can be understood as probabilistic feature-based SLAM [1], [2].

The key contributions of this paper are:

- A feature-based method for finding new VAs during tracking of the agent, allowing to infer the floor plan.
- Online tracking of VA positions as well as corresponding range uncertainties enables the evaluation of the reliability of the observed features.
- A proof-of-concept of the SLAM approach using measured data.

The paper is organized as follows: Section II introduces the geometric-stochastic signal model and provides an overview about the subject. Section III describes the components of the SLAM approach, while Sections IV and V wrap up the paper with results, discussions, and conclusions.

II. Problem Formulation

A. Signal Model

A UWB signal $s(t)$ is exchanged between the j-th anchor at position[3] $\mathbf{p}_1^{(j)} \in \mathbb{R}^2$ and the agent at position $\mathbf{p}_n \in \mathbb{R}^2$ at the n-th time step. The corresponding complex-baseband received signal is modeled as [5]

$$r_n^{(j)}(t) = \sum_{k=1}^{K_n^{(j)}} \alpha_{k,n}^{(j)} s(t - \tau_{k,n}^{(j)}) + (s * \nu_n^{(j)})(t) + w(t). \quad (1)$$

The first term describes a sum of $K_n^{(j)}$ deterministic MPCs with complex amplitudes $\{\alpha_{k,n}^{(j)}\}$ and delays $\{\tau_{k,n}^{(j)}\}$. We model these delays by VAs at positions $\mathbf{p}_{k,n}^{(j)} \in \mathbb{R}^2$, yielding $\tau_{k,n}^{(j)} = \frac{1}{c} d(\mathbf{p}_n, \mathbf{p}_{k,n}^{(j)}) = \frac{1}{c} \|\mathbf{p}_n - \mathbf{p}_{k,n}^{(j)}\|$ with $k = 2 \dots K_n^{(j)}$, where c is the speed of light. The delay $\tau_{1,n}^{(j)} = \frac{1}{c} d(\mathbf{p}_n, \mathbf{p}_1^{(j)})$ always defines the direct path between the agent and the j-th anchor. $K_n^{(j)}$ is equivalent to the number of visible VAs at the agent position $\mathbf{p}_n$ [6]. We assume the energy of $s(t)$ is normalized to one.

The second term denotes the convolution of the transmitted signal $s(t)$ with the DM $\nu_n^{(j)}(t)$, which is modeled as a zero-mean Gaussian random process. Note that the statistic of $(s * \nu_n^{(j)})(t)$ is non-stationary in the delay domain and colored due to the spectrum of $s(t)$. For DM $\nu_n^{(j)}(t)$ we assume uncorrelated scattering along the delay axis τ, hence the auto-correlation function (ACF) is given by $K_{\nu,n}^{(j)}(\tau, u) = \mathbb{E}_\nu \left\{ \nu_n^{(j)}(\tau)(\nu_n^{(j)})^*(u) \right\} = S_{\nu,n}^{(j)}(\tau)\delta(\tau - u)$, where $S_{\nu,n}(\tau)$ is the power delay profile (PDP) of DM at the agent position $\mathbf{p}_n$. The DM process is assumed to be quasi-stationary in the spatial domain, which means that $S_\nu(\tau)$ does not change in the vicinity of position $\mathbf{p}_n$ [12]. Finally, the last term $w(t)$ denotes an additive white Gaussian noise (AWGN) process with double-sided power spectral density (PSD) of $N_0/2$.

Using these channel model parameters, the signal-to-interference-plus-noise ratio (SINR) [5], [6] is defined as

$$\mathrm{SINR}_{k,n}^{(j)} = \frac{|\alpha_{k,n}^{(j)}|^2}{N_0 + T_\mathrm{p} S_{\nu,n}^{(j)}(\tau_{k,n}^{(j)})}. \quad (2)$$

The SINR is used to quantify the position-related information of the k-th MPC. From this, the measurement variance of the estimated delay $\mathrm{var}\left\{\hat{d}_{k,n}^{(j)}\right\}$ can be computed (see Section III-C).

B. Channel Estimation

The MPC arrival time estimation at agent position $\mathbf{p}_n$ is realized as an iterative least-squares approximation of the received signal [6]

$$\hat{\tau}_{k,n}^{(j)} = \arg\min_\tau \int_0^T \left| r_n^{(j)}(t) - \hat{r}_{n,k-1}^{(j)}(t) - \hat{\alpha}(\tau) s(t-\tau) \right|^2 dt \quad (3)$$

using a template signal for all MPCs up to the $(k-1)$-th defined as $\hat{r}_{n,k-1}^{(j)}(t) = \sum_{k'=1}^{k-1} \hat{\alpha}_{k',n}^{(j)} s(t - \hat{\tau}_{k',n}^{(j)})$. The path amplitudes are nuisance parameters, estimated using a projection of $\hat{r}_{n,k}^{(j)}(t)$ onto a unit energy pulse $s(t)$ as

$$\hat{\alpha}(\tau) = \int_0^T [\hat{r}_{n,k}^{(j)}(t)]^* s(t-\tau) dt; \quad \hat{\alpha}_{k,n}^{(j)} = \hat{\alpha}(\hat{\tau}_{k,n}^{(j)}). \quad (4)$$

The number of estimated MPCs $\hat{K}_n^{(j)}$ should be chosen according to the number of expected specular paths in an environment. With the assumptions of separable MPCs and white noise, (3) and (4) correspond to a maximum-likelihood (ML) estimation of the deterministic MPCs. The finite set of measured delays is written as $\mathcal{Z}_n = \bigcup_j \mathcal{Z}_n^{(j)} = \bigcup_j \{\hat{d}_{k,n}^{(j)}\}_{k=1}^{\hat{K}_n^{(j)}}$, where $\hat{d}_{k,n}^{(j)} = c\hat{\tau}_{k,n}^{(j)}$.

C. General SLAM Formulation

The presented work focuses on probabilistic feature-based SLAM with VAs of the according anchors as representative features of a floor plan. As stated, the VAs at position $\mathbf{p}_{k,n}^{(j)}$ are the mirror images of the anchors at position $\mathbf{p}_1^{(j)}$ at

[2] We note that the floor plan itself is not directly estimated, but its representation using the VAs. The reconstruction of the floor plan from this information is out of the scope of this paper.

[3] Two-dimensional position coordinates are used throughout the paper, for the sake of simplicity. The extension to three dimensional coordinates is straightforward.

flat surfaces, i.e. walls, of the surrounding environment and thus they are a parametric representation of the environment. Starting with the positions of the anchors $\mathbf{p}_1^{(j)}$ and optionally a small set of precomputed VAs (using optical ray-tracing [6]), channel information assisted SLAM comprises a method to find new VAs and also to estimate an according reliability measure, the $\mathrm{SINR}_{k,n}^{(j)}$ described in Equation (2), for those features.

Bayesian feature-based SLAM allows to compute the joint posterior $p(\mathbf{x}_n, \mathcal{A}_n|\mathbf{r}_{1:n})$ of the state vector of the agent $\mathbf{x}_n = [\mathbf{p}_n, \mathbf{v}_n]^{\mathrm{T}}$, where $\mathbf{p}_n$ is the position and $\mathbf{v}_n$ the velocity of the agent, respectively, and $\mathcal{A}_n = \bigcup_j \mathcal{A}_n^{(j)}$, which represents the finite set of all VA positions at time instance n that are associated with measured delays (see Section III-A).

As a consequence of using just one antenna at the anchor- and the agent-side, and the partial observability of the VAs, delayed mapping [13] has to be applied, which means that the set of past measurements $\mathcal{Z}_{1:n}$ and the according estimated states of the agent $\mathbf{x}_{1:n}$ are needed to initialize new possible VAs.

In the most generic form, the prediction equation for a feature map and an agent state, using the Markovian assumption, can be written as

$$p(\mathbf{x}_n, \mathcal{A}_n|\mathcal{Z}_{1:n-1}) = \int_{\mathbf{x}_{n-1}, \mathcal{A}_{n-1}} p(\mathbf{x}_{n-1}, \mathcal{A}_{n-1}|\mathcal{Z}_{1:n-1}) \times p(\mathbf{x}_n|\mathbf{x}_{n-1}) p(\mathcal{A}_n|\mathcal{A}_{n-1}) d\{\mathbf{x}_{n-1}, \mathcal{A}_{n-1}\} \quad (5)$$

where $p(\mathbf{x}_n|\mathbf{x}_{n-1})$ and $p(\mathcal{A}_n|\mathcal{A}_{n-1})$ are the state transition probability distribution functions of the agent and the VAs, respectively. The latter one is represented by an identity function. The update equation is then

$$p(\mathbf{x}_n, \mathcal{A}_n|\mathcal{Z}_{1:n}) = \frac{p(\mathcal{Z}_n|\mathbf{x}_n, \mathcal{A}_n) p(\mathbf{x}_n, \mathcal{A}_n|\mathcal{Z}_{1:n-1})}{p(\mathcal{Z}_{1:n}|\mathcal{Z}_{1:n-1})} \quad (6)$$

where $p(\mathcal{Z}_n|\mathbf{x}_n, \mathcal{A}_{1:n})$ represents the general likelihood function of the current measurements. The state space and measurement model that are used in the presented approach are described in Section III-B.

III. SLAM Approach

The general approach for tracking the agent position and for discovering new VAs is depicted in Fig. 2. This section explains the different parts.

A. Data Association

The set of expected MPC delays $\mathcal{D}_n^{(j)}$ at time step n is computed as the distances of each VA in $\mathcal{A}_n^{(j)}$ to the predicted position

$$\mathcal{D}_n^{(j)} = \left\{ d(\mathbf{p}_{n,k}^{(j)}, \mathbf{p}_n) : \mathbf{p}_{n,k}^{(j)} \in \mathcal{A}_n^{(j)} \right\}. \quad (7)$$

As $\mathcal{D}_n^{(j)}$ and the set of measured delays $\mathcal{Z}_n^{(j)}$ are sets of usually different cardinalities, i.e. $|\mathcal{Z}_n^{(j)}| = \hat{K}_n^{(j)} \neq |\mathcal{D}_n^{(j)}| = K_n^{(j)}$, no conventional distance measure is defined and therefore there is no straightforward way of an association. We employ a well-known multi-target miss-distance, the *optimal sub-pattern assignment* (OSPA) metric [14]. For $\hat{K}_n^{(j)} \geq K_n^{(j)}$, which can be ensured by filling up $\mathcal{Z}_n^{(j)}$ with dummy clutter, it is defined as

$$d_{\mathrm{OSPA}}(\mathcal{D}_n^{(j)}, \mathcal{Z}_n^{(j)}) = \left[\frac{1}{\hat{K}_n^{(j)}} \left(\min_{\boldsymbol{\pi} \in \Pi_{\hat{K}_n^{(j)}}} \sum_{i=1}^{K_n^{(j)}} \left[d^{(d_{\mathrm{c}})}(d_{i,n}^{(j)}, \hat{d}_{\boldsymbol{\pi}_i,n}^{(j)}) \right]^p + d_{\mathrm{c}}^p (\hat{K}_n^{(j)} - K_n^{(j)}) \right) \right]^{\frac{1}{p}}, \quad (8)$$

where Π_N is defined as the set of permutations of positive integers up to N. The function $d^{(d_{\mathrm{c}})}(x, y) = \min(d_{\mathrm{c}}, d(x, y))$, i.e. an arbitrary distance metric $d(\cdot)$ that is cut off at a $d_{\mathrm{c}} > 0$, the so-called *cut-off distance*, which is a design parameter. The metric order is denoted as p. The first sum in the metric is the cumulative distance over the optimal sub-pattern assignment of $\mathcal{Z}_n^{(j)}$ to $\mathcal{D}_n^{(j)}$, i.e. where $K_n^{(j)}$ entries of $\mathcal{Z}_n^{(j)}$ are assigned optimally to the entries of $\mathcal{D}_n^{(j)}$. The Hungarian or Munkres algorithm can be used for this assignment [14], [15]. For the remaining $\hat{K}_n^{(j)} - K_n^{(j)}$ entries of $\mathcal{Z}_n^{(j)}$, d_{c} is assigned as penalty distance.

For performing the data association (DA), we introduce a set $\mathcal{C}_n^{(j)}$ of correspondence variables [16], whose i-th entry $c_{n,i}^{(j)}$ is defined as

$$c_{n,i}^{(j)} = \begin{cases} k, & \text{if } \hat{d}_{i,n}^{(j)} \text{ corresponds to VA } \mathbf{p}_k^{(j)} \\ 0, & \text{if } \hat{d}_{i,n}^{(j)} \text{ corresponds to clutter.} \end{cases} \quad (9)$$

The optimal sub-pattern assignment between $\mathcal{D}_n$ and $\mathcal{Z}_n$ is reflected by the first part of (8)

$$\boldsymbol{\pi}_{\mathrm{opt}} = \arg \min_{\boldsymbol{\pi} \in \Pi_{\hat{K}_n^{(j)}}} \sum_{i=1}^{K_n^{(j)}} d^{(d_{\mathrm{c}})}(d_{i,n}^{(j)}, \hat{d}_{\boldsymbol{\pi}_i,n}^{(j)})^p. \quad (10)$$

With this, the correspondence variables are set as

$$c_{n,i}^{(j)} = \begin{cases} k, & \text{if } [\boldsymbol{\pi}_{\mathrm{opt}}]_k = i \text{ and } d^{(d_{\mathrm{c}})}(d_{n,k}^{(j)}, \hat{d}_{n,i}^{(j)}) < d_{\mathrm{c}} \\ 0, & \text{else,} \end{cases} \quad (11)$$

where $[\boldsymbol{\pi}_{\mathrm{opt}}]_k$ denotes the k-th entry of the optimal sub-pattern assignment. After the DA was applied for all anchors, the following union sets are defined:

- The set of associated discovered (and optionally a-priori known) VAs $\mathcal{A}_{n,\mathrm{ass}} = \bigcup_j \mathcal{A}_{n,\mathrm{ass}}^{(j)}$.
- The according set of associated measurements $\mathcal{Z}_{n,\mathrm{ass}} = \bigcup_j \mathcal{Z}_{n,\mathrm{ass}}^{(j)}$.
- The set of remaining measurements $\mathcal{Z}_{n,\overline{\mathrm{ass}}} = \bigcup_j \mathcal{Z}_{n,\overline{\mathrm{ass}}}^{(j)}$, which are not associated to VAs of $\mathcal{A}_n$.

B. State Space and Measurement Model

The distance estimates for all anchors $\mathcal{Z}_n$ are stacked in the EKF's measurement input vector. These measurements are modeled as

$$\mathbf{z}_n = \left[\ldots,\ d(\mathbf{p}_{n,k}^{(j)}, \mathbf{p}_{\mathrm{n}}),\ \ldots \right]^T + \mathbf{n}_{z,n},\ \mathbf{p}_{k,n}^{(j)} \in \mathcal{A}_{n,\mathrm{ass}}. \quad (12)$$

The cardinality of the VA set $\mathcal{A}_{n,\mathrm{ass}}$ is defined as $K_n = \sum_j K_n^{(j)}$. The vector $\mathbf{n}_{z,n}$ contains Gaussian measurement

noise with covariance matrix $\mathbf{R}_n$. The choice of $\mathbf{R}_n$ depends on the amount of prior information and will be explained in Section III-C.

The tracking of the agent is done as in [17] using an extended Kalman filter (EKF) with DA. We choose a simple linear Gaussian constant-velocity motion model for the agent state

$$\begin{aligned}\mathbf{x}_n =& \mathbf{F}\mathbf{x}_{n-1} + \mathbf{G}\mathbf{n}_{\mathrm{a},n} \\ =& \begin{bmatrix} 1 & 0 & \Delta T & 0 \\ 0 & 1 & 0 & \Delta T \\ 0 & 0 & 1 & 0 \\ 0 & 0 & 0 & 1 \end{bmatrix} \mathbf{x}_n + \begin{bmatrix} \frac{\Delta T^2}{2} & 0 \\ 0 & \frac{\Delta T^2}{2} \\ \Delta T & 0 \\ 0 & \Delta T \end{bmatrix} \mathbf{n}_{\mathrm{a},n}.\end{aligned} \tag{13}$$

The state vector of the agent is $\mathbf{x}_n = [\mathbf{p}_n, \mathbf{v}_n]^{\mathrm{T}}$, and ΔT is the update rate. The driving acceleration noise term $\mathbf{n}_{\mathrm{a},n}$ with zero mean and covariance matrix $\mathbf{I}\sigma_a^2$ models motion changes that deviate from the constant-velocity assumption.

To incorporate the discovered and associated VAs $\mathcal{A}_{n,\mathrm{ass}}$ into the state space, the model is extended to

$$\begin{aligned}\tilde{\mathbf{x}}_n &= \tilde{\mathbf{F}}_n \tilde{\mathbf{x}}_{n-1} + \tilde{\mathbf{G}}_n \mathbf{n}_{\mathrm{a},n} \\ &= \begin{bmatrix} \mathbf{F} & \mathbf{0}_{4\times 2K_n} \\ \mathbf{0}_{2K_n\times 4} & \mathbf{I}_{2K_n\times 2K_n} \end{bmatrix} \tilde{\mathbf{x}}_{n-1} + \begin{bmatrix} \mathbf{G} \\ \mathbf{0}_{2K_n\times 2} \end{bmatrix} \mathbf{n}_{\mathrm{a},n},\end{aligned} \tag{14}$$

where $\tilde{\mathbf{x}}_n = [\mathbf{x}_n^{\mathrm{T}}, \mathbf{p}_{2,n}^{\mathrm{T}}, \ldots, \mathbf{p}_{K_n,n}^{\mathrm{T}}]^{\mathrm{T}}$ represents the stacked state vector, where $\{\mathbf{p}_{k,n}\} \in \mathcal{A}_{n,\mathrm{ass}}$. The according measurement model is defined as

$$\tilde{\mathbf{z}}_n = \tilde{\mathbf{H}}_n \tilde{\mathbf{x}}_n + \tilde{\mathbf{n}}_{z,n}, \tag{15}$$

where $\tilde{\mathbf{z}}_n = [\mathbf{z}_n^{\mathrm{T}}, \mathbf{z}_{2,\mathcal{P}_{2,n}}^{\mathrm{T}}, \ldots, \mathbf{z}_{K_n,\mathcal{P}_{K_n,n}}^{\mathrm{T}}]^{\mathrm{T}}$ is the stacked measurement vector. The vector $\mathbf{z}_{k,\mathcal{P}_{k,n}}$ represents the set of measurements over time that have been associated with the k-th VA, where $\mathcal{P}_{k,n}$ defines the according set of time indices at which the DA was possible. The stack vector $\tilde{\mathbf{n}}_{z,n}$ contains the according measurement noise. The linearized measurement matrix $\tilde{\mathbf{H}}_n$ is described in Equation (16) on the top of the next page. Note that (16) shows the general structure of the fully occupied measurement matrix, but for time instance n just columns are present for which the corresponding VAs are in $\mathcal{A}_{n,\mathrm{ass}}$, and rows for which measurements of $\mathbf{z}_n$ and $\mathbf{z}_{k,\mathcal{P}_{k,n}}^{\mathrm{T}}$ $\forall\, k \in \mathcal{A}_{n,\mathrm{ass}}$ are available. To compute all derivatives in $\tilde{\mathbf{H}}_n$, also all past agent positions $\mathbf{p}_i$ $i \in \mathcal{P}_{k,n}$ $\forall k$ are needed. The covariance matrix $\mathbf{R}_n$ contains the according past range variances.

The upper left block in (16) comprises the linearized measurement equations for the agent position $\mathbf{p}_n$. The other K_n blocks of linearized measurement equations are for the VA positions $\{\mathbf{p}_{k,n}^{(j)}\} \in \mathcal{A}_{n,\mathrm{ass}}$.

C. Range Uncertainty Estimation

For the measurement noise model of the tracking filter, the range estimation uncertainties $\mathrm{var}\left\{\hat{d}_{k,n}^{(j)}\right\}$ to the associated VAs are used to build the measurement noise covariance matrix as

$$\mathbf{R}_n = \mathrm{diag}\left\{\mathrm{var}\left\{\hat{d}_{k,n}^{(j)}\right\}\right\} \quad \forall\, k, j : \mathbf{p}_{k,n}^{(j)} \in \mathcal{A}_{n,\mathrm{ass}}. \tag{17}$$

The MPC range uncertainties can be related to the SINR of the k-th MPC at agent position $\mathbf{p}_n$ (2) using the Fisher information of the corresponding distances [6]

$$\mathrm{J}_r^{-1}(d_{k,n}^{(j)}) = \left(\frac{8\pi^2\beta^2}{c^2}\mathrm{SINR}_{k,n}^{(j)}\right)^{-1} \leq \mathrm{var}\left\{\hat{d}_{k,n}^{(j)}\right\}. \tag{18}$$

Here, β denotes the effective (root mean square) bandwidth of $s(t)$. These SINRs are estimated with a method of moments estimator [6] using the associated complex amplitudes $\{\alpha_{k,i}^{(j)}\}_{i=n_0}^{n}$ over a window of past estimated agent positions where the MPC was associated.

The online estimation is started once an initial window size of measurements is available for the respective newly detected VA. Until then, a default value $\sigma^2_{\mathrm{d,init}}$ is assigned. The VA-filter block in Fig. 2 allows to exclude VAs with too unreliable position information, i.e. too large range standard deviation, from the DA, using a threshold value $\sigma^2_{\mathrm{d,max}}$. For a VA without associated measurements at time step n, the previous value of the estimated range variance is assigned.

D. Feature Detection: VA Discovery

The set of measurements $\mathcal{Z}_{n,\overline{\mathrm{ass}}}$ that are not associated for the tracking phase described above is used for discovering new VAs. In principle, the channel information assisted SLAM algorithm tries to associate these measurements with candidates for new VAs at different stages. This process is illustrated in Figure 2 and is summarized in the following way:

- The potential subset $\mathcal{Z}_n^{\mathrm{ca}} \subset \mathcal{Z}_{n,\overline{\mathrm{ass}}}$ of the non-associated measurements contains measurements that can be associated with already existing VA candidates $\mathbf{p}_{k'}^{\mathrm{ca}}$ with $k' = 1, \ldots, C_n$, which have not yet been estimated unambiguously[4]. These VA-candidate-associated measurements $\{z_{1,n}^{\mathrm{ca}}, \ldots, z_{C_n,n}^{\mathrm{ca}}\}$ are used to improve the position estimate of the corresponding VA candidates and to resolve the ambiguity in their positions.
- As soon as the position ambiguity is resolved, a new VA is initialized at position $\mathbf{p}_{K+1,n}$[5], with covariance matrix $\mathbf{P}_{K+1,K+1,n}$ and added to the geometry data-base. This new VA can be used in next time step.
- Measurements that have not yet been associated with a VA candidate are comprised in $\mathcal{Z}_n^{\overline{\mathrm{ca}}}$ and further grouped into vectors of similar delays $\{\mathbf{z}_{1,\mathcal{P}_{1,n}}^{\mathrm{gr}}, \ldots, \mathbf{z}_{G_n,\mathcal{P}_{G_n,n}}^{\mathrm{gr}}\}$, where $\mathcal{P}_{g,n}$ represents the set of time-indices of delays associated with the g-th group. G_n is the current number of groups. If the size of a group reaches a certain threshold, a new VA candidate is estimated with the grouped delays and according past agent positions.

Estimate new VA candidate pairs: In the case that a vector of similar group delays $\mathbf{z}_{g,\mathcal{P}_{g,n}}^{\mathrm{gr}}$ has reached a certain number of entries, a new VA candidate pair $\mathbf{p}_{k'}^{\mathrm{ca}}$ is estimated using the range Bancroft algorithm [18] and the according agent

[4] A reason for ambiguity in the position of a newly estimated VA is that the circles spanned by the measured delays around the according agent positions may intersect in two points (e.g. due to agent movement on a straight line).

[5] The symbol K defines the number of all discovered VA—until time instance n—that are stored in the geometry memory (see Figure 2).

$$\tilde{\mathbf{H}}_n = \begin{bmatrix} \frac{\partial d(\mathbf{p}_{2,n},\mathbf{p}_n)}{\partial x_n} & \frac{\partial d(\mathbf{p}_{2,n},\mathbf{p}_n)}{\partial y_n} & 0 & 0 & \frac{\partial d(\mathbf{p}_{2,n},\mathbf{p}_n)}{\partial x_{2,n}} & \frac{\partial d(\mathbf{p}_{2,n},\mathbf{p}_n)}{\partial y_{2,n}} & \dots & 0 & 0 \\ \vdots & \vdots & \vdots & \vdots & \vdots & \vdots & & \vdots & \vdots \\ \frac{\partial d(\mathbf{p}_{K_n,n},\mathbf{p}_n)}{\partial x_n} & \frac{\partial d(\mathbf{p}_{K_n,n},\mathbf{p}_n)}{\partial y_n} & 0 & 0 & 0 & 0 & \dots & \frac{\partial d(\mathbf{p}_{K_n,n},\mathbf{p}_n)}{\partial x_{K_n,n}} & \frac{\partial d(\mathbf{p}_{K_n,n},\mathbf{p}_n)}{\partial y_{K_n,n}} \\ 0 & 0 & 0 & 0 & \frac{\partial d(\mathbf{p}_{2,n},\mathbf{p}_1)}{\partial x_{2,n}} & \frac{\partial d(\mathbf{p}_{2,n},\mathbf{p}_1)}{\partial y_{2,n}} & \dots & 0 & 0 \\ \vdots & \vdots & \vdots & \vdots & \vdots & \vdots & & \vdots & \vdots \\ 0 & 0 & 0 & 0 & \frac{\partial d(\mathbf{p}_{2,n},\mathbf{p}_{n-1})}{\partial x_{2,n}} & \frac{\partial d(\mathbf{p}_{2,n},\mathbf{p}_{n-1})}{\partial y_{2,n}} & \dots & 0 & 0 \\ 0 & 0 & 0 & 0 & 0 & 0 & \dots & \frac{\partial d(\mathbf{p}_{K_n,n},\mathbf{p}_1)}{\partial x_{K_n,n}} & \frac{\partial d(\mathbf{p}_{K_n,n},\mathbf{p}_1)}{\partial y_{K_n,n}} \\ \vdots & \vdots & \vdots & \vdots & \vdots & \vdots & & \vdots & \vdots \\ 0 & 0 & 0 & 0 & 0 & 0 & \dots & \frac{\partial d(\mathbf{p}_{K_n,n},\mathbf{p}_{n-1})}{\partial x_{K_n,n}} & \frac{\partial d(\mathbf{p}_{K_n,n},\mathbf{p}_{n-1})}{\partial y_{K_n,n}} \end{bmatrix} \tag{16}$$

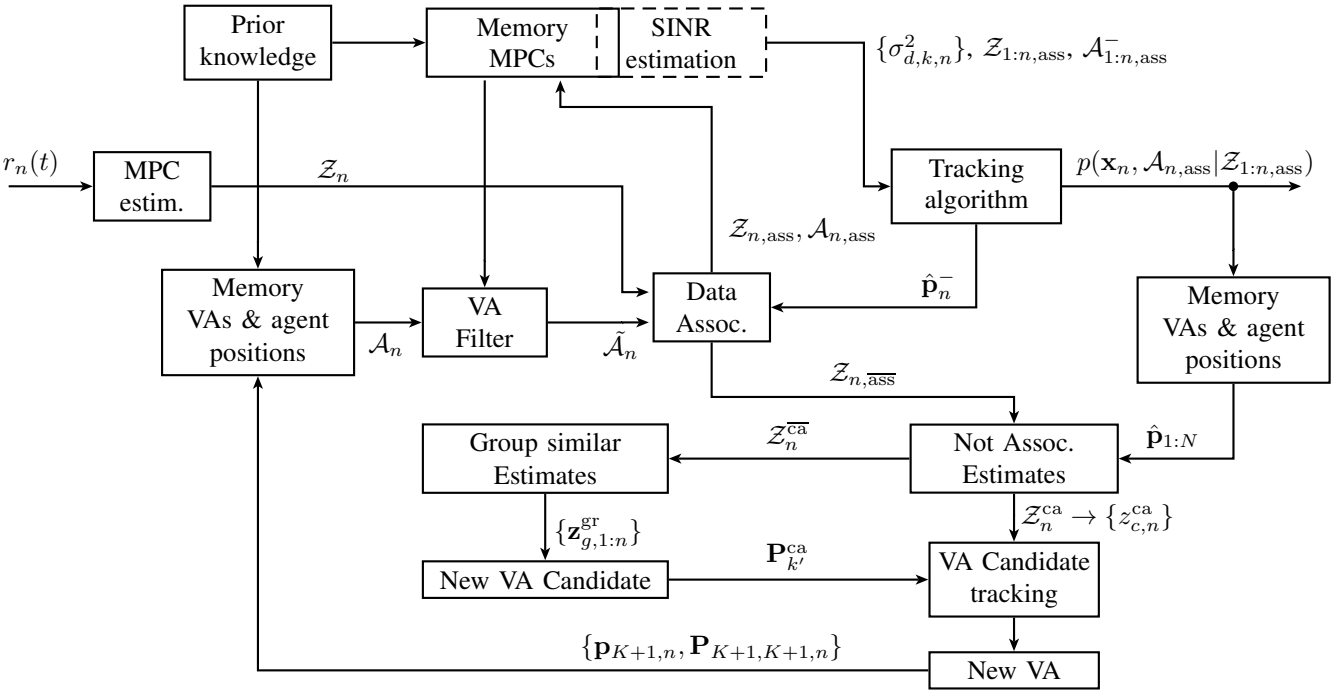

Fig. 2. Block Diagram of channel information assisted SLAM

positions $\mathbf{p}_{\mathcal{P}_{g,n}}$. A VA candidate pair $\mathbf{p}^{\text{ca}}_{k'} = \{\mathbf{p}^{1,\text{ca}}_{k'}, \mathbf{p}^{2,\text{ca}}_{k'}\}$ is given by the two possible solutions of the range Bancroft method.

Tracking of VA candidate pairs: Already found VA candidate pairs $\mathbf{P}^{\text{ca}}_{k'}$ are then updated with a recursive least square (RLS) algorithm using the new associated measurements $\{z^{\text{ca}}_{1,n}, \dots, z^{\text{ca}}_{C_n,n}\}$ and the currently estimated agent position $\mathbf{p}_n$ until the above described ambiguities are resolved.

Initialize new VA: Resolved VAs are stored in the geometry memory and further used in the state space model. The last update of the RLS algorithm provides the initial position $\mathbf{p}_{K+1,n}$ and covariance matrix $\mathbf{P}_{K+1,K+1,n}$ of the newly found VA. The cross-covariance $\mathbf{P}_{K+1,m,n}$ between the new VA and the agent position and the covariances $\mathbf{P}_{K+1,K,n}$ between the new VA and all other VAs are initialized with zero matrices.

IV. Results

For the evaluation of this SLAM approach, we use the seminar room scenario of the MeasureMINT database [19]. We use an agent trajectory as shown in Fig. 1, consisting of 220 points spaced by 5 cm. At each position, UWB measurements of the channel between the agent and the two anchors at the positions $\mathbf{p}^{(1)}_1$ and $\mathbf{p}^{(2)}_1$ are available. The measurements allow for 25 quasi-parallel trajectories, as in total 25×220 points have been measured at a 1 cm grid spacing [6], [7]. These measurements have been performed using an M-sequence correlative channel sounder developed by *Ilmsens*. This sounder

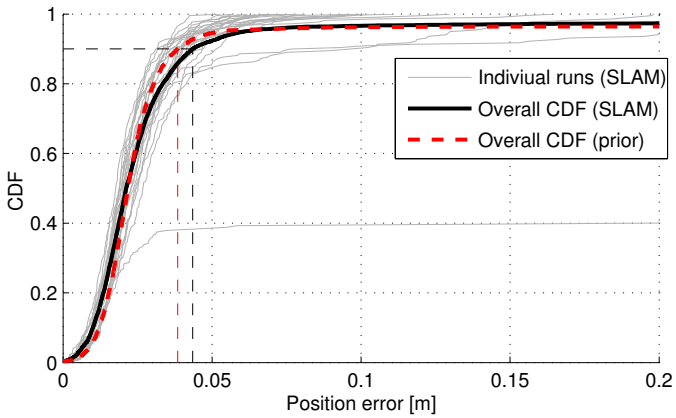

Fig. 3. Performance CDFs for $T_\mathrm{p} = 0.5\,\mathrm{ns}$ and $f_\mathrm{c} = 7\,\mathrm{GHz}$. The grey CDFs indicates the tracking error of the agent using the presented SLAM approach over the 25 trajectories, and the black line denotes the respective overall CDF. Only the anchor coordinates are known. The red dashed line shows the overall CDF using all VAs up to third order as a-priori known and online tracking of their positions and range variances.

provides measurements over the whole FCC frequency range from $3.1 - 10.6\,\mathrm{GHz}$. Out of this range, we select the desired frequency band using filtering with a raised cosine pulse with a pulse duration $T_\mathrm{p} = 0.5\,\mathrm{ns}$ (corresponding to a bandwidth of $2\,\mathrm{GHz}$) at a center frequency of $f_\mathrm{c} = 7\,\mathrm{GHz}$.

Fig. 1 shows the final result of the tracking along the trajectory together with the obtained knowledge of the floor plan in terms of the detected VAs and their uncertainties. This is evaluated at the end of the tracking phase for trajectory run 25. Black squares indicate positions of geometrically calculated VAs up to order two. For many of the detected VAs, shown by red (Anchor 1) and blue (Anchor 2) plus markers, there is an underlying expected VA. This is especially the case for these VAs that have a small position variance, indicated by their standard deviation ellipses. The latter are enlarged by a factor of 30 for better visibility. Some detected VAs, e.g. the one at approximately $\mathbf{p} = [-1.4, 13.4]^T$, correspond to VAs of order three, which are not shown in the plot. The dark crosses show those detected VAs whose range standard deviation exceeds the threshold of $\sigma_\mathrm{d,max} = 6.23\,\mathrm{cm}$, corresponding to a SINR of $0\,\mathrm{dB}$, c.f. (18) and (2). These are discarded from the tracking process. Some of the detected VAs do not correspond to any geometrically explainable positions, i.e. they represent clutter. This may correspond to scattering objects which are visible for a significant time span. These do not comply to the geometric model of VAs and will be mapped to erroneous positions. However, for many of these false detections, the variance in the position domain is large, in principle allowing for a treatment of these errors on a higher layer.

Fig. 3 shows CDFs of the position error of the agent. The grey curves represents the performance of the presented SLAM approach over the 25 individual trajectory runs. Only the two anchor positions $\mathbf{p}_1^{(1)}$ and $\mathbf{p}_1^{(2)}$ are used as prior knowledge. It can be seen that despite the fact that one run was diverging, the overall performance is excellent, i.e. $90\,\%$ of the errors are within $4.4\,\mathrm{cm}$. As a comparison, the black line shows the overall performance over the 25 runs using all VAs up to order three as prior knowledge. The expected visibility regions of these VAs are precomputed using geometrical ray-tracing and used in the prediction process to find the set of expected VAs [6], [7]. The corresponding VA positions are tracked using the EKF, and their range variances are estimated online based on the estimated positions of the agent. This provides a performance of $90\,\%$ within $3.8\,\mathrm{cm}$, i.e. only slightly better than for SLAM. We suspect that a reason for the good performance of the SLAM approach is that in the VA discovery process, many unreliable MPCs are not detected and thus do not impair the localization. In the case of a-priori known VAs, these MPCs will be associated to the signal features and may cause errors. Due to the variance tracking, they should be weighted down after some time, but until then, they influence the tracking. A deeper understanding of the influences as well as an analysis of more measurements to evaluate the significance of the difference is subject of ongoing research.

Fig. 4 contains the estimated standard deviations of the ranging to the selected VAs marked in Fig. 1. The default value assigned to newly detected VAs, $0.07\,\mathrm{m}$, is shown (black line) as well as the threshold $\sigma_\mathrm{d,max}$ that is used to select VAs to become candidates for the data association (grey line). As Fig. 4(a) and (b) show, the blackboard is nicely detectable and usable for tracking, both for Anchor 1 and 2. In the expected regions where the MPC should be invisible, the uncertainty raises, indicating the decrease in position information. For the door and window on the right side and Anchor 1, Fig. 4(c) shows that the corresponding uncertainty is very low. This is expected, as the door is made of metal and the window is metal coated. Interestingly, the estimation continues to yield good values also in the NLOS region. This means that in this region, still a measurement is associated to the discovered VA, otherwise only the previous value is reused. This is an indication of some uncertainty in the geometry, i.e. the reflection from the slightly displaced wall between door and window is associated to the measurement, leading to a VA merging these elements. For the left window and Anchor 2, the estimation is shown in Fig. 4(d). After the VA has been discovered, the variance is estimated well. In the NLOS region, only a few erroneous associations are made, mostly the previous values are used. As the VA becomes visible again, the estimation continues with low uncertainty values.

V. Conclusions and Outlook

We have presented a proof-of-concept of a SLAM approach that extracts geometry information from single-antenna UWB measurements. We show the general applicability of using information from specular MPCs for localization, without any prior floor plan information. The proposed *channel information assisted* SLAM algorithm is able to learn efficiently a feature-based representation of the environment using VAs, while tracking the agent position.

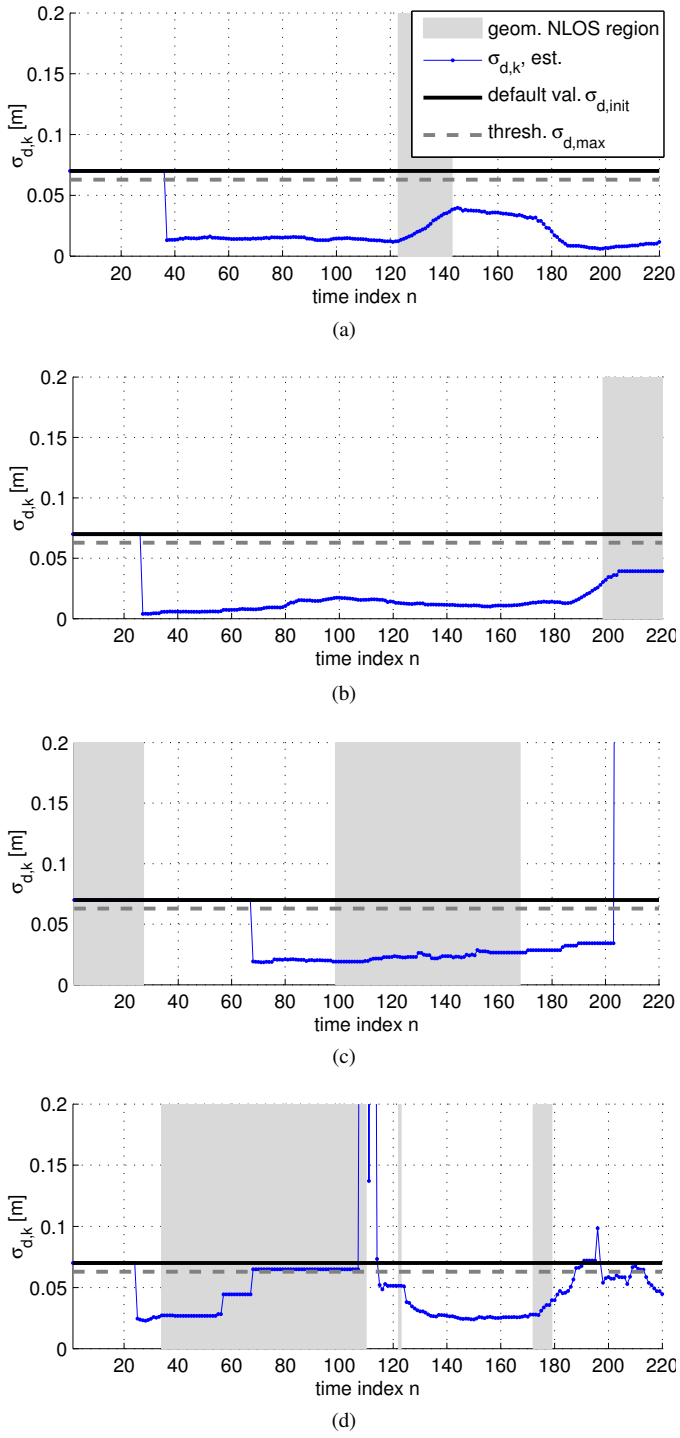

Fig. 4. Estimated standard deviations of the ranging to selected VAs, i.e. the reflections w.r.t. the blackboard and Anchor 1 (a) as well as Anchor 2 (b), the right hand door and window and Anchor 1 (c), and the left window and Anchor 2 (d). Grey regions indicate geometrically computed regions where the corresponding MPC is not visible. Blue lines denote the estimated ranging uncertainty, and black and grey lines the default value and the threshold, respectively.

An important issue for future work is the consideration of synthetic signals in simplified environments. With this, it is easier to provide a ground truth for the geometry that should be learned by the SLAM algorithm. In this way, a more structured analysis of influence factors on the performance can be performed. Also, in the initialization of a VA candidate pair, the chosen method may not be optimal. In the case of closely-spaced agent positions, the measurement geometry is often bad, caused by multiple similar circles that do not clearly intersect. A more sophisticated initialization and tracking—using particle filtering and filters based on random finite set statistic—of the candidate positions may help here.

Acknowledgement

Part of this work has been funded by the Austrian Research Promotion Agence (FFG) under Grant 845630 “REFlex”.

References

[1] H. Durrant-Whyte and T. Bailey, “Simultaneous localization and mapping (SLAM): Part I,” *IEEE Robotics and Automation Magazine*, vol. 13, no. 2, pp. 99 –110, june 2006.

[2] T. Bailey and H. Durrant-Whyte, “Simultaneous localization and mapping (SLAM): Part II,” *IEEE Robotics and Automation Magazine*, vol. 13, no. 3, pp. 108 –117, sept. 2006.

[3] Y. Bar-Shalom and T. Fortmann, *Tracking and Data Association*. Academic Press, 1988.

[4] E. Leitinger, P. Meissner, C. Ruedisser, G. Dumphart, and K. Witrisal, “Evaluation of position-related information in multipath components for indoor positioning,” *Selected Areas in Communications, IEEE Journal on*, 2014, submitted.

[5] K. Witrisal and P. Meissner, “Performance bounds for multipath-assisted indoor navigation and tracking (MINT),” in *IEEE International Conference on Communications (ICC)*, 2012.

[6] P. Meissner, E. Leitinger, and K. Witrisal, “UWB for Robust Indoor Tracking: Weighting of Multipath Components for Efficient Estimation,” *IEEE Wireless Communications Letters*, vol. 3, no. 5, pp. 501–504, Oct. 2014.

[7] P. Meissner, “Multipath-Assisted Indoor Positioning,” Ph.D. dissertation, Graz University of Technology, 2014.

[8] J. Borish, “Extension of the image model to arbitrary polyhedra,” *The Journal of the Acoustical Society of America*, 1984.

[9] N. Michelusi, U. Mitra, A. Molisch, and M. Zorzi, “UWB Sparse/Diffuse Channels, Part I: Channel Models and Bayesian Estimators,” *IEEE Transactions on Signal Processing*, 2012.

[10] C. Gentner and T. Jost, “Indoor positioning using time difference of arrival between multipath components,” in *International Conference on Indoor Positioning and Indoor Navigation (IPIN)*, Oct 2013, pp. 1–10.

[11] T. Deissler and J. Thielecke, “Uwb slam with rao-blackwellized monte carlo data association,” in *International Conference on Indoor Positioning and Indoor Navigation (IPIN)*, Sept 2010, pp. 1–5.

[12] A. Molisch, “Ultra-wide-band propagation channels,” *Proceedings of the IEEE*, 2009.

[13] J. J. Leonard, R. J. Rikoski, P. M. Newman, and M. Bosse, “Mapping partially observable features from multiple uncertain vantage points,” *The International Journal of Robotics Research*, 2002.

[14] D. Schuhmacher, B.-T. Vo, and B.-N. Vo, “A Consistent Metric for Performance Evaluation of Multi-Object Filters,” *IEEE Transactions on Signal Processing*, 2008.

[15] J. Munkres, “Algorithms for the Assignment and Transportation Problems,” *Journal of the Society for Industrial and Applied Mathematics*, vol. 5, no. 1, pp. pp. 32–38, 1957.

[16] S. Thrun, W. Burgard, and D. Fox, *Probabilistic Robotics*. MIT, 2006.

[17] P. Meissner, E. Leitinger, M. Froehle, and K. Witrisal, “Accurate and Robust Indoor Localization Systems Using Ultra-wideband Signals,” in *European Navigation Conference (ENC)*, Vienna, Austria, 2013. [Online]. Available: http://arxiv.org/abs/1304.7928

[18] S. Bancroft, “An Algebraic Solution of the GPS Equations,” *Aerospace and Electronic Systems, IEEE Transactions on*, vol. AES-21, no. 1, pp. 56–59, Jan 1985.

[19] P. Meissner, E. Leitinger, M. Lafer, and K. Witrisal, “MeasureMINT UWB database,” 2013, Publicly available database of UWB indoor channel measurements. [Online]. Available: www.spsc.tugraz.at/tools/UWBmeasurements

Evaluation of Position-related Information in Multipath Components for Indoor Positioning

Erik Leitinger, *Student Member, IEEE*, Paul Meissner, *Member, IEEE*, Christoph Rüdisser, Gregor Dumphart, and Klaus Witrisal, *Member, IEEE*

***Abstract*—Location awareness is a key factor for a wealth of wireless indoor applications. Its provision requires the careful fusion of diverse information sources. For agents that use radio signals for localization, this information may either come from signal transmissions with respect to fixed anchors, from cooperative transmissions inbetween agents, or from radar-like monostatic transmissions. Using a-priori knowledge of a floor plan of the environment, specular multipath components can be exploited, based on a geometric-stochastic channel model. In this paper, a unified framework is presented for the quantification of this type of position-related information, using the concept of equivalent Fisher information. We derive analytical results for the Cramér-Rao lower bound of multipath-assisted positioning, considering bistatic transmissions between agents and fixed anchors, monostatic transmissions from agents, cooperative measurements inbetween agents, and combinations thereof, including the effect of clock offsets. Awareness of this information enables highly accurate and robust indoor positioning. Computational results show the applicability of the framework for the characterization of the localization capabilities of a given environment, quantifying the influence of different system setups, signal parameters, and the impact of path overlap.**

***Index Terms*—Cramér-Rao bounds, channel models, ultra wideband communication, localization, cooperative localization, clock synchronization**

I. Introduction

Location awareness is a key component of many future wireless applications. Achieving the needed level of accuracy *robustly*[1] is still elusive, especially in indoor environments which are characterized by harsh multipath conditions. Promising candidate systems thus either use sensing technologies that provide remedies against multipath or they fuse information from multiple information sources [1], [2]. WLAN-based systems make use of existing infrastructure and exploit the position dependence of the received signal strength [3]. However, the latter shows a relatively large variance w.r.t. the position-related parameters such as the distance, even with an optimized deployment [4].

E. Leitinger, P. Meissner, C. Rüdisser, and K. Witrisal are with Graz University of Technology, Graz, Austria, email: {erik.leitinger, paul.meissner, witrisal}@tugraz.at

G. Dumphart is with ETH Zurich, Zurich, Switzerland, email: dumphart@nari.ee.ethz.ch

Manuscript received Aug. 14, 2014; revised Dec. 6, 2014 and Jan. 23, 2015, accepted Feb. 16, 2015.

This work was supported by the Austrian Science Fund (FWF), National Research Network SISE, Project S10610 and by the Austrian Research Promotion Agency (FFG), KIRAS PL3, grant no. 832335 "LOBSTER".

[1]We define robustness as the percentage of cases in which a system can achieve its given potential accuracy.

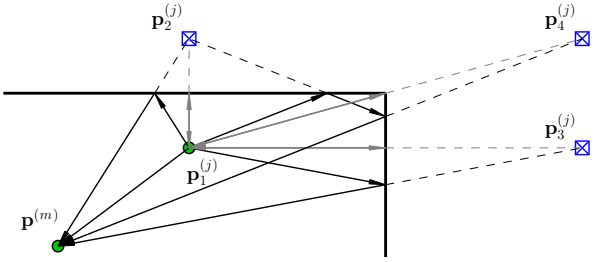

Fig. 1. Illustration of multipath geometry using VAs for (i) bistatic transmissions (black) between an anchor at $\mathbf{p}_1^{(j)}$ and an agent at $\mathbf{p}^{(m)}$ and for (ii) a monostatic measurement (gray) by an agent at $\mathbf{p}_1^{(j)}$.

In *Multipath-assisted indoor positioning,* multipath components (MPCs) can be associated to the local geometry using a known floor plan. In this way, MPCs can be seen as signals from additional (virtual) anchors (VAs). Ultra-wideband (UWB) signals are used because of their superior time resolution and to facilitate the separation of MPCs. Hence, additional position-related information is exploited that is contained in the radio signals.

This is in contrast to competing approaches, which either detect and avoid non-line-of-sight (NLOS) measurements [5], mitigate errors induced by strong multipath conditions [6], or employ more realistic statistical models for the distribution of the range estimates [7]. Cooperation between agents is another method to increase the amount of available information [8] and thus to reduce the localization outage. Actual exploitation of multipath propagation requires prior knowledge [9]. This can be the floor plan, like in this work and related approaches [10], or a set of known antenna locations to enable beamforming (e.g. in imaging [11]). In an inverse problem, the room geometry can be inferred from the multipath and known measurement locations [12].

Insight on the position-related information that is conveyed in the signals [13] can be gained by an analysis of performance bounds, such as the Cramér-Rao lower bound (CRLB), which is the lower bound of the covariance matrix of an unbiased estimator for a vector parameter. Using the concept of equivalent Fisher information matrices (EFIMs) [14], [15], allows for analytic evaluation of the CRLB by blockwise inversion of the Fisher information matrix (FIM) [16], [17].

A proper channel model is paramount to capture the information contained in MPCs. It is common [18]–[22] to differentiate between resolvable MPCs which origin from

specular reflections or scatterers and so-called dense or diffuse multipath (DM), which comprises all other "energy producing" components that can not be resolved by the measurement aperture. This part of the channel is often modeled statistically since many unresolvable components add up in one delay bin of the channel impulse response. An established approach to describe these statistics is to use parametric models for the power delay profile (PDP) [18], [19]. The overall models are often referred to as hybrid geometric-stochastic channel models (GSCMs). For the analysis presented in this paper, propagation effects other than the geometrically modeled MPCs constitute interference to useful position-related information. This interference is also called diffuse multipath (DM) [23] and modeled as a colored noise process with non-stationary statistic.

Fig. 1 illustrates the geometric model for multipath-assisted positioning. A signal exchanged between an anchor at position $\mathbf{p}_1^{(j)}$ and an agent at $\mathbf{p}^{(m)}$ contains specular reflections at the room walls, indicated by the black lines.[2] These reflections can be modeled geometrically using VAs $\mathbf{p}_k^{(j)}$, mirror images of the anchor w.r.t. walls that can be computed from the floor plan [24]–[26]. We call this the *bistatic* setup, where the fixed anchors and the floor plan constitute the available infrastructure. In a *cooperative* setup, agents localize themselves using bistatic measurements inbetween them. Here, the node at $\mathbf{p}_1^{(j)}$ is an agent that plays the role of an anchor (and thus provides a set of VAs) for the agent at $\mathbf{p}^{(m)}$. If the agents are equipped accordingly, they can use *monostatic* measurements, indicated by the gray lines. Here, the node at $\mathbf{p}_1^{(j)}$ acts as anchor for itself with its own set of VAs.

For these measurement setups, we analyze the following scenarios isolated to get insights on different effects of interest: (i) Multipath-Sync with known clock-offset between anchors and agents, (ii) Multipath-NSync with unknown clock-offset between anchors and agents and optionally also between the individual anchors, and (iii) Multipath-Coop with cooperation between the agents, monostatic measurements, and possibly additional fixed anchors. Clock-synchronization for impulse radio UWB has shown to achieve a synchronization accuracy in order of 1 ns, which results still in large localization errors [27]. As a consequence, we estimate the clock-offset jointly, solely based on the received signal and the a-priori known floor plan. Only the differences between the arrival times of MPCs carry position-related information in this case, not the time of arrival as in the synchronized one.

For a tracking application, we have coined the terms *multipath-assisted indoor navigation and tracking (MINT)* for the bistatic setup [23], and Co-MINT [28] for the cooperative setup. The robustness and accuracy of MINT have been reported in [24], [29], [30] and references therein. Also, a real-time demonstration system has been realized [29].

The key contributions of this paper are:

- We present a mathematical framework for the quantification of position-related information contained in geometrically modeled specular reflections in (ultra) wideband wireless signals under DM.
- This information is quantified for conventional bistatic, monostatic, and cooperative measurement scenarios, optionally including unknown clock offsets, allowing for important insights that can be used in the design of a localization system.
- The results show the relevance of a site-specific, position-related channel model for indoor positioning and the components it comprises of. This position-related FIM is a measure for *accuracy* and as a further consequence, it can also be seen as indicator for *robustness*, since it increases with the number of useful MPCs, which also makes algorithms based on multipath-assisted approach more *robust*.
- We validate, using real measurements, the usefulness of the derived bounds and of the introduced signal-to-interference-plus-noise-ratio (SINR) as a measure for position-related information.

The paper is organized as follows: Section II introduces the geometric-stochastic signal model that is used in Section III to derive the CRLB on the position estimation error. Section IV describes the relationship between signal parameters and node positions in a generic form. These results are used in Section V to derive the CRLB for the different scenarios. Finally, Sections VI and VII wrap up the paper with results, discussions, and conclusions.

Mathematical notations: $\mathbb{E}_z\{\cdot\}$ represents the expectation operator with respect to the random variable z. $[\mathbf{A}]_{n,m}$ is the (n,m)-th element of matrix $\mathbf{A}$; $\mathbf{A}_{N\times M}$ indicates the size of a matrix. $\|\cdot\|$ is the Euclidean norm, $|\cdot|$ is the absolute value, and $(*)$ denotes convolution. $\mathbf{A} \succeq \mathbf{B}$ means that $\mathbf{A}-\mathbf{B}$ is positive semidefinite. $\mathbf{I}_N$ is the identity matrix of size N. $(\cdot)^{\mathrm{H}}$ is the Hermitian conjugate. $\mathrm{tr}\{\cdot\}$ and $\mathrm{diag}\{\cdot\}$ are the trace and the diagonal of a square matrix, respectively.

II. Signal Model

In Sections II and III, we simplify the setup—for the ease of readability—to a single (fixed) anchor located at position $\mathbf{p}_1 \in \mathbb{R}^2$ and one agent at position $\mathbf{p} \in \mathbb{R}^2$. Note that two-dimensional position coordinates are used throughout the paper, for the sake of simplicity[3]. A *baseband* UWB signal $s(t)$ is exchanged between the anchor and the agent. The corresponding received signal is modeled as [23]

$$\begin{aligned} r(t) &= r_{\mathrm{det}}(t) + r_{\mathrm{diff}}(t) + w(t) \\ &= \sum_{k=1}^{K} \alpha_k s(t-\tau_k) + (s * \nu)(t-\epsilon) + w(t). \end{aligned} \quad (1)$$

The first term $r_{\mathrm{det}}(t)$ describes a sum of K deterministic MPCs with complex amplitudes $\{\alpha_k\}$ and delays $\{\tau_k\}$. We model these delays by VAs at positions $\mathbf{p}_k \in \mathbb{R}^2$, yielding $\tau_k = \frac{1}{c}\|\mathbf{p}-\mathbf{p}_k\| + \epsilon$, with $k = 1 \ldots K$, where c is the speed of light and ϵ represents the clock-offset due to clock asynchronism. K is equivalent to the number of visible VAs

[2]Since the radio channel is reciprocal, the assignment of transmitter and receiver roles to anchors and agents is arbitrary and this choice can be made according to higher-level considerations.

[3]The extension to three dimensional coordinates is straightforward.

at the agent position $\mathbf{p}$ [24]. We assume the energy of $s(t)$ is normalized to one.

The second term $r_{\text{diff}}(t)$ denotes the convolution of the transmitted signal $s(t)$ with the DM $\nu(t)$, which is modeled as a zero-mean Gaussian random process. Note that the statistic of $r_{\text{diff}}(t)$ is non-stationary in the delay domain and it is colored due to the spectrum of $s(t)$. For DM we assume uncorrelated scattering along the delay axis τ, hence the auto-correlation function (ACF) of $\nu(t)$ is given by

$$K_\nu(\tau, u) = \mathbb{E}_\nu\left\{\nu(\tau)[\nu(u)]^*\right\} = S_\nu(\tau)\delta(\tau - u), \quad (2)$$

where $S_\nu(\tau)$ is the PDP of DM at the agent position $\mathbf{p}$. The DM process is assumed to be quasi-stationary in the spatial domain, which means that $S_\nu(\tau)$ does not change in the vicinity of position $\mathbf{p}$ [31]. The PDP $S_\nu(\tau)$ is crucial to represent the power ratio between useful deterministic MPCs and DM (along the delay axis τ) and it is represented by an arbitrary function which can be estimated from an ensemble of measurements [19] [4], rather than a parametric PDP [18]. We will assume that the DM statistic is known a-priori to be able to analyze the influence of DM on the CRLB in closed form, with no parametric restriction on the DM PDP $S_\nu(\tau)$. With this, our results will show that information coming from MPCs is quantified by a signal-to-interference-plus-noise-ratio (SINR) for these MPCs, which represents the power ratio between useful deterministic MPC and impairing DM plus noise. Finally, the last term $w(t)$ denotes an additive white Gaussian noise (AWGN) process with double-sided power spectral density (PSD) of $N_0/2$.

In the following, we will drop the clock-offset ϵ. We will re-introduce it in Section V-B where the Multipath-NSync setup is studied.

III. Cramér-Rao Lower Bound

The goal of multipath-assisted indoor positioning is to estimate the agent's position $\mathbf{p}$ from the signal waveform (1), exploiting the knowledge of the VA positions $\{\mathbf{p}_k\}$, in presence of diffuse multipath and AWGN with known statistics. Let $\hat{\boldsymbol{\theta}}$ denote the estimate of the position-related parameter vector $\boldsymbol{\theta} = [\mathbf{p}^{\mathrm{T}}\ \Re\boldsymbol{\alpha}^{\mathrm{T}}\ \Im\boldsymbol{\alpha}^{\mathrm{T}}]^{\mathrm{T}} \in \mathbb{R}^{D_{\boldsymbol{\theta}}}$, where $\Re\boldsymbol{\alpha} = [\Re\alpha_1, \ldots, \Re\alpha_K]^{\mathrm{T}}$ and $\Im\boldsymbol{\alpha} = [\Im\alpha_1, \ldots, \Im\alpha_K]^{\mathrm{T}}$ are the real and imaginary parts of the complex amplitudes $\boldsymbol{\alpha}$, respectively, which are nuisance parameters. According to the information inequality, the error covariance matrix of $\boldsymbol{\theta}$ is bounded by [32]

$$\mathbb{E}_{\mathbf{r}|\boldsymbol{\theta}}\left\{\left(\hat{\boldsymbol{\theta}} - \boldsymbol{\theta}\right)\left(\hat{\boldsymbol{\theta}} - \boldsymbol{\theta}\right)^{\mathrm{H}}\right\} \succeq \boldsymbol{\mathcal{I}}_{\boldsymbol{\theta}}^{-1}, \quad (3)$$

where $\boldsymbol{\mathcal{I}}_{\boldsymbol{\theta}} \in \mathbb{R}^{D_{\boldsymbol{\theta}} \times D_{\boldsymbol{\theta}}}$ is the Fisher information matrix (FIM) and its inverse represents the CRLB of $\boldsymbol{\theta}$. We apply the chain rule to derive this CRLB (cf. [14], [17]), i.e., the FIM $\boldsymbol{\mathcal{I}}_{\boldsymbol{\theta}}$ is computed from the FIM of the signal parameter vector $\boldsymbol{\psi} = \left[\boldsymbol{\tau}^{\mathrm{T}}, \Re\boldsymbol{\alpha}^{\mathrm{T}}, \Im\boldsymbol{\alpha}^{\mathrm{T}}\right]^{\mathrm{T}} \in \mathbb{R}^{D_{\boldsymbol{\psi}}}$, where $\boldsymbol{\tau} = [\tau_1, \ldots, \tau_K]^{\mathrm{T}}$ represents the vector of position-related delays. We get

$$\boldsymbol{\mathcal{I}}_{\boldsymbol{\theta}} = \mathbf{J}^{\mathrm{T}}\boldsymbol{\mathcal{I}}_{\boldsymbol{\psi}}\mathbf{J} \quad (4)$$

[4]The PDP for instance can be estimated globally for an anchor placed in a room from sets of measurements distributed over the according floor plan and then it can be updated during tracking of an agent [24].

with the Jacobian

$$\mathbf{J} = \frac{\partial\boldsymbol{\psi}}{\partial\boldsymbol{\theta}} \in \mathbb{R}^{D_{\boldsymbol{\psi}} \times D_{\boldsymbol{\theta}}}. \quad (5)$$

The FIM $\boldsymbol{\mathcal{I}}_{\boldsymbol{\psi}} \in \mathbb{R}^{D_{\boldsymbol{\psi}} \times D_{\boldsymbol{\psi}}}$ of the signal model parameters can be computed from the likelihood function $f(\mathbf{r}|\boldsymbol{\psi})$ of the received signal $\mathbf{r}$ conditioned on parameter vector $\boldsymbol{\psi}$,

$$\boldsymbol{\mathcal{I}}_{\boldsymbol{\psi}} = \mathbb{E}_{\mathbf{r}|\boldsymbol{\psi}}\left\{\left[\frac{\partial}{\partial\boldsymbol{\psi}}\ln f(\mathbf{r}|\boldsymbol{\psi})\right]\left[\frac{\partial}{\partial\boldsymbol{\psi}}\ln f(\mathbf{r}|\boldsymbol{\psi})\right]^{\mathrm{T}}\right\}. \quad (6)$$

A. Likelihood Function

The likelihood function $f(\mathbf{r}|\boldsymbol{\psi})$ is defined for the sampled received signal vector $\mathbf{r} = [r(0), r(T_{\mathrm{s}}), \ldots, r((N-1)T_{\mathrm{s}})]^{\mathrm{T}} \in \mathbb{C}^N$, containing N samples at rate $1/T_{\mathrm{s}}$. Using the assumption that AWGN and DM are both Gaussian, it is given by

$$\begin{aligned} f(\mathbf{r}|\boldsymbol{\psi}) &\propto \exp\left\{-(\mathbf{r} - \mathbf{S}\boldsymbol{\alpha})^{\mathrm{H}}\mathbf{C}_{\mathrm{n}}^{-1}(\mathbf{r} - \mathbf{S}\boldsymbol{\alpha})\right\} \\ &\propto \exp\left\{2\Re\left\{\mathbf{r}^{\mathrm{H}}\mathbf{C}_{\mathrm{n}}^{-1}\mathbf{S}\boldsymbol{\alpha}\right\} - \boldsymbol{\alpha}^{\mathrm{H}}\mathbf{S}^{\mathrm{H}}\mathbf{C}_{\mathrm{n}}^{-1}\mathbf{S}\boldsymbol{\alpha}\right\} \end{aligned} \quad (7)$$

where $\mathbf{S} = [\mathbf{s}_{\tau_1}, \ldots, \mathbf{s}_{\tau_K}] \in \mathbb{R}^{N \times K}$ is the signal matrix containing delayed versions $\mathbf{s}_{\tau_k} = [s(-\tau_k), s(T_{\mathrm{s}} - \tau_k), \ldots, s((N-1)T_{\mathrm{s}} - \tau_k)]^{\mathrm{T}}$ of the sampled transmit pulse and $\mathbf{C}_{\mathrm{n}} = \sigma_{\mathrm{n}}^2\mathbf{I}_N + \mathbf{C}_{\mathrm{c}} \in \mathbb{R}^{N \times N}$ denotes the co-variance matrix of the noise processes. The vector of AWGN samples has variance $\sigma_{\mathrm{n}}^2 = N_0/T_{\mathrm{s}}$; the elements of the DM co-variance matrix are given by $[\mathbf{C}_{\mathrm{c}}]_{n,m} = T_{\mathrm{s}}\sum_{i=0}^{N-1} S_\nu(iT_{\mathrm{s}})s(nT_{\mathrm{s}} - iT_{\mathrm{s}})s(mT_{\mathrm{s}} - iT_{\mathrm{s}})$ (see Appendix A).

B. FIM for the Signal Model Parameters

1) General Case: The FIM $\boldsymbol{\mathcal{I}}_{\boldsymbol{\psi}}$ is obtained from (6) with (7). Following the notation of [14], it is decomposed according to the subvectors of $\boldsymbol{\psi}$ into

$$\boldsymbol{\mathcal{I}}_{\boldsymbol{\psi}} = \begin{bmatrix} \boldsymbol{\Lambda}_{\mathrm{A}} & \boldsymbol{\Lambda}_{\mathrm{B}}^{\mathrm{R}} & \boldsymbol{\Lambda}_{\mathrm{B}}^{\mathrm{I}} \\ (\boldsymbol{\Lambda}_{\mathrm{B}}^{\mathrm{R}})^{\mathrm{T}} & \boldsymbol{\Lambda}_{\mathrm{C}}' & \mathbf{0} \\ (\boldsymbol{\Lambda}_{\mathrm{B}}^{\mathrm{I}})^{\mathrm{T}} & \mathbf{0} & \boldsymbol{\Lambda}_{\mathrm{C}}' \end{bmatrix} = \begin{bmatrix} \boldsymbol{\Lambda}_{\mathrm{A}} & \boldsymbol{\Lambda}_{\mathrm{B}} \\ \boldsymbol{\Lambda}_{\mathrm{B}}^{\mathrm{T}} & \boldsymbol{\Lambda}_{\mathrm{C}} \end{bmatrix}. \quad (8)$$

Its elements are defined as [32], for example (see also (A.5)),

$$[\boldsymbol{\Lambda}_{\mathrm{B}}^{\mathrm{R}}]_{k,k'} = \mathbb{E}_{\mathbf{r}|\boldsymbol{\psi}}\left\{-\frac{\partial^2 \ln f(\mathbf{r}|\boldsymbol{\psi})}{\partial\tau_k\partial\Re\alpha_{k'}}\right\}$$

which yields with (7)

$$[\boldsymbol{\Lambda}_{\mathrm{A}}]_{k,k'} = 2\Re\left\{\alpha_k\alpha_{k'}^*\left(\frac{\partial\mathbf{s}_{\tau_{k'}}}{\partial\tau_{k'}}\right)^{\mathrm{H}}\mathbf{C}_{\mathbf{n}}^{-1}\frac{\partial\mathbf{s}_{\tau_k}}{\partial\tau_k}\right\} \quad (9)$$

$$[\boldsymbol{\Lambda}_{\mathrm{B}}^{\mathrm{R}}]_{k,k'} = 2\Re\left\{\alpha_k\left(\mathbf{s}_{\tau_{k'}}\right)^{\mathrm{H}}\mathbf{C}_{\mathbf{n}}^{-1}\frac{\partial\mathbf{s}_{\tau_k}}{\partial\tau_k}\right\} \quad (10)$$

$$[\boldsymbol{\Lambda}_{\mathrm{B}}^{\mathrm{I}}]_{k,k'} = 2\Im\left\{\alpha_k\left(\mathbf{s}_{\tau_{k'}}\right)^{\mathrm{H}}\mathbf{C}_{\mathbf{n}}^{-1}\frac{\partial\mathbf{s}_{\tau_k}}{\partial\tau_k}\right\} \quad (11)$$

$$[\boldsymbol{\Lambda}_{\mathrm{C}}']_{k,k'} = 2\Re\left\{\left(\mathbf{s}_{\tau_k}\right)^{\mathrm{H}}\mathbf{C}_{\mathbf{n}}^{-1}\mathbf{s}_{\tau_{k'}}\right\}. \quad (12)$$

These equations can be used to numerically evaluate the FIM without further assumptions. The CRLB can thus be evaluated, but the inverse of the covariance matrix $\mathbf{C}_{\mathrm{n}}$, which is needed as a whitening operator [33] to account for the non-stationary DM process, limits the insight it can possibly provide. More insight can be gained under the assumption that the received deterministic MPCs $\{\alpha_k s(t - \tau_k)\}$ are orthogonal, which occurs in practice when MPCs are non-overlapping.

2) Orthogonal MPCs: In this case, the columns of the signal matrix $\mathbf{S}$ are orthogonal and $\mathbf{\Lambda}_\mathrm{A}$ becomes diagonal (since $\mathbf{C}_\mathbf{n}^{-1}$ is symmetric). Furthermore, $[\mathbf{\Lambda}_\mathrm{B}]_{k,k'}$ is zero (due to the symmetry of the autocorrelation function of $s(t)$) and as a consequence $[\mathbf{\Lambda}_\mathrm{C}]_{k,k'}$ is not needed. The elements of $\mathbf{\Lambda}_\mathrm{A}$ can then be written as (see Appendix A)

$$[\mathbf{\Lambda}_\mathrm{A}]_{k,k} = 8\pi^2\beta^2 \mathrm{SINR}_k \gamma_k \tag{13}$$

where $\beta^2 = \int_f f^2 |S(f)|^2 \mathrm{d}f$ is the effective (mean square) bandwidth of the energy-normalized transmit pulse $s(t) \overset{\mathcal{F}}{\longleftrightarrow} S(f)$,

$$\mathrm{SINR}_k := \frac{\left|\alpha_k\right|^2}{N_0 + T_\mathrm{p} S_\nu(\tau_k)} \tag{14}$$

is the signal-to-interference-plus-noise ratio (SINR) of the k-th MPC, and γ_k is the so-called bandwidth extension factor. The product of these three factors quantifies the delay information provided by the k-th MPC. It hence provides the following insight for the investigated estimation problem: The interference term $T_\mathrm{p} S_\nu(\tau_k)$ is determined by the PDP of DM $S_\nu(\tau_k)$ at the delay τ_k of the MPC. It scales with the effective pulse duration T_p of the pulse $s(t)$, the reciprocal of its equivalent Nyquist bandwidth $B_\mathrm{N} = 1/T_\mathrm{p}$. An increased bandwidth is hence beneficial to suppress DM.

The bandwidth extension quantifies the SINR-gain due to the whitening operation. It is defined as $\gamma_k = \beta_k^2/\beta^2$, where β_k^2 is the mean square bandwidth of the whitened pulse,

$$\beta_k^2 = \int_f f^2 |\mathrm{S}(f)|^2 \frac{N_0 + T_\mathrm{p} S_\nu(\tau_k)}{N_0 + |\mathrm{S}(f)|^2 S_\nu(\tau_k)} \mathrm{d}f. \tag{15}$$

If the pulse has a block spectrum, we have (due to the energy normalization of $s(t)$) $|S(f)|^2 = T_\mathrm{p}$ for $|f| \leq B_\mathrm{N}/2$, hence $\beta_k^2 = \beta^2$ and $\gamma_k = 1$. I.e., in this case, there is *no* bandwidth extension due to whitening[5]. The same holds if DM is negligible, i.e. $N_0 \gg T_\mathrm{p} S_\nu(\tau_k)$. For the asymptotic case that AWGN is negligible, i.e. $|\mathrm{S}(f)|^2 S_\nu(\tau_k) \gg N_0$, we drop N_0 in (15) and get a block spectrum that corresponds to the *absolute* bandwidth of $S(f)$.

In general, γ_k is a function of the interference-to-noise ratio (INR) $T_\mathrm{p} S_\nu(\tau_k)/N_0$ and can be evaluated numerically. Closed-form results can be given for special cases. E.g. for a root-raised-cosine pulse with roll-off factor R, we have $\beta^2 = B_\mathrm{N}^2(\frac{1}{12} + \frac{\pi^2-8}{4\pi^2}R^2)$ which scales slightly with R. In the asymptotic case where DM dominates, we get $\beta_k^2 = \frac{(1+R)^3}{12} B_\mathrm{N}^2$. Hence the bandwidth extension due to the whitening operation can result in an SINR gain of up to about 7 dB at $R = 1$. Numerical evaluation shows a γ_k of 4 dB at $R = 0.6$ and INR of 15 dB.

For further analysis, we define the extended SINR

$$\widetilde{\mathrm{SINR}}_k = \mathrm{SINR}_k \gamma_k \tag{16}$$

which quantifies the delay information provided by MPC k as a function of the signal, interference, and noise levels.

[5]This specialization was assumed in our previous paper [23].

C. Position Error Bound

The FIM $\boldsymbol{\mathcal{I}}_{\boldsymbol{\psi}}$ of the signal model parameters quantifies the information gained from the measurement $\mathbf{r}$. The position-related part of this information lies in the MPC delays $\boldsymbol{\tau}$, which are a function of the position $\mathbf{p}$. To compute the position error bound (PEB), the square-root of the trace of the CRLB on the position error, we need the upper left 2×2 submatrix of the inverse of FIM $\boldsymbol{\mathcal{I}}_{\boldsymbol{\theta}}$,

$$\mathcal{P}\{\mathbf{p}\} = \sqrt{\mathrm{tr}\left\{\left[\boldsymbol{\mathcal{I}}_{\boldsymbol{\theta}}^{-1}\right]_{2\times 2}\right\}} = \sqrt{\mathrm{tr}\left\{\boldsymbol{\mathcal{I}}_\mathbf{p}^{-1}\right\}}, \tag{17}$$

which can be obtained with (4) and (5) using the blockwise inversion lemma. This results in the so-called *equivalent* FIM (EFIM) $\boldsymbol{\mathcal{I}}_\mathbf{p}$ [14],

$$\boldsymbol{\mathcal{I}}_\mathbf{p} = \mathbf{H}^\mathrm{T}\big(\mathbf{\Lambda}_\mathrm{A} - \mathbf{\Lambda}_\mathrm{B}\big(\mathbf{\Lambda}_\mathrm{C}\big)^{-1}\mathbf{\Lambda}_\mathrm{B}^\mathrm{T}\big)\mathbf{H},$$

which represents the information relevant for the position error bound. Matrix $\mathbf{H} = \partial\boldsymbol{\tau}/\partial\mathbf{p}$ is the submatrix of Jacobian (5) that relates to the position-related information, the derivatives of the delay vector $\boldsymbol{\tau}$ w.r.t. postition $\mathbf{p}$. It describes the variation of the signal parameters w.r.t. the position and can assume different, scenario-dependent forms, depending on the roles of anchors and agents. General expressions for these *spatial delay gradients* are derived in the next section.

IV. Spatial Delay Gradients

The following notations are used to find the elements of matrix $\mathbf{H}$: $\mathbf{p}^{(m)} \in \mathbb{R}^2$ is the position of the m-th agent, where $m \in \mathcal{N}_m = \{1, 2, \ldots, M\}$. $\mathbf{p}_1^{(j)} \in \mathbb{R}^2$ is the position of the j-th fixed anchor, $j \in \mathcal{N}_j = \{M+1, \ldots, M+J\}$, with VAs at positions $\mathbf{p}_k^{(j)} \in \mathbb{R}^2$. In the cooperative scenario, we replace j with an arbitrary index ξ to cover fixed anchors as well as agents which act as anchors. The corresponding VAs are at $\mathbf{p}_k^{(\xi)} \in \mathbb{R}^2$. To describe gradients w.r.t. anchor or agent position, we use an index η, introducing $\mathbf{p}^{(\eta)} \in \mathbb{R}^2$.

The delay of the k-th MPC is defined by the distance between the k-th VA and the m-th agent,

$$\tau_k^{(\xi,m)} = \frac{1}{c}\left\|\mathbf{p}^{(m)} - \mathbf{p}_k^{(\xi)}\right\| \tag{18}$$

$$= \frac{1}{c}\sqrt{\left(x^{(m)} - x_k^{(\xi)}\right)^2 + \left(y^{(m)} - y_k^{(\xi)}\right)^2}. \tag{19}$$

The angle of vector $(\mathbf{p}^{(m)} - \mathbf{p}_k^{(\xi)})$ is written as $\phi_k^{(\xi,m)}$. To describe the relation between the signal parameter $\tau_k^{(\xi,m)}$ and the geometry, we need to analyze the spatial delay gradient, the derivative of the delay $\tau_k^{(\xi,m)}$ w.r.t. position $\mathbf{p}^{(\eta)}$,

$$\begin{aligned}
\mathbf{h}_k^{(\xi,\eta,m)} =& \frac{\partial \tau_k^{(\xi,m)}}{\partial \mathbf{p}^{(\eta)}} = \frac{1}{c}\frac{\partial\left\|\mathbf{p}^{(m)} - \mathbf{p}_k^{(\xi)}\right\|}{\partial \mathbf{p}^{(\eta)}} \\
=& \frac{1}{c}\frac{\partial\left(x^{(m)} - x_k^{(\xi)}\right)}{\partial \mathbf{p}^{(\eta)}} \frac{x^{(m)} - x_k^{(\xi)}}{\left\|\mathbf{p}^{(m)} - \mathbf{p}_k^{(\xi)}\right\|} \\
&+ \frac{1}{c}\frac{\partial\left(y^{(m)} - y_k^{(\xi)}\right)}{\partial \mathbf{p}^{(\eta)}} \frac{y^{(m)} - y_k^{(\xi)}}{\left\|\mathbf{p}^{(m)} - \mathbf{p}_k^{(\xi)}\right\|} \\
=& \frac{1}{c}\left(\delta_{m,\eta}\mathbf{I}_2 - \delta_{\eta,\xi}\frac{\partial \mathbf{p}_k^{(\xi)}}{\partial \mathbf{p}^{(\xi)}}\right)^\mathrm{T} \mathbf{e}\left(\phi_k^{(\xi,m)}\right)
\end{aligned} \tag{20}$$

where $\mathbf{e}(\phi) := [\cos(\phi), \sin(\phi)]^{\mathrm{T}}$ is a unit vector in direction of the argument angle and $\delta_{m,\eta}$ is the Kronecker delta.Using (B.9) for the Jacobian $\mathbf{p}_k^{(\xi)}/\mathbf{p}^{(\xi)}$ of a VA position w.r.t. its respective anchor's position from Appendix B, we get

$$\mathbf{h}_k^{(\xi,\eta,m)} = \frac{1}{c}\Big[\delta_{m,\eta}\mathbf{e}\Big(\phi_k^{(\xi,m)}\Big) - \delta_{\eta,\xi}\mathbf{e}\Big((-1)^{Q_k^{(\xi)}}\phi_k^{(\xi,m)} + 2\bar{\zeta}_k^{(\xi)}\Big)\Big], \tag{21}$$

where the first summand represents the influence of the agent position while the second summand is linked to the anchor position. The parameter $\bar{\zeta}_k^{(\xi)}$ (see Appendix B) describes the effective wall angle of the k-th MPC w.r.t. to the η-th anchor (or agent) and $Q_k^{(\xi)}$ represents the according VA order. We stack the transposed gradient vectors (21) for the entire set of multipath components in the gradient matrix $\mathbf{H}^{(\xi,\eta,m)} \in \mathbb{R}^{K^{(\xi,m)}\times 2}$ and the matrices for all the agents' derivatives into matrix $\mathbf{H}^{(\xi,m)} \in \mathbb{R}^{K^{(\xi,m)}\times 2M}$.

The following specializations will be used:

1) Bistatic scenario: $k = 1, \ldots, K^{(\xi,m)}$

a) The gradient with respect to the agent: This case describes the derivatives of delay $\tau^{(\xi,m)}$ w.r.t. the agent position, i.e. $\eta = m$, yielding the gradient

$$\mathbf{h}_k^{(\xi,m,m)} = \frac{\partial \tau^{(\xi,m)}}{\partial \mathbf{p}^{(m)}} = \frac{1}{c}\mathbf{e}\Big(\phi_k^{(\xi,m)}\Big) \tag{22}$$

which represents a vector pointing from an agent to the k-th VA of the according anchor. We define the gradient matrix $\mathbf{H}_{\mathrm{Ag}}^{(\xi,m)} = \mathbf{H}^{(\xi,m,m)} \in \mathbb{R}^{K^{(\xi,m)}\times 2}$.

b) The gradient with respect to the anchor: In this case, the derivatives w.r.t. the anchor position $\mathbf{p}^{(\xi)} = \mathbf{p}_1^{(\xi)}$ are described, i.e. $\eta = \xi$. For the k-th MPC, the gradient is expressed as

$$\begin{aligned}\mathbf{h}_k^{(\xi,\xi,m)} &= \frac{\partial \tau_k^{(\xi,m)}}{\partial \mathbf{p}^{(\xi)}} \\ &= -\frac{1}{c}\mathbf{e}\Big((-1)^{Q_k^{(\xi)}}\phi_k^{(\xi,m)} + 2\bar{\zeta}_k^{(\xi)}\Big) = \frac{1}{c}\mathbf{e}\Big(\phi_k^{(m,\xi)}\Big)\end{aligned} \tag{23}$$

which in this case is a vector pointing from an agent acting as anchor to the k-th VA of a cooperating agent. The proof for the final equality can be obtained graphically. The gradient matrix is $\mathbf{H}_{\mathrm{An}}^{(\xi,m)} = \mathbf{H}_{\mathrm{Ag}}^{(m,\xi)} = \mathbf{H}^{(\xi,\xi,m)} \in \mathbb{R}^{K^{(\xi,m)}\times 2}$.

2) Monostatic scenario: Here we restrict the VA set to $k = 2, \ldots, K^{(m,m)}$, the agent is as well the anchor, $\xi = m$, and both move synchronously, $\eta = m$, i.e., the two terms in (21) interact with each other. The gradient

$$\begin{aligned}\mathbf{h}_k^{(m,m,m)} &= \frac{\partial \tau_k^{(m,m)}}{\partial \mathbf{p}^{(m)}} \\ &= \frac{1}{c}\left(\mathbf{e}\Big(\phi_k^{(m,m)}\Big) - \mathbf{e}\Big((-1)^{Q_k^{(m)}}\phi_k^{(m,m)} + 2\bar{\zeta}_k^{(m)}\Big)\right) \\ &= \begin{cases} \frac{2}{c}\sin\Big(\bar{\zeta}_k^{(m)}\Big)\mathbf{e}\Big(\phi_k^{(m,m)} + \bar{\zeta}_k^{(m)} - \frac{\pi}{2}\Big) & \text{If } Q_k^{(m)}\text{is even} \\ \frac{2}{c}\sin\Big(\bar{\zeta}_k^{(m)} - \phi_k^{(m,m)}\Big)\mathbf{e}\Big(\bar{\zeta}_k^{(m)} - \frac{\pi}{2}\Big) & \text{If } Q_k^{(m)}\text{is odd}\end{cases}\end{aligned} \tag{24}$$

has been decomposed—as shown in Appendix C—into a magnitude term $0 \le \big\|\mathbf{h}_k^{(m,m,m)}\big\| \le \frac{2}{c}$ and a resulting direction vector. Both depend on the angle $\phi_k^{(m,m)}$, the VA order, and the angles of all contributing walls comprised in $\bar{\zeta}_k^{(m)}$. The gradient matrix is $\mathbf{H}_{\mathrm{Mo}}^{(m)} = \mathbf{H}^{(m,m,m)} \in \mathbb{R}^{(K^{(m,m)}-1)\times 2}$.

The following interpretations apply for the monostatic case: Single reflections ($Q_k^{(m)} = 1$, $\bar{\zeta}_k^{(m)} = \phi_k^{(m,m)} \pm \frac{\pi}{2}$) and reflections on rectangular corners ($Q_k^{(m)} = 2$, $\bar{\zeta}_k^{(m)} = \pm\frac{\pi}{2}$) constitute important types of monostatic VAs. Both have $\partial\tau_k^{(m,m)}/\partial\mathbf{p}^{(m)} = \frac{2}{c}\mathbf{e}(\phi_k^{(m,m)})$, which is twice as much spatial sensitivity of delays as in the bistatic cases (22) and (23), thus providing higher ranging information. The simplest case of a vanishing gradient (magnitude zero) is a second-order reflection between parallel walls ($Q_k^{(m)} = 2$, $\bar{\zeta}_k^{(m)} = 0$).

V. CRLB on the Position Error

In this Section, the CRLB on the position error is derived for the three scenarios Multipath-Sync, Multipath-NSync, and a Multipath-Coop scenario.

Using a stack vector $\mathbf{\Psi} = [\mathbf{T}^{\mathrm{T}}, \Re\mathbf{A}^{\mathrm{T}}, \Im\mathbf{A}^{\mathrm{T}}]^{\mathrm{T}}$ of the signal parameters for all relevant nodes, with $\mathbf{T}$ combining the delays and $\mathbf{A}$ combining the amplitudes, the Jacobian (5) has the following general structure.

$$\begin{aligned}\mathbf{J} = \frac{\partial\mathbf{\Psi}}{\partial\mathbf{\Theta}} &= \begin{bmatrix}\mathbf{H} & \mathbf{L} & \mathbf{0}\\ \mathbf{0} & \mathbf{0} & \mathbf{I}\end{bmatrix} \\ &= \begin{bmatrix}\partial\mathbf{T}/\partial\mathbf{P} & \partial\mathbf{T}/\partial\boldsymbol{\epsilon} & \partial\mathbf{T}/\partial\Re\mathbf{A} & \partial\mathbf{T}/\partial\Im\mathbf{A}\\ \partial\Re\mathbf{A}/\partial\mathbf{P} & \partial\Re\mathbf{A}/\partial\boldsymbol{\epsilon} & \partial\Re\mathbf{A}/\partial\Re\mathbf{A} & \partial\Re\mathbf{A}/\partial\Im\mathbf{A}\\ \partial\Im\mathbf{A}/\partial\mathbf{P} & \partial\Im\mathbf{A}/\partial\boldsymbol{\epsilon} & \partial\Im\mathbf{A}/\partial\Re\mathbf{A} & \partial\Im\mathbf{A}/\partial\Im\mathbf{A}\end{bmatrix}\end{aligned} \tag{25}$$

Vector $\mathbf{\Theta} = [\mathbf{P}^{\mathrm{T}}, \boldsymbol{\epsilon}^{\mathrm{T}}, \Re\mathbf{A}^{\mathrm{T}}, \Im\mathbf{A}^{\mathrm{T}}]^{\mathrm{T}}$, spatial delay gradient $\mathbf{H} = \partial\mathbf{T}/\partial\mathbf{P}$, and gradient $\mathbf{L} = \partial\mathbf{T}/\partial\boldsymbol{\epsilon}$ are specifically defined for the different cases in the following subsections.

A. Derivation of the CRLB for Multipath-Sync

Assuming that only one agent is present in Multipath-Sync and Multipath-NSync, we drop the agent index m so that $\mathbf{P} = \mathbf{p}$, and define $\mathcal{N}_j = \{1, 2, \ldots, J\}$. We use the geometry for the bistatic scenario, case (a) Section B. The clock-offset $\boldsymbol{\epsilon}$ is considered to be known and zero. Using a suitable signaling scheme[6], measurements $\mathbf{r}^{(j)}$ from all J anchors are independent. Hence, the log-likelihood function is defined as

$$\ln f(\mathbf{R}|\mathbf{\Psi}) = \sum_{j\in\mathcal{N}_j} \ln f\big(\mathbf{r}^{(j)}|\boldsymbol{\tau}^{(j)}, \boldsymbol{\alpha}^{(j)}\big), \tag{26}$$

where $\mathbf{R} = \big[\big(\mathbf{r}^{(1)}\big)^{\mathrm{T}}, \ldots, \big(\mathbf{r}^{(J)}\big)^{\mathrm{T}}\big]^{\mathrm{T}}$ combines all measurements and $\boldsymbol{\tau}^{(j)}$ and $\boldsymbol{\alpha}^{(j)}$ are the delay and amplitude vectors respectively, corresponding to measurement $\mathbf{r}^{(j)}$. The Jacobian $\mathbf{J}$ has the following structure,

$$\mathbf{J} = \begin{bmatrix}\mathbf{H}_{K^{(1)}\times 2}^{(1)} & & \\ \vdots & & \\ \mathbf{H}_{K^{(J)}\times 2}^{(J)} & & \\ & & \mathbf{I}_{D_{\mathbf{I}}\times D_{\mathbf{I}}}\end{bmatrix}, \tag{27}$$

where zero-matrices in the off-diagonal blocks are skipped for clarity and $D_{\mathbf{I}} = 2\sum_{j=1}^{J} K^{(j)}$. The subblocks $\mathbf{H}^{(j)} = \mathbf{H}_{\mathrm{Ag}}^{(j,1)}$

[6] E.g conventional multiple access schemes, like time-division-multiple-access (TDMA).

account for the geometry as described in Section IV. Due to the independence of the measurements $\mathbf{r}^{(j)}$, the EFIMs $\boldsymbol{\mathcal{I}}_{\mathbf{p}}^{(j)}$ from the J different anchors are additive. Using Equation (4), we can write the EFIM as

$$\boldsymbol{\mathcal{I}}_{\mathbf{p}} = \sum_{j\in\mathcal{N}_j} \left(\mathbf{H}^{(j)}\right)^{\mathrm{T}} \left(\boldsymbol{\Lambda}_{\mathrm{A}}^{(j)} - \boldsymbol{\Lambda}_{\mathrm{B}}^{(j)} \left(\boldsymbol{\Lambda}_{\mathrm{C}}^{(j)}\right)^{-1} \left(\boldsymbol{\Lambda}_{\mathrm{B}}^{(j)}\right)^{\mathrm{T}}\right) \mathbf{H}^{(j)} \tag{28}$$

where $\boldsymbol{\Lambda}_{\mathrm{A}}^{(j)}$, $\boldsymbol{\Lambda}_{\mathrm{B}}^{(j)}$, and $\boldsymbol{\Lambda}_{\mathrm{C}}^{(j)}$ are subblocks of $\boldsymbol{\mathcal{I}}_{\boldsymbol{\psi}}^{(j)}$ defined in (8). Expression (28) simplifies when we assume no path overlap (i.e. orthogonality) between signals from different VAs. In this case, $\boldsymbol{\Lambda}_{\mathrm{B}} = \mathbf{0}$ and $\boldsymbol{\Lambda}_{\mathrm{A}}$ will be diagonal, as discussed in Section III-B2 and we can then write

$$\begin{aligned}\boldsymbol{\mathcal{I}}_{\mathbf{p}} &= \sum_{j\in\mathcal{N}_j} \left(\mathbf{H}^{(j)}\right)^{\mathrm{T}} \boldsymbol{\Lambda}_{\mathrm{A}}^{(j)} \mathbf{H}^{(j)} \\ &\approx \frac{8\pi^2\beta^2}{c^2} \sum_{j\in\mathcal{N}_j} \sum_{k=1}^{K^{(j)}} \widetilde{\mathrm{SINR}}_k^{(j)} \mathbf{D}_{\mathrm{r}}(\phi_k^{(j)})\end{aligned} \tag{29}$$

where $\widetilde{\mathrm{SINR}}_k^{(j)}$ is the extended SINR (eq. 16) for the j-th anchor and

$$\mathbf{D}_{\mathrm{r}}(\phi_k^{(j)}) = \mathbf{e}(\phi_k^{(j)})\mathbf{e}(\phi_k^{(j)})^{\mathrm{T}} \tag{30}$$

is called ranging direction matrix (cf. [14]), a rank-one matrix with an eigenvector in direction of $\phi_k^{(j)}$.

Valuable insight is gained from (29) and (14). In particular,

- Each VA (i.e. each deterministic MPC) adds some positive term to the EFIM in direction of $\phi_k^{(j)}$ and hence reduces the PEB in direction of $\phi_k^{(j)}$.
- The $\widetilde{\mathrm{SINR}}_k^{(j)}$ determines the magnitude of this contribution as discussed in Section III-B2 (cf. ranging intensity information (RII) in [14]). It is limited by diffuse multipath—an effect that reduces with increased bandwidth—and it can show a significant gain due to the interference whitening if the interference-to-noise ratio is large.
- The effective bandwidth β scales the EFIM. Any increase corresponds to a decreased PEB.

Discussion of *path overlap* (cf. [14]):

- $\tau_k - \tau_{k'} \ll T_{\mathrm{p}}$: In this case the MPCs can not be distinguished and the position-related information is entirely lost.
- $\tau_k - \tau_{k'} \approx T_{\mathrm{p}}$: In this case the MPCs are correlated, but the position-related information can still partly be used. The discrete-time formulation of the CRLB based on (7) can quantify this information gain, in contrast to our previous, continuous formulation in [23].
- $\tau_k - \tau_{k'} \gg T_{\mathrm{p}}$: If this holds, the MPCs are considered to be orthogonal and (29) can be used if it holds for all $k \neq k'$.

B. Derivation of the CRLB for Multipath-NSync

Next we consider the same setup as before, but assume the clock offsets $\boldsymbol{\epsilon}$ to be unknown parameters. The differences between arrival times still provide position information in this case. When using multiple anchors, we distinguish two different scenarios where either the clocks of all anchors are synchronized among each other, or alternatively no synchronization is present at all. While this does not affect the signal parameter FIM, we need to take it into account when performing the parameter transformation. Apart from the partial derivatives $\mathbf{L} = \partial\mathbf{T}/\partial\boldsymbol{\epsilon}$, the terms of the Jacobian are identical for Multipath-Sync and Multipath-NSync, resulting in

$$\mathbf{J} = \begin{bmatrix} \mathbf{H}_{K^{(1)}\times 2}^{(1)} & \mathbf{L}_{K^{(1)}\times D_{\boldsymbol{\epsilon}}}^{(1)} & & \\ \vdots & \vdots & & \\ \mathbf{H}_{K^{(J)}\times 2}^{(J)} & \mathbf{L}_{K^{(J)}\times D_{\boldsymbol{\epsilon}}}^{(J)} & & \\ & & & \mathbf{I}_{D_{\mathbf{I}}\times D_{\mathbf{I}}} \end{bmatrix}, \tag{31}$$

where $\mathbf{L}^{(j)} = \partial\boldsymbol{\tau}^{(j)}/\partial\boldsymbol{\epsilon}$ and $D_{\boldsymbol{\epsilon}}$ is the length of $\boldsymbol{\epsilon}$.

Synchronized anchors: When assuming $\epsilon^{(1)} = \cdots = \epsilon^{(J)} = \epsilon$, the vector $\boldsymbol{\epsilon}$ reduces to $\boldsymbol{\epsilon} = \epsilon$. The derivatives of the arrival times with respect to the clock offset are then given by $\mathbf{L}^{(j)} = \mathbf{l}_{\mathrm{syn}}^{(j)} = [1,\ldots,1]^{\mathrm{T}}$. Applying the parameter transformation and computing the block inverse similarly as in (28) leads to additivity of the 3×3 EFIMs $\boldsymbol{\mathcal{I}}_{\mathbf{p},\epsilon}^{(j)}$ for the extended parameter vector $[\mathbf{p}^{\mathrm{T}}, \epsilon]^{\mathrm{T}}$ (see Appendix D). When neglecting path overlap this expression simplifies to

$$\boldsymbol{\mathcal{I}}_{\mathbf{p},\epsilon} = \sum_{j\in\mathcal{N}_j} \boldsymbol{\mathcal{I}}_{\mathbf{p},\epsilon}^{(j)} = 8\pi^2\beta^2 \sum_{j\in\mathcal{N}_j} \sum_{k=1}^{K^{(j)}} \widetilde{\mathrm{SINR}}_k^{(j)} \mathbf{D}_{\mathrm{r},\epsilon}(\phi_k^{(j)}), \tag{32}$$

with

$$\mathbf{D}_{\mathrm{r},\epsilon}(\phi_k^{(j)}) = \mathbf{v}\mathbf{v}^{\mathrm{T}},\ \mathbf{v} = \left[\frac{1}{c}\cos(\phi_k^{(j)}),\ \frac{1}{c}\sin(\phi_k^{(j)}),\ 1\right]^{\mathrm{T}}.$$

The inner sum in (32) reveals that the 3×3 EFIMs $\boldsymbol{\mathcal{I}}_{\mathbf{p},\epsilon}^{(j)}$ are in canonical form. Since $\mathbf{D}_{r,\epsilon}$ is a positive semidefinite matrix, it highlights that each VA adds information for the estimation of $\mathbf{p}$ and ϵ, scaled by its extended $\widetilde{\mathrm{SINR}}_k$ and β.

The EFIM $\boldsymbol{\mathcal{I}}_{\mathbf{p}}$ can be computed from $\boldsymbol{\mathcal{I}}_{\mathbf{p},\epsilon}$ by again applying the blockwise inversion lemma. When neglecting path overlap, the expression for $\boldsymbol{\mathcal{I}}_{\mathbf{p}}$ becomes

$$\boldsymbol{\mathcal{I}}_{\mathbf{p}} = \frac{8\pi^2\beta^2}{c^2} \left[\sum_{j\in\mathcal{N}_j} \sum_{k=1}^{K^{(j)}} \widetilde{\mathrm{SINR}}_k^{(j)} \mathbf{D}_{\mathrm{r}}(\phi_k^{(j)}) - \boldsymbol{\mathcal{C}}\right], \tag{33}$$

where $\boldsymbol{\mathcal{C}}$ accounts for the (negative) influence of the clock offset estimation with

$$\boldsymbol{\mathcal{C}} = \frac{1}{\sum_{j\in\mathcal{N}_j}\sum_{k=1}^{K^{(j)}} \widetilde{\mathrm{SINR}}_k^{(j)}} \mathbf{c}\mathbf{c}^{\mathrm{T}},$$

$$\mathbf{c} = \sum_{j\in\mathcal{N}_j} \sum_{k=1}^{K^{(j)}} \widetilde{\mathrm{SINR}}_k^{(j)} \mathbf{e}(\phi_k^{(j)}).$$

Note that Multipath-NSync can theoretically achieve equal performance as Multipath-Sync under the (rather unlikely) condition $\mathbf{c} = \mathbf{0}$. Otherwise $\boldsymbol{\mathcal{C}}$ reduces the information, and thereby increases the PEB.

Asynchronous anchors: When having $\epsilon^{(i)} \neq \epsilon^{(j)}$, $\forall i \neq j$, $i, j \in \mathcal{N}_j$, we stack all clock offsets in the vector $\boldsymbol{\epsilon} =$

$[\epsilon^{(1)},\dots,\epsilon^{(J)}]^{\mathrm{T}}$. The derivatives of the arrival times with respect to the clock offsets are then given by a gradient matrix $\mathbf{L} = \partial\mathbf{T}/\partial\boldsymbol{\epsilon}$ of size $\sum_{j\in\mathcal{N}_j} K^{(j)} \times J$ which stacks submatrices $\mathbf{L}^{(j)}_{\text{asyn}}$ with one nonzero column $[\mathbf{L}^{(j)}_{\text{asyn}}]_{i,j} = 1$, $i = 1,\dots,K^{(j)}$. This leads to an additivity of the 2×2 EFIMs as shown in Appendix D, i.e. $\boldsymbol{\mathcal{I}}_{\mathbf{P}} = \sum_{j\in\mathcal{N}_j} \boldsymbol{\mathcal{I}}^{(j)}_{\mathbf{P}}$. When neglecting path overlap, $\boldsymbol{\mathcal{I}}_{\mathbf{P}}$ takes the form of (33), but with

$$\boldsymbol{\mathcal{C}} = \sum_{j\in\mathcal{N}_j} \frac{1}{\sum_{k=1}^{K^{(j)}} \widetilde{\mathrm{SINR}}^{(j)}_k} \mathbf{c}^{(j)} \big(\mathbf{c}^{(j)}\big)^{\mathrm{T}}, \qquad (34)$$

$$\mathbf{c}^{(j)} = \sum_{k=1}^{K^{(j)}} \widetilde{\mathrm{SINR}}^{(j)}_k \mathbf{e}(\phi^{(j)}_k).$$

Again, equality with Multipath-Sync is obtained if each $\mathbf{c}^{(j)} = \mathbf{0}$, otherwise the PEB is increased.

C. Derivation of the CRLB for Multipath-Coop

We assume M agents $m \in \mathcal{N}_m = \{1,2,\dots,M\}$ and J fixed anchors $j \in \mathcal{N}_j = \{M+1,\dots,M+J\}$, which cooperate with one another. As outlined in the Introduction, every agent conducts a monostatic measurement, meaning it emits a pulse and receives the multipath signal reflected by the environment, and conventional bistatic measurements with all other agents and the fixed anchors. All measurements are distributed such that every agent is able to exploit information from any of its received and/or transmitted signals. The clock-offsets $\boldsymbol{\epsilon}$ are considered to be zero.

The signal parameter vectors for the (j,m)-th received signal $\mathbf{r}^{(j,m)}$ are defined as $\boldsymbol{\tau}^{(j,m)} = \big[\tau^{(j,m)}_1,\dots,\tau^{(j,m)}_{K^{(j,m)}}\big]^{\mathrm{T}}$ and $\boldsymbol{\alpha}^{(j,m)} = \big[\alpha^{(j,m)}_1,\dots,\alpha^{(j,m)}_{K^{(j,m)}}\big]^{\mathrm{T}}$. For deriving the cooperative EFIM, we stack positions $\mathbf{p}^{(m)}$ of the M agents into the vector

$$\mathbf{P} = \big[\big(\mathbf{p}^{(1)}\big)^{\mathrm{T}},\dots,\big(\mathbf{p}^{(M)}\big)^{\mathrm{T}}\big]^{\mathrm{T}} \in \mathbb{R}^{2M\times 1} \qquad (35)$$

and all measurements $\mathbf{r}^{(j,m)}$ in the vector

$$\mathbf{R} = \big[\big(\mathbf{r}^{(1,1)}\big)^{\mathrm{T}},\dots,\big(\mathbf{r}^{(1,M)}\big)^{\mathrm{T}},\dots,\big(\mathbf{r}^{(M,M)}\big)^{\mathrm{T}}, \big(\mathbf{r}^{(M+1,1)}\big)^{\mathrm{T}},\dots,\big(\mathbf{r}^{(M+J,M)}\big)^{\mathrm{T}}\big]^{\mathrm{T}} \in \mathbb{C}^{D_{\mathbf{R}}\times 1}, \qquad (36)$$

where $D_{\mathbf{R}} = NM(M+J)$. Further, we stack the signal parameters correspondingly in the vectors

$$\mathbf{T} = \big[\big(\boldsymbol{\tau}^{(1,1)}\big)^{\mathrm{T}},\dots,\big(\boldsymbol{\tau}^{(1,M)}\big)^{\mathrm{T}},\dots,\big(\boldsymbol{\tau}^{(M+J,M)}\big)^{\mathrm{T}}\big]^{\mathrm{T}} \qquad (37)$$

and

$$\mathbf{A} = \big[\big(\boldsymbol{\alpha}^{(1,1)}\big)^{\mathrm{T}},\dots,\big(\boldsymbol{\alpha}^{(1,M)}\big)^{\mathrm{T}},\dots,\big(\boldsymbol{\alpha}^{(M+J,M)}\big)^{\mathrm{T}}\big]^{\mathrm{T}} \qquad (38)$$

of length $D_{\mathbf{T}} = D_{\mathbf{A}} = \sum_{j\in(\mathcal{N}_m\cup\mathcal{N}_j)}\sum_{m\in\mathcal{N}_m} K^{(j,m)}$ to construct vector $\boldsymbol{\Psi} = [\mathbf{T}^{\mathrm{T}}, \Re\mathbf{A}^{\mathrm{T}}, \Im\mathbf{A}^{\mathrm{T}}]^{\mathrm{T}}$. The corresponding joint log-likelihood function, assuming independent measurements $\mathbf{r}^{(j,m)}$ between the cooperating nodes, is defined as

$$\ln f(\mathbf{R}|\boldsymbol{\Psi}) = \sum_{j\in(\mathcal{N}_m\cup\mathcal{N}_j)} \sum_{m\in\mathcal{N}_m} \ln f\big(\mathbf{r}^{(j,m)}|\boldsymbol{\tau}^{(j,m)},\boldsymbol{\alpha}^{(j,m)}\big). \qquad (39)$$

The EFIM $\boldsymbol{\mathcal{I}}_{\mathbf{P}}$ is described by (see Appendix E)

$$\boldsymbol{\mathcal{I}}_{\mathbf{P}} = \sum_{j\in(\mathcal{N}_m\cup\mathcal{N}_j)} \sum_{m\in\mathcal{N}_m} \big(\mathbf{H}^{(j,m)}\big)^{\mathrm{T}} \boldsymbol{\Lambda}^{(j,m)} \mathbf{H}^{(j,m)} \qquad (40)$$

where

$$\boldsymbol{\Lambda}^{(j,m)} = \boldsymbol{\Lambda}^{(j,m)}_{\mathrm{A}} - \boldsymbol{\Lambda}^{(j,m)}_{\mathrm{B}} \big(\boldsymbol{\Lambda}^{(j,m)}_{\mathrm{C}}\big)^{-1} \big(\boldsymbol{\Lambda}^{(j,m)}_{\mathrm{B}}\big)^{\mathrm{T}} \qquad (41)$$

yields the sub-blocks $\boldsymbol{\mathcal{I}}^{(j,m)}_{\boldsymbol{\psi}}$ of the FIM for the likelihood function (39), for independent measurements, and $\mathbf{H}^{(j,m)}$ are the spatial delay gradients[7] of the Jacobian

$$\mathbf{J} = \begin{bmatrix} \mathbf{H}^{(1,1)}_{K^{(1,1)}\times 2M} & & \\ \vdots & & \\ \mathbf{H}^{(1,M)}_{K^{(1,M)}\times 2M} & & \\ \vdots & & \\ \mathbf{H}^{(M+J,M)}_{K^{(M+J,M)}\times 2M} & & \\ & & \mathbf{I}_{D_{\mathbf{I}}\times D_{\mathbf{I}}} \end{bmatrix}, \qquad (42)$$

where $D_{\mathbf{I}} = 2D_{\mathbf{A}}$.[8] As shown in Appendix E, one gets the following final result for the EFIM $\boldsymbol{\mathcal{I}}_{\mathbf{P}}$ for all agents

$$\boldsymbol{\mathcal{I}}_{\mathbf{P}} = \begin{bmatrix} \boldsymbol{\mathcal{I}}^{(1)}_{\mathrm{Mo}} + 2\boldsymbol{\mathcal{I}}^{(1)}_{\mathrm{Ag}} + \boldsymbol{\mathcal{I}}^{(1)}_{\mathrm{An}} & 2\boldsymbol{\mathcal{I}}^{(1,2)}_{\mathrm{C}} & \dots & 2\boldsymbol{\mathcal{I}}^{(1,M)}_{\mathrm{C}} \\ 2\boldsymbol{\mathcal{I}}^{(2,1)}_{\mathrm{C}} & \ddots & & \\ \vdots & & & \\ 2\boldsymbol{\mathcal{I}}^{(M,1)}_{\mathrm{C}} & & & \boldsymbol{\mathcal{I}}^{(M)}_{\mathrm{Mo}} + 2\boldsymbol{\mathcal{I}}^{(M)}_{\mathrm{Ag}} + \boldsymbol{\mathcal{I}}^{(M)}_{\mathrm{An}} \end{bmatrix}. \qquad (43)$$

The diagonal blocks $\boldsymbol{\mathcal{I}}^{(\eta)}_{\mathrm{Ag}} = \sum_{m\in\mathcal{N}_m\setminus\{\eta\}} \big(\mathbf{H}^{(m,\eta)}_{\mathrm{Ag}}\big)^{\mathrm{T}} \boldsymbol{\Lambda}^{(m,\eta)} \mathbf{H}^{(m,\eta)}_{\mathrm{Ag}}$ account for the bistatic measurements between agent η and all other agents, $\boldsymbol{\mathcal{I}}^{(\eta)}_{\mathrm{An}} = \sum_{j\in\mathcal{N}_j} \big(\mathbf{H}^{(j,\eta)}_{\mathrm{Ag}}\big)^{\mathrm{T}} \boldsymbol{\Lambda}^{(j,\eta)} \mathbf{H}^{(j,\eta)}_{\mathrm{Ag}}$ account for the bistatic measurements between agent η and all fixed anchors, and $\boldsymbol{\mathcal{I}}^{(\eta)}_{\mathrm{Mo}} = \big(\mathbf{H}^{(\eta)}_{\mathrm{Mo}}\big)^{\mathrm{T}} \boldsymbol{\Lambda}^{(\eta,\eta)} \mathbf{H}^{(\eta)}_{\mathrm{Mo}}$ account for the monostatic measurement of agent η. The off-diagonal blocks $\boldsymbol{\mathcal{I}}^{(\eta,\eta')}_{\mathrm{C}} = \big(\mathbf{H}^{(\eta',\eta)}_{\mathrm{Ag}}\big)^{\mathrm{T}} \boldsymbol{\Lambda}^{(\eta',\eta)} \mathbf{H}^{(\eta,\eta')}_{\mathrm{Ag}}$ account for the uncertainty about the cooperating agents in their role as anchors (cf. (E.2) and (E.3)). This has a negative effect on the localization performance of the agents. The factors of two in (43), related to the EFIM of measurements inbetween agents, results from the fact that those measurements are performed twice. This simplifies the notations in this section. If such repeated measurements are avoided, the same result would apply but with these factors removed.

Finally, the CRLB on position $\mathbf{p}^{(\eta)}$ of agent η is

$$\mathcal{P}\{\mathbf{p}^{(\eta)}\} = \sqrt{\mathrm{tr}\Big\{\big[\boldsymbol{\mathcal{I}}^{-1}_{\mathbf{P}}\big]^{(\eta,\eta)}_{2\times 2}\Big\}}. \qquad (44)$$

VI. Results

Computational results are presented in this section for two environments. We first validate the theoretical results using experimental data for a room illustrated in Fig. 2 and then discuss in detail the trade-offs of different measurement scenarios for a synthetic room shown in Fig. 3.

[7] Multipath-Coop can be seen as the most general setup, if clock offset issues are also included. This can be done by combining the results of Multipath-NSync and Multipath-Coop by replacing $\mathbf{H}^{(j,m)}$ with $\mathbf{G}^{(j,m)} = [\mathbf{H}^{(j,m)}, \mathbf{L}^{(j,m)}]$ (see Appendix D), which accounts for the geometry and clock offset. For monostatic measurements $\mathbf{L}^{m,m} = \mathbf{0}$.

[8] Assuming no path overlap, (40) can be simplified as in (29), using the result from Appendix A.

TABLE I
CHANNEL PARAMETERS FOR NUMERICAL EVALUATIONS.

	Param.	Value for Room Valid.	Synth.	Description
Deterministic MPCs		2		max. VA order
		3 dB		attenuation per reflection
Signal parameters	f_c	8 GHz	7 GHz	carrier freq.
	T_p	1 ns, (0.5 ns,2 ns)		pulse duration
		RRC		pulse shape
	R	0.6		roll-off factor
PDP of diffuse multipath	Ω_1	$2.67e^{-6}$	$1.16e^{-6}$	norm. power
	γ_1	10 ns	20 ns	
	γ_{rise}	3 ns	5 ns	shape param.
	χ	0.98		
E_{LOS}/N_0		29.5 dB (at 1 m)		LOS SNR

TABLE II
MPC SINRS FOR THE VALIDATION ENVIRONMENT, ESTIMATED FROM MEASURED SIGNALS AND COMPUTED FROM THE CHANNEL MODEL.

MPC	SINR (measurem.) / SINR (model) [dB] $T_p = 0.5$ ns	$T_p = 1$ ns	$T_p = 2$ ns
LOS Anchor 1	23.1 / 25.8	24.7 / 24.7	23.2 / 23.7
lower wall	11.1 / 18.3	5.4 / 15.9	4.1 / 13.7
right window	13.5 / 12.6	7.6 / 10.2	6.9 / 7.7
upper wall	2.2 / 11.7	-0.6 / 9.5	5.2 / 7.1
lower wall – right win.	9.5 / 7.3	7.6 / 4.9	4.9 / 2.4
LOS Anchor 2	25.9 / 26.4	26.0 / 25.3	26.5 / 24.2
right window	11.9 / 12.6	10.5 / 10.8	9.3 / 8.8
upper window	10.1 / 14.0	8.2 / 11.6	5.1 / 9.1
left wall	3.1 / 14.4	4.2 / 11.9	5.5 / 9.4
upper wall – right win.	10.6 / 5.7	11.7 / 3.9	3.5 / 1.8
upper win. – left wall	7.2 / 9.7	4.8 / 7.3	2.1 / 4.8

For the transmit signal $s(t)$, we use a root-raised-cosine (RRC) pulse with unit energy and a roll-off factor $R = 0.6$, modulated on a carrier at $f_c = 7\,\text{GHz}$ and $f_c = 8\,\text{GHz}$ (see Table I). The computations are done for pulse durations of $T_p = 0.5\,\text{ns}$, $T_p = 1\,\text{ns}$ and $T_p = 2\,\text{ns}$. In the synthetic environments, we assume for all antennas isotropic radiation patterns in the azimuth plane and gains of 0 dB. The free-space pathloss has been modeled by the Friis equation. To account for the material impact, we assume 3 dB attenuation per reflection. As in our previous paper [23], the PDP of the DM is considered to be a fixed double-exponential function, as introduced by [22, eq. (9)]. This choice reflects the common assumption of an exponential decay of the DM power and also the fact that the LOS component is not impaired by DM as severely as MPCs arriving later [34]. The model has been fitted in [22] to measurements collected in an industrial environment. We have used $\chi = 0.98$ as in [22] to describe the impact of DM on the LOS component and adapted γ_{rise} and γ_1 to reflect the smaller dimensions of our environments. Table I summarizes the parameters of the channel and signal models.

We would like to emphasize that this parametric model was introduced for simplicity and reproducibility, to analyze the impact of DM on the PEB in various scenarios. In practice, the SINR values can be estimated from channel measurements and used with the results from Section V to compute the PEB for real environments. This approach is used next to validate the theoretical results and the parametric channel model.

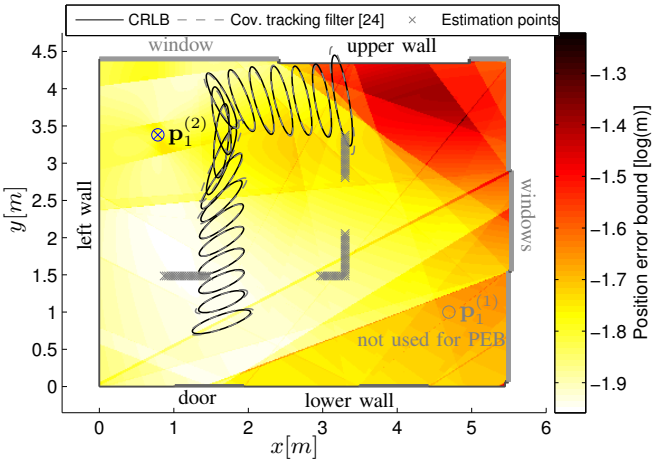

Fig. 2. Logarithmic PEB (17) for estimated SINRs in the validation environment using measured signals with $T_p = 0.5\,\text{ns}$ and $f_c = 8\,\text{GHz}$ and only MPCs corresponding to the anchor at $\mathbf{p}_1^{(2)}$. 30-fold standard deviation ellipses are shown for the CRLB and a tracking algorithm (c.f. [24]).

A. Validation with Measurement Data: Multipath-Sync

The validation is conducted in an example environment shown in Fig. 2, c.f. [29]. The MPC SINRs (14) are estimated from channel measurement data as discussed in [13], [24], using fixed positions for two anchors and a set of "estimation points" for the agent as illustrated in the figure. Table II shows the obtained values for selected MPCs. It also lists the corresponding SINRs computed from the parametric channel model, with parameters given in Table I. The choice of the parameters of the double exponential PDP of the DM has been made to account for the smaller room dimensions in comparison to the synthetic environment used below.

The *estimated SINRs* in Table II show the relevance of the corresponding MPCs. The LOS is the most significant one. Its SINR is approximately constant over all bandwidths used, indicating that it is only slightly influenced by DM. The reflections at the windows and at the lower wall also provide significant position-related information. A scaling with bandwidth—as suggested by (14)—is observable reasonably well. Other MPCs provide less information, such as the left wall (plasterboard) and the upper wall. This is caused by a reduced reflection coefficient, increased interference by DM, and increased variance of the MPC amplitude over the estimation points. Reference [35] contains further results supporting the presented findings based on measurement data from other environments [36].

Table II also shows that the *parametric channel model* yields realistic SINRs in many cases and therefore valid performance bounds. It has to be stressed that the global PDP model as used here cannot describe the local behavior of DM. However, based on the provided framework, it is straightforward to introduce more realism by fitting separate parameterized or sampled models to any appropriate local area.

Figure 2 shows the logarithmic PEB for the validation environment using the estimated SINRs from Table II for Anchor 2 and $T_p = 0.5\,\text{ns}$. Equation (29) has been employed to compute the PEB, i.e. path overlap has been neglected and

synchronization assumed. Clearly, one can observe from this figure the visibility regions and the relative importance (c.f. Table II) of specific MPCs. The PEB is better than 10 cm at almost the entire area. The ellipses encode the geometrically decomposed PEB with 30-fold standard deviation, computed from (17). Dashed ellipses are for a multipath-assisted tracking algorithm [24] that makes use of the estimated SINRs for properly weighting the information from MPCs. It can be observed that both results match closely.

B. Synthetic Environment

The synthetic environment shown in Fig. 3 is used to compare different measurement scenarios. The PEB is evaluated across the entire room, assuming one or two fixed anchor at positions $\mathbf{p}_1^{(1)} = [10, 7]^{\mathrm{T}}$ and $\mathbf{p}_1^{(2)} = [2, 1]^{\mathrm{T}}$. We use a point grid with a resolution of 2 cm, resulting in 180,000 points. VAs up to order two are considered, unless otherwise specified.

1) Multipath-Sync: Fig. 3 shows the PEB over the floorplan for Multipath-Sync and $T_{\mathrm{p}} = 1\,\mathrm{ns}$. Figs. 3(a) and (b) compare the simplified PEB neglecting path-overlap (cf. (29)) with the full PEB considering it (cf. (28)). A single anchor is employed in both cases at position $\mathbf{p}_1^{(1)}$, yielding a PEB below 10 cm for most of the area. One can clearly see the visibility regions of different VA-modeled MPCs encoded by the level of the PEB. A valid PEB is obtained over the entire room even though the anchor is partly not visible from the agent positions. If path-overlap is considered (Fig. 3(b)) in the computation of the CRLB, the adverse effect of room symmetries is observable, corresponding to regions where deterministic MPCs overlap. In case of *unresolvable* path overlap, i.e. the delay difference of two MPCs is less than the pulse duration $\tau_k - \tau_{k'} \ll T_{\mathrm{p}}$, the information of the components is entirely lost (see Section V-A). The ellipses illustrate the geometrically decomposed PEB with 20-fold standard-deviation.

Fig. 3(c) shows the PEB with path-overlap for the same parameters but for two anchors. The error ellipses clearly indicate that the PEB is much smaller and the impact of path overlap has been reduced.

A quantitative assessment of this scenarios is given in Figs. 4 and 5, showing the CDFs of the PEB for different pulse durations ($T_{\mathrm{p}} = 0.5\,\mathrm{ns}$, $T_{\mathrm{p}} = 1\,\mathrm{ns}$ and $T_{\mathrm{p}} = 2\,\mathrm{ns}$). One can observe that the PEB increases vastly w.r.t. this parameter. The "no PO" results account for the proportional scaling of Fisher information with bandwidth and additionally for the increased interference power due to DM, both of which are clearly seen in approximation (29). The influence of path overlap, which is neglected by (29), magnifies this effect even further because its occurrence becomes more probable. It almost diminishes—on the other hand—for the shortest pulse $T_{\mathrm{p}} = 0.5\,\mathrm{ns}$. Over all, the error magnitude scales by a factor of almost ten, while the bandwidth is scaled by a factor of four.

Our work in [24], [29], [30] shows algorithms based on the presented signal model that can closely approach these bounds. I.e. cm-level accuracy is obtained for 90 % of the estimates.

2) Multipath-NSync: Fig. 6 compares the CDFs of the PEB for Multipath-NSync and different synchronization states in-between anchors, obtained from (33). The CDFs are shown for

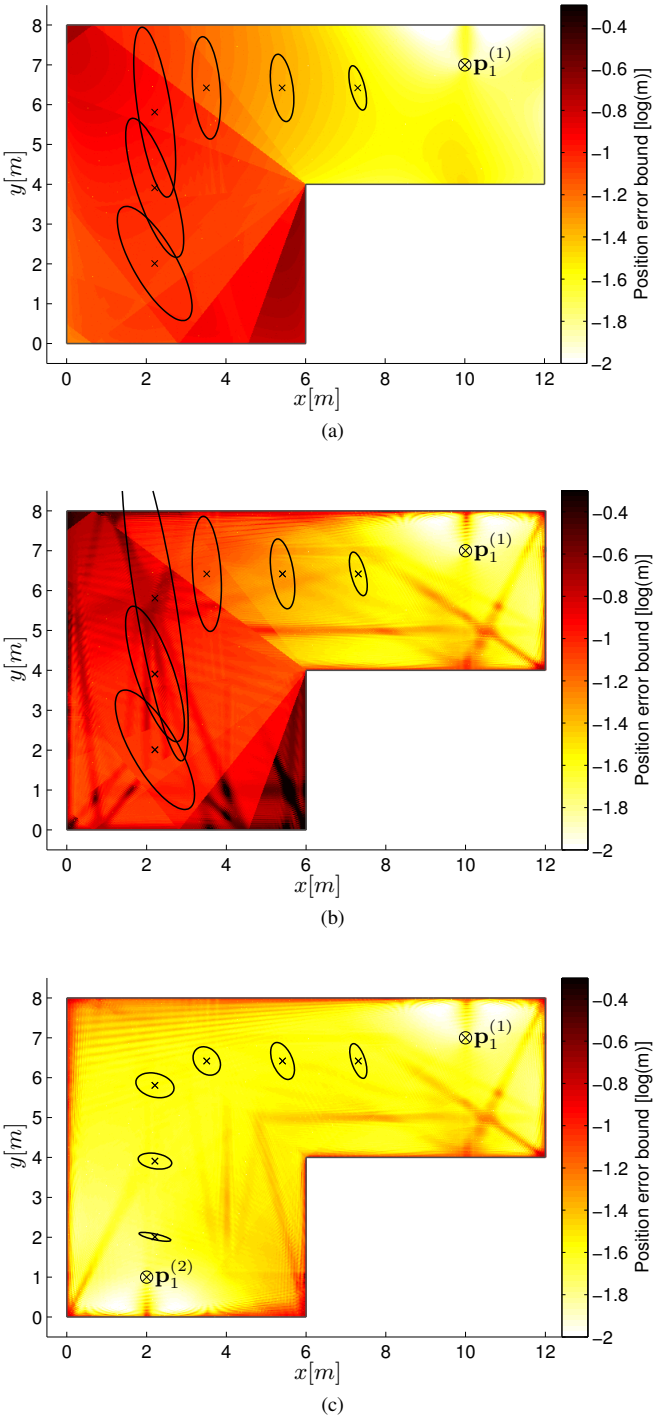

Fig. 3. Logarithmic PEB (17) for Multipath-Sync with $T_{\mathrm{p}} = 1\,\mathrm{ns}$ over the example room for VAs up to order two. (a) One anchor at $\mathbf{p}_1^{(1)}$; path overlap neglected. (b) same as (a) but considering the influence of path overlap. (c) a second anchor has been introduced at $\mathbf{p}_1^{(2)}$; path overlap included. At some sample points, 20-fold standard deviation ellipses are shown.

either two anchors at $\mathbf{p}_1^{(1)}$ and $\mathbf{p}_1^{(2)}$ which can be synchronized or not, or just the first anchor. A pulse duration of $T_{\mathrm{p}} = 1\,\mathrm{ns}$ is used. The performance deteriorates w.r.t. the Multipath-Sync case in Figs. 4 and 5, which can be explained by the fact that some of the delay information is used for clock-offset

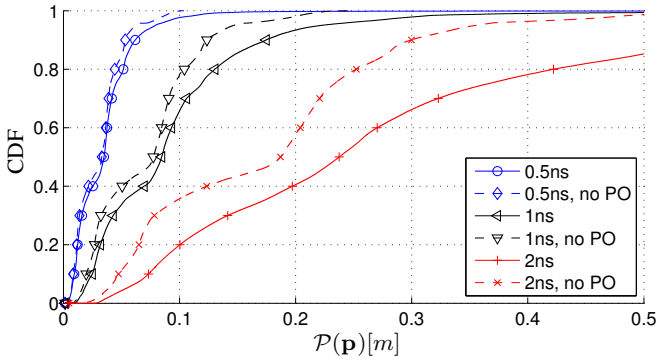

Fig. 4. CDFs of the PEB (17) for Multipath-Sync, pulse durations $T_\mathrm{p} = 0.5\,\mathrm{ns}$, $T_\mathrm{p} = 1\,\mathrm{ns}$ and $T_\mathrm{p} = 2\,\mathrm{ns}$, and one anchor at $\mathbf{p}_1^{(1)}$. Path overlap is neglected in results marked by dashed lines.

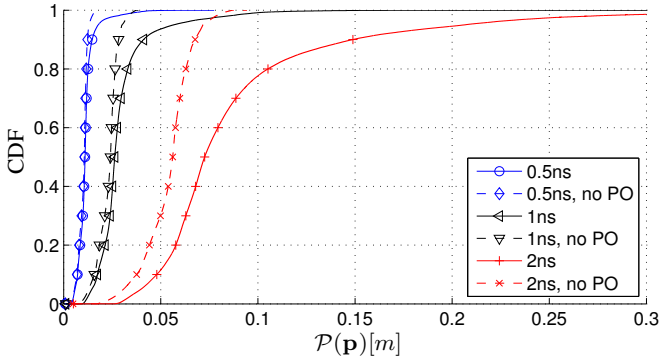

Fig. 5. CDFs of the PEB (17) for Multipath-Sync, pulse durations $T_\mathrm{p} = 0.5\,\mathrm{ns}$, $T_\mathrm{p} = 1\,\mathrm{ns}$ and $T_\mathrm{p} = 2\,\mathrm{ns}$, and two anchors at $\mathbf{p}_1^{(1)}$ and $\mathbf{p}_1^{(2)}$. Path overlap is neglected in results marked by dashed lines.

estimation, resulting in a loss of *position*-related information. A second anchor helps to counteract this effect. Here, one can recognize an additional gain of information if the two anchors are synchronized. The impact of path overlap is smaller if two anchors are used and even less pronounced if the anchors are synchronized.

A qualitative representation of the PEB is shown in Fig. 7 for Multipath-NSync over the example room, with two anchors at $\mathbf{p}_1^{(1)}$ and $\mathbf{p}_1^{(2)}$, and $T_\mathrm{p} = 1\,\mathrm{ns}$. Comparing this result with the synchronized case shown in Fig. 3(c), one can observe an increase due to the need of extracting syncronization information. Also, the impact of path overlap has increased.

Fig. 8 compares Multipath-Sync and Multipath-NSync for the two-anchors case and $T_\mathrm{p} = 1\,\mathrm{ns}$, considering VAs of order one or two and an NLOS scenario where the LOS component has been set to zero across the entire room. One can observe the importance of the LOS component which usually has a significantly larger SINR and provides thus more position-related information than MPCs arriving later. Increasing the VA order leads in general also to an information gain. However, in a few cases this trend is reversed since a larger VA-order can lead to more positions with unresolvable path overlap. This occurs especially at locations close to walls and in corners.

3) Multipath-Coop: Fig. 9 contains 2D-plots of the different contributions to the PEB in (44) for the cooperative case.

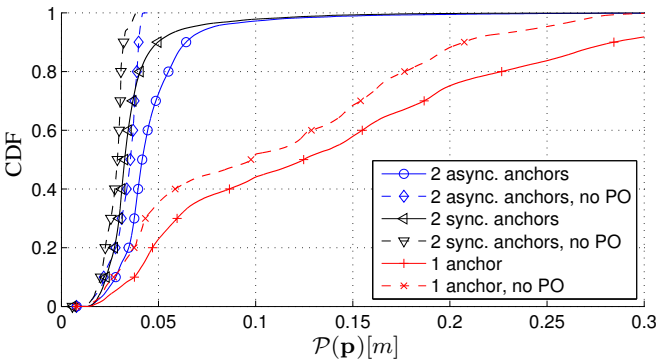

Fig. 6. CDFs of the PEB (17) for Multipath-NSync and different synchronization states at pulse duration $T_\mathrm{p} = 1\,\mathrm{ns}$. Either two anchors are used at $\mathbf{p}_1^{(1)}$ and $\mathbf{p}_1^{(2)}$, which can be synchronized or not, or just the first anchor.

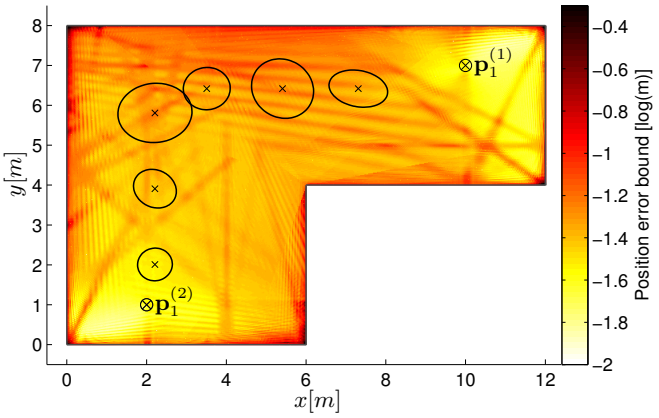

Fig. 7. Logarithmic PEB (17) for Multipath-NSync over the example room with $T_\mathrm{p} = 1\,\mathrm{ns}$, using two asynchronous anchors at $\mathbf{p}_1^{(1)}$ and $\mathbf{p}_1^{(2)}$. 20-fold standard deviation ellipses are shown at some sample points.

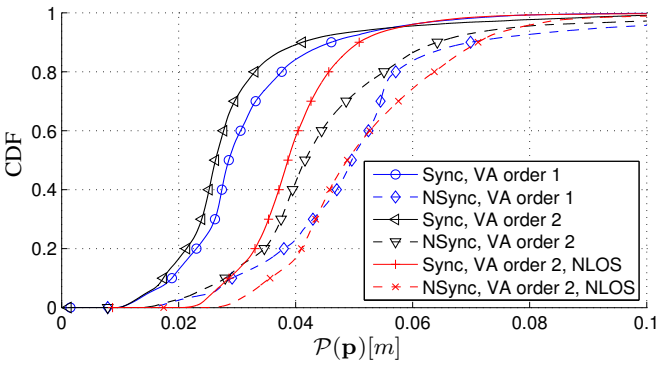

Fig. 8. CDFs of the PEB in (17) for Multipath-Sync and Multipath-NSync and $T_\mathrm{p} = 1\,\mathrm{ns}$ with two anchors at $\mathbf{p}_1^{(1)}$ and $\mathbf{p}_1^{(2)}$. VAs of order one or two are considered; for the latter case also for an artificial NLOS situation over the whole room.

The PEB has been evaluated for Agent 3 across the entire room with two resting, cooperating agents at $\mathbf{p}^{(1)}$ and $\mathbf{p}^{(2)}$. In Fig. 9(a), only the monostatic measurements of Agent 3 are considered, illustrating the adverse effect of room symmetries and resulting unresolvable path overlap. In particular, areas close to the walls are affected as well as the diagonals of the room. Fig. 9(b) shows the information provided by the agents

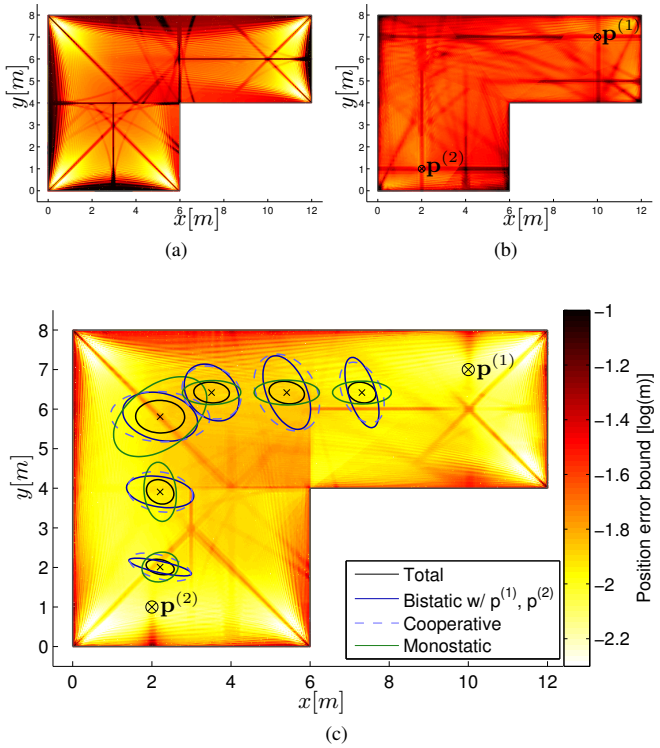

Fig. 9. Logarithmic PEB (44) with $T_\mathrm{p} = 1\,\mathrm{ns}$ over the example room for three cooperating agents, two of which are resting at positions $\mathbf{p}^{(1)}$ and $\mathbf{p}^{(2)}$. The PEB is decomposed into its (a) monostatic and (b) cooperative components. Plot (c) shows the total PEB for Multipath-Coop. In (c), also the 40-fold standard deviation ellipses are shown at some sample points for these three cases and—in addition—for the (bistatic) case with fixed anchors.

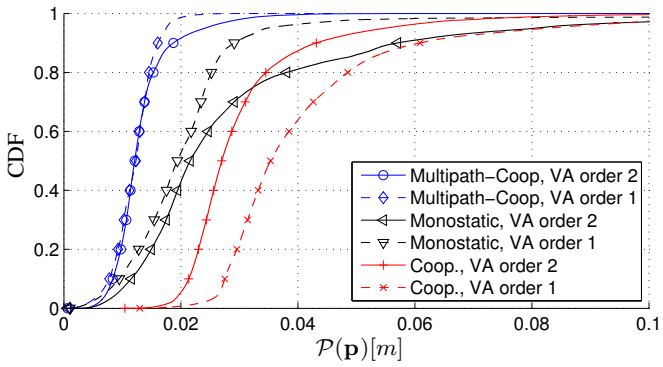

Fig. 10. CDFs of the PEB (44) for Multipath-Coop with $T_\mathrm{p} = 1\,\mathrm{ns}$, for VAs of order one and two, analyzing contributions of different measurements.

at $\mathbf{p}^{(1)}$ and $\mathbf{p}^{(2)}$ in their role as anchors. Their contribution is similar to the fixed-anchor case analyzed in Fig. 3(c), but due to uncertainties in their own positions, this information is not fully accessible. A robust, infrastructure-free positioning system is obtained if these two components can complement one another. Indeed Fig. 9(c) indicates excellent performance across the entire area. The distinction between the parts of the position-related information is further highlighted by the CRLB ellipses in Fig. 9(c), which also include the fixed-anchor (bistatic) case of Fig. 3(c). It shows the decreased information of the cooperative part in comparison to the bistatic case with

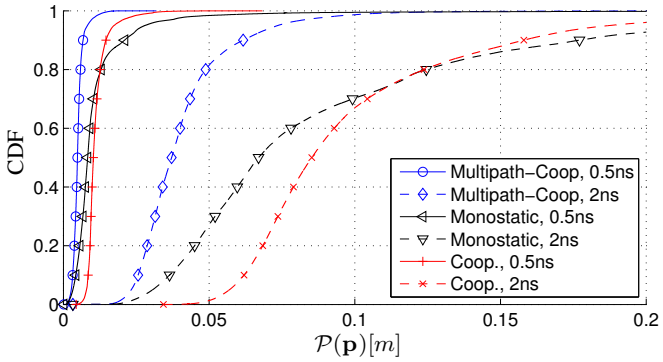

Fig. 11. CDFs of the PEB in (44) for Multipath-Coop with $T_\mathrm{p} = 0.5\,\mathrm{ns}$ and $T_\mathrm{p} = 2\,\mathrm{ns}$ for VAs of order two, showing contributions of different measurements types.

fixed anchors. The monostatic ellipses are mostly oriented towards the nearest wall, where the most significant information comes from. In many cases, this information is nicely complemented by the cooperative contribution.

Fig. 10 shows the CDFs of the PEB in (44) for $T_\mathrm{p} = 1\,\mathrm{ns}$ and VAs of order one and two. It is interesting to note that Multipath-Coop does not benefit from taking into account second-order MPCs. This is explained by the large influence of the monostatic measurements, for which second-order reflections cause many regions with unresolvable path overlap (c.f. Fig. 9(a)). For cooperative measurements, increasing the VA order is still beneficial.

Fig. 11 illustrates the influence of bandwidth on Multipath-Coop, using $T_\mathrm{p} = 0.5\,\mathrm{ns}$ and $T_\mathrm{p} = 2\,\mathrm{ns}$ for VAs of order two. Especially for the monostatic measurements, the occurrence of unresolvable path overlap is significantly reduced, leading to a clear advantage of a larger bandwidth.

VII. Conclusions and Outlook

In this article, we have introduced and validated a unified framework for evaluating the accuracy of radio-based indoor-localization methods that exploit geometric information contained in deterministic multipath components. The analysis shows and quantifies fundamental relationships between environment properties and the position-related information that can potentially be acquired. This is due to two mechanisms: (i) Diffuse multipath, which is related to physical properties of the propagation environment, acts as interference to useful specular multipath components. (ii) Path overlap, which relates to system design choices as the placement of agents but also to the given geometry of an environment, may render deterministic components useless. An increased signal bandwidth allows to counteract those effects since it improves the time-resolution of the measurements: The power of DM thus decreases and path overlap becomes less likely.

The framework allows for the analysis of different measurement setups: For instance, (i) in absence of synchronization, position information can be extracted from the time-difference between MPCs. The need for clock-offset estimation reduces thereby the positioning accuracy in comparison to a synchornized setup. (ii) Cooperation between agents increases

the available position-related information, but the uncertainty of the unknown positions of agents *acting* as anchors partly levels this effect. (iii) With monostatic measurements, the VAs move synchronously with the agents, which leads to a scaling of the information provided by MPCs. These MPC-geometry-dependent scaling factors lie between zero and two w.r.t. a conventional bistatic measurement.

The quantification of position-related information, as provided by the presented framework, can be used for designing positioning and tracking algorithms (e.g. [24], [29], [30]). The proper parametrization of the underlying geometric-stochastic channel model optimizes such algorithms and provides valuable insight for system design choices such as antenna placements and signal parameters. Algorithms that can learn and extract these environmental parameters online from measurements may achieve such optimization without the need for manual system optimization and are thus an important topic for further research on robust indoor localization.

Appendix A
FIM for orthogonal MPCs

For a sampled received signal, the covariance matrix of AWGN and the DM is written as

$$\mathbf{C}_\mathrm{n} = \sigma_\mathrm{n}^2\mathbf{I}_N + \mathbf{C}_\mathrm{c} = \sigma_\mathrm{n}^2\mathbf{I}_N + \bar{\mathbf{S}}^\mathrm{H}\mathbf{S}_\nu\bar{\mathbf{S}} \tag{A.1}$$

where $\bar{\mathbf{S}} = [\mathbf{s}_0, \cdots, \mathbf{s}_{N-1}]^\mathrm{T} \in \mathbb{R}^{N\times N}$ is the *full* signal matrix with $\mathbf{s}_i = \left[s((-i)_{\mathrm{mod}\,N}T_\mathrm{s}), \ldots, s((N-1-i)_{\mathrm{mod}\,N}T_\mathrm{s})\right]^\mathrm{T}$, defined as a circulant matrix. The covariance matrix of DM is

$$[\bar{\mathbf{S}}^\mathrm{H}\mathbf{S}_\nu\bar{\mathbf{S}}]_{n,m} = \sum_{i=0}^{N-1} T_\mathrm{s}S_\nu(iT_\mathrm{s})s((n-i)_{\mathrm{mod}\,N}T_\mathrm{s}) \times s((m-i)_{\mathrm{mod}\,N}T_\mathrm{s}). \tag{A.2}$$

Using the Woodbury matrix identity, the inverse of $\mathbf{C}_\mathrm{n}$ can be written as

$$\mathbf{C}_\mathrm{n}^{-1} = \frac{1}{\sigma_\mathrm{n}^2}\Big[\mathbf{I}_N - \bar{\mathbf{S}}^\mathrm{H}\big(\sigma_\mathrm{n}^2\mathbf{S}_\nu^{-1} + \bar{\mathbf{S}}\bar{\mathbf{S}}^\mathrm{H}\big)^{-1}\bar{\mathbf{S}}\Big]. \tag{A.3}$$

In (7), this inverse is multiplied from the right by $\mathbf{S}\boldsymbol{\alpha}$, which can be re-written as

$$\begin{aligned}\mathbf{C}_\mathrm{n}^{-1}\mathbf{S}\boldsymbol{\alpha} &= \sum_{k=1}^{K}\alpha_k\mathbf{C}_\mathrm{n}^{-1}\mathbf{s}_{\tau_k}\\ &= \frac{1}{\sigma_\mathrm{n}^2}\sum_{k=1}^{K}\alpha_k\Big[\mathbf{I}_N - \bar{\mathbf{S}}^\mathrm{H}\big(\sigma_\mathrm{n}^2\mathbf{S}_\nu^{-1} + \bar{\mathbf{S}}\bar{\mathbf{S}}^\mathrm{H}\big)^{-1}\bar{\mathbf{S}}\Big]\mathbf{s}_{\tau_k}\end{aligned}$$

where the factor $\bar{\mathbf{S}}\mathbf{s}_{\tau_k}$ on the very right is an autocorrelation vector of the transmitted signal shifted to delay time τ_k. The desired properties of $s(t)$—a large bandwidth and favorable autocorrelation properties—imply that this autocorrelation has most of its energy concentrated at delay τ_k. It hence samples the nonstationary PDP at time τ_k and we can replace $\mathbf{S}_\nu$ for each summand by a stationary PDP $\mathbf{S}_\nu^{(\tau_k)} = T_\mathrm{s}S_\nu(\tau_k)\mathbf{I}_N$. Using this assumption, we define

$$\big[\mathbf{C}_\mathrm{n}^{(\tau_k)}\big]^{-1} = \big[\sigma_\mathrm{n}^2\mathbf{I}_N + T_\mathrm{s}S_\nu(\tau_k)\bar{\mathbf{S}}^\mathrm{H}\bar{\mathbf{S}}\big]^{-1}$$

which involves the inverse of a cyclic matrix that can be diagonalized by a DFT. We introduce a unitary DFT matrix $\mathbf{W}$, $\mathbf{W}^\mathrm{H}\mathbf{W} = \mathbf{W}\mathbf{W}^\mathrm{H} = \mathbf{I}$, and use $\bar{\mathbf{S}} = \mathbf{W}\widetilde{\mathbf{S}}\mathbf{W}^\mathrm{H}$, where $\widetilde{\mathbf{S}} = \mathrm{diag}(\sqrt{N}\mathbf{W}\mathbf{s}_0)$ is a diagonal matrix containing the DFT of $\mathbf{s}_0^\mathrm{T}$ (the first row of $\bar{\mathbf{S}}$), to obtain

$$\begin{aligned}\big[\mathbf{C}_\mathrm{n}^{(\tau_k)}\big]^{-1} &= \big[\mathbf{W}\big(\sigma_\mathrm{n}^2\mathbf{I}_N + T_\mathrm{s}S_\nu(\tau_k)\widetilde{\mathbf{S}}^\mathrm{H}\widetilde{\mathbf{S}}\big)\mathbf{W}^\mathrm{H}\big]^{-1}\\ &= \mathbf{W}\big(\sigma_\mathrm{n}^2\mathbf{I}_N + T_\mathrm{s}S_\nu(\tau_k)\widetilde{\mathbf{S}}^\mathrm{H}\widetilde{\mathbf{S}}\big)^{-1}\mathbf{W}^\mathrm{H}.\end{aligned} \tag{A.4}$$

With this, we can approximate the second summand of likelihood function (7) by

$$\begin{aligned}[\boldsymbol{\alpha}^\mathrm{H}\mathbf{S}^\mathrm{H}\mathbf{C}_\mathrm{n}^{-1}\mathbf{S}\boldsymbol{\alpha}]_{k,k'} &\approx \alpha_k^*\alpha_{k'}\mathbf{s}_{\tau_k}^\mathrm{H}\big[\mathbf{C}_\mathrm{n}^{(\tau_k)}\big]^{-1}\mathbf{s}_{\tau_{k'}}\\ &= \sum_{i=0}^{N-1}\frac{\alpha_k^*\alpha_{k'}|\mathrm{S}_f[i]|^2}{\sigma_\mathrm{n}^2 + T_\mathrm{s}|\mathrm{S}_f[i]|^2S_\nu(\tau_k)}\exp\left\{\frac{-j2\pi i(\tau_k-\tau_{k'})}{N}\right\}\end{aligned}$$

where $\mathrm{S}_f[i]$ are samples of the DFT of $\mathbf{s}_0$ and the exponential accounts for the delays τ_k and $\tau_{k'}$. Approximating the sum by an integral yields

$$[\boldsymbol{\alpha}^\mathrm{H}\mathbf{S}^\mathrm{H}\mathbf{C}_\mathrm{n}^{-1}\mathbf{S}\boldsymbol{\alpha}]_{k,k'} \approx \int_f \frac{\alpha_k^*\alpha_{k'}|\mathrm{S}(f)|^2}{N_0 + |\mathrm{S}(f)|^2S_\nu(\tau_k)}\exp\{-j2\pi f(\tau_k-\tau_{k'})\}\,\mathrm{d}f.$$

With this expression, the diagonal elements of submatrix $\boldsymbol{\Lambda}_\mathrm{A}$ of the FIM can be written as

$$\begin{aligned}[\boldsymbol{\Lambda}_\mathrm{A}]_{k,k} &= \mathbb{E}_{\mathbf{r}|\boldsymbol{\psi}}\left\{-\frac{\partial^2\ln f(\mathbf{r}|\boldsymbol{\psi})}{\partial\tau_k\partial\tau_k}\right\}\\ &\approx 8\pi^2|\alpha_k|^2\int_f f^2\frac{|\mathrm{S}(f)|^2}{N_0 + S_\nu(\tau_k)|\mathrm{S}(f)|^2}\mathrm{d}f\\ &= \frac{8\pi^2}{N_0}\mathrm{SINR}_k\int_f f^2|\mathrm{S}(f)|^2\frac{N_0 + T_\mathrm{p}S_\nu(\tau_k)}{N_0 + |\mathrm{S}(f)|^2S_\nu(\tau_k)}\mathrm{d}f\\ &= 8\pi^2\beta^2\mathrm{SINR}_k\gamma_k\end{aligned} \tag{A.5}$$

where $\beta^2 = \int_f f^2|S(f)|^2\mathrm{d}f$ is the mean square bandwidth of $s(t)$, $\mathrm{SINR}_k = |\alpha_k|^2/(N_0 + T_\mathrm{p}S_\nu(\tau_k))$ is the signal-to-interference-plus-noise ratio (SINR) of the k-th MPC, and $\gamma_k = \beta_k^2/\beta^2$ is called bandwidth extension factor, expressing the influence of the whitening. The latter relates the mean square bandwidth of the *whitened* pulse $\beta_k^2 = \int_f f^2|\mathrm{S}(f)|^2\frac{N_0+T_\mathrm{p}S_\nu(\tau_k)}{N_0+|\mathrm{S}(f)|^2S_\nu(\tau_k)}\mathrm{d}f$ to β^2. Its value is a function of the interference-to-noise ratio $T_\mathrm{p}S_\nu(\tau_k)/N_0$. Note that $s(t)$ is assumed to be normalized to unit energy. Hence we have $|S(f)|^2 = T_\mathrm{p}$ for $|f| \le 1/(2T_\mathrm{p})$ if $s(t)$ has a block spectrum.

Appendix B
Jacobian of VA Position w.r.t. Anchor Position

We want to find a simple expression for $\partial\mathbf{p}_k^{(\xi)}/\partial\mathbf{p}^{(\xi)}$. We restrict our derivation on a single VA of a specific node w.l.o.g., so we drop all ξ, k-indexing and use a simpler notation $\partial\mathbf{p}_\mathrm{VA}/\partial\mathbf{p}$. As explained in Section I, $\mathbf{p}_\mathrm{VA}$ is obtained by mirroring $\mathbf{p}$ on walls Q times where Q is the VA order. We use index q for this iteration and refer to the intermediate positions as $\tilde{\mathbf{p}}_q$ where $\tilde{\mathbf{p}}_0 = \mathbf{p}$ and $\tilde{\mathbf{p}}_Q = \mathbf{p}_\mathrm{VA}$. We need to express $\mathbf{p}_\mathrm{VA}$ as a function of $\mathbf{p}$ and room geometry. We account for the latter by considering walls with line equations

$$y - y_q = \tan(\zeta_q)(x - x_q) \tag{B.1}$$

where ζ_q is the wall angle and $\mathbf{d}_q = (x_q, y_q)^{\mathrm{T}}$ is an offset vector. We obtain the q-th position by mirroring position $q-1$ on the q-th wall, or more formally

$$\tilde{\mathbf{p}}_q = \mathbf{Mir}(\tilde{\mathbf{p}}_{q-1}, \zeta_q, \mathbf{d}_q) \ . \tag{B.2}$$

where **Mir** is defined as the mirroring operator. Starting at $q = Q$ and using recursive substitution down to $q = 0$, we get

$$\mathbf{p}_{\mathrm{VA}} = \mathbf{Mir}(\ldots \mathbf{Mir}(\mathbf{Mir}(\mathbf{p}, \zeta_1, \mathbf{d}_1), \zeta_2, \mathbf{d}_2) \ldots, \zeta_Q, \mathbf{d}_Q) \ . \tag{B.3}$$

The mirroring operation is given by

$$\begin{aligned} \mathbf{Mir}(\tilde{\mathbf{p}}_{q-1}, \zeta_q, \mathbf{d}_q) &= \mathbf{M}(\zeta_q)(\tilde{\mathbf{p}}_{q-1} - \mathbf{d}_q) + \mathbf{d}_q \\ &= \mathbf{M}(\zeta_q)\tilde{\mathbf{p}}_{q-1} + \big(\mathbf{I} - \mathbf{M}(\zeta_q)\big)\mathbf{d}_q \end{aligned} \tag{B.4}$$

where we use a mirror matrix that acts w.r.t. a line through the origin at angle ζ_q,

$$\begin{aligned} \mathbf{M}(\zeta_q) &= \begin{bmatrix} \cos(2\zeta_q) & \sin(2\zeta_q) \\ \sin(2\zeta_q) & -\cos(2\zeta_q) \end{bmatrix} \\ &= \mathbf{Rot}(2\zeta_q) \begin{bmatrix} 1 & 0 \\ 0 & -1 \end{bmatrix} = \mathbf{Rot}(2\zeta_q)\mathbf{F} \end{aligned} \tag{B.5}$$

and can be decomposed into a rotation by $2\zeta_q$, $\mathbf{Rot}(2\zeta_q)$ and a sign-flip $\mathbf{F}$ in the second dimension. $\mathbf{M}(\zeta_q)$ has eigenvalues $\{-1, +1\}$ and bears analogies to rotation. For breaking down (B.3), we prefer the latter form of (B.4) because of the separated $\tilde{\mathbf{p}}_{q-1}$-summand. By carefully repeated application, we obtain a formula

$$\begin{aligned} \mathbf{p}_{\mathrm{VA}} &= \mathbf{M}(\zeta_Q) \cdot \tilde{\mathbf{p}}_{Q-1} + \big(\mathbf{I} - \mathbf{M}(\zeta_Q)\big)\mathbf{d}_Q \\ &= \mathbf{M}(\zeta_Q)\mathbf{M}(\zeta_{Q-1}) \cdot \tilde{\mathbf{p}}_{Q-2} + \\ &\quad \mathbf{M}(\zeta_Q)\big(\mathbf{I} - \mathbf{M}(\zeta_{Q-1})\big)\mathbf{d}_{Q-1} + \big(\mathbf{I} - \mathbf{M}(\zeta_Q)\big)\mathbf{d}_Q \\ &= \ \ldots \ = \left(\prod_{q=0}^{Q-1} \mathbf{M}(\zeta_{Q-q})\right)\mathbf{p} + \\ &\quad \sum_{q=1}^{Q} \left(\prod_{\tilde{q}=1}^{Q-q} \mathbf{M}(\zeta_{Q+1-\tilde{q}})\right) \left(\mathbf{I} - \mathbf{M}(\zeta_q)\right) \mathbf{d}_q \end{aligned} \tag{B.6}$$

where the derivative w.r.t. $\mathbf{p}$ is just the leading product of mirror matrices. Transposition reverses multiplication order

$$\left(\frac{\partial \mathbf{p}_{\mathrm{VA}}}{\partial \mathbf{p}}\right)^{\mathrm{T}} = \prod_{q=1}^{Q} \mathbf{M}(\zeta_q) \ . \tag{B.7}$$

To resolve this product, we derive a pseudo-homomorphism property of the mirror matrix. We note that both $\mathbf{F}$ and $\mathbf{M}(\zeta)$ are symmetric, orthogonal, and self-inverse. Thus, $\mathbf{M}(\zeta) = \mathbf{Rot}(2\zeta)\mathbf{F}$ implies $\mathbf{M}(\zeta)\mathbf{F} = \mathbf{Rot}(2\zeta)$. We rearrange the product of two mirror matrices

$$\begin{aligned} \mathbf{M}(\zeta_a)\mathbf{M}(\zeta_b) &= \mathbf{M}(\zeta_a)\mathbf{M}(\zeta_b)^{\mathrm{T}} = \mathbf{Rot}(2\zeta_a)\mathbf{F}\mathbf{F}^{\mathrm{T}}\mathbf{Rot}(2\zeta_b)^{\mathrm{T}} \\ &= \mathbf{Rot}(2\zeta_a)\mathbf{I}\ \mathbf{Rot}(-2\zeta_b) = \mathbf{Rot}(2(\zeta_a - \zeta_b)) \end{aligned}$$

and obtain the property

$$\mathbf{M}(\zeta_a)\mathbf{M}(\zeta_b) = \mathbf{M}(\zeta_a - \zeta_b)\mathbf{F} \ . \tag{B.8}$$

Applying (B.8) to (B.7) $(Q-1)$-times the Jacobian of a VA position w.r.t. its respective anchor's position yields

$$\left(\frac{\partial \mathbf{p}_{\mathrm{VA}}}{\partial \mathbf{p}}\right)^{\mathrm{T}} = \mathbf{M}(\bar{\zeta})\mathbf{F}^{Q-1} = \mathbf{Rot}(2\bar{\zeta})\mathbf{F}^{Q} \tag{B.9}$$

where we refer to $\bar{\zeta} := \zeta_1 - \zeta_2 + \ldots + (-1)^{Q-1}\zeta_Q = \sum_{q=1}^{Q}(-1)^{q-1}\zeta_q$ as the effective wall angle, where index q iterates the order of occurrence of walls during MPC reflection or VA construction.

Appendix C
Delay Gradient for the Monostatic Setup

We transform the initial gradient from Appendix B into a magnitude-times-unit-vector form by component-wise application of basic trigonometric identities. This yields an insightful expression for the monostatic case, cf. (24). We consider

$$\begin{aligned} \mathbf{e}(\phi) - \mathbf{e}((-1)^Q\phi + 2\bar{\zeta}) &= \begin{bmatrix} \cos(\phi) - \cos((-1)^Q\phi + 2\bar{\zeta}) \\ \sin(\phi) - \sin((-1)^Q\phi + 2\bar{\zeta}) \end{bmatrix} \\ &= \begin{bmatrix} 2\sin\left(\frac{((-1)^Q+1)\phi+2\bar{\zeta}}{2}\right)\sin\left(\frac{((-1)^Q-1)\phi+2\bar{\zeta}}{2}\right) \\ 2\cos\left(\frac{((-1)^Q+1)\phi+2\bar{\zeta}}{2}\right)\sin\left(-\frac{((-1)^Q-1)\phi+2\bar{\zeta}}{2}\right) \end{bmatrix}. \end{aligned}$$

By defining symbols for the arguments that contain ϕ depending on the even/odd parity of Q

$$\begin{aligned} O &:= \frac{(-1)^Q - 1}{2}\phi + \bar{\zeta} = \begin{cases} \bar{\zeta} & \text{If } Q \text{ is even} \\ \bar{\zeta} - \phi & \text{If } Q \text{ is odd} \end{cases} \\ E &:= \frac{(-1)^Q + 1}{2}\phi + \bar{\zeta} = \begin{cases} \bar{\zeta} + \phi & \text{If } Q \text{ is even} \\ \bar{\zeta} & \text{If } Q \text{ is odd} \end{cases} \end{aligned}$$

we further get

$$\begin{aligned} \mathbf{e}(\phi) - \mathbf{e}((-1)^Q\phi + 2\bar{\zeta}) &= 2\sin(O)\ \mathbf{e}\Big(E - \frac{\pi}{2}\Big) \\ &= \begin{cases} 2\sin(\bar{\zeta})\mathbf{e}(\phi + \bar{\zeta} - \frac{\pi}{2}) & \text{If } Q \text{ is even} \\ 2\sin(\bar{\zeta} - \phi)\mathbf{e}(\bar{\zeta} - \frac{\pi}{2}) & \text{If } Q \text{ is odd} \end{cases} . \end{aligned} \tag{C.1}$$

Appendix D
Derivation of the NSync CRLB

Synchronized anchors: In order to derive the 3×3 EFIM $\boldsymbol{\mathcal{I}}_{\mathbf{p},\epsilon}$ we need to repartition the transformation matrix $\mathbf{J}$ by combining the submatrices $\mathbf{H}^{(j)}$ and $\mathbf{L}^{(j)} = \mathbf{l}_{\mathrm{syn}}^{(j)}$ to $\mathbf{G}^{(j)} = [\mathbf{H}^{(j)}, \mathbf{l}_{\mathrm{syn}}^{(j)}]$. Applying the transformation leads to

$$\boldsymbol{\mathcal{I}}_{\mathbf{P}} = \mathbf{J}^{\mathrm{T}}\boldsymbol{\mathcal{I}}_{\boldsymbol{\psi}}\mathbf{J} = \tag{D.1}$$

$$\begin{bmatrix} \sum\limits_{j\in\mathcal{N}_j} \big(\mathbf{G}^{(j)}\big)^{\mathrm{T}}\boldsymbol{\Lambda}_{\mathrm{A}}^{(j)}\mathbf{G}^{(j)} & \big(\mathbf{G}^{(1)}\big)^{\mathrm{T}}\boldsymbol{\Lambda}_{\mathrm{B}}^{(1)} & \cdots & \big(\mathbf{G}^{(J)}\big)^{\mathrm{T}}\boldsymbol{\Lambda}_{\mathrm{B}}^{(J)} \\ \big(\boldsymbol{\Lambda}_{\mathrm{B}}^{(1)}\big)^{\mathrm{T}}\mathbf{G}^{(1)} & \boldsymbol{\Lambda}_{\mathrm{C}}^{(1)} & & \\ \vdots & & \ddots & \\ \big(\boldsymbol{\Lambda}_{\mathrm{B}}^{(J)}\big)^{\mathrm{T}}\mathbf{G}^{(J)} & & & \boldsymbol{\Lambda}_{\mathrm{C}}^{(J)} \end{bmatrix}.$$

The 3×3 EFIM is then given as the sum over the EFIMs of the corresponding anchors

$$\boldsymbol{\mathcal{I}}_{\mathbf{p},\epsilon} = \tag{D.2}$$

$$\sum_{j\in\mathcal{N}_j} \big(\mathbf{G}^{(j)}\big)^{\mathrm{T}}\Big[\boldsymbol{\Lambda}_{\mathrm{A}}^{(j)} - \boldsymbol{\Lambda}_{\mathrm{B}}^{(j)}\big(\boldsymbol{\Lambda}_{\mathrm{C}}^{(j)}\big)^{-1}\big(\boldsymbol{\Lambda}_{\mathrm{B}}^{(j)}\big)^{\mathrm{T}}\Big]\mathbf{G}^{(j)}.$$

When neglecting path overlap, this reduces to

$$\boldsymbol{\mathcal{I}}_{\mathbf{p},\epsilon} = \sum_{j\in\mathcal{N}_j} \left(\mathbf{G}^{(j)}\right)^{\mathrm{T}} \boldsymbol{\Lambda}_{\mathrm{A}}^{(j)} \mathbf{G}^{(j)}, \tag{D.3}$$

which leads finally to (32).

Asynchronous anchors: The result for $\boldsymbol{\mathcal{I}}_{\boldsymbol{\theta}}$ (D.1) is also valid when considering asynchronous anchors, provided that we respect $\mathbf{L}^{(j)} = \mathbf{L}_{\text{asyn}}^{(j)}$ and $\mathbf{G}^{(j)} = [\mathbf{H}^{(j)}, \mathbf{L}_{\text{asyn}}^{(j)}]$. We apply the blockwise inversion lemma twice, first to derive the EFIM $\boldsymbol{\mathcal{I}}_{\mathbf{p},\boldsymbol{\epsilon}}$ (note that now $\boldsymbol{\epsilon}$ is a vector), and then again to proof the additivity of the EFIMs $\boldsymbol{\mathcal{I}}_{\mathbf{p}}^{(j)}$.

The EFIM $\boldsymbol{\mathcal{I}}_{\mathbf{p},\boldsymbol{\epsilon}}$ is now a square matrix of order $2+J$. It can be expressed as in (D.2), but taking account of the changed definition of $\mathbf{G}^{(j)}$. We can write its structure as

$$\boldsymbol{\mathcal{I}}_{\mathbf{p},\boldsymbol{\epsilon}} = \sum_{j\in\mathcal{N}_j} \begin{bmatrix} \boldsymbol{\mathcal{I}}_A^{(j)} & \boldsymbol{\mathcal{I}}_B^{(j)} \\ \left(\boldsymbol{\mathcal{I}}_B^{(j)}\right)^{\mathrm{T}} & \boldsymbol{\mathcal{I}}_D^{(j)} \end{bmatrix}, \tag{D.4}$$

with $\boldsymbol{\mathcal{I}}_A^{(j)} \in \mathbb{R}^{2\times 2}$, $\boldsymbol{\mathcal{I}}_B^{(j)} \in \mathbb{R}^{2\times J}$ and $\boldsymbol{\mathcal{I}}_D^{(j)} \in \mathbb{R}^{J\times J}$. Further evaluation yields, that only the j-th column of $\boldsymbol{\mathcal{I}}_B^{(j)}$ is nonzero, and the sum over $\boldsymbol{\mathcal{I}}_B^{(j)}$ can be written as

$$\sum_{j\in\mathcal{N}_j} \boldsymbol{\mathcal{I}}_B^{(j)} = \left[\mathbf{b}^{(1)}, \ldots, \mathbf{b}^{(J)}\right], \ \mathbf{b}^{(j)} \in \mathbb{R}^2, \tag{D.5}$$

meaning that each column is determined by the contribution of a different anchors. Similarly, $\boldsymbol{\mathcal{I}}_D^{(j)}$ has only one nonzero entry $\left[\boldsymbol{\mathcal{I}}_D^{(j)}\right]_{j,j}$, leading to

$$\sum_{j\in\mathcal{N}_j} \boldsymbol{\mathcal{I}}_D^{(j)} = \operatorname{diag}\left(\left[\boldsymbol{\mathcal{I}}_D^{(1)}\right]_{1,1}, \ldots, \left[\boldsymbol{\mathcal{I}}_D^{(J)}\right]_{J,J}\right). \tag{D.6}$$

Rewriting $\boldsymbol{\mathcal{I}}_{\mathbf{p},\boldsymbol{\epsilon}}$ (D.4) and again applying the blockwise inversion lemma yields the additivity of the EFIMs $\boldsymbol{\mathcal{I}}_{\mathbf{p}}^{(j)}$:

$$\boldsymbol{\mathcal{I}}_{\mathbf{p}} = \sum_{j\in\mathcal{N}_j} \boldsymbol{\mathcal{I}}_A^{(j)} - \frac{1}{\left[\boldsymbol{\mathcal{I}}_D^{(j)}\right]_{j,j}} \mathbf{b}^{(j)} \left(\mathbf{b}^{(j)}\right)^{\mathrm{T}} = \sum_{j\in\mathcal{N}_j} \boldsymbol{\mathcal{I}}_{\mathbf{p}}^{(j)}. \tag{D.7}$$

The involved terms are defined by

$$\boldsymbol{\mathcal{I}}_A^{(j)} = \left(\mathbf{H}^{(j)}\right)^{\mathrm{T}} \left(\boldsymbol{\Lambda}_{\mathrm{A}}^{(j)} - \boldsymbol{\Lambda}_{\mathrm{B}}^{(j)} \left(\boldsymbol{\Lambda}_{\mathrm{C}}^{(j)}\right)^{-1} \left(\boldsymbol{\Lambda}_{\mathrm{B}}^{(j)}\right)^{\mathrm{T}}\right) \mathbf{H}^{(j)},$$

$$\left[\boldsymbol{\mathcal{I}}_D^{(j)}\right]_{j,j} = \sum_{u=1}^{K^{(j)}} \sum_{v=1}^{K^{(j)}} \left[\boldsymbol{\Lambda}_{\mathrm{A}}^{(j)} - \boldsymbol{\Lambda}_{\mathrm{B}}^{(j)} \left(\boldsymbol{\Lambda}_{\mathrm{C}}^{(j)}\right)^{-1} \left(\boldsymbol{\Lambda}_{\mathrm{B}}^{(j)}\right)^{\mathrm{T}}\right]_{u,v},$$

and

$$\mathbf{b}^{(j)} = \left(\mathbf{H}^{(j)}\right)^{\mathrm{T}} \left(\boldsymbol{\Lambda}_{\mathrm{A}}^{(j)} - \boldsymbol{\Lambda}_{\mathrm{B}}^{(j)} \left(\boldsymbol{\Lambda}_{\mathrm{C}}^{(j)}\right)^{-1} \left(\boldsymbol{\Lambda}_{\mathrm{B}}^{(j)}\right)^{\mathrm{T}}\right) [1 \ldots 1]_{1\times K^{(J)}}^{\mathrm{T}}.$$

Appendix E
Derivation of the Multipath-Coop CRLB

The EFIM for the cooperative setup is defined as

$$\boldsymbol{\mathcal{I}}_{\mathbf{P}} = \mathbf{H}^{\mathrm{T}} \operatorname{diag}\left(\boldsymbol{\Lambda}^{(1,1)}, \ldots, \boldsymbol{\Lambda}^{(1,M)}, \ldots, \boldsymbol{\Lambda}^{(M+J,M)}\right) \mathbf{H},$$

being of size $2M \times 2M$. It can be written with subblock $\mathbf{H}$ from (42) in the canonical form (40). Matrix $\boldsymbol{\Lambda}^{(j,m)}$ is defined in (41). The canonical form decomposes the EFIM $\boldsymbol{\mathcal{I}}_{\mathbf{P}}$ into contributions from independent transmissions inbetween the agents or between agents and fixed anchors. Matrix $\boldsymbol{\mathcal{I}}_{\mathbf{P}}$ consists of the following subblocks for $\eta, \eta' \in \mathcal{N}_m = \{1, \ldots, M\}$,

$$[\boldsymbol{\mathcal{I}}_{\mathbf{P}}]_{2\times 2}^{\eta,\eta'} = \sum_{j\in(\mathcal{N}_m\cup\mathcal{N}_j)} \sum_{m\in\mathcal{N}_m} \left(\mathbf{H}^{(j,\eta,m)}\right)^{\mathrm{T}} \boldsymbol{\Lambda}^{(j,m)} \mathbf{H}^{(j,\eta',m)} \tag{E.1}$$

where $\mathbf{H}^{(j,\eta,m)}$ stacks the spatial delay gradients (21) as defined in Section IV. Considering that only summand (j,m) of (E.1) contributes to a block, for which either index j or index m equals η or η', we get the following subblocks:

1) Off-diagonal blocks $\eta \neq \eta'$:

$$\begin{aligned}
[\boldsymbol{\mathcal{I}}_{\mathbf{P}}]_{2\times 2}^{(\eta,\eta')} &= \left(\mathbf{H}^{(j,\eta,m)}\right)^{\mathrm{T}} \boldsymbol{\Lambda}^{(j,m)} \mathbf{H}^{(j,\eta',m)}\Big|_{j=\eta,m=\eta'} \\
&\quad + \left(\mathbf{H}^{(j,\eta,m)}\right)^{\mathrm{T}} \boldsymbol{\Lambda}^{(j,m)} \mathbf{H}^{(j,\eta',m)}\Big|_{j=\eta',m=\eta} \\
&= \left(\mathbf{H}_{\text{An}}^{(\eta,\eta')}\right)^{\mathrm{T}} \boldsymbol{\Lambda}^{(\eta,\eta')} \mathbf{H}_{\text{Ag}}^{(\eta',\eta)} \\
&\quad + \left(\mathbf{H}_{\text{Ag}}^{(\eta',\eta)}\right)^{\mathrm{T}} \boldsymbol{\Lambda}^{(\eta',\eta)} \mathbf{H}_{\text{An}}^{(\eta',\eta)},
\end{aligned}$$

using the definitions for $\mathbf{H}_{\text{An}}^{(\eta,\eta')}$ and $\mathbf{H}_{\text{Ag}}^{(\eta,\eta')}$ from Section IV-1. With $\mathbf{H}_{\text{An}}^{(\eta,\eta')} = \mathbf{H}_{\text{Ag}}^{(\eta',\eta)}$ (Section IV-1) and $\boldsymbol{\Lambda}^{(\eta,\eta')} = \boldsymbol{\Lambda}^{(\eta',\eta)}$ we get

$$[\boldsymbol{\mathcal{I}}_{\mathbf{P}}]_{2\times 2}^{(\eta,\eta')} = 2\boldsymbol{\mathcal{I}}_{\mathrm{C}}^{(\eta,\eta')} = 2\left(\mathbf{H}_{\text{Ag}}^{(\eta',\eta)}\right)^{\mathrm{T}} \boldsymbol{\Lambda}^{(\eta',\eta)} \mathbf{H}_{\text{Ag}}^{(\eta,\eta')}. \tag{E.2}$$

2) Diagonal blocks $\eta = \eta'$:

$$\begin{aligned}
[\boldsymbol{\mathcal{I}}_{\mathbf{P}}]_{2\times 2}^{\eta,\eta} &= \left(\mathbf{H}^{(\eta,\eta,\eta)}\right)^{\mathrm{T}} \boldsymbol{\Lambda}^{(\eta,\eta)} \mathbf{H}^{(\eta,\eta,\eta)} \\
&\quad + \sum_{\substack{j\in\mathcal{N}_m\setminus\{\eta\} \\ m=\eta}} \left(\mathbf{H}^{(j,\eta,m)}\right)^{\mathrm{T}} \boldsymbol{\Lambda}^{(j,m)} \mathbf{H}^{(j,\eta,m)} \\
&\quad + \sum_{\substack{m\in\mathcal{N}_m\setminus\{\eta\} \\ j=\eta}} \left(\mathbf{H}^{(j,\eta,m)}\right)^{\mathrm{T}} \boldsymbol{\Lambda}^{(j,m)} \mathbf{H}^{(j,\eta,m)} \\
&\quad + \sum_{j\in\mathcal{N}_j} \left(\mathbf{H}^{(j,\eta,\eta)}\right)^{\mathrm{T}} \boldsymbol{\Lambda}^{(j,\eta)} \mathbf{H}^{(j,\eta,\eta)} \\
&= \left(\mathbf{H}_{\text{Mo}}^{(\eta)}\right)^{\mathrm{T}} \boldsymbol{\Lambda}^{(\eta,\eta)} \mathbf{H}_{\text{Mo}}^{(\eta)} \\
&\quad + \sum_{j\in\mathcal{N}_m\setminus\{\eta\}} \left(\mathbf{H}_{\text{Ag}}^{(j,\eta)}\right)^{\mathrm{T}} \boldsymbol{\Lambda}^{(j,\eta)} \mathbf{H}_{\text{Ag}}^{(j,\eta)} \\
&\quad + \sum_{m\in\mathcal{N}_m\setminus\{\eta\}} \left(\mathbf{H}_{\text{An}}^{(\eta,m)}\right)^{\mathrm{T}} \boldsymbol{\Lambda}^{(\eta,m)} \mathbf{H}_{\text{An}}^{(\eta,m)} \\
&\quad + \sum_{j\in\mathcal{N}_j} \left(\mathbf{H}_{\text{Ag}}^{(j,\eta)}\right)^{\mathrm{T}} \boldsymbol{\Lambda}^{(j,\eta)} \mathbf{H}_{\text{Ag}}^{(j,\eta)}
\end{aligned}$$

using again $\mathbf{H}_{\text{An}}^{(\eta,\eta')}$ and $\mathbf{H}_{\text{Ag}}^{(\eta,\eta')}$ from Section IV-1 and $\mathbf{H}_{\text{Mo}}^{(\eta)}$ from Section IV-2. With $\mathbf{H}_{\text{An}}^{(\eta,m)} = \mathbf{H}_{\text{Ag}}^{(m,\eta)}$ and $\boldsymbol{\Lambda}^{(j,m)} = \boldsymbol{\Lambda}^{(m,j)}$ due to reciprocity, we get

$$\begin{aligned}
[\boldsymbol{\mathcal{I}}_{\mathbf{P}}]_{2\times 2}^{(\eta,\eta)} &= \boldsymbol{\mathcal{I}}_{\text{Mo}}^{(\eta)} + 2 \sum_{m\in\mathcal{N}_m\setminus\{\eta\}} \boldsymbol{\mathcal{I}}_{\text{Ag}}^{(m,\eta)} + \sum_{j\in\mathcal{N}_j} \boldsymbol{\mathcal{I}}_{\text{An}}^{(j,\eta)} \\
&= \boldsymbol{\mathcal{I}}_{\text{Mo}}^{(\eta)} + 2\boldsymbol{\mathcal{I}}_{\text{Ag}}^{(\eta)} + \boldsymbol{\mathcal{I}}_{\text{An}}^{(\eta)}
\end{aligned} \tag{E.3}$$

which implicitly defines the contributions from monostatic measurements, bistatic measurements inbetween agents, and bistatic measurements between agents and fixed anchors.

REFERENCES

[1] Y. Shen, S. Mazuelas, and M. Win, "Network Navigation: Theory and Interpretation," *IEEE Journal on Selected Areas in Communications*, 2012.

[2] A. Conti, D. Dardari, M. Guerra, L. Mucchi, and M. Win, "Experimental Characterization of Diversity Navigation," *IEEE Systems Journal*, 2014.

[3] S. Mazuelas, A. Bahillo, R. Lorenzo, P. Fernandez, F. Lago, E. Garcia, J. Blas, and E. Abril, "Robust Indoor Positioning Provided by Real-Time RSSI Values in Unmodified WLAN Networks," *IEEE Journal of Selected Topics in Signal Processing*, vol. 3, no. 5, pp. 821–831, Oct 2009.

[4] M. Ficco, C. Esposito, and A. Napolitano, "Calibrating indoor positioning systems with low efforts," *IEEE Transactions on Mobile Computing*, vol. 13, no. 4, pp. 737–751, April 2014.

[5] S. Marano and, W. Gifford, H. Wymeersch, and M. Win, "NLOS identification and mitigation for localization based on UWB experimental data," *IEEE Journal on Selected Areas in Communications*, 2010.

[6] H. Wymeersch, S. Marano, W. Gifford, and M. Win, "A Machine Learning Approach to Ranging Error Mitigation for UWB Localization," *IEEE Transactions on Communications*, 2012.

[7] H. Lu, S. Mazuelas, and M. Win, "Ranging likelihood for wideband wireless localization," in *IEEE International Conference on Communications (ICC)*, 2013.

[8] H. Wymeersch, J. Lien, and M. Z. Win, "Cooperative Localization in Wireless Networks," *Proceedings of the IEEE*, 2009.

[9] Y. Shen and M. Win, "On the Use of Multipath Geometry for Wideband Cooperative Localization," in *IEEE Global Telecommunications Conference (GLOBECOM)*, 2009.

[10] R. Parhizkar, I. Dokmanic, and M. Vetterli, "Single-Channel Indoor Microphone Localization," in *39th International Conference on Acoustics, Speech, and Signal Processing*, 2014.

[11] M. Leigsnering, M. Amin, F. Ahmad, and A. Zoubir, "Multipath Exploitation and Suppression for SAR Imaging of Building Interiors: An overview of recent advances," *IEEE Signal Processing Magazine*, 2014.

[12] I. Dokmanic, R. Parhizkar, A. Walther, Y. M. Lu, and M. Vetterli, "Acoustic Echoes Reveal Room Shape," *Proceedings of the National Academy of Sciences*, 2013.

[13] P. Meissner and K. Witrisal, "Analysis of Position-Related Information in Measured UWB Indoor Channels," in *6th European Conference on Antennas and Propagation (EuCAP)*, 2012.

[14] Y. Shen and M. Win, "Fundamental Limits of Wideband Localization; Part I: A General Framework," *IEEE Transactions on Information Theory*, 2010.

[15] Y. Shen, H. Wymeersch, and M. Win, "Fundamental Limits of Wideband Localization - Part II: Cooperative Networks," *IEEE Transactions on Information Theory*, 2010.

[16] Y. Qi, H. Kobayashi, and H. Suda, "Analysis of wireless geolocation in a non-line-of-sight environment," *IEEE Transactions on Wireless Communications*, vol. 5, no. 3, pp. 672 – 681, 2006.

[17] H. Godrich, A. Haimovich, and R. Blum, "Target Localization Accuracy Gain in MIMO Radar-Based Systems," *IEEE Transactions on Information Theory*, vol. 56, no. 6, pp. 2783 –2803, June 2010.

[18] A. Richter and R. Thoma, "Joint maximum likelihood estimation of specular paths and distributed diffuse scattering," in *IEEE Vehicular Technology Conference, VTC 2005-Spring*, 2005.

[19] N. Michelusi, U. Mitra, A. Molisch, and M. Zorzi, "UWB Sparse/Diffuse Channels, Part I: Channel Models and Bayesian Estimators," *IEEE Transactions on Signal Processing*, 2012.

[20] N. Decarli, F. Guidi, and D. Dardari, "A Novel Joint RFID and Radar Sensor Network for Passive Localization: Design and Performance Bounds," *IEEE Journal of Selected Topics in Signal Processing*, 2014.

[21] T. Santos, F. Tufvesson, and A. Molisch, "Modeling the Ultra-Wideband Outdoor Channel: Model Specification and Validation," *IEEE Transactions on Wireless Communications*, 2010.

[22] J. Karedal, S. Wyne, P. Almers, F. Tufvesson, and A. Molisch, "A Measurement-Based Statistical Model for Industrial Ultra-Wideband Channels," *IEEE Transactions on Wireless Communications*, 2007.

[23] K. Witrisal and P. Meissner, "Performance bounds for multipath-assisted indoor navigation and tracking (MINT)," in *IEEE International Conference on Communications (ICC)*, 2012.

[24] P. Meissner, E. Leitinger, and K. Witrisal, "UWB for Robust Indoor Tracking: Weighting of Multipath Components for Efficient Estimation," *IEEE Wireless Communications Letters*, vol. 3, no. 5, pp. 501–504, Oct. 2014.

[25] J. Borish, "Extension of the image model to arbitrary polyhedra," *The Journal of the Acoustical Society of America*, 1984.

[26] J. Kunisch and J. Pamp, "An ultra-wideband space-variant multipath indoor radio channel model," in *IEEE Conference on Ultra Wideband Systems and Technologies*, 2003.

[27] P. Carbone, A. Cazzorla, P. Ferrari, A. Flammini, A. Moschitta, S. Rinaldi, T. Sauter, and E. Sisinni, "Low complexity uwb radios for precise wireless sensor network synchronization," *Instrumentation and Measurement, IEEE Transactions on*, vol. 62, no. 9, pp. 2538–2548, Sept 2013.

[28] M. Froehle, E. Leitinger, P. Meissner, and K. Witrisal, "Cooperative Multipath-Assisted Indoor Navigation and Tracking (Co-MINT) Using UWB Signals," in *IEEE ICC 2013 Workshop on Advances in Network Localization and Navigation (ANLN)*, 2013.

[29] P. Meissner, E. Leitinger, M. Lafer, and K. Witrisal, "Real-Time Demonstration System for Multipath-Assisted Indoor Navigation and Tracking (MINT)," in *IEEE ICC 2014 Workshop on Advances in Network Localization and Navigation (ANLN)*, 2014.

[30] E. Leitinger, M. Froehle, P. Meissner, and K. Witrisal, "Multipath-Assisted Maximum-Likelihood Indoor Positioning using UWB Signals," in *IEEE ICC 2014 Workshop on Advances in Network Localization and Navigation (ANLN)*, 2014.

[31] A. Molisch, "Ultra-wide-band propagation channels," *Proceedings of the IEEE*, 2009.

[32] S. Kay, *Fundamentals of Statistical Signal Processing: Estimation Theory*. Prentice Hall Signal Processing Series, 1993.

[33] H. L. Van Trees, *Detection, Estimation and Modulation, Part I*. Wiley Press, 1968.

[34] G. Steinböck, T. Pedersen, B. Fleury, W. Wang, and R. Raulefs, "Distance Dependent Model for the Delay Power Spectrum of In-room Radio Channels," *IEEE Transactions on Antennas and Propagation*, vol. 61, no. 8, pp. 4327–4340, Aug 2013.

[35] P. Meissner, "Multipath-Assisted Indoor Positioning," Ph.D. dissertation, Graz University of Technology, 2014.

[36] P. Meissner, E. Leitinger, M. Lafer, and K. Witrisal, "MeasureMINT UWB database," 2014, Publicly available database of UWB indoor channel measurements. [Online]. Available: www.spsc.tugraz.at/tools/UWBmeasurements

Erik Leitinger (S'12) was born in Graz, Austria, on March 27, 1985. He received the B.Sc. degree (with distinction) in electrical engineering from Graz University of Technology, Graz, Austria, in 2009, and the Dipl.-Ing. degree (with distinction) in electrical engineering from Graz University of Technology, Graz, Austria, in 2012.

He is currently pursuing his PhD degree at the Signal Processing and Speech Communication Laboratory (SPSC) of Graz University of Technology, Graz, Austria focused on UWB wireless communication, indoor-positioning, estimation theory, Bayesian inference and statistical signal processing.

Paul Meissner (S'10–M'15) was born in Graz, Austria, in 1982. He received the B.Sc. and Dipl.-Ing. degree (with distinction) in information and computer engineering from Graz University of Technology, Graz, Austria in 2006 and 2009, respectively. He received the Ph.D. degree in electrical engineering (with distinction) from the same university in 2014.

Paul is currently a postdoctoral researcher at the Signal Processing and Speech Communication Laboratory (SPSC) of Graz University of Technology, Graz, Austria. His research topics include statistical signal processing, localization, estimation theory and propagation channel modeling. He served in the TPC of the IEEE Workshop on Advances in Network Localization and Navigation (ANLN) at the IEEE Intern. Conf. on Communications (ICC) 2015 and of IEEE RFID 2015.

Christoph Rüdisser was born in Hohenems, Austria, in 1984. He received the Dipl.-Ing. degree in electrical engineering (with distinction) from the Graz University of Technology, Graz, Austria, in 2014.

Prior to his studies, he was at High Q Laser Production GmbH in Hohenems, Austria, doing electronics and software development for four years. At present he is looking for interesting career opportunities in the field of wireless communications, with focus on statistical signal processing.

Gregor Dumphart received the B.Sc. and Dipl.-Ing. degrees (with distinction) in information and computer engineering from Graz University of Technology, Graz, Austria in 2011 and 2014, respectively.

He was a Student Assistant at the Department of Analysis and Computational Number Theory from 2009 to 2011 and at the Signal Processing and Speech Communication Laboratory from 2011 to 2013, both of Graz University of Technology. Since October 2014, he is pursuing the PhD degree at the Communications Technology Laboratory, ETH Zurich, Zurich, Switzerland. His research is concerned with localization and communication in dense networks (swarms) of low-complexity, sub-mm nodes by means of inductive coupling.

Klaus Witrisal (S'98–M'03) received the Dipl.-Ing. degree in electrical engineering from Graz University of Technology, Graz, Austria, in 1997 and the Ph.D. degree (cum laude) from Delft University of Technology, Delft, The Netherlands, in 2002.

He is currently an Associate Professor at the Signal Processing and Speech Communication Laboratory (SPSC) of Graz University of Technology, Graz, Austria, where he has been participating in various national and European research projects focused on UWB communications and positioning. He is co-chair of the Technical Working Group "Indoor" of the COST Action IC1004 "Cooperative Smart Radio Communications for Green Smart Environments." His research interests are in signal processing for wideband and UWB wireless communications, propagation channel modeling, and positioning.

Prof. Witrisal served as a leading chair for the IEEE Workshop on Advances in Network Localization and Navigation (ANLN) at the IEEE Intern. Conf. on Communications (ICC) 2013, 2014, and 2015, as a TPC co-chair of the Workshop on Positioning, Navigation and Communication (WPNC) 2011, 2014, and 2015, and as a co-organizer of the Workshop on Localization in UHF RFID at the IEEE 5th Annual Intern. Conf. on RFID, 2011. He is an associate editor of IEEE Communications Letters since 2013. From 2007 to 2011, he was a co-chair of the MTT/COM Chapter of IEEE Austria.

Monostatic Indoor Localization: Bounds and Limits

Gregor Dumphart*, Erik Leitinger†, Paul Meissner†, and Klaus Witrisal†
* Communication Technology Laboratory, ETH Zurich, Switzerland, Email: dumphart@nari.ee.ethz.ch
† Graz University of Technology, Austria, Email: {erik.leitinger, paul.meissner, witrisal}@tugraz.at

***Abstract*—Multipath-assisted localization is a promising concept for cooperative agent networks to guarantee *robust* and *accurate* positioning in indoor environments with harsh radio channel characteristics. It uses two types of measurements: (i) bistatic measurements between agents and (ii) monostatic (bat-like) measurements by the individual agents. This paper presents an in-depth analysis of the position-related information provided by monostatic measurements. The CRLB on the position error is computed and used to analyze the impact of the indoor geometry and to find the limitations of such measurements. A general form of multipath delay gradients, crucial terms in the CRLB relating geometry and channel parameters, is derived for this purpose.**

I. Introduction

Multipath-assisted indoor localization [1]–[3] is able to robustly achieve a high level of accuracy in indoor environments with harsh multipath conditions. Ultra-wideband (UWB) systems provide the needed separability of multipath components (MPCs). With an a priori known floor plan, these MPCs can be linked to the local geometry and used as (additional) virtual anchors (VAs) [4]. All other, not geometrically modeled propagation effects constitute interference to the exploitable position-related information and are called diffuse multipath (DM) [5]. Our work [2] has shown the significant increase in performance when using prior knowledge of a geometric-stochastic channel model.

In [6] we showed that multipath-assisted concepts are applicable to a cooperative setup where agents perform two types of measurements (cf. Figure 1): (i) bistatic measurements between agents and (ii) monostatic (bat-like) measurements.[1]

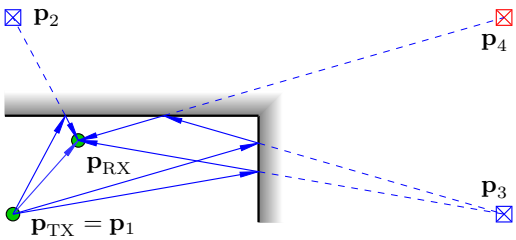

(a) Bistatic VAs

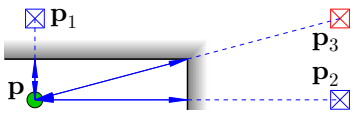

(b) Monostatic VAs

Fig. 1. Virtual anchors (VAs) on an exemplary indoor wall corner for bistatic and monostatic measurements. For (a), the LOS path is considered as VA $\mathbf{p}_1$ at $\mathbf{p}_{\mathrm{TX}}$. For (b), $\mathbf{p} = \mathbf{p}_{\mathrm{RX}} = \mathbf{p}_{\mathrm{TX}}$ holds.

In the bistatic case, one agent acts as anchor and the cooperating partner agent is localized. An agent in monostatic mode acts as both transmitter and receiver, and the received signal represents an image of the surrounding geometry.[2] The joint Cramér-Rao lower bound (CRLB) on the position error was analyzed in [3] for the cooperative approach, where monostatic contributions arise as additive Fisher information, valuable for self-localization [7], [8] for tracking agents over time. A related cooperative SLAM approach was studied in [9].

This paper presents an in-depth analysis of the position-related information provided by monostatic measurements, using a general form of multipath delay gradients and the CRLB on the position error. Monostatic measurements alone are unsuitable for robust agent localization. They do provide valuable ranging information to surrounding walls but geometric ambiguities are hard to resolve. The analysis of the monostatic CRLB reveals the position-related information content of such measurements, but also their limitations. Our key contributions are:

1) Derivation of the spatial multipath delay gradient, which connects geometry with the channel parameters. The general result covers all bistatic and monostatic setups.
2) Investigation of the CRLB on the monostatic position error using the previously derived gradients.

The paper is structured as follows. Section II introduces the used indoor UWB signal model and the relationship between position error CRLB and multipath delay gradients. Section III rigorously derives said gradient as a function of room geometry and node position. Section IV evaluates monostatic VA types and gives numerical results of the monostatic CRLB over an example room. Section V concludes the paper.

Notation: All vectors are column vectors and written boldface. Jacobians $\partial \boldsymbol{y}/\partial \boldsymbol{x}$ have dimension $\dim \boldsymbol{y} \times \dim \boldsymbol{x}$ but gradients $\partial s/\partial \boldsymbol{x}$ are column vectors $\dim \boldsymbol{x} \times 1$. $\mathbf{e}(\phi) = [\cos(\phi), \sin(\phi)]^{\mathrm{T}}$ is a unit vector of tilt angle ϕ.

II. Problem Formulation

A. Signal Model

We suppose a transmitted UWB pulse $s(t)$ of duration T_s and employ for the received signal the model [1], [3]

$$r(t) = \sum_{k=1}^{K} \alpha_k s(t - \tau_k) + (\nu * s)(t) + w(t) \qquad (1)$$

Gregor Dumphart thanks the co-authors for supervising his master's thesis at the Signal Processing and Speech Communication Laboratory of Graz University of Technology, which resulted in the research at hand.

[1]The terms *bistatic* and *monostatic* are well-established in radar.

[2]Think of a bat navigating in a cave: It emits ultrasonic sound, listens to the echoes and in this way estimates its position w.r.t. the nearby cave walls.

over a total of K considered paths. $\tau_k \in \mathbb{R}^+$ are path delays, $\alpha_k \in \mathbb{C}$ complex path amplitudes and $k \in \{1 \dots K\}$. K is equivalent to the number of visible virtual anchors (VAs) at agent position $\mathbf{p}$. Diffuse multipath (DM) is modeled as zero-mean Gaussian random process $\nu(t)$ with autocorrelation $R_\nu(\tau, u) = S_\nu(\tau)\delta(\tau - u)$, where we assume uncorrelated scattering. $w(t)$ is additive white Gaussian noise (AWGN) with two-sided power spectral density (PSD) $N_0/2$.

Figure 1 illustrates the concept of multipath-assisted indoor localization: In Figure 1(a), a transmitter at position $\mathbf{p}_{\text{TX}}$ isotropically sends an UWB pulse $s(t)$. The received signal includes, besides the line-of-sight path, reflections of the room walls, shown by the blue lines. These reflected paths can be modeled geometrically using VAs at positions $\mathbf{p}_k$, mirror images of the anchor w.r.t. walls that can be computed from the a priori known floor plan [10]. Since transmitter and receiver are separate, we call this the *bistatic* setup. For *monostatic* measurements, shown in Figure 1(b), the agent is both receiver and transmitter collocated at $\mathbf{p}$, and acts as anchor for itself with its own set of VAs at $\mathbf{p}_k$. In a *cooperative* multipath-assisted indoor localization setup [3], [6], both types of measurements are being used in order to perform robust, unambiguous position estimation.

The distance between agent $\mathbf{p}_{\text{RX}}$ and VA $\mathbf{p}_k$ equals the actual path length $c\tau_k$ [4], [11] where c is the speed of light. Thus

$$\tau_k = \frac{1}{c}||\mathbf{p}_{\text{RX}} - \mathbf{p}_k||_2 \tag{2}$$

constitutes the main link between geometry and signal model. We consider two-dimensional localization[3], i.e. $\mathbf{p}_{\text{RX}}, \mathbf{p}_k \in \mathbb{R}^2$.

B. CRLB on the Position Error

We want to obtain an estimate $\hat{\mathbf{p}}$ of agent position $\mathbf{p}$ from the received signal $r(t)$ by exploiting the knowledge of the VA positions $\{\mathbf{p}_k\}$, in presence of DM and AWGN.

The position-related parameter vector $\boldsymbol{\theta} = [\mathbf{p}^{\text{T}}\ \Re\boldsymbol{\alpha}^{\text{T}}\ \Im\boldsymbol{\alpha}^{\text{T}}]^{\text{T}}$ where nuisance parameters $\Re\boldsymbol{\alpha}, \Im\boldsymbol{\alpha}$ are the real and imaginary parts of amplitudes $\boldsymbol{\alpha} = [\alpha_1 \dots \alpha_K]^{\text{T}}$. $\boldsymbol{\mathcal{I}}_{\boldsymbol{\theta}}$ is the Fisher information matrix (FIM) of $\boldsymbol{\theta}$. As described in [1], [3], [11], only the upper left block of its inverse $[\boldsymbol{\mathcal{I}}_{\boldsymbol{\theta}}^{-1}]_{2\times 2} =: \boldsymbol{\mathcal{I}}_{\mathbf{p}}^{-1}$ is relevant to position estimation. $\boldsymbol{\mathcal{I}}_{\mathbf{p}}$ is called *equivalent Fisher information matrix* and yields the CRLB on the position error

$$\mathbb{E}_{\mathbf{r}|\boldsymbol{\theta}}\{(\hat{\mathbf{p}} - \mathbf{p})(\hat{\mathbf{p}} - \mathbf{p})^{\text{T}}\} \geq \boldsymbol{\mathcal{I}}_{\mathbf{p}}^{-1} \ .$$

The position error bound (PEB) is then the root of the trace

$$\mathcal{P}(\mathbf{p}) = \sqrt{\text{tr}(\boldsymbol{\mathcal{I}}_{\mathbf{p}}^{-1})} \ . \tag{3}$$

$\boldsymbol{\mathcal{I}}_{\boldsymbol{\theta}}$ is connected to signal model (1) by the chain rule

$$\boldsymbol{\mathcal{I}}_{\boldsymbol{\theta}} = \frac{\partial \boldsymbol{\psi}}{\partial \boldsymbol{\theta}}^{\text{T}} \boldsymbol{\mathcal{I}}_{\boldsymbol{\psi}} \frac{\partial \boldsymbol{\psi}}{\partial \boldsymbol{\theta}} \tag{4}$$

where matrix $\boldsymbol{\mathcal{I}}_{\boldsymbol{\psi}}$ is the FIM of the channel parameter vector $\boldsymbol{\psi} = \left[\boldsymbol{\tau}^{\text{T}}, \Re\boldsymbol{\alpha}^{\text{T}}, \Im\boldsymbol{\alpha}^{\text{T}}\right]^{\text{T}}$ with $\boldsymbol{\tau} = [\tau_1 \dots \tau_K]^{\text{T}}$ holding the delays. $\boldsymbol{\mathcal{I}}_{\boldsymbol{\psi}}$ is given by likelihood function $f(\mathbf{r}|\boldsymbol{\psi})$ through

$$\boldsymbol{\mathcal{I}}_{\boldsymbol{\psi}} = \mathbb{E}_{\mathbf{r}|\boldsymbol{\psi}} \left\{ \left(\frac{\partial \ln f(\mathbf{r}|\boldsymbol{\psi})}{\partial \boldsymbol{\psi}} \right) \left(\frac{\partial \ln f(\mathbf{r}|\boldsymbol{\psi})}{\partial \boldsymbol{\psi}} \right)^{\text{T}} \right\}. \tag{5}$$

To obtain a more insightful expression for $\boldsymbol{\mathcal{I}}_{\mathbf{p}}$, we break down the submatrices of Jacobian (4) and channel FIM $\boldsymbol{\mathcal{I}}_{\boldsymbol{\psi}}$ (5) to

$$\frac{\partial \boldsymbol{\psi}}{\partial \boldsymbol{\theta}} = \begin{bmatrix} \partial\boldsymbol{\tau}/\partial\mathbf{p} & \mathbf{0}_{K\times 2K} \\ \mathbf{0}_{2K\times 2} & \boldsymbol{I}_{2K\times 2K} \end{bmatrix}, \quad \boldsymbol{\mathcal{I}}_{\boldsymbol{\psi}} = \begin{bmatrix} \boldsymbol{\Lambda}_{\text{A}} & \boldsymbol{\Lambda}_{\text{B}} \\ \boldsymbol{\Lambda}_{\text{B}}^{\text{T}} & \boldsymbol{\Lambda}_{\text{C}} \end{bmatrix} \tag{6}$$

where $\boldsymbol{\Lambda}_{\text{A}} \in \mathbb{R}^{K\times K}$, $\boldsymbol{\Lambda}_{\text{B}} \in \mathbb{R}^{K\times 2K}$, $\boldsymbol{\Lambda}_{\text{C}} \in \mathbb{R}^{2K\times 2K}$ are specified in Appendix C. By expanding the products of (4) using (6) and employing blockwise inversion lemma [3], [11], we obtain

$$\boldsymbol{\mathcal{I}}_{\mathbf{p}} = \frac{\partial \boldsymbol{\tau}}{\partial \mathbf{p}}^{\text{T}} \left(\boldsymbol{\Lambda}_{\text{A}} - \boldsymbol{\Lambda}_{\text{B}} \boldsymbol{\Lambda}_{\text{C}}^{-1} \boldsymbol{\Lambda}_{\text{B}}^{\text{T}} \right) \frac{\partial \boldsymbol{\tau}}{\partial \mathbf{p}} \ . \tag{7}$$

The term in brackets describes the delay information of MPCs $\alpha_k s(t - \tau_k)$ in the noisy $r(t)$. The subtractive term represents the impact of path overlap which is significant whenever there is a pair of overlapping MPCs, i.e. k, k' that fulfill $|\tau_k - \tau_{k'}| < T_s$, but essentially zero otherwise [12].

The Jacobian $\partial\boldsymbol{\tau}/\partial\mathbf{p}$ translates delay information into position information. The underlying gradients $\partial\tau_k/\partial\mathbf{p}$ are determined by the surrounding room geometry at the current agent position. They show very particular behavior in the monostatic case, which is the focus of this paper.

For further analysis on the impact of the gradients on localization accuracy, we simplify (7) for non-overlapping MPCs. Then, $\boldsymbol{\Lambda}_{\text{B}}$ is zero and $\boldsymbol{\Lambda}_{\text{A}}$ diagonal, which by [11, eq. (15)] allows for decomposing $\boldsymbol{\mathcal{I}}_{\mathbf{p}}$ into a sum over MPCs

$$\boldsymbol{\mathcal{I}}_{\mathbf{p}} = 8\pi^2\beta^2 \sum_{k=1}^{K} \text{SINR}_k \frac{\partial \tau_k}{\partial \mathbf{p}} \cdot \frac{\partial \tau_k}{\partial \mathbf{p}}^{\text{T}} \tag{8}$$

where $\text{SINR}_k = |\alpha_k|^2/(N_0 + T_s S_\nu(\tau_k))$ is the signal-to-interference-plus-noise ratio [3] and β the effective bandwidth.

III. Spatial Delay Gradients

A. Gradient Derivation in General Form

As per (2), the length of the k-th path is

$$c\tau_k = \|\mathbf{p}_{\text{RX}} - \mathbf{p}_k\| = \sqrt{(x_{\text{RX}} - x_k)^2 + (y_{\text{RX}} - y_k)^2}$$

and the gradient w.r.t. some position $\mathbf{p} \in \{\mathbf{p}_{\text{RX}}, \mathbf{p}_{\text{TX}}\}$ is[4]

$$\begin{aligned} c\frac{\partial \tau_k}{\partial \mathbf{p}} &= \frac{x_{\text{RX}} - x_k}{\sqrt{(x_{\text{RX}} - x_k)^2 + (y_{\text{RX}} - y_k)^2}} \frac{\partial (x_{\text{RX}} - x_k)}{\partial \mathbf{p}} \\ &\quad \frac{y_{\text{RX}} - y_k}{\sqrt{(x_{\text{RX}} - x_k)^2 + (y_{\text{RX}} - y_k)^2}} \frac{\partial (y_{\text{RX}} - y_k)}{\partial \mathbf{p}} \\ &= \cos(\phi_k) \left(\frac{\partial x_{\text{RX}}}{\partial \mathbf{p}} - \frac{\partial x_k}{\partial \mathbf{p}} \right) + \sin(\phi_k) \left(\frac{\partial y_{\text{RX}}}{\partial \mathbf{p}} - \frac{\partial y_k}{\partial \mathbf{p}} \right) \\ &= \left(\frac{\partial \mathbf{p}_{\text{RX}}}{\partial \mathbf{p}} - \frac{\partial \mathbf{p}_k}{\partial \mathbf{p}} \right)^{\text{T}} \cdot \mathbf{e}(\phi_k) \end{aligned}$$

[3] We refrain from a general 3D treatment because, to our current knowledge, results and especially derivation steps involving rotation matrices turn out considerably more complicated than in the 2D case. Fortunately, a 2D treatment is often sufficient for typical right-angled indoor environments.

[4] We refer to nodes as RX and TX by communications engineering habit, even though the particular roles and the signal flow direction is irrelevant in this context. This reciprocity is later emphasized by (22) and Figure 3.

where $\mathbf{e}(\phi_k) = (\mathbf{p}_{\text{RX}} - \mathbf{p}_k)/\|\mathbf{p}_{\text{RX}} - \mathbf{p}_k\|$. Jacobian $\partial\mathbf{p}_{\text{RX}}/\partial\mathbf{p}$ is identity if $\mathbf{p} = \mathbf{p}_{\text{RX}}$ and zero otherwise. VAs $\mathbf{p}_k$ are a function of $\mathbf{p}_{\text{TX}}$ and room geometry, thus $\partial\mathbf{p}_k/\partial\mathbf{p}$ is nonzero only for $\mathbf{p} = \mathbf{p}_{\text{TX}}$. This motivates the use of indicator functions:

$$\mathbb{1}_{\text{RX}}(\mathbf{p}) := \begin{cases} 1 & \text{If } \mathbf{p} = \mathbf{p}_{\text{RX}} \\ 0 & \text{If } \mathbf{p} \neq \mathbf{p}_{\text{RX}} \end{cases} \tag{9}$$

$$c\,\frac{\partial\tau_k}{\partial\mathbf{p}} = \left(\mathbb{1}_{\text{RX}}(\mathbf{p})\cdot\mathbf{I}_{2\times 2} - \mathbb{1}_{\text{TX}}(\mathbf{p})\cdot\frac{\partial\mathbf{p}_k}{\partial\mathbf{p}_{\text{TX}}}\right)^{\text{T}}\cdot\mathbf{e}(\phi_k) \tag{10}$$

Jacobian $\partial\mathbf{p}_k/\partial\mathbf{p}_{\text{TX}}$, the last missing piece, is comprehensively derived in the following section.

B. Derivation of the Virtual Anchor Jacobian

We derive Jacobian $\partial\mathbf{p}_k/\partial\mathbf{p}_{\text{TX}}$ in closed form as a function of node position and indoor geometry. Thereby, we examine the characteristics of the underlying reflections. We consider a fixed MPC, so w.l.o.g. we drop index k and write $\partial\mathbf{p}_{\text{VA}}/\partial\mathbf{p}_{\text{TX}}$. Derivation and notation are guided by Figure 2.

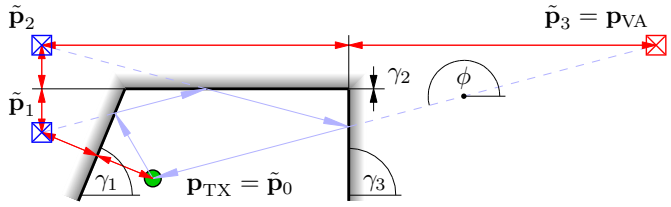

Fig. 2. Exemplary construction of a virtual anchor $\mathbf{p}_{\text{VA}}$ via intermediate anchors $\tilde{\mathbf{p}}_q$ by Q-fold mirroring of $\mathbf{p}_{\text{TX}}$ on the walls in such order as defined by the MPC at hand. Here, $Q = 3$, $\gamma_1 = 3\pi/8$, $\gamma_2 = 0$, $\gamma_3 = \pi/2$.

We introduce index $q \in \{1, \ldots, Q\}$ to iterate the VA construction where Q is the VA order (the number of reflections of the MPC at hand). Each q-step involves a particular wall, which we model with a line equation

$$\mathbf{p}' = t\cdot\mathbf{e}(\gamma_q) + \mathbf{d}_q,$$

where $t \in \mathbb{R}$, $\gamma_q \in (-\pi, +\pi]$ is the angle of the q-th wall,[5] and $\mathbf{d}_q \in \mathbb{R}^2$ is a wall offset vector. In order to obtain the Jacobian, we have to find a representation $\mathbf{p}_{\text{VA}} = f(\mathbf{p}_{\text{TX}}, \gamma_1, \mathbf{d}_1, \ldots, \gamma_Q, \mathbf{d}_Q)$ first. $\mathbf{p}_{\text{VA}}$ is obtained by mirroring $\mathbf{p}_{\text{TX}}$ on walls Q times. We refer to intermediate positions as $\tilde{\mathbf{p}}_q$ with the understanding that $\tilde{\mathbf{p}}_0 = \mathbf{p}_{\text{TX}}$ and $\tilde{\mathbf{p}}_Q = \mathbf{p}_{\text{VA}}$. We obtain the q-th intermediate anchor position by mirroring position $q-1$ on the q-th wall, or more formally

$$\tilde{\mathbf{p}}_q = \mathcal{S}(\tilde{\mathbf{p}}_{q-1}, \gamma_q, \mathbf{d}_q)$$

where function $\mathcal{S}$ denotes mirroring. Considering $\mathbf{p}_{\text{VA}} = \tilde{\mathbf{p}}_Q$ and by using recursive substitution down to $q = 0$, we get

$$\mathbf{p}_{\text{VA}} = \mathcal{S}(\ldots\mathcal{S}(\mathcal{S}(\mathbf{p}_{\text{TX}}, \gamma_1, \mathbf{d}_1), \gamma_2, \mathbf{d}_2)\ldots, \gamma_Q, \mathbf{d}_Q)\ . \tag{11}$$

Appendix A concretizes the mirroring function

$$\mathcal{S}(\tilde{\mathbf{p}}_{q-1}, \gamma_q, \mathbf{d}_q) = \mathbf{M}(\gamma_q)\cdot(\tilde{\mathbf{p}}_{q-1} - \mathbf{d}_q) + \mathbf{d}_q \tag{12}$$

$$= \mathbf{M}(\gamma_q)\cdot\tilde{\mathbf{p}}_{q-1} + \big(\mathbf{I} - \mathbf{M}(\gamma_q)\big)\cdot\mathbf{d}_q \tag{13}$$

where we use mirror matrix $\mathbf{M}(\gamma_q)$ that acts w.r.t. a line through the origin with angle γ_q,

$$\mathbf{M}(\gamma_q) := \begin{bmatrix} \cos(2\gamma_q) & \sin(2\gamma_q) \\ \sin(2\gamma_q) & -\cos(2\gamma_q) \end{bmatrix}$$

$$= \mathbf{R}(2\gamma_q)\cdot\begin{bmatrix} 1 & 0 \\ 0 & -1 \end{bmatrix} = \mathbf{R}(2\gamma_q)\cdot\mathbf{F}\ . \tag{14}$$

Thus, mirroring $\mathbf{M}(\gamma_q)$ is the composition of sign-flip $\mathbf{F}$ in the second dimension

$$\mathbf{F} = \begin{bmatrix} 1 & 0 \\ 0 & -1 \end{bmatrix} \tag{15}$$

and rotation $\mathbf{R}$ about angle $2\gamma_q$.[6,7] For breaking down (11), we prefer (13) with the separated $\tilde{\mathbf{p}}_{q-1}$-summand. Repeated application, where non-commutative matrices require care, yields an involved closed-form formula

$$\mathbf{p}_{\text{VA}} = \left(\prod_{q=0}^{Q-1}\mathbf{M}(\gamma_{Q-q})\right)\mathbf{p}_{\text{TX}} + \sum_{q=1}^{Q}\left(\prod_{\tilde{q}=1}^{Q-q}\mathbf{M}(\gamma_{Q+1-\tilde{q}})\right)\big(\mathbf{I} - \mathbf{M}(\gamma_q)\big)\,\mathbf{d}_q\ .$$

Fortunately, the derivative w.r.t. $\mathbf{p}_{\text{TX}}$ is just the leading product

$$\frac{\partial\mathbf{p}_{\text{VA}}}{\partial\mathbf{p}_{\text{TX}}} = \prod_{q=0}^{Q-1}\mathbf{M}(\gamma_{Q-q})\ .$$

Transposition and symmetry $\mathbf{M}(\gamma_q)^{\text{T}} = \mathbf{M}(\gamma_q)$ give

$$\left(\frac{\partial\mathbf{p}_{\text{VA}}}{\partial\mathbf{p}_{\text{TX}}}\right)^{\text{T}} = \prod_{q=1}^{Q}\mathbf{M}(\gamma_q)\ . \tag{16}$$

To resolve this product, we use a pseudo-homomorphism property of the mirror matrix derived in Appendix B,

$$\mathbf{M}(\gamma)\mathbf{M}(\beta) = \mathbf{M}(\gamma - \beta)\cdot\mathbf{F}. \tag{17}$$

By $(Q-1)$-fold application of (17) in (16), we obtain

$$\left(\frac{\partial\mathbf{p}_{\text{VA}}}{\partial\mathbf{p}_{\text{TX}}}\right)^{\text{T}} = \mathbf{M}\left(\gamma_1 - \gamma_2 + \gamma_3 - \ldots + (-1)^{Q-1}\gamma_Q\right)\cdot\mathbf{F}^{Q-1}$$

$$= \mathbf{M}(\bar{\gamma})\cdot\mathbf{F}^{Q-1} = \mathbf{R}(2\bar{\gamma})\cdot\mathbf{F}^{Q} \tag{18}$$

where (14) was used. We define the *effective wall angle* of the VA or MPC at hand

$$\bar{\gamma}_k = \sum_{q=0}^{Q_k}(-1)^{q-1}\gamma_{k,q}\ , \tag{19}$$

an oscillated sum of the wall angles $\gamma_{k,q}$ involved in the reflection[8] of the k-th path.

[5] In this context, we do not consider wall boundaries $t \in [a, b]$.

[6] Mirroring is hence also termed *rotoreflection* or *improper rotation* [13].

[7] $\mathbf{M}(\gamma_q)$ has eigenvalue 1 along $\mathbf{e}(\gamma_q)$, i.e. in parallel to the wall, and -1 perpendicular. This, with (12), formally reveals key properties of $\mathcal{S}$:
- Invariance of parallel moves $\mathcal{S}(\mathbf{p} + t\cdot\mathbf{e}(\gamma), \gamma, \mathbf{d}) = \mathcal{S}(\mathbf{p}, \gamma, \mathbf{d}) + t\cdot\mathbf{e}(\gamma)$.
- Mirroring $\mathcal{S}(\mathbf{p} + t\cdot\mathbf{e}(\gamma + \pi/2), \gamma, \mathbf{d}) = \mathcal{S}(\mathbf{p}, \gamma, \mathbf{d}) - t\cdot\mathbf{e}(\gamma + \pi/2)$.
- Arbitrary choice of offset $\mathcal{S}(\mathbf{p}, \gamma, \mathbf{d} + t\cdot\mathbf{e}(\gamma)) = \mathcal{S}(\mathbf{p}, \gamma, \mathbf{d})$.

[8] For a bistatic LOS path, $Q_k = 0$ and (19) is an empty sum, thus $\bar{\gamma}_k = 0$. This makes our formalism compatible with conventional anchor utilization.

C. Gradient Summary and Conclusions

Using (18) in (10) and the geometric meanings of $\mathbf{F}$ and $\mathbf{R}(2\bar{\gamma}_k)$ leads to the final result for the spatial delay gradient:

$$\begin{aligned} c\frac{\partial \tau_k}{\partial \mathbf{p}} &= \left(\mathbb{1}_{\text{RX}}(\mathbf{p}) \cdot \mathbf{I} - \mathbb{1}_{\text{TX}}(\mathbf{p}) \cdot \mathbf{R}(2\bar{\gamma}_k) \cdot \begin{bmatrix} 1 & 0 \\ 0 & (-1)^{Q_k} \end{bmatrix} \right) \cdot \mathbf{e}(\phi_k) \\ &= \mathbb{1}_{\text{RX}}(\mathbf{p}) \cdot \mathbf{e}(\phi_k) - \mathbb{1}_{\text{TX}}(\mathbf{p}) \cdot \mathbf{R}(2\bar{\gamma}_k) \cdot \mathbf{e}((-1)^{Q_k}\phi_k) \\ &= \mathbb{1}_{\text{RX}}(\mathbf{p}) \cdot \mathbf{e}(\phi_k) - \mathbb{1}_{\text{TX}}(\mathbf{p}) \cdot \mathbf{e}((-1)^{Q_k}\phi_k + 2\bar{\gamma}_k) \quad (20) \end{aligned}$$

where $\bar{\gamma}_k$ is the *effective wall angle* (19) and ϕ_k is the angle of arrival of the k-th path. Indicator functions were defined in (9) and suggest the following case analysis.

For bistatic cases $\mathbf{p}_{\text{RX}} \neq \mathbf{p}_{\text{TX}}$, only one summand of (20) remains for a fixed choice $\mathbf{p} \in \{\mathbf{p}_{\text{RX}}, \mathbf{p}_{\text{TX}}\}$. Particularly,

$$\frac{\partial \tau_k}{\partial \mathbf{p}_{\text{RX}}} = \frac{1}{c}\mathbf{e}(\phi_k), \quad \frac{\partial \tau_k}{\partial \mathbf{p}_{\text{TX}}} = -\frac{1}{c}\mathbf{e}((-1)^{Q_k}\phi_k + 2\bar{\gamma}_k) \ . \quad (21)$$

Bistatic gradients w.r.t. TX can be simplified with the trivial property of forward and reverse path lengths being equal, i.e. $\tau_k = \tau_k^{\text{rev}}$ and so $\|\mathbf{p}_{\text{RX}} - \mathbf{p}_k\| = \|\mathbf{p}_{\text{TX}} - \mathbf{p}_k^{\text{rev}}\|$.[9] The concept is shown in Figure 3. Considering switched roles for $\mathbf{p}_{\text{RX}}$ and $\mathbf{p}_{\text{TX}}$ then suggests

$$\frac{\partial \tau_k}{\partial \mathbf{p}_{\text{TX}}} = \frac{\partial \tau_k^{\text{rev}}}{\partial \mathbf{p}_{\text{TX}}} = \frac{1}{c}\mathbf{e}(\phi_k^{\text{rev}}) \ . \quad (22)$$

Then, (22) in (21) gives the (from a geometrical optics perspective) intuitive angle relation $\phi_k^{\text{rev}} = (-1)^{Q_k}\phi_k + 2\bar{\gamma}_k + \pi$.

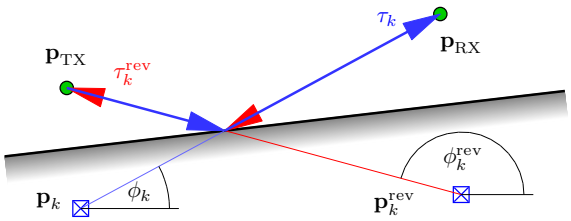

Fig. 3. Forward and reverse paths of a bistatic MPC and the corresponding VAs and angles of arrival.

In the monostatic case, we are facing a single mobile $\mathbf{p} = \mathbf{p}_{\text{TX}} = \mathbf{p}_{\text{RX}}$ and so both summands of (20) remain.

$$\begin{aligned} \frac{\partial \tau_k}{\partial \mathbf{p}} &= \frac{1}{c}\left(\mathbf{e}(\phi_k) + \mathbf{e}(\phi_k^{\text{rev}})\right) \\ &= \begin{cases} \frac{2}{c}\sin(\bar{\gamma}_k)\mathbf{e}\left(\phi_k + \bar{\gamma}_k - \frac{\pi}{2}\right) & \text{If } Q_k \text{ is even} \\ \frac{2}{c}\sin(\bar{\gamma}_k - \phi_k)\mathbf{e}\left(\bar{\gamma}_k - \frac{\pi}{2}\right) & \text{If } Q_k \text{ is odd} \end{cases} \quad (23) \end{aligned}$$

Formula (23) has magnitude-times-direction form which is often useful for assessing monostatic reflections.

IV. Results

A. Evaluation of Monostatic Virtual Anchor Types

We write the general gradient as magnitude times direction

$$\frac{\partial \tau_k}{\partial \mathbf{p}} = \frac{1}{c}a_k\mathbf{e}(\mu_k)$$

where a_k represents spatial sensitivity and $\mathbf{e}(\mu_k)$ is the direction of greatest change of τ_k. Monostatic gradients (23) satisfy $0 \leq a_k \leq 2$ while bistatic gradients (21) are of constant magnitude $a_k = 1$. The reason is the two summands in (20): They represent changes in path length due to movement of $\mathbf{p}_{\text{RX}}$ and $\mathbf{p}_{\text{TX}}$, respectively. For bistatic gradients, only one influence is active at a time, and the characteristics of either are alike, cf. (22). Monostatic gradients are affected by both, so the two influences may add up or cancel, depending on the multipath geometry, and thus allow for zero or double sensitivity.

Knowing the spatial delay gradients, we use (8) to write FIM $\boldsymbol{\mathcal{I}}_{\mathbf{p}}$ as a sum of contributions from the individual VAs

$$\boldsymbol{\mathcal{I}}_{\mathbf{p}} = \frac{8\pi^2\beta^2}{c^2}\sum_{k=1}^{K} \text{SINR}_k \ a_k^2 \ \mathbf{e}(\mu_k)\cdot\mathbf{e}(\mu_k)^T$$

where $\mathbf{e}(\mu_k)\cdot\mathbf{e}(\mu_k)^T$ is a ranging direction matrix[10] [11].

The above sum reveals that each MPC contributes one-dimensional position information in direction $\mathbf{e}(\mu_k)$, scaled by the individual SINR and the square of spatial sensitivity a_k [3], [11]. For bistatic cases, a technical evaluation is facilitated by $a_k = 1$ and was done in [1]. For monostatic cases, a_k depends heavily on the multipath geometry, which necessitates further investigation.

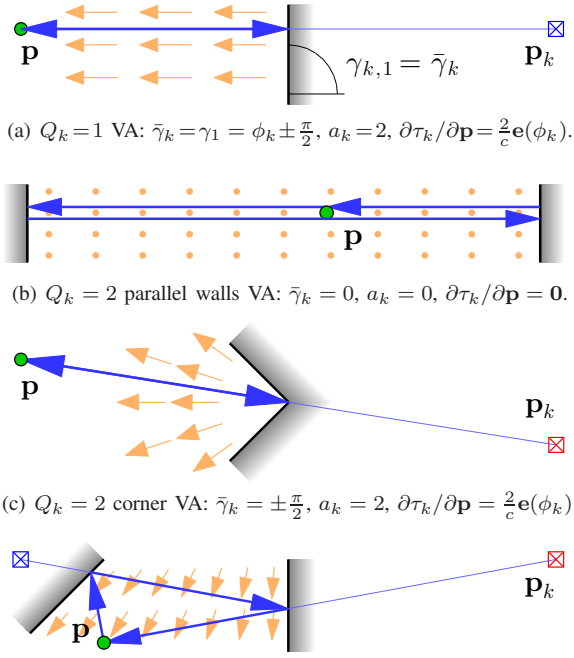

(a) $Q_k = 1$ VA: $\bar{\gamma}_k = \gamma_1 = \phi_k \pm \frac{\pi}{2}$, $a_k = 2$, $\partial\tau_k/\partial\mathbf{p} = \frac{2}{c}\mathbf{e}(\phi_k)$.

(b) $Q_k = 2$ parallel walls VA: $\bar{\gamma}_k = 0$, $a_k = 0$, $\partial\tau_k/\partial\mathbf{p} = \mathbf{0}$.

(c) $Q_k = 2$ corner VA: $\bar{\gamma}_k = \pm\frac{\pi}{2}$, $a_k = 2$, $\partial\tau_k/\partial\mathbf{p} = \frac{2}{c}\mathbf{e}(\phi_k)$.

(d) $Q_k = 2$ arbitrary VA: $\bar{\gamma}_k = \gamma_1 - \gamma_2$, $a_k = 2\sin(\bar{\gamma}_k)$, $\partial\tau_k/\partial\mathbf{p} = \frac{2}{c}\sin(\bar{\gamma}_k)\mathbf{e}\left(\phi_k + \bar{\gamma}_k - \frac{\pi}{2}\right)$, cf. (23) even case.

Fig. 4. Monostatic VAs of order 1 and 2 and their properties for significant indoor geometries. The orange vector field illustrates the spatial delay gradient $\partial\tau_k/\partial\mathbf{p}$ and thus the direction of position information provided by the VA.

Figure 4 shows four important types of monostatic VAs in indoor setups. Figure 4(a) shows a first-order VA (i.e. a single reflection), providing position information orthogonal to the

[9] τ_k^{rev}, $\mathbf{p}_k^{\text{rev}}$ are just temporary symbols used to show the reciprocity idea.
[10] $\mathbf{e}(\mu_k)\cdot\mathbf{e}(\mu_k)^T$ has eigenvalue 1 towards $\mathbf{e}(\mu_k)$ and 0 perpendicular.

wall with twice the sensitivity a_k than in bistatic cases (e.g., with anchors). Second-order reflections between parallel walls are useless for localization because of their constant delay: Figure 4(b) shows that the path length is twice the room width, independent of agent position.[11,12] The gradient of the rectangular corner VA from Figure 4(c) is radially pointing away from the corner and has double sensitivity. For an arbitrary second-order VA like in Figure 4(d), the behavior is a mixture of the parallel and corner cases, depending on the wall angle mismatch.

VAs of order $Q_k \geq 3$ are insignificant in practice [10] since their SINR is usually below detectability, due to limited reflectivity of construction materials and path loss. Also, the PEB (3) is dominated by the few highest-SINR paths [12], so even detectable paths of $Q_k \geq 3$ would contribute very little.

B. Numerical Results for the Monostatic PEB

We assume a raised-cosine pulse of duration $T_s = 1$ns on an $f_c = 7$ GHz carrier. Like in [3], we set the power delay profile $S_\nu(\tau)$ of DM to a double-exponential (time constants: 5ns rise, 20ns decay). We use AWGN with double-sided PSD $N_0/2$ such that $E_{\text{LOS}}/N_0 = 80$dB at 1m of propagation.

Figure 5 shows the floorplan of an example room, where the CRLB on the monostatic position error (3) is shown for agent positions therein. First-order and second-order corner VAs with $-3\text{dB} \cdot Q_k$ attenuation are considered. The possible localization performance is particularly promising for agent positions close to the room corners. This is because an accurate position estimate requires high-SINR ranging information (i.e., low path loss and DM interference) in both horizontal and vertical directions, which is best provided by the nearest first-order VAs. Path overlap (PO) inevitably causes poor performance in certain regions: overlap of nearby first-order VAs leads to a performance drop along the room's symmetry axes. The parabola-shaped outage regions close to walls are due to a corner VA and an adjoining first-order VA having low delay separation there.

Figure 6 shows the upper left 3m × 3m corner of the previous room for different assumptions. We observe how the additional consideration of second-order VAs helps performance in principle, but also leads to severe problems with PO.

For quantitative analysis, Figure 7 shows the CDF of PEB over the entire floor plan for pulse duration $T_\text{s} = 1$ ns and different maximum VA orders (1 and 2). For the neglected PO case, one can observe that the PEB decreases when adding higher-order VAs (dashed lines). Obviously, PO leads to a degradation of the PEB, since useful position information is lost. This effect is even stronger when $Q_k \leq 2$, which is mostly due to overlap of first-order and corner paths close to walls, as described earlier.

[11]This property could prove useful in indoor mapping, i.e. estimation of an unknown floor plan from reflections. Observing those MPCs whose delays are invariant under agent movements could extend approaches like [14].

[12]The reverse path has the same constant length, causing inevitable overlap and singular $\mathbf{\Lambda}'_C, \mathcal{I}_\mathbf{p}$ when both VAs are considered. This problem affects all higher-order paths with non-coinciding directions of departure and arrival.

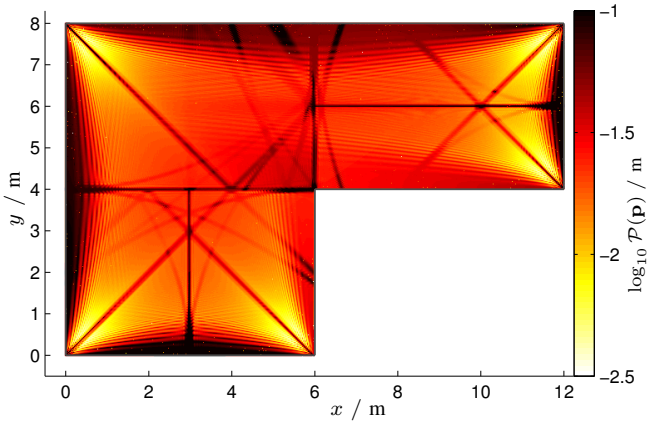

Fig. 5. Position error bound (PEB) of monostatic localization over a simple L-room. VAs are of order $Q_k \leq 2$ and path overlap (PO) is considered.

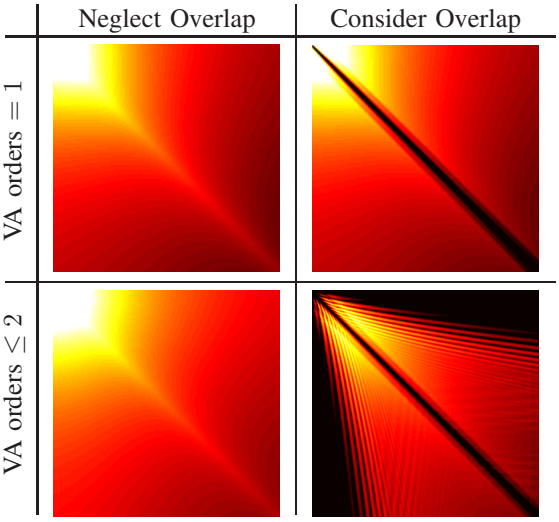

Fig. 6. The upper left 3m × 3m corner of the room in Figure 5 for different parameters. Here, the value range [white, black] $\hat{=}$ $[10^{-2.5}\text{m}, 10^{-1.5}\text{m}]$.

V. Conclusions

The CRLB on the position error of monostatic multipath-assisted indoor localization has been decomposed into Jacobians of multipath delays over agent position and the Fisher information matrix of signal model parameters. To compute the Jacobians, we formulated the spatial gradients of multipath delays. This general result shows that the influence of room geometry reduces to a single scalar quantity, termed effective wall angle. We analyzed the gradient for the most significant types of monostatic VAs to understand their behavior. The latter could be used for measuring room dimensions.

Numerical results show that, besides outage regions caused by path overlap, monostatic concepts are applicable for highly accurate node localization. However, monostatic position estimation is intrinsically ambiguous and utilizing it for robust localization is possible only as part of a more sophisticated concept, e.g. a cooperative approach.

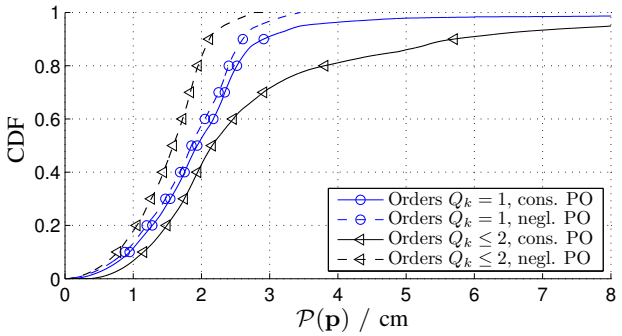

Fig. 7. CDFs of the PEB with $T_\mathrm{s} = 1\,\mathrm{ns}$ for VAs of order one and two. Path overlap is neglected in the results marked by dashed lines.

Appendix A
Proof of Mirroring Formula (12)

Recall definition (15) of $\mathbf{F}$ and (14) of $\mathbf{M}(\gamma)$. To find a formula for mirror image $\mathcal{S}(\mathbf{p},\gamma,\mathbf{d})$ of $\mathbf{p}$ about wall γ, $\mathbf{d}$, we first switch to a more suitable coordinate system where wall and horizontal axis coincide. To do so, we move the origin onto the wall by subtracting $\mathbf{d}$ and then compensate the wall angle with rotation $\mathbf{R}(-\gamma)$, so $\mathbf{p}$ moves to $\mathbf{p}' = \mathbf{R}(-\gamma)(\mathbf{p}-\mathbf{d})$. Now, mirroring equals a simple vertical flip $\mathbf{p}'_\mathrm{mir} = \mathbf{F}\mathbf{p}'$. Lastly, we undo coordinate transformations $\mathbf{p}_\mathrm{mir} = \mathbf{R}(\gamma)\mathbf{p}'_\mathrm{mir}+\mathbf{d}$. Broken down to $\mathbf{p}$, the mirror image is located at

$$\mathcal{S}(\mathbf{p},\gamma,\mathbf{d}) = \mathbf{p}_\mathrm{mir} = \mathbf{R}(\gamma)\mathbf{F}\mathbf{R}(-\gamma)(\mathbf{p}-\mathbf{d})+\mathbf{d}\ .$$

Some basic trigonometry reveals $\mathbf{R}(\gamma)\mathbf{F}\mathbf{R}(-\gamma) = \mathbf{M}(\gamma)$, thus

$$\mathcal{S}(\mathbf{p},\gamma,\mathbf{d}) = \mathbf{M}(\gamma)(\mathbf{p}-\mathbf{d})+\mathbf{d}\ .$$

Appendix B
Proof of Mirror Matrix Property (17)

Mirror matrices $\mathbf{M}(\gamma)$ are symmetric and orthogonal and thus self-inverse. Sign-flip $\mathbf{F} = \mathbf{M}(0)$ inherits these properties. Rotation is a well-known homomorphism $\mathbf{R}(\gamma)\mathbf{R}(\beta) = \mathbf{R}(\gamma+\beta)$. Definition $\mathbf{M}(\gamma) = \mathbf{R}(2\gamma)\mathbf{F}$ from (14) implies $\mathbf{R}(2\gamma) = \mathbf{M}(\gamma)\mathbf{F}$. We rearrange the following product to derive the desired pseudo-homomorphism property of the mirror matrix:

$$\begin{aligned}\mathbf{M}(\gamma)\mathbf{M}(\beta) &= \mathbf{M}(\gamma)\mathbf{M}(\beta)^\mathrm{T} = \mathbf{R}(2\gamma)\mathbf{F}\big(\mathbf{R}(2\beta)\mathbf{F}\big)^\mathrm{T}\\ &= \mathbf{R}(2\gamma)\mathbf{F}\mathbf{F}^{-1}\mathbf{R}(2\beta)^\mathrm{T} = \mathbf{R}(2\gamma)\mathbf{R}(-2\beta)\\ &= \mathbf{R}(2(\gamma-\beta)) = \mathbf{M}(\gamma-\beta)\cdot\mathbf{F}\end{aligned}$$

Appendix C
Likelihood Function and Fisher Information Matrix of Signal Model Parameters

The likelihood function (LHF) of the sampled received signal $\mathbf{r}$ in AWGN and diffuse multipath (DM) is given as [1], [3]

$$f(\mathbf{r}|\boldsymbol{\psi}) \propto \exp\left\{2\Re\left\{\mathbf{r}^\mathrm{H}\mathbf{C}_\mathrm{n}^{-1}\mathbf{S}\boldsymbol{\alpha}\right\} - \boldsymbol{\alpha}^\mathrm{H}\mathbf{S}^\mathrm{H}\mathbf{C}_\mathrm{n}^{-1}\mathbf{S}\boldsymbol{\alpha}\right\} \quad \text{(C.1)}$$

where $\mathbf{S} = [\mathbf{s}_{\tau_1},\ldots,\mathbf{s}_{\tau_K}] \in \mathbb{R}^{N\times K}$ is the signal matrix containing delayed versions $\mathbf{s}_{\tau_k} = [s(T_\mathrm{s}-\tau_k),\ldots,s(NT_\mathrm{s}-\tau_k)]^\mathrm{T}$ of the sampled transmit pulse and $\mathbf{C}_\mathrm{n} = \sigma_\mathrm{n}^2\mathbf{I}_{N\times N}+\mathbf{C}_\mathrm{c}$ is the noise co-variance matrix. AWGN samples have variance $\sigma_\mathrm{n}^2 = N_0/T_\mathrm{s}$; the elements of the DM co-variance matrix are given by $[\mathbf{C}_\mathrm{c}]_{n,m} = T_\mathrm{s}\sum_{i=1}^{N} S_\nu(iT_\mathrm{s})s(nT_\mathrm{s}-iT_\mathrm{s})s(mT_\mathrm{s}-iT_\mathrm{s})$. Using (C.1) in (5) yields FIM $\boldsymbol{\mathcal{I}}_{\boldsymbol{\psi}}$ (see (6)), whose submatrices are given [3] as follows:

$$\boldsymbol{\Lambda}_\mathrm{B} = [\boldsymbol{\Lambda}_\mathrm{B}^R\ \boldsymbol{\Lambda}_\mathrm{B}^I], \qquad \boldsymbol{\Lambda}_\mathrm{C} = \begin{bmatrix}\boldsymbol{\Lambda}'_\mathrm{C} & 0\\ 0 & \boldsymbol{\Lambda}'_\mathrm{C}\end{bmatrix}$$

$$\begin{aligned}[\boldsymbol{\Lambda}_\mathrm{A}]_{k,k'} &= 2\Re\Big(\alpha_k\alpha_{k'}^*\Big(\frac{\partial\mathbf{s}_{\tau_{k'}}}{\partial\tau_{k'}}\Big)^\mathrm{H}\mathbf{C}_\mathbf{n}^{-1}\frac{\partial\mathbf{s}_{\tau_k}}{\partial\tau_k}\Big)\\ [\boldsymbol{\Lambda}_\mathrm{B}^R]_{k,k'} &= 2\Re\Big(\alpha_k\big(\mathbf{s}_{\tau_{k'}}\big)^\mathrm{H}\mathbf{C}_\mathbf{n}^{-1}\frac{\partial\mathbf{s}_{\tau_k}}{\partial\tau_k}\Big)\\ [\boldsymbol{\Lambda}_\mathrm{B}^I]_{k,k'} &= 2\Im\Big(\alpha_k\big(\mathbf{s}_{\tau_{k'}}\big)^\mathrm{H}\mathbf{C}_\mathbf{n}^{-1}\frac{\partial\mathbf{s}_{\tau_k}}{\partial\tau_k}\Big)\\ [\boldsymbol{\Lambda}'_\mathrm{C}]_{k,k'} &= 2\Re\Big(\big(\mathbf{s}_{\tau_k}\big)^\mathrm{H}\mathbf{C}_\mathbf{n}^{-1}\mathbf{s}_{\tau_{k'}}\Big)\end{aligned}$$

References

[1] K. Witrisal and P. Meissner, "Performance bounds for multipath-assisted indoor navigation and tracking (MINT)," in *Communications (ICC), 2012 IEEE International Conference on*, June 2012, pp. 4321–4325.

[2] P. Meissner, E. Leitinger, and K. Witrisal, "UWB for Robust Indoor Tracking: Weighting of Multipath Components for Efficient Estimation," *Wireless Communications Letters, IEEE*, vol. 3, no. 5, pp. 501–504, Oct 2014.

[3] E. Leitinger, P. Meissner, C. Ruedisser, G. Dumphart, and K. Witrisal, "Evaluation of Position-related Information in Multipath Components for Indoor Positioning," *IEEE Journal on Selected Areas in Communications*, 2015, to appear.

[4] J. Borish, "Extension of the image model to arbitrary polyhedra," *The Journal of the Acoustical Society of America*, vol. 75, no. 6, 1984.

[5] N. Michelusi, U. Mitra, A. Molisch, and M. Zorzi, "UWB Sparse/Diffuse Channels, Part I: Channel Models and Bayesian Estimators," *IEEE Transactions on Signal Processing*, vol. 60, no. 10, pp. 5307–5319, Oct 2012.

[6] M. Froehle, E. Leitinger, P. Meissner, and K. Witrisal, "Cooperative Multipath-Assisted Indoor Navigation and Tracking (Co-MINT) Using UWB Signals," in *IEEE ICC 2013 Workshop on Advances in Network Localization and Navigation (ANLN)*, June 2013, pp. 16–21.

[7] Y. Shen, H. Wymeersch, and M. Win, "Fundamental Limits of Wideband Localization - Part II: Cooperative Networks," *IEEE Transactions on Information Theory*, vol. 56, no. 10, pp. 4981–5000, Oct 2010.

[8] Y. Shen, S. Mazuelas, and M. Win, "Network Navigation: Theory and Interpretation," *IEEE Journal on Selected Areas in Communications*, vol. 30, no. 9, pp. 1823–1834, October 2012.

[9] M. des Noes and B. Denis, "Benefits from cooperation in simultaneous anchor-less tracking and room mapping based on Impulse Radio - Ultra Wideband devices," in *International Conference on Systems, Signals and Image Processing (IWSSIP)*, April 2012, pp. 17–21.

[10] P. Meissner and K. Witrisal, "Analysis of Position-Related Information in Measured UWB Indoor Channels," in *6th European Conference on Antennas and Propagation (EuCAP)*, March 2012, pp. 6–10.

[11] Y. Shen and M. Win, "Fundamental Limits of Wideband Localization - Part I: A General Framework," *Information Theory, IEEE Transactions on*, vol. 56, no. 10, pp. 4956–4980, Oct 2010.

[12] ——, "Effect of Path-Overlap on Localization Accuracy in Dense Multipath Environments," in *Communications, 2008. ICC '08. IEEE International Conference on*, May 2008, pp. 4197–4202.

[13] H. Coxeter, *Introduction to Geometry*, ser. Wiley Classics Library. Wiley, 1989.

[14] T. Deissler and J. Thielecke, "UWB SLAM with Rao-Blackwellized Monte Carlo data association," in *Indoor Positioning and Indoor Navigation (IPIN), 2010 International Conference on*, Sept 2010.

High-Accuracy Localization for Assisted Living

Klaus Witrisal, Paul Meissner, Erik Leitinger, Yuan Shen,
Carl Gustafson, Fredrik Tufvesson, Katsuyuki Haneda,
Davide Dardari, Andreas F. Molisch, Andrea Conti, and Moe Z. Win

***Abstract*—Assisted living (AL) technologies, enabled by technical advances such as the advent of the Internet-of-Things, are increasingly gaining importance in our ageing society. This article discusses the potential of future high-accuracy localization systems as a key component of AL applications. Accurate location information can be tremendously useful to realize, e.g., behavioral monitoring, fall detection, and real-time assistance. Such services are expected to provide older adults and people with disabilities with more independence and thus to reduce the cost for caretaking. Total cost of ownership and ease of installation are paramount to make sensor systems for AL viable. In case of a radio-based indoor localization system, this implies that a conventional solution is unlikely to gain widespread adoption because of its requirement to install multiple fixed nodes (anchors) in each room. This paper therefore places its focus on (i) discussing radiolocalization methods that reduce the required infrastructure by exploiting information from reflected multipath components and (ii) showing that knowledge about the propagation environment enables localization with high accuracy and robustness. It is demonstrated that new millimeter-wave (mm-wave) technology, under investigation for 5G communications systems, will be able to provide cm-accuracy indoor localization in a robust manner, ideally suited for AL.**

***Index Terms*—Assisted living technologies, localization, location aware communications, ultra-wideband systems, mm-wave systems, fundamental limits, channel models**

I. Introduction

The robust provisioning of accurate location information is a key enabler for AL systems. A recent survey on ambient intelligence in healthcare [1] illustrates the wide range of applications that could be supported by a cm-accuracy indoor positioning system *alone*: Activity recognition, behavioral pattern discovery, anomaly detection, and decision support methods can all be based on such a sensor modality. Application examples include behavioral monitoring to assess the physical and mental health of individuals, emergency (fall) detection to alert caretakers or emergency services, real-time assistance to provide context awareness to medication management systems (to remind—for instance—to take medications before/during/after meals) or as an orthotic and rehabilitation tool for individuals suffering from cognitive decline, geofencing for people with dementia, and even as a navigation aid for visually impaired (see [1] and the references therein).

However, as of today, the technologies for indoor localization have not converged towards a unique winning approach, hence the topic is still subject of research and competitions [2]. Among the many location sensing methods proposed [3]–[9], active or passive radiolocalization[1] are most promising, because radio transceivers can be integrated in existing devices like smartphones and built at small form factors with low power consumption. Video cameras and microphones [11]–[13], for example, suffer from occlusions and a lack of acceptance because of privacy concerns. But the influence of the dense multipath radio channel in indoor environments still makes accurate and robust radiolocalization a challenging task. Ultra-wideband (UWB) signals have been shown to deliver excellent accuracy, since they allow for a separation of the multipath components (MPCs) [14]–[17]. Hence, on the one hand, the direct signal path can be isolated from interfering MPCs; on the other hand, position-related information in later-arriving MPCs becomes accessible as well and turned into an advantage [18].

Unfortunately, dedicated technology is required to implement traditional UWB systems operating in the microwave band (at $3.1 - 10.6$ GHz). With the advent of mm-wave communications in the 60 GHz band [19]–[21], a UWB localization system could operate synergetically with an existing communication system, e.g. using the IEEE 802.11ad standard [22]. Furthermore, 60 GHz regulations allow much higher transmit power compared to microwave UWB systems. Beamforming technologies proposed for these systems [19] perfectly complement the needs of the localization system and vice versa: also the beamforming algorithms will benefit from the location information and from environmental radio maps, i.e. spatial characterizations of the propagation channel that can be estimated and tracked in realtime. Location awareness is created, which is beneficial for different layers of the protocol stack of a communications system [23].

The reduction of the required infrastructure is of key importance for a viable localization system for AL. At the same time, localization with high accuracy and robustness is needed. This paper discusses a range of multipath-assisted localization approaches that actively take environmental propagation information into account to cope with these seemingly conflicting requirements. Even with only *a single anchor node* within each room, highly-accurate and robust location estimates can be obtained [18], [24], [25]. As a side effect, this method also reduces the amount of electromagnetic radiation, possibly increasing its acceptance by users. High accuracy and robustness are more easily achieved with active systems [18], [24] where the user has to wear, e.g. a bracelet as illustrated in Fig. 1, while passive systems [25], [26] prevent the risk of lacking user compliance.

This paper highlights the following issues:

- A model of the received signal using a geometry-based stochastic channel model and the concept of virtual sources/anchors. This leads to an *environment model*

[1] In active localization, devices to be localized are equipped with a radio device participating in the communication, which is not the case in passive localization [10].

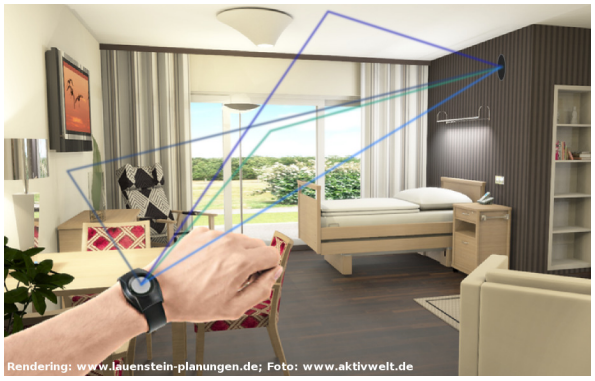

Fig. 1. Illustration of a high-accuracy, multipath-enabled indoor localization system for assisted-living applications. Information from reflected signals (such as the exemplary rays depicted) can be exploited if the geometry of the environment is taken into account.

that describes the localization capability in a specific environment.
- Performance limits for indoor localization employing multipath propagation, showing the relevance of geometrically modeled MPCs.
- Algorithms for multipath-assisted localization and tracking: Maximum likelihood localization, tracking filters with data association, algorithms for passive localization and multi-target identification.
- Experimental and numerical results demonstrating the localization accuracy and robustness using a current experimental microwave-band system and the potential performance of a mm-wave system.
- Discussions and conclusions, evaluating the usefulness of the presented concepts for accurate and robust localization as a key component of an AL system.

Creating the proposed infrastructure, developing the appropriate distributed processing algorithms, and validating the applications in challenging AL environments will require significant multidisciplinary work over the coming years.

The remainder of this paper is structured as follows: Section II discusses the signal modeling and the resulting performance bounds for multipath-assisted localization. The separated text box contains details on the models and derivations. An extensive overview over multipath-assisted localization and tracking algorithms together with representative results is found in Section III, while the discussion of mm-wave systems for localization is given in Section IV. The paper is wrapped up with a summary and conclusions in Section V.

II. Signal Models and Performance Bounds

A suitable signal model supporting the analysis of a multipath-assisted localization system requires a description of the geometry to address the position dependence of signal features and stochastic elements to represent signal impairments and noise. We hence use a geometry-based stochastic channel model to describe the signal transmitted from a mobile agent node to a fixed anchor node (or the other way around, from anchor to agent). The received signal is thus modeled as a convolution of a UWB transmit pulse $s(t)$ with the channel

$$r(t) = \sum_{k=1}^{K} \alpha_k s(t-\tau_k) + s(t) * \nu(t) + w(t) \qquad (1)$$

where the sum accounts for K deterministic MPCs with complex amplitudes $\{\alpha_k\}$ whose delays $\{\tau_k\}$ yield useful position-related information, while the stochastic process $\nu(t)$ represents diffuse multipath (DM) which is *interference* to these useful components. The signal $w(t)$ denotes white Gaussian measurement noise at power spectral density (PSD) N_0. We assume a unit-energy pulse $s(t)$, such that the energy of the k-th MPC is given as $|\alpha_k|^2$. DM is everything that is not or can not be described by the deterministic components. It is modeled as a (Gaussian) random process with auto-covariance $\mathrm{E}\{v(t)v^*(\tau)\} = S_\nu(\tau)\delta(t-\tau)$, where $S_\nu(\tau)$ is a power delay profile (PDP) accounting for the non-stationary variance of the DM in the delay domain [27].

We assume that the result of a possible linear beamformer is already incorporated in $r(t)$. Beamforming will have an impact on the energies $|\alpha_k|^2$ and the DM, but for simplicity we do not indicate these dependencies in our equations.

To describe the *localization environment*, we propose a model for the signal-to-interference-plus-noise ratios (SINRs) of MPCs along with their propagation delays. The delays are deterministically related to the geometry at hand. We model the delay τ_k of the k-th MPC using a virtual anchor (VA) [18], [28] at position $\mathbf{a}_k$, yielding $\tau_k = \frac{1}{c}\|\mathbf{p} - \mathbf{a}_k\|$, where $\mathbf{p}$ is the position to be determined and c is the speed of light. For reflections at plane surfaces, the positions of the VAs can be computed straightforwardly: physical anchors are simply mirrored w.r.t. the planes; iterated mirroring operations account for higher-order reflections [27].

The SINR of the k-th component is defined as

$$\mathrm{SINR}_k = \frac{|\alpha_k|^2}{N_0 + T_\mathrm{p} S_\nu(\tau_k)} \qquad (2)$$

relating the *useful* MPC energy $|\alpha_k|^2$ to the combined effects of the noise and the *interfering* DM. The latter is characterized by its PDP at the corresponding delay. The influence of the DM scales with the effective pulse duration T_p, i.e. with the inverse of the bandwidth of the measurement signal.

The model for the received signal in (1) enables the derivation of a Cramér-Rao lower bound (CRLB) on the position estimation error. (The derivation is briefly discussed in boxed text.) Using the information inequality, we obtain a bound for the position error as $\mathbb{E}_{\mathbf{r}|\mathbf{p}}\left\{\|\hat{\mathbf{p}} - \mathbf{p}\|^2\right\} \geq \mathrm{tr}\{\mathbf{J}_\mathbf{p}^{-1}\}$, where the square root of the right hand side is defined as the position error bound (PEB), $\hat{\mathbf{p}}$ is the estimated position and $\mathbf{J}_\mathbf{p}$ is the equivalent Fisher information matrix (EFIM) [29]–[32]. The EFIM can be written—under the assumption of resolvable, "non-overlapping" MPCs (see also the boxed text)—in the form [27]

$$\mathbf{J}_\mathbf{p} = \frac{8\pi^2\beta^2}{c^2} \sum_{k=1}^{K} \mathrm{SINR}_k \mathbf{J}_r(\phi_k) \qquad (3)$$

where β denotes the effective (root mean square) bandwidth of the measurement signal and $\mathbf{J}_r(\phi_k)$ is a rank-one matrix

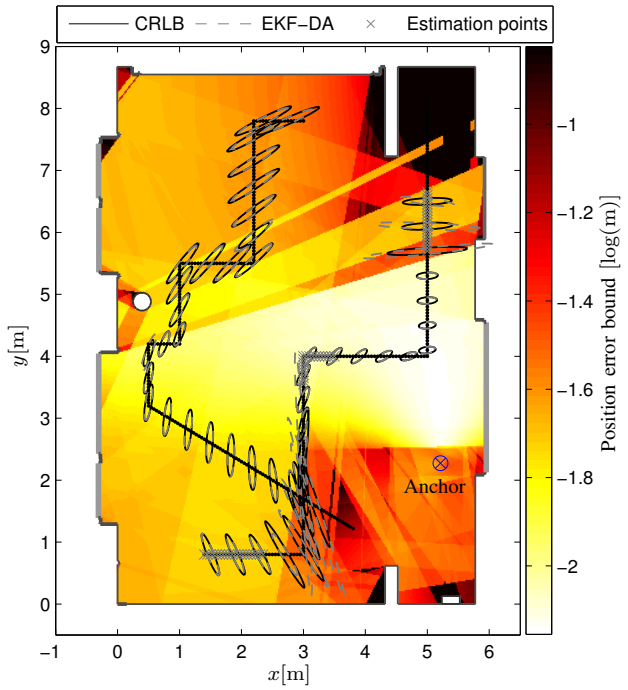

Fig. 2. Position error bound (PEB) and tracking results for $T_\mathrm{p} = 0.5\,\mathrm{ns}$, $f_\mathrm{c} = 7\,\mathrm{GHz}$, and a single fixed anchor. The PEB (3) has been computed from estimated SINRs (2); grey crosses are 60 positions used for this SINR estimation [18]. Solid and dashed ellipses denote the standard deviation ellipses corresponding to the CRLB and to the error covariance matrices of an extended Kalman tracking filter, respectively, at several points along two trajectories. These ellipses are enlarged by a factor of 20 for better visibility.

with an eigenvector pointing along the angle of arrival (AoA) ϕ_k of the k-th MPC. This simple, canonical form of the EFIM allows for important conclusions regarding localization:

- Each geometrically modeled (deterministic) MPC yields additional position-related information which is quantified by its SINR value. In fact, the range $\hat{d}_k$ estimated from the k-th MPC has an error variance bounded as $\mathrm{var}\left\{\hat{d}_k\right\} \geq c^2/(8\pi^2\beta^2\mathrm{SINR}_k)$; i.e. the SINRs indicate the uncertainties of the MPC ranges.
- The equations relate to the system parameters (e.g. bandwidth expressed by β and T_p), the environment model (the SINR values), and the geometry (the AoAs) and thus indicate the expected performance *in a specific scenario*.

Figure 2 shows an evaluation of the PEB according to (3) for a single fixed anchor, for SINR values estimated from measured channel impulse response data [33]. The evaluation takes into account the visibility of the VAs across the floor plan but it assumes a "global" model of SINRs for the entire room shown[2]. Two-dimensional positioning is considered here; the measurement data have been acquired over a bandwidth of 2 GHz at a 7 GHz carrier [33]. According to this result, the expected precision lies in between one and ten centimeters for most of the area.

The figure provides a prediction of the spatial distribution of the achievable performance. It can thus be considered as an indication for the robustness of the localization system for a specific environment. As mentioned in Section II, the set of VAs and the quantification of their relevance as given by the SINR model represents an *environment model* which reflects the potential localization accuracy. Using (2) and (3), the influence of system parameters, such as the signal bandwidth, can be quantified.

[2]To create a more detailed picture, one could estimate individual SINR-sets for different parts of a room or even estimate the SINR values online [34].

III. Algorithms for Multipath-assisted Environment-aware Localization

For the practical application of a multipath-assisted positioning and tracking system, two core challenges need to be tackled. (i) Algorithms are needed that can properly exploit the position-related information provided by each MPC; and (ii) algorithms are needed that can estimate the required side information, i.e. the environment model. Efficient solutions must be able to capture the relevant information from measurements at a reasonable computational complexity.

A. Multipath-assisted Localization and Tracking

Fig. 3 shows the block diagram of a multipath-assisted tracking scheme that is based on a Bayesian tracking filter [18], [33]. A core component of this scheme is the data association block. It associates, at each timestep n, the arrival times of a number of MPCs to the predicted delays. The arrival times (collected in the set $\mathcal{Z}_n$) are estimated from the received signal $r_n(t)$ by a high-resolution maximum-likelihood channel estimation algorithm; the predicted delays are computed from the VA positions $\{\mathbf{a}_k\}$ (collected in the set $\mathcal{A}_n$) and the predicted agent position $\hat{\mathbf{p}}_n^-$. The data association is needed to identify the potential (virtual) signal sources, to discard false detections due to dense multipath, and to ignore missing arrival-time measurements. It has been accomplished in [18], [33] using a constrained optimal subpattern assignment approach [35]. This means that the predicted and estimated MPC delays are matched using combinatorial optimization with the constraint that associations at a distance larger than a so-called cut-off distance are discarded. The output of the data association block, i.e the positions of the associated VAs $\mathcal{A}_{n,\mathrm{ass}}$ and corresponding MPC delays $\mathcal{Z}_{n,\mathrm{ass}}$, are fed into the tracking algorithm as measurement inputs.

In the upper branch of the block diagram, the SINR model is updated, which reflects the *reliability* of the range measurements: the SINRs are estimated using past measurements of the MPC amplitudes [34]. The SINRs can also be estimated from offline training data [18]. Using this side information, the tracking filter can perform an appropriate measurement weighting of the extracted delays [18]. Furthermore, the SINRs allow for relevance determination: the overall set of VAs $\mathcal{A}_n$ can be reduced to a set of relevant VAs $\tilde{\mathcal{A}}_n$. Also geometric considerations, like the visibilities of certain VAs, can be incorporated at this stage [33].

Fig. 4 illustrates the efficiency of this approach based on experimental data in the microwave-UWB band at a bandwidth of 2 GHz [18], [33]. It compares the CDFs of the position errors for algorithms having different levels of environment

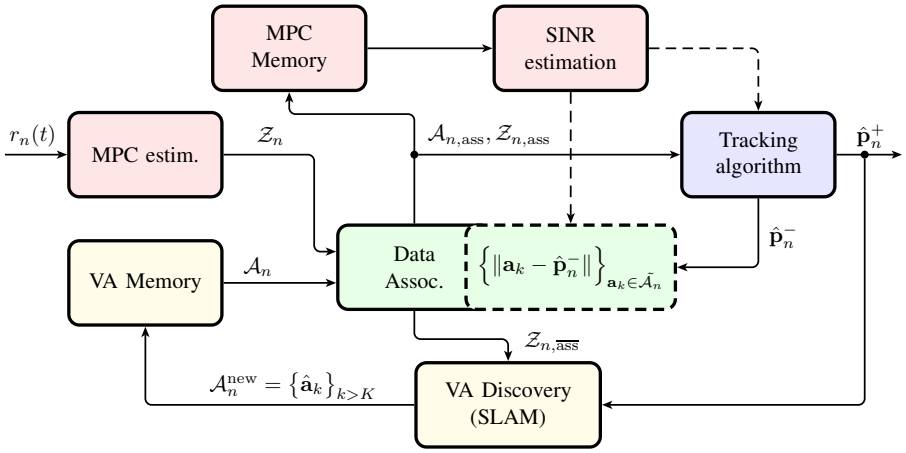

Fig. 3. Block diagram of state space tracking and data association scheme using MPC range estimates. The input is the received signal $r_n(t)$, the overall output is the estimated agent position $\hat{\mathbf{p}}_n^+$ at timestep n. The estimation is performed using the environment model represented by the memory blocks.

models available. The data have been obtained on 25 measurement trajectories with two fixed anchors. Trajectory points were spaced by 5 cm, while the different trajectories were obtained by shifting the entire tracks in 1 cm steps. An algorithm that exploits SINR information (red curves) obtains excellent robustness *and* accuracy: all 25 runs have similar performance with 90 % of the errors below 4 cm. Without SINR information (black and gray), 10 of 25 runs diverge. This occurs mostly in a short part of the trajectory where the LOS to one of the anchors is lost, being a strong indication of a reduced robustness. The overall CDF for the 15 non-diverging runs is shown by the black bold dashed line; 90 % of the errors are within 7 cm. Tracking results are also observable in Fig. 2, showing two example trajectories and the performance using only a single anchor. The standard deviation ellipses of the tracking filter match those corresponding to the CRLB and indicate the relevance of position information available in different directions.

Fig. 4 also shows the influence of a correction of the VA positions which has been done to refine the environment model in comparison to a VA model computed from the floorplan. A maximum a-posteriori (MAP) estimator has been used for this refinement, employing a set of training data at known locations. The performance without this MAP refinement is indicated by the blue dash-dotted curve. It shows a similar robustness but a reduced accuracy. We see this result as an evidence that the SINR model improves the robustness, while the VA-position refinement is needed to optimize the accuracy.

The environment model, e.g. the SINR information, thus is the key to obtain *efficient* tracking algorithms; not only in terms of achieving optimal performance, but also in terms of complexity: The set of relevant VAs in a scenario is significantly smaller than the overall set of VAs that would be taken into account by visibility considerations [18][3]. By also considering the uncertainty of the VA positions in the environment model, i.e. including the VAs to the state space, the position refinement can be done online at low complexity [34], eliminating the need for training measurements. Processing steps such as environment model tracking and relevance determination are potential features of a *cognitive* localization system. "Cognition" is aimed at understanding the surrounding world as found for instance in human visual perception (cf. [36], [37]).

[3]Usually, the number of MPCs carrying relevant information is on the order of 5–10 per radio link.

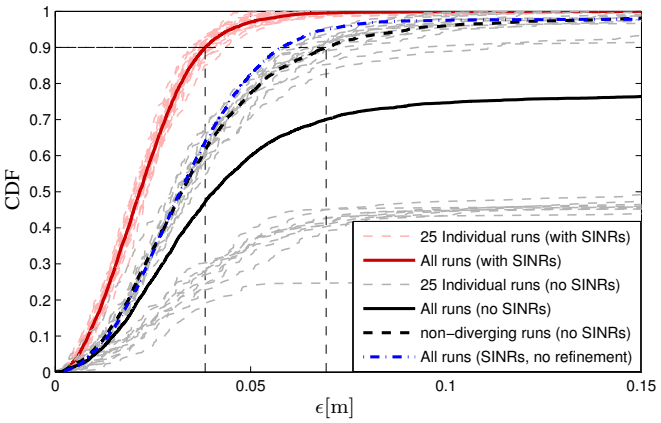

Fig. 4. CDFs of the position error $\epsilon = \|\hat{\mathbf{p}}_n^+ - \mathbf{p}_{\mathrm{true}}\|$ for $T_{\mathrm{p}} = 0.5\,\mathrm{ns}$ and $f_{\mathrm{c}} = 7\,\mathrm{GHz}$. Thin dashed lines show the individual 25 runs over the trajectories. Red and gray indicate the performance of the EKFs with and without estimated SINRs. Bold lines denote the total performance for all runs, the dashed line indicates the performance without SINRs on all non-diverging runs (15 out of 25).

The presented tracking approach naturally makes use of the position estimate obtained in the previous time step. Hence, an initialization strategy is also needed, i.e. a *localization* algorithm. Reference [24] proposes a maximum likelihood estimation algorithm based on (4). The important role of DM is taken into account by directly estimating the corresponding PDP $S_\nu(\tau)$ from the sampled received signals. No data association is necessary, since the entire received signal is used. In this way, a similar performance is achieved as in Fig. 4. Examples of the likelihood as a function of position $\mathbf{p}$ are shown in Section IV for mm-wave measurements.

This maximum likelihood approach can also be used in a tracking manner, resulting in particle-filter-based implementations of the scheme in Fig. 3. Although such algorithms have increased computational complexity, they provide enhanced

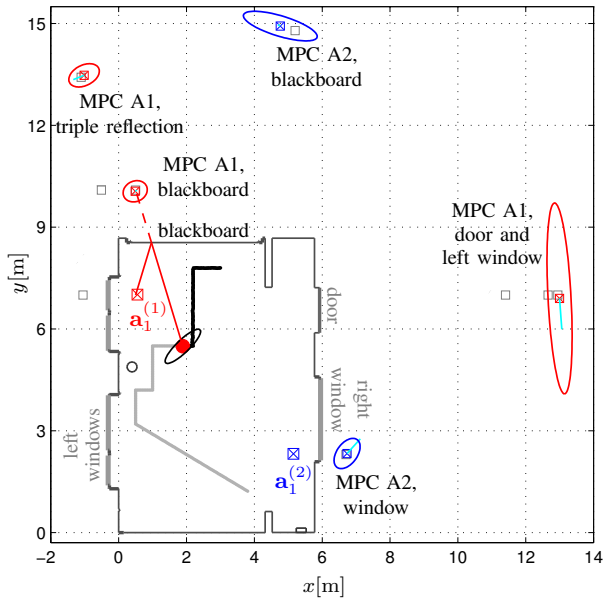

Fig. 5. Illustration of the environment map obtained by a SLAM algorithm. Two anchors at $\mathbf{a}_1^{(1)}$ and $\mathbf{a}_1^{(2)}$ represent the infrastructure. The agent position as well as the floor plan (represented by virtual anchors (VAs)) are estimated using specular multipath, for which one example path is shown. Grey squares indicate geometrically expected VAs, blue and red square-cross markers with uncertainty ellipses (30-fold) represent discovered VAs. An agent tracking result is shown in black with an error ellipse (100-fold).

robustness because the particles can represent multiple position hypotheses. This helps to avoid cases where Kalman filter-based schemes diverge.

B. Simultaneous Localization and Mapping Using Multipath Channel Information

How the environment model information can be obtained in practice, remains as a problem. In particular in assisted living scenarios, "plug-and-play" installation is of prime importance. That is, ideally, the environment model has to be acquired "online" while the system is in operation. Simultaneous localization and mapping (SLAM) is a well-known approach to learn a map of the environment with a mobile agent and at the same time to localize the agent within this map [38]. Its application to multipath-assisted indoor localization has been discussed in [34]. In this case, the learned map contains the data of the environment model, the VA positions and the SINR values; i.e. the requirement of plug-and-play installation is fulfilled. In [39], a structure-from-motion approach has been proposed to also estimate the agent and (virtual) anchor locations simultaneously from a set of UWB measurements.

The SLAM algorithm presented in [34] includes map features (the VA positions) within a joint state-space of a tracking filter with the agent and thus updates the VAs whenever new data are available. Again a data association is needed for this purpose, which has been accomplished by a similar subpattern assignment approach as discussed before. Sets of associated past measurements are then used to estimate the current SINR values. Non-associated measurements $\mathcal{Z}_{n,\overline{\text{ass}}}$, on the other hand, are grouped by their delays and used to compute "candidate" VAs that will be included in the environment model, if observed for a sufficiently long time. These new VAs are described by the set $\mathcal{A}_n^{\text{new}}$ shown in Fig 3.

It has been demonstrated in [34] that a 2D-map can be constructed with no prior information about the scenario other than the absolute positions of two fixed anchors. Fig. 5 shows an illustrative example of this SLAM approach, which has been obtained from the same measurement data as the CDFs in Fig. 4. Grey squares indicate the positions of some "expected" VAs computed from the floor plan. Discovered VAs are shown by red (Anchor 1) and blue (Anchor 2) square-cross markers; their marginal position covariance matrices are indicated by standard deviation ellipses, enlarged by a factor of 30 for better visibility. The corresponding true agent trajectory is indicated in grey. The current estimated agent position is shown by the red dot; its standard deviation ellipse is in black (enlarged by a factor of 100).

As shown in the figure—after 68 time steps—a number of relevant VAs have been identified that match very well with the geometrically computed VAs. Some of these VAs have only been associated for a few time steps, corresponding to rather large variances due to large geometric dilution of precision and/or low SINR values (e.g. MPC "A1 door and left window"). On the other hand, some VAs already have converged accurately to their true location (e.g. MPC "A1 blackboard"). Falsely discovered VAs often show a very large variance of their associated amplitudes, corresponding to a low SINR. Thus, their influence on the tracking process remains limited. The overall tracking performance almost matches up the performance of the approach discussed in Fig. 4. 90 % of the errors are within 4.4 cm. Assuming the availability of side information, e.g. from an inertial measurement unit (IMU), we expect that the robustness of this SLAM algorithm against divergence gets even higher.

C. Passive Localization Exploiting Multipath

As mentioned above, passive localization has the great advantage that no specific user compliance is necessary—in other words, the person to be helped does not need to remember to carry a specific device. At the same time, the passive principle makes it more challenging to handle multipath. While in an active system, localization can be achieved based on the triangulation with line-of-sight paths, in passive localization we have to base it on "direct paths" that go from the transmitter, via reflection at the target, to the receiver. Furthermore, these "direct paths" are embedded in background paths—paths that propagate from transmitter to receiver without participation of the target—and the delay of the background paths can be larger *or* smaller than those of the direct path. Secondly, there are also indirect paths, which involve reflection at both target and additional objects. And analogously to active localization, where the LOS path might be shadowed off, the direct path might be blocked. This overall makes target localization much more difficult.

Despite these difficulties, passive vital sign monitoring has a long history (the main motivation used to be in a military/surveillance context, but the principles can be applied

to AL as well). Narrowband Doppler radar was used to detect the presence of breathing already in the 1970s. However, this does not allow to *localize* the breathing person, and is thus of somewhat limited utility for AL applications. A more promising approach seems to be the use of wideband MIMO radar. Ref. [40] demonstrated a prototype that could precisely localize a person and track the small-scale movement of the chest that occurs during breathing from a distance of several meters away. This was enabled with a sounding waveform extending over 7 GHz bandwidth (within the UWB band from 3 to 10 GHz), combined with an 8-element transmit array, and high-resolution (iterative maximum-likelihood estimation) evaluation. Most noteworthy, the localization can be achieved *without* a direct path, as long as the environment (location of walls), etc., is known. The figures in [40] demonstrate the relative location of the echo reflected from head and chest when the target is breathing in or breathing out.

The situation is more difficult when more than one possible target is present. In contrast to active devices that send out unique signatures and thus allow identification of all associated signals, it is difficult (and often impossible) to distinguish between the multipath components belonging to different targets. Such multi-target localization is another difficult but important problem—obviously, in many AL situations (e.g., elder care homes), multiple targets might be present simultaneously, and if they are moving, their trajectories might intersect. From an algorithmic point of view, we have to distinguish the cases where transmitter and receiver have multiple antenna elements (and thus can resolve directions of the echoes), versus the (much more difficult) case of distributed single-antenna transceivers (e.g., [41]).

In addition to localization and tracking, radio signals may be used for the reconstruction of a 3D map of the surrounding environment, e.g. to assist people with impaired vision capabilities. This is of course strongly related to the mapping task of the SLAM approach. The "passive" reflections of the radio waves from the environment are exploited together with additional reflections from targets and walls. A single sensor through-the-wall radar with data association is discussed in [25], multipath-assisted through-the-wall imaging in [26]. The suitability of UWB radars for mapping, imaging, and also breathing detection was shown in [42]. Recently, the concept of the *personal radar* has been proposed as a smartphone-centric low cost solution for the navigation and mapping problem [43]. A personal radar could be an additional feature offered by 5G smartphones, exploiting mm-wave massive antenna arrays with electronic pencil-beam steering capability and high ranging accuracy. The small wavelength of mm-wave technology permits to pack a massive antenna array in pocket-size space [44]. In fact, mm-wave technologies could provide a most suitable platform for the purpose of high-accuracy localization for AL, as discussed next.

IV. MM-WAVE LOCALIZATION SYSTEMS FOR ASSISTED LIVING

Insights gained so far show the promising features of a multipath-assisted indoor localization system. However, the price to pay is a very large signal bandwidth, to enable the separation of MPCs at sufficiently high SINRs. Microwave-band UWB systems can fulfill this promise, but their mass-market adoption seems unlikely [9], given the recent developments of indoor wireless systems. For conventional wireless systems it would also be possible to utilize the phase evolution of the MPCs for precise localization and tracking [45]. This technique, however, requires large arrays for separating the MPCs at moderate bandwidths and hence might not be relevant in an AL context. 5G wireless systems—on the other hand—will include ultra-wideband radios in the mm-wave frequency band. The IEEE 802.11ad standard [22], for example, already defines an air-interface for a 2 GHz bandwidth system in the 60 GHz frequency band. Beamforming and tracking of MPCs are key elements of such systems. Despite the promising features of mm-wave systems for localization, only few papers address this aspect so far, and even less discuss measurement data and realistic channel models [46], [47].

This section highlights the great potential of mm-wave technologies for realizing multipath-assisted indoor localization. We analyze, for this purpose, exemplary measurement data discussed in [19], [20] that mimic the intended AL application scenario. It is shown that a single access point provides enough position-related information to enable high accuracy localization. A properly parameterized environment model is a key ingredient to achieve this.

A. Measurement Scenario and Setup

The mm-wave channel measurements of [19], [20] are MIMO measurements with 7x7 locations on both TX and RX sides obtained by a vector network analyzer. In the intended application, one array assumes the role of the agent to be localized, while the other corresponds to the anchor, i.e. the fixed infrastructure. (The floorplan is shown in Fig. 7a.) The measurement grid on the agent side was moved to 22 different locations in the room. Both LOS and obstructed LOS (OLOS) situations have been measured; the latter were obtained using a laptop screen to shadow the direct link to the anchor. These measurements have been conducted at a center frequency of 63 GHz. To mimic the IEEE 802.11ad standard [22], we selected a subband of 2 GHz from the total measured bandwidth of 4 GHz, using a raised cosine filter (cf. [33]).

B. Measurement Results

We first analyze the SINRs of the MPCs as defined in (2), i.e. the ratio of the useful energies of the deterministic MPCs to the interference by DM and AWGN. The SINRs are estimated using the technique of [18], [33], a method-of-moments estimator operating directly on the MPC amplitudes. In this way, the PDP $S_\nu(\tau)$ does not explicitly have to be estimated. We use the array positions on the anchor-side to provide the required signal ensemble. The array at the agent-side is used to show the potential of beamforming. In a practical setup, it may be advantageous to implement the beamforming at the anchor side, i.e. at the infrastructure, where the array has a known orientation, while at the agent side, low-complexity terminals may be used that have only one

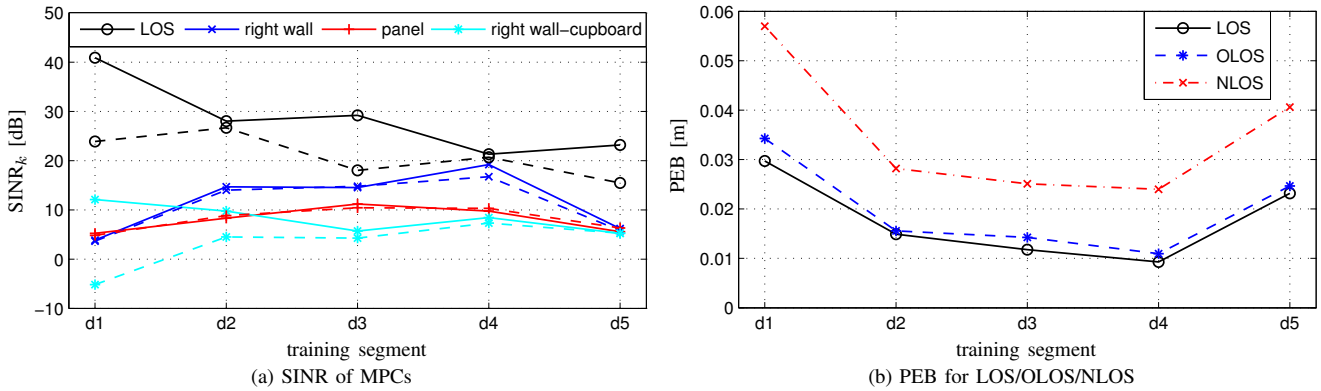

(a) SINR of MPCs (b) PEB for LOS/OLOS/NLOS

Fig. 6. (a) Estimated SINRs of selected reflections using $T_\mathrm{p} = 0.5\,\mathrm{ns}$ and $f_\mathrm{c} = 63\,\mathrm{GHz}$ and (b) PEB for LOS, OLOS, and NLOS (complete lack of the LOS component) scenarios. Solid lines indicate LOS measurements; while dashed and dash-dotted lines correspond to OLOS and NLOS measurements, respectively. The x-axis labeling refers to the measurement sets acquired at different positions $d_1, d_2, \ldots, d_5$ as reported in [19], [20].

or a few fixed antennas. We reverse these roles here, since the horizontal array geometry at the agent-side was better suited for a proof-of-principle.

The *estimated SINRs* in Fig. 6a show the relevance of selected MPCs in this environment for several agent positions. The LOS is the MPC providing most position-related information. Besides the fact that it is usually the strongest component of a radio channel, this significance is due to the relatively low impact of DM on the LOS component at a bandwidth of 2 GHz [33]. Interestingly, in some cases, the SINR of the LOS component drops only slightly in the OLOS situation, although its energy drops significantly (the average LOS K-factor over the estimation positions decreases from $8.9\,\mathrm{dB}$ to $-7.4\,\mathrm{dB}$). This implies that the component is still exploitable for localization. The reflected components also show significant SINRs over the estimation points but there is quite some location-dependence of the SINRs. It is more pronounced than for microwave band UWB measurements [33], highlighting the need for online estimation (tracking) of the environment model, as explained in Section III-B and [34].

Fig. 6b shows the PEB corresponding to the estimated SINRs of Fig. 6a. The PEB is a measure of the potentially achievable localization accuracy, hence highly-accurate single-anchor localization is possible in this scenario. The PEB increases only slightly in the OLOS situations, due to the still significant SINR of the LOS component. Even if the LOS component is not taken into account at all, (NLOS; the red dash-dotted line), the agent is still localizable at centimeter level, easily satisfying requirements of most AL applications. A proper operation in total absence of an LOS indicates the "good" robustness of the discussed techniques.

Fig. 7 shows the likelihood (4) for a sampled received signal $r(t)$ as a function of position $\mathbf{p}$, evaluated over the floorplan. It compares (a) LOS and (b) OLOS conditions with (c) OLOS with the use of beamforming. The bold black lines indicate the directions to the anchor, thin black lines the directions to first-order VAs, and black dashed lines the directions to second-order VAs. The black diamonds mark the estimated positions of the agent. Using a maximum likelihood positioning algorithm as in [24], an error in the centimeter level is achieved ($2\,\mathrm{cm}$ for the LOS and $3\,\mathrm{cm}$ for the OLOS situations). Only a small degradation results in the OLOS case, as anticipated from the analysis of the SINR values.

The potential use of beamforming shows a different great advantage: the multimodality of the likelihood function is reduced, which reduces the risk of converging to a wrong local maximum. Large modes at locations farther away from the true agent position are suppressed due to the angular resolution of the array antenna. Note, however, that MPC delays are still responsible for providing a high accuracy in a direction orthogonal to the LOS path. Without the processing of multipath, we would see a smooth maximum (along the circle) in stead of a sharp peak. The likelihood function in Fig. 7c has been computed by using a phased-array beamformer for each exploited MPC. This is achieved by coherently adding the signals at the agent-side array positions, taking into account the relative phase shifts that correspond to the known arrival angles of the MPCs. The figure exemplary shows that such a processing, envisioned for 5G mm-wave communication systems, can greatly improve the robustness of the localization, since many local maxima can be ruled out.

V. Discussion and Conclusion

This paper envisions accurate and robust indoor localization as a key sensing modality of an AL systems. It has been shown that awareness to the signal propagation conditions enables the robustness and allows to reduce the needed infrastructure. Experimental, measurement-based results support the discussion of theoretical findings.

A geometry-based stochastic model of the received signal allows the derivation of theoretical position error bounds and thus provides the theoretical background for a number of multipath-assisted localization and tracking algorithms. More specifically, an environment model, consisting of a geometrical model (based on VA positions) and a measurement uncertainty model (based on the SINR of MPCs), yields insight in the potential location information that can be acquired at a certain position, in a certain environment. Several algorithms have been discussed that exploit such information: Maximum likelihood localization, tracking filters with data association,

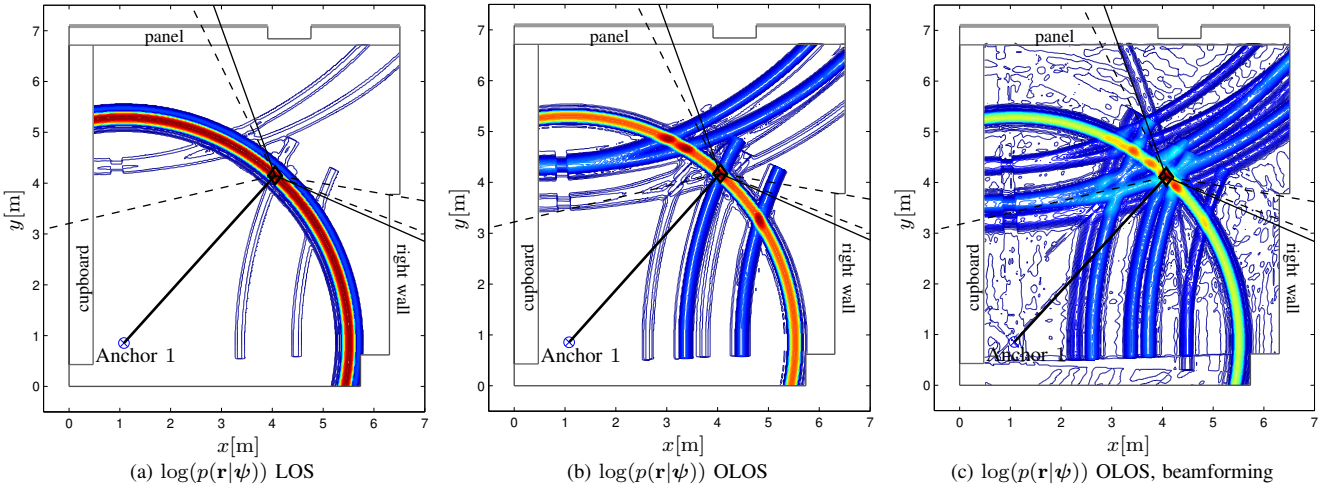

(a) $\log(p(\mathbf{r}|\boldsymbol{\psi}))$ LOS (b) $\log(p(\mathbf{r}|\boldsymbol{\psi}))$ OLOS (c) $\log(p(\mathbf{r}|\boldsymbol{\psi}))$ OLOS, beamforming

Fig. 7. Likelihood function over the floor plan for (a) LOS, (b) OLOS situation, and (c) OLOS situation with phased-array beamforming. The position error of the MLE is 2 cm and 3 cm for LOS and OLOS situations, respectively. Bold black lines show the directions to the anchors, thin black line the directions to first-order VAs, and black dashed lines the directions to second-order VAs. The black diamonds mark the estimated positions of the agent.

and algorithms for passive localization. The benefit of using this environmental information has been shown.

Future 5G mm-wave communication systems could be an ideal platform for achieving high-accuracy indoor localization with this concept. In addition to a large signal bandwidth, beamforming capabilities are envisioned for such systems, which can be exploited to make the localization and tracking more robust and efficient. It becomes feasible to obtain accurate and robust indoor localization with only a single anchor node in a room, with a system that also serves as a standard-compliant access point for 5G communications.

Note that vice-versa the environment model can be exploited by the communications system. "Location awareness" is created by providing a site-specific propagation model that can be used to improve the robustness of the radio air-interface. For example the arrival and departure angles of the most significant radio paths are encoded in the environment model, which will be useful for efficient beamsteering algorithms for communications in highly dynamic environments, extending the scope of the proposed concepts well beyond AL scenarios.

Proposed Call-outs

- A cm-accuracy indoor positioning system *alone* enables a wide range of AL applications.
- Radio technology is promising for positioning as low-power transceivers can be built at small size.
- Awareness to the signal propagation conditions enables robustness and reduces the requirements on the infrastructure.
- Multipath-assisted methods enable high-accuracy indoor localization with only a single 5G access point in a room.

Acknowledgments

The work of K. Witrisal and E. Leitinger was partly supported by the Austrian Research Promotion Agency (FFG) within the project REFlex (project number: 845630).

Appendix

Derivation of the PEB

The Cramér-Rao bound is a lower bound on the error variance of a parameter estimator. It is obtained from the second derivative of the log of the measurement likelihood function w.r.t. the estimation parameters, quantifying the curvature of this likelihood function. For an unbiased estimator, this curvature relates to the potential measurement precision [48]. Assuming zero-mean complex Gaussian noise processes, a likelihood function derived from a discrete-time version of the signal model (1) can be written as

$$f(\mathbf{r}|\boldsymbol{\psi}) \propto \exp\left\{-(\mathbf{r}-\mathbf{S}\boldsymbol{\alpha})^{\mathrm{H}}{\mathbf{C_n}}^{-1}(\mathbf{r}-\mathbf{S}\boldsymbol{\alpha})\right\} \quad (4)$$

where $\mathbf{r}$ is the received signal sampled at rate $1/T_\mathrm{s}$, the parameter vector $\boldsymbol{\psi} = [\boldsymbol{\alpha}^T,\ \boldsymbol{\tau}^T]^T$ stacks the complex amplitudes $\{\alpha_k\}$ and delays $\{\tau_k\}$, $\mathbf{S} = [\mathbf{s}_{\tau_1},\ldots,\mathbf{s}_{\tau_K}] \in \mathbb{R}^{N\times K}$ is the signal matrix containing delayed versions $\mathbf{s}_{\tau_k} = [s(-\tau_k), s(T_\mathrm{s}-\tau_k),\ldots,s((N-1)T_\mathrm{s}-\tau_k)]^\mathrm{T}$ of the sampled transmit pulse, and the matrix $\mathbf{C_n} = {\sigma_\mathrm{n}}^2\mathbf{I}_N + \mathbf{C_c} \in \mathbb{R}^{N\times N}$ denotes the co-variance matrix of the noise processes. The elements of the DM co-variance matrix are given by $[\mathbf{C_c}]_{n,m} = T_\mathrm{s}\sum_{i=0}^{N-1} S_\nu(iT_\mathrm{s})s(nT_\mathrm{s}-iT_\mathrm{s})s(mT_\mathrm{s}-iT_\mathrm{s})$; the AWGN samples have variance ${\sigma_\mathrm{n}}^2 = N_0/T_\mathrm{s}$.

A number of analytical manipulations are needed to obtain the insightful expressions (2) and (3) for the CRLB[a]. The difficulty lies in finding the inverse of the covariance matrix $\mathbf{C_n}$. Under the assumption that the useful components in (1) are non-overlapping, it is fair to assume that each of these components can be observed independently. The DM process is then treated as stationary for each MPC at a variance defined by the PDP at the MPC's corresponding excess delay, $S_\nu(\tau_k)$.

We can then use the Fourier transform to compute the inverse and obtain for the Fisher information of the k-th delay estimate the expression [27]

$$\mathbb{E}_{\mathbf{r}|\boldsymbol{\psi}}\left\{-\frac{\partial^2 \ln f(\mathbf{r}|\boldsymbol{\psi})}{\partial\tau_k\partial\tau_k}\right\} \approx 8\pi^2|\alpha_k|^2 \times \int_f f^2 \frac{|\mathrm{S}(f)|^2}{N_0 + S_\nu(\tau_k)|\mathrm{S}(f)|^2}\mathrm{d}f \overset{(\mathrm{BS})}{=} 8\pi^2\beta^2\mathrm{SINR}_k \quad (5)$$

where $\beta^2 = \int_f f^2|S(f)|^2\mathrm{d}f$ is the mean square bandwidth of (the Fourier transform $S(f)$ of) pulse $s(t)$, $\mathrm{SINR}_k = |\alpha_k|^2/(N_0 + T_\mathrm{p}S_\nu(\tau_k))$ is the SINR of the k-th MPC. The second line only holds for a block spectrum (BS) $|S(f)|^2 = T_\mathrm{p}$ for $|f| \leq 1/(2T_\mathrm{p})$; a generalized version of this equation has been derived in [27].

To compute the EFIM for the position vector from the Fisher information matrix of the parameter vector $\boldsymbol{\psi}$, we evoke the matrix inversion lemma to account for the nuisance parameters $\{\alpha_k\}$ and a parameter transformation to convert the delays $\{\tau_k\}$ to the position vector $\mathbf{p}$ [30]. The latter requires the computation of the Jacobian $\mathbf{H} = \partial\boldsymbol{\tau}/\partial\mathbf{p}$, the derivative of the delays $\{\tau_k\}$ w.r.t. position $\mathbf{p}$. It describes the variation of the delays w.r.t. the position and can assume different, scenario-dependent forms, depending on the roles of anchors and agents. General expressions for these *spatial delay gradients* have been derived in [27]. For an MPC arriving from direction ϕ_k we get $\partial\tau_k/\partial\mathbf{p} = \mathbf{e}(\phi_k)$ with unit-norm vector $\mathbf{e}(\phi_k)$ pointing in direction ϕ_k, which leads to the matrices $\mathbf{J}_r(\phi_k) = \mathbf{e}(\phi_k)\mathbf{e}^\mathrm{T}(\phi_k)$ in (3).

[a] It can be intuitively argued that (4) satisfies the regularity condition required for the CRLB derivation [48] for all points within the room: Considering a correct geometry and a sufficiently large signal bandwidth, the likelihood has a maximum at the true position whose spatial extent is small w.r.t. the room dimensions. It can be shown that the regularity condition is satisfied even without these assumptions, but this is out of scope here.

References

[1] G. Acampora, D. Cook, P. Rashidi, and A. Vasilakos, "A Survey on Ambient Intelligence in Healthcare," *Proc. IEEE*, vol. 101, no. 12, pp. 2470–2494, Dec 2013.

[2] P. Barsocchi, S. Chessa, F. Furfari, and F. Potorti, "Evaluating Ambient Assisted Living Solutions: The Localization Competition," *IEEE Pervasive Comp.*, vol. 12, no. 4, pp. 72–79, Oct 2013.

[3] P. Rashidi and A. Mihailidis, "A Survey on Ambient-Assisted Living Tools for Older Adults," *IEEE J. Biomed. Health Inform.*, vol. 17, no. 3, pp. 579–590, May 2013.

[4] M. Z. Win, A. Conti, S. Mazuelas, Y. Shen, W. M. Gifford, D. Dardari, and M. Chiani, "Network Localization and Navigation via Cooperation," *IEEE Commun. Mag.*, vol. 49, no. 5, pp. 56–62, May 2011.

[5] S. Gezici, Z. Tian, G. B. Giannakis, H. Kobayashi, A. F. Molisch, H. V. Poor, and Z. Sahinoglu, "Localization via Ultra-wideband Radios: A Look at Positioning Aspects for Future Sensor Networks," *IEEE Signal Process. Mag.*, vol. 22, no. 4, pp. 70–84, Jul. 2005.

[6] S. Bartoletti, W. Dai, A. Conti, and M. Z. Win, "A Mathematical Model for Wideband Ranging," *IEEE J. Sel. Topics Signal Process.*, vol. 9, no. 2, pp. 216–228, Mar. 2015.

[7] D. Dardari, A. Conti, U. J. Ferner, A. Giorgetti, and M. Z. Win, "Ranging with Ultrawide Bandwidth Signals in Multipath Environments," *Proc. IEEE*, vol. 97, no. 2, pp. 404–426, Feb. 2009.

[8] H. Wymeersch, J. Lien, and M. Z. Win, "Cooperative Localization in Wireless Networks," *Proc. IEEE*, vol. 97, no. 2, pp. 427–450, 2009.

[9] A. Conti, M. Guerra, D. Dardari, N. Decarli, and M. Win, "Network experimentation for cooperative localization," *IEEE J. Sel. Areas Commun.*, vol. 30, no. 2, pp. 467–475, 2012.

[10] S. Bartoletti, A. Giorgetti, M. Z. Win, and A. Conti, "Blind Selection of Representative Observations for Sensor Radar Networks," *IEEE Trans. Veh. Technol.*, vol. 64, no. 4, pp. 1388–1400, Apr. 2015.

[11] B. U. Töreyin, Y. Dedeoğlu, and A. Çetin, "HMM based falling person detection using both audio and video," in *Computer Vision in Human-Computer Interaction*, ser. Lecture Notes in Computer Science, N. Sebe, M. Lew, and T. Huang, Eds. Springer Berlin Heidelberg, 2005, vol. 3766, pp. 211–220.

[12] D. Weinland, R. Ronfard, and E. Boyer, "A survey of vision-based methods for action representation, segmentation and recognition," *Computer Vision and Image Understanding*, vol. 115, no. 2, pp. 224 – 241, 2011. [Online]. Available: http://www.sciencedirect.com/science/article/pii/S1077314210002171

[13] Y. Li, K. Ho, and M. Popescu, "A microphone array system for automatic fall detection," *IEEE Trans. Biomed. Eng.*, vol. 59, no. 5, pp. 1291–1301, May 2012.

[14] M. Z. Win and R. A. Scholtz, "Impulse radio: How it works," *IEEE Commun. Lett.*, vol. 2, no. 2, pp. 36–38, Feb. 1998.

[15] ——, "Ultra-Wide Bandwidth Time-Hopping Spread-Spectrum Impulse Radio for Wireless Multiple-Access Communications," *IEEE Trans. Commun.*, vol. 48, no. 4, pp. 679–691, Apr. 2000.

[16] ——, "Characterization of Ultra-Wide Bandwidth Wireless Indoor Communications Channel: A Communication-Theoretic View," *IEEE J. Sel. Areas Commun.*, vol. 20, no. 9, pp. 1613–1627, Dec. 2002.

[17] A. F. Molisch, D. Cassioli, C.-C. Chong, S. Emami, A. Fort, B. Kannan, J. Karedal, J. Kunisch, H. Schantz, K. Siwiak, and M. Z. Win, "A Comprehensive Standardized Model for Ultrawideband Propagation Channels," *IEEE Trans. Antennas Propag.*, vol. 54, no. 11, pp. 3151–3166, Nov. 2006.

[18] P. Meissner, E. Leitinger, and K. Witrisal, "UWB for Robust Indoor Tracking: Weighting of Multipath Components for Efficient Estimation," *IEEE Wireless Commun. Lett.*, vol. 3, no. 5, pp. 501–504, Oct. 2014.

[19] S. Wyne, K. Haneda, S. Ranvier, F. Tufvesson, and A. Molisch, "Beamforming Effects on Measured mm-Wave Channel Characteristics," *IEEE Trans. Wireless Commun.*, vol. 10, no. 11, pp. 3553–3559, November 2011.

[20] C. Gustafson, K. Haneda, S. Wyne, and F. Tufvesson, "On mm-Wave Multipath Clustering and Channel Modeling," *IEEE Trans. Antennas Propag.*, vol. 62, no. 3, pp. 1445–1455, March 2014.

[21] A. Molisch and F. Tufvesson, "Propagation channel models for next-generation wireless communications systems," *IEICE Transactions on Communications*, vol. E97B, no. 10, pp. 2022–2034, 2014.

[22] *ISO/IEC/IEEE International Standard for Information technology–Telecommunications and information exchange between systems–Local and metropolitan area networks–Specific requirements-Part 11: Wireless LAN Medium Access Control (MAC) and Physical Layer (PHY) Specifications Amendment 3: Enhancements for Very High Throughput in the 60 GHz Band (adoption of IEEE Std 802.11ad-2012)*, IEEE Std., 2014.

[23] R. Di Taranto, S. Muppirisetty, R. Raulefs, D. Slock, T. Svensson, and H. Wymeersch, "Location-Aware Communications for 5G Networks: How location information can improve scalability, latency, and robustness of 5G," *IEEE Signal Process. Mag.*, vol. 31, no. 6, pp. 102–112, Nov 2014.

[24] E. Leitinger, M. Froehle, P. Meissner, and K. Witrisal, "Multipath-Assisted Maximum-Likelihood Indoor Positioning using UWB Signals," in *IEEE ICC Workshop on Advances in Network Localization and Navigation (ANLN)*, 2014, pp. 170–175.

[25] P. Setlur, G. Smith, F. Ahmad, and M. Amin, "Target Localization with a Single Sensor via Multipath Exploitation," *IEEE Trans. Aerosp. Electron. Syst.*, vol. 48, no. 3, pp. 1996–2014, July 2012.

[26] M. Leigsnering, M. Amin, F. Ahmad, and A. Zoubir, "Multipath Exploitation and Suppression for SAR Imaging of Building Interiors: An overview of recent advances," *IEEE Signal Process. Mag.*, vol. 31, no. 4, pp. 110–119, 2014.

[27] E. Leitinger, P. Meissner, C. Ruedisser, G. Dumphart, and K. Witrisal, "Evaluation of position-related information in multipath components for indoor positioning," *IEEE J. Sel. Areas Commun.*, vol. 33, no. 11, pp. 2313–2328, Nov 2015.

[28] Y. Shen and M. Win, "On the Use of Multipath Geometry for Wideband Cooperative Localization," in *IEEE Global Telecommunications Conference (GLOBECOM)*, 2009, pp. 1–6.
[29] D. B. Jourdan, D. Dardari, and M. Z. Win, "Position Error Bound for UWB Localization in Dense Cluttered Environments," *IEEE Trans. Aerosp. Electron. Syst.*, vol. 44, no. 2, pp. 613–628, Apr. 2008.
[30] Y. Shen and M. Win, "Fundamental Limits of Wideband Localization; Part I: A General Framework," *IEEE Trans. Inf. Theory*, vol. 56, no. 10, pp. 4956–4980, 2010.
[31] Y. Shen, H. Wymeersch, and M. Win, "Fundamental Limits of Wideband Localization - Part II: Cooperative Networks," *IEEE Trans. Inf. Theory*, vol. 56, no. 10, pp. 4981–5000, 2010.
[32] Y. Qi, H. Kobayashi, and H. Suda, "Analysis of wireless geolocation in a non-line-of-sight environment," *IEEE Trans. Wireless Commun.*, vol. 5, no. 3, pp. 672–681, 2006.
[33] P. Meissner, "Multipath-Assisted Indoor Positioning," Ph.D. dissertation, Graz University of Technology, 2014.
[34] E. Leitinger, P. Meissner, M. Lafer, and K. Witrisal, "Simultaneous Localization and Mapping using Multipath Channel Information," in *IEEE ICC Workshop on Advances in Network Localization and Navigation (ANLN)*, June 2015, pp. 754–760.
[35] D. Schuhmacher, B.-T. Vo, and B.-N. Vo, "A Consistent Metric for Performance Evaluation of Multi-Object Filters," *IEEE Trans. Signal Process.*, vol. 56, no. 8, pp. 3447–3457, 2008.
[36] S. Haykin, "Cognitive radar: a way of the future," *IEEE Signal Process. Mag.*, vol. 23, pp. 30–40, Jan. 2006.
[37] K.Witrisal, E. Leitinger, P. Meissner, and D. Arnitz, "Cognitive radar for the localization of RFID transponders in dense multipath environments," in *IEEE Radar Conference*, Ottawa, Canada, Apr. 2013.
[38] H. Durrant-Whyte and T. Bailey, "Simultaneous localization and mapping: part I," *IEEE Robot. Autom. Mag.*, vol. 13, no. 2, pp. 99–110, June 2006.
[39] Y. Kuang, K. Astrom, and F. Tufvesson, "Single antenna anchor-free UWB positioning based on multipath propagation," in *IEEE International Conference on Communications (ICC)*, June 2013, pp. 5814–5818.
[40] J. Salmi and A. F. Molisch, "Propagation Parameter Estimation, Modeling and Measurements for Ultrawideband MIMO Radar," *IEEE Trans. Antennas Propag.*, vol. 59, no. 11, pp. 4257–4267, 2011.
[41] J. Shen and A. Molisch, "Estimating multiple target locations in multipath environments," *IEEE Trans. Wireless Commun.*, vol. 13, no. 8, pp. 4547–4559, 2014.
[42] R. Zetik, J. Sachs, and R. Thoma, "UWB short-range radar sensing - The architecture of a baseband, pseudo-noise UWB radar sensor," *IEEE Instrum. Meas. Mag.*, vol. 10, no. 2, pp. 39–45, April 2007.
[43] F. Guidi, A. Guerra, and D. Dardari, "Personal Mobile Radars with Millimeter-Wave Massive Arrays for Indoor Mapping," *IEEE Trans. Mobile Comput.*, vol. PP, no. 99, pp. 1–1, 2015.
[44] W. Hong, K.-H. Baek, Y. Lee, Y. Kim, and S.-T. Ko, "Study and prototyping of practically large-scale mmWave antenna systems for 5G cellular devices," *IEEE Commun. Mag.*, vol. 52, no. 9, pp. 63–69, Sep. 2014.
[45] M. Zhu, J. Vieira, Y. Kuang, K. Astrom, A. F. Molisch, and F. Tufvesson, "Tracking and positioning using phase information from estimated multipath components," in *IEEE ICC Workshop on Advances in Network Localization and Navigation (ANLN)*, London, UK, Jun. 2015, pp. 712–717.
[46] H. El-Sayed, G. Athanasiou, and C. Fischione, "Evaluation of localization methods in millimeter-wave wireless systems," in *IEEE 19th International Workshop on Computer Aided Modeling and Design of Communication Links and Networks (CAMAD)*, Dec 2014, pp. 345–349.
[47] A. Guerra, F. Guidi, and D. Dardari, "Position and orientation error bound for wideband massive antenna arrays," in *IEEE ICC Workshop on Advances in Network Localization and Navigation (ANLN)*, 2015, pp. 853–858.
[48] S. Kay, *Fundamentals of Statistical Signal Processing: Estimation Theory*. Prentice Hall Signal Processing Series, 1993.

Klaus Witrisal (S'98–M'03) received his Ph.D. degree from Delft University of Technology, The Netherlands, in 2002 and the Habilitation from Graz University of Technology, Austria in 2009, where he is currently an Associate Professor. He has been an associate editor of IEEE Communications Letters, a co-chair of the TWG "Indoor" of the COST Action IC1004, a leading chair of the IEEE Workshop on Advances in Network Localization and Navigation (ANLN), and TPC (co)-chair of the Workshop on Positioning, Navigation and Communication (WPNC). His research interests are in signal processing for wireless communications, propagation channel modeling, and positioning. He is a member of the IEEE.

Paul Meissner (S'10–M'15) received the B.Sc. and Dipl.-Ing. degree (with distinction) in information and computer engineering from Graz University of Technology, Graz, Austria in 2006 and 2009, respectively. He received the Ph.D. degree in electrical engineering (with distinction) from the same university in 2014. In 2015, he received the award of the Association of German Engineers for his Ph.D. thesis. Dr. Meissner is currently a postdoctoral researcher at the Signal Processing and Speech Communication Laboratory (SPSC) of Graz University of Technology, Graz, Austria. His research topics include statistical signal processing, localization, estimation theory and channel modeling.

Erik Leitinger (S'12) was born in Graz, Austria, on March 27, 1985. He received the B.Sc. degree (with distinction) in electrical engineering from Graz University of Technology, Graz, Austria, in 2009, and the Dipl.-Ing. degree (with distinction) in electrical engineering from Graz University of Technology, Graz, Austria, in 2012. He is currently pursuing his PhD degree at the Signal Processing and Speech Communication Laboratory (SPSC) of Graz University of Technology, Graz, Austria focused on UWB wireless communication, indoor-positioning, estimation theory, Bayesian inference and statistical signal processing.

Yuan Shen received the Ph.D. degree and the S.M. degree in EECS from MIT in 2014 and 2008, respectively, and the B.E. degree (with highest honor) in EE from Tsinghua University in 2005. He is now an Associate Professor with the EE Department at Tsinghua University. His research focuses on network localization and navigation, inference techniques, resource allocation, and intrinsic wireless secrecy. Dr. Shen is elected Secretary (2015-2017) for the IEEE ComSoc Radio Communications Committee. He is serving as an Editor for the IEEE Communications Letters, Guest-Editor for the International Journal of Distributed Sensor Networks (2015).

Carl Gustafson received the Ph.D. degree in Radio Systems from the department of Electrical and Information Technology, Lund University, where he now is working as a post-doctoral researcher. His main research interests include channel measurements and modeling for mm-wave wireless systems, for cellular systems operating above 6 GHz and for vehicular wireless communication systems. Other research interests include massive MIMO, antenna array processing, statistical estimation and electromagnetic wave propagation.

Fredrik Tufvesson received his Ph.D. in 2000 from Lund University in Sweden. After two years at a startup company, he joined the department of Electrical and Information Technology at Lund University, where he is now professor of radio systems. His main research interests are channel modelling, measurements and characterization for wireless communication, with applications in various areas such as massive MIMO, UWB, mm wave communication, distributed antenna systems, vehicular communication systems and radio based positioning. Fredrik is heading the wireless propagation group at the department and has authored and co-authored around 50 journal papers and 120 conference papers.

Katsuyuki Haneda (S'03-M'07) received the Doctor of Engineering from the Tokyo Institute of Technology, Japan, in 2007. He is presently as an assistant professor in the Aalto University School of Electrical Engineering. Dr. Haneda was the recipient of the best paper awards in VTC2013-Spring and EuCAP2013. Dr. Haneda has been serving as an associate editor for the IEEE Transactions on Antennas and Propagation since 2012 and as an editor of the IEEE Transactions on Wireless Communications since 2013. His current research activity includes millimeter-wave radios, wireless for medical and post-disaster scenarios, radio wave propagation prediction, and in-band full-duplex radio technologies.

Davide Dardari (M'95-SM'07) is an Associate Professor at the University of Bologna, Italy. Since 2005, he has been a Research Affiliate at Massachusetts Institute of Technology, USA. His interests are on wireless communications, localization techniques and distributed signal processing. He received the IEEE Aerospace and Electronic Systems Society's M. Barry Carlton Award (2011) and the IEEE Communications Society Fred W. Ellersick Prize (2012). He is Senior Member of the IEEE where he was the Chair for the Radio Communications Committee of the IEEE Communication Society. He served as an Editor for IEEE Transactions on Wireless Communications from 2006 to 2012.

Andreas F. Molisch is Professor of Electrical Engineering at the University of Southern California, where he is also currently Director of the Communication Sciences Institute. His research interest is wireless communications, with emphasis on wireless propagation channels, multi-antenna systems, ultrawideband signaling and localization, novel cellular architectures, and cooperative communications. He is the author of four books, 16 book chapters, more than 420 journal and conference papers, as well as 70 patents. He is a Fellow of IEEE, AAAS, and IET, Member of the Austrian Academy of Sciences, and recipient of numerous awards.

Andrea Conti (S'99-M'01-SM'11) is an associate professor at the University of Ferrara. His research interests involve theory and experimentation

of wireless systems and networks including network localization, adaptive diversity communications, cooperative relaying techniques, and network secrecy. He has been elected Chair of the IEEE Communications Society Radio Communications Committee and an IEEE Distinguished Lecturer. He received the HTE Puskas Tivadar Medal, the IEEE Fred W. Ellersick Prize, and the IEEE Stephen O. Rice Prize in the Field of Communications Theory.

Moe Win (S'85-M'87-SM'97-F'04) (moewin@mit.edu) is a professor at the Massachusetts Institute of Technology (MIT) and the founding director of the Wireless Communication and Network Sciences Laboratory. Prior to joining MIT, he was with AT&T Research Laboratories for five years and with the Jet Propulsion Laboratory for seven years. His current research topics include network localization and navigation, network interference exploitation, intrinsic wireless secrecy, adaptive diversity techniques, and ultra-wideband systems. He is an elected Fellow of the AAAS and the IET, and was an IEEE Distinguished Lecturer.

Bibliography

[1] P. Meissner, "Multipath-Assisted Indoor Positioning," Ph.D. dissertation, Graz University of Technology, 2014.

[2] B. Hofmann-Wellenhof, H. Lichtenegger, and E. Wasle, *GNSS – Global Navigation Satellite Systems*. Springer Press, 2008.

[3] J. Pearl, *Probabilistic Reasoning in Intelligent Systems: Networks of Plausible Inference*. San Francisco, CA, USA: Morgan Kaufmann Publishers Inc., 1988.

[4] P. Gregory, *Bayesian Logical Data Analysis for the Physical Sciences*. New York, NY, USA: Cambridge University Press, 2005.

[5] D. S. Sivia and J. Skilling, *Data analysis : a Bayesian tutorial*, ser. Oxford science publications. Oxford, New York: Oxford University Press, 2006.

[6] F. Pernkopf, R. Peharz, and S. Tschiatschek, *Introduction to Probabilistic Graphical Models*, 2014, pp. 989–1064. [Online]. Available: http://mrw.elsevier.com/sigp/menu.htm

[7] D. Dardari, E. Falletti, and M. Luise, *Satellite and Terrestrial Radio Positioning Techniques - A signal processing perspective*. Elsevier Academic Press, 2012.

[8] M. Z. Win, A. Conti, S. Mazuelas, Y. Shen, W. M. Gifford, D. Dardari, and M. Chiani, "Network Localization and Navigation via Cooperation," *IEEE Commun. Mag.*, vol. 49, no. 5, pp. 56–62, May 2011.

[9] Y. Shen, S. Mazuelas, and M. Win, "Network Navigation: Theory and Interpretation," *Selected Areas in Communications, IEEE Journal on*, vol. 30, no. 9, pp. 1823–1834, Oct. 2012.

[10] A. Conti, M. Guerra, D. Dardari, N. Decarli, and M. Win, "Network Experimentation for Cooperative Localization," *Selected Areas in Communications, IEEE Journal on*, vol. 30, no. 2, pp. 467–475, February 2012.

[11] A. Conti, D. Dardari, M. Guerra, L. Mucchi, and M. Win, "Experimental Characterization of Diversity Navigation," *Systems Journal, IEEE*, vol. 8, no. 1, pp. 115–124, March 2014.

[12] R. Mautz, "Indoor Positioning Technologies," Habilitation Thesis, ETH Zurich, 2012.

[13] H. L. Van Trees, *Detection, Estimation and Modulation, Part I*. Wiley Press, 1968.

[14] S. Kay, *Fundamentals of Statistical Signal Processing: Estimation Theory.* Prentice Hall Signal Processing Series, 1993.

[15] M. Win and R. Scholtz, "Characterization of Ultra-Wide Bandwidth Wireless Indoor Channels: a Communication-Theoretic View," *Selected Areas in Communications, IEEE Journal on*, vol. 20, no. 9, pp. 1613 – 1627, dec 2002.

[16] ——, "Impulse Radio: How it Works," *IEEE Commun. Lett.*, vol. 2, no. 2, pp. 36–38, Feb. 1998.

[17] ——, "Ultra-Wide Bandwidth Time-Hopping Spread-Spectrum Impulse Radio for Wireless Multiple-Access Communications," *IEEE Trans. Commun.*, vol. 48, no. 4, pp. 679–691, Apr. 2000.

[18] S. Gezici, Z. Tian, G. B. Giannakis, H. Kobayashi, A. F. Molisch, H. V. Poor, and Z. Sahinoglu, "Localization via Ultra-Wideband Radios: A Look at Positioning Aspects for Future Sensor Networks," *IEEE Signal Processing Magazine*, vol. 22, no. 4, pp. 70–84, Jul. 2005.

[19] "IEEE Standard for Information Technology- Telecommunications and Information Exchange Between Systems-Local and Metropolitan Area Networks-Specific Requirements-Part 11: Wireless LAN Medium Access Control (MAC) and Physical Layer (PHY) Specifications," *IEEE Std 802.11-1997*, 1997.

[20] S. Mazuelas, A. Bahillo, R. Lorenzo, P. Fernandez, F. Lago, E. Garcia, J. Blas, and E. Abril, "Robust Indoor Positioning Provided by Real-Time RSSI Values in Unmodified WLAN Networks," *Selected Topics in Signal Processing, IEEE Journal of*, vol. 3, no. 5, pp. 821–831, Oct 2009.

[21] C. Yang and H.-R. Shao, "WiFi-based Indoor Positioning," *Communications Magazine, IEEE*, vol. 53, no. 3, pp. 150–157, March 2015.

[22] A. Gaber and A. Omar, "A Study of Wireless Indoor Positioning Based on Joint TDOA and DOA Estimation Using 2-D Matrix Pencil Algorithms and IEEE 802.11ac," *Wireless Communications, IEEE Transactions on*, vol. 14, no. 5, pp. 2440–2454, May 2015.

[23] M. Ficco, C. Esposito, and A. Napolitano, "Calibrating Indoor Positioning Systems with Low Efforts," *Mobile Computing, IEEE Transactions on*, vol. 13, no. 4, pp. 737–751, April 2014.

[24] Z. Sahinoglu, S. Gezici, and I. Guvenc, *Ultra-wideband Positioning Systems – Theoretical Limits, Ranging Algorithms and Protocols.* Cambridge University Press, 2008.

[25] D. Dardari, A. Conti, U. Ferner, A. Giorgetti, and M. Win, "Ranging with Ultrawide Bandwidth Signals in Multipath Environments," *Proceedings of the IEEE*, vol. 97, no. 2, pp. 404–426, 2009.

[26] S. Bartoletti, W. Dai, A. Conti, and M. Win, "A Mathematical Model for Wideband Ranging," *Selected Topics in Signal Processing, IEEE Journal of*, vol. 9, no. 2, pp. 216–228, March 2015.

[27] J. Ziv and M. Zakai, "Some Lower Bounds on Signal Parameter Estimation," *Information Theory, IEEE Transactions on*, vol. 15, no. 3, pp. 386–391, May 1969.

[28] C. Steiner, "Location Fingerprinting for Ultra-Wideband Systems - The Key to Efficient and Robust Localization ," Ph.D. dissertation, PhD Thesis, 2010. [Online]. Available: http://www.nari.ee.ethz.ch/wireless//pubs/p/Diss_CS

[29] C. Steiner and A. Wittneben, "Efficient Training Phase for Ultrawideband-Based Location Fingerprinting Systems," *Signal Processing, IEEE Transactions on*, vol. 59, no. 12, pp. 6021–6032, Dec 2011.

[30] J. Borish, "Extension of the Image Model to arbitrary Polyhedra," *The Journal of the Acoustical Society of America*, 1984.

[31] J. Kunisch and J. Pamp, "An Ultra-Wideband space-variant Multipath Indoor Radio Channel Model," in *Ultra Wideband Systems and Technologies, 2003 IEEE Conference on*, Nov 2003, pp. 290–294.

[32] Y. Shen and M. Win, "On the Use of Multipath Geometry for Wideband Cooperative Localization," in *Global Telecommunications Conference, 2009. GLOBECOM 2009. IEEE*, Dec. 2009, pp. 1–6.

[33] P. Setlur, G. Smith, F. Ahmad, and M. Amin, "Target Localization with a Single Sensor via Multipath Exploitation," *Aerospace and Electronic Systems, IEEE Transactions on*, vol. 48, no. 3, pp. 1996–2014, JULY 2012.

[34] R. Parhizkar, I. Dokmanic, and M. Vetterli, "Single-Channel Indoor Microphone Localization," in *Acoustics, Speech and Signal Processing (ICASSP), 2014 IEEE International Conference on*, May 2014, pp. 1434–1438.

[35] M. Leigsnering, M. Amin, F. Ahmad, and A. Zoubir, "Multipath Exploitation and Suppression for SAR Imaging of Building Interiors: An overview of recent advances," *Signal Processing Magazine, IEEE*, vol. 31, no. 4, pp. 110–119, July 2014.

[36] I. Dokmanic, R. Parhizkar, A. Walther, Y. M. Lu, and M. Vetterli, "Acoustic Echoes Reveal Room Shape," *Proceedings of the National Academy of Sciences*, 2013.

[37] I. Dokmanic, "Listening to Distances and Hearing Shapes," Ph.D. dissertation, Ecole polytechnique federale de Lausanne (EPFL), Lausanne, 2015.

[38] S. Marano and, W. Gifford, H. Wymeersch, and M. Win, "Nlos identification and mitigation for localization based on uwb experimental data," *Selected Areas in Communications, IEEE Journal on*, vol. 28, no. 7, pp. 1026 –1035, september 2010.

[39] H. Wymeersch, S. Marano, W. Gifford, and M. Win, "A Machine Learning Approach to Ranging Error Mitigation for UWB Localization," *Communications, IEEE Transactions on*, vol. 60, no. 6, pp. 1719–1728, June 2012.

[40] H. Lu, S. Mazuelas, and M. Win, "Ranging Likelihood for Wideband Wireless Localization," in *Communications (ICC), 2013 IEEE International Conference on*, June 2013, pp. 5804–5808.

[41] H. Wymeersch, J. Lien, and M. Win, "Cooperative Localization in Wireless Networks," *Proceedings of the IEEE*, vol. 97, no. 2, pp. 427 –450, Feb. 2009.

[42] Y. Shen, H. Wymeersch, and M. Win, "Fundamental Limits of Wideband Localization; Part II: Cooperative Networks," *Information Theory, IEEE Transactions on*, vol. 56, no. 10, pp. 4981 –5000, Oct. 2010.

[43] F. Meyer, O. Hlinka, H. Wymeersch, E. Riegler, and F. Hlawatsch, "Cooperative Simultaneous Localization and Tracking in Mobile Agent Networks," *Signal Processing, IEEE Transactions on*, vol. abs/1403.1824, 2014, submitted. [Online]. Available: http://arxiv.org/abs/1403.1824

[44] W. Dai, Y. Shen, and M. Win, "Energy-Efficient Network Navigation Algorithms," *Selected Areas in Communications, IEEE Journal on*, vol. PP, no. 99, pp. 1–1, 2015.

[45] P. Meissner and K. Witrisal, "Analysis of position-related information in measured UWB indoor channels," in *Antennas and Propagation (EUCAP), 2012 6th European Conference on*, March 2012, pp. 6–10.

[46] Y. Shen and M. Win, "Fundamental Limits of Wideband Localization; Part I: A General Framework," *Information Theory, IEEE Transactions on*, vol. 56, no. 10, pp. 4956–4980, Oct. 2010.

[47] Y. Qi, H. Kobayashi, and H. Suda, "Analysis of Wireless Geolocation in a Non-Line-of-Sight Environment," *IEEE Transactions on Wireless Communications*, vol. 5, no. 3, pp. 672 – 681, 2006.

[48] H. Godrich, A. Haimovich, and R. Blum, "Target Localization Accuracy Gain in MIMO Radar-Based Systems," *Information Theory, IEEE Transactions on*, vol. 56, no. 6, pp. 2783 –2803, June 2010.

[49] T. Santos, F. Tufvesson, and A. Molisch, "Modeling the Ultra-Wideband Outdoor Channel: Model Specification and Validation," *Wireless Communications, IEEE Transactions on*, vol. 9, no. 6, pp. 1987 –1997, june 2010.

[50] T. Santos, J. Karedal, P. Almers, F. Tufvesson, and A. Molisch, "Modeling the Ultra-Wideband Outdoor Channel: Measurements and pParameter Extraction Method," *Wireless Communications, IEEE Transactions on*, vol. 9, no. 1, pp. 282 –290, january 2010.

[51] J. Salmi and A. Molisch, "Propagation Parameter Estimation, Modeling and Measurements for Ultrawideband MIMO Radar," *Antennas and Propagation, IEEE Transactions on*, vol. 59, no. 11, pp. 4257 –4267, nov. 2011.

[52] J. Salmi, A. Richter, and V. Koivunen, "Detection and Tracking of MIMO Propagation Path Parameters Using State-Space Approach," *Signal Processing, IEEE Transactions on*, vol. 57, no. 4, pp. 1538–1550, April 2009.

[53] A. Richter, "Estimation of Radio Channel Parameters: Models and Algorithms," Ph.D. dissertation, Ilmenau University of Technology, 2005.

[54] A. Richter and R. Thoma, "Joint Maximum Likelihood Estimation of Specular Paths and Distributed Diffuse Scattering," in *Vehicular Technology Conference, 2005. VTC 2005-Spring. 2005 IEEE 61st*, vol. 1, 2005, pp. 11–15 Vol. 1.

[55] N. Michelusi, U. Mitra, A. Molisch, and M. Zorzi, "UWB Sparse/Diffuse Channels, Part I: Channel Models and Bayesian Estimators," *Signal Processing, IEEE Transactions on*, vol. 60, no. 10, pp. 5307–5319, 2012.

[56] ——, "UWB Sparse/Diffuse Channels, Part II: Estimator Analysis and Practical Channels," *Signal Processing, IEEE Transactions on*, vol. 60, no. 10, pp. 5320–5333, 2012.

[57] N. Decarli, F. Guidi, and D. Dardari, "A Novel Joint RFID and Radar Sensor Network for Passive Localization: Design and Performance Bounds," *Selected Topics in Signal Processing, IEEE Journal of*, vol. 8, no. 1, pp. 80–95, Feb 2014.

[58] J. Karedal, S. Wyne, P. Almers, F. Tufvesson, and A. Molisch, "A Measurement-Based Statistical Model for Industrial Ultra-Wideband Channels," *Wireless Communications, IEEE Transactions on*, vol. 6, no. 8, pp. 3028–3037, Aug. 2007.

[59] K. Witrisal and P. Meissner, "Performance Bounds for Multipath-Assisted Indoor Navigation and Tracking (MINT)," in *Communications (ICC), 2012 IEEE International Conference on*, June 2012, pp. 4321–4325.

[60] H. Durrant-Whyte and T. Bailey, "Simultaneous Localization and Mapping: Part I," *Robotics Automation Magazine, IEEE*, vol. 13, no. 2, pp. 99 –110, june 2006.

[61] T. Bailey and H. Durrant-Whyte, "Simultaneous Localization and Mapping (SLAM): Part II," *Robotics Automation Magazine, IEEE*, vol. 13, no. 3, pp. 108 –117, sept. 2006.

[62] J. Mullane, B.-N. Vo, and M. Adams, "Rao-Blackwellised PHD SLAM," in *Robotics and Automation (ICRA), 2010 IEEE International Conference on*, may 2010, pp. 5410 –5416.

[63] J. Mullane, B.-N. Vo, M. Adams, and B.-T. Vo, "A Random-Finite-Set Approach to Bayesian SLAM," *Robotics, IEEE Transactions on*, vol. 27, no. 2, pp. 268–282, April 2011.

[64] ——, *Random Finite Sets for Robot Mapping & SLAM: New Concepts in Autonomous Robotic Map Representations.* Springer Publishing Company, Incorporated, 2013.

[65] R. Mahler, ""Statistics 101" for Multisensor, Multitarget Data Fusion," *Aerospace and Electronic Systems Magazine, IEEE*, vol. 19, no. 1, pp. 53–64, Jan 2004.

[66] ——, ""Statistics 102" for Multisource-Multitarget Detection and Tracking," *Selected Topics in Signal Processing, IEEE Journal of*, vol. 7, no. 3, pp. 376–389, 2013.

[67] ——, *Statistical Multisource-Multitarget Information Fusion.* Norwood, MA, USA: Artech House, Inc., 2007.

[68] R. Perharz, "Foundations of Sum-Product Neworks for Probabilistic Modeling," Ph.D. dissertation, Graz University of Technology.

[69] Y. Bar-Shalom and T. Fortmann, *Tracking and Data Association.* Academic Press, 1988.

[70] S. Thrun, W. Burgard, and D. Fox, *Probabilistic Robotics (Intelligent Robotics and Autonomous Agents).* The MIT Press, 2005.

[71] T. Bailey, J. Nieto, J. Guivant, M. Stevens, and E. Nebot, "Consistency of the EKF-SLAM Algorithm," in *Intelligent Robots and Systems, 2006 IEEE/RSJ International Conference on*, 2006, pp. 3562–3568.

[72] C. Gentner and T. Jost, "Indoor Positioning using Time Difference of Arrival between Multipath Components," in *International Conference on Indoor Positioning and Indoor Navigation (IPIN)*, Oct 2013, pp. 1–10.

[73] T. Deissler and J. Thielecke, "UWB SLAM with Rao-Blackwellized Monte Carlo Data Association," in *Indoor Positioning and Indoor Navigation (IPIN), 2010 International Conference on*, 2010.

[74] S. Haykin, Y. Xue, and P. Setoodeh, "Cognitive Radar: Step Toward Bridging the Gap Between Neuroscience and Engineering," *Proceedings of the IEEE*, vol. 100, no. 11, pp. 3102 –3130, nov. 2012.

[75] S. Haykin and J. Fuster, "On Cognitive Dynamic Systems: Cognitive Neuroscience and Engineering Learning From Each Other," *Proceedings of the IEEE*, vol. 102, no. 4, pp. 608–628, April 2014.

[76] S. Haykin, "Cognitive Radar: A way of the future," *Signal Processing Magazine, IEEE*, vol. 23, no. 1, pp. 30 – 40, jan. 2006.

[77] S. Haykin, M. Fatemi, P. Setoodeh, and Y. Xue, "Cognitive Control," *Proceedings of the IEEE*, vol. 100, no. 12, pp. 3156 –3169, dec. 2012.

[78] J. M. Fuster, *Cortex and Mind - Unifying Cognition.* Oxford University Press, 2003.

[79] M. Fatemi and S. Haykin, "Cognitive Control: Theory and Application," *Access, IEEE*, vol. 2, pp. 698–710, 2014.

[80] E. Leitinger, B. Geiger, and K. Witrisal, "Capacity and Capacity-Achieving Input Distribution of the Energy Detector," in *Ultra-Wideband (ICUWB), 2012 IEEE International Conference on*, sept. 2012, pp. 57 –61.

[81] M. Gan, P. Meissner, F. Mani, E. Leitinger, M. Froehle, C. Oestges, K. Witrisal, and T. Zemen, "Calibration of Indoor UWB Sub-band Divided Ray Tracing Using Multiobjective Simulated Annealing," in *IEEE ICC*, Sydney, 2014.

[82] ——, "Low-Complexity Sub-band Divided Ray Tracing for UWB Indoor Channels," in *IEEE WCNC*, Sydney, 2014.

[83] P. Meissner, E. Leitinger, M. Froehle, and K. Witrisal, "Accurate and Robust Indoor Localization Systems Using Ultra-wideband Signals," in *European Navigation Conference (ENC)*, Vienna, Austria, 2013. [Online]. Available: http://arxiv.org/abs/1304.7928

[84] P. Meissner, E. Leitinger, M. Lafer, and K. Witrisal, "Method, device and system for indoor localization and tracking using ultrawideband radio signals," Patent 14 171 612.6, Jun. 6., 2014, patent filed.

[85] R. Liepins, "Acoustic Source Localization using Reflected Signals," Master's thesis, Graz University of Technology, 2014.

[86] M. Lafer, "Real-Time Multipath-Assisted Indoor-Localization using a Channel Sounder," Master's thesis, Graz University of Technology, 2014.

[87] G. Dumphart, "Performance Bounds for Anchorless Cooperative Indoor Localization exploiting Multipath," Master's thesis, Graz University of Technology, 2014.

[88] C. Rüdisser, "Synchronisation for Multipath-assisted Indoor Localization and Tracking," Master's thesis, Graz University of Technology, 2014.

[89] A. Molisch, *Wireless Communications*. Wiley-IEEE Press, 2005.

[90] ——, "UltrawidebandPropagation Channels-Theory, Measurement, and Modeling," *Vehicular Technology, IEEE Transactions on*, vol. 54, no. 5, pp. 1528–1545, Sept. 2005.

[91] ——, "Ultra-Wide-Band Propagation Channels," *Proceedings of the IEEE*, vol. 97, no. 2, pp. 353–371, Feb. 2009.

[92] H. Wymeersch, "The Impact of Cooperative Localization on Achieving higher-level Goals," in *Communications Workshops (ICC), 2013 IEEE International Conference on*, June 2013, pp. 1–5.

[93] F. Meyer, H. Wymeersch, M. Frohle, and F. Hlawatsch, "Distributed Estimation With Information-Seeking Control in Agent Networks," *Selected Areas in Communications, IEEE Journal on*, vol. 33, no. 11, pp. 2439–2456, Nov 2015.

[94] B. Grocholsky and B. Grocholsky, "Information-Theoretic Control of Multiple Sensor Platforms," Ph.D. dissertation, Department of Aerospace, Mechatronic and Mechanical Engineering, 2002.

[95] K. Chaloner and I. Verdinelli, "Bayesian Experimental Design: A Review," *Statistical Science*, vol. 10, no. 3, pp. pp. 273–304, 1995. [Online]. Available: http://www.jstor.org/stable/2246015

[96] C. Shannon, "A Mathematical Theory of Communication," *Bell System Technical Journal, The*, vol. 27, no. 4, pp. 623–656, Oct 1948.

[97] T. M. Cover and J. A. Thomas, *Elements of Information Theory (Wiley Series in Telecommunications and Signal Processing)*. Wiley-Interscience, 2006.

[98] G. Hoffmann and C. Tomlin, "Mobile Sensor Network Control Using Mutual Information Methods and Particle Filters," *Automatic Control, IEEE Transactions on*, vol. 55, no. 1, pp. 32–47, Jan 2010.

[99] B. J. Julian, M. Angermann, M. Schwager, and D. Rus, "Distributed Robotic Sensor Networks: An Information-theoretic Approach," *Int. J. Rob. Res.*, vol. 31, no. 10, pp. 1134–1154, Sep. 2012. [Online]. Available: http://dx.doi.org/10.1177/0278364912452675

[100] P. Carbone, A. Cazzorla, P. Ferrari, A. Flammini, A. Moschitta, S. Rinaldi, T. Sauter, and E. Sisinni, "Low complexity uwb radios for precise wireless sensor network synchronization," *Instrumentation and Measurement, IEEE Transactions on*, vol. 62, no. 9, pp. 2538–2548, Sept 2013.

[101] G. Steinböck, T. Pedersen, B. Fleury, W. Wang, and R. Raulefs, "Distance Dependent Model for the Delay Power Spectrum of In-room Radio Channels," *IEEE Transactions on Antennas and Propagation*, vol. 61, no. 8, pp. 4327–4340, Aug 2013.

[102] P. Meissner, E. Leitinger, M. Lafer, and K. Witrisal, "MeasureMINT UWB database," www.spsc.tugraz.at/tools/UWBmeasurements, 2013, Publicly available database of UWB indoor channel measurements. [Online]. Available: www.spsc.tugraz.at/tools/UWBmeasurements

[103] J. Hu, Y. Wang, E. Zhou, M. Fu, and S. Marcus, "A Survey of Some Model-Based Methods for Global Optimization," in *Optimization, Control, and Applications of Stochastic Systems*, ser. Systems & Control: Foundations & Applications. Birkhäuser Boston, 2012, pp. 157–179.

[104] G. Tong, Z. Fang, and X. Xu, "A Particle Swarm Optimized Particle Filter for Nonlinear System State Estimation," in *Evolutionary Computation, 2006. CEC 2006. IEEE Congress on*, 2006, pp. 438–442.

[105] M. Arulampalam, S. Maskell, N. Gordon, and T. Clapp, "A Tutorial on Particle Filters for online Nonlinear/Non-Gaussian Bayesian Tracking," *Signal Processing, IEEE Transactions on*, vol. 50, no. 2, pp. 174–188, Feb 2002.

[106] T. Li, M. Bolic, and P. Djuric, "Resampling Methods for Particle Filtering: Classification, implementation, and strategies," *Signal Processing Magazine, IEEE*, May 2015.

[107] P. Meissner and K. Witrisal, "Multipath-Assisted Single-Anchor Indoor Localization in an Office Environment," in *Systems, Signals and Image Processing (IWSSIP), 2012 19th International Conference on*, April 2012, pp. 22–25.

[108] S. Julier and J. Uhlmann, "Unscented Filtering and Nonlinear Estimation," *Proceedings of the IEEE*, vol. 92, no. 3, pp. 401 – 422, mar 2004.

[109] R. Merwe and E. Wan, "Sigma-Point Kalman Filters For Integrated Navigation," 2004.

[110] R. Merwe, A. Doucet, N. de Freitas, and E. Wan, "The Unscented Particle Filter," 2000.

[111] D. Schuhmacher, B.-T. Vo, and B.-N. Vo, "A Consistent Metric for Performance Evaluation of Multi-Object Filters," *IEEE Transactions on Signal Processing*, 2008.

[112] J. Munkres, "Algorithms for the Assignment and Transportation Problems," *Journal of the Society for Industrial and Applied Mathematics*, vol. 5, no. 1, pp. pp. 32–38, 1957.

[113] S. Thrun, W. Burgard, and D. Fox, *Probabilistic Robotics*. MIT, 2006.

[114] Y. Bar-Shalom and T. Fortmann, *Tracking and Data Association*. Academic Press, 1988.

[115] Y. Bar-Shalom, F. Daum, and J. Huang, "The probabilistic data association filter," *Control Systems, IEEE*, vol. 29, no. 6, pp. 82–100, Dec 2009.

[116] F. Meyer, P. Braca, P. Willett, and F. Hlawatsch, "Scalable Multitarget Tracking using Multiple Sensors: A belief propagation approach," in *Information Fusion (Fusion), 2015 18th International Conference on*, July 2015, pp. 1778–1785.

[117] J. J. Leonard, R. J. Rikoski, P. M. Newman, and M. Bosse, "Mapping Partially Observable Features from Multiple Uncertain Vantage Points," *International Journal of Robotics Research*, vol. 21, pp. 943–975, 2002.

[118] D. Simon, *Optimal State Estimation: Kalman, H Infinity, and Nonlinear Approaches*. Wiley-Interscience, 2006.

[119] P. Tichavsky, C. Muravchik, and A. Nehorai, "Posterior Cramer-Rao Bounds for Discrete-Time Nonlinear Filtering," *Signal Processing, IEEE Transactions on*, vol. 46, no. 5, pp. 1386–1396, 1998.

[120] S. Bancroft, "An Algebraic Solution of the GPS Equations," *Aerospace and Electronic Systems, IEEE Transactions on*, vol. AES-21, no. 1, pp. 56–59, Jan 1985.

[121] T. Deissler and J. Thielecke, "Feature based Indoor Mapping using a Bat-Type UWB Radar," in *Ultra-Wideband, 2009. ICUWB 2009. IEEE International Conference on*, Sept 2009, pp. 475–479.

[122] T. Deissler, J. Thielecke, R. Salman, T. Schultze, and I. Willms, "UWB Radar Object Recognition for SLAM," in *Radar Symposium (IRS), 2010 11th International*, 2010.

[123] S. Särkkä, A. Vehtari, and J. Lampinen, "Rao-Blackwellized Particle Filter for Multiple Target Tracking," *Information Fusion*, 2007.

[124] S. Haykin, *Cognitive Dynamic Systems: Perception-action Cycle, Radar and Radio*. New York, NY, USA: Cambridge University Press, 2012.

[125] R. Bellman, *Dynamic Programming*. Princeton, NJ, USA: Princeton University Press, 1957.

[126] D. P. Bertsekas, *Dynamic Programming and Optimal Control*. Athena Scientific, 2000.

[127] R. S. Sutton and A. G. Barto, *Introduction to Reinforcement Learning*, 1st ed. Cambridge, MA, USA: MIT Press, 1998.

[128] J. G. Proakis and M. Salehi, *Digital Communications*, 5th ed. Prentice-Hall.